Osiris Canciglieri Junior
Miroslav D. Trajanovic *Editors*

Personalized Orthopedics

Contributions and Applications of Biomedical Engineering

PUCPR
GRUPO MARISTA

PUCPRESS

Springer

Personalized Orthopedics

Osiris Canciglieri Junior · Miroslav D. Trajanovic
Editors

Personalized Orthopedics

Contributions and Applications of Biomedical Engineering

PUCPR GRUPO MARISTA
PUCPRESS
Springer

Editors
Osiris Canciglieri Junior
Polytechnic School
Pontifical Catholic University of Paraná
Curitiba, PR, Brazil

Miroslav D. Trajanovic
Faculty of Mechanical Engineering
University of Nis
Nis, Serbia

ISBN 978-3-030-98278-2 ISBN 978-3-030-98279-9 (eBook)
https://doi.org/10.1007/978-3-030-98279-9

Jointly published with Associação Paranaense de Cultura

This Springer imprint is published by the registered company Springer Nature Switzerland AG
The registered company address is: Gewerbestrasse 11, 6330 Cham, Switzerland

Foreword

I had the opportunity to read the first draft of the book *Personalized Orthopedics: Contributions and Applications of Biomedical Engineering*, edited by Profs. Osiris Canciglieri Junior and Miroslav D. Trajanovic. The book was created as a result of many years of work of their teams on projects of application of biomedical engineering in orthopedics. Innovative solutions resulting from the work on these projects have led to the application of a personalized approach in the treatment of orthopedic patients. The collaboration of these teams is obvious, and it has given new value to their research.

Authors cover, present, analyze, compare and discuss, self-experiences state of the art in personalized medicine in orthopedics. The book first deals with a 3D geometric model of human bones, as a necessary basis for a personalized approach to the production of implants, fixators, scaffolds and other orthopedic aids. The book presents Method of anatomical feature—new method which enables geometrical reverse engineering of human bones both for the case when there is a computer tomography (CT) scan of the whole bone, and for the case when there is a CT scan of only a part of the bone. The following chapters illustrate the application of the method for reverse engineering of long bones, pelvis and mandible. The book further shows the application of a 3D geometric model of bone for the design of personalized implants and prostheses. Also, the book covers application of additive technologies in personalized orthopedics as well as prediction, simulation and optimization in personalized orthopedics.

I am convinced that the book will attract a lot of attention from two types of readers. The first group are orthopedists, surgeons, maxillofacial specialists who want to apply the principles of personalized medicine in their work. The second group includes engineers from companies engaged in the production of orthopedic devices, implants, scaffolds and fixators. Due to competition in the market, they are forced to offer personalized solutions to their customers.

Prof. Dr. Yuri Dekhtyar
Head of the Institute of Biomedical
Engineering and Nanotechnologies
Riga Technical University
Riga, Latvia

Preface

The recent development of many technologies, such as artificial intelligence, additive manufacturing, computed tomography would be better biomedical engineering, personalized medicine, which was once an unattainable dream, is becoming a reality. Based on the analysis of data on the Web of Science portal, the first papers on the topic of personalized medicine appeared at the beginning of the 21st century, but that their number began to grow exponentially in 2007. Personalized medicine is most often mentioned in papers in the field of pharmacology and oncology.

From 1999 to 2020, a total of 16.445 papers dealing with personalized medicine were published. The largest number of papers is in the field of pharmacology (2.364) and oncology (2.084). In the same period, only 15 papers mention the terms "personalized medicine" and "orthopedics" at the same time, while 126 papers mention the terms "personalized" (without medicine) and "orthopedics" at the same time. It is obvious that the number of published papers in the field of personalized orthopedics is very small compared to other fields of medicine. This does not mean that a personalized approach is not interesting for orthopedics. Because of the many benefits that personalized orthopedics offers for both orthopedists and patients, orthopedists are more than interested in this approach.

The book *Personalized Medicine in Orthopedic* covers the most important topics in the field of personalized orthopedics from the engineering point of view. This is because, above all, developments in the field of biomedical engineering have made personalized orthopedics much more applicable in clinical practice. It starts with 3D geometry of the bones, focusing on the problem of reverse engineering of the bones, both for the case when there is a volumetric medical image of the whole bone, and for the case when there is a volumetric medical image of only the remaining part of the bone. The book further shows the application of a 3D geometric model of bone for the design of personalized implants and prostheses. Also, the book covers application of additive technologies in personalized orthopedics as well as prediction, simulation and optimization in personalized orthopedics.

The book is aimed first towards biomedical engineers, master students in biomedical engineering, and any other technically oriented people who are dealing with design, optimization and production of personalized orthopedics product. They will gain a broad understanding of methods and techniques necessary for their mission. Also, the book is intended for orthopedists who want to understand the engineering methods by which they can provide personalized orthopedics services to their patients.

The optimal treatment process is always based on the principles of personalized medicine. That is why the future of medicine is in a personalized approach. This also applies to orthopedics. This book provides the necessary knowledge for the transition from classical to personalized orthopedics. So, the book, addresses issues of personalized orthopedics, which has not received enough attention in the existing literature the following themes:

- **Part I—Personalized Orthopedics** (Chapter 1—State of the Art);
- **Part II—Reverse Engineering of Human Bones** (Chapter 2—Creation of geometrical models of human bones by using method of anatomical features; Chapter 3—Geometrical model of human mandible: Potential for Application in personalized maxillofacial surgery; Chapter 4—Reverse modeling of human long bones by the application of method of anatomical features; and Chapter 5—Building 3D surface model of the human hip bone from 2D radiographic images using parameter-based approach);
- **Part III—Personalized Implants** (Chapter 6—Design and manufacturing of the personalized plate implants; Chapter 7—Method of Support to Decision-Making in the Dental Implant Process; Chapter 8—Application of artificial materials in thoracic surgery; and Chapter 9—Implant personalization needs in dynamic internal fixation of bone fractures);
- **Part IV—Personalized Prothesis** (Chapter 10—The influence of human factors in the functional analysis of the support device for users with upper limb agenesis; Chapter 11—Modelling of the personalized skull prosthesis based on Artificial intelligence; Chapter 12—Application Study of Electroencephalographic Signals in the Upper Limb Prosthesis Field; Chapter 13—Maxillofacial prostheses: Assistive Technology in Mutilated Facial Patients);
- **Part V—Additive Manufacturing and Personalized Materials** (Chapter 14—3D Printing in Orthopedic Surgery; and Chapter 15—Natural hydrogels and 3D-Bioprinting);
- **Part VI—Prediction, Optimization and Monitoring** (Chapter 16—Computational Modelling and Machine Learning based Image Processing in Spine Research; Chapter 17—Structural analysis and optimization of fixation devices used in treatment of proximal femoral fractures; and Chapter 18—Overview of AI-based approaches to remote monitoring and assistance in orthopedic rehabilitation).

The book represents a significant contribution to the orthopedic community on its path to fully personalized orthopedics integrated to Product Development context. The authors of the book first presented the original method for reverse bone engineering—the Method of Anatomical Features (MAF). This method is unique in that it enables the reconstruction of the original geometry and topology of the bone, even when only data on its part are available. The application of this method is shown on the examples of human long bones, mandible and hip bone reconstruction.

A particularly interesting part of the book is the application of 3D bone models for the design of personalized implants and prostheses. The book contains a review of several real cases of personalized implants. Another important application of the 3D geometric bone model is for making personalized prostheses. The book gives several examples of prostheses for the design of which a 3D model of bones was used, as well as other patient data based on which personalized prostheses were designed.

The book raises important questions whose answers will help orthopedists implement personalized orthopedics in clinical practice. Why do we need personalized orthopedics and what are the benefits of it? Furthermore, the book deals with the reverse engineering of human bones. *Why we need 3D geometrical models of human bones in personalized orthopedics and what type they can be?* Is it possible, and with what precision, to obtain a 3D geometric model of bones when anatomical entities are recognizable? Is it possible to get a 3D model even when the bone is partially destroyed due to cancer, great trauma or osteoporosis? What are methods for reverse engineering available?

Another very important issue that book addresses is the application of 3D geometrical model to design and manufacture personal implants and prothesis. What are the benefits of personalized implants and dentures? What is the process of designing a personalized implant and prosthesis based on a 3D geometric model? What materials and technologies are available to produce implants and prostheses?

The behavior of prothesis, and especially implants, is a very important issue. Even in the design phase, it is necessary to predict what the behavior will be. Are the implants or stretches strong enough to withstand the load? Are they optimal in terms of weight, productivity or price? The answers to these and other questions are given in the last part of the book.

Finally, we would like to thank immensely the contributing authors, reviewers and editorial team for their fundamental contributions in the realization of book. We hope that the contributions presented in this book will provide timely support for the continued implementation of more integrated design initiatives between Medicine, Dentistry, Health Technology, Product Engineering, Industrial Engineering and other areas in order to promote better development practices.

Curitiba, Brazil Osiris Canciglieri Junior, Ph.D.
Nis, Serbia Miroslav D. Trajanovic, Ph.D.
November 2021

Contents

Editors and Contributors

About the Editors

Prof. Osiris Canciglieri Junior (Ph.D.) is a full Professor of Industrial Engineering and Control and Automation Engineering (Mechatronic) at Pontifical Catholic University of Paraná in the Brazil (PUCPR). He is also Managing Director of Industrial and Systems Engineering Graduate Program (PPGEPS). He has more than 30 years of experience in new product development and manufacturing engineering, working both in Brazilian industry and in academia. Prof. Canciglieri Junior's research has been funded directly by PUCPR, industry and Brazilian funding agencies *(CNPq, CAPES* and *Fundação Araucária).* He has strong experience in product design, information modelling to support product design and manufacturing. His work has led over than 160 research publications and some 20 PhD completions. The research of professor Osiris is focused on support the design of prosthesis including dental field, Design for Manufacturing and Assembly (DFM/DFA), Design for Sustainability, Concurrent Engineering, Assistive Technology, Development of Sustainable Products focused on the production, generation and use of renewable energy and sustainable development. Professor Osiris Canciglieri Junior is an editorial member and reviewer of scientific journals in his research field area.

Prof. Miroslav D. Trajanovic (Ph.D.) is a full Professor of the University of Nis, Faculty of mechanical engineering, Serbia. He has more than 35 years of experience in application of IT in mechanical engineering and medicine. Those experiences include problems modelling, writing programs for solving different engineering problems and educating students in ICT and biomedical engineering. He is expert for computer programming, CAD, finite element method, additive technology, reverse engineering, and biomedical engineering.

Professor Trajanovic is the author of more than 300 scientific and professional papers and five books. He has also taken part in realization of 15 scientific projects supported by Serbian government and industry and was project leader or workpackage leader of 10 projects mainly in IT, mechanical and biomedical engineering, as well as two FP6, six FP7 and three HORIZON 2020 European projects. Inter alia, he was leader of the projects the Application of Information Technologies in Orthopedic Surgery, 2008-2010, and Virtual human osteoarticular system and its application in preclinical and clinical practice, 2011-2019, sponsored by Ministry for Education, science, and technological development of the Republic of Serbia.

Contributors

Jovan Arandjelovic Faculty of Mechanical Engineering, University of Nis, Nis, Serbia

Stojanka Arsić Faculty of Medicine, University of Niš, Niš, Serbia

Osiris Canciglieri Junior Industrial and Systems Engineering Graduate Program (PPGEPS), Pontifical Catholic University of Paraná (PUCPR), Curitiba, Paraná, Brazil;
Product Development Research Center oriented to assistive technology of PPGEPS/PUCPR, Curitiba, Brazil

Paola F. Corso Reconstructive Facial Prosthesis Service of Trabalhador Hospital, Curitiba, PR, Brazil

Luiz Gustavo Schitz da Rocha Control and Automation Engineering, Pontifical Catholic University of Paraná (PUCPR), Curitiba, Brazil

Geane Aparecida Poteriko da Silva Product Development Research Center oriented to assistive technology of PPGEPS/PUCPR, Curitiba, Brazil;
Paraná State Department of Education, Curitiba, Brazil

Clayton Fernandes de Souza School of Education and Humanities, Chemistry Undergraduate Course, Pontifícia Universidade Católica do Paraná, Curitiba, Paraná, Curitiba, Brazil

Leandro dos Santos Coelho Industrial and Systems Engineering Graduate Program, Pontifical Catholic University of Parana, Curitiba, Parana, Brazil;
Department of Electrical Engineering (PPGEE), Federal University of Parana (UFPR), Curitiba, Brazil

Beatriz Luci Fernandes Health Technology Graduate Program, Pontifícia Universidade Católica do Paraná, Curitiba, Paraná, Brazil;
Polytechnic School, Chemical Engineering Undergraduate Course, Pontifícia Universiade Católica do Paraná, Curitiba, Brazil

Nenad Filipović Bioengineering Research and Development Center (BioIRC), Kragujevac, Serbia;
Steinbeis Advanced Risk Technologies Institute Doo Kragujevac (SARTIK), Kragujevac, Serbia

Yohan Boneski Gumiel Health Technology Graduate Program (PPGTS), Pontifical Catholic University of Paraná (PUCPR), Curitiba, Brazil

Alexandre Ferreira Kleppa Control and Automation Engineering Department, Pontifical Catholic University of Parana (PUCPR), Curitiba, Parana, Brazil

Nikola Korunovic Faculty of Mechanical Engineering, University of Nis, Nis, Serbia

Vojin Kovačević Faculty of Engineering, University of Kragujevac, Kragujevac, Serbia;
Bioengineering Research and Development Center (BioIRC), Kragujevac, Serbia;
Steinbeis Advanced Risk Technologies Institute Doo Kragujevac (SARTIK), Kragujevac, Serbia

Maria Elizete Kunkel Institute of Science and Technology of Federal, University of São Paulo, São José Dos Campos, SP, Brazil

Ana Lukovic Department of Surgery, Faculty of Medical Sciences, University of Kragujevac, Kragujevac, Serbia

Miodrag Manic Faculty of Mechanical Engineering, University of Nis, Nis, Serbia

Celso Júnio Aguiar Mendonça Postgraduate Program in Electrical Engineering and Industrial Informatics—CPGEI, Federal Technological University of Paraná—UTFPR, Curitiba, Brazil;
Musculoskeletal System Unit—USME, Hospital of the Federal University of Parana—CHC UFPR, Curitiba, Brazil

Slobodan Milisavljevic Department of Surgery, Faculty of Medical Sciences, University of Kragujevac, Kragujevac, Serbia

Dragan Misic Facuty of Mechanical Engineering, Nis, Serbia

Jelena Mitic Faculty of Sciences and Mathematics, University of Nis, Nis, Serbia

Milan M. Mitkovic Faculty of Medicine, University of Nis, Nis, Serbia;
Clinic for Orthopedics and Traumatology, University Clinical Center Nis, Nis, Serbia

Maria Lucia Miyake Okumura Industrial and Systems Engineering Graduate Program, Pontifical Catholic University of Paraná (PPGEPS/PUCPR), Curitiba, Paraná, Brazil;
Product Development Research Center oriented to assistive technology of PPGEPS/PUCPR, Curitiba, Brazil

Vesna Ranković Faculty of Engineering, University of Kragujevac, Kragujevac, Serbia;
Bioengineering Research and Development Center (BioIRC), Kragujevac, Serbia;
Steinbeis Advanced Risk Technologies Institute Doo Kragujevac (SARTIK), Kragujevac, Serbia

Lukas Rasulić Faculty of Engineering, University of Kragujevac, Kragujevac, Serbia;
Bioengineering Research and Development Center (BioIRC), Kragujevac, Serbia;
Steinbeis Advanced Risk Technologies Institute Doo Kragujevac (SARTIK), Kragujevac, Serbia

Marcelo Rudek Production and System Engineering Graduate Program—PPGEPS, Pontifical Catholic University of Parana - PUCPR, Curitiba, Brazil

João Antônio Palma Setti Postgraduate Program in Biomedical Engineering—PPGEB, Federal Technological University of Paraná—UTFPR, Curitiba, Brazil

Roberta T. Stramandinoli-Zanicotti Reconstructive Facial Prosthesis Service of Trabalhador Hospital, Curitiba, PR, Brazil

Tijana Šušteršič Faculty of Engineering, University of Kragujevac, Kragujevac, Serbia;
Bioengineering Research and Development Center (BioIRC), Kragujevac, Serbia;
Steinbeis Advanced Risk Technologies Institute Doo Kragujevac (SARTIK), Kragujevac, Serbia

Anderson Luis Szejka Industrial and Systems Engineering Graduate Program, Pontifical Catholic University of Paraná, Curitiba, Paraná, Brazil

Sabrina Tinfer Industrial and Systems Engineering Graduate Program, Pontifical Catholic University of Paraná, Curitiba, Paraná, Brazil

Miroslav D. Trajanovic Mechanical Engineering Faculty, University of Niš, Niš, Serbia;
Faculty of Science and Mathematics, University of Nis, Nis, Serbia

Milica Tufegdzic Department of Information Technology, Academy of Professional Studies Sumadija, Trstenik, Serbia

Nikola Vitković Faculty of Mechanical Engineering, University of Nis, Nis, Serbia

Milan Zdravkovic Facuty of Mechanical Engineering, Nis, Serbia

Part I
Personalized Orthopedics

Chapter 1
Personalized Medicine in Orthopedic—State of the Art

Miroslav D. Trajanovic and Osiris Canciglieri Junior

1.1 Introduction

Personalized medicine does not have a generally accepted definition, which, among other things, can be seen from the fact that the same concept is encountered in the literature under different names. Thus, the terms personalized medicine, precise medicine, stratified medicine and P4 (Predictive, Preventive, Personalized and Participatory) medicine, although differ in nuances, are used for the same meaning. In health communication, there are, although less often, other names such as Genomic medicine, Genotype-based therapy, Individualized medicine, Information-based medicine, or Omics-based medicine, to name just a few.

There are many attempts to make definition of personalized medicine. For Kewal K. Jain personalized medicine simply means the prescription of specific treatments and therapeutics best suited for an individual taking into consideration both genetic and environmental factors that influence response to therapy (Jain 2015).

U.S. Food and Drug Administration in so called Blue book—Paving the Way for Personalized Medicine: FDA's Role in a New Era of Medical Product Development (FDA 2013) states that personalized medicine "may be thought of as the tailoring of medical treatment to the individual characteristics, needs and preferences of a patient during all stages of care, including prevention, diagnosis, treatment and follow-up".

European Union definition of personalized medicine is based on the Horizon 2020 Advisory Group. This definition says that personalized medicine is: "a medical model using characterization of individuals' phenotypes and genotypes (e.g., molecular

M. D. Trajanovic (✉)
Mechanical Engineering Faculty, University of Nis, Nis, Serbia
e-mail: miroslav.trajanovic@gmail.com

O. Canciglieri Junior
Industrial and Systems Engineering Graduate Program (PPGEPS), Pontifical Catholic University of Paraná (PUCPR), Curitiba, Paraná, Brazil
e-mail: osiris.canciglieri@pucpr.br

O. Canciglieri Junior and M. D. Trajanovic (eds.), *Personalized Orthopedics*,
https://doi.org/10.1007/978-3-030-98279-9_1

profiling, medical imaging, lifestyle data) for tailoring the right therapeutic strategy for the right person at the right time, and/or to determine the predisposition to disease and/or to deliver timely and targeted prevention" (EU 2015).

The term 'P4' encompasses personalized approach within a broader frame which also recognizes the increasingly predictive, preventive and participatory nature of modern medicine (AMS 2015).

It can be said that stratified medicine is the precursor of personalized medicine. According to this approach, all patients suffering from the same disease are divided into distinct groups according to some characteristics. The optimal approach to the diagnosis, prevention or treatment of this disease is determined for each group. Personalized medicine goes a step further. Instead of a group, it treats each person separately. In that way, personalized medicine gives much more precise treatment and hence much better outcomes.

As in other branches of medicine, the personalized approach to the treatment of the patient in orthopedics should be determined by his genetical constitution, phenotype and state. Although there is some research in the field of application of genetic techniques in orthopedic practice, the results of this research have so far not significantly contributed to a personalized approach in orthopedics (Aicale et al. 2019). The vast majority of personalized treatments in today's orthopedic practice are based on patient's phenotype and state.

Personalized orthopedics takes into account the individual characteristics of a specific patient, such as his previous and current psycho-physical condition, anatomical features, and the environment in which the patient lives and in which he will be treated in order to define an individual approach in prevention, diagnosis and treatment.

1.2 Enabling Technologies

Doctors have always tried to provide prevention, diagnosis and treatment that best suits a specific patient. However, a large number of restrictions prevented them from achieving that intention. Unlike the situation in the twenty-first century, there were not enough good diagnostic devices, tools and methods, not enough strong computer support for their work, and also not enough suitable materials and production technologies that could meet the requirements of a personalized approach in medicine.

At the end of the 20th and the beginning of the twenty-first century, the existing technologies were perfected and new technologies were developed, which all together enabled personalized medicine in orthopedics. Most of the new devices, techniques and methods that have enabled personalized orthopedics are based on digital technologies, so that the term "digital orthopedics" is increasingly encountered in the scientific journals and books (Pei 2018; Xianlong and Kunzheng 2021; Bini et al. 2020). Important technologies that have enabled the application of a personalized approach in orthopedics include 3D imaging, computer aided design (CAD), reverse

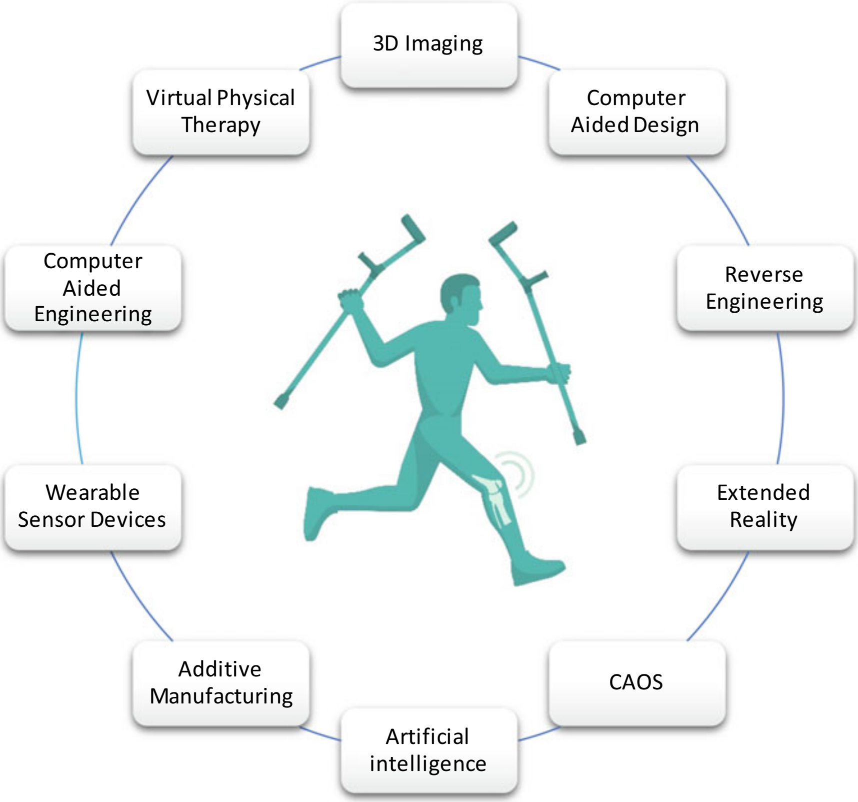

Fig. 1.1 Enabling technologies in personalized orthopedics

engineering, extended reality, computer-assisted orthopedic surgery (CAOS), artificial intelligence, additive manufacturing, wearable sensor devices, computer aided engineering (CAE), virtual physical therapy and virtual physical therapy (Fig. 1.1).

1.3 3D Imaging

Medical imaging is a method that provides images of organs using various devices, such as X-ray, Computed Tomography (CT) scanner, Magnetic Resonance Imaging (MRI) scanner or ultrasound scanners. Medical images are of great help to doctors in all phases of patient treatment because they provide a view of the patient's internal organs.

During most of the twentieth century, 2D medical images obtained by radiography (X-ray) were of invaluable assistance to orthopedists in the process of diagnosis and treatment of patients. With the advent of the first CT scanner in 1971, 3D images were also available to orthopedists. Very quickly, in the early eighties, the first MRI devices appeared, which also produced a 3D image of the patient's organs. Although 2D X-ray images are still used today, CT with spatial resolution of 0.5 mm and MRI with spatial resolution of 1–2 mm are becoming irreplaceable. Both CT and MRI devices produce so-called volumetric medical images by stacking multiple cross-sectional images of the patient's body.

The volumetric image consists of a series of 2D images of the human body, so-called slices, which are sampled with a constant step, usually 0.5–2 mm. The image of each slice, which is actually 2D, consists of a series of pixels. A volume bounded by pixels at the same x–y coordinate in two adjacent slices is called a voxel. Each voxel is associated with a value of gray expressed in Hounsfield units (HU). The value of gray ranges from -1024 HU for the air, trough 0 HU for the water, to more than 3000 HU for the most of metals. The fact that individual organs and their parts have different HU values is used to segment organs in the human body. For example, as Fat et al. (2011) reported, cortical bone geometry in the proximal humerus can be segmented in HU range of 500–900 HU.

Segmentation is widely used in orthopedics for bones (Zhang et al. 2010) and muscles segmentation (Kamiya 2018), as well as for segmentation of bone fragments after major trauma (Moldovan et al. 2021).

Despite many efforts, there is still no general method that completely automatically performs bone segmentation in volumetric medical images, ensuring high accuracy. However, such solutions exist for specific bones. Yu et al. (2018) presented methods for the automatic segmentation of five lumbar vertebrae from a CT image which offers excellent results. By testing their method on 21 samples of volumetric medical images, the authors achieved an average Dice coefficient of $93.9 \pm 1.0\%$ and an average symmetric surface distance of 0.41 ± 0.08 mm.

Successful segmentation can also be performed using MRI medical images. Zeng and Zheng (2018) presented artificial intelligence-based method for automatic segmentation of proximal femur from the MRI volumetric medical image. More specifically, authors applied deeply supervised 3D Unet-like fully convolutional network for segmentation and proved its efficiency on the example of 20 femur samples. Similar research was reported by Deniz et al. (2018). The authors presented a method for automatic proximal femur segmentation based on deep convolutional neural networks (CNN). The results show better results for 3D CNN than 2D CNN and high accuracy, which is illustrated with the Dice score of 0.95 ± 0.02.

In some cases of orthopedic practice, the only correct approach in treating a patient is to apply a personalized approach. This is especially true in cases of great trauma when the bone turns into a large number of smaller and larger fragments. Because each major trauma is unique in place, number of fragments, and shape, a personalized approach is the only possible solution. Successful treatment in such cases requires the orthopedist to place the broken fragments, sometimes very small, with each other so that they all together take on the shape of the bone before the trauma. Reconstruction of the position of fragments during orthopedic surgery is a long-term process that takes place on a trial-and-error basis. Therefore, before the beginning of the surgical reconstruction, it is necessary to perform meticulous planning and simulation of the fragments positioning based on data from CT image.

One of the first solutions for the semi-automatic system alignment of fragments of human broken bone was created as an upgrade of the system for the reconstruction of archaeological bones (Willis et al. 2007). Process begins with segmentation of CT data with the aim to mark the boundaries of individual fragments. Then, a surface network of fragments is created, assigning a Hounsfield intensity value to each network node. Using Hounsfield intensity value each surface is segmented into intact surface and fracture surface, which enable interactive alignments of the fragments.

Team of researchers from the "George Emil Palade" University of Medicine, Pharmacy, Science, and Technology of Targu Mures developed a method of aligning broken parts of the bones (Moldovan et al. 2021). The application of this method is performed according to the proposed clinical process which consists of three steps: (a) making a 3D image using CT scanners, (b) segmentation of broken parts of bones and intact bone, and (c) alignment of all parts of bone. The core of this method is the modified method of the Iterative Closest Point (ICP) algorithm for alignment developed by the authors.

Research in the field of medical image processing has resulted in commercial software solutions that have different purposes. Taken as a whole, such software solutions are used for image digitization and formatting, image quality improvement, visualization, image content analysis and data management generated during the medical image processing process. Some of the available software is for general use, while some are specialized for work in the field of orthopedics. So, for example, the company Simpleware offers solution for 3D image processing for orthopedics (Simpleware 2021). The software provides functions of 3D medical image processing and generation of bone models for further use in design of personalized osteofixation material by integration of image data and CAD (Computer Aided Design) 3D geometrical model of implants. It also generates mesh for finite element analysis and models for 3D printing.

Software mediCAD offers, beside segmentation and image analysis, specialized modules for surgical planning through specialized modules 3D Spine, 3D Hip, 3D Knee, and 3D Shoulder (mediCAD 2021).

1.4 Computer Aided Design

CAD programs are widely used today for creation of 3D geometrical models of implants, scaffolds, fixators, prostheses and other osteofixation materials tailored for specific person. When a patient 3D bone geometrical model is created by one of the reverse engineering methods, it is relatively easy to design personalized osteofixation material using the functions of the CAD program.

The use of CAD in orthopedics began in the 1980s (Klasson 1985; Staats 1985; Fernie 1984). Since then, computers have become much more powerful, and CAD programs have been enriched with a large number of new functions. This has led to the huge application of CAD technologies in the design of osteofixation material.

CAD programs are very often used to construct customized auxiliary tools in orthopedics such as jigs that are used as cutting guides. Khan et al. (2013) used (CAD) software (Pro/Engineer Wildfire 5.0 to design custom jig in order to investigate if such a jig will improve accuracy of wide resection of bone tumors for the case of joint-sparing hemimetaphyseal resection. Similar research is presented in Helguero et al. (2015). They concluded that application of personalized jigs gives better accuracy in the case of skeletal tumor resection than freehand techniques.

Mandolini et al. (2020) presented a procedure for designing custom-made implants for forehead augmentation in people suffering from Apert syndrome. They first used CAD tool Rhinoceros to design the anterior surface of the prosthesis and base on it they designed the custom-made mold for directly shaping the implant during surgery.

Trajanovic et al. (2010) presented application of 3D solid model of Mitkovic self-dynamisable internal fixator made by CAD program Pro/Engineer for pre-operative planning of surgical intervention. The geometric model was used to simulate the placement of the fixator on the bone and to analyze the behavior of the fixator and bone assembly under the real load (Fig. 1.2).

Due to the complex topology of the bones, designers typically use the costly CAD programs such as Catia, PTC Creo, Siemens NX or Rhinoceros 3D. However, the tremendous development of CAD programs has made it possible for even some

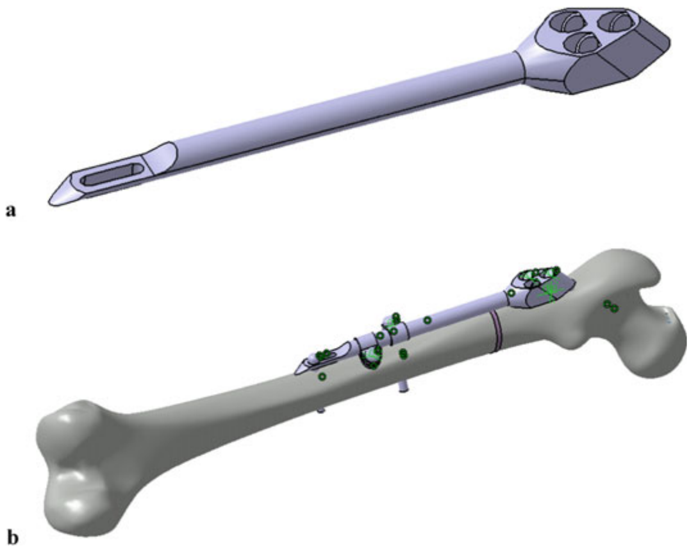

Fig. 1.2 Application of 3D geometrical model of Mitkovic selfdynamisable internal fixator. **a** Basic part of selfdynamizing implant with trochanteric unit—trochanteric bar. **b** Femur-fixator assembly (Trajanovic et al. 2010)

freeware programs to be able to design very complex elements of osteofixation material. Hertzberg-Boelch et al. (2021) presented a design of sophisticated custom made monoflanged acetabular component made by powerful freeware Wincad 2D/3D CAD program.

The development of programs and methods for Computer Aided Design has enabled also the emergence of the first pre-operative planning systems in orthopedics. Murphy et al. (1985) have shown that 3D models obtained by CT images can be converted in 3D geometrical models and use for the pre-operative planning of orthopedic reconstructive procedures.

1.5 Reverse Engineering

The three-dimensional (3D) geometric model of bones is of great importance in personalized orthopedics. These models are used for training, preoperative planning, simulations, analysis of bone behavior with and without osteofixation material by finite element method, design of personalized osteofixation material, computer assisted orthopedic surgery, orthopedic extended reality systems, production of physical bone models and personalized osteofixation material, etc.

Due to the complex topology of human bones, it is not possible to design them directly, but various reverse engineering techniques are used, which are based on data extracted from medical images. In order to get the best results of the application of the 3D geometric model of bones in personalized medicine, the accuracy of the model is of great importance. Research by Schmutz et al. (2021) has shown that commercial fracture fixation plates anatomically fit only in 13% of cases. The plates designed using statistical bone geometrical model fit in 20% of cases but using exact 3D personalized bone models anatomically fit rises to 67%. This clearly shows importance of exact 3D models of human bones.

Most of medical images made by X-ray, CT, MRI, ultrasound and similar devices are stored in DICOM (Digital Imaging and Communications in Medicine) format. It is an international widely accepted standard for storing and transmitting information recorded in medical imaging (DICOM 2021). There are many viewers for medical image in DICOM format. These viewers can usually only display a 3D image consisting of voxels, although some allow orthopedists to measure some dimensions or calculate volume. This can be useful in personalized medicine, but for complex tasks that use advanced technologies, much richer geometric models, such as 3D polygonal or solid models, are needed.

Computer Aided Design (CAD) programs have possibility to transform medical image in DICOM format in 3D polygonal model. Typically, such models are written in STL (STereoLithography) format. A very common problem of polygonal models generated from medical images are gaps between polygons, overlapping or intersections of polygons, or sometimes wrong orientations of polygons normal, which makes them unsuitable for further application. To solve such problems Patel et al.

(2006) proposed method for an automatic CAD model topology generation using iterative vertex pair contraction and expansion technique.

Although it is possible to obtain a 3D geometrical solid model of bone based on X-ray images (Filippi et al. 2009), volumetric images are more often used in modern practice for reverse bone engineering. There are many methods for converting a polygonal geometric model to a solid model when a complete volumetric medical image is available (Trajanovic et al. 2012; Veselinovic et al. 2013; Mitic et al. 2020). One of the simple methods for conversion of complete volumetric medical image, obtained by CT, to the 3D surface geometrical model was presented in Veselinovic et al. (2011). In order to create valid 3D model of human tibia, the authors, based on anatomical and morphological properties, divided tibia into proximal end, shaft and distal end. Each of these geometric entities has a specific topology, so an adequate modeling method was applied for each part. Eventually all three entities were joined and thus a 3D surface geometric model of the complete tibia was obtained (Fig. 1.3).

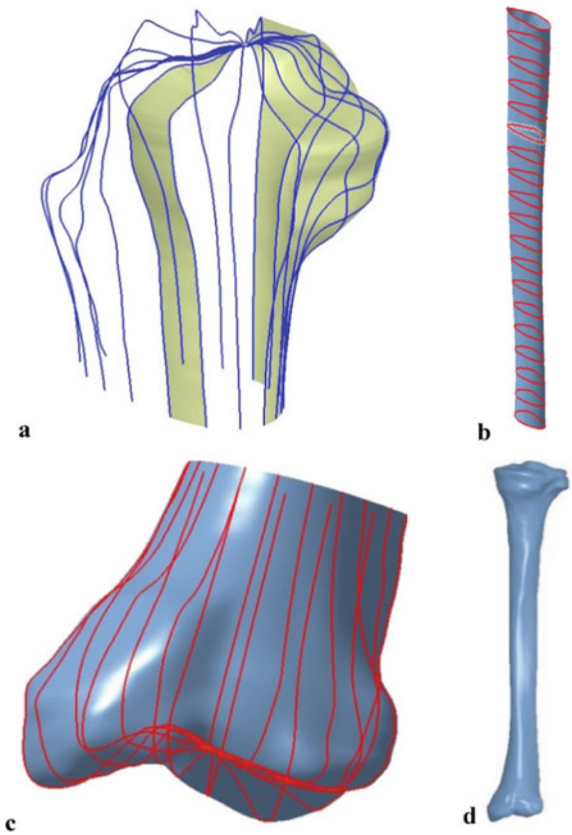

Fig. 1.3 Creation of 3D surface geometrical model of tibia. **a** Proximal end, **b** shaft, **c** distal end, **d** complete model of tibia (posterior view). Veselinovic et al. (2011)

Recently, Leordean et al. (2021) presented three methods for conversion of polygonal model to the solid model for the left zygomatic bone and proximal femur using CAD programs CATIA and Creo Parametric.

However, building accurate 3D solid models when a complete volumetric medical image is not available is much more complex task and is the goal of numerous studies. The lack of data can be caused by a bone medical condition (bone cancer, osteoporosis or big trauma) or if only X-ray image is available.

Majstorovic et al. (2013), presented Method of Anatomical Features (MAF) for creation of geometrical models in the case when only partial volumetric medical image of a patient's bone is available. The main structure of the method is described, as well as the algorithm that was applied for model creation. Referential Geometrical Entities are defined as the basis of the MAF method. A detailed description of the applied methods (modeling and statistical processing) is given, as well as the analysis of the achieved results for the cases of the human tibia and femur. Based on the analysis, it was concluded that the MAF method is applicable for the development of accurate geometric models of the human femur and tibia.

In paper Vitkovic et al. (2013) a software system created to build a personalized geometrical model of human bones is presented. This system enables the creation of geometric models of bones when there is a lack of input bone data. The testing of the system was performed by creating geometric models of a number of human femurs and checking their deviation from the original bone geometry. The analysis showed that a high level of geometrical and morphological accuracy of the bone geometrical models can be achieved by using this system. The improved Method of anatomical features is presented in Vitkovic et al. (2019). The authors introduced a new aspect of geometry and anatomy analysis of human bones based on the Regions of Interest (ROI). The improved Method of Anatomical Features (MAF) has been created, which enables the creation of ROI and their use for creating accurate personalized 3D geometric models of human bones and plate implants.

In addition to long bones, MAF can be successfully applied to irregular bones such as the ilium or mandible, whose shape is considerably more complex than long bones. In the paper Tufegdzic et al. (2013) authors proposed method for reverse engineering of hip bone based on the MAF method with some improvement by introducing parametric regions (Fig. 1.4). For the case of the ilium bone, complete subject specific morphometry of the wing of the human ilium bone was defined by measuring only the 10 parameter's values, described as linear distances between selected anatomical landmarks, from the anterior–posterior radiographic projection of the hip bone. The values for additional 12 parameters are easy to calculate, using obtained nonlinear one-parameter regression models (three square, six exponential, and three logarithmic) (Tufegdzic et al. 2015).

Patient-specific bone reconstruction of the ilium bone, in the cases of incomplete volumetric data, was done using the method of parametric regions for determining a point model from two biplanar X-ray projections. The method enables creating a complete polygonal model, chosen regions or some parts of the regions, so called subregions. Results expressed in the form of regression equations are applicable to the left ilium bone (Trajanovic et al. 2018).

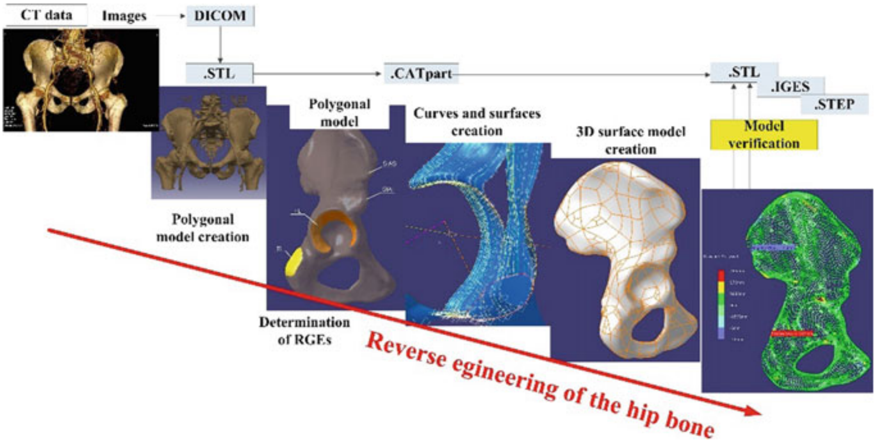

Fig. 1.4 Process of reverse engineering of the hip bone

The process of obtaining coordinate values for anatomical landmarks and parameters' values at human ilium bone was further simplified. It was done using landmark-driven approach with the aid of statistical tools. From the set of 15 anatomical points, four anatomical points, whose positions are easy to localize and determine, were separated. The coordinate values for 11 landmarks were calculated in simple Graphical User Interface (GUI), using established regression dependencies. GUI also allows for calculating the parameters' values (Tufegdžić and Trajanović 2021).

The Method of anatomical features enables for the reverse engineering of the complete mandible or its anatomical parts, with sufficient accuracy from the point of view of orthodontics. In the paper Vitkovic et al. (2015), the MAF is implemented for the creation of the parametric model of the human mandible coronoid process. The parametric model is defined as a point cloud model, where each point coordinate in the point cloud is defined by an individual parametric function realized by applying multiple linear regression. To personalize a model to the specific patient, values of morphometric parameters are measured from patient's medical images (CT, X-ray) and applied in parametric functions. The geometric accuracy of resulting model is tested by analyzes of the surface deviations and results are quite satisfactory. The same method is applied for the whole mandibula (Mitic et al. 2020). The Referential Geometrical Entities (RGEs) have been defined in accordance with anatomical properties of the mandible. The scientific significance is reflected in the identification of a minimal set of RGEs important for the creation of all other geometrical features of higher order (e.g., curves, surfaces) on the human mandible. In order to test the geometrical accuracy, a comparative analyzes is performed on the resulting model (Fig. 1.5) created by two approaches: MAF and classical techniques of reverse engineering. Considering the results, it can be concluded that the correct identification of RGEs directly affects the speed and accuracy of reverse engineering of human mandible.

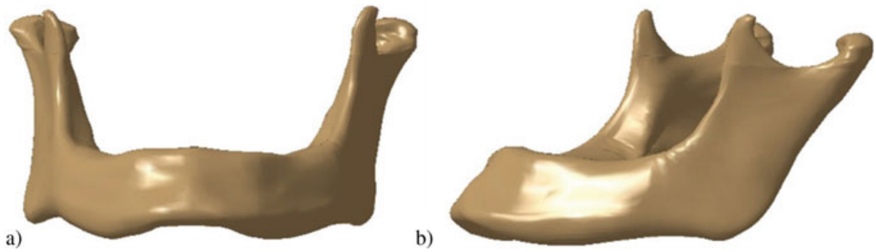

Fig. 1.5 3D surface model of the human mandible: **a** lateral aspect, **b** anterior aspect

Yunnan et al. (2017) presented method for generating 3D human femur geometrical models for the cases when volumetric medical image exists only for a part of the bone. The method is combination of parametric method and deformation method. Their approach consists of two processes. In the preparatory process they process volumetric medical image of femur samples by determining feature points, segmentation of the mesh, parameters calculation and averaging models. In modelling process, based on partial parameters, authors compare patient's bone (or its part) with the bones in samples library with the aim to select best suited geometric model of the femur. After global interpolation and regional deformation 3D geometrical model of patient's bone is obtained.

Rudek et al. (2013) proposed a method to create the geometric model for correction of skull defects by applying anatomical pros-thesis modeling by means of three-dimensional images obtained by tomography. This method automatically generates the pre-processing parameters for the machining of the prosthesis. The method decides which ellipse represents the best fit for each bone border in a given CT scan slice. It generates the super ellipse by adjusting the parameters to estimate the data representing its curvature. PSO (Particle Swarm Optimization) was used to define the parameters that can be achieved through the optimization methods. It can be used to decide which is the best solution (best ellipse) that represents the bone curvature for each CT slice.

Rudek et al. (2015) performed an autonomous content retrieval search on a large database of medical images in order to find healthy shape-similar bones to replace missing regions. Their method is based on a CT-by-CT approach concerning the amount of data to be compared by defining a small set of parameters applying Cubic Bezier Curves. The fit is evaluated by the ABC optimization algorithm as a user-form tool to evaluate the best of the descriptor parameters.

1.6 Extended Reality

Extended reality technologies (XR) enable humans to integrate the physical and virtual worlds in a single perception through the use of computers technologies and wearables. At the moment XR encompasses three technologies: augmented reality (AR), mixed reality (MR) and virtual reality (VR), but some new ones may appear soon. XR may help orthopedic surgeons in the processes of training, pre-operative planning, simulation of the surgical intervention, navigation during surgical intervention, and interaction with remote orthopedists (Fig. 1.6).

Virtual reality provides totally virtual computer-generated environment to the users. While using VR users cannot see anything from the real word. Instead, in the case of orthopedics, users are fully immersed in a simulated world by presentation of more or less faithful 3D geometric model of the human body that shows, among other things, bones, muscles, cartilage, and ligaments. This environment is ideal for training unexperienced residents and staff surgeons outside the operating room (Verhey et al. 2020). 3D geometric models used in orthopedic VR systems are mostly standard so they can only be used for training. However, VR is increasingly encountered with systems that use patient-specific models of the musculoskeletal system. Such systems are a strong support to personalized orthopedics because they provide pre-operative planning, and even intra-operative navigational guidance (Vaughan et al. 2016).

AR has a much greater application in personalized orthopedics because it enriches the image of the real world with digital information usually, but not only, in visual form. Comparing with VR, AR is much more useful during surgical intervention, especially for reduction, drilling, screwing, needle insertion and wiring (Negrillo-Cardenas et al. 2020). In an extensive study of the application of augmented reality in orthopedic surgery, Jud et al. (2020) have identified a large number of applications of this technology in personalized orthopedics, and the most significant are in the field of instrument and implant placement, osteotomy, tumor surgery and trauma. AR is used successfully in the pre-operative, intra-operative and post-operative phase of personalized orthopedics.

Mixed reality is the youngest type of extended reality technologies. It provides additional benefits to users compared with AR. As in AR, in mixed reality environment users can see virtual computer-generated objects in the real-world environment, but now they can interact with virtual objects like they would in the real environment.

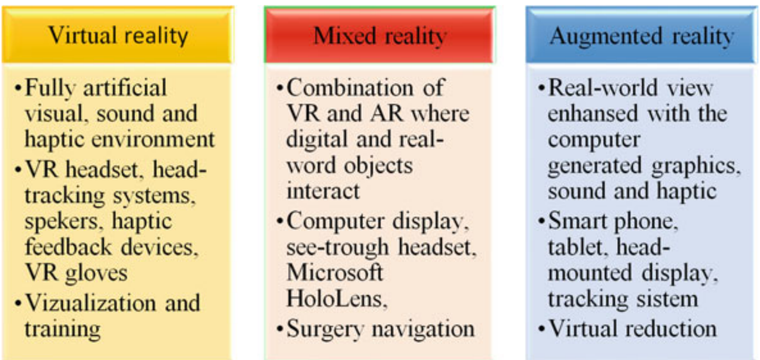

Fig. 1.6 Virtual, mixed and augmented reality in orthopedics

Thanks to its advantages over AR, MR significantly facilitates a personalized approach in orthopedics, but since it is a relatively young technology, there are only a few published papers showing the application of MR technology in orthopedics. Lee et al. (2017) presented mixed reality system supporting screw placement in orthopedic surgery. The system is based on data fusion from cone-beam CT and a red–green–blue–depth camera, and model-based surgical tool tracking. Xinghuo et al. (2018) announced new MR surgical navigation system which consist of a display, a magnetic launcher, a passenger sensor, and a processor. Teatini et al. (2021) presented novel MR surgical navigation tool which visualize bones with the illusion of possessing "X-ray" vision and thus enable tracking a location at the tip of the surgical instrument in holographic space.

1.7 Computer Assisted Orthopedic Surgery

Computer Assisted Orthopedic Surgery (CAOS) is a method of orthopedic surgery that uses various engineering technologies to provide better results of surgical procedures in orthopedics. CAOS can also be defined as an integrative orthopedic surgical approach based on computers, software, medical imaging, fluoroscopy, extended reality, robots, sensors and additive manufacturing. It enables the surgeons, inter alia, to optimize the surgical outcome, avoid surgical errors, perform minimally invasive surgery and rise surgical accuracy by using real-time feedback and robots. Based on patient's medical image, CAOS enable fully personalized approach during preoperative, intraoperative, and postoperative phases (Fig. 1.7).

The first CAOS solutions appeared in the second half of the 1990s (Joskowicz and Hazan 2016). It started with the development of method of bone segmentation from CT images and design patient's specific 3D surface geometrical model of the bone. At the same time first surgical robot ROBODOC became commercially available. According to Picard et al. (2019), CAOS systems can be divided into three categories: active systems with autonomous robot, semi-active systems which utilize handheld or robotic assisted devices, and passive systems which only provide navigation information without direct action.

The basis of any CAOS system is a good and accurate visualization of the patient's body in the form of 3D geometrical model, as well as osteofixation material and surgical instruments. The medical images used to visualize the patient's body can come from X-rays, CT, MRI, ultrasound or fluoroscopy devices, and those in CAOS are combined into a so-called multimodal view. All data from the medical images represent a single patient data set. In order for such a data set to be usable, it is necessary to perform data fusion for the anatomical region in which the surgical intervention is performed. The final result is virtual model which is the base for CAOS functioning. A virtual model is used to navigate the surgeon during the intraoperative phase or to program robot movements during the preoperative phase. In order to ensure the correlation between the virtual model and the physical space in which the patient's body is located, the so-called registration, it is necessary to place fiducial markers. There are several different registration techniques that are described in detail in the paper (Langlotz and Nolte 2004).

Robots can be part of a CAOS system. Their precision and resistance against tremor and fatigue is a great help to surgeons during surgical operations (Langlotz and Nolte 2004). Today, there are several modern robots that are capable of performing very demanding orthopedic interventions, such as total and partial knee replacement, total hip replacement or complex interventions on the spine. The ROSA Knee System (Zimmer Biomet) is robot based on CAOS system which supports surgeons in performing total knee arthroplasty. Company Medtronic offers Mazor X Stealth Edition robotic guidance system for spinal surgery which provides preoperative planning, robotic guidance, and surgical navigation. Mako SmartRobotics (Stryker, USA) helps surgeons in total hip replacement as well as in partial and total knee replacement, by combining 3D CT-based planning, AccuStop haptic technology, and data analytics. Although the use of robots in personalized orthopedics has many advantages, there are still some limitations to keep in mind. Robotic CAOS systems are still expensive, requiring large space and additional surgeon training (Beyaz 2020).

Performing surgical interventions requires great knowledge and skills from orthopedists. That is why great attention is paid to their training. The classic approach implies many years of presence and assistance to experienced surgeons during orthopedic operations. However, for ethical reasons, it is not good for patients to be a means of learning. The use of cadaveric or animal models for learning is also not completely ethical, while the lack of phantom models is low fidelity. The advent of the CAOS system has provided a much more efficient way to learn and acquire skills. CAOS allows trainees to learn from their mistakes without fear of injuring the patient. They can repeat the same operation several times until they acquire a satisfactory level of specific knowledge and skill such as selection of appropriate surgical tool, implants or fixation device, navigation of surgical instruments through the patient's body, reduction of a fracture, cutting or drilling of bones, placement of an implant, to name a few.

According to Ruikar et al. (2018), CAOS systems can serve as a training simulator that may be non-interactive, interactive simulator with visual feedback and interactive simulator with visio-haptic feedback.

Many software tools for surgery planning are available to orthopedists today. Some of them are EOSapps, PeekMed, Materialise OrthoView, MediCAD and Brainlab. Most applications are intended for personalized planning of knee, hip, spine and long bone surgeries (Table 1.1).

Despite the best preoperative planning, orthopedic surgeries require exceptional precision of the surgeon during the operation process. Even the slightest mistake in the surgeon's precision can cause fatal consequences for the patient. With the development of technologies for making volumetric medical images, fluoroscopy, CAD and others, conditions have been created for the application of the computer navigation in clinical practice. Intraoperative navigation is most important function of CAOS. Today, two computer navigation techniques are used in orthopedics. In passive navigation, the surgeon performs the surgery autonomously with visual navigational

Table 1.1 Prominent software tools for surgery planning in orthopedics

Software suite	Applications	Website
EOSapps	hipEOS and spineEOS	https://www.eos-imaging.com/
PeekMed	Osteotomy, fracture reduction, templating, 2D/3D hybrid planning	https://www.peekmed.com/#/
Materialise OrthoView	Primary and revision hip and knee arthroplasties, shoulder and small joint replacements, fracture management, deformity correction and spine procedures	https://www.materialise.com/en/medical/orthoview
MediCAD	2D/3D Spine, Knee, Shoulder, Hip, Long Leg	https://medicad.eu/en/
Brainlab	Digital spine surgery, TraumaCad orthopedic digital templating	https://www.brainlab.com/

support from the CAOS system. Active navigation uses a robot surgeon (Rambani and Varghese 2014).

Despite the best preoperative planning, orthopedic surgeries require exceptional precision of the surgeon during the operation process. Even the slightest mistake in the surgeon's precision can cause fatal consequences for the patient. With the development of technologies for making volumetric medical images, fluoroscopy, CAD and others, conditions have been created for the application of the computer navigation in clinical practice. Intraoperative navigation is most important function of CAOS. Today, two computer navigation techniques are used in orthopedics. In passive navigation, the surgeon performs the surgery autonomously with visual navigational support from the CAOS system. Active navigation uses a robot surgeon (Rambani and Varghese 2014).

CAOS is widely used in the intraoperative phase for the spinal, hip and knee surgery (Wang et al. 2020), shoulder arthroplasty, anterior cruciate ligament reconstruction, trauma surgery (Hernandez et al. 2017), and sacrum surgery (Joyce 2017). CAOS is also used during the postoperative phase, but to a lesser extent. Most frequent application in postoperative phase are surgical outcome evaluation, monitoring of recovery process, and assessing need for revision surgery (Joskowicz 2017). Zheng et al. (2018) presented 3X-Knee solution for preoperative planning and postoperative evaluation of total knee arthroplasty.

Szejka et al. (2013) proposed a reasoning system based on CT images to support the implant planning process. The system generates a three-dimensional model of the dental arch and interacts with the dental surgeon specialist in selecting the most appropriate implants for each specific case. The reasoning process is divided into 3 phases, the first selects the region of interest within the bone, the second defines the bone density of the region of interest, and the third selects the most appropriate implants that can be used.

With this, it is possible to increase interactivity in surgical planning through a three-dimensional geometric model of the dental arch, improve the decision-making process of choosing the most suitable implant and significantly reduce surgical time.

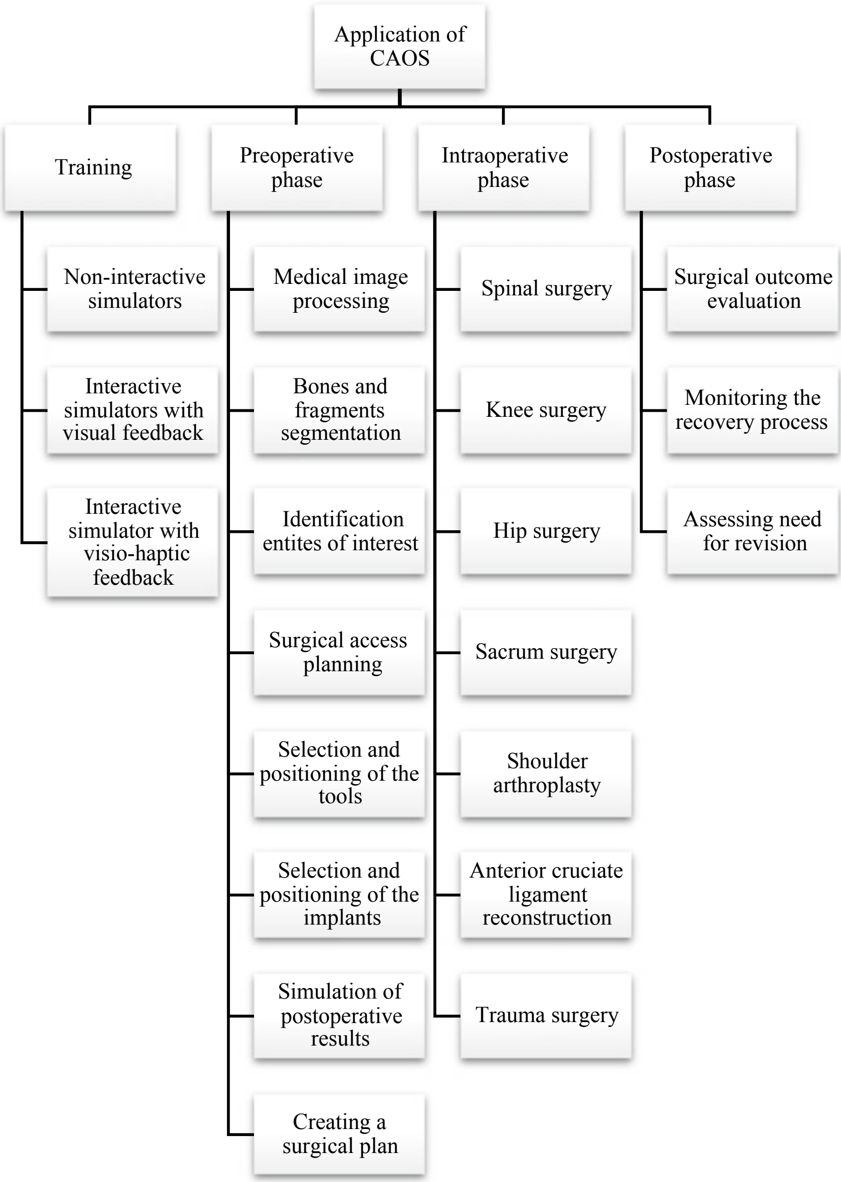

Fig. 1.7 Application of CAOS systems

1.8 Artificial Intelligence

Artificial intelligence (AI) has been used for decades in various fields of science and technology, including orthopedics. Thanks to technical solutions such as medical images, electronic health record, wearable sensors, to name just a few, orthopedists have at their disposal a huge amount of data that is impossible to process completely in real time and interpret without errors. The ability of artificial intelligence techniques to analyze large amounts of data, recognize patterns and draw conclusions is the main reason for the increasing use of artificial intelligence in medicine, and especially in personalized orthopedics. Since its inception in 1956, a large number of innovative algorithms have been developed in the field of artificial intelligence, such as knowledge based expert system, Artificial Neural Network (ANN), Machine Learning (ML), Deep Learning (DL) and Convolutional Neural Network (CNN), which are widely used in orthopedics.

The most common areas of research on the application of artificial intelligence in orthopedics relate to the interpretation of medical images, diagnosis, the prediction of the outcomes of orthopedic interventions, bone fragility assessment and decision support systems for preoperative evaluation (Han and Tian 2019). Thanks to all these AI techniques, many solutions have appeared in the form of virtual assistants in the field of personalized orthopedics. Virtual assistants provide reliable information and solutions, but the primary role of orthopedic specialists is still retained.

Pranata et al. (2019) presented novel method for automated classification and detection of fracture locations in calcaneus CT images by using two different Convolutional Neural Network algorithms. To obtain feature vectors, authors applied Speeded-Up Robust Features (SURF) local descriptors. The presented method classified fractures in calcaneus CT images with 98% sensitivity.

AI is widely applied in musculoskeletal trauma (Ajmera et al. 2021). In the form of review article, authors presented many applications of AI for automatic fracture detection based on X-ray, CT, MRI, and ultrasound images. In most of the cases CNN method as a subtype of DL was applied for fracture detection. Majority of the techniques presented are specialized in detecting fractures in narrow anatomical regions such as the ribs, wrist, hip, vertebra and ankle, based on X-ray images, rib, calcaneus, based on CT images, and vertebra, knee and hip, based on MRI images. AI tools use ultrasound images mainly for tendons.

AI can help not only in recognizing bones, but also in recognizing the type and model of implants implanted. In the process of planning re-operations and revisions of total shoulder arthroplasty, it is necessary to identify the model and manufacturer of the implant. Sultan et al. (2021) proposed DL-based framework which can recognize implant with the accuracy of 85.92%.

Artificial intelligence is also widely used in prediction of the clinical outcome. In an extensive systematic review, Ogink et al. (2021) analyzed 77 prediction models in orthopedic surgical outcome based on machine learning. The results show that the most common focus of prediction models is medical management (22%), following with survival prediction (21%), complication (19), passive range of motion (16%)

and intraoperative complication (3,9). The analyzed prediction models are specialized and are intended for application in the treatment of the spine (36%), arthroplasty (27%), trauma (17%) oncology (7.8%), and other (12%). Most of applied ML algorithms are neural network, but also DL and CNN are used.

1.9 Additive Manufacturing

During its short history, Additive Manufacturing has changed many names. The first name of these technologies was rapid prototyping because prototypes of future products were mainly produced. With the advent of 3D printers, which are cheap and have therefore become widely used, most people, as is the case today, have started using the term 3D printing. It should be said that 3D printing is just one of the additive technologies. Today, there are many additive technologies available that can be classified into the following categories: binder jetting, material extrusion, material jetting, powder bed fusion, sheet lamination, vat photopolymerization and directed energy deposition. Many of these technologies are used in personalized medicine for the production of fixators as well as their prototypes, implants, scaffolds, orthoses, prostheses, guides, surgical instrumentation and other auxiliary orthopedic tools and devices.

The immobilization in case of distal radius fractures, which are one of the most common fractures in clinical practices, requires firm immobilization in the period of initial bone healing, and at a later stage a certain flexibility. In order to produce personalised orthosis which can address both the healing and rehabilitation needs of a patient (Aranđelović et al. 2021a, b) used cheap Fused Deposition Modelling machines. The body of the orthosis was made of a flexible Ninja Flex (Fenner Inc. Manheim, PA, USA) material and additional reinforcing detachable plates were produced to fully immobilize the fracture region during healing period (Fig. 1.8).

Canciglieri et al. (2019) proposed an advanced manufacturing method for the design and manufacturing of dental implants prosthesis (dental crown). They used the advanced manufacturing concepts to standardize and speed up the manufacturing process, increasing standardization and agility. Their research also provided a

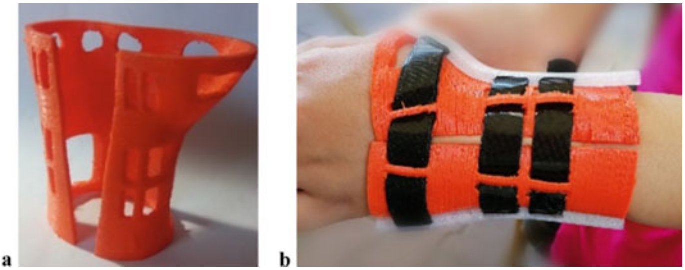

Fig. 1.8 Flexible personalized distal radius orthosis (Aranđelović et al. 2021a, b)

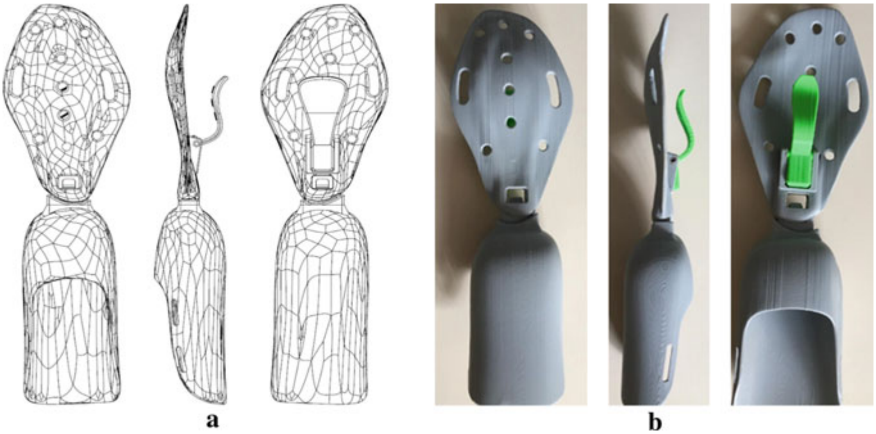

Fig. 1.9 Prototype Modeling of the prosthetic device and prosthetic device obtained by rapid prototyping (Francisco 2020; Francisco et al. 2022). **a** 3D geometrical model of the prosthetic device. **b** Prototype of the prosthetic device obtained by additive manufacturing

contribution in dentistry and its integration with engineering in order to speed up and improve the manufacturing of prostheses based on the use of digital medical images processing in DICOM formats, additive manufacturing systems, and subtractive rapid prototyping systems.

Francisco (2020) have developed a prosthetic device to assist the patient with agenesis at the wrist level in the process of learning to swim. The method applied in this development was part of the reference model for the product development process, which allowed the conception, modeling and prototyping through 3D printing. The preliminary proposal of the prosthetic device presents itself as a facilitating opportunity for the access of patients with hand agenesis to physical activity, allowing for a better quality of life and social inclusion through sport as illustrate in (Fig. 1.9). The observation of existing models allowed the identification of relevant features implemented in the design of the prosthetic device. The upper limb prosthesis model has a mechanism that allows the use of an accessory for the initial process of learning to swim, defining the central idea of the product and identifying the basic requirements, so it was possible to outline the initial design of the product (Francisco et al. 2022).

1.10 Wearable Sensor Devices

The development of the lightweight sensors, smartphones and communication technologies, such as 5G, have contributed to the emergence of wearable sensor devices. They are smart electronic devices attached to wearer in such a way that can collect, process, transmit and/or present data and information. In the case of orthopedics, the wearer can be a patient or a physician. Sensors usually collect data related to the patient, but they can also collect other data from the environment.

The wearable sensor devices may have different forms such as simple sensor attached to the patient's body, smart bracelet, smart watch, smart belt, smart ring, smart glasses, smart clothes or smart shoes. This list is not exhaustive because new forms of these devices are constantly appearing. Smartphones are the most widespread wearable sensor devices. Typical smartphone has many sensors such as accelerometer, gyroscope, magnetometer, GPS, barometer, proximity, ambient light and others. In addition, smartphones can receive data from sensors or other wearable sensor devices worn by the owner, process it, display it and forward it to remote servers. In addition to sensors that can be found in smartphones, sensors of force, pressure, vibration, temperature can also be used in orthopedics. They are used alone or as part of a wearable device. In addition to sensors that can be found in telephones, sensors of force, pressure, vibration, temperature can also be used in orthopedics. They are used either as a separate sensor or as part of a device. Also, sensors that can be implanted in the human body have appeared, so now the term werable-inplantable sensor is used (Andreu-Perez et al. 2015).

Current research has shown that wearable sensors devices can be used in diagnosis, preoperative planning, intraoperative assistance, and monitoring during rehabilitation (Shah et al. 2021). However, some unresolved issues remain, such as ethical and legal rules, approved clinical procedures, patient privacy protection, sensors power supply, and data security, which need to be addressed before widespread application in clinical practice.

The main problem of the wearable sensor devices is the supply of energy that is needed for their work and communication. This is a particularly critical issue for implantable sensors. Thanks to the development of a new energy harvesting sources, it is possible to have battery-free wearable sensor devices. Most promising sources are electromagnetic energy, human skin temperature, photovoltaic, ultrasound, mechanical energy, and biofuels (Kim et al. 2021; Sheng et al. 2021).

The ever-improving quality of wearable motion sensors and the drop in their price have made their application in rehabilitation significantly expanded. Especially, they are very useful in movement evaluation. However, many issues, such as the optimal position of the sensor on human body, have not yet been resolved. In the paper Derungs and Amft (2020) authors concluded that personally selected sensor positions is necessary to gain accuracy of the measurement. Wide review of 61 articles related to the use of wearable sensor devices for walking and running gait analysis outside of the laboratories shows that more similar studies over long periods of time with large numbers of participants are necessary to analyze real-world gait patterns (Benson et al. 2018). It would be of great help for the personalized orthopedics.

Wearable sensor devices can be also part of external fixation devices. Misic et al. (2018) proposed the improvement of external fixator by attaching sensors, processing, and communication devices to it in order to enable real-time monitoring of patient's behavior during recovery process.

One of the devices that is often used in orthopedics is the Inertial Measurement Unit (IMU). Usually, IMU consists of accelerometers, gyroscopes, and magnetometers, so it is possible to measure forces, limb rotation and body orientation of the patient. Bolam et al. (2021) reported results of the research on usability of IMU for monitoring state of 14 patients undergoing primary knee arthroplasty for osteoarthritis. On the ankles of each patient were placed two IMU in order to measure impact load, limb impact load asymmetry and knee range of motion. Authors concluded that results obtained by commercially available IMU sensors are promising. Similar research, using IMU as a wearable sensor device, but for the patients suffering from adhesive capsulitis of the shoulder, was reported by Yu-Pin et al. (2020).

1.11 Computer Aided Engineering

Computer aided engineering (CAE) is a group of numerical analysis methods used to solve engineering analysis tasks. CAE includes, inter alia, finite element analysis, multibody dynamics, and optimization. These methods are widely used in personalized orthopedics especially in the pre-operative phase.

The Finite Element Method (FEM) is numerical method widely used in biomedical engineering, or more specifically in the biomechanics, for solving structural, fluid flow and heat transfer problems in human body. The first attempts to use FEM in orthopedics were made in the 1970s to solve the problem of determining the stresses in the host bone in the proximity of internal fracture fixation plates as well (Vangala et al. 1982). Today FEM is used for analysis of behavior of bones with or without implants (Vulovic et al. 2011), crack propagation (Kruzic et al. 2006), simulation of bone remodeling (Idhammad et al. 2013), and other patient-specific simulation.

During the preoperative planning process, FEM is used to determine the optimal shape, configuration, and position of implants and fixators (Ingrassia et al. 2020). In the paper by Korunovic et al. (2015), a sensitivity study of Selfdynamisable Internal Fixator (SIF) stress to the change of bar length, number of distal screws and fracture zone elasticity modulus was presented. SIF is a type of fixator used in treatment of subtrochanteric femoral fractures. The specific approach was used in the research, where in the same FE assembly two different methods for defining the material properties were used. Local material mapping was employed to assign a location-specific value of elastic modulus to each finite element of the femur, while a constant value of elasticity modulus was assigned to all finite elements belonging to components of SIF.

Korunovic et al. (2019) also performed the optimization of position and configuration of SIF. Bidirectionally associative computer-aided design (CAD) and finite element (FE) models of femur- fixator assembly were thereby created to facilitate the automatic optimization process. This research stands out by flexibility and robustness of CAD and FE models of a complex medical implant, which were achieved by using the proper anatomical landmarks and assembly constraints.

Multibody dynamics analysis is an important pillar of personalized orthopedics. Such an analysis use model of human musculoskeletal system consisting of bones, joints, contact elements, ligaments and muscle actuators (Seth et al. 2011). Software solutions such as AnyBody Modeling System version 6.0.5 (AnyBody Technology A/S, Aalborg, Denmark), SIMM (Software for Interactive Musculoskeletal Modeling) from Motion Analysis Corp, OpenSim (National Center for Simulation in Rehabilitation Research) or LifeMOD (LifeModeler, Inc., USA) are widely used for such analyzes. Those analysis include inverse kinematics, inverse dynamics, static optimization, and forward dynamics of human musculoskeletal system.

Kang et al. (2018) investigated effects of deficient posterolateral corner structures on the kinematics of the knee joint under gait and squat loading conditions. Simulation was done using AnyBody Modeling System on the five subject-specific models. The same software was used by Benditz et al. (2018) to investigate sagittal balance of the spine and to compare spinal load before and after spinal fusion.

In order to prepare input data for the finite element analysis of total knee replacement, Loi et al. (2021) used OpenSim for the kinematic and dynamic analysis of patient-specific gait trials. Bheemreddy et al. (2020) used also OpenSim to do functional neuromuscular stimulation of individuals paralyzed due to spinal cord injury.

1.12 Virtual Physical Therapy

After orthopedic interventions, some kind of rehabilitation of the patient is usually performed. Rehabilitation can take place as traditional clinical in-person physiotherapy or as telerehabilitation with distant patients. Physical therapy with distant patients is called in the literature by various names such as telehealth physical therapy, computer assisted rehabilitation, remote physical therapy, telerehabilitation, and virtual physical therapy, but the meaning is the same. Remote patients may be equipped with smartphones, personal computers, sensors and haptic devices and have opportunity to communicate with their physicians who can collect measured data in order to monitor patient's state.

Some methods of orthopedic physiotherapy, such as cryotherapy or massage, cannot be performed with distant patients. Due to the specifics of each patient, the best results are achieved with personalized individual exercises, regardless of whether the therapy is performed in-person at the clinic or remotely.

Virtual physical therapy shows no signs of inferiority to in-person clinical therapy. In an extensive prospective study, Crawford et al. (2021) evaluated the results of the use of the exercise educational care management system, based on smartwatch and smartphone application, after primary knee arthroplasty. A control group of 244 patients receiving in-person rehabilitation physiotherapy and treatment group of 208 patients, receiving distance physiotherapy using a smartphone application, were monitored for three months and several indicators were measured. Based on results obtained, they concluded that platform could have positive effect on decreasing post-operative costs, while improving patient engagement. A similar comparative study of the results of in-person physiotherapy and telerehabilitation of the knee joints of patients with polytrauma was performed by Tsvyakh et al. (2021). For each patient, physicians created a personalized rehabilitation plan. The study included 16 in-person rehabilitated patients and 96 who underwent telerehabilitation. Each patient was equipped with the sensors attached to the injured limb, and measured data were collected and processed. The results showed that remote patients spent much less physician time (1.9 min vs. 15.2 min), with their degree of satisfaction being much higher than patients undergoing in-person therapy (78.3% vs. 36.7%).

Burdea et al. (2000) presented telerehabilitation system based on virtual reality and haptic interfaces. The system was intended for rehabilitation of patients with hand, elbow, knee and ankle impairments. Hardware and software component of this telerehabilitation system is presented in Popescu et al. (2000).

1.13 Conclusion

In recent years, there has been a significant increase in the personalized approach in orthopedics, primarily due to the availability of new innovative engineering technologies. Personalized orthopedics today, thanks to the application of engineering technologies, applies patient specifics or small group specific prevention, diagnostic, treatment, and recovery actions, in such a way that patients obtain optimal patient-centric health services without trial-and-error attempts.

In this study, ten enabling technologies were identified that significantly contributed to the practice of personalized medicine, namely 3D Imaging, Computer Aided Design, Reverse Engineering, Extended Reality, CAOS, Artificial intelligence, Additive Manufacturing, Wearable Sensor Devices, Computer Aided Engineering, Virtual Physical Therapy. Although all of these engineering technologies are still evolving, some of them are mature, while some are at an early stage of development. Accordingly, each of them is more or less represented in orthopedic practice. Technologies such as 3D medical imaging, reverse engineering, and computer aided engineering, are very widespread in orthopedics. In contrast, technologies such as mixed reality (class of extended reality) or wearable sensor devices are still in the development stage and are rarely encountered in practice. What is certain is that further development of these technologies can be expected, which will contribute to further personalization in the field of orthopedics, and hence better treatment outcomes.

References

Aicale R, Tarantino D, Maccauro G et al (2019) Genetics in orthopaedic practice. J Biol Regul Homeost Agents. 33(2 Suppl. 1):103–117. XIX Congresso Nazionale S.I.C.O.O.P. Societa' Italiana Chirurghi Ortopedici Dell'ospedalita' Privata Accreditata

Ajmera P, Kharat A, Botchu R et al (2021) Real-world analysis of artificial intelligence in musculoskeletal trauma. J Clin Orthop Trauma 27(22):101573. https://doi.org/10.1016/j.jcot.2021.101573

AMS (2015) Stratified, personalised or P4 medicine: a new direction for placing the patient at the centre of healthcare and health education. Academy of Medical Sciences. https://acmedsci.ac.uk/viewFile/564091e072d41.pdf. Accessed 15 Oct 2021

Andreu-Perez J, Leff DR, Ip HMD et al (2015) From wearable sensors to smart implants—toward pervasive and personalized healthcare. IEEE Trans Biomed Eng 62(12):2750–2762. https://doi.org/10.1109/TBME.2015.2422751

Aranđelović J, Korunović N, Stamenković B et al (2021a) Design Methodology of a personalised wrist orthosis for fractures and rehabilitation. In: Zdravković M, Trajanović M, Konjović Z (eds) ICIST 2021a Proceedings, pp 154–157

Aranđelović J, Korunović N, Stamenković B et al (2021b) Methodology for topological optimization and 3D printing of a personalised wrist orthosis for fractures and rehabilitation. In: Proceedings of the 38th international conference on production engineering—Serbia, pp 57–61

Beyaz S (2020) A brief history of artificial intelligence and robotic surgery in orthopedics & traumatology and future expectations. Joint Dis Relat Surg 31(3):653–655. https://doi.org/10.5606/ehc.2020.75300

Benditz A, Auer S, Spörrer JF et al (2018) Regarding loads after spinal fusion, every level should be seen separately: a musculoskeletal analysis. Eur Spine J 27:1905–1910. https://doi.org/10.1007/s00586-018-5476-5

Benson LC, Clermont CA, Bosnjak E et al (2018) The use of wearable devices for walking and running gait analysis outside of the lab: a systematic review. Gait Posture 63:124–138. https://doi.org/10.1016/j.gaitpost.2018.04.047

Bheemreddy A, Friederich A, Lombardo L (2020) Estimating total maximum isometric force output of trunk and hip muscles after spinal cord injury. Med Biol Eng Comput 58(4):739–751. https://doi.org/10.1007/s11517-020-02120-0

Bini S et al (2020) Digital orthopaedics: a glimpse into the future in the midst of a pandemic. J Arthroplasty 35(7):S68–S73. https://doi.org/10.1016/j.arth.2020.04.048

Bolam S et al (2021) Remote patient monitoring with wearable sensors following knee arthroplasty. Sensors 21(15):5143. https://doi.org/10.3390/s21155143

Burdea G, Popescu V, Hentz V, Colbert K (2000) Virtual reality-based orthopedic telerehabilitation. IEEE Trans Rehabil Eng 8(3):430–432. https://doi.org/10.1109/86.867886

Canciglieri MB, Leite AFCSM, Szejka AL, Canciglieri Junior O (2019) An approach for dental prosthesis design and manufacturing through rapid manufacturing technologies. Int J Comput Integr Manuf 32:1–16. https://doi.org/10.1080/0951192x.2019.1636410

Crawford D et al (2021) 2021 Mark Coventry Award: use of a smartphone-based care platform after primary partial and total knee arthroplasty: a prospective randomized controlled trial. Bone Joint J 103-B(6 Suppl. A):3–12. https://doi.org/10.1302/0301-620X.103B6.BJJ-2020-2352.R1

Deniz CM, Xiang S, Hallyburton RS et al (2018) Segmentation of the proximal femur from MR images using deep convolutional neural networks. Sci Rep 8:16485. https://doi.org/10.1038/s41598-018-34817-6

Derungs A, Amft O (2020) Estimating wearable motion sensor performance from personal biomechanical models and sensor data synthesis. Sci Rep 10:11450. https://doi.org/10.1038/s41598-020-68225-6

DICOM (2021) About DICOM: overview. https://www.dicomstandard.org/about. Accessed 20 Sept 2021

EU (2015) Council conclusions on personalised medicine for patients. Official Journal of the European Union. 2015/C 421/03
Fat DL et al (2011) The Hounsfield value for cortical bone geometry in the proximal humerus—an in vitro study. Skeletal Radiol 41:557–568
FDA (2013) Report. Paving the way for personalized medicine. https://www.fdanews.com/ext/resources/files/10/10-28-13-Personalized-Medicine.pdf. Accessed 10 Oct 2021
Fernie G (1984) Computer aided design and manufacture for prosthetics and orthotics. Biomedizinische Technik. Band 29 Heft 12. https://doi.org/10.1515/bmte.1984.29.12.335
Filippi S, Motyl B, Bandera C (2009) Comparing parametric solid modelling/reconfiguration, global shape modelling and free-form deformation for the generation of 3D digital models of femurs from X-ray images. Comput Methods Biomech Biomed Engin 12(1):101–108. https://doi.org/10.1080/10255840802178582
Francisco MG (2020) Design for six sigma reference model oriented to the product development process. Thesis (Doctorate Thesis in Industrial and Systems Engineering—in Portuguese), Pontifical Catholic University of Paraná, PUCPR, Brazil
Francisco M, Canciglieri Junior O, Sant'Anna MO et al (2022) Assistive technology: development of a prosthetic device for swimming learning. In: Product lifecycle management—green and blue technologies to support smart and sustainable organizations, vol 640, pp 1–11
Han XG, Tian W (2019) Artificial intelligence in orthopedic surgery: current state and future perspective. Chin Med J 132(21):2521–2523. https://doi.org/10.1097/CM9.0000000000000479
Helguero C et al (2015) Improving the accuracy of wide resection of bone tumors and enhancing implant fit: a cadaveric study. J Orthop 12(Suppl. 2):188–194
Hernandez D, Garimella R, Eltorai AEM, Daniels AH (2017) Computer-assisted orthopaedic surgery. Orthop Surg 9:152–158. https://doi.org/10.1111/os.12323
Hertzberg-Boelch SP et al (2021) Custom made Monoflange Acetabular components for the treatment of Paprosky Type III defects. J Pers Med 11(4):283. https://doi.org/10.3390/jpm11040283
Idhammad A, Abdali A, Alaa N (2013) Computational simulation of the bone remodeling using the finite element method: an elastic-damage theory for small displacements. Theor Biol Med Model 10:32. https://doi.org/10.1186/1742-4682-10-32
Ingrassia T, Nigrelli V, Pecorella D et al (2020) Influence of the screw positioning on the stability of locking plate for proximal tibial fractures: a numerical approach. Appl Sci 10(14):4941. https://doi.org/10.3390/app10144941
Jain K (2015) Textbook of personalized medicine, 2nd edn. Springer
Joyce DM (2017) Computer navigation in the sacrum. In: Ruggieri P, Angelini A, Vanel D, Picci P (eds) Tumors of the sacrum. Springer, Cham. https://doi.org/10.1007/978-3-319-51202-0_22
Joskowicz L, Hazan E (2016) Computer aided orthopaedic surgery: incremental shift or paradigm change? Med Image Anal 33:84–90. https://doi.org/10.1016/j.media.2016.06.036
Joskowicz L (2017) Computer-aided surgery meets predictive, preventive, and personalized medicine. EPMA J 8(1):1–4. https://doi.org/10.1007/s13167-017-0084-8
Jud L et al (2020) Applicability of augmented reality in orthopedic surgery—a systematic review. BMC Musculoskelet Disord 21:103. https://doi.org/10.1186/s12891-020-3110-2
Kamiya N (2018) Muscle segmentation for orthopedic interventions. In: Zheng G, Tian W, Zhuang X (eds) Intelligent orthopaedics. Advances in experimental medicine and biology, vol 1093. Springer, Singapore. https://doi.org/10.1007/978-981-13-1396-7_7
Kang et al (2018) Biomechanical influence of deficient posterolateral corner structures on knee joint kinematics: a computational study. J Orthop Res 36(8):2202–2209. https://doi.org/10.1002/jor.23871
Kim KK, Choi J, Ko SH (2021) Energy harvesting untethered soft electronic devices. Adv Healthcare Mater 10(17). https://doi.org/10.1002/adhm.202002286
Klasson B (1985) Computer aided design, computer aided manufacture and other computer aids in prosthetics and orthotics. Prosthet Orthot Int 9:3–11

Khan F et al (2013) Surgical technique: computer-generated custom jigs improve accuracy of wide resection of bone tumors. Clin Orthop Relat Res 471(6):2007–2016. https://doi.org/10.1007/s11999-012-2769-6

Korunovic N, Trajanovic M, Mitkovic M, Vitkovic N, Stevanovic D (2015) A parametric study of selfdynamisable internal fixator used in femoral fracture treatment. Paper presented at the NAFEMS World Congress 2015 inc. the 2nd International SPDM Conference, San Diego, 21–24 June

Korunovic N, Marinkovic D, Trajanovic M, Zehn M, Mitkovic M, Affatato S (2019) In silico optimization of femoral fixator position and configuration by parametric CAD model. Materials 12(14):2326. https://doi.org/10.3390/ma12142326

Kruzic J, Scott J, Nalla R et al (2006) Propagation of surface fatigue cracks in human cortical bone. J Biomech 39:968–972

Langlotz F, Nolte LP (2004) Technical approaches to computer-assisted orthopedic surgery. Eur J Trauma 30:1–11. https://doi.org/10.1007/s00068-004-1374-0

Lee SC et al (2017) Multi-modal imaging, model-based tracking, and mixed reality visualisation for orthopaedic surgery. Healthcare Technol Lett. https://doi.org/10.1049/htl.2017.0066

Leordean D, Vilău C, Dudescu MC (2021) Generation of computational 3D models of human bones based on STL data and CAD software packages. Appl Sci 11(17):7964. https://doi.org/10.3390/app11177964

Loi I, Stanev D, Moustakas K (2021) Total knee replacement: subject-specific modeling, finite element analysis, and evaluation of dynamic activities

Mandolini M, Caragiuli M, Brunzini A et al (2020) A procedure for designing custom-made implants for forehead augmentation in people suffering from Apert syndrome. J Med Syst 44:146. https://doi.org/10.1007/s10916-020-01611-9

Majstorovic V, Trajanovic M, Vitkovic N, Stojkovic M (2013) Reverse engineering of human bones by using method of anatomical features. CIRP Ann Manuf Technol 62(1):167–170. https://doi.org/10.1016/j.cirp.2013.03.081

MediCAD (2021) The mediCAD 6.x version of the medical planning software. https://www.medicad.eu/en/medicad/medicad-classic. Accessed 21 Sept 2021

Misic D, Zdravkovic M, Mitkovic M et al (2018) Real-time monitoring of bone fracture recovery by using aware, sensing, smart, and active orthopedic devices. IEEE Internet Things J 5:4466–4473. https://doi.org/10.1109/JIOT.2018.2819623

Mitic J, Vitkovic N, Manic M et al (2020) Reverse modeling of the human mandible 3D geometric model. Vojnosanit Pregl 77(3):262–270. https://doi.org/10.2298/VSP170727063M

Moldovan F, Gligor A, Bataga T (2021) Structured integration and alignment algorithm: a tool for personalized surgical treatment of tibial plateau fractures. J Pers Med 11:190. https://doi.org/10.3390/jpm11030190

Murphy S, Kijewski P, Walker P, Scott R (1985) Computer-assisted pre-operative planning of orthopedic reconstructive surgery. In: Lemke H, Rhodes ML, Jaffee CC, Felix R (eds) Computer assisted radiology/Computergestützte Radiologie. Springer, Berlin, Heidelberg. https://doi.org/10.1007/978-3-642-52247-5_64

Negrillo-Cardenas J et al (2020) The role of virtual and augmented reality in orthopedic trauma surgery: from diagnosis to rehabilitation. Comput Methods Programs Biomed. https://doi.org/10.1016/j.cmpb.2020.105407

Ogink PT, Groot OQ, Karhade AV et al (2021) Wide range of applications for machine-learning prediction models in orthopedic surgical outcome: a systematic review. Acta Orthop 92(5):526–531. https://doi.org/10.1080/17453674.2021.1932928

Patel P, Marcum D, Remotigue M (2006) Automatic CAD model topology generation. Int J Numer Meth Fluids 52:823–841. https://doi.org/10.1002/fld.1166

Pei G (eds) (2018) Digital orthopedics. Springer Nature B.V. and People's Medical Publishing House. https://doi.org/10.1007/978-94-024-1076-1

Picard F, Deakin AH, Riches PE et al (2019) Computer assisted orthopaedic surgery: past, present and future. Med Eng Phys 72:55–65. https://doi.org/10.1016/j.medengphy.2019.08.005

Popescu VG, Burdea GC, Bouzit M et al (2000) A virtual-reality-based telerehabilitation system with force feedback. IEEE Trans Inf Technol Biomed 4(1):45–51. https://doi.org/10.1109/4233.826858

Pranata YD, Wang KC, Wang JC et al (2019) Deep learning and SURF for automated classification and detection of calcaneus fractures in CT images. Comput Methods Programs Biomed 171:27–37. https://doi.org/10.1016/j.cmpb.2019.02.006

Rambani R, Varghese M (2014) Computer assisted navigation in orthopaedics and trauma surgery. Orthopaedics and Trauma 28(1):50–57. https://doi.org/10.1016/j.mporth.2014.01.002

Rudek M, Canciglieri Junior O, Greboge T (2013) A PSO application in skull prosthesis modelling by superellipse. Electron Lett Comput Vision Image Anal 12(2):1–12. https://doi.org/10.5565/rev/elcvia.514

Rudek R, Gumiel YB, Canciglieri Junior O (2015) Autonomous CT replacement method for the skull prosthesis modelling. Facta Univ Ser Mech Eng 13(3):283–294

Ruikar DD, Hegadi RS, Santosh KC (2018) A systematic review on orthopedic simulators for psycho-motor skill and surgical procedure training. J Med Syst 42:168. https://doi.org/10.1007/s10916-018-1019-1

Schmutz B, Rathnayaka K, Albrecht T (2021) Anatomical fitting of a plate shape directly derived from a 3D statistical bone model of the tibia. J Clin Orthopaedics Trauma 10:S236–S241. https://doi.org/10.1016/j.jcot.2019.04.019

Seth A, Sherman M, Reinbolt JA, Delp SL (2011) OpenSim: a musculoskeletal modeling and simulation framework for in silico investigations and exchange. Procedia Iutam. 2:212–232. https://doi.org/10.1016/j.piutam.2011.04.021

Shah NV, Gold R, Dar QA et al (2021) Smart technology and orthopaedic surgery: current concepts regarding the impact of smartphones and wearable technology on our patients and practice. Curr Rev Musculoskelet Med. https://doi.org/10.1007/s12178-021-09723-6

Sheng H et al (2021) Recent advances of energy solutions for implantable bioelectronics. Adv Healthcare Mater 10(17). https://doi.org/10.1002/adhm.202100199

Simpleware (2021) Simpleware 3D image processing for orthopedics. https://www.synopsys.com/simpleware/life-sciences/orthopedics.html. Accessed 21 Sept 2021

Staats T (1985) Advanced prosthetic techniques for below knee amputations. Orthopedics 8(2). https://doi.org/10.3928/0147-7447-19850201-13

Sultan H, Owais M, Park C et al (2021) Artificial intelligence-based recognition of different types of shoulder implants in X-ray scans based on dense residual ensemble-network for personalized medicine. J Pers Med 27, 11(6):482. https://doi.org/10.3390/jpm11060482

Szejka AL, Rudek M, Canciglieri Junior O (2013) A reasoning system to support the dental implant planning process. In: Concurrent engineering approaches for sustainable product development in a multi-disciplinary environment, 1st edn, vol 2. Springer, London, pp 909–919. https://doi.org/10.1007/978-1-4471-4426-7_77

Teatini A, Kumar RP, Elle OJ et al (2021) Mixed reality as a novel tool for diagnostic and surgical navigation in orthopaedics. Int J CARS 16:407–414. https://doi.org/10.1007/s11548-020-02302-z

Trajanovic M et al (2010) Application of computer models of Mitkovic selfdynabizable internal fixator in rehabilitation of femur traumas. Facta Univ Seri Mech Eng 8(1):27–38

Trajanovic M, Tufegdžić M, Arsic S (2012) Reverse engineering of the human fibula. In: 11th international scientific conference MMA 2012. https://doi.org/10.13140/2.1.1655.5203

Trajanovic M, Tufegdzic M, Arsic S (2018) Obtaining patient-specific point model of the human ilium bone in the case of incomplete volumetric data using the method of parametric regions. Australas Phys Eng Sci Med 41:931–944. https://doi.org/10.1007/s13246-018-0689-9

Tsvyakh AI, Hospodarskyy AY, Marchenkova NO et al (2021) Telerehabilitation of the knee joints of patients with polytrauma. Wiad Lek 74(1):48–51

Tufegdžić M, Trajanović M (2021) Landmark-driven statistical morphometry of the human ilium bone as a base for obtaining subject specific 3D model. In: Zdravković M, Trajanović M, Konjović

Z (eds) ICIST 2021 Proceedings, pp. 109–112. https://www.eventiotic.com/eventiotic/library/paper/650
Tufegdzic M, Trajanovic M, Arsic S et al (2013) Toward reverse engineering of hip bone, Proceedings of 35th International conference on production engineering. Kraljevo - Kopaonik, Serbia, pp 319–326
Tufegdzic M, Arsic S, Trajanovic M (2015) Parameter-based morphometry of the wing of ilium. J Anat Soc India 64(2):129–135. https://doi.org/10.1016/j.jasi.2015.10.008
Vangala S, Ghista D, Repo R (1982) The scope of finite element models in providing answers to clinical orthopaedic problems. In: Biomedical engineering I, Recent developments: Proceedings of the first southern biomedical engineering conference. Pergamon Press, pp 159–163
Vaughan N, Dubey V, Wainwright T, Middleton R (2016) A review of virtual reality based training simulators for orthopaedic surgery. Med Eng Phys 38(2):59–71. https://doi.org/10.1016/j.medengphy.2015.11.021
Verhey J, Haglin J, Verhey E et al (2020) Virtual, augmented, and mixed reality applications in orthopedic surgery. Int J Med Robot 16(2):e2067. https://doi.org/10.1002/rcs.2067
Veselinovic M, Stevanovic D, Trajanovic M et al (2011) Method for creating 3D surface model of the human tibia. In: Proceedings of the 34th international conference on production engineering 2011, Niš, Serbia. University of Niš, Faculty of Mechanical Engineering, pp 355–358
Veselinovic M, Vitković N, Trajanović M et al (2013) Different approaches for creation of human tibia 3D models based on CT data. In: The 35th international conference on production engineering, Kraljevo-Kopaonik. pp 283–289
Vitković N, Milovanović J, Korunović N et al (2013) Software system for creation of human femur customized polygonal models. Comput Sci Inf Syst 10(3):1473–1497
Vitkovic N, Mitic J, Manic M et al (2015) The parametric model of the human mandible coronoid process created by method of anatomical features. Comput Math Methods Med 3:1–10. https://doi.org/10.1155/2015/574132
Vitkovic N, Radovic L, Trajanovic M et al (2019) 3D point cloud model of human bio form created by the application of geometric morphometrics and method of anatomical features: human tibia example. Filomat Univ Nis, Fac Sci Math 33(4):1217–1225. https://doi.org/10.2298/Fil1904217v
Vulovic S, Korunovic N, Trajanovic M et al (2011) Finite element analysis of CT based femur model using finite element program PAK. J Serb Soc Comput Mech 5(2):160–166
Wang M, Li D, Shang X, Wang J (2020) A review of computer-assisted orthopaedic surgery systems. Int J Med Robotics Comput Assist Surg 16:e2118. https://doi.org/10.1002/rcs.2118
Willis A et al (2007) 3D reconstruction of highly fragmented bone fractures. In: Pluim J, Reinhardt J (ed) Proceedings of SPIE 6512, Medical Imaging 2007: Image Processing, 65121P. https://doi.org/10.1117/12.708683
Xinghuo W et al (2018) Mixed reality technology-assisted orthopedics surgery navigation. Surg Innov 25(3):304–305. https://doi.org/10.1177/1553350618771413
Xianlong Z, Kunzheng W (2021) The future of joint surgery-the application of digital orthopedics technology in joint surgery. Chin J Orthop. 41(8):525–531. https://doi.org/10.3760/cma.j.cn121113-20210303-00214
Yunyan W, Zhengming C, Kunjin H et al (2017) Rapid generation of human femur models based on morphological parameters and mesh deformation. Biotechnol Biotechnol Equip 31(1):162–174. https://doi.org/10.1080/13102818.2016.1255156
Yu-Pin C et al (2020) Wearable motion sensor device to facilitate rehabilitation in patients with shoulder adhesive capsulitis: pilot study to assess feasibility. J Med Internet Res 22(7):e17032. https://doi.org/10.2196/17032
Yu W, Liu W, Tan L, Zhang S, Zheng G (2018) Multi-object model-based multi-atlas segmentation constrained grid cut for automatic segmentation of lumbar vertebrae from CT images. In: Zheng G, Tian W, Zhuang X (eds) Intelligent orthopaedics. advances in experimental medicine and biology, vol 1093. Springer, Singapore. https://doi.org/10.1007/978-981-13-1396-7_5
Zeng G, Zheng G (2018) Deep learning-based automatic segmentation of the proximal femur from MR images. In: Zheng G, Tian W, Zhuang X (eds) Intelligent orthopaedics. Advances in

experimental medicine and biology, vol 1093. Springer, Singapore. https://doi.org/10.1007/978-981-13-1396-7_6

Zhang J, Yan C, Chui C, Ong S (2010) Fast segmentation of bone in CT images using 3D adaptive thresholding. Comput Biol Med 40(2):231–236. https://doi.org/10.1016/j.compbiomed.2009.11.020

Zheng G, Alcoltekin A, Thelen B et al (2018) 3X-Knee: a novel technology for 3D preoperative planning and postoperative evaluation of TKA based on 2D X-Rays. Adv Exp Med Biol 1093:93–103. https://doi.org/10.1007/978-981-13-1396-7_8

Part II
Reverse Engineering of Human Bones

Chapter 2
Creation of Geometrical Models of Human Bones by Using Method of Anatomical Features

Nikola Vitković, Miroslav D. Trajanovic, and Stojanka Arsić

2.1 Introduction

We are witnessing the great influence of engineering technologies on orthopedics. Thanks to them, conditions are created for the wider application of personalized orthopedics. Increasingly high-quality devices for recording volumetric medical images enable orthopedists to better perform preventive, diagnostic, intraoperative and postoperative procedures. The outputs from medical imaging methods are various, and one potential output is geometrical data. This data is acquired from special software integrated into medical scanners, and usually requires post-processing in some medical and Computer-Aided Design (CAD) software. Post-processing presumes application of different methods for the complete reconstruction of the geometrical model of the specific patient. To improve geometrical accuracy and anatomical correctness, new methods for creating geometric models of human bones, based on acquired medical data, are being developed. Based on the data that provide, medical scanners can be divided into devices that allow the creation of 2D images of the scanning object, such are X-rays or standard 2D ultrasound and devices that allow the creation of 3D images (volumetric models), such are Computed Tomography (CT) or Magnetic Resonance Imaging (MRI). With such data, different types of processing can be performed, and as a result, accurate geometrical models of human bones can be obtained. For the processing of medical images, specialized commercial software packages can be used, which enable 3D visualization of certain parts of the human body, but their price is extremely high. A typical example of

[1] https://www.materialise.com/en/medical/mimics-innovation-suite/mimics.

N. Vitković (✉) · M. D. Trajanovic
Mechanical Engineering Faculty, University of Niš, Niš, Serbia
e-mail: nikola.vitkovic@masfak.ni.ac.rs

S. Arsić
Faculty of Medicine, University of Niš, Niš, Serbia

O. Canciglieri Junior and M. D. Trajanovic (eds.), *Personalized Orthopedics*,
https://doi.org/10.1007/978-3-030-98279-9_2

commercial software is Materialize Mimics,[1] which is intended to segment medical images to create precise 3D anatomical models of the human body. 3D geometrical models created by given software solutions can be used for further processing using CAD software packages, production of bone implants with Additive Technologies (AT), planning of orthopedic operations and more. As an alternative to commercial software solutions, open-source applications offer a smaller range of possibilities or are narrowly specialized for a specific anatomical region. Therefore, they are free and provide the possibility of upgrading according to user needs. An example of a software for creating applications that work with DICOM[2] images (Digital Imaging and Communications in Medicine) are ClearCanvas[3] and 3D Slicer,[4] but with a limited capabilities concerning model processing. Such solutions are often developed in scientific institutions, during the scientific research. A common feature of the described software packages is that they offer an appropriate type of visualization of medical information in the form of 2D or 3D geometric models of the human skeleton and soft tissue. Based on the presented models, orthopedic surgeons can detect a problem (fracture or bone defect on a certain bone, etc.) and determine the appropriate therapy for a given patient.

To build accurate 3D geometrical model of the bones, it is important to have good medical images, with valid geometrical and other data about patient organs. The medical data acquired from scanners can be complete, i.e., it contains complete geometrical data about the affected organ, or incomplete, i.e., there is not enough data about patient organ, due to the bad imaging, lack of adequate scanner, patient organ affected by some medical condition, etc. For the physician it is important to have accurate geometrical model of the patient organ(s), in both cases. When data is complete, that is not so hard to achieve, but in the cases, where is lack of data, the problem arise. To improve model creation process in both cases, and specifically in the second case, authors of this chapter developed the Method of Anatomical Features (MAF), which brings new modern techniques combined in one method for the creation of geometrically accurate, and anatomically and morphologically correct 3D models of human bones. MAF is the focus of this chapter, and in the following sections it will be explained in detail.

This chapter is organized as follows. In the following Sect. 2.2, introduction to computer graphics important for MAF is presented; In Sect. 2.3 medical imaging is described; State of the art in the bone remodeling methods is presented in Sect. 2.4; Sect. 2.5 provides insight into human skeletal system; In Sect. 2.6, MAF description is provided, which includes: Anatomical and morphometric aspect of the human bones and the Method application on the femur bone. The conclusion is presented in the final Sect. 2.7.

[2] https://www.dicomstandard.org/.

[3] https://clearcanvas.github.io/.

[4] https://www.slicer.org/.

2.2 Definition of the Important Topics

Computer graphics is a field in computer science in which visual content is created, with the application of appropriate methods and with the use of computer technology. Computer graphics involves the visualization of two-dimensional content (e.g., photographs, images), as well as three-dimensional content (e.g., 3D presentation of objects).

Computer model—Computer representation of physical objects. A computer model can be the visualization of a physical object shape (e.g., a 3D model of a house displayed on a monitor screen) or for example a graphical presentation of a change in temperature in area over a period.

Geometrical modelling—A scientific field in which the application of various methods and algorithms defines a mathematical description of the geometry, topology, and shape of physical objects.

Geometrical models—Geometrical models are a special group of computer models created through the application of geometric modelling. The basic classification of geometric models is into 2D models that allow the display of objects in 2D space and 3D models that allow 3D visualization of physical object shapes. 2D models are widely used in mechanical engineering (e.g., technical drawings), construction (e.g., building plans), electronics (e.g., electrical diagrams). 3D models are applied in CAD, but also in construction (e.g., 3D visualization of houses, buildings) and entertainment industries (e.g., computer games, movies).

Computer-Aided Design (CAD)—Methods involving the use of computer techniques to create, modify, optimize, and analyze objects. In mechanical engineering, the term CAD refers to the creation of geometric models of machine elements and assemblies, both in 3D and in 2D. Software packages used to create such models are CATIA, Solid Works, PRO/Engineer, etc.

CAD models—Geometric models created using CAD methods. There are several types of such models and some of them are:

- *Point cloud model*—A model in 2D or 3D space whose boundaries are defined by points. Each point is defined by coordinates in Euclidean space.
- *Wireframe model*—A special type of model that defines the edges (lines) between points in space. This model can be used as a preview of more complex types of models because it takes up fewer computing resources.
- *Polygonal model*—A model in which the boundary surfaces of an object are defined by polygons. Polygons are defined as planar objects bounded by edges. A set of polygons defines a polygonal model. Polygons are usually of the triangle type, but they can also be defined with several edges. Polygonal models nowadays, in addition to their application in mechanical engineering, are also widely used in computer graphics in the entertainment industry (computer games, movies).
- *Surface model*—A model that describes the boundary surfaces of objects. NURBS (Non-uniform Rational B-Splines) curves, polygonal models and Subdivision Surfaces are commonly used as elements to enable this.

- *Volumetric model*—A model that defines the volume of an object, both inside and outside. Usually defined by discretely sampled 3D set.
- *Solid model*—Solid models contain information about the edges, faces, and the interior of the physical objects. This type of model has a wide application in additive manufacturing, machining, and stress–strain analysis.
- *Parametric model*—Mathematical model which geometry is described with a set of parametric function. By changing input parameters, the shape and size of modeled object is changing.
- *Generic models*—These models can be defined as global geometrical models applicable to the whole specific domain. The application to the specific entity in the domain is achieved by using entity properties defined as input arguments of the generic model. The CAD parametric model is one of the examples of generic model.

Computer-Aided Manufacturing (CAM)—Methods that involve using computer techniques and computer equipment to control the operation of machine tools and process machine and other parts. The main purpose of the mentioned methods is to improve the accuracy of processing and on the other hand to speed up the whole process of production of parts.

Computer-Aided Engineering (CAE)—Methods that involve using of computers and appropriate software to analyze and predict behavior of physical object in real word. Programs for the finite element analysis and computational fluid dynamic are typical representatives.

Medical Image Processing (MIP)—A set of methods and algorithms that can be used to process medical images obtained by radiological methods. By applying these methods, it is possible to obtain a volumetric model of the human musculoskeletal system, in which the patient is scanned using computed tomography.

2.3 Medical Imaging

Medical imaging is a technique and procedure of imaging the inside of the body for clinical analysis and medical intervention, as well as a visual presentation of the function of some organs or tissues (physiology). Medical imaging seeks to reveal the internal body structures, as well as to diagnose and treat diseases. Furthermore, medical imaging allows the creation of a database of normal anatomy and physiology to enable the detection of abnormalities. Medical imaging devices can be grouped by the technologies that they use (X-Rays, Ultrasound) and may include X-ray radiography, magnetic resonance imaging (MRI), ultrasound, endoscopy, elastography, positron emission tomography (PET) and single photon computed tomography (SPECT). It may also include measurement and recording techniques that are not primarily intended for imaging, such as electroencephalography (EEG), magnetoencephalography (MEG), electrocardiography (ECG). Medical imaging procedures result in various data which can be stored for later use. For example, CT devices can provide large amounts of information for the whole human body as visual 3D representation of the organs. Another example is MRI, which uses magnetic fields to create 3D visualization of organs.

2.3.1 Devices for Diagnostics, Monitoring and Therapy

Radiology can be defined as the science of radiation, where radiation includes emissions of different types of waves (gamma rays, X-rays, etc.), with application for medical purposes for diagnosis and therapy of the patient.

Radiological methods—There are various radiological methods used to diagnose the condition of patients, and some of them are**:**

- X-ray—The most common form of acquisition of patient body data when X-rays are used to create images. The procedure is invasive, and it is not desirable for regular check-ups, because X-rays are ionizing. During imaging, the patient is placed between the emitter and the detector. Recording is performed by emitting a short X-ray pulse, whereby the detector captures different levels of energy transmitted through the patient's body. In the resulting image, organs that absorb more X-ray energy are shown in a lighter (white level) shade of grey (e.g., bone), and those that have less ability to absorb X-rays are represented as a darker shade of grey (e.g., soft tissue).
- Computed Tomography—A method of medical imaging that provides information about the internal structure of the human body. The patient is imaged on a CT scanner, which uses X-rays to acquire data about the patient's body. The recording process is performed by rotating the X-ray source and the receiver around the patient's body (during which it is possible to move the table on which the patient lies, so-called spiral scanning) and by recording the amount of absorbed energy as in the case of classic X-ray machines. During the scanning process, many individual 2D images (cross-sections) of the patient's body (or a certain part) are formed. A virtual 3D model can be created with the use of appropriate software. Due to the use of X-rays, CT is one of the invasive radiological methods.
- Magnetic Resonance Imaging—Data acquisition that is very similar to tomography (2D images of cross-sections of the patient's body are also formed), with the important difference that instead of X-rays, this technique uses magnetic fields and radio waves. Due to the nature of the waves that are used, MRI unlike CT is not an invasive method. MRI is mainly used for imaging soft tissues, but it is also possible to use MRI for imaging bones (although it is better to use CT for the bone and joint system).

2.3.2 Organ and Process Modeling

Organs and processes modelling is based on the application of medical and CAE (Computer-Aided Engineering) software for the creation of a medical process model, or a 3D CAD model of the organ. Furthermore, organ modelling can be defined through the creation of a 3D model of a human organ by using geometrical modelling software, like CAD. It is extremely hard to design a geometrical model of human organs, because of their very complex shape, other methods are used. The most used method is the reverse modelling method which is based on the medical imaging outputs. This method is a part of reverse engineering (RE), which can often be applied in medicine. It is important to note that the RE method depends on the output from medical imaging methods, i.e., the better the input model is, the better the output CAD model will be. The resulting models can be used for various purposes, such as diagnostics, preoperative planning, Computer-Assisted Surgery (CAS), etc.

Process simulation can be carried out in software for Finite Element Analysis (FEA). The CAD model of the human organ, which can be used for the simulation of the process, is usually acquired from CAD software, or in some cases from medical software. Materialise Mimics as medical software has the capabilities to perform basic meshing of models for later FEA analysis. Process modelling can also be used for modelling the cardiovascular or other dynamic systems, when there is a requirement to simulate blood flow, or implant insertion (like stent).

2.4 Related Research

Geometric models of human bones are of high importance in modern medicine and anthropology and other related sciences. The possibilities of applying high-quality geometric models which, according to their geometric, topological, anatomical and morphological characteristics, correspond to physical models of human skeletal bones, are diverse. Computer-Assisted Surgery (CAS) is one of the most common applications of computer-generated geometric models (Adams et al. 2002; Gomez et al. 2021). The application of geometrically accurate models enables the correct preparation and execution of the surgical intervention using appropriate computer, different techniques, and software tools, and reduces the possibility of error. The basic components of a CAS can be: a console operated by a surgeon and through which it controls mechanical components (e.g., a robotic arm); mechanical arm with an endoscopic camera and surgical instruments; auxiliary equipment (pumps, sensors, etc.). A comparative review of conventional methods and CAS is given in Weng et al. (2009). Based on the facts presented in this paper, it can be concluded that the new technique of performing surgical procedures, i.e., surgical interventions, can significantly improve the quality of the procedure itself and significantly improve the patient's recovery. The same paper presents the application of CAS in bilateral Total Knee Arthroplasty (TKA), which is also one of the possible applications of geometric models. When performing such an intervention, it is very important to achieve the correct orientation of the knee components, which is a measure of the success of the operation. If the geometric models of bones, muscles, and other tissues are properly constructed, then the CAS will be successfully realized.

As already mentioned, CAS also includes preoperative planning of surgical procedures. Preoperative planning usually involves the use of appropriate models of human organs in certain software, which allows the surgeon to plan the course of surgery to a certain level, which is defined by the limitations of the applied software. The advantages of using preoperative planning are described in other studies (Hak and Rose 2010). Preparation of surgery includes:

- Simulation of the procedure with all the necessary elements such as fixators, implants, bone and other tissue models, and other auxiliary elements (screws, needles, couplings, clamps, etc.)
- Fully defined surgical procedure with all clearly defined guidelines as well as the members of the surgical team who will perform them.
- Clearly defined logistics of the surgical procedure with all the necessary instruments and other surgical equipment identified.
- Clearly defined responsibility of each team member for each procedure that must be performed during the procedure.
- All other actions that precede the execution of surgical (orthopedic) intervention.

The application of CAS in orthopedics is presented in the work of Young et al. (2013), in which the authors define the application of CAS in sports medicine (e.g., application in knee surgery). The application of CAS in orthopedics is defined through a specific area which is defined as Computer-Assisted Orthopedic Surgery (CAOS), (Sugano 2013; Min et al. 2021). Sugano (2013) explains the use of CAOS and the advantages and disadvantages of its application in total hip arthroplasty (THA). Weber (2014) defines a novel rigid point set registration (PSR) approach that aims to accurately map the pre-operative space with the intra-operative space to enable successful image guidance for surgery. It can be concluded that CAOS has the greatest application in joint surgery, bone fractures and spine surgery, which of course does not prevent its use for other purposes, such as: remediation of various bone diseases (e.g., osteoporosis, bone tumors) using appropriate implants (tissue matrices, fixators, etc.) (Young et al. 2013; Sugano 2013; Min et al. 2021).

Geometric models of human bones created in the already mentioned way can find their application in the field of Virtual Anthropology (VA). VA is a field that deepens comparative morphology, and sets the interconnections between anthropology, mathematics, statistics, engineering and all other fields of science and technology, aimed at digitization of observed objects (e.g., fossil specimens). Within VA, advanced statistical methods, computer graphics and information technologies are applied in order to obtain geometric, topological and morphological data about the observed object (e.g., fossil specimens). A detailed description of virtual anthropology (VA) and the methods used in this field of research is further described in other studies (Weber 2014; Benazzi et al. 2009).

2.4.1 Geometrical Modelling of Bones

Geometric bone models can be used for various purposes, as mentioned above. However, before applying them, it is necessary to create them. There are different methods of creating a geometric model of bones, and the fundamental division can be made based on the modeling approach, namely (1) RE and (2) direct modeling.

RE is the common way in which bone models are created, while direct modeling is less commonly used. RE involves acquiring bone data using a medical scanner (volumetric—CT, or 2D such as X-ray), processing the data, and constructing a bone model (Filippi et al. 2008). Direct modeling involves the use of various technical elements of appropriate CAD packages to construct bone models and is based on conceptual design and known anatomical/morphological and topological characteristics. It is mainly used to visualize skeletal models or the human body as a whole. An example of a web application for visualizing the human body is the application "ZygoteBody", formerly known as "Google Body", which provides a spatial representation of the organs of the human body. Regardless of which approach is applied, modeling can be performed with complete and incomplete data on bone geometry, anatomy/morphology, and topology. Complete data include all necessary geometric, anatomical and topological data that enable the correct formation of 3D models of a particular human bone. Incomplete data do not contain enough data to form a complete bone model, but only a specific part of bone (Stojkovic et al. 2010; Vitkovic et al. 2013). The software system that provides support for the modelling of bone with complete and incomplete scanned data is shown in the study by Filippi et al. (2008), and the procedure for the creation and implantation of the part of the sternum bone and ribs, based on the incomplete bone data due to the tumor, is presented in Stojković et al. (2010).

2.4.2 Creating 3D Bone Models Using Methods Based on Complete Bone Data

Complete Data-based methods commonly involve use of volumetric scanning methods to acquire geometrical and topological data of bone(s). Volumetric scanning methods include methods that enable a three-dimensional display of bones and models of other human organs. The most widely used methods today are CT and MRI. Tomography involves scanning sections of a certain thickness, the so-called scanning by slice. CT is a standard volumetric and tomographic method based on X-rays and is mainly used to scan patients "in vivo" (Filippi et al. 2008; Benazzi et al. 2009; Weber 2014; Min et al. 2021), although it is possible to apply "in vitro" (Min et al. 2021). ST is mainly used to acquire data on higher density organs, such as bones, teeth, although objects such as stones, ammunition, and others can also be scanned. Unlike CT, MRI is used in cases when it is necessary to scan patients with a lower dose of radiation. MRI uses harmless electromagnetic radiation, caused by a strong magnetic field. The type of radiation is limited by the scanning area, which is mainly soft tissue, although in special cases it can also be used to scan bones, specifically the skull (Brown and Semelka 2010; Min et al. 2021).

As a result of the CT and MRI scanning process, 2D sections of a certain thickness are obtained, which together form a 3D volume. Each 2D cross section consists of two-dimensional raster elements called pixels (Min et al. 2021). By adding the thickness of the cross section, 3D elements called voxels are formed. Voxels carry information about the X, Y, Z position in 3D space and other important information, including the value of the shade of gray. Organs of different material densities transmit rays differently, so that the result is a different shade of gray in 2D images. There are two basic resolutions that are defined in CT and MRI scanners: spatial and contrast. The size of the voxel defines spatial resolution, and since voxels are three-dimensional elements, this resolution can be different in three different directions. Generally, spatial resolution is defined in the section plane (2D image plane) and in depth (section thickness). Contrast resolution is defined by the number of gray levels that can represent the mean tissue density in a single voxel. MRI has better contrast resolution, while spatial resolution is higher with CT scanners. The cross-sectional thickness conditions the spatial resolution and in CT scanners it generally ranges from 0.5 mm to 1 mm. The lowest resolution can be achieved on μCT scanners where a resolution of up to 100 μm can be achieved (Noser et al. 2011; Rathnayaka et al. 2012; Min et al. 2021). As for the resolution in the 2D cross-sectional plane, the resolution usually ranges up to 512 × 512 pixels in CT and up to 1024 × 1024 in MRI, although the resolution has recently increased with new ways of creating scanners. Contrast resolution depends on the number of bits that can be stored per pixel. If it is necessary to create high-contrast images, then the number of bits per pixel must be higher. For example, for CT it is 12 bits, i.e., $2^{12} - 1$ different levels of gray, in order to register all the necessary values of ST numbers (Bushberg 2002; Brown and Semelka 2010). An important feature of volumetric scanners, which refers to the image quality, is the pixel size. The pixel size is determined by the ratio between the real dimension of the scanned object (the distance between two points) and the number of pixels in 2D image between those two points. The size of the image is determined with FOV (Field Of View), which is a characteristic of the scanner, and for example if the FOV is 25 cm, and the number of pixels in the image is 512 × 512, then the pixel size is 25/512 = 0.048 cm = 0.48 mm. Number of columns and rows, i.e., the number of pixels, is defined by the scanner matrix.

All the above parameters depend on the design of the volumetric scanner itself and the algorithms applied for image processing (Bushberg 2002; Goldman 2007). Images formed in 2D sections consist of pixels with different values of gray levels, i.e., with clearly defined scalar value. The scalar value corresponds to the so-called CT number defined as a linear transformation of the value of the attenuated radiation coefficient when imaging on volumetric scanners in radiology (Noser et al. 2011). This means that it is possible to form pixels (voxels) in adjacent sections that have the same CT number values at the basic level. The presented feature enables volumetric and surface reconstruction of scanning objects. Volumetric reconstruction involves showing the volume structure of the scanning object, while surface reconstruction involves showing the envelope of the surface of the scanning object.

Surface reconstruction using 2D contours is based on methods that can generally be divided into methods that create polygonal models by using contours in adjacent planes (tiling), and methods that use surfaces defined with iso-curves on basis of the volumetric model (the so-called indirect method) (Majstorović et al. 2013). The first method is described in more detail in the dissertation of Zsemlye (2005) as well as in the work of Fuchs et al. (1977). This method involves several processes:

1. Joining the appropriate contours—Determining which contours are connected and in what way. If there are several contours along the plane of the section, then topological problems in the connection can occur, which are solved by using prior knowledge about the object.
2. Joining the vertices of contours into polygons—Polygons are usually triangles that contain one edge of the contour and two edges that connect two adjacent contours.
3. Solving branching problems—This problem occurs if it is not possible to clearly identify the vertices that join in adjacent planes, and this happens in situations where there are a different number of contours. In such cases, there is a one-to-one connection, and the problem is often solved by adding additional segments to form multi-contour to multiple contours, or one contour to one contour. In principle, as in the first step, if there is prior knowledge about the object to be reconstructed, then the problem of branching is reduced.
4. Surface display is performed by shading the polygon. The more polygons, the better the surface, but it requires more computer power for further processing. It is possible to introduce parametrically defined surfaces (NURBS surfaces) into appropriate CAD software packages, which would include the vertices of the polygon.

The second method (indirect method) is based on the creation of so-called binary masks over the volume model expressed through unit elements of volume, i.e., voxels. In this method, it is necessary to find a certain iso-surface with a defined value, i.e., it is necessary to find voxels that contain a given iso-surface. Based on the appropriate segmentation, it is possible to make a detailed delineation of the anatomical entities of the human body based on the value of the CT number, i.e., to define the value that defines the iso-surface. For example, it is possible to visualize the enveloping surface of the cortical bone because it is known that the CT number for that part of the bone is around 3000 HU (Hounsfield Unit). Extraction of such iso-surfaces is performed using the marching cubes algorithm (Raman and Wenger 2008; Wang et al. 2020).

Volumetric reconstruction includes methods based on volumetric shading (Noon 2012; Liang et al. 2019). Volumetric shading, in contrast to surface reconstruction, also includes the definition of volume, i.e., it enables the display of objects that are above and/or below the observed surface. This is made possible by adding RGBA (Red–Red, Green–Green, Blue–Blue, Alpha–Transparency) components to the voxel. The given components define a certain color and transparency of the voxel, and it is possible to completely visualize the human body, i.e., the object of scanning by depth. The methods used today for volumetric shading are: Maximum/Minimum Intensity Projection, Multi-Planar Reconstruction (MPR), as well as all other reconstructions under Volume Rendering Reconstruction (VRR) (Cavalcanti et al. 2021; Noon 2012). Maximum/Minimum reconstruction defines a 2D projection of a 3D object as a set of pixels with a maximum / minimum value, which are projected in the direction of a defined view of the projection plane. Multi-plane projection is a method of volumetric shading that enables the formation of a 2D projected view based on cutting a set of 2D sections in one of the normal planes (middle, frontal) in relation to the axial plane (plane of 2D images). It is possible to use a projection of maximum or minimum intensity to define the display. These methods enable the visualization of the organs of the human body with a defined shading by depth, i.e., volume. In this way, it is possible for the surgeon to make certain conclusions related to the patient's condition by analyzing the volumetric model. Based on the CT number value, it is possible to distinguish bones from other organs of the human body by segmentation and forming adequate 3D models (polygonal, surface, volume) using techniques such as marching cube technique. 2D images obtained by volumetric scanning can be processed directly in the scanner software, or in specialized software designed to process the given images (e.g., 3D Physician, Materialize Mimics, etc.). In general, specialized software provides more options for processing scanned images and allows the application of the reconstruction methods mentioned earlier. To exchange scanned data in medicine, the mentioned DICOM format is used. DICOM is a defined standard (or format) for textual and graphic data exchange in medicine (Tashiro et al. 2014). Using the DICOM format, it is possible to transfer patient data from the volumetric scanner to the appropriate specialized software. By performing reconstructive methods, it is possible to create adequate models that can be used for visualization, or for post-processing if the software has adequate modules (e.g., Materialize Mimics enables FEA and preparation of models for processing with AT) (Tashiro et al. 2014).

In addition to specialized medical software, the processing of geometric models can also be performed using CAD software packages. In CAD, the most common way to form geometrically defined models from CT or MRI is to export segmented polygonal models from specialized medical software in an adequate format (usually STereoLithography—STL), and their further processing in CAD software (Stojković et al. 2010; Vitković et al. 2013; Majstorović et al. 2013). The main feature of CAD applications is the use of NURBS surfaces to define the envelope structure (surface model) of certain Free Form Surfaces. For example, bones are typical representatives of free-form objects due to their complex topology and geometry. Therefore, they are used to form geometric models of the bone-joint system (Ciocca et al. 2012; Majeed et al. 2017), use parametric surfaces (NURBS). The technical elements of CAD software can be used to define the geometry of imported models in detail and thus enable subsequent operations with models such as: creating FEA models, creating physical models with AT, creating adaptive fixators and implants, making missing bone parts (McCullough et al. 2006; Vitković et al. 2013; Stevanović et al. 2013; Veselinovic et al. 2013).

2.4.3 Creating 3D Bone Models Using Methods Based on Incomplete Bone Data

In clinical practice, it is very common that it is not possible to obtain complete data about scanned bone, which creates a problem in building a 3D model of a complete bone or some part of it. The reasons can be that the bone is affected by some pathological process (e.g., osteoporosis, tumor) or trauma (e.g., bone fracture). In such cases it is not possible to perform a volumetric scan, or it is possible to make only one or an insufficient number of 2D images (e.g., X-ray, ultrasound). In such cases, it is necessary to define/apply a procedure or method, which application can enable reconstruction of a complete 3D model of a bone or a certain part of a bone. The basic division of currently applied methods can be done according to the method of creation, into methods based on a generic (template) model, and those based on other techniques (Filippi et al. 2008). In general, it is difficult to define a strict classification, because most approaches are based on methods connected to both cases. Methods based on a template model mainly use statistical bone models, parametric bone models (which in most cases can be classified as statistical), methods that use the FFD (Free Form Deformation) approach, or a combination of these models or methods. Statistical bone models are formed over set of input bone models (Lorenz and Krahnstöver 1999; Benameur et al. 2003; Zheng et al. 2012). The given models are created based on statistical methods and enable the prediction of the geometry and shape of the bone of a certain patient. These models adapt to the patient geometry and anatomy by applying certain values acquired from medical images. An example of creating a statistical-parametric model based on quadric surfaces is provided in Sholukha et al. (2011). This is a typical example of using statistics to form a model that can be modified depending on certain morphometric parameters (and even other parameters), acquired mostly from medical images. Statistically based models such as ASM (Active Shape Models) (Cootes et al. 1995; Montufar et al. 2018), are used for iterative deformation and to fit the statistical model with the subject model (e.g., X-ray image). Their application in radiography is given in study by Montufar et al. (2018), where novel technique for automatic cephalometric landmark localization on 3-dimensional (3D) cone-beam computed tomography (CBCT) volumes by using an active shape model to search for landmarks in related projections is presented. The other approach can be application of "smart" template model, where neural networks are trained by using a combination of CT and X-ray data, to predict bone (radius and ulna) shape based on patient radiographs (Shiode et al. 2021).

FFD methods are based on the use of a mesh model defined over a certain control volume (e.g., parallelepiped) and subsequent deformation of a given model by changing certain parameters (Filippi et al. 2008; Chenna et al. 2018). In general, FFD models adapt to an input model by deforming the control volume grid to fit the boundaries of the input model, which can be a 2D X-ray image of bone in a particular projection (Gunay and Shimada 2004; Gunay et al. 2007). A technique like the above (FFD) is a technique in which a previously created template CT image is deformed based on parameters read from X-rays (Lee et al. 2008).

There is a possibility of using the database of previously created bone models (Matthews et al. 2009) or fracture models (Sourina et al. 2000). Such models can be used for various purposes, such as creating composite bone models, planning, and simulating orthopedic interventions and the like.

Methods that are not based on a template model mainly use contour projections and certain curves in those projections. Typical examples are the creation of cross sections based on a predefined projection in a certain plane (e.g., Anterior–Posterior–AP plane) (Filippi et al. 2008; Kasten et al. 2020). An example of such a reconstruction is the creation of 3D models based on anatomical characteristics and contours created over X-rays as shown in the work of Gamage et al. (2009).

In conclusion, it is essential to note that it is difficult to make a general classification because often a combination of certain methods is performed to create a geometrically accurate and anatomically/morphologically correct model of a complete bone.

2.5 Anatomy of the Human Bones

Patient-specific bone modeling is considered an important tool for diagnosing and treating skeletal disease and for clinical research aimed to develop different types of treatments that differ for each patient. Therefore, it is necessary to perform parameterization of the bone, which requires excellent knowledge of anatomy, morphological, structural, and developmental characteristics of the bones and their anatomical variation. For this reason, this section of the chapter contains short overview of general osteology with the aim to explain an important aspect of the bones to biomedical engineers.

The science concerned with the study of bones is termed osteology. Bones, joints, and muscles are the components of the locomotor system. Bones and joints are the passive part of the locomotor apparatus. Its active part are the muscles attached to the bones.

2.5.1 Human Skeleton

The skeletal system of an adult is composed of 206 bones, and it is divided into axial and appendicular parts (Table 2.1).

The axial skeleton consists of 80 bones that form the axis of the body. It supports and protects the organs of the head, neck, and trunk. The components of the axial skeleton are skull bones, auditory ossicles, hyoid bone, vertebral column (vertebrae) and the bones of the thoracic cage (sternum and ribs) (Adams 2015; Moore et al. 2019; Salhotra et al. 2020).

The appendicular skeleton is composed of 126 bones of the upper and lower limbs and the bones of the bony girdles (pectoral and pelvic), which anchor the appendages

Table 2.1 Division of the human skeleton

Type of skeleton		Number of bones
Axial skeleton	Skull bones and hyoid bone + auditory bones	23 + 6 = 29
	Vertebral column	26
	Sternum and ribs	25
		80
Appendicular skeleton	Bones of the upper limb	64
	Bones of the lower limb	62
		126
Axial skeleton + Appendicular skeleton		**206**

to the axial skeleton. The bones of the shoulder girdle are the scapula and clavicle. The bones of the upper limb are humerus, ulna, radius, and bones of the hand. The bones of the pelvic girdle are the hip bones (sacral bone made of the five fused sacral vertebrae is the part of the vertebral column and pelvic girdle). The bones of the lower limb are femur, tibia, fibula and bones of the foot (Adams 2015; Moore et al. 2019; Salhotra et al. 2020).

It should be noted that the bones are extremely dynamic, living organs, specifically vascularized and innervated. The bones change during growth, aging, but also due to some pathological process by which they are affected. The bones show numerous morphological and structural variations that depend on the sex, age, race, genetic and endocrine status and health condition of a particular person.

2.5.2 *Morphological Characteristics of the Bones*

According to the shape the bones are classified on long, short, flat, irregular, pneumatic and sesamoid.

The long bones (*ossa longa*) have a particularly pronounced one dimension—length, which is considerably more pronounced than the other two—width and thickness. They are the parts of the upper and lower extremities. The main parts of a long bone are: middle part called diaphysis or the body (*lat.corpus*) or the shaft and two ends called epiphysis. Between the diaphysis and epiphyses is the metaphysis**,** which represents a part of bone which grows most intensively. The diaphysis is made up mostly of compact bone, externally and medullary canal/cavity with bone marrow internally. The epiphyses are made mostly of the spongy, cancellous bone.

In the short bones (*ossa brevia*) none of the dimensions is particularly conspicuous. The short bones are carpal and tarsal bones. They have only a thin layer of compact bone surrounding a spongy interior.

Flat bones (*ossa plana*) have one dimension (thickness) much smaller of the other two (width and length. The structure of flat bones is very specific: their external and internal surfaces are lined with a layer of compact bone tissue *(lamina externa and lamina interna*), and between them is a layer of spongy tissue, called *diploë*. The examples of the flat bones are occipital, parietal, frontal, nasal, and lacrimal bones, vomer, scapula, sternum, ribs and the bones of the roof of skull (*calvaria*).

Irregular bones (*ossa irregularia*) as implied by the name, have an irregular shape due to their many centers of ossification They consist of thin layers of compact bone surrounding a spongy interior. Examples include the facial bones (*viscerocranium*), ethmoid and sphenoid bone, vertebrae and the hip bones.

Pneumatic bones (*ossa pneumatica*) contain cavities filled with the air and lined with mucous membrane. This group includes mastoid cells in mastoid process of the temporal bone (*cellulae mastoideae*), but also the paranasal sinuses made by invagination of the respiratory mucous membranes of the nasal cavity into the adjacent bones: frontal, maxillary, sphenoid and ethmoid sinuses.

Sesamoid bones (*ossa sesamoidea*) have the shape like sesame seeds. They are embedded in the tendons of some muscles and hold the tendon further away from the joint at the sites of the high pressure and friction between the tendon and the bone.

In the leg, the largest permanent sesamoid bone is the patella that develops in the tendon of quadriceps femoris muscle, while fabella, often exists in the tendon of the lateral head of gastrocnemius muscle.

The bones not constantly present, sutural bones (*ossa suturalia*) and fonticular bones (*ossa fonticulorum*), are not included in the classification according to the shape of bones. They are classified according to the position.

Knowledge of the morphological variation of bones are very important, especially in orthopedic surgery, but also in the radiology, because of their proper description and avoidance of diagnostic errors (Adams 2015).

2.5.3 Morphological Elements of Bone Surfaces

The bone surface is morphologically specific. It has numerous prominences (articular and non-articular), depressions/impressions (articular and non-articular) as well as various openings (Table 2.2) (Adams 2015).

2.5.4 Structure of the Bone

The components of the bone structure are: (a) bone tissue - compact and spongy and b) bone marrow (*medulla osium*) (Florencia-Silva et al. 2015). Bone tissue is specialized supporting connective tissue, made of (a) bone cells (osteoprogenitor, osteoblasts, osteocytes and osteoclasts) and (b) extracellular mineralized matrix (ECM). Bone is a metabolically active tissue composed of four types of bone cells: osteoprogenitor, osteoblasts, osteocytes and osteoclasts (Rančić and Nikolić 2007; Lačković 2014; Mohamed 2008).

Table 2.2 Morphological elements on the bone surface

Prominences		
Name	Definition	Example
Articular prominences		
Condylus	Wide rounded articular prominence	Condylar procesus of mandible
Head	Prominent round articular end of proximal epiphysis	Head of femur
Trochlea	Pulley, cylindric part of bone	Trochlea of humerus
	narrowed in the middle	
Non- articular prominences		
Linear		
Linea	Elongated, narrow edge/protrusion	Linea aspera (femur)
Crest	Ridge or more protruding edge	Iliac crest (hip bone)
Round		
Tubercule	**S**mall round extension	Greater tubercle (humerus)
Epicondyle	Bone structure above condyle	Lateral epicondyle (humerus)
Tuber	Large round extension	Ischial tuberosity (ischium)
Trochanter	Pronounced bump	Greater trochanter (femur)
Protuberance	Irregular circular bulge	External occipital protuberans
Sharp		
Spine	Spike, spike-like process	Spine of scapula
Process	Any bony extension	Styloid process of radius
Impressions		
Articular impressions		
Acetabulum	A hemispherical impression shape of a Roman wine glass	Acetabulum (Hip bone)
Cavity	Shallow, articular impression	Glenoid cavity
Fovea	**A** small shallow depression	Articular fovea (radius)
Fossa	Pit, deeper depression	Articular fossa
Incisure	Notch in an edge or surface	Ulnar incisure of radius
Non-articular impressions		
Impression	shallow, rough **impression**	Maseteric impression (mandible)
Sulcus	Groove on bone surfaces for passage of blood vessels or nerves	Intertubercul groove (humerus) Sulcus of subclavian artery (1st rib)
Fissure	Split between two bones or passage of blood vessels and nerves	Superior orbital fissure
Fossa	Pit, depression	Fossa coronoidea (humerus)
Incisure	Notch on the bone	Scapular notch
Foramens		

(continued)

Table 2.2 (continued)

Impressions		
Foramen	Opening, hole on the bone for passage blood vessels and nerves	*Foramen magnum* (*occipital bone*)
		Foramen rotundum (sphenoid bone)
Canalis	The bony canal that runs through the bone	Hypoglossal canal
Meatus	A canal that enters the bone but does not pass through the bone	Internal acoustic meatus (temporal bone)
Sinus	Pneumatic cavity in the bone, filled with air and coated with mucose membrane	Maxillary sinus

Osteoprogenitor Cells Osteiprogenitor cells are dormant bone cells that coat the internal layer of the periosteum, endosteum, medullary cavity and the Haversian and Volkman's canals. They originated from the mezenhimal cells and have potential to differentiate into the osteoblasts.

Osteoblasts Osteoblasts are young bone cells responsible for the formation and mineralization of the extracellular matrix. An unmineralized bone matrix is called osteoid. Osteoblasts synthesize all osteoid components (collagen type 1, proteoglycans, glycoproteins). When an osteoblast become completely surrounded by osteoid, it become osteocytes.

Osteocytes Osteocytes are mature, immobile bone cells"trapped" in a solid intercellular substance. They synthesize a minimal amount of extracellular matrix to maintain bone structure, transmit mechanical stimuli, and mediate bone remodeling.

Osteoclasts Osteoclasts are large multinucleated cells that resorb bone tissue. They are situated on the surface of bone tissue on the places where bone is decomposed. By erosive action they make shallow depressions on bone surface, so-called Howship's lacunae. The activity leads to an increase in the concentration of calcium ions in the blood which supply osteoclasts situated in—*Howship's lacunae*. The osteoclast attaches to the bone through integrin which bind to specific bone glycoproteins of the bone matrix (bone sialoprotein, osteonectin). Bright zone does not contain organelles, but it has multitude of actin filaments which help integrins to maintain contact with the bone matrix, narrow subosteoclast space. By the action of osteoclasts, in this space, a specific, acidic microenvironment, which affects demineralization of bone and decomposition of its organic components is created (Rančić and Nikolić 2007; Lačković 2014; Mohamed 2008).

Extracellular Matrix of Bone Tissue Extracellular matrix of bone tissue is composed of the organic and inorganic part.

Organic part synthesized mainly by osteoblasts makes 35% of the extracellular matrix. It is composed of the collagen fibers (type I) (90%), glycosaminoglycans (chondroitin sulfate, keratin sulfate, hyaluronic acid) glycoproteins or non-collagen proteins (osteocalcin, osteopontin, and osteonectin), grow factors (bone morphogenic protein, BMPs) and cytokines.

Inorganic part of the bone matrix (65%) is composed of the calcium and phosphorus ions that form hydroxyapatite crystals. Mineralization of the extracellular matrix is binding of hydroxyapatite crystals to collagen fibers, where the crystals, with the participation of glycoproteins, bind at the sites of intermolecular lateral gaps, between tropocollagen molecules (Florencia-Silva et al. 2015).

Bone Marrow (medulla osium) Bone marrow is soft, gelatinous tissue that fills the medullary cavities of bones. There are two types of bone marrow, red and yellow. Red bone contains hematopoietic stem cells. These are blood-forming stem cells. Yellow bone marrow contains mesenchymal stem cells, or marrow stromal cells. These produce fat, cartilage, and bone (Florencia-Silva et al. 2015).

2.5.5 *Bone Development*

Process of bone formation is called osteogenesis or ossification. There are two types of ossification: intramembranous and endochondral (Rančić and Nikolić 2007).

Intramembranous or direct ossification begins between 6 and 12 weeks of the intrauterine development. At the site of the future bone, a condensation of mesenchymal cells which form connective tissue membranes is present (Fig. 2.1). Osteoblasts migrate to the membranes and deposit bony matrix around themselves. Most of the bones in the human skeleton, such as certain flat bones of the neurocranium, viscerocranium and partially the clavicle, are formed in this manner (Rančić and Nikolić 2007).

Endochondral or indirect ossification begins in the third month of the intrauterine development. Condensed mesenchymal cells differentiate into chondroblasts that form hyaline cartilage. On that way the future bones are first formed as hyaline cartilage models. The blood vessels and osteoblasts infiltrate the perichondrium that surrounds the hyaline cartilage "model of the future bone". The osteoblasts form

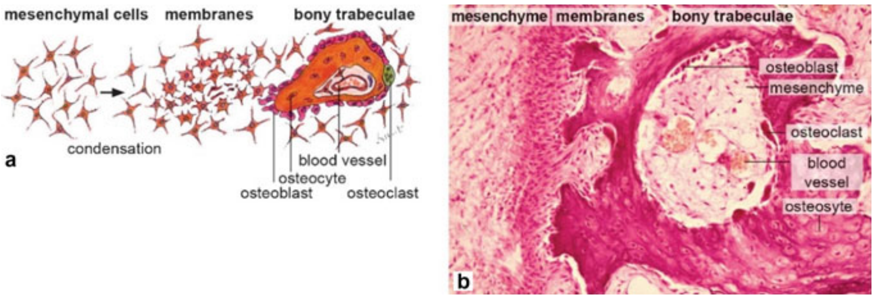

Fig. 2.1 Direct (intamembranous, endesmal ossification). **a** Condensed mesenchymal cells form membranes that mineralized and form trabeculae; **b** histological structures in the area of bone formation by direct ossification (© Copyright 2007 Data Status, all rights reserved)

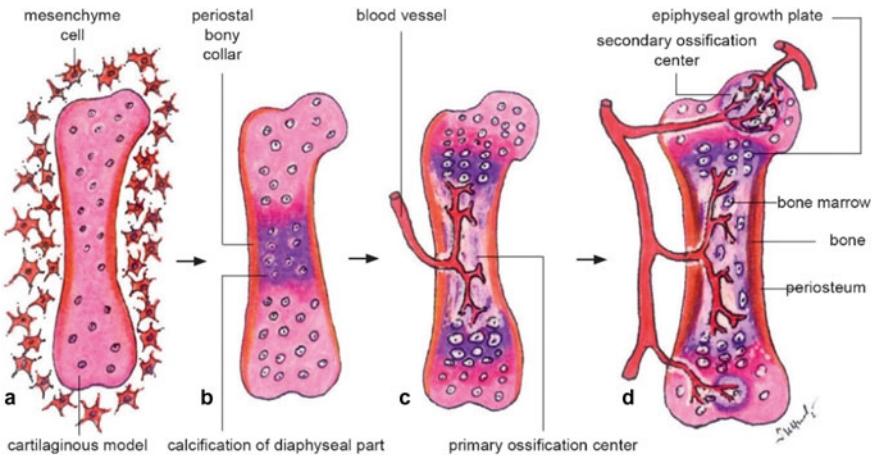

Fig. 2.2 Indirect (enchondral) ossification during the formation of long bones. **a** Hyaline cartilage model of the bone is formed by condensation and differentiation of the mesenchyme cells (central) part of the osteocyte; **b** diaphyseal (central) part of the hyaline cartilage model calcified; **c** from the periosteum, a blood vessel (vascular bud) enters in the diaphysis of the cartilaginous model, where the primary ossification center is formed; **d** creation of the secondary (epiphyseal) ossification centers (© Copyright 2007 Data Status, all rights reserved)

a collar of compact bone around the diaphysis. At the same time, the cartilage in the center of the diaphysis begins to disintegrate. Osteoblasts penetrate the disintegrating cartilage forming a primary ossification center. Ossification continues from this center toward the ends of the bones. The cartilage in the epiphyses continues to grow so the developing bone increases in length. Later, usually after birth, secondary ossification centers form in the epiphyses. The long bones, vertebrae, phalanges, sternum, ribs and skull base are formed by this type of ossification (Rančić and Nikolić 2007). During bone formation, the primary bone is formed first and by its remodeling with the action of osteoclasts and osteoblasts, a secondary or definitive bone is formed (Figs. 2.2, 2.3 and 2.4). The secondary or definitive bone is composed of two bone tissue types: compact and spongy (Lačković 2014).

The compact bone tissue has dense, lamellar structure. It forms external surface of the long bone dyaphises. The main morphofunctional unit of the compact bone is the osteon, or Haversian system. The osteon is like a cylinder consists of a system of bony lamellae arranged concentrically around a central canal called Haversian canal. This canal contains nerves and blood vessels. The bone lamellae consist of multiple layers of osteocytes and interconnecting canaliculi and matrix. From the periosteum into the bone matter, in special canals called Volkmann's canals, pass blood vessels and nerves.

The spongy bone is present in epiphyses of the long bones and in the flat bones. Spongy (cancellous) bone also called trabecular bone. Is lighter and less dense than compact bone. It is composed of the numerous large spaces that give a honeycombed or spongy appearance and 3D latticework of bony plates, called trabeculae,

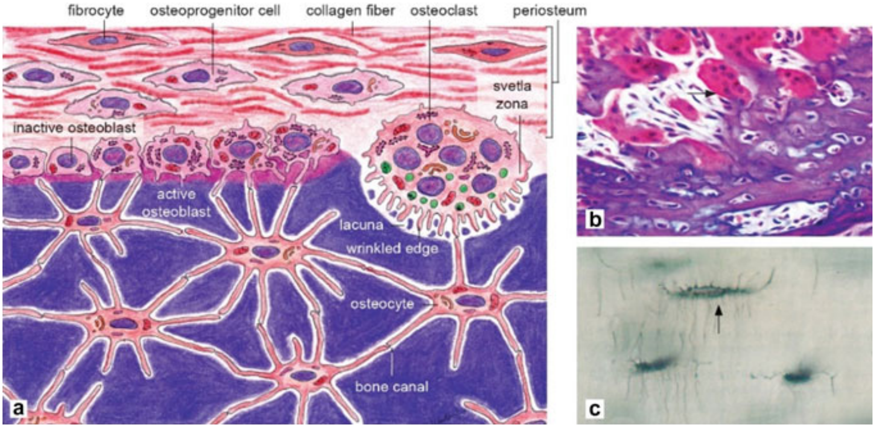

Fig. 2.3 Structure of the mature bone. **a** Perichondrium, bone cells and mineralized bony matrix; **b** osteoclasts (arrow); **c** osteocytes (arrow) (© Copyright 2014 Data Status, all rights reserved)

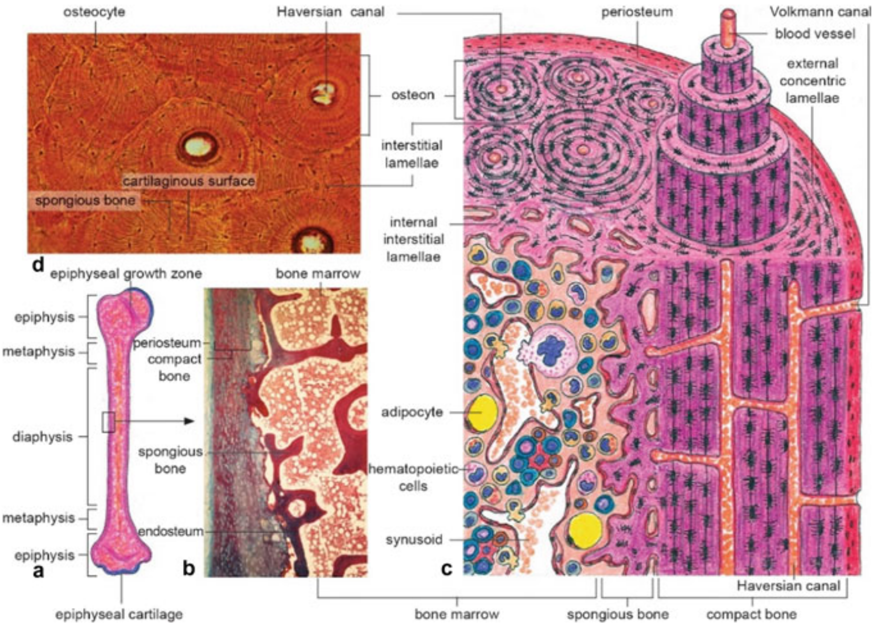

Fig. 2.4 Structure of the mature bone. **a** Long bone appearance and morphology; **b** histological section of the long bone diaphysis; **c** histological organization of mature bone; **d** cross section of lamellar bone (© Copyright Data Status, all rights reserved)

arranged along the lines of stress. Spongy bone is the main structural component in the epiphyses of the long bones, vertebrae, flat bones of the skull, ribs and scapula (Rančić and Nikolić 2007).

2.5.6 Biological Properties of Bone

Bone Growth in Length During longitudinal bone growth (interstitial growth; growth of bone length) cartilage continuously grows and is being replaced by bone tissue. The cartilage is by its properties built for fast and efficient growth. Its cells form high pillars. The chondroblast's fragments present on the top of the pillar divide by suppressing epiphysis away from the diaphysis. Older chondrocytes signal to the surrounding matrix to calcify, and then they die and be destroyed. The trabeculae are partial eroded by osteoclasts. Osteoblasts then cover the trabeculae with bone tissue. During the growth, the bone lengthens by the growth of the cartilaginous epiphyseal plate, which divides and creates more and more cartilage while diaphyseal cartilage in the epiphyseal plate, located near the diaphysis, transforms into the bone. This leads to an increase in the length of the bone shaft and the bone length as whole (Florencia-Silva et al. 2015).

Growth of the Bone Thickness The osteoblasts below the periosteum secrete a bone matrix at the external (periosteal) surface of the bone. This makes the bone thicker. At the same time, the osteoclasts in the endosteum remove bone and so they expand the medullary cavity. This leads to an increase in the diameter of the bone shaft, although the total amount of bone in the shaft of the bone remains unchanged (Florencia-Silva et al. 2015).

Fractures of the Bones and Their Repair Despite their firmness, the bones can break if they are suddenly exposed to a large load, beating, hitting or stretching. Bone damage that occurs is called the fracture. The proper healing (repair) of the fracture, depends on whether or not blood and cellular components of the periosteum and endosteum are preserved. Fracture repair takes place in some phases (Schindeler et al. 2008).

Bone Remodeling Remodeling (reshaping) of the bone after the fracture, involves two processes: the process of resorption (decomposition) and the process of the bone formation according to the activity of osteoclasts and osteoblasts. Resorption of the old and creation of a new bony matrix (enabling continuous renewal and maintenance of the bone tissue) takes place during the whole life. In the bone remodeling participate osteoblasts, osteoclasts, bone matrix, hormones (parathormone and calcitonin), various growth factors and cytokines (Schindeler et al. 2008).

Vascular Supply of the Bones The bones of an adult are not tissues that are actively growing, but need a constant blood supply to stay vital. Vascularization of the long bone depends on several sources of supply: nutritive, periosteal, epiphyseal, and metaphyseal artery (Florencia-Silva et al. 2015).

Nerve Supply of the Bones All bones except the auditory ossicles (ossicula auditoria) have nerves. They are most numerous on the articular surfaces of long bones, vertebrae and in larger flat bones. Nerves in long bones follow the nutritional arteries and have a vasomotor functions. The nerves that innervate the periosteum enter in the bone with the periosteal arteries. They are in the perivascular spaces of the Haversian canals. Periosteum is richly innervated, which explains the severe pain during the bone fractures (Florencia-Silva et al. 2015).

2.6 The Method of Anatomical Features—MAF

This section presents a comprehensive description of the MAF. The basic understanding of computer graphics, different computer models, medical imaging, and supporting software is essential for the full understanding of this method and its contribution to biomedical engineering.

2.6.1 Introduction to MAF

The human skeletal system is often affected by some pathological process (e.g., tumor), injuries and fractures. In many cases, it is, therefore, necessary to perform surgery, sometimes in a very short time. It is especially important for the success of the surgical intervention to have a good operation plan and adequate implants. The development of such computer-aided technologies and methods that will enable surgery planning and rapid production of quality implants is essential in orthopedic surgery.

A key factor in bone and joint surgery success is the planning and simulation of orthopedic surgery. Surgery planning means choosing the optimal method of correcting the position of bone and joint elements, choosing the safest surgical approach (including muscles, tendons, and neurovascular elements) and choosing the optimal method of fixing bone fragments. The more time is spent on planning the probability of intraoperative complications (unexpected problems during the operation) will be minimal.

Another important success factor is the quality and fast production of implants. Implants are metal, plastic or components made of other non-resorptive or resorbable materials, which are temporarily or permanently implanted in the patient's body. These components can be screws, wedges, rods, plates or artificial parts of bones or joints. The production of standard components such as screws can be done with classic production technologies. The problem, however, is the production of parts of bones or joints that, due to their shape and complexity, cannot be produced by conventional production technologies. Therefore, in this study, AT for implant manufacturing is proposed as implant fabrication technologies. AT allow the production of implants of any complexity only based on its 3D model. Production is fully computerized and can be performed in a hospital setting and without special knowledge in the field of production technologies. Thanks to that, it is possible to quickly produce an implant that completely fits the shape of a certain patient. In addition, AT can also be used to make anatomical models of bones, which play a significant role in the process of planning operations.

Quality production of AT implants requires multidisciplinarity, i.e., close collaboration of anatomists, orthopedic surgeons, and radiologists on the one hand and AM and RE engineers on the other. Making AT implants involves a series of steps: Development of a method for efficient medical modeling of bones using scanned models of the same with the most suitable imaging diagnostic method. Depending on the case, scanning of either damaged bone or healthy bone, processing of the obtained image data in DICOM format (using appropriate medical modeling software), healing of the obtained model, conversion of the same into the appropriate format; Making a 3D geometric model of the implant; Selection of adequate AT and appropriate biocompatible material and making a specific implant using AT.

All the above models are, as already mentioned, extremely important for the proper planning of orthopedic interventions, as well as to produce implants and fixators adapted to humans. To create the mentioned models, it is possible to use different approaches. The analysis of the state of research gives a general overview of how to create different geometric models, while in this part, a brief overview is presented, and two general approaches are defined.

The first approach is based on the creation of 3D geometric models of the bones based on geometric data obtained by medical imaging methods. These methods can be based on volumetric scanning methods, or on application of more than one two-dimensional images of the patient's bones (X-ray, ultrasound). This approach involves the formation of 3D geometric models in several ways: by using specialized software that is part of a medical scanner (e.g., Vitrea), post-processing of medical images in medically oriented CAD programs (e.g., Materialize Mimics), or post-processing in one of the CAD software packages (e.g., CATIA). One of the main disadvantages of this approach is the inability to create models of whole bones in cases where the scanned bone is incomplete due to disease (osteoporosis, arthritis, tumor, etc.) or trauma (multiple fractures, crushed bone, etc.), or when medical images are not of appropriate quality. Examples of methods used in this approach are given in (Filippi et al. 2008; Rathnayaka et al. 2012; Noser et al. 2011).

Another approach for creating 3D geometric models of bones or bone segments is based on a predefined predictive model. In predictive models, geometric entities are described by mathematical functions, whose arguments are morphometric parameters, which can be read from the medical images of a particular patient. This approach makes it possible to create a 3D geometric model that corresponds as closely as possible to the physical model of the patient's bone. Potential disadvantages of this approach are the inability to read all parameters (for the same reasons as in the first approach), the insufficient number of parameters included in the prediction functions, and inadequately selected parameters. Examples of creating 3D bone models based on incomplete data are given in the cited literature (Vitković et al., 2013; Majstorovic et al. 2013; Sholukha et al. 2011).

In this part of the study, it is essential to note that one of the methods that greatly influenced the creation of MAF is the PD method (Point Distribution Method—PDM) (Lorenz and Krahnstöver 1999). The PDM defines each model as a set of reference points, calculating the mean position of the points and calculating the deviation of each point relative to the mean position. The PDM used in medicine is based on the use of anatomical landmarks (points). Anatomical experts define the anatomical points of each human organ as input to PDM. Together with PDM, Active Shape Model—ASM is used to describe morphological forms in medicine. With this method, it is possible to adjust the statistical model (PDM) created over the input set of objects, to the corresponding new image obtained by one of the methods for data acquisition in medicine. Mentioned methods work on the principle of image segmentation and the creation of appropriate anatomical points on the contours that separate the anatomical entities. One of the possible problems that can be noticed with such approaches is the selection of anatomical points on 2D images to form a segmentation contour. To successfully create a model, it is necessary to select multiple points along the contour of the image. These do not have to be points that delimit anatomical units, but simply points based on which a contour is formed.

MAF introduces a new approach to describe geometrical entities of human bones, and it enables the creation of various geometrical models of the human bones. MAF method has already been presented in research (Vitković et al., 2013; Vitkovic et al. 2018). The main objective of MAF application is to provide complete 3D geometrical models of human bones and bone fragments, even in cases where input data about a patient's bone is not complete, due to the bone illness, fracture, or some other trauma. Two different types of models can be created by MAF:

- 3D geometrical models—Standard polygonal, surface, and volume models used in CAD for many years.
- Generic models of the human bones—Defined as parametrical models formed over the input set of bone samples.

Both types of models are created on the basis of data (input models) acquired from medical imaging methods (e.g., CT or MRI). MAF is a complex method, and because of that, Structured Analysis and Design Technique (SADT) is used for its description. SADT diagrams are used for the graphical representation of system processes, and they enable detailed analysis of the system and involved resources. The main components of SADT diagrams are input elements, recourses, control elements, and output elements. To apply SADT on MAF, it was essential to define the main components of the method. MAF analysis was performed, and main components are presented in Fig. 2.5 and defined as:

1. Input elements—labeled with the capital I:
   (a) Volumetric images of the patient (bone) created by CT or MRI.
   (b) 2D images of the patient (bone) are usually created using X-ray.

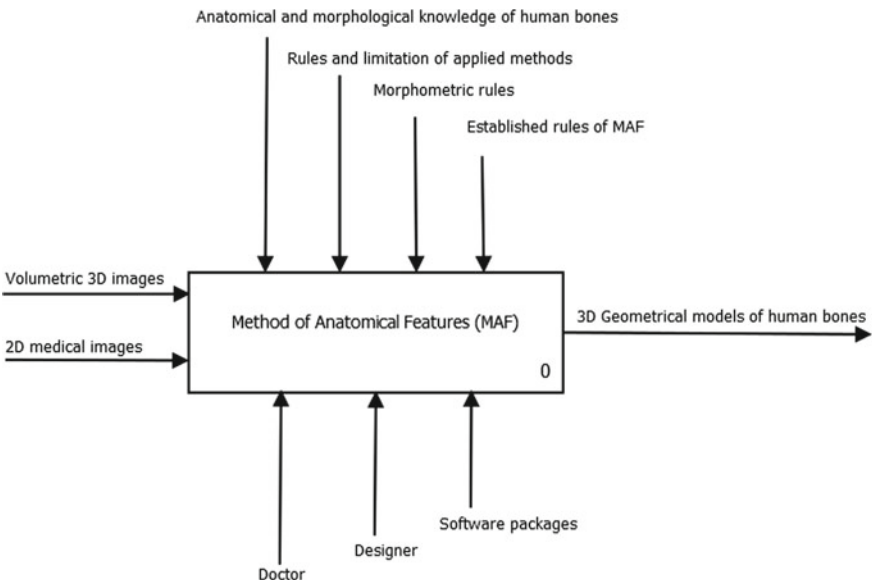

Fig. 2.5 Basic components of MAF—A-0 (Vitkovic et al. 2019)

2. Mechanisms (Resources)—labeled with capital M:
   (a) Physician—surgeon, orthopedic surgeon.
   (b) Designer—Expert in CAD and medical software.
   (c) Software packages: Materialise Mimics, CATIA etc.
3. Control elements—labeled with capital C:
   (a) Medical knowledge about anatomy, morphology and morphometric of human bones.
   (b) Rules and limitations of applied methods in MAF.
   (c) Morphometric rules—Rules about morphometric parameters (values and relationships between parameters).
   (d) Rules defined in MAF-a—Rules which define proper way of creating geometrical models of human bones.
4. Output elements—labeled with capital O:
   Geometrical models of human bones—polygonal, NURBS (surface), solid.

MAF contains basic and additional processes (Fig. 2.6). Basic processes are presented in Fig. 2.7 and additional processes are presented in Fig. 2.8. Basic processes enable complete geometrical and anatomical definition of the specific human bone, and they are:

- Creation of initial polygonal model (A11)—This process contains several procedures, which must be performed in sequential order: Scanning of human bone by

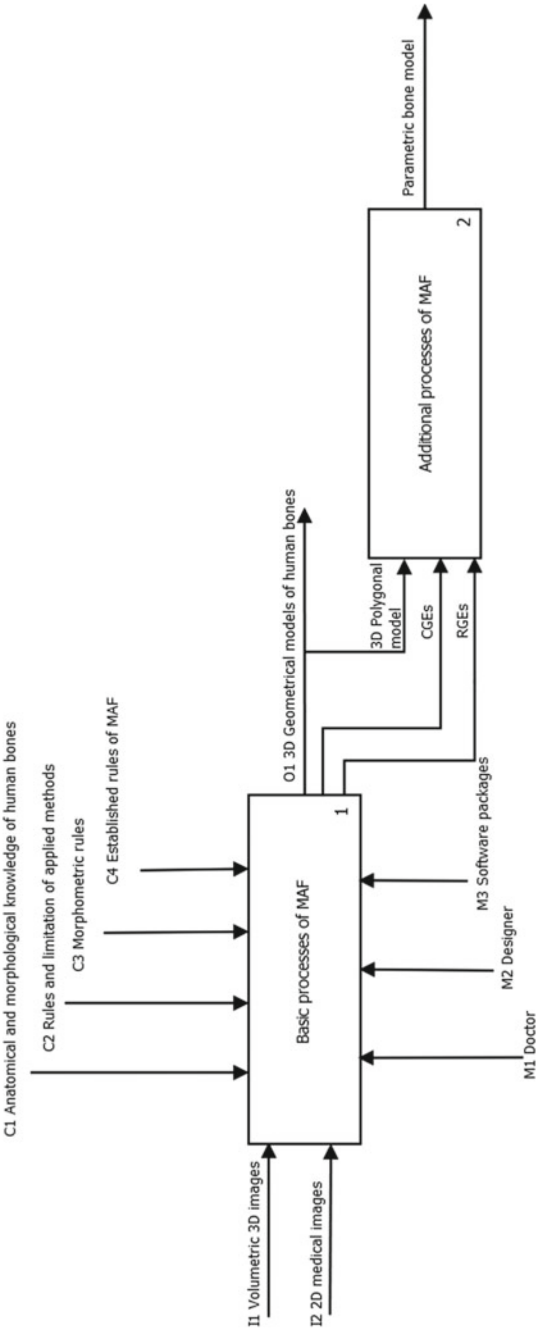

Fig. 2.6 Basic and additional processes of MAF (Vitkovic et al. 2019)

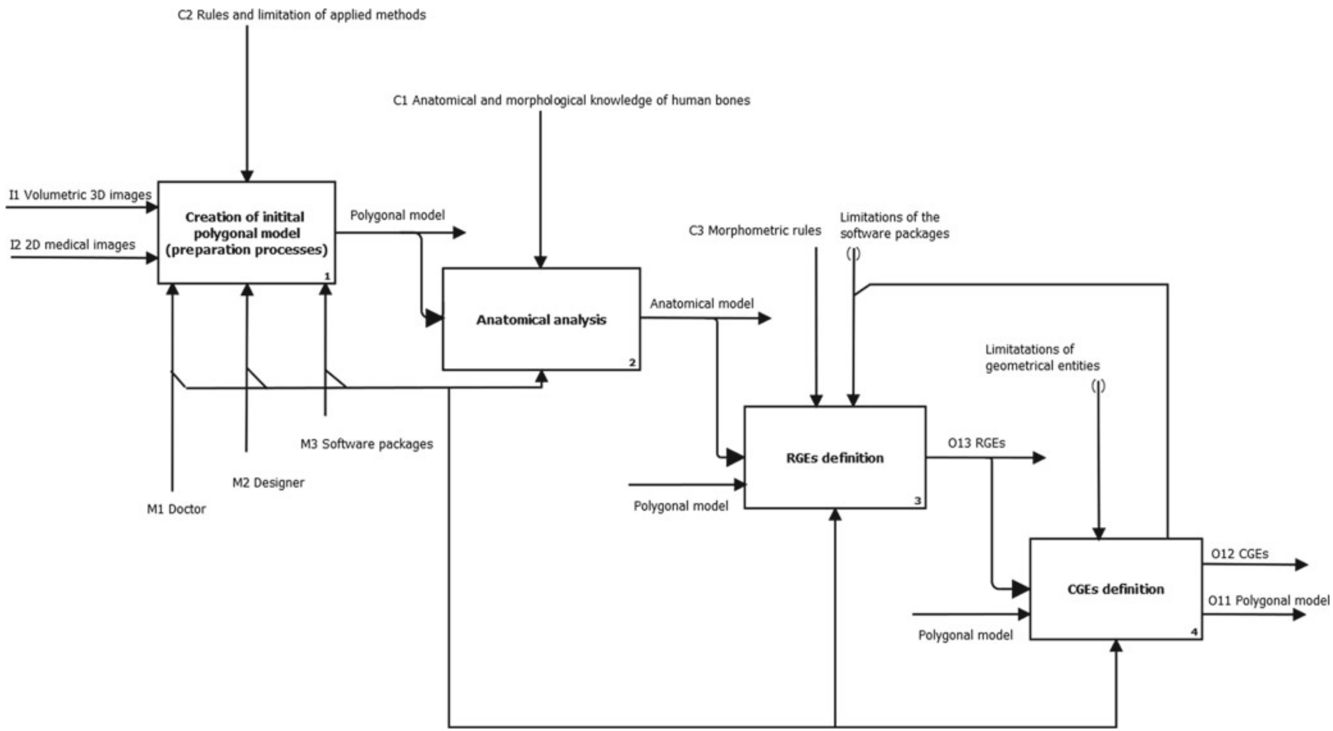

Fig. 2.7 Basic processes of the MAF—A1 (Vitkovic et al. 2019)

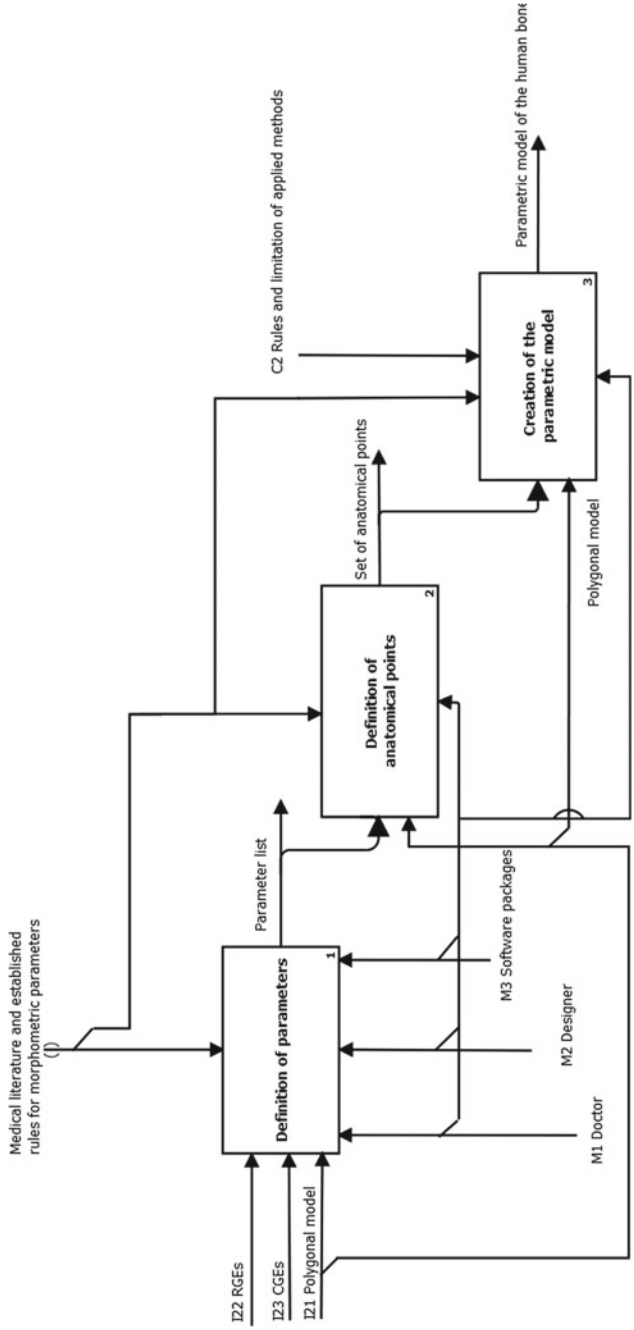

Fig. 2.8 Additional processes of MAF—A2 (Vitkovic et al. 2019)

the application of CT scanner; Segmentation of the acquired images, Forming of the polygonal model and its conversion to STL format—creation of the initial point cloud; Cleaning of the point cloud; Creation of the tessellation model; Additional processing of the tessellated model (filling holes, fixing irregularities in model, etc.). The output from this process is a polygonal model of the specific human bone.

- Anatomical analysis (A12)—The anatomical analysis presumes anatomical and morphological analysis of the human bone to create an anatomical model of the human bone. This model is a semantic model that connects geometrical elements on the polygonal bone model with anatomical and morphological terms already defined in medical literature. The outcome of this process is anatomical model of the specific human bone.
- Definition of Referential Geometrical Entities (RGEs) (A13)—RGEs are geometrical entities (points, lines, planes, axes, etc.) which are created on the polygonal model of the human bone. These entities represent basic geometry used to create all other geometrical elements like curves or surfaces.
- Creation of Constitutive Geometrical Entities (CGEs) (A14)—RGEs are the basis on which CGEs are created. These entities are called constitutive because they are used for the creation of surface and solid models of the human bones, and parts of the bones. CGEs are the best geometrical entities that conform to the morphology (shape) of the human bone. The morphology of the human bone is complex, and shape of the human bone can be defined as free form shape. To geometrically describe free form shape, parametric curves (splines) were applied. It is generally known that splines curves are used to define parametric (NURBS) free form surfaces, so they were an adequate choice for CGEs. It is important to mention that splines curves are not the only geometrical entities that can be used to describe the bone shape. If some other entity (line, arcs, etc.) can geometrically describe certain parts of the bone, it can be used as CGEs.

Polygonal model, RGEs and CGES are output from the basic MAF processes. By the application of these outputs, different geometrical models of the human bone can be created. For example, surface and volume models of the human bone can be created by the application of standard technical features like sweep or loft, and they can be used for: the creation of presentational models, for the preparation of surgical interventions, for the Finite Element Analysis (FEA) of bones, etc.

Created outputs can be also used for the creation of parametric model of the specific human bone. The parametric model is a generic model which shape, and anatomy are defined by the formed parametric functions, and conditioned by the values of the morphometric parameters acquired from medical imaging methods. Processes that are used to create such a model are called additional processes of MAF and they are presented in Fig. 2.8. These processes are:

- Definition of parameters (A21)—First step in this process is to define morphometric parameters, which are clearly visible and measurable dimensions in medical images and defined in medical literature and traditional morphometrics. These parameters are defined individually for each human bone. This means that morphometric parameters determined for femur are different from parameters defined for tibia. Parameters can be: Femoral Head Radius (FHR), angle between mechanical and anatomical axes of femur, angle of inclination (femoral neck), etc. (Rathnayaka et al. 2012; Bushberg 2002).

- Definition of anatomical points (A22)—Anatomical points are defined on CGEs or other important anatomical landmarks (true, pseudo and semi landmarks) on polygonal model, in relation to anatomical model of specific human bone and defined morphometric properties. This means that for each specific human bone distinctive set of anatomical points is defined. The number of points in set is determined by the parametric model's required geometrical and anatomical quality, i.e., more points will define a better model. This set of anatomical points must be defined for each bone in an input set, i.e., if the set contains fifty (50) bone samples, then fifty (50) sets of points must be created. Output from this process is point cloud of anatomical points. It is important to note that landmark geometric morphometrics states that the number of landmarks should correspond to the number of specimens, but that is not the case in this research. This is not important because this research is only based on the landmark geometric as a basic theory, but reversed principle is applied, i.e., landmark points are created on the CGEs which are geometric elements used to describe bone shape, and not on the bone itself.
- Creation of the parametric model (A23)—The last step in the parametric model definition is to measure coordinates of points and morphometric parameters for each created polygonal model in a set. Measured values are applied in statistical analysis, and as a result, parametric functions with morphometric parameters as arguments, are created. These functions define values for coordinates of anatomical points in relation to morphometric parameters. Each coordinate of every anatomical point can be calculated by applying parametric functions width input arguments defined as values of morphometric parameters measured for a specific patient. In the first iteration of the MAF, multiple linear regression was chosen as statistical functions (Raman and Wenger 2008), but other statistical methods, or machine learning methods can be also applied.

The output from MAF additional processes is parametric model of the specific human bone. The parametric model can be transformed into the point cloud model by applying unique values of morphometric parameters acquired from specific patient's medical images. Furthermore, the transformation of point cloud into some other geometrical models (polygonal, surface, and solid) can be done by applying known CAD techniques in CAD software.

2.6.2 MAF Application

MAF can be applied to create a geometric model of bone in two basic ways:

- By using RE methods to reconstruct a geometrical bone model based on medical images from volumetric scanners.
- By applying methods based on the use of a parametric bone model and values of morphometric parameters acquired from medical images.

The basic application process (A0) is identical to the process shown in Fig. 2.5, with the same inputs, outputs, and resources, but the lower-level processes differ. It is important to note that MAF and its application are separate processes and, as such, are presented in this section.

2.6.2.1 Reconstruction of a Geometric Bone Model Based on a Volumetric Image

The first method is the application of MAF for the reconstruction of a bone model based on a volumetric image of the bone, using the procedure shown in Fig. 2.9. The volumetric image of the bone is formed by using a computed tomography procedure. The bone is affected by trauma and depending on the type of trauma, a complete or incomplete bone scan can be obtained. If a disease such as osteoporosis or a tumor affects the bone, parts of the bone may be missing on the image, so the image is incomplete. In addition, the bone scan may be partial in the sense that if there has been extensive bone destruction, the bone fragments may separate from the parent bone, and therefore, it will be difficult to identify on the scan. Regardless of whether the image is complete or incomplete, the reconstruction procedure should enable the creation of a valid geometric model of the complete bone or parts of the bone. A valid geometric model is one that has the required degree of geometric and anatomical accuracy.

The first step in the reconstruction is forming a polygonal bone model based on a volumetric image. The given process takes place in medical software, during which the formed volumetric model is initially processed, and a polygonal model is formed in a certain format (e.g., STL). Further processing is performed in a CAD application, whereby the imported polygonal model (point clouds in this case) is cleaned and filtered. After forming the final polygonal model, the creation of RGEs and CGEs can be conducted. The formation of a certain geometric model of bone is done according to each patient's individual needs or depending on the clinical case. If it is necessary to create presentation models for medical/biological sciences education, it is even possible to omit the creation of CGEs and RGEs. It is possible to use the formed polygonal model and create bone models with additive technologies (3D printers). Suppose it is necessary to perform preoperative planning. In that case, it is possible to create a set of fixator models and combine them with a bone geometric model to define the best possible orientation and position of the components of the bone-fixator assembly.

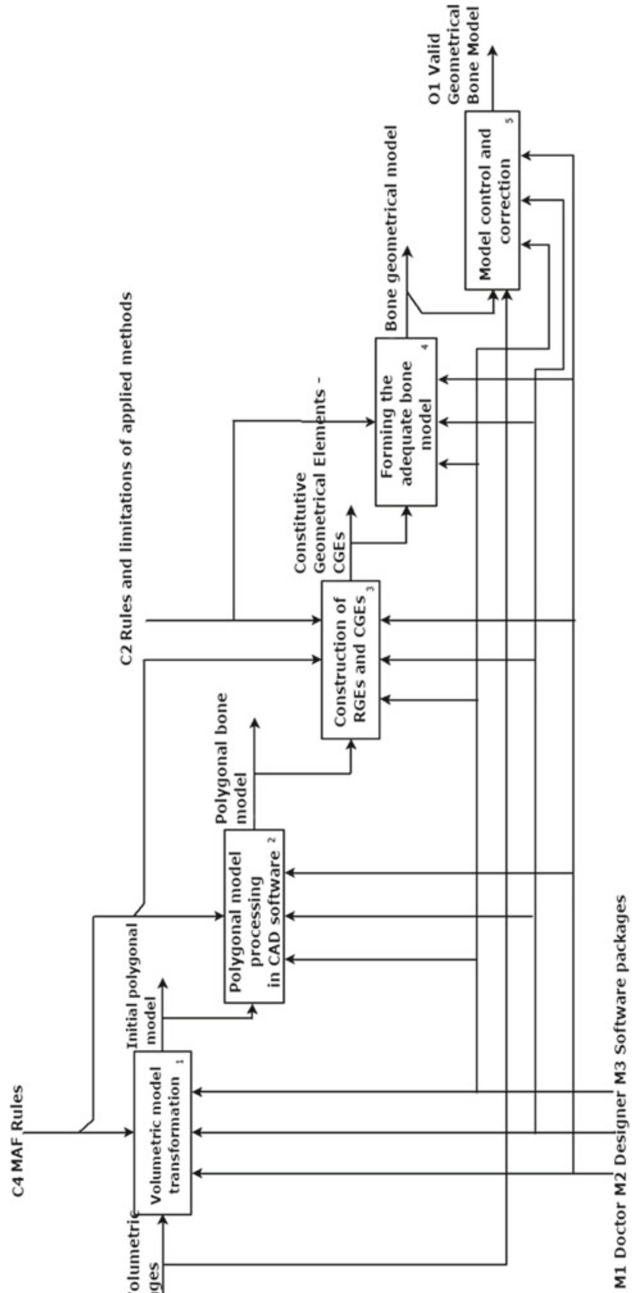

Fig. 2.9 The reconstruction process based on volumetric data—A1 (Vitković 2016)

2.6.2.2 Reconstruction of a Geometric Bone Model Using a Parametric Model

Another way of building a valid geometric bone model is based on a parametric bone model, and the process is shown in Fig. 2.10. In this case, the input bone image may be an incomplete volumetric model or insufficient number of 2D bone images (which may also be incomplete). This method also includes the case when it is not possible to create a volumetric image of the bone, because it is impossible to record the patient for various, already defined reasons. In a given case, it is necessary to read the parameters from the available images and apply the parameter values in the parametric functions defined for a given bone. Then, based on the application of parametric functions, a point cloud with calculated point coordinates is formed, which can be applied for further processing, and geometric models that have already been defined in the first approach can be created. It is important to note that, if a particular part of the bone is missing, applying a parametric model makes it possible to form that part of the bone and thus create a complete bone model based on insufficient data obtained from the input images. Also, since the parametric model is based on a certain number of parameters, it is possible to form parametric models based on a larger and smaller number of parameters. This means that, if it is not possible to read all parameters from medical images, then it is desirable to apply a parametric model with functions defined with a smaller number of parameters. Therefore, a geometric bone model of lower accuracy will be created, but it is sufficient for specific applications (e.g., presentation models).

2.6.3 The Reverse Modelling Procedure

The importance of rapid creation of geometrically accurate and anatomically correct geometrical models of the human bones by applying RE methods was already stated and demonstrated. Such models were used for additive manufacturing and as a basis for the development of models intended for FEA analysis using finite element methods. The creation of non-parametric volume models is performed through the following phases:

2.6.3.1 Geometrical Model Creation

A CT scan (tomogram) of the lower extremities of different patients were used as the starting point for creating a polygonal model of human bone (Fig. 2.11).

1. Creating a polygonal model of a particular bone
   (a) Scanning the subject on a CT scanner
   (b) Defining regions of interest
   (c) Creating point clouds based on CT model

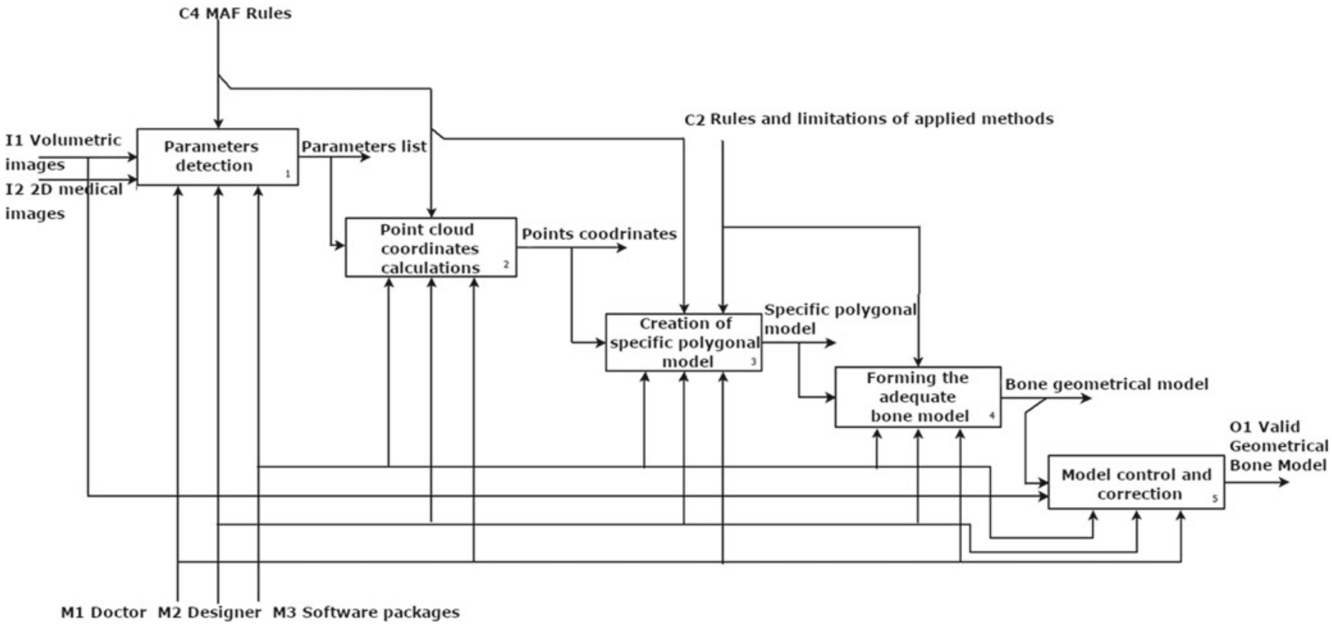

Fig. 2.10 The reconstruction process based on the parametric model—A2 (Vitković 2016)

Fig. 2.11 The polygonal model of the femur bone with additional "noise" (Korunović et al. 2010; Vitković, 2016)

   (d) Creating a polygonal model based on point clouds

2. Creating a CAD model of a specific bone
   (a) "Cleaning" and "healing" of the polygonal model
   (b) Creating a closed group of NURBS surfaces
   (c) Creating a volume model based on surfaces.

Using a computer application for processing medical images, a zone of interest was selected on the tomogram of the lower extremities, which included a certain human bone (e.g., femur, tibia, fibula). Using the function for recognizing the type of tissue based on its density, the so-called "point cloud" corresponds to the human bone's outer surface and the surface which separate the compact bone from the central medullary cavity. However, this procedure inevitably highlights a number of points that do not belong to these surfaces but are located inside the compact bone, and whose number is significantly higher in bones that are more affected by the process of osteoporosis. Such points represent "noise" which makes it difficult to create a geometric model. In addition, the used CT scans were acquired from patients who had problems with the vascular system, and contrast was injected into their veins during the scan (whose density is similar to bone density). Therefore, the isolated point clouds also contained a part of the vascular system, as observed in Fig. 2.11, which represents a polygonal model obtained on the basis of one of the point clouds.

The polygonal model was obtained by creating a network of triangular surfaces above the point cloud, which is primarily intended for better visualization of data and their transfer to the CAD software package (Brown and Semelka 2010).

2.6.3.2 Creating a CAD Model of Human Bone

The process of creating a CAD model of bone will be shown on the example of the femur. Processing of the polygonal model, which is the basis for creating the CAD model, begins with removing segments that do not belong to human bones, such as parts of the vascular system or surrounding soft tissues and bones. The cleaned polygonal model is shown in Fig. 2.12, and the segment of the polygonal model with prominent polygons in Fig. 2.13.

Fig. 2.12 Polygonal model of the femur after removal of the remaining segments of the surrounding objects (Korunović et al. 2010; Vitković, 2016)

Fig. 2.13 Segment of the polygonal model with prominent polygons (Korunović et al. 2010; Vitković, 2016)

After removing the obvious "noise", we move on to "cleaning" the model interior and removing the "noise" that originated mainly from the internal trabecular bone structure (Fig. 2.14).

The internal structure of the polygonal bone model consists of the boundary between the solid bone and the central medullary cavity and the "chaotically" arranged triangles created on the basis of the trabecular structure of the spongy bone.

After removing the inside, the remaining outer surface of the bone is still connected to the segments that penetrate deeper into the inside, and it also contains cracks and openings that need to be filled (Fig. 2.15).

In order to prepare such a model for the creation of surface and volume models that are geometrically correct, methods for "healing" the polygonal model are used. The most important of them are:

Fig. 2.14 Internal structure of a polygonal human bone model (Korunović et al. 2010; Vitković, 2016)

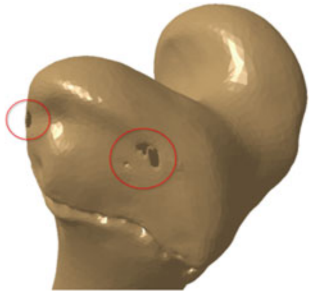

Fig. 2.15 Openings in the polygonal model of the distal part of the femur are most often associated with larger groups of irregularly spaced polygons that penetrate deep into the model's interior (Korunović et al. 2010; Vitković, 2016)

- Removal of redundant polygons based on visual inspection, i.e., removing points from point clouds
- Automated "cleaning" of the polygonal net, using appropriate software tools:
  - Removal of incorrectly formed polygons
  - Removing identical copies of the polygon
  - Alignment of polygon orientation
  - Removal of edges and vertices that are not correctly oriented
  - Removal of isolated polygons, isolated within smaller groups
  - Removing too long edges
  - Increasing too small angles
- Filling of openings on the polygonal network, whose area is smaller than the set threshold
- Manual, interactive creation of missing polygons, where it is not possible to use other healing methods.
- Reduction of the number of polygons
- Polygon shape optimization
- Increasing the smoothness of the polygonal surface (smoothing).

After the polygonal model satisfactorily "heals" and, if necessary, increases its "smoothness", a closed NURBS surface is created by approximation, which represents the outer shell of the model (Fig. 2.16).

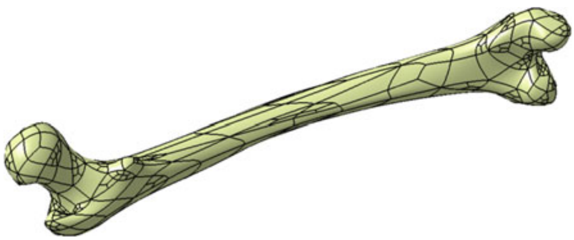

Fig. 2.16 Closed complex NURBS surface representing the outer shell of human bone (Korunović et al. 2010; Vitković, 2016)

2.6.3.3 Reference Geometric Entities and Surface Model on the Example of the Femur

The definition of RGEs of human bones necessarily precedes the procedure of reverse modeling and the parameterization of the geometry of the femur with the help of CAD software. Bone RGEs are formed by using characteristic points, directions, planes, and views in accordance with anatomical and morphological properties of the bones. All other geometric entities, of a higher order, such as curves, surfaces and solids are spatially referenced in relation to the RGEs. The procedure of determining RGEs aims to propose a way to identify the minimum set of RGEs to make the procedure of reverse modeling and parameterization of femur geometry as robust as possible in terms of required geometric adaptations to the specific anatomy of an individual patient (Vitković et al. 2013; Vitković et al. 2015a, b). Therefore, all other geometric constraints and relations, which will later exist in the 3D bone model and control the changes, are based on this minimal set of RGEs. At the same time, this method should enable the parameterization of the geometry of the bone model, and quick and simple changes according to the specific morphology of the femur in an individual patient. Also, the correct identification of RGEs directly affects the speed and accuracy of RE of implants and fixators, which is the basic imperative in urgent cases.

In anatomy, two basic views of the femur are defined, observing the spatial orientation of the femur. The first is the so-called anterior–posterior view/direction or orientation (A-P) and the other is lateral-medial (L-M) view/direction or orientation. For reverse modeling of the geometry of the femur, it is necessary to form several (not always orthogonal) directions and corresponding projections of the bone or part of the bone. Unlike medical situations, RE and the manufacturing of custom implants and fixators require very precisely defined rules for the development of all directions and views to be used, including A-P and L-M. For the development of methods for identification of RGEs of the femur and, later, reverse modeling of the femur, CAD software was used: CATIA V5 R19 (R21), i.e., its set of modules for reverse modeling. Identifying RGEs begins with importing and geometric processing of point clouds (removal of redundant points and spatial binding of clouds with the existing initial geometric entities of the model). Before RGEs identification, a polygonal model is created above the point cloud by tesalation, i.e., by creating a large number of polygons (in this case triangles), between the corresponding points. In this phase, additional processing of the polygonal model is performed to correct appropriate irregularities, normalization, etc. After the preparation of the polygonal model, the anatomical model application follows. Anatomical model is a descriptive model which describes important anatomical landmarks on the polygonal model. By using anatomical landmarks and entities (axis, points, surfaces), RGEs are formed. As it is presented in Fig. 2.17, RGEs are formed on the femur polygonal model. By using these RGEs, CGEs are created, and then used to create the surface femur model and define the parametric femur model.

The CGEs on femur are generally defined as splines which are good for describing free form surfaces, and they are used as the basis for the surface model creation. They are also used for the definition of anatomical points (descriptively presented in

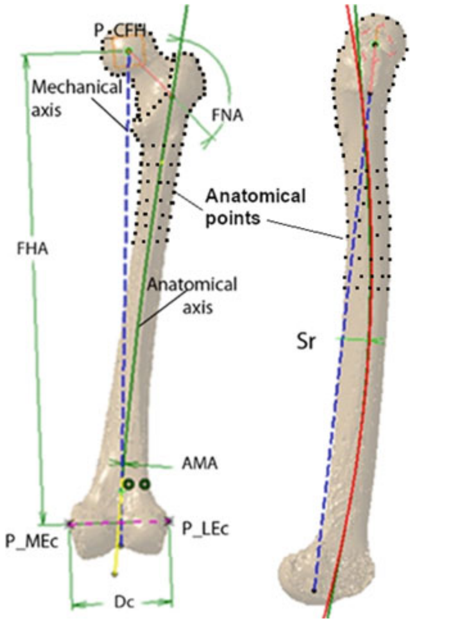

- P_LEc - The point of the lateral epicondyle.
- P_MEc - The point of the medial epicondyle.
- P_CFH - Femoral Head Center.
- FHR - Femoral Head Radius.
- FNA – Femoral Neck Angle.
- FHA – Distance between P_CFH and line connecting P_MEc and P_LEc.
- DC – Distance between P_MEc and P_LEc.
- AMA – Angle between Anatomical and Mechanical Axis.
- Sr – Shaft radius.

Fig. 2.17 Femur's referential geometrical entities (RGEs) (Majstorovic et al. 2013)—modified figure

Fig. 2.17) applied for the creation of femur parametric cloud point model described in next section, and in the (Majstorović et al. 2013).

2.6.3.4 The Parametric Model Creation

Predictive (parametric) models of human bones: these models are statistical models formed over the input set of bone samples. They are defined as point cloud models, which represent an approximation of the human bone boundary surface. Each point coordinate (X, Y, and Z) in the point cloud is defined by an individual parametric function Eq. (2.1).

$$X = f_1(p_1, p_2, \ldots p_n),\ \ Y = f_2(p_1, p_2, \ldots p_n),\ \ Z = f_3(p_1, p_2, \ldots p_n) \tag{2.1}$$

Currently, multilinear regression is applied for the creation of parametric functions, and the used algorithm is presented in Eq. (2.2) and defined in (Majstorović et al. 2013; Vitkovic et al. 2018).

$$\begin{aligned} P &= [ones(size(p_1))\ p_1 p_2 p_3 p_4 \ldots p_n]; \\ P_i &= P' * P; \\ B &= P_i \backslash P' * X; \end{aligned}$$

$$M = P * B; \tag{2.2}$$

X—Vector of X coordinates defined for the input set cloud of point; P_i—Morphometric parameters (i = 1,…n); B—Coefficient Vector; M—Vector of calculated values (multilinear regression).

As a result of regression application, parameter functions that give the linear functional dependence between the coordinates of points and parameters are created. The example of parametric function for particular anatomical point is presented in Eq. (2.3).

$$X_{\mathrm{f11}} = b_0 + b_1 \cdot D_{\mathrm{ci}} + b_2 \cdot \mathrm{FHA}_i + b_3 \cdot \mathrm{FNA}_i + b_4 \cdot \mathrm{AMA}_i + b_5 \cdot S_{\mathrm{ri}} + b_6 \cdot \mathrm{FHR}_i \tag{2.3}$$

Parametric function is a function whose arguments are morphometric parameters. Morphometric parameters are dimensions which can be acquired (measured) from medical images by using adequate software, like Materialise Mimics, 3D physician (http://www.ablesw.com/3d-physician/), or GIMP (https://www.gimp.org/). For the femur bone, morphometric parameters used in the parametric model are defined using its RGEs and graphically presented in Fig. 2.17. By the application of individually defined values of morphometric parameters, these models can be customized to the geometry and morphology of a human bone of a specific patient. Currently, the process of acquiring parameter data is done externally by using medical or other image processing software, but the intention is to create in-house software solution which will enable accurate measuring of parameters from medical images. After the point cloud personalization, the model can be further processed in any CAD application, and other types of 3D geometrical models can be created.

Another example of parametric model application is provided in study by (Vitković et al. 2015a, b), where MAF is implemented for the creation of the parametric model of the Human Mandible Coronoid Process (HMCP). The obtained results about geometrical accuracy of the model are quite satisfactory, as the medical practitioners state it and confirmed in the literature.

It is important to note that parametric models are used in clinical cases when 3D data of human bone are missing (e.g., due to tumour, osteoporosis, and complex fractures), and therefore, a complete 3D model cannot be created. By using medical software (e.g., Mimics or 3D Slicer) or X-ray images, a surgeon can acquire values of measurable morphometric parameters by using standard techniques and apply them in parametric functions. Parametric functions may be created with variable number of parameters. Suppose the values of all the parameters are not legible due to the incomplete data acquired from the medical images of the human bone. In that case, it is possible to apply the parametric functions with the number of available parameters. As the result of the process, a complete point cloud model of the bone is created, despite the lack of input data.

2.7 Conclusion

The techniques presented in this chapter are part of the Method of Anatomical Features (MAF), which introduces a new approach to describe geometrical entities of human bones. It enables the creation of various geometrical models of human bones. The main objective of MAF application is to provide complete 3D geometrical models of human bones and bone fragments, even in cases where input data about patient's bone is not complete, due to the bone illness, fracture, or some other trauma. It is shown that MAF can create two different types of models:

- 3D geometrical models—Standard polygonal, surface and volume models used in CAD for many years. They are created by the application of standard CAD technical features in CAD software packages.
- Predictive (parametric) models of the human bones—Statistical models formed over the input set of bone samples. By applying the morphometric parameters acquired from medical imaging methods, anatomical landmarks, these models can be adjusted to the geometry and morphology of the human bone of a specific patient.

Various types of geometrical models (polygonal, surface, volumetric, and parametric) of certain human body bones have been created to verify MAF, and they are already referenced. All created geometrical models have satisfied the necessary accuracy in geometrical and anatomical terms defined in scientific literature. This chapter provides examples of created geometrical models of femur; however, more geometrical models of other bones (tibia, fibula, humerus, mandible, etc.) have been created during this research. Nevertheless, MAF has been applied for other purposes, both directly and indirectly (geometrical models of bones created with MAF have been used). These are characteristic cases which can appear in clinical practice: case of creation of customized sternum implant, use of MAF to create parametric model of internal fixator by Mitkovic, application of Finite Element Method (FEM) to analyse stress and strain of femur bone and internal fixator by Mitkovic.

Research results presented in this chapter display a significant scientific result that greatly contributes to the improvement of methods used in reverse engineering and geometrical modelling of bones of the skeletal-joint system in humans.

References

Adams L, Krybus W, Meyer-Ebrecht D et al (2002) Computer-assisted surgery. IEEE Comput Graph Appl 10(3):43–51

Adams MA (2015) Functional anatomy of the musculoskeletal system. In: Wigley CB (ed) Gray's anatomy: the anatomical basis of clinical practice, 41st edn. Churchill Livingstone/Elsevier, Philadelphia, PA, USA, pp 84–85

Benameur S, Mignotte M, Parent S et al (2003) 3D/2D registration and segmentation of scoliotic vertebrae using statistical models. Comput Med Imag Graph 27(5):321–337

Benazzi S, Stansfield E, Kullmer O et al (2009) Geometric morphometric methods for bone reconstruction: the mandibular condylar process of Pico della Mirandola. Anat Rec—Adv Integr Anat Evol Biol—ANAT REC 292(8):1088–1097

Brown MA, Semelka RC (2010) MRI: basic principles and applications. Wiley, Hobooken, NJ, p 245. https://doi.org/10.1002/9781119013068

Bushberg JT (2002) The essential physics of medical imaging. Lippincot Williams & Wilkins, Philadelphia, USA, p 1048

Cavalcanti M, Rocha S, Vannier M (2021) Craniofacial measurements based on 3D-CT volume rendering: implications for clinical applications. Dentomaxillofac Radiol 33(3):170–176. https://doi.org/10.1259/dmfr/13603271

Chenna D, Yedukondala N, Ghassemi P et al (2018) Free-form deformation approach for registration of visible and infrared facial images in fever screening. Sensors 18(1):125. https://doi.org/10.3390/s18010125

Ciocca L, Mazzoni S, Fantini M et al (2012) A CAD/CAM-prototyped anatomical condylar prosthesis connected to a custom-made bone plate to support a fibula free flap. Med Biol Eng Comput 50(7):743–749. https://doi.org/10.1007/s11517-012-0898-4

Cootes TF, Taylor CJ, Cooper DH, Graham J (1995) Active shape models—their training and application. Comput vis Image Und 61(1):38–59

Filippi S, Motyl B, Bandera C (2008) Analysis of existing methods for 3D modelling of femurs starting from two orthogonal images and development of a script commercial software package. Comput Methods Programs Biomed 89(1):76–82

Florencia-Silva R, Rodrigues G, Sasso-Cerri E et al (2015) Biology of bone tissue: Structure, function, and factors that influence bone cells. Biolmed Res Int 2015:1–17

Fuchs H, Kedem Z, Uselton S (1977) Optimal surface reconstruction from planar contours. Commun ACM 20(10):693–702

Gamage P, Xie SQ, Delmas P, Xu P (2009) 3D reconstruction of patient specific bone models from 2D radiographs for image guided orthopedic surgery. In: Proceedings of digital image computing: techniques and applications, pp 212–216. https://doi.org/10.1109/DICTA.2009.42

Goldman LW (2007) Principles of CT and CT technology. J Nucl Med Technol 35(3):115–128. https://doi.org/10.2967/jnmt.107.042978

Gomez NL, Boccalatte LA, Lopez RÁ et al (2021) Total temporomandibular joint replacement and simultaneous orthognathic surgery using computer-assisted surgery. J Maxillofac Oral Surg 20:394–403. https://doi.org/10.1007/s12663-020-01422-y

Gunay M, Shimada K (2004) Three-dimensional bone shape reconstruction from X-ray images using hierarchical free-form deformation and nonlinear optimization. In: CARS 2004—computer assisted radiology and surgery, proceedings of the 18th international congress and exhibition, p 1291. https://doi.org/10.1016/j.ics.2004.03.154

Gunay M, Shim MB, Shimada K (2007) Cost-and time-effective three-dimensional bone-shape reconstruction from X-ray images. Int J Med Robot 3(4):323–335. https://doi.org/10.1002/rcs.162

Hak J, Rose J (2010) Preoperative planning in orthopedic trauma: benefits and contemporary uses. Orthopedics 33(8):581–584

Kasten Y, Doktofsky D, Kovler I (2020) End-to-end convolutional neural network for 3D reconstruction of knee bones from bi-planar X-Ray images. ArXiv preprint. doi: arxiv.org/abs/2004.00871

Korunović N, Trajanović M, Mitković M, Vulović S (2010) Od CT snimka do modela za analizu naponskog stanja u femuru primenom metoda konačnih elemenata. IMK-14 - Istraživanje i razvoj 16(2):45–48

Lačković V (2014) Vezivno tkivo. In: Lačković et al. Osnovna i oralna histologija i embriologija. Data Status, Beograd, pp 69–76

Lee M, Lee S, Kim A et al (2008) The study of femoral 3D reconstruction process based on anatomical parameters using a numerical method. J Biomech Sci Eng 3(3):443–451

Liang X, Li N, Zhang Z et al (2019) Shading correction for volumetric CT using deep convolutional neural network and adaptive filter. Quant Imaging Med Surg 9(7):1242–1254. https://doi.org/10.21037/qims.2019.05.19

Lorenz C, Krahnstöver N (1999) 3D statistical shape models for medical image segmentation. In: Proceedings. Second international conference on 3-D digital imaging and modeling. https://doi.org/10.1109/IM.1999.805372

Majeed A, Piah ARM, Rafique M et al (2017) NURBS curves with the application of multiple bones fracture reconstruction. Appl Math Comput 315:70–84. https://doi.org/10.1016/j.amc.2017.05.061

Majstorovic V, Trajanovic M, Vitkovic N, Stojkovic M (2013) Reverse engineering of human bones by using method of anatomical features. CIRP Ann Manuf Technol 62(1):167–170

Matthews F, Messmer P, Raikov V et al (2009) Patient-specific three-dimensional composite bone models for teaching and operation planning. J Digit Imaging 22(5):473–482

McCullough CJ, Remedios D, Tytherleigh-Strong G et al (2006) The use of hydroxyapatite-coated CAD-CAM femoral components in adolescents and young adults with inflammatory polyarthropathy: ten-year results. J Bone Joint Surg 88(7):860–864

Min Z, Zhu D, Liu J et al (2021) Aligning 3D curve with surface using tangent and normal vectors for computer-assisted orthopedic surgery. IEEE Trans Med Robot Bionics 3(2):372–383. https://doi.org/10.1109/TMRB.2021.3075784

Mohamed AM (2008) Review article an overview of bone cells and their regulating. Malays J Med Sci 15(1):4–12

Montúfar J, Romero M, Scougall-Vilchis RJ (2018) Automatic 3-dimensional cephalometric landmarking based on active shape models in related projections. Am J Orthod Dentofac Orthop 153(3):449–458. https://doi.org/10.1016/j.ajodo.2017.06.028

Moore KL, Persuad TVN, Torchia MG (2019) Skeletal system: development of appendicular skeleton. In: Moore KL, Persuad TVN, Torchia MG (eds) The developing human, 11th edn. Elsevier, pp 328–329

Noon CJ (2012) A volume rendering engine for desktops, laptops, mobile devices and immersive virtual reality systems using GPU-based volume raycasting. Ph.D. thesis, Graduate College at Digital Repository @ Iowa State University, p 185. https://doi.org/10.31274/ETD-180810-1752

Noser H, Heldstab T, Schmutz B, Kamer L (2011) Typical accuracy and quality control of a process for creating CT-based virtual bone models. J Digit Imaging 24:437–445. https://doi.org/10.1007/s10278-010-9287-4

Raman S, Wenger R (2008) Quality isosurface mesh generation using an extended marching cubes lookup table. Comput Graph Forum 27(3):791–798

Rančić G, Nikolić I. (2007) Razviće vezivnog tkiva. In: Nikolić et al (eds) Embriologija čoveka tekst i atlas, treće dopunjeno izdanje, Data Status, Beograd, pp 109–115

Rathnayaka K, Momot KI, Noser H (2012) Quantification of the accuracy of MRI generated 3D models bones compared to CT generated 3D models. Med Eng Phys 34(3):357–363. https://doi.org/10.1016/j.medengphy.2011.07.027

Salhotra A, Shah HN, Levi B et al (2020) Mechanisms of bone development and repair. Nat Rev Mol Cell Biol 21:696–711. https://doi.org/10.1038/s41580-020-00279-w

Schindeler A, McDonald MM, Bokko P, Little DG (2008) Bone remodeling during fracture repair: the cellular picture. Semin Cell Dev Biol 19:459–466. https://doi.org/10.1016/j.semcdb.2008.07.004

Shiode R, Kabashima M, Hiasa Y et al (2021) 2D–3D reconstruction of distal forearm bone from actual X-ray images of the wrist using convolutional neural networks. Sci Rep 11:15249. https://doi.org/10.1038/s41598-021-94634-2

Sholukha V, Chapman T, Salvia P, Moiseev F, Euran F, Rooze M, Van Sint JS (2011) Femur shape prediction by multiple regression based on quadric surface fitting. J Biomech 44(4):712–718

Sourina O, Sourin A, Howe TS (2000) Virtual orthopedic surgery training on personal computer. Int J Inf Technol 6(1):16–29

Stevanović D, Vitković N, Veselinović M et al (2013) Parametrization of internal fixator by Mitkovic. In: Proceedings of the international working conference “Total quality management—advanced and intelligent approaches”, 4–7 June 2013, Belgrade, Serbia, pp 541–544
Stojković M, Milovanović J, Vitković N et al (2010) Reverse modeling and solid free-form fabrication of sternum implant. Australas Phys Eng Sci Med 33(3):243–250
Sugano N (2013) Computer-assisted orthopaedic surgery and robotic surgery in total hip arthroplasty. Clin Orthop Surg 5(1):1–9. https://doi.org/10.4055/cios.2013.5.1.1
Tashiro Y, Okazaki K, Uemura M et al (2014) Comparison of transtibial and transportal techniques in drilling femoral tunnels during anterior cruciate ligament reconstruction using 3D-CAD models. Open Access J Sports Med 4(5):65–72. https://doi.org/10.2147/OAJSM.S59297
Veselinovic M, Vitković N, Trajanović M et al (2013) Different approaches for creation of human tibia 3D models based on CT data. In: The 35th international conference on production engineering, Kraljevo-Kopaonik, pp 283–289
Vitković N (2016) Reverse engineering of human long bones based on morphometric parameters. University of Niš, Faculty of Mechanical Engineering in Niš
Vitković N, Manić M, Trajanović M et al (2014) Geometrically defined cloud of anatomical points of human femur trochanteric and neck region. In: ICT Forum 2014, ICT Conference 2014, Niš, Serbia, pp 126–129
Vitković N, Milovanović J, Korunović N et al (2013) Software system for creation of human femur customized polygonal models. Comput Sci Inf Syst 10(3):1473–1497
Vitković N, Mitić J, Manić M (2015a) The parametric model of the human mandible coronoid process created by method of anatomical features. Comput Math Methods Med 2015:574132. https://doi.org/10.1155/2015/574132
Vitković N, Mitković MM, Mitković BM et al (2015b) Reverse engineering of the mitkovic type internal fixator for lateral tibial plateau. Facta Univ Ser Mech Eng 13(3):259–268
Vitkovic N, Mladenovic S, Trifunovic M et al (2018) Software framework for the creation and application of personalized bone and plate implant geometrical models. J Healthcare Eng 2018(Article ID 6025935). https://doi.org/10.1155/2018/6025935
Vitkovic N, Radovic LJ et al (2019) 3D point cloud model of human bio form created by the application of geometric morphometrics and method of anatomical features: human tibia example. Filomat Univ Nis, Fac Sci Math 33(4):1217–1225. https://doi.org/10.2298/Fil1904217v
Wang J, Huang Z, Yang X et al (2020) Three-dimensional reconstruction of jaw and dentition CBCT images based on improved marching cubes algorithm. Procedia CIRP 89:239–244. https://doi.org/10.1016/j.procir.2020.05.148
Weber GW (2014) Virtual anthropology. Am J Phys Anthropol. https://doi.org/10.1002/ajpa.22658
Weng YJ, Hsu RW, Hsu WH (2009) Comparison of computer-assisted navigation and conventional instrumentation for bilateral total knee arthroplasty. J Arthroplasty 24(5):668–673. https://doi.org/10.1016/j.arth.2008.03.006
Young SW, Safran MR, Clatworthy M (2013) Applications of computer navigation in sports medicine knee surgery: an evidence-based review. Curr Rev Musculoskelet Med 6(3):150–157. https://doi.org/10.1007/s12178-013-9166-y
Zheng G, Von Recum J, Nolte LP et al (2012) Validation of a statistical shape model-based 2D/3D reconstruction method for determination of cup orientation after THA. Int J CARS 7(2):225–231. https://doi.org/10.1007/s11548-011-0644-7
Zsemlye G (2005) Shape prediction from partial information. Ph.D. thesis, ETH Zurich, Zürich. https://doi.org/10.3929/ethz-a-005181558

Chapter 3
Geometrical Model of the Human Mandible: Potential for Application in Personalized Maxillofacial Surgery

Jelena Mitic and Miroslav D. Trajanovic

3.1 Introduction

The human skeletal system represents a highly complex structure, and therefore, some orthopedic interventions applied on its deformed parts are in many cases complicated. Hence, most surgical interventions for the treatment of fractures, some pathological processes, and injuries require a good preoperative plan.

A number of research studies have reported that the 3D geometrical model of a human bone (including models of other anatomical structures—models of muscles, tissues) for medical applications is a powerful tool in numerous stages of the planning. Ganguli et al. (2018) provide a detailed review on that.

In brief, the 3D geometrical model of a human bone (polygonal, surface, and solid) is defined as a model which according to its geometric, topological, anatomical, and morphological characteristics, corresponds to the physical shape of the human skeleton bone. It is created from individual patient data, obtained from medical images, and can be represented as a model of a complete bone structure and/or specific segments. According to published articles, the application of geometrical models of human bones in today's medicine and other related disciplines is various.

Based on published studies in the scientific literature, the application of geometrical models of human bones depends on their geometrical accuracy. The tolerance of two millimeters is a regular requirement regarding geometrical accuracy. The anatomically correct, geometrically accurate and topologically similar models of human bones in most cases can provide the surgeons to properly prepare and plan the course of surgical intervention. Clearly defined procedures and responsibilities of team members require the minimal occurrence of possible problems and errors that may occur during the intervention (Hammoudeh et al. 2015; Bell 2010; Gateno et al. 2007). On the other hand, a less accurate 3D geometrical model can provide the

J. Mitic (✉) · M. D. Trajanovic
Faculty of Science and Mathematics, University of Nis, Nis, Serbia
e-mail: jelena.mitic3@pmf.edu.rs

O. Canciglieri Junior and M. D. Trajanovic (eds.), *Personalized Orthopedics*,
https://doi.org/10.1007/978-3-030-98279-9_3

students with: not only better visualization of the anatomical structure, and understanding the anatomy but also could be used to train new surgeons to prepare for the surgery.

In the last few years, software packages have been developed offering numerous approaches for preoperative planning and postoperative evaluation of the Computer—Aided Surgery (CAS) process. CAS is a scientific and technical discipline where computer technology and medical images of a patient are applied to create 3D models of anatomical structures that topologically and anatomically correspond to physical shape (Fuessinger et al. 2018). The application of 3D geometric models in specific software packages allow performing surgical planning and surgical simulations of interventions with maximum respect to procedure. However, in order to assess the accuracy of the reconstruction and compare the postoperative results, it is necessary to standardize the methods (van Baar et al. 2018).

The turning point in the complex surgical intervention was the advent of 3D Computer-Aided Surgical Simulation (CASS). In recent decades, a revolution in complex surgical intervention began due to new methods of CASS. The CASS is a planning method for the treatment of patients with complex deformities. This method can provide accurate guidance for assessment and treatment planning in clinical practice. Complex surgical interventions of craniomaxillofacial deformities have so far been planned by traditional methods. However, there have been problems associated with such methods that can result in less than the ideal surgical outcome. Compared to traditional methods, the method of 3D CASS is significantly better with surgical outcomes (Xia et al. 2011). To reduce potential risks, Gateno et al. (2007), presented a model of the skull with a high degree of accuracy of the reproduction of bone structures. To modify the surgical plan and prevent potential unsatisfactory outcomes, the intervention simulation was performed after the model was created. The result indicated that a precise and high-quality 3D geometric model of a bone is in a direct correlation with the successful realization of CASS.

The fact that a face represents symmetrical structure enabled the use of a 3D model of a healthy part for the reconstruction of a complete 3D model of the mandible. Such fact is supported by the results of the study by Watson et al. (2014) and Lee et al. (2007). 3D model of the mandible has a pivotal role in the correction of: deformities, post-traumatic defect, defect after disease and tumor. These types of models have proper geometrical definitions, and thus, they are suitable for Finite Element Method (FEM) based software packages as Abaqus, Ansys, etc. (Vajgel et al. 2013; Lisiak-Myszke et al. 2020). The results also indicated that by using the 3D model of the mandible as a guide for a surgical planning, it is possible to achieve satisfactory functioning and aesthetic results. In the area of the defect, such models enable a creation of bone implants, scaffolds and fixators adapted to the morphological characteristics of the bone using engineering technologies (Computer-Aided Design and Manufacturing (CAD/CAM) and additive manufacturing).

In the field of Virtual Anthropology, the importance of geometric models is reflected in the providing the topological and morphological information about bones (Weber et al. 2001). This information is as important for anthropology students as well as for doctors. The application of geometrical models of bone structures is also present in forensic anthropology. In forensic anthropology, it is necessary to collect, report, and evaluate as much individual data and samples as possible to create an anthropological database of virtual skeletons. Data comparability was analyzed to understand the limitations of applied anthropological methods on virtual bones.

In summary, anatomically correct, geometrically accurate, and topologically similar models of a human bone are necessary for the field of reconstructive surgery, engineering, material science, and other scientific disciplines. Because of that, it is of essential importance to put efforts into the creation and definition of the human bone geometry and morphology. The first step on the path towards the reaching of the previously listed goals is the knowledge of possible approaches for the creation of the geometrical model of human bones and its possible disadvantages.

The chapter is organized in a following manner: Sect. 3.2 introduces the anatomy of human mandible. Section 3.3 presents two approaches for the creation of the mandible bone geometrical model and its adequate application in a personalized maxillofacial surgery. The final Sect. 3.4 is the conclusion.

3.2 Anatomy of Human Mandible

The lower jaw (mandible) is the largest and strongest face bone of the viscerocranium, connected with the skull by temporomandibular joint. The temporomandibular joint is the only movable joint of the head. The main parts of the mandible is the mandible body located inferior to the maxilla (Moore 1992).

The mandible body has a horseshoe shape and represents it's the horizontal part. Its upper part called the alveolar part, makes the inferior dental arch. The body of the mandible has two sides, external (it contains the mandibular symphysis at midline) and internal (it contains the median ridge at midline and mental spines) and two edges, the upper one which matches the dental arc and a lower edge or the basis of the mandible. The ramus of the mandible has an approximately rectangular shape, located upward and backward in the relation to the mandibular body forming an angle of 90° to 140°. To summarize, it has two sides: external and internal, and four edges: upper, lower, anterior and posterior. The upper edge has two processes: coronoid and condylar, which are divided into two parts: the head and the neck. The head of the mandible is triangular, flattened in the anteroposterior direction, and contributes to the temporomandibular junction by articulating with the articular disk. The neck of the mandible represents the lower, narrow part of the condylar process that projects from the ramus (Sokolovic 1997; Juodzbalys et al. 2010). Anatomy of human mandible is presented in Fig. 3.1.

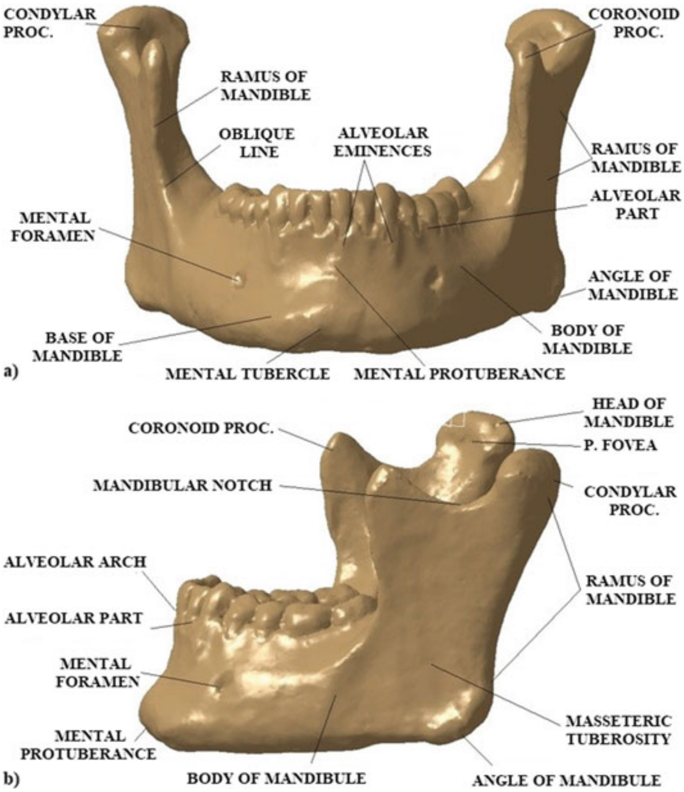

Fig. 3.1 The mandible **a** lateral aspect, **b** anterior aspect

3.3 Methods

The development of computer science and computer aided modeling enabled significant support in the development of new approaches, which provides us with almost ideal geometrical models of human bones. The basic way to create a geometrical model of human bones is based on the application of Reverse Engineering (RE). RE is a process that allows the reconstruction of the geometry of 3D models of anatomical structures and objects of interest (Page et al. 2007). Its application is described in case studies from the fields of computer arts, medicine, dentistry, and biomedical research (Bradley and Currie 2005). The application of RE in the creation 3D of the geometrical model of a human bone is divided into several phases with the aim of providing higher geometric and anatomical accuracy of the models. To the best of the author knowledge, there are two methods for the generation of 3D geometrical models of a human bone by the RE methods. The first method for the creation of a geometric model is based on the use of volumetric scanning methods while the second approach is based on the bone shape prediction (Majstorovic et al. 2013).

3.3.1 Creation of a Geometric Model of Human Mandible by Volumetric Scanning Method

Volumetric scanning methods enable the creation of the geometric model of human bone by the application of a medical software and Computer-Aided Design (CAD) software packages. As described by Vitkovic et al. (2018), such models can be created in three phases: data acquisition, processing of medical images in medical-oriented CAD programs (e.g., Materialise Mimics), and building a solid model in a CAD software packages (e.g., CATIA).

Depending on the level of accuracy, a variety of techniques can be used for the RE data acquisition (Adate et al. 2017). Scanning methods, which allow a three-dimensional representation of anatomical structures with complex geometries and shapes, primarily use the non-contact methods (Galantucci et al. 2006). The noncontact methods use light to capture the data, and the geometry of an object is represented by 2D cross-sections or point clouds (Hieu et al. 2010). The non-contact volumetric scanning techniques, such as CT and MRI are the most widely used for the acquisition of the data of bone structures (Ghafoor 2018). The advantage of this method is that volumetric images can accurately reproduce the bone geometry (Aroeira et al. 2017). CT, which is excellent for bone imaging, uses specialized X–rays to provide a detailed insight into the bone structure (Petrovic and Korunovic 2018). Compared to CT, MRI acquisition takes a considerably longer time, and it is used in cases when it is necessary to scan patients with a lower radiation dose. In the phase of the data acquisition, special attention is paid to some scanning parameters, which define the accuracy and the resolution of the scanned images (Taleghani and Fatahi 2018). These parameters depend on the construction of the volumetric scanners, as well as on the algorithms applied for processing of images. Processing scanned images can be done directly in the scanner software which is a part of a medical device or in specialized programs. The specialized programs provide more options. Their advantage is reflected in the application of reconstruction methods. The transfer of the patient data into appropriate specialized programs is performed in some file formats: Analyze, Neuroimaging Informatics Technology Initiative (NIFTI), Minc, and Digital Imaging and Communications in Medicine (DICOM) (Sriramakrishnan et al. 2019). However, the DICOM format has been widely accepted and successfully used for storing and transmitting medical images thanks to great flexibility to follow the medical imaging advances (Larobina and Murino 2014).

The next phase is processing of medical images and is usually performed in medical-oriented CAD programs (Materialise Mimics, 3D Doctor, 3D Slicer, MeVisLad). Within this phase, the chosen anatomical structure is separated based on similarity or heterogeneity measures by applying different segmentation methods. The existing published data indicate a different classification of techniques available in the image segmentation. However, segmentation methods were classified into two classes: method based on gray level features and textural feature-based methods (Sharma and Aggarwal 2010). The methods based on gray level features, such as thresholding (Indraswari et al. 2019) and region-based segmentation (Kaur et al.

2014) are the techniques with the simplest approach to the problem of segmentation. Methods based on the textural features subdivide the image into a regions with different texture properties depending on its tone and structure. Compared to the methods based on gray level features, the texture-based methods are more appropriate for the segmentation of medical images (Tesar et al. 2008). However, the performance of various segmentation techniques can be improved by integrating them with a different neural network-based algorithms in order to ensure accuracy, reliability, and repeatability, robustness (Sharma and Aggarwal 2010). During an adequate process, volumetric data can be visualized in the form of the 3D anatomical model, which is described in Budzik and Turek (2018). The export of the model from specialized medical software is usually done in STL (STereoLithography) file format. In medical-oriented CAD programs such as Materialise Mimics, it is possible to create 3D adequate models of anatomical structures by performing reconstructive methods that can be used for building a solid model.

The processing of the geometrical model of anatomical structures formed from CT or MRI is the last phase, and is usually performed in a CAD software packages. This process is performed on an imported segmented model from a specialized medical software in an adequate format (usually STL) and consists of a set of operations (removing the unnecessary entities which are not a part of the bone, healing, optimization, and mesh smoothing) to create a polygonal model (Trajanovic et al. 2009), which can be used for the creation of different types of models (surface and solid), as presented in Tufegdzic et al. (2013). In CAD software packages, the Non-Uniform Rational B-Splines (NURBS) are used to define the surface of objects with complex geometry and topology, such as a human bone (Au et al. 2008). However, the study by Stojkovic et al. (2019) considers the application of T-NURCCs (Non-Uniform Rational Catmull-Clark Surfaces with T-junctions) in geometric modeling of objects characterized by complex topologies such as a mandible bone due to a clear advantage in comparison to the surface created with NURBS, especially regarding surface quality, geometric flexibility, and local refinement. Technical elements of CAD software packages allow the detailed definition of the model geometry and thus enable subsequent operations with models such as application of Finite Element Analysis (FEA) (Lisiak-Myszke et al. 2020), development of physical models with additive technologies (Kontio et al. 2012), creation of customized fixators and implants, etc.

The main disadvantage of this approach is the inability to create models of complete bones in cases when the scanned bone is incomplete due to some disease or trauma or when medical images are not of appropriate quality.

3.3.1.1 Application of the Method of Anatomical Features for Creation Geometrical Model of Human Mandible

One of the methods that have proven success in the creation of geometric models of human bones is the Method of Anatomical Features (MAF). Initially, the method was applied to long bones (humerus, tibia, and femur), but it gained its universality by applying it for the creation of the geometric model also for other bones of the human skeletal system. The method is based on a set of techniques and procedures that aim to create anatomically accurate and morphologically correct 3D geometric models. The main goal of applying the MAF method is to create 3D geometric models of complete bones, as well as bone parts of high geometric precision and anatomical accuracy, even in cases when the patient's bone image is not complete (Majstorovic et al. 2013).

To demonstrate the MAF, a human mandible sample without any deformities was used, scanned by 64-slice CT (MSCT) (Aquillion 64, Toshiba, Japan) according to the standard protocol recording. The human geometrical model creation procedure is based on the application of medical imaging software and CAD software going two phases:

- creating a polygonal model,
- creating a 3D geometrical (surface and solid) model.

The preprocessing of medical images starts in medical imaging software which enables the creation of the 3D model of the scanned mandible by applying adequate segmentation methods (using the Hounsfield scale). The next step is exporting a 3D model of the mandible from the medical imaging software to STL format. This format is easy to use and describes only the surface geometry of the 3D model without common CAD model attributes. Importing and processing the 3D model of mandible in CAD software (CATIA V5 R19) is based on reconstructing and healing the surfaces, eliminating errors, with the aim to obtaining a polygonal model of the mandible bone.

The human geometrical model creation procedure consists of the following steps (Mitic et al. 2020a):

- definition of the Referential Geometrical Entities (RGEs),
- definition of the Constitutive Geometrical Entities (CGEs),
- creation of a surface and solid model of the human mandible.

The determination of RGEs of the human mandible bone is a prerequisite for the successful reverse modeling. This step of the reverse modeling of the human mandible geometric model is based on the definition of characteristic points, axes, planes (bone RGEs) according to the anatomical and morphological characteristics of the bone, with the aim of referencing Constitutive Geometrical Entities (such as curves, surface, and solids). For the reverse modeling of the mandibular geometry, the rules for the formation of several directions and views are defined in order to describe the projections of bone parts or the whole bone.

The process of identifying RGEs begins with the creation of characteristic anatomical points as geometrical elements. They are defined as RGEs on the polygonal model of the mandible, shown in Fig. 3.2 and described in Table 3.1. It is very important to note that we analyzed only the characteristic anatomical landmarks (points) that are important for creating a 3D geometrical model of the mandible. In accordance with the needs (such as, dental practice) more precise analyzes of anatomical landmarks is necessary (Arsic 2019).

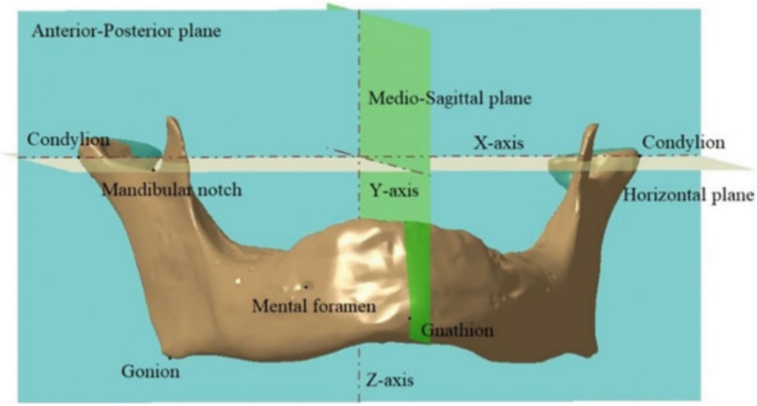

Fig. 3.2 Referential geometrical entities defined on the polygonal model of mandible

Table 3.1 Anatomical landmark (MP) (Arsic et al. 2010)

Anatomical landmark	Definition
Mental foramen (MF)	Is one of two holes located on the anterior surface of the mandible
Gnathion (Gn)	It is the most inferior midline point on the mandible
Gonion (Go)	It is a point along the rounded posteroinferior corner of the mandible between the ramus and the body
Condylion (Con)	It is the most prominent point on the mandibular condyle
Mandibular cut (MU)	It is the central point on the mandibular notch

The initial mandible RGE is Medio-Sagittal (MS) plane, and defining all other planes of the coordinate system, as well as the axis, defined depending on it. To define the MS plane, two points (the RGEs of the mandible) are used:

- Condylion (Con) defined on the left and right condylar process,
- Gnathion (Gn).

MS plane was constructed as the plane normal to the distance between the most lateral points on the right and left condyles (Con) and contained the Gnathion (Gn) anatomical point. MS plane divides the human mandible into two halves—left and right. Based on the previously defined RGEs, the following geometric entities were constructed: Horizontal Plane (HP), Anterior–Posterior (AP) plane, X-axis, Y-axis, and Z-axis, shown in Fig. 3.2.

Horizontal Plane (HP) is constructed as normal to the MS plane and containes the most inferior point on the mandibular angle—Gonion (Go). Anterior–Posterior (AP) plane is constructed as normal to the HP dividing the mandible into two anatomical sections—anterior and posterior. Origin of the coordinate system was defined as the middle of the distance between the most lateral points on the right and left condyles.

MS plane and AP are constructed as the planes which contain the Origin of the OBC. To be used as a plane of OBC, the HP plane is translated to the origin of OBC.

The X-axis of the mandible RGEs is very important for procedures of reverse modeling of the mandible, which is based on a rotating set of the cross-section. The X-axis is created as normal to the MS plane. The Y-axis is created as normal to the AP plane, and Z-axis is created as normal to HP. This axis is necessary for the procedure of reverse modeling of the body of the human mandible. Referential Geometrical Entities defined on the polygonal model are presented in Fig. 3.2.

Definition of the CGEs (geometrical entities higher order) such as curves, surface, and solid are based on RGEs. Then follows the construction of CGEs along the body and ramus follows.

Body cross-section curves are constructed using an outer surface and a series of sixteen planes. These planes are defined to form a certain angle with the MS plane and passing through the Z-axis (in this case, axis of rotation). The center of a series of rotational planes is defined as the middle of the distance between anatomical point Con positioned on the left and right condylar process. Body cross-section curves created in rotational planes are usually closed, however, in case, when cross-section results with separated curves it is necessary to close curves by merging. To create a surface model of the mandibular body, B-splines are used. Body cross-section curves are used to create a B-spline that follows the shape of the mandibular body, preserving the morphology (form or shape) of the bone. Constructed B-spline curves on the mandibular body are presented in Fig. 3a.

To obtain a surface of the mandibular ramus, a similar procedure is performed. B-spline curves are created by the cross-section of the 14 planes (defined to form a certain angle with the Horizontal plane and passing through the X-axis) and polygonal models, defined to follow the bone geometry and its specific morphology. Constructed B-spline curves on mandibular ramus are presented in Fig. 3b.

With appropriate operations, such as merging and joining on constructed individual surfaces of the mandibular body and ramus, the surface model of the whole

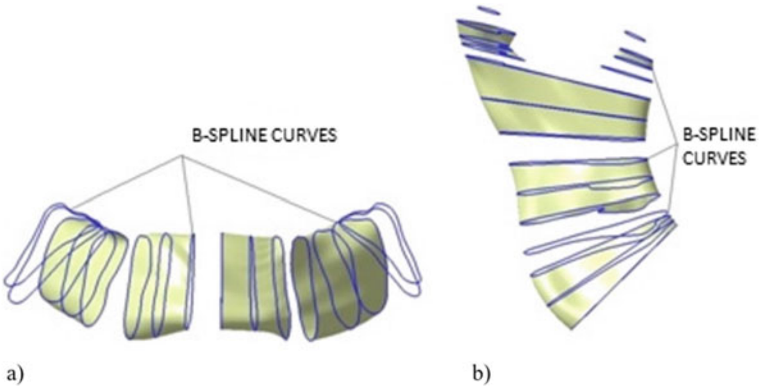

Fig. 3.3 **a** B-spline curves on the body, **b** ramus of the human mandible (Mitic et al. 2020a)

Fig. 3.4 3D surface model of the human mandible (Mitic et al. 2020a)

mandible was created. The surface model of the whole mandible is presented in Fig. 3.4.

As a final remark, it is important to mention that by using a large number of cross-sectional planes in order to obtain a more precise 3D model, problems arise in the later formation of the surface model of the mandible. Namely, it comes to unwanted deformation of the surface in places where the morphology of the mandible is more complex (Fig. 5a, b). These irregularities and wrinkles could be partially corrected by using smaller number B-spline curves.

In order to test the geometrical accuracy, a comparative analyzes is performed on the resulting models created by two approaches: MAF and classical techniques of reverse engineering. The methods are demonstrated on the same bone sample. Geometrical accuracy is tested by applying analyzes of the deviations between the input and the resulting model in CATIA software. The maximal deviation value of the surface model created by MAF is 1.66 mm, 22.3% better than the surface models created by classical techniques of the reverse engineering (2.03 mm) (Mitic et al. 2020a). Considering the results of the study, it can be concluded that MAF represents the basis for defining and identifying morphological entities that are particularly

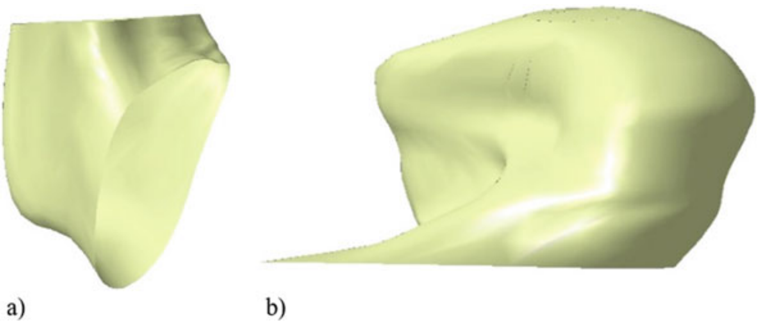

Fig. 3.5 Irregularities and wrinkles on **a** angle of human mandible, **b** condylar process

important in creating geometric models and directly affect the speed and accuracy of the reverse engineering process, which is a basic imperative in emergencies.

3.3.1.2 Application of the Geometrical Model of a Human Mandible

One of the most common problems in maxillofacial surgery is rebuilding bones or bone parts which are exposed to trauma with the aim of proper functioning, repairing, or replacing a lost or damaged bone, accelerate healing and improving the quality of patient's recovery (Olson et al. 1982). Various techniques have been used for reduction and fixation process of fractures which can provide biomechanical stability to the assembly of fractured mandible and adequate implant (different kind of plates with a specific dimension range, screws, etc.) (Stacey et al. 2006). However, the reduction of bone fragments and their fixation may be problematic if the geometry and morphology of the human bone and plates are not properly defined. This problem prevents quality improvement and increases duration of the intervention and postoperative recovery of patients.

The importance of the geometric model of the human mandible created by using application MAF and the benefits it brings may be summarized as follows:

- Geometrically accurate and anatomically correct 3D model of the bones allows the creation of personalized plate implant for the fixation of mandible internal fractures (Fig. 6a). In that way, the geometry, and morphology of the specific human bone and osteofixation material (in this case, plates type of implant shaped as a trapezoid) are properly defined (Mitic et al. 2017).
- The healthcare procedure in maxillofacial surgery based on precise 3D bone model enables the surgeons to improve surgical interventions (Fig. 6b) (Manic et al. 2015).

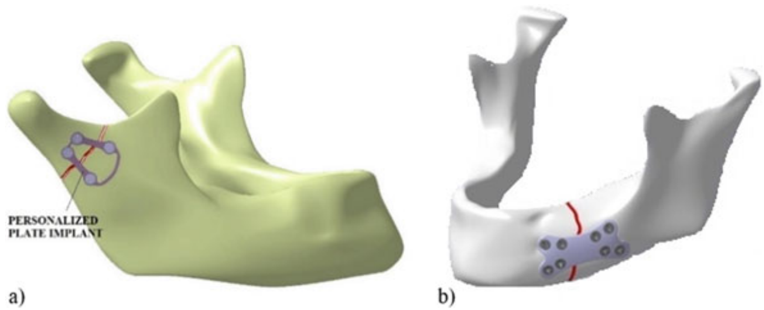

Fig. 3.6 Personalized plate implant for the fixation of mandible internal fractures **a** on condylar process (Mitic et al. 2017), **b** on body of mandible (Manic et al. 2015)

3.3.2 *Creation of the Geometric Model of Human Mandible Based on Shape Prediction*

Methods based on the prediction of a shape and geometry enable the development of a 3D model that describes the typical human bone anatomy of a particular population. These methods enable the creation of bone geometrical models applying the parametric or statistical models.

Statistical Shape Models (SSMs) are 3D geometric models that describe a collection of semantically similar objects in a very compact way and represent an average shape as well as their variation in shape (Ambellan et al. 2019). The statistical shape model describes the natural variation of the shape structure, and for that reason they are often applied in research related to recognizing and changing the shape of anatomical structures. The method for the creation of SSM is based on the identification of landmarks on elements of the initial set of samples and establishing correspondence between them where the shape variation is modelled by statistical analyzes.

To generate the statistical model of human bones, the biggest challenge is to collect a sufficient number of input samples of the same bone. A very large number of scans are performed in clinical practice; however, the problem is collecting quality images of healthy bones in accordance with ethical and legal rules. Medical images of patients with the bones affected by pathological changes, fractures and deformities are excluded from the data set. It is generally known that the number of healthy bone samples determines the quality of the resulting model. According to the data from the literature, the number of samples that allow the construction of a statistical model should be greater than 10.

Research dealing with the generation of statistical models of human bones, in most cases, uses volumetric images of bones obtained by a CT device (Coogan et al. 2018; Valenti 2015), because it provides accurate spatial information about bone structures.

Only a few papers described the development of geometric models directly from medical images (Lamecker et al. 2005). The usual approach is to use some segmentation methods to separate the object of interest from the background (Tian et al. 2009). The segmentation of the object gives a direct representation of areas, without redundant information that is not the subject of interest. By choosing an adequate Hounsfield unit (NU) value from 226 to 3072, background objects classified as bones could be extracted in most cases. Choosing a lower NU value, threshold would classify even softer tissue, while a higher threshold would miss the actual bone. One solution would be to create automatic segmentation algorithms. However, none of the available algorithms can completely solve the problem of classification the object of interest. The results of the study suggest that manual editing is a more reliable method due to the compromise between classifying too many or few voxels. Attention should be drawn to another problem and that is the position of the sample. Each sample should be placed in a similar position. This requirement especially refers to the creation of statistical models where the objects of interest should be placed in the same position as precisely as possible in order to avoid differences in measures due to different position or angle of view to the bone.

The most important step in creating geometric models is to represent the shape of the objects. The simplest way to represent shapes is correspondence where the positioning of points on each input sample is done in the same way, according to a comparable position. In the scientific literature, points correspondence can be anatomical landmarks (biologically meaningful points defined by experts to ensure their correspondences within the same species), mathematical landmarks (points located on an object as a description of a mathematical or geometric property), and pseudo-landmarks (points located between anatomical or mathematical landmarks) (Gomes et al. 2013). The number of landmarks depends on the complexity of the shape. Most statistical shape models are based on Point Distribution Models (PDMs) where each shape is represented by a set of labelled landmark points (Vasconcelos and Tavares 2018). Morphological forms in medicine can be described by a method based on the use of Active Shape Models (ASMs). With this method, it is possible to perform an iterative deformation of the statistical model created over the input set of the object, to fit an example of the object in the new image obtained by one of the methods for the data acquisition in medicine.

Predicting the shape of a human mandible or its part is usually performed by the statistical method named Principal Component Analysis (PCA) (Zachowa et al. 2005; Kim et al. 2012). PCA is a fundamental tool in the shape modelling, which can be used as a prediction technique when shapes need to be predicted based on available information.

It is very difficult to assess the accuracy of statistical models. According to the scientific literature, a good statistical model should be able to "capture" 90% of the total variance in a training set (Heimann and Meinzer 2009). However, this is not the only criterion. The research based on a facial reconstruction indicates that it is necessary to pay attention to the reconstructive error. The authors of the study Berar et al. (2005), which deals with the research based on the facial reconstruction, created a statistical model that was additionally tested for the reconstruction error. The testing was performed on samples of the initial data set and on samples that are not part of the original data set. According to the obtained results, the authors indicate that the global reconstruction is correct, with a model accuracy of 0.5 mm for samples of the original data set. On the other hand, the test sample is reconstructed with an average accuracy of 7 mm. For the research purposes, a statistical model of the shape has been developed that would enable the reconstruction of mandibular dysplasia (Zachowa et al. 2005). Checking the accuracy of the created statistical model was done on three pathological conditions. In all three cases, the distances of the anatomical parts of the mandible that will be reconstructed were measured. About 70–83% of the selected areas had a deviation of less than 2 mm, while only 2–6.6% of the surface had a deviation of 4 mm. The authors consider the maximum deviation of 8.3–10.4 mm to be a consequence of the small number of samples (11) in the training set.

3.3.2.1 Parametric Model of Human Mandible

Only a few published papers described the development of the parametric model of the human bone (Trajanovic et al. 2018; Breglia 2006). The process of creating a parametric model of the human bone is complex and requires the use of appropriate medical and CAD software packages. In order to achieve a complete geometrical definition of the human bone, the knowledge of human bone anatomy, medical image analyzes knowledge, and anatomical and morphological rules is of an essential importance.

One of the methods that have proven to be successful for the creation of parametric models is the MAF method. The parametric model of the human bone is one of the output models obtained by the MAF, and it is defined by a set of parametric functions, whose arguments are morphometric parameters (specific dimensions which can be measured from medical images by using adequate software). By the application of individually defined values of morphometric parameters, these models can be transformed into a 3D personalized geometrical model of the specific human bone (Majstorovic et al. 2013, Mitic 2019a).

To demonstrate the MAF, a samples of 22 CT scans of the human mandible are used, obtained with Toshiba MSCT scanner Aquillion according to the standard protocol recording. The samples came from adults (ages from 22 to 72 years), different heights and weights.

Data from CT scans, written in DICOM format are converted to STL format in a medical software and imported into CAD application CATIA. The model reconstruction (eliminate the unnecessary entities, healing, optimization and mesh smoothing) is performed in CATIA with the aim to obtain polygonal models of bones.

The research is composed of a few steps, presented in Fig. 3.7.

The identification and creation of RGE on each polygonal model represent the initial phase in the MAF method. This phase is also the main precondition for the successful reverse modeling of the human bone geometry. As already mentioned, RGE includes characteristic points, directions, planes and views that serve to define other elements of the bone curve and surface geometry. In the beginning, anatomical landmarks (characteristic anatomical points) are created as geometrical elements on each polygonal model of the human mandible. In this research, 5 characteristic anatomical points are singled out: MF, Gn, Go, Con and Mu (present and described in Table 3.1), which served as a basis for defining other elements on the mandible.

After the creation of characteristic anatomical points, morphometric parameters are defined as geometrical elements on the polygonal model of the human mandible. Morphometric parameters are specific dimension defined with the aim to describe the shape, position, and size of individual elements of the mandible. Due to the position of the mandible, 10 morphometric parameters (Con-ConD, BMB, Go-GoD, LMB, max RH, HCon, Min RB, Gn-ConD, HMB, and Gn-IdD) are used to describe the configuration of the mandible (Fig. 3.8). The values of 10 morphometric parameters are measured in the characteristic anatomical planes on each polygonal model. Morphometric parameters at the mandible bone are presented and described in Table 3.2.

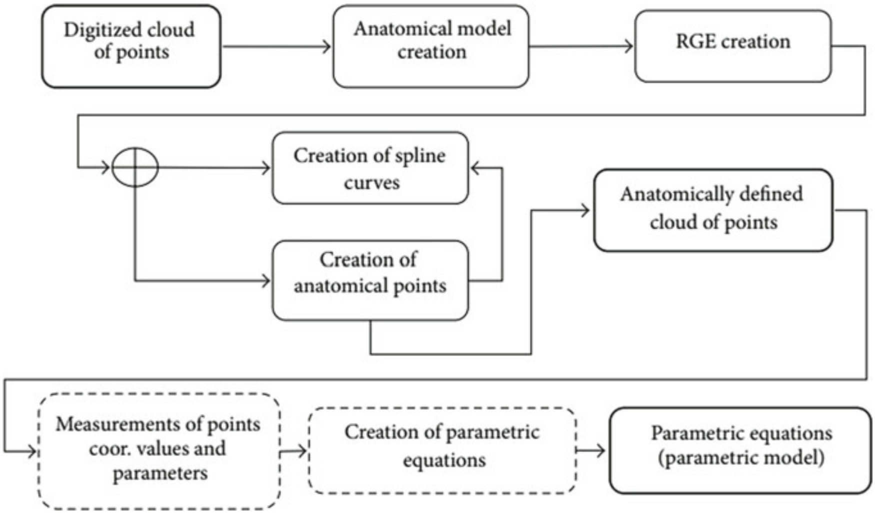

Fig. 3.7 The process of creation of parametric model of the human bone by MAF method (Vitkovic et al. 2015)

Fig. 3.8 Morphometric parameters defined on human mandible (Vitkovic et al. 2015)

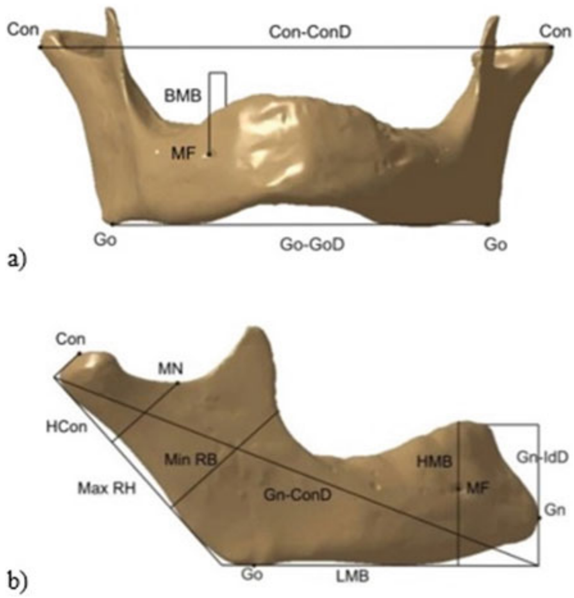

Table 3.2 Morphometric parameters (MP) (Arsic et al. 2010)

MP	Definition
Gnathion-interdental distance (Gn-IdD)	Distance from the gnathion (Gn) to the alveolar septum between two incisors
Bigonial width (Go-GoD)	Direct distance between right and left gonion (Go)
Bicondylar distance (Con-ConD)	Direct distance between the most lateral points on the right and left condyles
Height of the mandibular body (HMB)	Distance from the alveolar border to the mandibular base at the level of the mental foramen (MF)
Breadth of the mandibular body (BMB)	Maximum breadth measured at the level of the mental foramen perpendiculary to the long axis of the mandible
Length of the mandibular body (LMB)	Distance between Go to Gn
Minimum ramus breadth (Min RB)	Minimum breadth of the mandibular ramus measured perpendiculary to the plane of the maximal height of the ramus
Maximum ramus height (Max RH)	Distance between the highest point on the mandibular condyle (condylion) (Con) to Go
Height of the condyle (HCon)	Distance between the Condylion (Con) and axis of the most inferior point of mandibular notch perpendiculary to Max RH
Gnathion-condylar distance (Gn-ConD)	Distance between Gnation (Gn) and Condylion (Con)

The next step is the creation of the model coordinate system on the polygonal model of the human mandible. The coordinate system is created on each polygonal model with the aim of measuring the coordinates of the anatomical points. The origin of the coordinate system is defined as the middle of the distance between the two characteristic anatomical points—Mental Foreman, positioned on the left and right condylar process. The constructed planes of the coordinate system of the mandible are:

- Medio—Sagittal plane (MS)—normal to the line which connects mental foreman middle points.
- Horizontal (Mandibular) plane—normal to the MS plane and it contains the Gonion anatomical point.
- Coronal plane—normal to the mandibular plane and divides mandible into two anatomical sections, anterior and posterior.

In the intersection of the constructed plane of the coordinate system and the polygonal model, spline curves are created serving to position the anatomical points. For a complete description of the shape of the mandible, the position of 156 anatomical points are defined: 52 anatomical points at the body of the human mandible, 36 at ramus, 28 at the angle of the human mandible, 14 at the condylar process, and 26 at coronoid process. Defining the position of anatomical points is done following the anatomical and morphological properties of the bone and their position is determined by the orthodontist. The coordinate's values of the anatomical points were measured in relation to the defined coordinate system.

To describe the functional dependence between the coordinates of anatomical points and morphometric parameters, multilinear regression is applied. Multilinear regression is a statistical technique, that uses an independent variables (in this case, measured values of morphometric parameters) to predict dependent variable (predict values of coordinates of the anatomical points) (Brown 2009).

However, in any statistical modeling based on regression analyzes, the goal is to develop the "best" model (equation) that fits the data the most. It is well known that the regression model that includes all the independent variables has the highest coefficient of determination, however. However, as a rule, all variables do not contribute significantly to explaining the variability. As a part of regression analyzes, multicollinearity is a problem because it undermines the statistical significance of an independent variable (Allen 1997).

Using Minitab software, the values of Pearson's correlation coefficient are determined. High values of correlation coefficients between the independent variable C1 (morphometric parameter Gn-ConD) and C4 (morphometric parameter BMB) (presented in Fig. 3.9) indicate a strong correlation between them which conditioned the elimination of the independent variable C4 from the regression model.

Based on the value of the coefficient of determination (a statistical measurement that examines how much of the variation in outcome can be explained by the variation in the independent variables) and value of statistical significance (*p*-value), it can be concluded that the new regression model with a smaller number of independent variables is just as good as the regression model that contains all the independent variables. By applying the multiple regression, for all of 156 anatomical points, 468 parametric equations were formed for each of the *X*, *Y*, and *Z* coordinates. The

	C1	C2	C3	C4	C5	C6	C7	C8	C9
C2	0.389								
	0.055								
C3	0.010	0.169							
	0.964	0.420							
C4	0.937	0.468	0.086						
	0.000	0.018	0.683						
C5	0.057	0.170	0.284	0.063					
	0.787	0.416	0.169	0.765					
C6	0.297	0.663	0.173	0.468	0.066				
	0.150	0.000	0.408	0.018	0.753				
C7	0.292	0.525	0.427	0.105	0.146	0.693			
	0.157	0.007	0.033	0.617	0.488	0.000			
C8	0.235	0.092	0.152	0.227	0.173	0.235	0.060		
	0.259	0.662	0.467	0.275	0.407	0.258	0.774		
C9	-0.014	0.292	0.581	0.011	0.192	0.368	0.474	0.514	
	0.946	0.157	0.002	0.957	0.359	0.070	0.017	0.009	
C10	0.423	0.738	-0.049	0.588	0.151	0.744	0.455	0.483	0.442
	0.035	0.000	0.817	0.002	0.472	0.000	0.022	0.015	0.027

Fig. 3.9 The values of the Pearson's correlation coefficient (Mitic 2019a)

Anatomical part		b_0	b_1	b_2	b_3	b_4	b_5	b_6	b_7	b_8	b_9
Body of the mandible	x	-27.025	-0.101	-0.083	0.173	0.007	0.055	0.216	0.098	-0.298	-0.04
	y	-12.989	0.509	-0.341	0.095	0.136	-0.663	1.225	-0.211	-0.150	0.286
	z	-33.744	-0.646	0.392	0.169	-0.317	0.285	-0.864	0.302	-0.188	-0.23
Angle of the mandible	x	-39.255	0.160	-0.390	0.054	-0.292	0.201	-0.164	0.217	-0.205	0.015
	y	-39.014	-0.618	0.099	0.266	0.019	0.684	-1.218	-0.138	-0.520	0.526
	z	-12.233	-0.198	0.191	0.082	-0.165	0.141	-0.265	0.197	-0.065	-0.25
Ramus	x	-39.008	0.005	-0.265	0.008	-0.090	0.289	-0.247	-0.029	-0.226	0.094
	y	-34.772	-0.385	0.165	0.148	-0.132	0.286	-0.962	-0.173	-0.637	0.739
	z	-3.576	-0.181	0.054	0.070	-0.053	0.033	-0.027	0.259	-0.159	-0.06
Condylar processes	x	-16.15	-0.204	-0.085	-0.225	0.028	0.689	-0.805	0.169	0.331	-0.29
	y	18.56	-0.195	-0.047	-0.145	-0.087	-0.269	-0.668	-0.762	0.164	1.357
	z	-55.737	-1.036	0.136	0.443	-0.229	0.167	-0.383	1.109	-1.144	0.021
Coronoid processes	x	-39.989	0.128	-0.273	0.351	0.0351	0.308	-0.306	-0.204	-0.032	0.124
	y	-16.851	-0.016	-0.066	0.030	-0.183	-0.329	-0.609	-0.531	-0.859	1.301
	z	-33.933	-1.024	0.279	0.290	-0.265	0.257	-0.634	1.107	-0.789	-0.16

Fig. 3.10 Values of regression coefficients for arbitrarily selected points on the anatomical regions of the mandible (Mitic 2019a)

regression coefficients for selected anatomical points at each anatomical region of the mandible are presented in the Fig. 3.10.

Statistical function for X coordinate of Point 1 is presented in the equation:

$$\begin{aligned} X &= b_0 + b_1 C_1 + b_2 C_2 + \cdots + b_8 C_8 + b_9 C_9 \\ &= -27.025 - 0.101 C_1 - 0.083 C_2 + \cdots - 0.298 C_8 - 0.04 C_9 \end{aligned} \quad (3.1)$$

where: X is value of X coordinate for defined point, $b_0, \ldots, b_9$ are the values of the regression coefficients, $C_1, \ldots, C_9$ are measured values of morphometric parameters.

The construction of the surface model is based on the obtained coordinate's values of the anatomical points. The surface models are created using the spline curves through the calculated points in the CATIA software package.

In order to present the efficiency and accuracy of the applied method, comparative analyzes were performed on all the resulting models. The results are verified through a comparative analyzes of the geometry and through a comparative analyzes of the surface deviation between the input and result models.

The results of the deviation analyzes between the surface model of human mandible created using the parametric functions (MAF method) and the surface models of the original mandible specimens indicate that the value for maximal positive deviation is 3.19 mm and the maximal negative deviation is −2.59 mm.

Based on the obtained results and the recommendation of the orthodontist, it is concluded that the deviations between the input and result models should be as small as possible (less than 2 mm) in order for the model to be suitable for further use.

It is very important to note that the MAF was initially applied to create a parametric model of an anatomical region (coronoid process) on the mandible. Due to its complex shape, this anatomical region was chosen to test the method (Vitkovic et al. 2015). As in the previous case, the generation of the human mandible coronoid process is based on the construction of a mathematical model to describe the functional dependence between the values of the coordinates of anatomical points (in this case, thirty-nine points were defined) and morphometric parameters. As a result of this process, a set of parametric functions is created, with a result in creating a 3D model with a completely satisfactory geometric accuracy and anatomical correctness.

3.3.2.2 Application of Artificial Neural Networks in Prediction of Human Mandible Geometry

The parametric model of the human mandible (MAF method) is defined by the set of parametric functions created by the application of a mathematical model. The quality and accuracy of the mathematical model depends on the complexity of the chosen function and the type of mathematical model. A multiple regression analyzis provided a statistical evaluation of the mathematical model. Using the chosen regression function, the mathematical model is estimated to be adequate, and the solutions obtained by this mathematical model are in the range of the values of the corresponding variables. However, in order to increase accuracy, more complex mathematical models are needed (Mitic et al. 2019b).

This section describes the development of the Artificial Neural Networks (ANN) model for the prediction of coordinates' values of anatomical points (X, Y, and Z). The reason for the selection of the ANN model is the ability to model complex patterns and prediction problems.

For developing the ANN model software package MATLAB is used. In order to develop an optimal ANN model of a high performance the following modeling steps must be considered Mitic (2019a):

- pre-processing of input–output data,
- selection of ANN training and architectural parameters,
- ANN models training,
- testing the ANN models and analyzes of the results.

Even though it is the case of a mathematical model, which is characterized by a large number of influential factors (morphometric parameters for the complete definition of mandible geometry), the previous analyzes has shown that this number can be reduced to 9 main influential factors.

The input layer of the ANN model consists of the nine neurons corresponding to the 9 morphometric parameters (Gn-ConD, LMB, Gn-IdD, Go-GoD, Con-ConD, HMB, min RB, max RH, Hcon), whereas the output layer has 3 neurons that correspond to measured values of points' coordinates X, Y and Z. Input–output pairs represent data obtained from 22 bone samples. In order to create a mathematical model, 75% of randomly selected bone samples are used, while the remaining 25% are used for validation. To stabilize and enhance ANN training, the pre-processing of input–output data is performed. All the data are normalized to a range of [0, 1] which corresponds to a sigmoid transfer function.

$$f(input) = \frac{1}{1 + e^{-input}} \tag{3.2}$$

Modern ANNs have a parallel-distributed architecture which consists of the input layer, a hidden layer (one or two, though there may be more of them), and an output layer. However, there is no clearly defined method for determining architectural parameters (number of hidden layers, the number of neurons in the hidden layer). Recently published literature has indicated that the number of hidden layers depends on the problem to be solved and indicate that the minimum number of layers is the most desirable. On the other hand, the addition of hidden neurons leads to a better prediction result, because the error is reduced in the training process. In this case, the authors warn that adding neurons over a certain level leads to overfitting problems. There are several recommendations for determining this parameter (Lippman 1987; Wong 1991) one of them is that the number of hidden neurons is determined by the equation:

$$m = \sqrt{nl} \tag{3.3}$$

where: n is number of neurons in input layer and l is the number of neurons in output layer.

In order to determine the optimal values of ANN training and architectural parameters (number of hidden layers, the number of neurons in the hidden layer, training algorithm, transfer functions, performance criterion, and other ANN parameters), the trial/error method is used. This method is most precise but also the most time-consuming. As described by Madic and Radovanovic (2011) and Dreyfus et al. (2005), the most used training algorithm for feed-forward backpropagation artificial neural network (BP-ANN) is Levenberg–Marquardt which offer some additional advantages in ANN training: less danger from entrapment in a local minimum, before reaching global minimum at error surface, and provide high accuracy of prediction. There are many different standard training algorithms such as Gradient Descent, Gradient Descent with Momentum, Scaled Conjugate Gradient. The choice of training algorithm conditions the adjustment of training parameters to determining high-performance ANN models.

Table 3.3 Topologies of neural networks (Mitic 2019a)

Model	Method	Number of hidden neurons	Number of hidden layer	Trans. fun. in hidden layer	Trans. fun. in output layer
1	Levenberg–Marquardt	50	1	Logsig	Logsig
2	Levenberg–Marquardt	70	1	Logsig	Logsig
3	Levenberg–Marquardt	50	1	Logsig	Purelin
4	Levenberg–Marquardt	20/30	2	Logsig	Logsig
5	Gradient descent	50	1	Logsig	Logsig
6	Gradient descent	20/30	2	Logsig	Purelin
7	Levenberg–Marquardt	50	1	Tansig	Tansig
8	Levenberg–Marquardt	50	1	Tansig	Purelin
9	Gradient descent	20/30	2	Tansig	Tansig

To determine the optimal values of ANN parameters, several neural networks of different structures are realized and tested. Table 3.3 presents the topologies of neural networks applied in this analyzes.

The ANN's performance during the training and testing was measured according to the Mean of Squared Errors (MSE) using the following equation:

$$MSE = \frac{1}{N}\sum_{i=1}^{N}(f_i - y_i)^2 \tag{3.4}$$

where: N is the number of data samples, f_i and y_i are predicted, and the measured values respectively.

To obtain a prediction accuracy of ANN models, one more statistical criterion (absolute error) needs to be applied. Therefore, the difference between the predicted values and the measured values are calculated for the X, Y, and Z coordinates of anatomical points. The absolute error is a very important criterion and the orthodontists and anatomist suggest that it should not exceed 2 mm in defined X, Y, and Z directions. The model performance is presented in Table 3.4.

The best-performing model is ANN model 1 (Table 3.3), trained by the Levenberg–Marquardt algorithm, and sigmoid (*logsig*) transfer functions are selected in a hidden and output layer. The learning rate is 0.045, while the momentum is 0.625.

Based on the structure of the ANN model and the type of activation functions, the mathematical relationship between input and output variables can be defined as follows:

$$\boldsymbol{Y} = \left[\frac{1}{1 + e^{-(Xw_{ji}+b_j)}}\right]w_{kj} + b_{ok} \tag{3.5}$$

Table 3.4 ANN performance (Mitic 2019a)

ANN	Number of training epochs	Mean squared error		Absolute error (mm)		
		Training data set	Test data set	X	Y	Z
Model 1	1464	0.038	0.002	0.296	0.580	0.388
Model 2	877	0.049	0.059	0.382	0.980	0.394
Model 3	594	0.102	0.307	0.510	0.787	0.659
Model 4	1201	0.121	2.212	0.558	1.573	0.358
Model 5	50,000	0.018	0.028	0.232	0.890	0.338
Model 6	3840	0.335	0.214	0.311	0.801	0.558
Model 7	623	0.065	0.177	0.480	1.415	0.409
Model 8	913	0.058	0.098	0.477	1.410	0.412
Model 9	20,980	0.033	0.077	0.475	1.365	0.413

where: $\boldsymbol{X}$ is the input vector, W_{ji}, b_j—coefficient in the hidden layer, W_{kj}, b_{ok}—coefficient in the output and $\boldsymbol{Y}$ is the output vector.

As an output from the ANN model with the best performance, the predictive values of the points' coordinates X, Y and Z are obtained. Based on the obtained predictive values of the points' coordinates, a cloud of points is formed, thus creating a surface model of the mandible.

The analyzes was performed by comparing the maximum surface deviations of the surface model created using the calculated coordinate's values and the surface model created using the measured coordinate's values. The surface models are created using the spline curves through the measured and calculated points in the CATIA software package. Maximal positive deviation and maximal negative deviation are measured in the anatomical regions on the mandible, and expressed in millimeters (Table 3.5).

The maximal positive deviation was 0.53 mm (measured on the angle of mandible) and maximal negative deviation was −0.46 mm (measured on the ramus of mandible). This means that 100% of the obtained surface has deviations in the range of −1 to 1 mm, which represents a more than satisfactory result. Analyzing the results of the value of maximal positive deviation and maximal negative deviation leads to conclusion. The resulted surface model created by the using of artificial intelligence technique is much more geometrically precise than the models created by the using multiple regression. The obtained values of the maximal positive deviation (0.53 mm) measured on the surface model created by using the artificial intelligence technique gave much better results than the obtained values of the maximal positive deviation (3.19 mm) measured on the surface model created by applying the multiple regression.

Considering the results of the comparative analyzes of geometry and deviations it can be concluded that by using the artificial intelligence technique a geometrical model of significantly higher geometric accuracy can be achieved, which proves the efficiency of the applied method. The created geometric models satisfy the geometric

Table 3.5 Analyzes of maximum deviations between surface model created by the calculated coordinates' values and the surface model created by the measured coordinates' values (Mitic 2019a)

	Maximum deviations (mm)				
Sample	Body of mandible	Ramus	Coronoid process	Condylar process	Angle of mandible
1	−0.31–**0.34**	−0.33–0.03	−0.21–0.02	−0.27–0.10	−0.24–0.25
2	−0.27–0.24	−0.34–0.05	−0.30–0.01	−**0.46**–0.08	−0.34–**0.53**
3	−0.27–0.25	−0.40–0.03	−0.27–0.02	−0.44–0.05	−0.33–0.51
4	−0.27–0.20	−**0.42**–0.10	−0.31–0.01	−0.44–0.07	−0.44–0.31
5	−0.28–0.23	−0.36–0.03	−0.25–0.02	−0.40–0.07	−0.29–0.46
6	−0.27–0.24	−0.32–0.07	−0.21–0.02	−0.34–0.11	−0.24–0.46
7	−0.28–0.21	−0.37–0.04	−0.24–0.07	−0.39–0.08	−0.27–0.45
8	−0.27–0.20	−0.33–0.03	−0.25–0.02	−0.37–0.09	−0.29–0.44
9	−0.28–0.23	−0.36–0.03	−0.24–0.01	−0.38–0.06	−0.26–0.48
10	−0.29–0.23	−0.40–0.06	−0.28–0.03	−0.42–0.10	−0.28–0.43
11	−0.28–0.22	−0.33–0.07	−0.26–0.02	−0.37–0.11	−0.26–0.48
12	−0.27–0.20	−0.31–0.05	−0.24–0.02	−0.36–0.08	−0.21–0.42
13	−0.27–0.27	−0.26–0.05	−0.26–0.02	−0.28–0.10	−0.30–0.50
14	−0.28–0.22	−0.33–0.02	−**0.34**–0.01	−0.37–0.07	−0.38–0.39
15	−0.28–0.23	−0.34–0.03	−**0.34**–0.03	−0.38–0.08	−0.39–0.43
16	−0.27–0.18	−**0.42**–0.02	−0.31–0.01	−0.44–0.05	−0.32–0.45
17	−0.29–0.26	−0.29–0.06	−0.23–0.03	−0.32–0.10	−0.20–0.43
18	−0.27–0.24	−0.40–0.05	−0.30–0.01	−0.45–0.08	−0.31–0.26
19	−0.29–0.27	−0.41–0.07	−0.29–0.05	−0.35–0.04	−0.30–0.40
20	−0.26–0.21	−0.36–0.02	−0.22–0.01	−0.37–0.06	−0.33–0.46
21	−0.22–0.19	−0.37–0.04	−0.25–0.07	−0.40–0.08	−0.29–0.39
22	−0.27–0.22	−0.33–0.05	−0.30–0.08	−0.44–0.10	−0.31–0.41

accuracy and anatomical/morphological correctness and can be used for medical purposes as a powerful tool in numerous stages of planning.

3.3.2.3 Comparison of ANN and Regression Results for the Case of Mandible with Fracture

Due to bone illness, fracture, or some other trauma, the human mandible can be significantly damaged. In these cases, the creation of a complete 3D bone model is based on available input data of a patient's bone, which in most cases is not adequate.

This case described the creation 3D geometrical model of the missing part of the body of the mandible by application of the parametric model of the human mandible

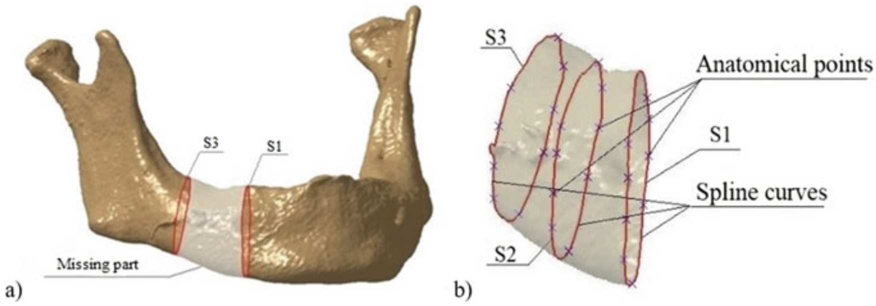

Fig. 3.11 **a** Complex fracture on the body of the human mandible, **b** anatomical points on the part of the human mandible (Mitic 2019a)

in the clinical case where the input data of a patient's bone are not complete. In this case, created damage on the mandible caused the inability to read the values of all defined specific parameters from the CT image, which led to problems in the formation of parametric equations (Mitic 2019a).

The case described the procedure for the development of parametric functions with morphometric parameters smaller than a strictly defined number. The inability to read a strictly defined number of morphometric parameters was influenced by a fracture created on the right side of the mandible body, in the area between the canine tooth and the second and third molar.

On the sample of the human mandible, which is not a part of the initial analyzes, the bone fracture was created on the right side, bounded by curves S1-S3, which corresponds to the lighter area in Fig. 11a. The bone fracture was created according to AO classifications (which is one of the most applied fracture classifications in traumatology today) (https://aotrauma.aofoundation.org) defined for mandible fractures, with the application of adequate operations in CAD software packages CATIA.

The reconstruction of the missing part will be performed using two methods. The first method for the reconstruction is the MAF, which is based on the application of the multiple regression in the creation of a geometrical personalized model of the missing part. The second method is an advanced MAF method. The aim of the preliminary analyzes is to present the obtained results of the mentioned reconstruction methods, which will serve to evaluate the resulting models and make a final conclusion about their geometric quality.

For this purpose, a sample of 22 CT scans of the human mandible is used. Common steps for both reconstruction methods include: obtaining a CT image, digitizing point clouds, preprocessing volumetric data, creating a polygonal model, and creating a model of the fracture bounded by the S1-S3 curves.

At the beginning of analyzes, the positioning of the characteristic anatomical points is performed in order to define morphometric parameters. The bone fracture affected the positioning of two morphometric parameters (Gn-ConD and LMB) and caused the impossibility of reading their values. The values of the remaining seven morphometric parameters (Gn-IdD, Go-GoD, Con-ConD, HMB, min RB, max RH, Hcon) were measured on each polygonal model, and a set of anatomical points on the bounded curves S1, S2, and S3 were extracted. 27 anatomical points are defined for a complete description of the shape of the missing part of the body of the mandible (Fig. 11b). On the each polygonal model, the values of the anatomical points are measured in a relation to the defined coordinate system. These values represent input vectors for analyzes. In order to create a surface model of the missing part, it is necessary to calculate predictive values for each of the 27 anatomical points.

The first method for the reconstruction involves the application of the MAF method, which has been explained several times. The inability to read morphometric parameters from the medical images caused the re-formation of parametric equations. In order to create a 3D geometrical model of the missing part, the available values of morphometric parameters are read from the sample of the human mandible, which is not a part of the initial analyzes and applied in new parametric equations (Mitic et al. 2020b). The example of equation for an X coordinate of one point is presented in:

$$\begin{aligned} X &= b_0 + b_1C_1 + b_2C_2 + \cdots + b_6C_6 + b_7C_7 \\ &= -23.5 - 0.115C_1 - 0.101C_2 + \cdots - 0.0720C_6 - 0.132C_7 \end{aligned} \tag{3.6}$$

where: X is the value of X coordinate for defined point, $b_0, \ldots, b_7$ are the values of the regression coefficients, $C_1, \ldots, C_7$ are measured values of morphometric parameters.

The calculated predictive values of the coordinates for all 27 points were used to construct the surface model of missing part in the CAD software CATIA (Fig. 3.12).

The second method for reconstruction applies a newly developed technique based on the application of the artificial intelligence in order to obtain predictive values of anatomical points (Mitic et al. 2020a).

MATLAB software was used for mathematical modeling. Using the MATLAB Neural Net Toolbox, precise connections were established between input and output variables. For the needs of training and testing the created ANN model, the whole sample (22) is randomly divided into a data subset for training (75% of whole

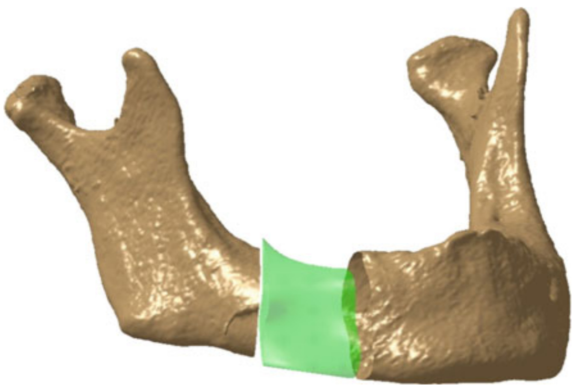

Fig. 3.12 Geometrical model of missing part (Mitic et al. 2020b)

samples) and a data subset for testing the ANN (25% of whole samples). Seven input parameters were used, and they are: Gn-IdD, Go-GoD, Con-ConD, HMB, min RB, max RH, Hcon, and 3 output parameters: measured values of X, Y, and Z coordinates. Before the training phase, the input–output data is normalized by the activation function of the ANN model.

The training of the ANN model for the prediction of the values of anatomical points was performed by the Levenberg- Marquardt algorithm. The choice of algorithm for training ANN models conditioned the adjustment of training parameters to realize high-performance ANN models. The optimal values of training parameters were determined by testing several neural networks of different structures. A value of 0.1 for the learning coefficient, 0.2 for momentum, and 1475 for the maximum number of epochs during training are specified values with which the backpropagation algorithm has the best prediction performance. By using the trial/error method, optimal values of the architecture parameters were obtained: one hidden layer, 30 neurons in the hidden layer, and sigmoid transfer functions in a hidden and output layer. All tested models represent a multilayer perception type of neural network. The MSE and the absolute error were used to evaluate the quality of the mathematical model. The ANN model with the best performance is presented in Table 3.6.

The mathematical relationship between input and output variables, according to the notation system of the software package MATLAB, it is presented in Fig. 3.13.

Based on the structure of the ANN model with the best performance (Fig. 3.10), the mathematical relation between input and output variables is defined. By applying a mathematical relation to the input values that were not part of the initial training set

Table 3.6 The ANN model with best performance (Mitic et al. 2020a)

ANN	Number of training epochs	MSE	
		Training data set	Test data set
Model 1	352	0.018	0.025

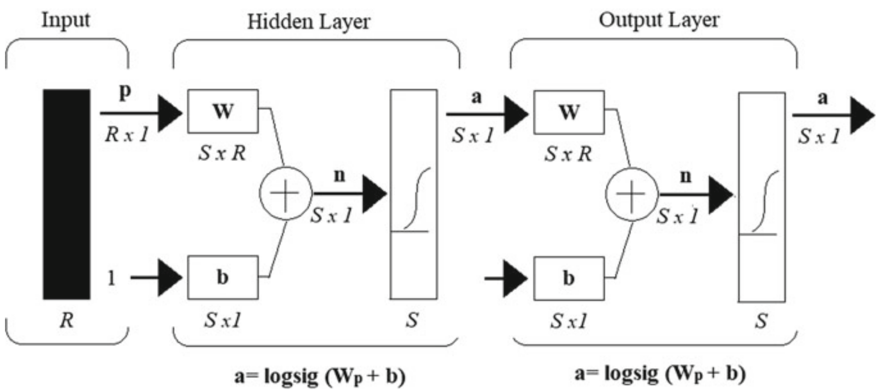

Fig. 3.13 Mathematical relation between input and output variables, where R is the number of elements in the input layer and S is the number of neurons in the hidden layer

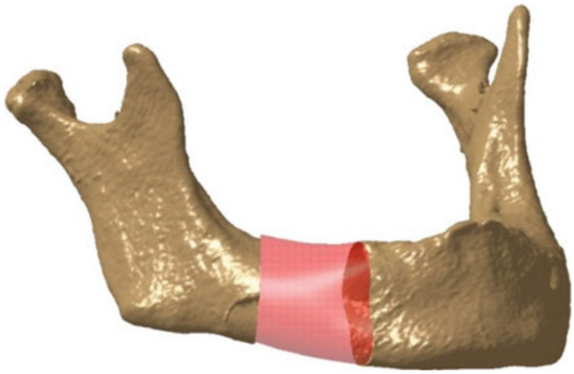

Fig. 3.14 Geometrical model of missing part (Mitic et al. 2020a)

(values of 7 morphometric parameters), the value of the output signals was obtained by entering the appropriate weights and biases in the mathematical relations.

The geometrical model of the missing part was created by the use of predictive coordinates values of the anatomical points in the CAD software CATIA. The obtained surface is presented in Fig. 3.14.

The comparison of the obtained surface models was performed based on the results acquired by analyzes of geometry and deviations between the initial and the obtained models.

The deviations analyzes between the initial, obtained from CT images and the surface model obtained by using of the first and second method of reconstruction was performed with an accuracy of 0.001 mm and shown in the form of a color-coded map in Fig. 15a, b.

Compared to the results, it can be concluded that the geometric accuracy of the resulting models is different depending on the applied mathematical model. The obtained values of the results of the deviation analyzes indicate that the model created by the use of ANN has the highest percentage of the resulting area in the range of −1 to 1 mm (85.40%), which represents a much better result compared to the analyzes of the model obtained by the use of multiple regression (25.86%). Additionally, with a maximum deviation of 2.77 mm, the obtained model is much more geometrically precise than the models created by applying multiple regression (maximum deviation of 7.66 mm). Considering the results of comparative analyzes of the deviation between the initial and the resulting models, it can be concluded that by applying ANN, a more than satisfactory accuracy of the resulting models can be achieved.

Analyzing the results on the geometric accuracy of the created surface models leads to the final conclusion. A smaller number of morphometric parameters than a strictly defined in parametric functions significantly affects the accuracy of the model. The geometrical bone model created by the application of parametric functions with strictly defined number of morphometric parameters is more anatomically correct and geometrically accurate. However, the result is a less accurate 3D model (but still personalized model) which can be adjusted to the surgeons needs in numerous stages of surgical planning.

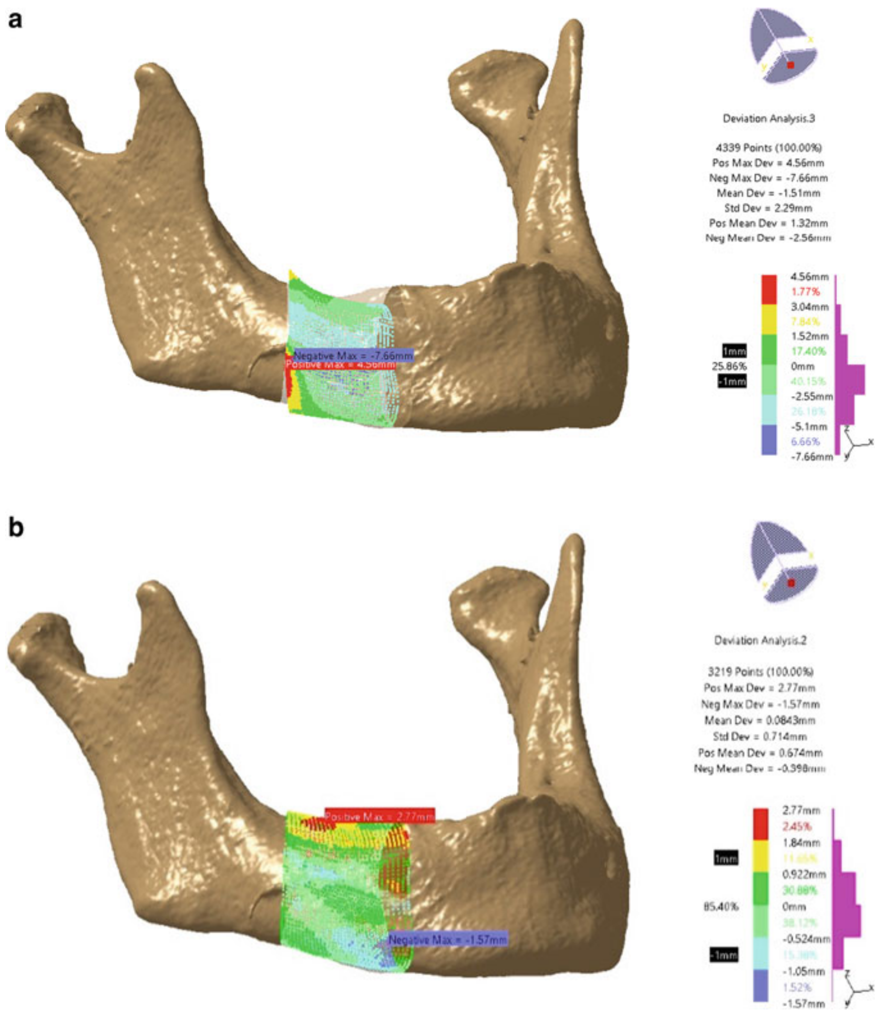

Fig. 3.15 **a** A deviations analyzes between the input and the resulting model created by the first method (Mitic et al. 2020b), **b** a deviations analyze between the input and the resulting model created by the second method (Mitic 2019a)

3.3.2.4 Application of the Geometrical Model of Human Mandible Based on Shape Prediction

Today, the creation and application of geometrical models based on the prediction of the shape and geometry are exclusively for research purposes. For now, commercial programs that use 3D models of human bones created in this way are unknown. On the other hand, numerous studies based on the prediction of the geometry of a particular bone and/or its parts aim to describe the natural shape variation.

The importance of the statistical model of the human mandible and the benefits it brings may be summarized as follows:

- A standard for the planning of surgical reconstruction of missing or malformed bony structures (Zachowa et al. 2005; Raith et al. 2017).
- Statistical shape models of the mandible can provide cephalometric parameters for 3D treatment planning and cephalometric measurements in orthognathic surgery (Kim et al. 2012).
- The statistical model has an important role in explaning sex differences in the anatomy of human temporomandibular joint mandibular condyles (Coogan et al. 2018).
- The statistical shape models can be used for 3D medical image segmentation with the aim of providing design parameters for personalized surgical instruments or providing directly yield anatomical measurements (Taghizadeh et al. 2019; Heimann and Meinzer 2009).

The application of statistical shape models of human bones is limited due to the inability to predict shape variations and geometry of the bone outside of the set the sample (Zachowa et al. 2005; Kim et al. 2012). The role of the parametric model of the human mandible in oral and maxillofacial surgery is more significant due to the possibility of transformation into a 3D personalized geometrical model of the specific human bone. The importance of the parametric model of the human mandible (created by using application MAF) and the benefits it brings may be summarized as follows:

- Geometric model of specific patient created by the application of the parametric model contains invaluable information about anatomical and morphological characteristics of the bone, related to possible the response of medical treatment.
- An integral element of the software framework that can be used independently in various institutions, for solving various problems in maxillofacial surgery (Vitkovic et al. 2018) (Fig. 16a, b).
- A parametric model can be used for the treatment of mandible fractures classified by the AO classification (https://aotrauma.aofoundation.org). The construction of 3D of personalized geometrical models of the mandible with fracture and plate implant allows the maxillofacial surgeon to improve pre-operative planning, intraoperative procedures, and postoperative recovery of the patient (faster and of better quality) (Husain et al. 2018).
- The parametric model has an important role in the reconstruction of the missing part of the bone structure. Its significance is reflected in the creation of personalized implants customized to the geometry, morphology, and anatomy of the specific patient (Mitic et al. 2020b) (Fig. 16c).
- Developed models and procedures can be used in the education of medical students and practitioners, with the aim to improve their techniques and knowledge in surgery planning and simulation.

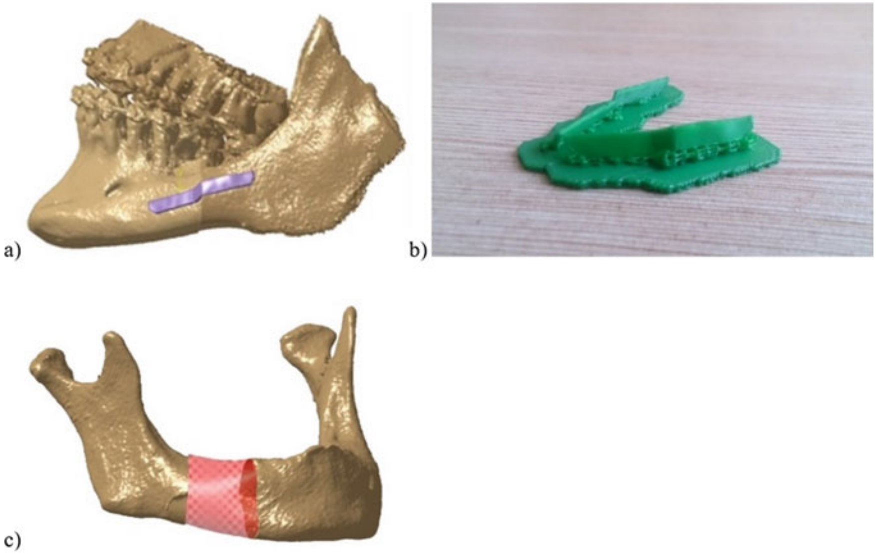

Fig. 3.16 **a** Solid model of the personalized plate (Vitkovic et al. 2018), **b** printed models of the plate implants (Vitkovic et al. 2018), **c** geometrical model of the missing part of the bone structure (Mitic 2019a)

3.4 Conclusion

The complexity of the human bone topology makes geometrical modelling quite challenging. Methods and techniques that have been used for this purpose are based on the combination of medical imaging for acquiring bone geometrical data and different 3D reverse modeling techniques. We analyzed the MAF for the generation of a 3D geometrical model of a human bone and demonstrated the method on human mandible samples. Applying the MAF, two different types of output models have been created and their application for medical purposes has been presented.

The additional significance of this research is reflected in improving the existent method of reverse engineering—MAF, aimed at solving the problem of the prediction of the human bone geometry. A new approach for the geometrical modeling of the human mandible based on the prediction of human bone geometry using ANN has been realized. The modeling methodology is based on the obtained mathematical model where input data represent the values of the specific parameters acquired from the medical images, while the output data represent the values of the anatomical entities (coordinates of anatomical points at the surface on the bone). By establishing mathematical relations between specific parameters and anatomical entities, a precise description of the geometrical entities of human bones is enabled. As a result of the applied approach the new algorithm for creation of a 3D parametric model of the human mandible is developed.

The modeling methodology is implemented through the process of creating the complete bone of the human mandible. In order to verify the method, the obtained results are compared with the results obtained by other statistical methods. Verification of the results is carried out through a comparative analyzes of geometry and deviation between initial and obtained models.

An additional aspect of the application of the method lies in the fact that the method can be applied to anatomical regions (according to the needs and available input data of a patient's) i.e., the parts of the bone.

Acknowledgements The work was supported by the Ministry of Education, Science and Technological Development of the Republic of Serbia (contract number 451-03-68/2022-14/200124).

References

Ambellan F, Lamecker H, Von Tycowicz C, Zachow S (2019) Statistical shape models: understanding and mastering variation in anatomy. In: Crusio W, Dong H, Radeke H, Rezaei N, Steinlein O, Xiao J (ed) Advances in Experimental Medicine and Biology, 1 st edn. Springer Nature, Switzerland, p 67–84

Adate P, Pandhare A (2017) Review on study of reverse engineering in mechanical. Paper presented at international conference on ideas, impact and innovation in mechanical engineering, Pune, India, 1–2 June 2017

Allen PM (1997) The problem of multicollinearity. In: Understanding Regression Analysis Springer, Germany. pp. 176–180.

AO Foundation, AO/OTA classification. https://aotrauma.aofoundation.org. Accessed 20 July 2021

Aroeira RM, Pertence AE, Kemmoku DT, Greco M (2017) Three-dimensional geometric model of the middle segment of the thoracic spine based on graphical images for finite element analysis. Res Biomed Eng 33(2):97–104

Arsic S (2019) Analysis of the human cephalometric parameters important for dental practice. Facta Univ Ser Med Biol 21(2):41–47

Arsic S, Peric P, Stojkovic M, Ilic D, Stojanovic M, Ajdukovic Z (2010) Komparativna analiza linearnih morfometrijskih parametara humane mandibule dobijenih direktnim i indirektnim merenjem. Vojnosanit Pregl 67(10):839–846

Au A, Palathinkal D, Liggins A, Raso VJ, Carey J, Lambert RG, Amirfazli A (2008) A nurbs-based technique for subject-specific construction of knee bone geometry. Comput Meth Prog Bio 92(1):20–34

Bell RB (2010) Computer planning and intraoperative navigation in cranio-maxillofacial surgery. Oral Maxillofac Surg Clin North Am 22(1):135–156

Berar M, Desvignes M, Bailly G, Payan Y (2005) 3D statistical facial reconstruction, paper presented at proceedings of the 4th international symposium on image and signal processing and analysis—ISPA 2005, Zagreb, Croatia, 15–17 Sept 2005

Bradley C, Currie B (2005) Advances in the field of reverse engineering. Comput Aided Des Appl 2(5):697–706

Breglia DP (2006) Generation of a 3-D parametric solid model of the human spline using anthropomorphic parameters. Dissertation, Russ College of Engineering and Technology of Ohio University

Brown S (2009) Multiple linear regression analysis: a matrix approach with MATLAB. Ala J Math 34:1–3

Budzik G, Turek P (2018) Improved accuracy of mandible geometry reconstruction at the stage of data processing and modeling. Australas Phys Eng S 41:687–695

Coogan JS, Kim DG, Bredbenner TL, Nicolella DP (2018) Determination of sex differences of human cadaveric mandibular condyles using statistical shape and trait modelinf. Bone 106:35–41

Dreyfus G (2005) Neural networks. Springer Verlag, Berlin

Fuessinger MA, Schwarz S, Cornelius CP, Metzger MC, Ellis E (2018) Planning of skull reconstruction based on a statistical shape model combined with geometric morphometrics. Int J Comput Assist Radiol Surg 13(4):519–529

Galantucci LM, Percoco G, Angelelli G, Lopez C, Introna F, Liuzzi C, Donno AD (2006) Reverse engineering techniques applied to a human skull, for CAD 3D reconstruction and physical replication by rapid prototyping. J Med Eng Technol 30(2):102–111

Ganguli A, Pagan-Diaz GJ, Grant L et al (2018) 3D printing for preoperative planning and surgical training: a review. Biomed Microdevices 20(3):65

Gateno J, Xia J, Teichgraeber et al (2007) Clinical feasibility of computer-aided surgical simulation (CASS) in the treatment of complex cranio-maxillofacial deformities. J Oral Maxillofac Surg 65(4):728–734

Ghafoor H (2018) Reverse engineering in orthodontics. Turk J Orthod 31(4):139–144

Gomes G, Cauter SV, Beule MD, Vigneron L, Pattyn C, Audenaert EA (2013) Patient-specific modeling in orthopedics: from image to surgery. In: Andreaus U, Iacoviello D (eds) Biomedical imaging and computational modeling in biomechanics. Springer Nederland. pp 109–129

Hammoudeh JA, Howell LK, Boutros S, Scott MA, Urata MM (2015) Current status of surgical planning for orthognathic surgery: traditional methods versus 3D surgical planning. Plast Reconstr Surg Glob Open 3(2):1–10

Heimann T, Meinzer HP (2009) Statistical shape models for 3D medical image segmentation: a review. Media 13(4):543–563

Hieu LC, Sloten JV, Khanh L, Soe S, Zlatov N, Phuoc LT, Trung PD (2010) Medical reverse engineering applications and methods. Paper presented at 2nd International Conference On Innovations, Recent Trends And Challenges In Mechatronics, mechanical engineering and new high-tech products development—MECAHITECH'10, Bucharest, Romania, 23–24 Sept 2010

Husain K, Rashid M, Manic M, Vitkovic N, Mitic J, Milovanovic J, Stojkovic M (2018) Geometrical models of mandible fracture and plate implant. Facta Univ Ser Mech Eng 16(3):369–379

Indraswari R, Arifin AZ, Suciati N, Astuti ER, Kurita T (2019) Automatic segmentation of mandibular cortical bone on cone-beam CT images based on histogram thresholding and polynomial fitting. Int J Intell Eng Syst 12(4):130–141

Juodzbalys G, Wang HL, Sabalys G (2010) Anatomy of mandibular vital structures. Part I: mandibular canal and inferior alveolar neurovascular bundle in relation with dental implantology. J Oral Maxillofac Res 1(1):1–8

Kaur A (2014) A review paper on image segmentation and its various techniques in image processing. Int J Sci Res 3(12):12–14

Kim SG, Yi JW, Hwang SJ, Choi SC et al (2012) Development of 3D statistical mandible models for cephalometric measurements. Imaging Sci Dent 42(3):175–182

Kontio R, Björkstrand R, Salmi M, Paloheimo M, Paloheimo KS, Tuomi J, Mäkitie AA (2012) Designing and additive manufacturing a prototype for a novel instrument for mandible fracture reduction. Surg: Curr Res. https://doi.org/10.4172/2161-1076.1000S1-002

Lamecker H, Zachow S, Wittmers A, Weber B, Hege HC, Elsholtz B, Stiller M (2005) Automatic segmentation of mandibles in low-dose CT-data. Int J Comput Assist Radiol Surg 1(1):393–395

Larobina M, Murino L (2014) Medical image file formats. J Digit Imaging 27(2):200–206

Lee J, Fang JJ, Chang LR, Yu CK (2007) Mandibular defect reconstruction with the help of mirror imaging coupled with laser stereolithographic modeling technique. J Formos Med Assoc 106(3):244–250

Lippmann RP (1987) An introduction to computing with neural nets. IEEE ASSP Mag 2(4):4–22

Lisiak-Myszke M, Marciniak D, Bielinski M, Sobczak H, Garbacewicz L, Drogoszewska B (2020) Application of finite element analysis in oral and maxillofacial surgery—a literature review. Materials 13(14):1–16

Madic M, Radovanovic MR (2011) Optimal selection of ANN training and architectural parameters using Taguchi method: a case study. FME Trans 39:79–86

Majstorovic V, Trajanovic M, Vitkovic N, Stojkovic M (2013) Reverse engineering of human bones by using method of anatomical features. CIRP Ann 62(1):167–170

Manic M, Stamenkovic Z, Vitkovic N, Stojkovic M, Trajanovic M, Mitić J (2015) Customized anatomically adjusted plate for fixation of mandible internal fractures. Paper presented at BIBE international conference on bioinformatics & bioengineering 1–6 Belgrade, Serbia, 02–04 Nov 2015

Mitic J, Vitkovic N, Manic M, Trajanovic M, Misic D (2017) Personalized anatomically adjusted plate for fixation of human mandible condyle process. Paper presented at ICIST 7th international conference on information society and technology, Kopaonik, Serbia 12–15 Mart 2017

Mitic J, Vitkovic N, Manic M, Trajanovic T (2019b) Application of artificial neural networks in prediction of human mandible geometry. Paper presented at ICIST 9th international conference on information society and technology, Kopaonik, Serbia, 10–13 Mart 2019b

Mitic J, Vitkovic N, Manic M, Trajanovic M, Petrovic S Arsic S (2020a) Reverse modeling of the human mandible 3D geometric model. Vojnosanit Pregl 77(3):262–270

Mitic J, Vitkovic N, Manic M, Trajanovic T (2020b) Reconstruction of the missing part in the human mandible. Paper presented at ICIST 10th International conference on information society and technology, Kopaonik, Serbia, 8–11 Mart 2019

Mitic J (2019a) Creating a 3D parametric model of human mandible using artificial intelligence techniques. Dissertation, University of Nis

Moore KL (1992) Clinically oriented anatomy. Williams & Wilikins, Baltimore

Olson RA, Fonseca RJ, Osbon DB (1982) Fractures of the mandible: a review of 580 cases. J Oral Maxillofac Surg 40(1):23–28

Page D, Koschan A Abidi M (2007) Methodologies and techniques for reverse engineering-the potential foe automation with 3-D laser scanners. In: Raja V, Fernandes KJ (eds) Reverse engineering—an industrial perspective. Springer, Germany. pp 11–32

Petrovic S, Korunovic N (2018) Imaging in clinical and preclinical practice. In: Zivic F, Affatato S, Trajanovic M, Schnabelrauch M, Grujovic N, Choy KL (eds) Biomaterials in clinical practice, 1st edn. Springer Nature, United Kingdom. pp 539–572

Raith S, Wolff S, Steiner T, Mobadder A, Weber M, Holzle F, Fischer H (2017) Planning of mandibular reconstructions based on statistical shape models. Int J Comput Assist Radiol Surg 12(1):99–112

Sharma N, Aggarwal L (2010) Automated medical image segmentation techniques. J Med Phys 35(1):3–14

Sokolovic B (1997) Toothlessness: clinic, diagnosis, treatment. 1st ed. Niš, Prosveta

Sriramakrishnan P, Kalaiselvi T, Padmapriya ST, Shanthi N, Ramkumar S, Kalaiche N (2019) An medical image file formats and digital image conversion. Int J Eng Adv Technol 9(1S4):74–78

Stacey DH, Doyle JF, Mount DL, Snyder MC, Gutowski KA (2006) Management of mandible fractures. Plast Reconstr Surg 117(3):48–60

Stojkovic M, Trajanovic M, Vitkovic N (2019) Personalized orthopedic surgery design challenge: human bone redesign method. Procedia CIRP 84:701–706

Taghizadeh E, Terrier A, Becce F, Farron A, Buchler P (2019) Automated CT bone segmentation using statistical shape modelling and local template matching. Comput Methods Biomech Biomed Engin 22(16):1303–1310

Taleghani SM, Fatahi L (2018) Application of medical imaging and image processing in creating 3D models of human organs. Paper presented at international conference on mechanics of advanced materials and equipment, Ahvaz, Iran 31 Jan 2018

Tesar L, Shimizu A, Smutek D, Kobatake H, Nawano S (2008) Medical image analysis of 3D CT images based on extension of Haralick texture features. Comput Med Imaging Graphics 32:513–520

Tian S, Hongsheng L, Zhen Q, Xiaolei H (2009) Active volume models for 3D medical image segmentation, Paper presented at IEEE Computer society conference on computer vision and pattern recognition, Miami Florida, USA, June 2009

Trajanovic M, Tufegdzic M, Arsic S (2018) Obtaining patient-specific point model of the human ilium bone in the case of incomplete volumetric data using the method of parametric regions. Australas Phys Eng Sci Med 41:931–944

Trajanovic M, Vitkovic N, Stojkovic M, Manic M, Arsic S (2009) The morphological approach to geometrical modeling of the distal femur. Paper presented at 2nd South-East European conference on computational mechanics An IACM-ECCOMAS Special Interest Conference Papadrakakis M, Kojic M, Papadopoulos V (eds) Rhodes, Greece, 22–24 June 2009

Tufegdzic M, Trajanovic M, Vitkovic N, Arsic S (2013) Reverse engineering of the human fibula by the anatomical features method. Facta Univ Ser Mech Eng 11(2):133–139

Vajgel A, Camargo I, Willmersdorf R, Menezes de Melo T, Filho J, Vasconcellos R (2013) Comparative finite element analysis of the biomechanical stability of 2.0 fixation plates in atrophic mandibular fractures. J Oral Maxillofac Surg 71(2):335–342

Valenti M (2015) Statistical shape models based 2D/3D registration methods for knee orthopaedic surgery. Dissertation, Politecnico di Milano

van Baar GC, Forouzanfar T, Liberton N, Winters HAH, Leusink FKJ (2018) Accuracy of computer-assisted surgery in mandibular reconstruction: a systematic review. Oral Oncol 84:52–60

Vasconcelos MJM, Tavares JMRS (2018) Methodologies to build automatic point distribution models for faces represented in images, computational modelling of object represented in images, Taylor and Francis Group, United Kingdom

Vitkovic N, Mladenovic S, Trifunovic M et al (2018) Software framework for the creation and application of personalized bone and plate implant geometrical models. J Healthc Eng 2018:1–11

Vitkovic N, Mitic J, Manic M, Trajanovic M, Husain K, Petrovic S, Arsic S (2015) The parametric model of the human mandible coronoid process created by method of anatomical features. Comput Math Methods Med 2015(3):1–10

Watson J, Hatamleh M, Alwahadni A, Srinivasan D (2014) Correction of facial and mandibular asymmetry using a computer aided design/computer aided manufacturing prefabricated titanium implant. J Craniofac Surg 25(3):1099–1101

Weber GW, Schare K, Prossinger H, Gunz P, Mitterocker P, Seidler H (2001) Virtual anthropology: the digital evolution in anthropological science. J Physiol Anthropol Appl Human Sci 20(2):69–80

Wong FS (1991) Time series forecasting using backpropagation neural networks. Neurocomputing 4:147–159

Xia JJ, Shevchenko L, Gateno J et al (2011) Outcome study of computer-aided surgical simulation in the treatment of patients with craniomaxillofacial deformities. J Oral Maxillofac Surg 69(7):2014–2024

Zachowa S, Lameckera H, Elsholtzb B, Stiller M (2005) Reconstruction of mandibular dysplasia using a statistical 3D shape model. Int Congr 1281:1238–1243

Chapter 4
Reverse Modeling of Human Long Bones by the Application of Method of Anatomical Features

Nikola Vitković and Miroslav D. Trajanovic

4.1 Introduction

Human bones can be classified as long, short, flat, irregular, and sesamoid bones. Long bones are specific in that they are mostly cylindrical in shape with one or two articulated ends, and much longer than their width. During a person's work activities (except during sleep), they allow a person to carry a load, including his own weight. In addition, long bones allow body mobility. As such, they are often subjected to injuries. Long bones include:

- bones of the arms: humerus, radius, and ulna
- bones of the legs: femur, tibia, and fibula
- bones of the hands and feet: metacarpals, metatarsals, and phalanges.

In orthopedic surgery, but also in all other sub-branches of surgery, where there is the need for pre-operative planning or creation of customized orthopedic devices, there is a specific requirement to know the exact geometrical model of the human bone. Therefore, it is very important to create geometry of the bone quickly and as accurately as possible. It is possible to build customized bone implants and fixators using rapid prototyping technologies or performing pre-operative planning procedures in adequate applications. Sometimes there is no (Computed Tomography) CT or (Magnetic Resonance Imaging) MRI scan, or part of the bone is missing, so it is not possible to create a required bone model. The presented research aims to create such a methodology that will enable the creation of anatomically correct, topologically, and geometrically accurate human long bone models, even when part of the bone is missing or only a single X-ray image is available. The methodology is based on Method of Anatomical Features (described in Chap. 2), and it represent its direct application and extension. The long bones geometrical models are built by

N. Vitković (✉) · M. D. Trajanovic
Mechanical Engineering Faculty, University of Niš, Niš, Serbia
e-mail: nikola.vitkovic@masfak.ni.ac.rs

O. Canciglieri Junior and M. D. Trajanovic (eds.), *Personalized Orthopedics*,
https://doi.org/10.1007/978-3-030-98279-9_4

using Referential Geometrical entities (RGEs) and Constitutive Geometrical Entities (CGEs) as the basis for the creation more complex geometry, like surface patches, or parametric models. Morphometric parameters are used as arguments for parametric model(s). They represent measurements which can be acquired from medical images (e.g., CT, MRI, or X-ray) for each human bone, as described in Chap. 2. The procedure for creating the geometrical models of several bones (femur, tibia and humerus) is presented and described in detail. Such models can be used mainly for pre-operative planning, but also in manufacturing process for custom implant and scaffold production, or for use in surgical interventions.

This chapter is organized as: Sect. 4.2 introduces the related work in the geometrical modeling of human bones. Section 4.3 presents summary of the geometrical models creation methods. The creation of RGEs, CGEs, geometrical models, and specifically parametric model are presented in Sect. 4.4. The novel approach to geometrical definition of Regions of Interest by using point cloud model is presented in Sect. 4.5. The final Sect. 4.6 is the conclusion, with guidelines to the future work.

4.2 Related Research

The related research concerning human bones remodeling methods is already presented in Chap. 2—"Creation of geometrical models of human bones by using method of anatomical features". In this section, only short review of remodeling methods for long bones will be presented.

With the advent of Computer Aided Orthopedic Surgery (CAOS) in the mid-1990s, the need for 3D geometric models of bones, implants and surgical aids and tools has been created. Today, the use of geometric models of bones in orthopedics is much wider and refers to pre-operative planning, decision-making and simulation (Atesok et al. 2015), training, design of personalized implants, Finite Element Analysis (FEA) of bone behavior. Because long bones are very often subject to trauma and disease, the need for their models is very pronounced.

Depending on the input data, reverse engineering of a patient's geometric bone model can take place in two different circumstances. A complete three-dimensional image of the patient's bone is available in the first case, most often obtained by computed tomography. In the second case, there is only a partial 3D medical image of the bone or even only a 2D image (X-ray). The reason for this circumstance can be great trauma, bone disease, or inability to do a CT scan.

In the case when there is a complete 3D medical image, the process of reverse engineering is much simpler. The input 3D point cloud model is transformed into a polygonal model which, after healing, is transformed into a 3D solid model by one of the computer-aided design (CAD) techniques. Although the methods used in this case are very mature, there is still research aimed at improving their efficiency and effectiveness.

To morph each partial functional region of a femur, Park et al. proposed novel morphing method for parameterizing patient-specific femur models based on femoral biomechanical functions (Park et al. 2014). Their function-based morphing method uses dimensional parameters, such as femoral head diameter or neck inclination angle to morph specific anatomical region. Such a models are very useful for various biomechanical sensitivity analyses.

Parametric approach to construct femur models and their fixation plates was presented in study Xiaozhong et al. (2016). Method uses average femur model to describes femur anatomy. The femur is divided in five anatomical regions: trochanter, head, neck, shaft, and condyle. Based on reconstructed femur geometrical model, fixation plate surface is designed. Finally, the patient-specific femur fixation plate was designed by feature parameterization.

In case there is no complete 3D medical image of the bone, various statistical methods or methods based on artificial intelligence are used to reconstruct the geometric model of the whole bone. Only one successful method will be presented here.

In the paper entitled Rapid generation of human femur models based on morphological parameters and mesh deformation (Yunyan et al. 2017) the authors presented a new method for creating a 3D geometric model of human femur by using measured pre-defined parameters from the patient's medical image. Method is based on data acquired from the 3D polygonal models of existing samples. Because the morphology of the femur is complex, and therefore cannot be geometrically defined by a single function, it is divided into seven segments (anatomical regions): femoral head, femoral neck, greater trochanter, lesser trochanter, femoral shaft, lateral condyle and medial condyle. Then, the authors identified three types of parameters that describe bone geometry and morphology. The parameters are divided into three groups: regional, inter-regional and key parameters. Regional parameters, such as femoral head diameter, femoral neck length or neck isthmus diameter, describe specific segments. The inter-regional parameters, such as distance from greater trochanter point to lesser trochanter point or neck–shaft angle, define structural relationship between two or more anatomical regions. There is only one key parameter and that is the length of the femur because it spans almost all segments of the femur. By processing 3D polygonal models of the samples, all parameters were measured. All geometric models of femur samples were divided into four groups depending on the length of the femur, and then an average model was created for each group. A combination of parametric technology and deformation technology is used to create a 3D geometric model of a specific patient. From the medical images of the patient, the pre-defined parameters are measured and based on them, the most similar sample and average model is found. Using global interpolation, the rough model of a specific patient is created. Then, by deformation of the rough geometrical model segments the final 3D model of patient's femur was obtained. The method enables obtaining a complete model of the femur, even in cases when there is no data on all parameters of the patient's femur.

4.3 Summary of the Human Geometrical Models Creation Procedures

Geometrical models of organs can be created by using different procedures, as already stated in Chap. 2—"Creation of geometrical models of human bones by using method of anatomical features". The short summary of stated procedures will be presented in this section. The first procedure is based on applying reverse engineering techniques, and the second is based on the use of generic models to create human organ models.

RE procedure (Fig. 4.1) is based on the application of medical imaging software for gathering and pre-processing data about the organ and CAD software which is usually used for additional processing and creation of models. These models are used for: pre-operative planning, creation of presentation models, Finite Element analysis (FEA), prototyping, rapid tooling of molds, etc. The procedure generally consists of the following steps:

- Medical imaging by using CT (for hard and soft tissue), and MRI (mainly for soft tissue).
- Pre-processing (Segmentation) in medical software which enables creation of adequate organ models, e.g., hard or soft tissue. Segmentation is usually done by using, Hounsfield scale, named after Sir Godfrey Hounsfield (De Vos et al. 2009). This is a quantitative scale for describing radiodensity, and it is often used in CT scans, where its value is also known as the CT number. By using this scale different organs can be extracted from the radiograph.
- Exporting a 3D model from medical imaging software to an adequate format. The usual export format is the STL format, which is widely used in RE, 3D printing and Computer graphics. This format describes 3D models as a set of triangles, with additional information about their normals. It is a very simple format, and easy to use.
- Importing and processing the 3D model in CAD software. It can be a very demanding and complex task, which mainly depends on the type of imported organ and its geometry and morphology. The processing in CAD software is based on the following: additional filtering of unnecessary data, tessellation and creation

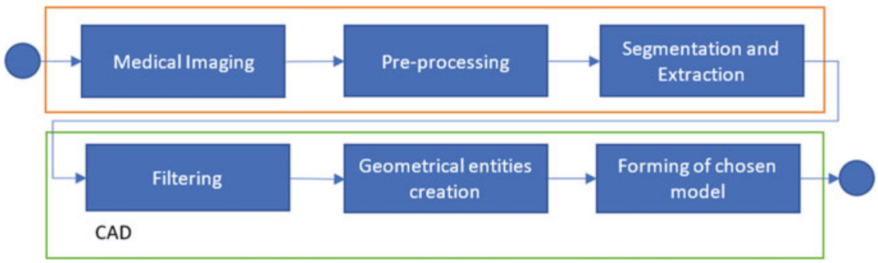

Fig. 4.1 Reverse engineering (modelling) procedure

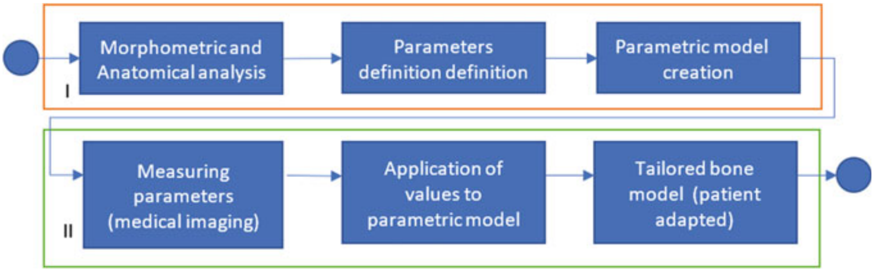

Fig. 4.2 Parametric model creation and application process: I—Definition of the parametric model (PM), II—application of the model

of a polygonal model, creation of geometrical entities, creation of different types of models (e.g., surface, solid).

Generic models, including template and parametric models (Fig. 4.2) are generally created as Free Form Deformation models. Different methods are used to adapt their shape and geometry to the personalized organ model or parametric bone models (Filippi et al. 2008). The latter are used for the creation of personalized bone models based on the morphometric and other values acquired from medical images.

4.4 The Application of Method of Anatomical Features for the Creation of Human Long Bones Geometrical Models

The Method of anatomical features (MAF) has already been described in Chap. 2, and all the rules and statements included in MAF are completely valid for the application in human long bone reconstruction processes (Vitković et al. 2013; Vitkovic et al. 2019; Tufegdžić et al. 2013). The focus of this section is to describe in detail the MAF application for the creation of human long models based on data acquired from medical imaging methods. Based on complete and incomplete bone data, both methods will be presented, together with descriptions of terms and definitions applied in MAF. The procedures will initially be described for the human femur, but MAF application for the reconstruction of human tibia and humerus will also be presented. The following will be presented:

- Definition of the Referential Geometrical Entities—Entities (axes, planes, points, etc.) important for the creation of all other geometrical features (e.g., curves, surfaces) on the human long bones.
- Definition of the Constitutive Geometrical Entities—Entities based on RGEs, used for the creation of geometrical models of higher order (e.g., surface, solid)

- Creation of the geometrical models of the human long bones—This contains description of procedure for the creation of surface and solid models of human long bones.
- Creation and application of the parametric model.
- The definition and application of geometric Regions of Interest—They are significant for the additional (in-depth) description of the bone geometry. They are based on ROI already defined in anatomy but transferred to the geometrical models of the human bones.

4.4.1 Referential Geometrical Entities and Constitutive Geometrical Entities on the Example of the Femur

The determination of Referential Geometric Entities (RGEs) of human bones precedes the procedure of reverse modeling and the parameterization of the geometry of the femur with the help of CAD software. Bone RGEs are formed by using characteristic points, directions, planes, and views. In addition, all other geometric entities, of a higher order, such as curves, surfaces, and solids, are referenced in relation to the RGEs. Therefore, the process of determining bone RGEs aims to propose a way to identify the minimum set of RGEs to make the procedure of reverse modeling and parametrization of femur geometry as robust as possible in terms of required geometrical adaptations to the specific anatomy of an individual patient (Vitković et al. 2013; Majstorovic et al. 2013). Therefore, all other geometric constraints and relations, which will exist in the 3D bone model, are to be based on this minimal set of RGEs. At the same time, this method should enable the parameterization of the geometry of the bone model and quick and straightforward changes according to the specific morphology of the femur of an individual patient. Also, the correct identification of RGEs directly affects the speed and accuracy of reverse engineering of implants and fixators, which is the primary imperative in urgent cases.

4.4.2 Referential Geometrical Entities and Surface Model on the Example of the Femur

In anatomy, two basic views of the femur are defined, observing the spatial orientation of the femur. The first is the so-called anterior–posterior view/direction or orientation (A-P) and the other is lateral-medial (L-M) view/direction or orientation. For reverse modeling of the geometry of the femur, it is necessary to form several (not always orthogonal) directions and corresponding projections of the bone or part of the bone. Unlike medical situations, reverse engineering and manufacturing of custom implants and fixators require very precisely defined rules for the development of all directions and views, including A-P and L-M (Stojkovic et al. 2009). For the development of methods for identification of reference geometric entities (RGEs) of the femur and, later, reverse modeling of the femur, CAD software, i.e., its set of modules for reverse modeling, was used (CATIA V5 R19-R21). Identifying RGEs begins with the import and geometric processing of point clouds (removal of redundant points and spatial binding of clouds with the existing initial geometric entities of the model). Before identifying RGEs, a polygonal model is created above the point cloud by tessellation, i.e., by creating many polygons (in this case triangles), between the corresponding points. In this phase, additional processing of the polygonal model is performed to correct appropriate irregularities, normalization, etc.

4.4.2.1 Determining the A-P Plane and Direction

The initial femur RGEs is the A-P plane. All other planes and views and directions are in direct dependence on the A-P plane and the A-P direction (line normal to the A-P plane). To define the A-P plane (direction and view), three points are used—referential geometrical entities of the femur geometry:

- Point of the center of the femoral head (P_CFH)
- Point of the lateral epicondyle (P_LEc)—the most prominent point on the lateral epicondyle
- Point of the medial epicondyle (P_MEc)—the most prominent point on the medial epicondyle.

4.4.2.2 Femoral Head Center (P_CFH)

The most important reference point of the femur geometry is the center of the femoral head (P_CFH). This point is defined as the intersection of the axes of the circles representing the approximate envelopes of the femoral head constructed on the initially orthogonal projections of the polygonal model of the femur (approximate A-P and L-M projections), Fig. 4.3.

4.4.2.3 Points of Lateral and Medial Epicondyle (P_LEc, P_MEc)

The points P_LEc and P_MEc are located in the intersection of the circles touching the most prominent points on the distal end of the femur, which are constructed in two initially orthogonal projections of the polygonal model of the femur (approximate A-P and Inferior-Superior or Down-Top projections).

The center of the femoral head (P_CFH) and (P_LEc, P_MEc) are used as reference points for defining the A-P plane or the so-called AP views, Fig. 4.4.

In addition to these three points, during the research it was noticed that there are three more points which, with a very small deviation, also lie on the A-P plane: Point of the intercondylar fossa (P_IcoF), The lowest point of the lateral condyle (Point of the lateral condyle—P_LC), The lowest point of the medial condyle (P_MC).

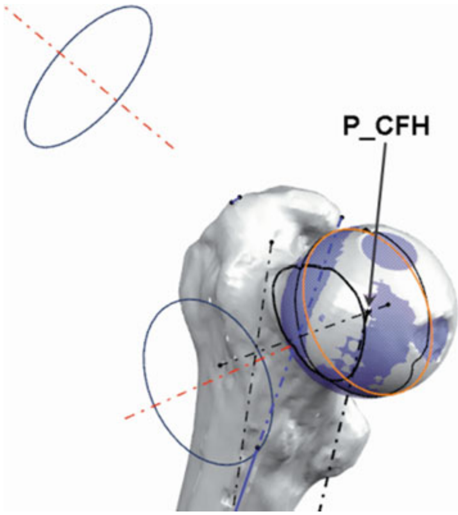

Fig. 4.3 Femoral head center (Stojkovic et al. 2009)

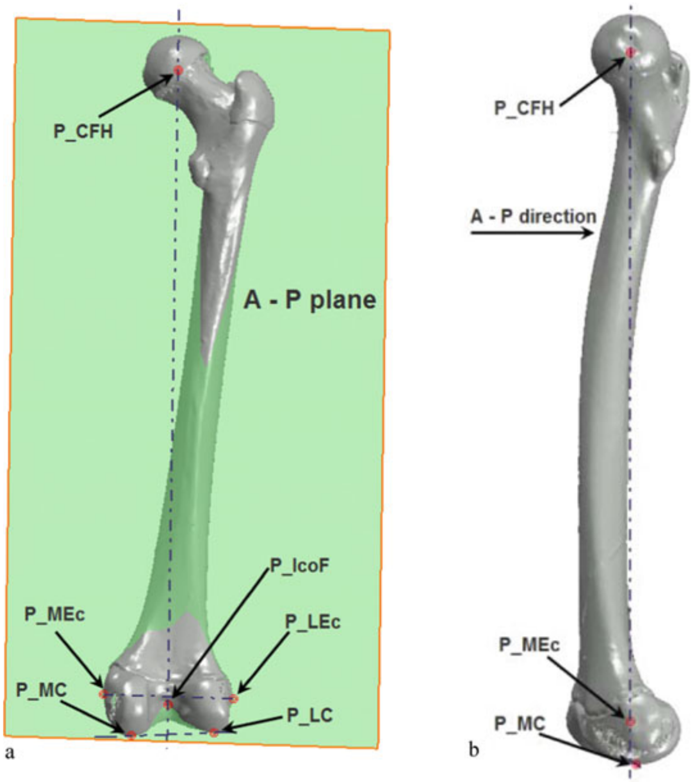

Fig. 4.4 Reference geometric entities shown on the femur: **a** AP view, **b** LM view (Stojkovic et al. 2009)

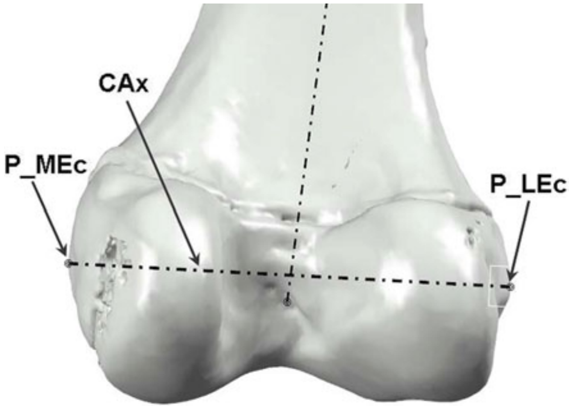

Fig. 4.5 The most prominent points on the distal end (lateral and medial condyle) and the axis of the distal end of the femur (Stojkovic et al. 2009)

These points (P_IcoF, P_LC and P_MC) are, within the method, used to check the accuracy, i.e., deviation of the A-P plane, Fig. 4.4.

4.4.2.4 The Axis of the Distal End of the Femur

The axis of the distal end of the femur (CAx) is RGEs which is necessary for a specially developed procedure for reverse condyle modeling which is based on a user-defined technical element—a rotating set of cross-sections (Trajanovic et al. 2009). The axis of the distal end is created by constructing a straight line connecting the points P_LEc and P_MEc, which are shown in Fig. 4.5.

4.4.2.5 Intercondylar Fossa Point (P_IcoF)

The point of the intercondylar fossa is constructed in the A-P plane as the maximum of the intercondylar bend (deep notch between the rear surfaces of the medial and lateral epicondyle of the femur). Additionally, to check its spatial location and deviation from the A-P plane, a point is created by direct digitization (choice of location) of the intercondylar fossa on the polygonal model, Fig. 4.4a.

4.4.2.6 Determining the L-M Plane and Direction

Before constructing P_LC and P_ MC points, it is necessary to define both the lateral-medial plane (L-M plane) and the L-M direction (the line normal to the L-M plane). To define L-M planes (directions and views), the A-P plane and the so-called mechanical axis—the next very important femur RGE are used.

4.4.2.7 Mechanical Axis

The mechanical axis of the femur is an axis constructed on the basis of two points: by definition it should pass through P_CFH and P_IcoF, as well as through the midpoint of the knee joint (it can be considered the midpoint of the axis created between P_MC and P_LC points). The mechanical axis defines the vertical orientation of the femur within this method of reverse modeling. From the point of view of anatomy, the mechanical axis is not the true vertical axis of the body of the femur, because the mechanical axis is about 3 degrees of valgus shifted in relation to the vertical axis of the body (Wheeless 2015; Cooke et al. 2007), as shown in Fig. 4.4a.

It is now possible to define the L-M plane, as a plane oriented orthogonally with respect to the A-P plane and passing through the mechanical axis of the femur (Fig. 4.4b).

4.4.2.8 Inferior/Lower/Lowest Points of Lateral and Medial Condyle (P_LC, P_MC)

The points P_LC and P_MC are in the intersection of the axes of the circles drawn in the A-P and L-M planes, as approximate envelopes of the base of the lateral and medial condyle, on the previously defined A-P and L-M projections of the polygonal femur model, Fig. 4.4.

4.4.2.9 The Guiding Curve of the Femoral Body

The femoral shaft guiding curve (FSC) is a spatial curve that is constructed by interpolation along the centers of gravity of the femoral body (Mahaisavariya et al. 2002; Vitković et al. 2012; Shui et al. 2021) In the A-P plane, the interpolation is linear (a line approximates the curve). In the L-M plane, the interpolation curve is approximated by a complex curve formed by the tangential connection of two circular arcs in the proximal or distal part of the femur. The proximal and distal ends of the curve-guide body of the femur are constructed as tangential lines to these arcs in the proximal, respectively distal part.

4.4.2.10 Gravity Points of the Femoral Body

The centers of gravity of the femur body are obtained by constructing the center of gravity of a series of cross-sections of the body with the help of a special technical element which allows to calculate the location of the center of gravity of surfaces framing body cross-section curves. Body cross-section curves are constructed using the cross-section of the femur model envelope (outer surface) and a series of sixteen (16) planes (optimal number obtained by creating multiple models). Cross-sections are orthogonal to the spatial curve formed by the cross section of the anterior/anterior

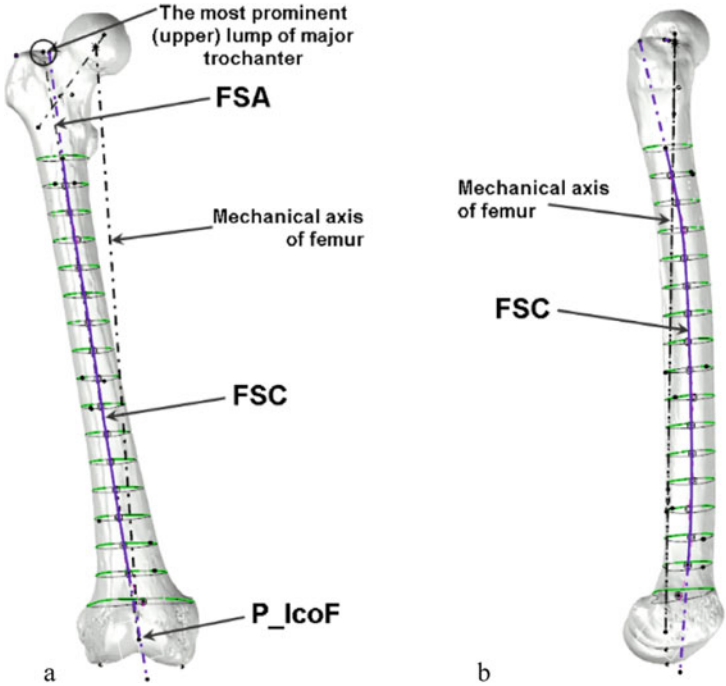

Fig. 4.6 Axis of the femoral body: **a** A-P view, **b** L-M view (Stojkovic et al. 2009)

part of the femur body envelope and the plane passing through the axis of the body of the femur and is normal to the A-P plane. The approximate femoral shaft axis (aFSA) is constructed in the A-P plane with the help of points: P_IcoF point, and a point constructed as an A-P projection of the inflection point of the great trochanter, Fig. 4.6a.

The construction of straight sections along the body of the femur, follows. It is important that the created sections are in the space between the lowest point of the small trochanter observed from the posterior aspect of the A-P plane (rear or back) and the transition part of the body to the distal end, which is characterized by a sudden change of section. This spatial limitation seeks to avoid considering the points of gravity of those sections which contain the influence of other morphological units (specifically, the trochanteric region and the femoral neck, on the proximal bone and condyle at its distal end). These straight sections are framed with sixteen (16) closed curves (sometimes, when the cross section did not result in one but in several smaller separated curves, it is necessary to perform their merging). This is followed by the construction of surfaces bounded by these curves, and then by the construction of the centers of gravity of these surfaces. It is important to note that these sections can be used as CGEs for the creation of the femoral shaft surface model.

The next step is to construct a rudimentary curve of the femoral body guide (rFSC) by interpolation, with the restriction that the curve passes through the centers of gravity of the16 sections. The rudimentary curve of the femoral body guide now serves as the basis for making projections of the femoral body guide curve in the A-P and L-M planes, Fig. 4.6a, b. Interpolation curves (arcs and lines) are created in each of the design planes. The interpolation curve of the femoral body guide is obtained as the cross section of the surfaces created above the interpolation projection curves in directions that are normal to the plane in which the interpolation curves were created.

4.4.2.11 Inferior/Lower Edge of the Trochanteric Region of the Femur

A very important RGEs of the proximal end of the femur is the so-called inferior margin of trochanter wedge—IMTW (the name is not in accordance with Terminologia Anatomica but the original term is provided in previous research (Stojkovic et al. 2009). This is the first line that geometrically identifies the morphological entity of the trochanteric wedge and connects the neck and body of the femur. Also, this RGE essentially influences the determination of the location of the axis of the neck of the femur, which is one of the most important RGEs of the femur. The construction of the IMTW begins with the projection of the lower edge of the trochanteric wedge in the A-P plane in the posterior aspect (rear view). It is constructed as a straight line connecting the lowest points of the large and small trochanters. The next step defines a plane that passes through this line and is normal to the A-P plane. This new plane—TCK plane, serves to define a new view of the trochanteric region/"wedge". The boundaries of the large and small trochanters are, in this plane, projected into two circular arcs. The centers of circular arcs are the points that determine the geometric location of a straight line that represents the IMTW projection in this (TCK) plane. In this way, the spatial location of IMTW is determined, i.e., the lower edge/inferior margin of the trochanteric region or wedge. Figure 4.7a, b shows the corresponding planes and IMTW.

4.4.2.12 Femoral Neck Guide Curve

The plane that is normal to IMTW is used to construct the so-called femoral neck axis (FNA). This plane is designated as the TKeel plane, Fig. 4.7a, in accordance with English terminology. Before constructing the femoral neck axis, it is necessary to construct two points that will define it. The first point is the projection of the center of the femoral head in the Tkeel plane (medial aspect). This is followed by drawing a circle representing the projection of the border of the base of the small trochanter (the place where the small trochanter passes into the body of the femur) into the Tkeel plane (medial aspect). The line starting from the projection P_CFH and tangenting the drawn circle at the anterior/anterior part, represents the projection of FNA in the Tkeel plane. The following procedure is similar to the procedure for constructing the focal points of the femoral body. In this case, the cross-sectional curves of the neck are constructed using the cross-section of the envelope of the femur model (outer

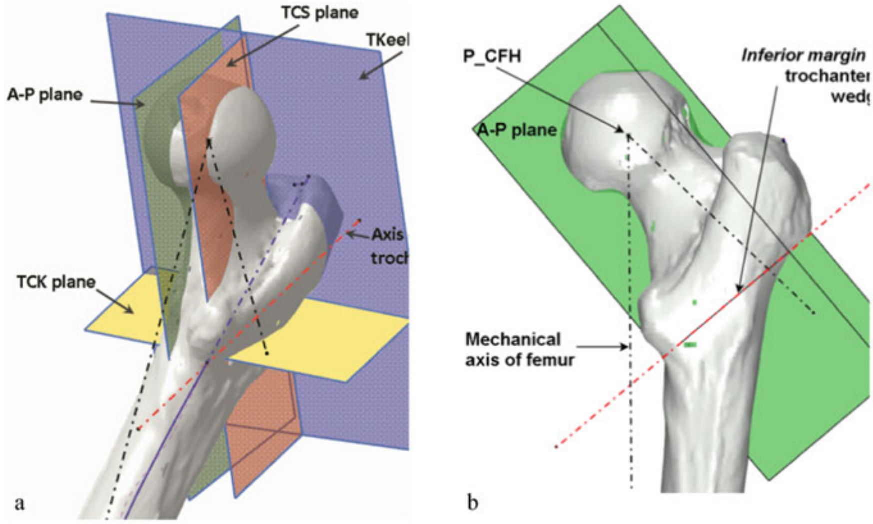

Fig. 4.7 RGEs flat and IMTW: **a** RGEs planes. **b** inferior margin lower edge of the trochanteric part of the femur (Stojkovic et al. 2009)

surface) and a series of five (5) planes (optimal number determined as for the femoral body axis) orthogonal to the FNA projection in the Tkeel plane.

It is important that these five (5) sections are in the space between the head and the trochanteric wedge in order to avoid considering the center of gravity of those sections which, in addition to the femoral neck, also contain the influence of other morphological units. This is followed by the construction of surfaces that are limited by the cross-sectional curves of the femoral neck, and then the center of gravity of these surfaces.

The next step is to construct a rudimentary curve of the femoral neck guide (rFNA) by interpolation, with the restriction that the curve passes through the points of gravity of five (5) sections. The rudimentary femoral body guide curve now serves as the basis for making projections of the femoral neck guide curve in the A-P and L-M planes in the same way as for the body guide curve.

The curve of the femoral neck guide—FNA is constructed at the intersection of two surfaces. The first surface is formed by extruding FNA in the direction normal to the A-P plane. The second surface is formed by extruding the L-M projection of the FNA in the direction normal to the L-M plane (Fig. 4.8).

4.4.2.13 Condylar Axes

Based on the lowest points of the lateral and medial condyle (P_LC, P_MC), the condyle axis (CAx) was created, (Fig. 4.5). The condyle axis defines the axis of rotation of the plane cross-sections that form the basic curves, over which the surface

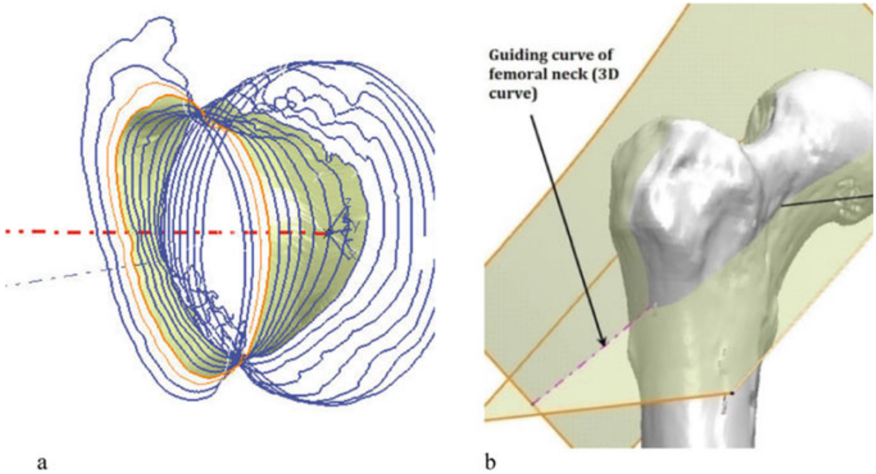

Fig. 4.8 The process of creating a curve of the femoral neck guide: **a** Intersections normal to the FNA plane, **b** guide curve in the intersection of two orthogonal surfaces (Stojkovic et al. 2009)

model of the condyle is created (Fig. 4.9). These curves are the CGEs for the creation of the condyle surface model, which can be connected to the shaft surface model.

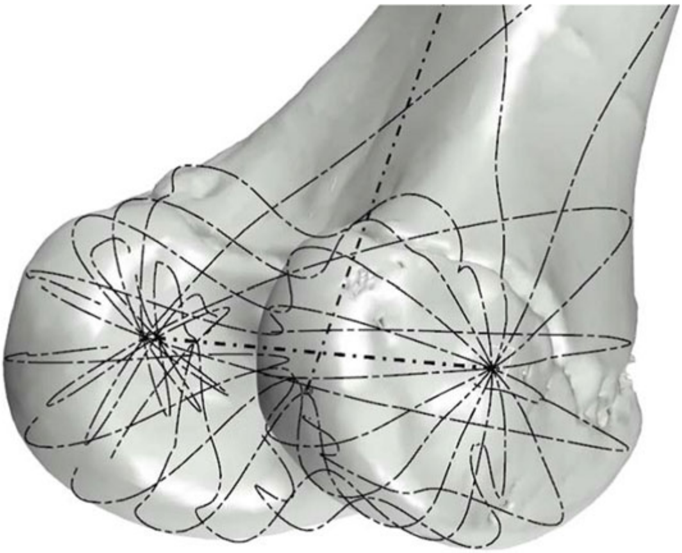

Fig. 4.9 Rotational plane sections with defined curves (Stojkovic et al. 2009)

4.4.2.14 Method Discussion

The presented method is the basis for geometrical definition of the morphological entities of the human femur. RGEs are especially important in terms of creating geometric models of the femur and other bones, and thus parametric models, which can later be used to create implants, plan orthopedic surgeries and the like. The method can be applied to other bones of the skeletal system, which enables the creation of a library of geometric models of all bones that make up the human skeleton. Using curves as CGEs defined through the construction of RGEs, and described in Chap. 2, with appropriate operations on individual surfaces, a surface model of the femur can be created. By comparing the deviation of the surface model obtained over the defined curves and the initial input polygonal model, the created model is quite satisfactory accuracy, with a maximum deviation of 1.71 mm and a mean deviation of 0.48 mm. Graphical representation of model deviation is shown in Fig. 4.10.

Fig. 4.10 Surface model of the femur and deviation of the given model in relation to the imported model

4.4.3 Parametric Geometrical Models of Long Bones

The algorithm used to create the parametric model was realized by applying multiple linear regression. The method used is well known (Brown 2009). The basic idea of linear regression is to predict the dependent variable Y in accordance with the values of the determined parameters, i.e., the independent variable X, (1).

$$Y = BX + E \tag{4.1}$$

Y—Dependent variable, X—Independent variable, B—Coefficients, E—Error.

Considering the defined model, it is necessary to determine the independent variable X. This variable is defined as a vector of morphometric parameters that are defined for every bone individually. All defined morphometric parameters are in relation to the anatomical and morphological entities on the bone. Also, the defined parameters can be clearly read from medical images, which is an imperative for fast creation of parametric models. It is important to note that it is possible to create individual anatomical sections with defined parameters only in that part, and to create parametric models of certain bone segments.

To successfully create a parametric model of a certain bone, it is necessary to clearly define anatomical points on the appropriate geometric elements, or on clearly defined anatomical landmarks on the bone itself. As for the parameters, it is necessary to measure the coordinates of the points on each individual bone specimen of the input bone set. The values of the coordinates of the points define the dependent variable Y. After the formation of the input elements, statistical processing is performed, and parametric functions are created. Using parametric functions, it is possible to create a point cloud adapted to a specific patient based on the values of parameters measured from medical images (CT, X-ray). In the following text, the process of creating parametric models of the femur and tibia will be presented.

4.4.3.1 Parametric Model of the Femur

The morphometric parameters defined on the polygonal model of the femur are shown in Fig. 4.11. Six parameters were defined for the complete femur. The more parameters, the greater the possibility of creating a higher quality model, but this requires more statistical analysis. It is important to note that it is possible to conduct an analysis with variable number of parameters and form parametric equations based on that. This means that if not all six parameters are available, only available ones can be used, which loses the quality of the model in terms of geometric and anatomical/morphometric accuracy, but on the other hand the model is still created and will allow the surgeon a basic operation simulation. Of course, because linear regression is used, the further analysis about parameters influence on the created parametric model should be conducted in the future work. Measurement of morphometric parameters

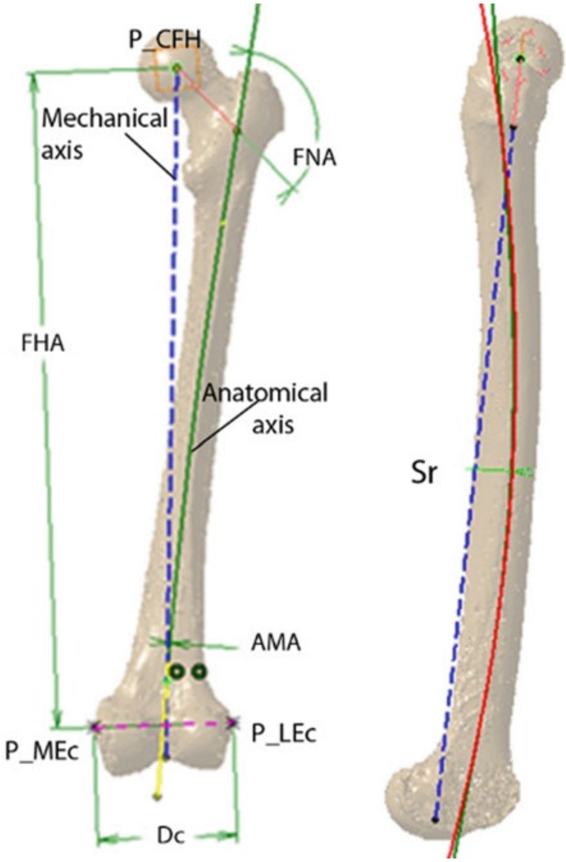

Fig. 4.11 Femur morphometric parameters (Majstorovic et al. 2013)

on femur models can be performed at any time, regardless of the measurement of point coordinates.

Input set was defined in detail in Majstorovic et al. (2013), and it included twenty femur samples, both men and women, with 0.5 mm scan thickness and 512 × 512 resolution.

The first and basic step is to define a coordinate system that will enable the correct measurement of the coordinates of points. It is possible to define several coordinate systems, one absolute (World Coordinate System—WCS) and several local or relative coordinate systems (Local Coordinate System—LCS). In the example of the femur, a WCS was created with in the center of the femoral head. The coordinate system planes are AP, LM, and the plane normal to these two planes (axial plane). Depending on the position of the points, appropriate measurements were performed in relation to the LCS, so the values were transformed in relation to the WCS. For example, a coordinate system is formed in the distal part/end of the femur so that the X and Y axes are defined as a direction defined by a line between the extreme points on the condyles, and a direction normal to a given direction in the corresponding rotational plane.

The Z axis is not necessary in this case, because the position of the points is defined in relation to the angle of rotation of the plane.

Example of Creating Parametric Functions.

Parametric functions will be first defined for ten samples because of clarity, and in the end, results for twenty samples will be presented. Parametric functions define the dependence of parameters ($p_1, p_2, \ldots p_n$) and coordinates (X, Y, Z) of points, and are shown in Eq. (4.2).

$$X = f_1(p_1, p_2, \ldots pn), Y = f_2(p_1, p_2, \ldots p_n), Z = f_3(p_1, p_2, \ldots p_n) \tag{4.2}$$

As stated above, multiple linear regression was used as a statistical function, and defined in Eq. (4.3).

$$\begin{aligned} X &= b_{x0} + b_{x1}p_1 + \cdots + b_{xn}p_n \\ Y &= b_{y0} + b_{y1}p_1 + \cdots + b_{yn}p_n \\ Z &= b_{z0} + b_{z1}p1 + \cdots + b_{zn}pn \end{aligned} \tag{4.3}$$

As an example of creating input vectors (matrices) of dependent and independent variables, the equations shown in Eq. (4.4) for the coordinate X (similar for Y and Z) are given.

$$\begin{aligned} &\mathrm{P_1, P_2, P_3, \ldots, P_n = X_i} \\ &p_{11},\ p_{12},\ p_{13},\ \ldots,\ p_{1n} = X_{1i} \\ &p_{21},\ p_{22},\ p_{23}, \ldots, p_{2n} = X_{2i} \\ &p_{31}, p_{32}, p_{33}, \ldots, p_{3n} = X_{3i} \\ &p_{m1}, p_{m2}, p_{m3}, \ldots, p_{mn} = X_{mi} \end{aligned} \tag{4.4}$$

$p_{i,j}$ are the values of the parameters measured on each of the bone samples of the input set. X_i is the coordinate value of the anatomical point on each bone specimen from the input set. An example of the formed equation for three parameters (e.g., if it is not possible to measure the other three) for the X_i coordinate is shown in Eq. (4.5). This is point 1 defined in Fig. 4.12a on the femur model and Fig. 4.12b on the spline curve.

$$\begin{aligned} &P_1(DC) \quad P_2(FNA) \quad P_3(FHA) = (X_1) \\ &81.383 \quad 127.456 \quad 386.675 = 12.149 \quad (X_{11}) \\ &82.297 \quad 125.67 \quad 391.734 = 12.149 \quad (X_{21}) \end{aligned} \tag{4.5}$$

To check the accuracy of the created parametric functions, it is important to determine the error vector for each coordinate of each point. The error vector for the mentioned point is given in Eq. (4.6) (Brown 2009).

$$E = X_1 - X \tag{4.6}$$

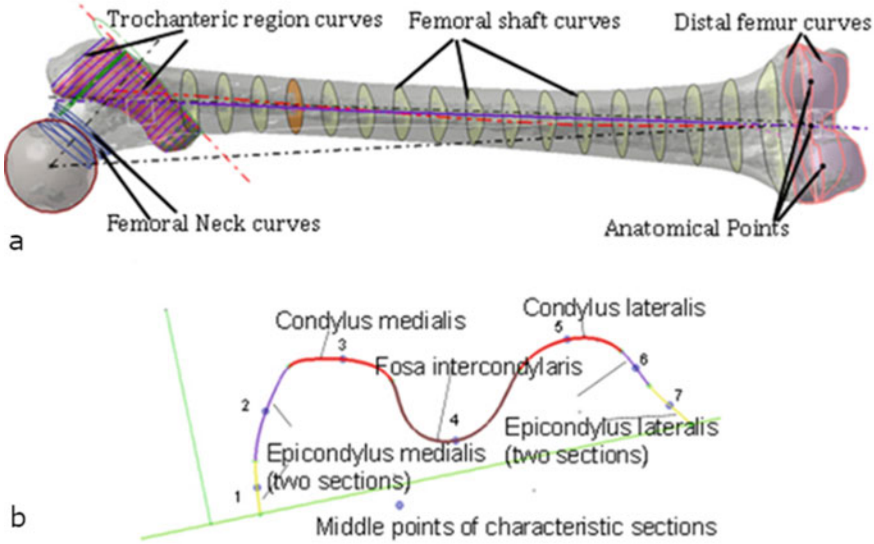

Fig. 4.12 RGEs and CGEs on the Femur model—**a** CGEs and anatomical points, **b** individual spline curve (Majstorovic et al. 2013)

Before presenting the regression application results, it is important to note why linear regression was chosen as a statistical function at all. The analysis of the behavior of the values of the coordinates of the points showed that the best approximation of the values of the coordinates is essentially a linear function. Of course, this is limited to the input set available in the research. In Figs. 4.13 and 4.14 the

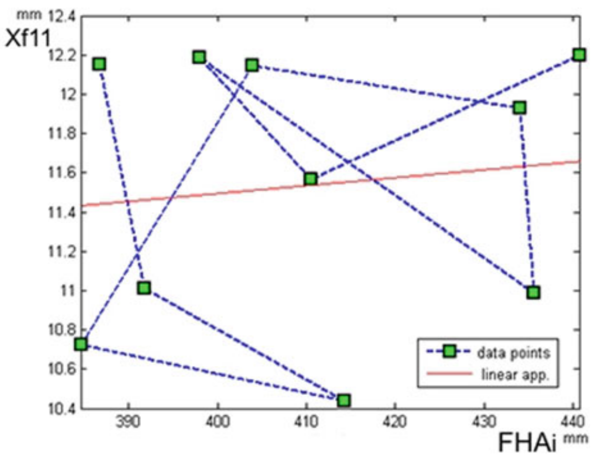

Fig. 4.13 X_{f11} coordinate of Point 1 (, f—Femur, Curve 1, Point 1) in relation to Dci (Distance between P_MEc and P_LEc) (Vitković et al. 2013)

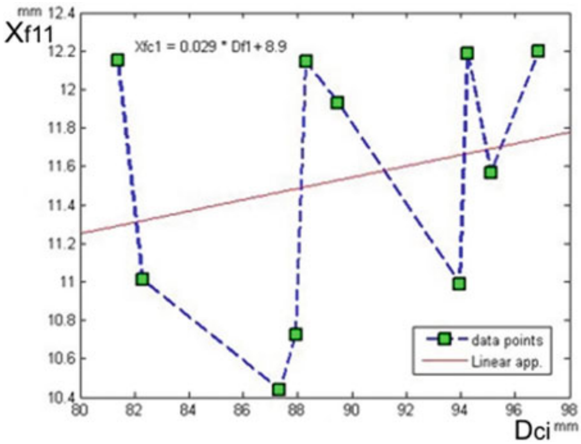

Fig. 4.14 X_{f11} coordinate of Point 1 (f—Femur, Curve 1, Point 1) with respect to FHAi (Distance between P_CFH and the line connecting P_MEc and P_LEc (Vitković et al. 2013)

variation of the X coordinate of point 1 with respect to the parameters FHA and DCi is quite well described by the linear approximate function Eqs. (4.7) and (4.8). Other types of functions such as cubic, higher degree polynomials and similar interpolations/approximations create results that make deviations on the defined input set that are greater than those given by the linear approximation. In this research, it was decided to apply a linear function, because it also defines an approximate mean value over the input set, which to some extent allows the application on bone specimens that do not meet the characteristics (age, regional affiliation, etc.) of the input set. Based on the applied analysis, it is possible to define an assumption for the selected input set that the points will be linearly distributed within a certain 3D space, which is exactly what linear regression provides. For further research, it is possible to apply other types of regression, as well as other methods of artificial intelligence, but in the current stage of research, linear regression was chosen.

$$X_{f11} = 0.029 D_{ci} + 8.9 \tag{4.7}$$

$$X_{f11} = 0.004 FHA_i + 9.9 \tag{4.8}$$

After the measurement, vectors of appropriate sizes Eq. (4.9) (DC, FNA, FHA) were created, and after the application of linear regression, the functions shown in Eq. (4.10) (B, E) for the input set of bones were obtained.

$$DC = [81.383\ 82.297\ 87.34\ 87.932\ 88.301$$
$$89.493\ 93.961\ 94.257\ 95.112\ 96.88]';$$
$$FNA = [127.456\ 125.67\ 129.45\ 127.67\ 130.56$$
$$129.1\ 128.7\ 126.2\ 129.5\ 128.015]';$$
$$FHA = [386.675\ 391.734\ 414.253\ 384.577\ 403.927$$

$$434.057\,435.555\,397.939\,410.45\,440.713]'; \tag{4.9}$$

$$\begin{aligned} &= [11.45090.0325 - 0.0007 - 0.0197] \\ E &= [0.8522 - 0.3480 - 0.9907 - 0.78110.70030.4381 \\ &\quad - 0.65500.4521 - 0.11830.4504] \end{aligned} \tag{4.10}$$

Analyzing the error vector, it can be concluded that the deviation is below one millimeter, which is considered a good result, and it can be said that the proposed model in this case met expectations and it conforms with results presented in other research (Sholukha et al. 2011).

As a result of the linear regression application, a functional dependence is formed between the point coordinate and the morphometric parameters, as defined in Eq. (4.11). This function can be used to define the position of Point 1 on a new specimen of the femur, i.e., this and other functions can be used to create a cloud of points adapted to the geometry and anatomy/morphology of the femur of a particular patient.

$$X_{f11} = 11.4509 - 0.0325DC - 0.0007FNA - 0.0197FHA \tag{4.11}$$

As an example of the use of all six parameters, the parametric function in Eq. (4.12) is shown. The error vector is shown in Eq. (4.13) and it can be seen that there are no major changes for this point. The error is still about 1 mm.

$$\begin{aligned} X_{\text{f11}} &= 9.168 + 0.033 \cdot DC_{\text{i}} - 0.033 \cdot \text{FHA}_i + 0.041 \cdot \text{FNA}_i \\ &\quad + 0.002 \cdot \text{AMA}_i + 0.055 \cdot \text{S}_{\text{ri}} - 0.033 \cdot \text{FHR}_i \end{aligned} \tag{4.12}$$

$$\begin{aligned} E &= [0.8322 - 0.4440 - 1.1607 - 0.58110.7503 \\ &\quad 0.421 - 0.61500.5521 - 0.01830.3504] \end{aligned} \tag{4.13}$$

Points Coordinates Deviation Analysis

Based on the analysis of all point errors for twenty (20) femur samples, certain results were obtained which are presented in Table 4.1. The maximum deviation is 4.19 mm. This point is at the point where certain input polygonal models were affected by osteoporosis, which led to the assumption about the position of the point. The position was assumed based on known anatomy and bone shape from the literature. Based on the Table 4.1 and the mean value of the maximum error for all points on the model, it can be concluded that the model is quite acceptable. If a larger number of samples were included, which is imperative in further research, as well as a larger number of parameters, the assumption is that the results would be even better. Also, the possibility of applying other methods of statistics and artificial intelligence enables another assumption about creating an even more accurate model.

Table 4.1 Deviation analysis [mm]

Point coordinates	Maximum deviation	Mean value of deviation	Mean value of maximum average error (EX, EY, EZ)	Standard deviation of deviation error
X	1.97	0.97	1.91	0.5
Y	4.19	1.45	1.93	0.58
Z	1.54	1.2	2.01	0.39

Another possibility available to researchers in this field is the use of limiting (boundary) functions. These functions should be created by using medical statistics, which would prevent the creation of coordinate values in an area that does not meet certain morphological/anatomical conditions.

The mean value of the maximum error shown in Table 4.1 was calculated for each coordinate of each point on the point cloud model for 20 specimens, and the formula for the X coordinate is shown in Eq. (4.14) and (4.15).

$$Ex_{1avg} = (Ex_1 + Ex_2 + \cdots Ex_n)/n \tag{4.14}$$

Ex1avg—Mean value of error (deviation) for point 1, for coordinate X (n = 20).

$$EX = \left(Ex_{1avg} + Ex_{2avg} + \cdots + Ex_{kavg}\right)/k \tag{4.15}$$

EX—Mean value of maximum average error for all points (k = 226).

4.4.3.2 Referential Geometrical Entities and Constitutive Geometrical Entities for the Human Tibia Geometrical Model

The basic anatomical elements that are important for defining the geometry of the human tibia are the anatomical and mechanical axes. In the A-P view (projection) these axes coincide. In accordance with the needs of this research, unlike the femur, the tibia is not considered in such detail in terms of anatomical and morphological characteristics, but only those anatomical landmarks that are important for creating appropriate models of the tibia are analyzed. In some future research, a more precise analysis of the morphological entities of the tibia will be done.

The mechanical axis of the tibia is defined as the line connecting the center of the upper articular surface of the tibia at its upper end, which corresponds to the point in the middle of the intercondylar bulge with the point corresponding to the center of the lower articular surface of the tibia at its lower end (Cooke et al. 2007).The upper articular surface of the tibia is approximated with an ellipse because it best encompasses its boundaries, i.e., geometrically it best corresponds to the shape of this particular surface. The first point of the mechanical axis is defined as the center of the ellipse. This point can also be defined as the center of the intercondylar elevation

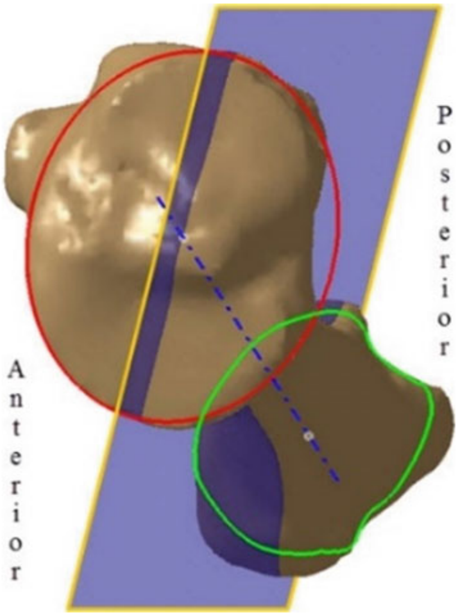

Fig. 4.15 RGEs defined on a polygonal model of the tibia: mechanical axis and A-P plane (Veselinovic et al. 2011)

of the proximal part of the tibia. The second point is defined as the center (center of gravity) of the section on the distal part of the tibia (lower articular surface of the tibia), Fig. 4.15.

When the mechanical axis is known, it is possible to place differently oriented planes in accordance with the anatomical characteristics of the tibia. The A-P plane is defined as a plane containing the longer axis of the ellipse and the mechanical axis of the tibia.

Two methods were used to create geometric models of the tibia. The first method is based on spline curves created in longitudinal rotational planes. The second method is based on merging individual geometric models of anatomical parts of the tibia, namely: the proximal part (upper end), the body of the tibia and the distal part (lower end) of the tibia. In both cases the spline curves (CGEs) based on the defined RGEs are created and used for the creation of the surface model. The model creation process is presented in Fig. 4.16.

To check the geometrical accuracy of the created surface model analysis was conducted (Veselinovic et al. 2011). The results were quite satisfactory, and the conclusion follows that the presented method can be used for the reconstruction of human tibia surface model.

4.4.3.3 Human Tibia Parametric Model

For the tibia in the first iteration, a parametric model of the proximal part was created to verify the claim about the possible use of parametrically defined implants, i.e.,

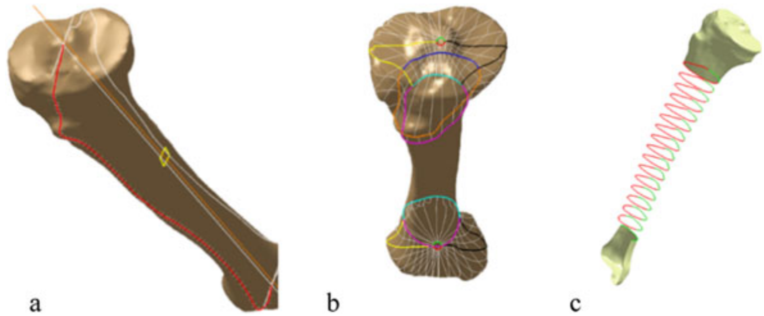

Fig. 4.16 Two methods for creating human tibia surface model: First method, **a** Rotational curves; second method, **b** guides and splines of the curve for creating the surface at the ends of the tibia, **c** surface of the proximal part and the back of the distal end and spline curve on the axis of the tibia (Veselinovic et al. 2011)

fixators for fixation of the proximal part of the bone. An input set of ten (10) bones of men and women of the same regional origin, with the same scanning parameters as for the femur bone, as described in Majstorovic et al. (2013). The defined morphometric parameters for the tibia are shown in Fig. 4.17a. In the case of the proximal end of the tibia, the parametric function for point 2 on curve 1 (Fig. 4.17b, point AP2) is shown in Eq. (4.16).

$$X_{f21} = 8.8236 - 0.2378P_1 + 0.1098P_2 - -0.0196P_3 - -0.1498P_4 \tag{4.16}$$

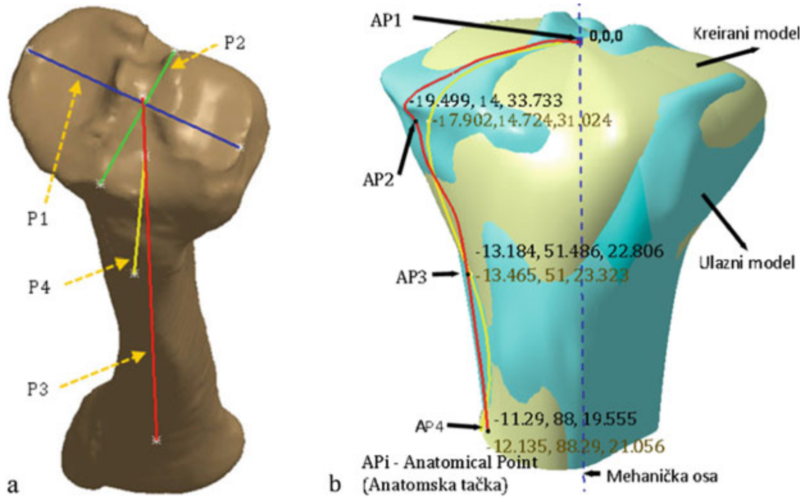

Fig. 4.17 The created surface model of the proximal end of the tibia: **a** Defined parameters on human tibia geometrical model, **b** proximal part accuracy analysis (Majstorovic et al. 2013)

Table 4.2 Deviations of coordinates of points of the entrance set of the human tibia [mm]

Point coordinates	Maximum deviation	Mean value of deviation	Mean value of maximum average error (EX, EY, EZ)	Standard deviation of mean deviation error
X	4.28	2.42	1.53	0.7
Y	0.72	0.64	1.32	0.55
Z	3.31	2.11	1.71	0.41

In Eq. (4.16), a parametric function is defined for the X coordinate of the point AP2. When all parametric functions for all anatomical points are determined, a parametric bone model is formed. Figure 4.16 shows the created surface model of the proximal end of the tibia that was created independently of the whole bone. If the patient is missing a part of the proximal part of the tibia and needs to be replaced with an implant, it is possible to take the geometry from the created model and make an implant (or a fixator in this case).

Analysis of the Obtained Results

The maximum deviation of the values of the coordinates of the points for the input set of polygonal models of the tibia is shown in Table 4.2.

Deviation values are determined for each point of the created models for the values of its coordinates. The deviation values are clearly defined in the error vectors obtained for each parametric function and represent the difference between the created values and the measured values from the input models. The mean deviation value was defined based on the deviation of the given coordinate for all specimens of the tibia. Based on the analysis of the geometry of the created models presented at the current stage, the MAF method provides quite satisfactory results, considering the mean geometric error shown in Table 4.2. It can be concluded that the created models are more than sufficient geometric precision and anatomical/morphological accuracy. In the next iteration of the parametric model of the tibia, a model of the complete tibia was created based on the rotational planes (Vitkovic et al. 2018a, b). After analyzing the results obtained on such a model, it was concluded that for the input defined set of tibia specimens, the errors for the complete bone set are within the already defined limits.

4.4.3.4 Referential Geometrical Entities and Constitutive Geometrical Entities for the Human Humerus Geometrical Model

The basic prerequisite for successful reverse modeling of a human bone's (humerus in this case) geometry is the identification of RGEs. RGEs include characteristic points, directions, planes and views. For the creation of humerus RGEs geometric and morphometric definition was acquired from literature. The definition of the coordinate system was acquired, where basic axes and planes (views) are defined (Rashid et al. 2017). The anatomical axis of the proximal part of the humerus (metaphyseal axis) is defined as the cylinder's axis formed in the upper part of the humeral shaft. It is set as the Z axis of the coordinate system. The X-axis is defined as a projection of the line which goes through tips of the epicondyles of the distal part of humerus on the plane perpendicular to Z axis. Y-axis is the line normal to the plane formed by Z and X axes. The planes are: Anterior–Posterior plane (X–Z), Lateral-Medial plane (Z-Y), and Axial plane (Y-X). Created RGEs are presented in Fig. 4.18.

Surface Model of Human Humerus

Spline curves were created in cross-sections of planes parallel to axial planes to create a surface (polygonal) model of the humerus. Polygonal model was created for three anatomical sections: proximal section, shaft section, distal section. The initial cross-section curves were adapted to the geometry and shape of humerus by inserting additional points or deleting unnecessary points. The positions of the spline curves were adjusted to the anatomical landmarks of the adequate anatomical sections of the humerus. The surface models of humerus anatomical sections together with constructed spline curves are presented in Fig. 4.19. The proximal part and the shaft were created using splines created in the axial planes (Fig. 4.19a, b). The distal section was created as an assembly of four surface parts. This is done because shape of the distal part is very complex. The upper part was created using spline curves positioned in rotational planes, with the upper ending curve (closer to the shaft) constructed in the axial plane. These planes follow the curvature of the distal part

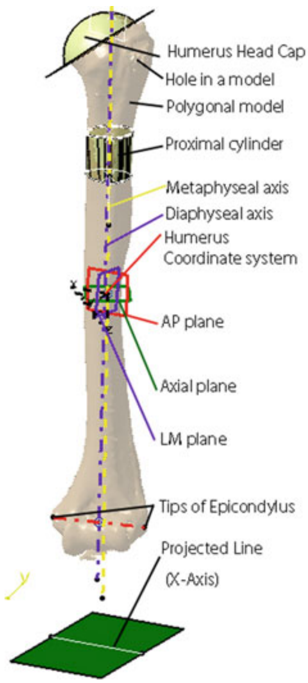

Fig. 4.18 RGEs of the humerus bone (Rashid et al. 2017)

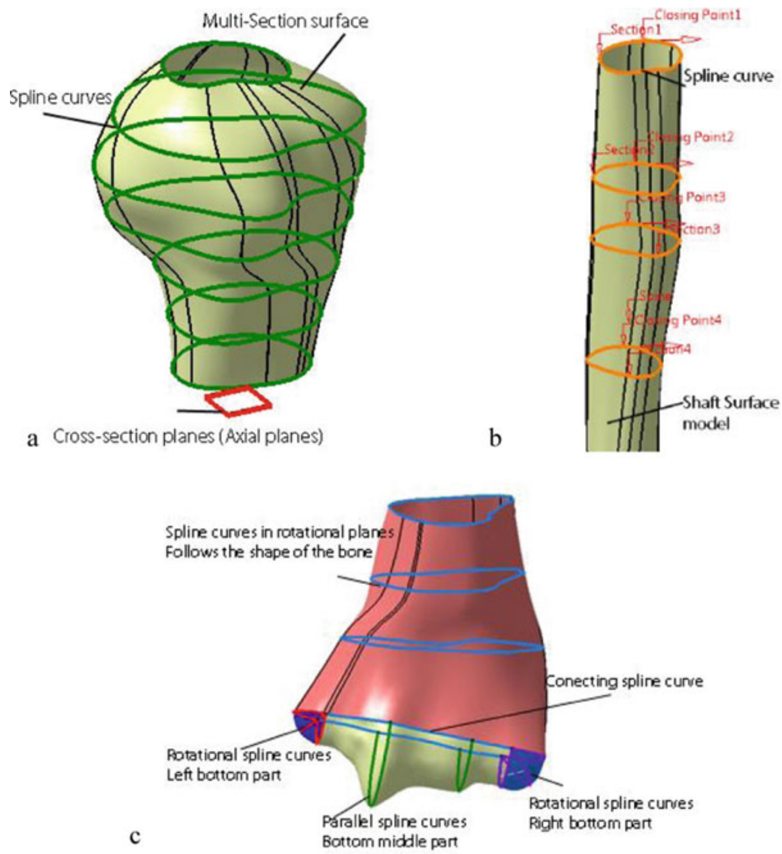

Fig. 4.19 Spline curves and adequate surface models of the human humerus anatomical sections. **a** proximal section, **b** shaft section, **c** distal section (Rashid et al. 2017)

of the humerus. The right and the left bottom parts were created by using rotational curves and the middle part was created with the parallel planes normal to the bottom ending plane of the upper part. The surface model of the distal part of the human humerus is presented in Fig. 4.19c.

Discussion of the Geometrical Accuracy of the Surface Model

The surface model of the whole humerus was created by merging constructed individual surfaces. The complete model is presented in the Fig. 4.20a.

The deviation values measured in reference to the input sample polygonal model show that the created surface model has adequate overall accuracy (Fig. 4.20b). The overall accuracy of the model is around 0.4–0.8 mm. The maximal deviation is in the range of 0.811–1.216 mm. In the area of the proximal shaft and greater tubercles max. deviation is 0.494 mm (one point, Fig. 4.20c). It should be noted that the initially

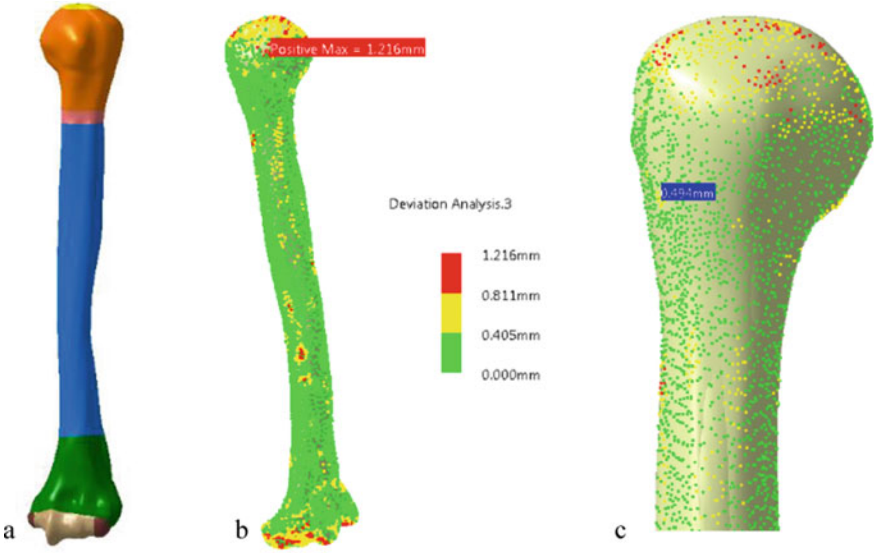

Fig. 4.20 Humerus bone surface model and deviation analysis. **a** Humerus surface model, **b** deviation analysis between input sample polygonal model and created surface model (surface based) **c** proximal part and supporting surface for plate positioning with deviation points (Rashid et al. 2017)

created surface model of the human humerus had greater deviations—Maximal deviations were around 3 mm. The occurrence of these points can be explained through irregularities (e.g., holes) in the initial polygonal model (probably due to the osteoporosis), the big change in curvature in the connected regions (e.g., head–neck). To correct these elements, additional points were added based on available medical literature information regarding the bone shape in adequate areas, and deviations were reduced as already stated.

Orthopedic surgeons included in this research stated that these deviations are more than acceptable, especially because they are not in the region of interest for placement of the plate. In the area of interest deviations are under 0.5 mm enabling proper definition of the plate geometry and position. If there is a requirement to improve the accuracy of a resulting model, it is possible to add more spline curves or add more points to the existing spline curves in the areas of interest (e.g., humeral head area, or distal part humerus).

4.4.4 Final Remarks on Parametric Long Bone Models

There are several activities whose application would increase the accuracy of the created parametric models:

- Increasing the number of samples of the input set of bones.

- Collection of better images of patients' bones in anatomical and geometric terms (without pathological or traumatic damage)
- Application of higher degree regression and detailed analysis of p number (and other factors) from the point of view of the influence of certain parameters on the accuracy of the geometric model of anatomical section(s) and the whole bone.
- Defining a number of morphometric and other parameters.
- Creation of a boundary model that would prevent excessive deviations of the values of morphometric parameters in relation to those defined in the literature and clinical practice.
- Application of other methods of artificial intelligence, such as neural networks, etc.

All the above elements represent the basis for further research and creation of geometrically more precise and anatomically/morphometrically more accurate bone models.

4.5 The Definition of Parametric Model and Regions of Interest (ROI)

To create parametric model of the specific human bone, input set of bone samples was analyzed, parameters and point cloud model was defined, and multilinear regression was applied, as already stated. The output of the applied process is a set of parametric functions which define correlation between bone morphometric and geometric parameters, and coordinates of points from point cloud. The parametric model was already tested, and results were more than promising. To provide better control of morphology and geometry of the formed Parametric bone 3D Point Cloud model (PPC), further steps were performed and previously described. The main step was creation of ROI, which were defined as point sets, formed by selecting specific points from the PPC model, from different regions of the bone surface. To define these sets, landmark, and outline morphometrics, and also bone anatomy and morphology were applied (Klingenberg 2016; Mitteroecker and Gunz 2009). To geometrically define ROI, point cloud model was separated into sections by using the interpolated splines which goes through the anatomical points (landmarks), as presented in Fig. 4.21 for the tibia bone. These sections can be defined arbitrary, because division into sections can be done as already stated, or by using recommendations from physicians and create Regions of Specific Interest (ROSI), with manually selected points from different predefined regions. Mathematically, ROI were defined as mathematical sets, presented in Eq. (4.17).

$$AS_k = \left\{P_{k,1}, P_{k,2}, P_{k,3}, \ldots, P_{k,n}\right\} \tag{4.17}$$

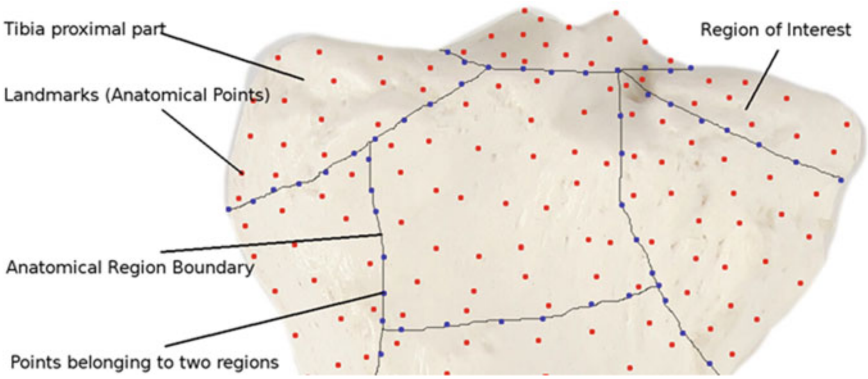

Fig. 4.21 Definition of the Region of Interest (ROI) on the tibia proximal part (Vitkovic et al. 2019)

$V = \{AS_1, AS_2, AS_3, \ldots AS_k\}$, AS_k—Kth—Anatomical section, $k = 1, \ldots, n$ (number of regions), $P_{i,j}$—Point in the Kth anatomical section; V—Set of anatomical sections.

Interpolated spline curves were defined in such a way that represent boundary between anatomical sections Eq. (4.18), which means that some points can belong to the more than one region Eq. (4.19)

$$PS_z = \{P_{z,1}, P_{z,2}, \ldots, P_{zm}\} \tag{4.18}$$

$$PSci \in (AS_v \cap AS_w) \tag{4.19}$$

where, v, w = indexes of the region, PS_z—Set of points belonging to individual spline, $z = 1, \ldots, s$ (number of splines), PS_{ci}—Set of anatomical points positioned on the boundary between regions.

Interpolated splines were defined as cubic splines Eq. (4.20). This means that $S_{3,n}$ (x) cubic spline is defined as C2 cubic piecewise polynomial of the third order, and therefore it can be defined as:

$$S_{3,n}(x) = \left\{ \begin{array}{c} p_1(x) = a_1 + b_1x + c_1x^2 + d_1x^3 x \in [x_0, x_1] \\ p_2(x) = a_2 + b_2x + c_2x^2 + d_2x^3 x \in [x_1, x_2] \\ \vdots \\ p_n(x) = a_n + b_nx + c_nx^2 + d_nx^3 x \in [x_{n-1}, x_n] \end{array} \right\} \tag{4.20}$$

C2 means that continuity of second and first derivate at any point in the defined interval is preserved, especially at the knots. To make these curves fully interpolated, one more condition must be met, and it is defined in Eq. (4.21)—function value, first and second derivate at the knot values should be the same.

$$S_{3,n}(X_i) = Y_i, i = 1, 2, \ldots, n; p_i^{'}(x_i) = p_{i+1}^{'}(x_i), p_i^{''}(x_i) \\ = p_{i+1}^{''}(x_i) i = 1, 2, \ldots, n-1 \tag{4.21}$$

It is not just enough to mathematically define anatomical points, section, and interpolated splines. They need to be defined in such a way, that they can be used for the creation of patient specific point cloud and surface model.

Procedure Definition The main procedure for surface forming is presented by using the flowchart diagram in Fig. 4.22. First step and most important is proper

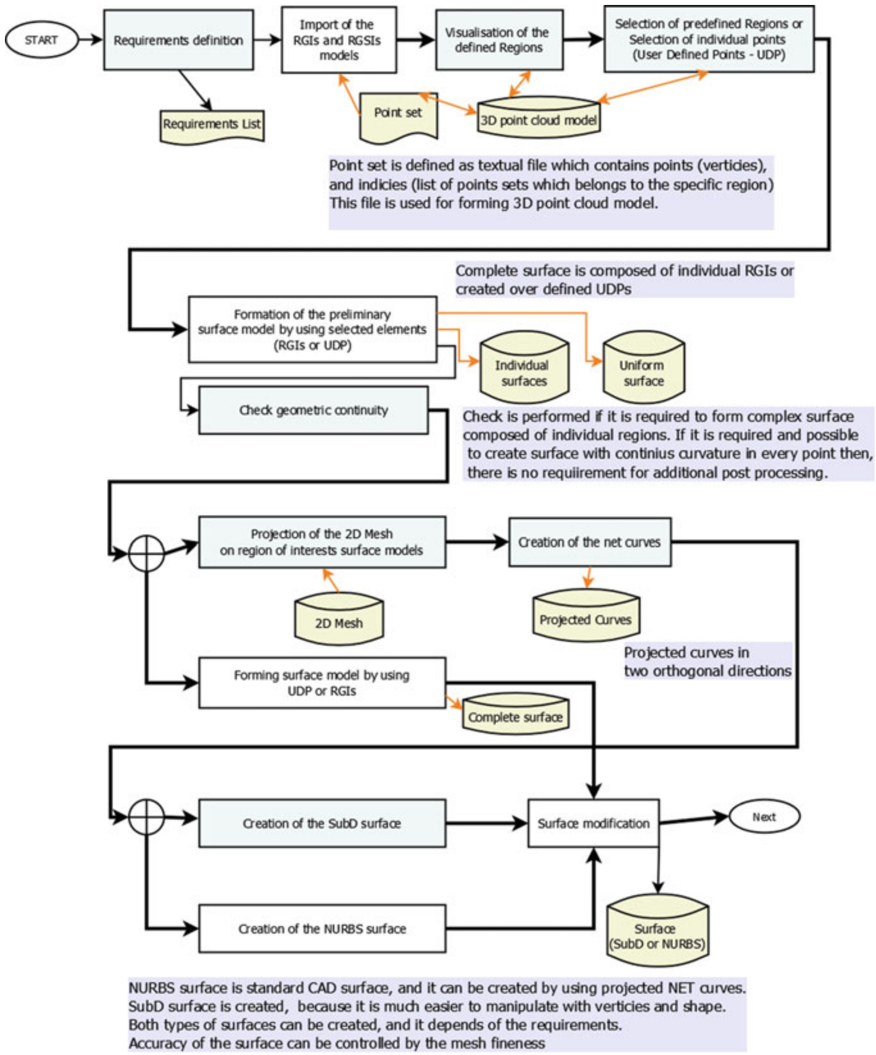

Fig. 4.22 Definition of the Region of interest (ROI) on the tibia proximal part (Vitkovic et al. 2021)

requirements definition. Requirements define resulting ROI and ROSI model(s) geometrical accuracy and anatomical correctness. It is already stated that ROI are predefined sets of anatomical and geometrical points, separated by defined boundaries, so how they will be used is defined in requirements definition process. Four main use cases are already defined:

UC1.Strict application of predefined unique ROI.
UC2.Combination of more than one ROI by defining specific surface connection rules.
UC3.Customized ROSI definition.
UC4.Specific requirements concerning surface curvature and tangency in specific areas of ROI or ROSI.

First use case is the easiest to accomplish, because the points are already properly defined to create surface of continuous curvature and tangency. Second use case has more complexity because it is generally known that connection between predefined surfaces can be hard to accomplish if there is a possibility of creating only contact connection (point by point or by connection curve), not a curvature continuity. In this case the proposed algorithm should provide possibility to connect individual ROI by establishing curvature continuity through connection curve, by using NURBS or by using SubD surfaces (Vitkovic et al. 2019). The radius defined in each point, can be continual and resulting surface will be topologically correct, which is the one of defined goals.

Third use case is oriented to define custom ROSI by selecting individual points in different regions, which can be observed as specific ROI. The points are selected by using CATIA grouped features, which means that individual cloud points regions, can be selected and validated, and then merged into one point cloud (ROSI). The process of defining points or points group is manual by using technical elements for selection (CATIA Features). The same rules apply here as for the use case one, and the addition is a manual point selection.

The last predefined use case is formed due to the requirements of different manufacturing technologies, and shape of standard and personalized implants (Vitkovic et al. 2018b). The further description and application of ROI is presented in additional study by Vitkovic et al. (2019).

4.6 Conclusion

In this chapter, different procedures for the creation of human long bone geometrical methods are presented. First, application of Method of Anatomical Features (MAF) for the creation of different human long bone geometrical models is demonstrated, by creating geometrical models of human femur tibia and humerus, both classic CAD models (polygonal, surface, solid) and parametric models (except humerus). Validity of this models is verified in this chapter, and by using external references.

The second procedure is defined as MAF improvement based on the novel methods which uses Regions of Interest (ROI) and Regions of Specific Interest (ROSI). ROI and ROSI are defined on human bone point cloud model, and created by using uniform mesh, NURBS and SubD elements. They can help physicians reconstruct bone surface during pre-operative planning processes in different areas of the affected bone, which can improve the outcome of the following surgical procedure. This procedure enables creation of more realistic, geometrically accurate, and anatomically correct 3D models of the human bones, which can be used for: pre-operative planning, surgical guidance, production of personalized plate implants and fixators, and educational purposes in medical science.

It is important to note that application of MAF is not restricted to the human bones only, but it can be extended to other bio-forms, like soft tissue. The main challenge in future research would be the application of MAF to develop the geometrical models of the human soft tissue by using ROI and ROSI. These adaptable models will enable better pre-operative planning in orthopedics, and automatic or semi-automatic creation of geometrical models of all human body parts, not just bones, enabling better manufacturing processes in personalized medicine.

References

Atesok K, Galos D et al (2015) Pre-operative planning in orthopaedic surgery: current practice and evolving applications. Bull Hosp Jt Dis 73(4):257–268

Brown S (2009) Multiple linear regression analysis: a matrix approach with MATLAB. Ala j math. Online: http://ajmonline.org/2009/brown.pdf

Cooke TDV, Sled EA, Scudamoore RA (2007) Frontal plane knee alignment: a call for standardized measurement. J Rheumatol 34(9):1796–1801

De Vos W, Casselman J, Swennen GRJ (2009) Cone-beam computerized tomography (CBCT) imaging of the oral and maxillofacial region: a systematic review of the literature. Int J Oral 38(6):609–625. https://doi.org/10.1016/j.ijom.2009.02.028

Filippi S, Motyl B, Bandera C (2008) Analysis of existing methods for 3D modelling of femurs starting from two orthogonal images and development of a script commercial software package. Comput Methods Programs Biomed 89(1):76–82

Klingenberg CP (2016) Size, shape, and form: concepts of allometry. Dev Genes Evol 226(3):113–137. https://doi.org/10.1007/s00427-016-0539-2

Mahaisavariya B, Sitthiseripratip K, Tongdee T et al (2002) Morphological study of the proximal femur: a new method of geometrical assessment using 3-dimensional reverse engineering. Med Eng Phys 24:617–622

Majstorovic V, Trajanovic M, Vitkovic N, Stojkovic M (2013) Reverse engineering of human bones by using method of anatomical features. CIRP Annals - Manufacturing Technology. 62(1):167–170

Mitteroecker P, Gunz P (2009) Advances in geometric morphometrics. Evol Biol 36:235–247. https://doi.org/10.1007/s11692-009-9055-x

Park BK Bae et al (2014) Function-based morphing methodology for parameterizing patient-specific models of human proximal femurs. Comput-Aided Des 5:31–38. https://doi.org/10.1016/j.cad.2014.02.003

Rashid MM, Husain KN, Vitković N et al (2017) Geometrical model creation methods for human humerus bone and modified cloverleaf plate. J Sci Ind Res 76(10):631–639

Sholukha V, Chapman T, Salvia P et al (2011) Femur shape prediction by multiple regression based on quadric surface fitting. J Biomech 44(4):712–718. https://doi.org/10.1016/j.jbiomech.2010.10.039

Shui W, Yang Y, Pi X et al (2021) A novel closed reduction technique for treating femoral shaft fractures with intramedullary nails, haemostatic forceps and the lever principle. BMC Musculoskelet Disord 22:187. https://doi.org/10.1186/s12891-021-04055-5

Stojkovic M, Trajanovic M, Vitkovic, N et al. (2009) Referential geometrical entities for reverse modeling of geometry of femur. In: Computational vision and medical image processing—VipIMAGE, Taylor & Francis Group, Porto, Portugal. pp 189–195

Trajanovic M, Vitkovic N, Stojkovic M et al. (2009) The morphological approach to geometrical modelling of the distal femur. In: SEECCM 2009, 2nd South-East European conference on computational mechanics. Rhodes, Greece, 22–24 June 2009

Tufegdžić M, Trajanovic M, Vitkovic N, Arsić S (2013) Reverse engineering of the human fibula by using method of anatomical features. Facta Univ Ser: Mech Eng 11(2):133–139

Veselinovic M, Vitkovic N, Stevanovic D et al (2011) Study on creating human tibia geometrical models. In: Proceedings of the 3rd international conference on E-health and bioengineering—EHB. Iaşi, Romania. pp 195–198

Vitković N, Milovanović J, Trajanović M et al (2012) Different approaches for the creation of femur anatomical axis and femur shaft geometrical models. STJSAO 54(3):247–255

Vitković N, Milovanović J, Korunović N et al (2013) Software system for creation of human femur customized polygonal models. Comput Sci Inf Syst 10(3):1473–1497. https://doi.org/10.2298/CSIS121004058V

Vitkovic N, Mladenovic S, Trifunovic M et al (2018a) Software framework for the creation and application of personalized bone and plate implant geometrical models. J Healthc Eng 2018:6025935. https://doi.org/10.1155/2018/6025935

Vitkovic N, Stojkovic M, Majstorovic V et al (2018b) Novel design approach for the creation of 3D geometrical model of personalized bone scaffold. CIRP Ann Manuf Technol 67(1):177–180. https://doi.org/10.1016/j.cirp.2018.04.064

Vitkovic N, Lj R et al (2019) 3D Point cloud model of human bio form created by the application of geometric morphometrics and method of anatomical features: human tibia example. Filomat 33(4):1217–1225. https://doi.org/10.2298/Fil1904217v

Vitkovic N, Trajanovic M, Manic M et al. (2021) Procedure for the creation of omplex free-form human bones surfaces for manufacturing of personalized implants. In: 18th international conference on product lifecycle management, IFIP PLM 2021, Brazil. Proceedings in Press

Wheeless CR (2015) Wheeless textbook of orthopaedics. Duke Orthopaedics, Durham. www.wheelessonline.com

Xiaozhong C, Kunjin H et al (2016) A parametric approach to construct femur models and their fixation plates. Biotechnol Biotechnol Equip 30(3):529–537. https://doi.org/10.1080/13102818.2016.1145555

Yunyan W, Zhengming C, Kunjin H, Weizhong G (2017) Rapid generation of human femur models based on morphological parameters and mesh deformation. Biotechnol Biotechnol Equip 31(1):162–174. https://doi.org/10.1080/13102818.2016.1255156

Chapter 5
Building 3D Surface Model of the Human Hip Bone from 2D Radiographic Images Using Parameter-Based Approach

Milica Tufegdzic and Miroslav D. Trajanovic

5.1 Introduction

Human hip bone represents a very complex morphological structure of irregular shape, resulting from the fusion of three primarily stand-alone bones: ilium, ischium and pubic bone. Being a part of the skeletal system, the hip bone can be significantly damaged due to various traumas, tumors and other pathological conditions. Hip bone fractures are fractures of any constitutive bone, such as pubic fractures, partial fractures of the ischium and ilium bone or pubic dislocations which involve acetabulum. Some of these traumas require the use of osteofixation materials (reconstructive plates, fixators, screws, clamps). Tumor resections have to be conducted with great precision and are followed by bone reconstruction process, which requires the existence of some personalized prosthesis and implants. They are constructed to completely match the lost part of the bone after tumor removal. In such cases, having a high-quality 3D model of the bones is necessary in order to simulate the correct placement of osteofixation materials and implants in a virtual environment, and to plan and simulate the surgical procedure.

Direct procedures for creating 3D models of hip bone are almost impossible to apply due to complex bone shapes, as well as lack of explicit knowledge about surface shape. The procedures used to reconstruct the 3D geometric model of individual bones are based on free-form technologies with a certain degree of approximation and reverse engineering technologies. Initial data for reverse engineering procedures are obtained from volumetric medical images, mostly by using procedures like CT or Magnetic Resonance Imaging (MRI). These digital images have different resolutions

M. Tufegdzic (✉)
Department of Information Technology, Academy of Professional Studies Sumadija, Trstenik, Serbia
e-mail: mtufegdzic@asss.edu.rs

M. D. Trajanovic
Faculty of Mechanical Engineering, University of Nis, Nis, Serbia

O. Canciglieri Junior and M. D. Trajanovic (eds.), *Personalized Orthopedics*,
https://doi.org/10.1007/978-3-030-98279-9_5

and therefore consist of point clouds of different densities. These point clouds need to be converted into usable 3D geometric models that can be translated into a digital representation of a physical object in reverse engineering procedures.

3D polygonal models are used for visualization purposes in the cases when high accuracy of the model is not required, since they have a certain degree of approximation of rough surfaces. However, for planning and simulating operations, as well as in the processes of osteofixation materials design, and similar applications, it is necessary to have a quality 3D volume model. This requirement is particularly pronounced in production of personalized implants. 3D polygonal and volume hip bone models can be acquired by reverse engineering methods only if there is a sufficiently dense point cloud of complete bone. Otherwise, in the case of incomplete data, it is not possible to obtain high-quality 3D model and to conduct accurate patient-specific bone reconstruction. For such cases, a new method of parametric regions was developed, using information about specific anatomical points and parameters, which represent a prerequisite for complete morphometry of the hip bone. Parameter-based approach, with the aid of statistical tools, allows for determining regression models for predicting the position of points on the hip bone surface. These positions are used for creating a surface model of the hip bone and/or its parts in the cases when all available input data are taken from two biplanar X-ray projections. The resulting 3D surface point models of the wing of ilium bone and its part as examples, are accurate enough for application in systems for planning and simulation of operative flow, as well as creating 3D models of missing parts of bone for the purpose of making implants and constructing personalized osteofixation material and similar applications.

5.1.1 Methods for 3D Models Reconstruction

Statistical modeling and analysis of anatomical shapes is the subject of research in the field of medical images (Styner et al. 2003; Chintalapani et al. 2007). Statistical shape analysis is important for 3D reconstruction of anatomical structures and improvement of shape prediction from incomplete input, while multivariate statistical analysis helps to determine the relevant shape variation in the population (Aguirre et al. 2007).

The anatomical structures of different individuals show large but limited natural variability that can be statistically represented. Appropriate parametric description of surfaces is needed to preserve variability and given characteristics. In methods that use parametric description of surfaces, deformable super-quadratics can be used in combination with local deformation modeling, a series of extensions, or coordinates of points on the surface (Sierra et al. 2006).

Similar to the representation of surfaces of any object, 3D bone surface models can be presented in the form of meshes or Non-uniform Rational B-Splines (NURBS) (Su et al. 2013). It is also possible to represent the surface of an object (like the bone) with the set of unique points in 3D space which have the same positions on each object (so-called “landmarks”). Each item belongs to a particular part of the object. Point Distribution Model (PDM) in 2D or 3D is obtained by statistical examination of the landmarks’ positions (Zsemlye 2005). Nonlinear models such as polynomial regression point distribution model, are based on polynomial regression, where the variation modes in linear model are replaced by polynomial curves (Kirschner 2013). In order to simplify and reduce the number of parameters describing the 3D object, modal analysis can be used, with the help of Delaunay methods in the reconstruction process (Angelopoulou et al. 2015).

Finding correspondent points is essential for the automatic production of statistical surface models from an initial set of 3D surfaces. In order to solve the problem of point correspondence, minimum description length function can be used for error reduction and generalization (Zsemlye 2005; Kirschner 2013; Chen and Shapiro 2009). The iterative closest point method can be used to establish correspondences (Zsemlye 2005; Blanc et al. 2012).

Predicting the shape of a particular organ or its part in practice, especially in the case of incomplete surface shape information, is performed on the basis of various predictors, using three methods: Principal Component Analysis (PCA), which is also known as principal component regression, partial least squares and canonical correlation analysis. Scalar predictors, such as morphometric and anthropometric parameters, can be directly included in the aforementioned regression models (Blanc et al. 2012). Prediction techniques, based on observing the population, are used when shapes need to be predicted based on partial information. Minimizing the Mahalonobis distance is an iterative technique for shape prediction. The surface is controlled by selected points on the surface that the user can directly identify in a given data set. The positions of these landmarks represent the boundary conditions for shapes (Zsemlye 2005). Some parametric shape description methods use deformable superquadrics combined with local deformable modeling or point coordinates of the vertices of the surface. It is possible to reduce the number of parameters to a certain degree using procedures such as PCA (Sierra et al. 2006). Spherical harmonic description allows parametric shape description, where shapes can be represented by an object that has a spherical topology (Styner et al. 2003; Zsemlye 2005; Besbes 2010).

A great number of anatomical researches of the human hip bone were conducted with the aim of studying its morphology and morphological variations that depend on age, sex, characteristics of a certain population, etc. In some previous studies, 3D polygonal models of the human hip bone have been created in specialized programs for processing medical images or statistical models for estimating shapes and variations, but the applied methods give results only when there is a complete and high-quality volumetric image of the whole bone.

Lamecker et al. (2004) have created a statistical surface model for semi-automatic segmentation of the pelvic bone, based on its polygonal model (mesh). A statistical surface model was generated from 23 CT images of the male pelvic bones. Statistical shape and intensity models of the pelvic bone were generated from a set of initial polygonal models, specific for given patient, using the PCA method and by generating virtual X-rays from deformable anatomical models (Ehlke et al. 2013). Statistical shape model was obtained from 50 CT scans which were manually segmented and converted into polygonal models (Seim et al. 2008). Statistical atlases of anatomical bone shapes from 110 CT images of individual patients were obtained using PCA and PDM, through procedures for identifying landmarks, establishing point-to-point correspondence and conducting statistical analysis to study shape variations (Chintalapani et al. 2007).

A hybrid method originating from combining incomplete data obtained from a CT image and geometric data from a visible human data set was used to generate the pelvis' finite element model, using higher-order Hermite cubic elements. Corresponding anatomical points were selected automatically from CT images, and the pelvic bone was divided into 4 regions (Shim et al. 2007). An anatomical model of the left half of the pelvic bone was constructed from input data in the form of a point cloud, obtained by a 3D laser scanner. Point cloud is further converted into triangle grid surface with certain assumptions and limitations (Phillips et al. 2007).

The hip bone is generated by a reverse engineering process through several steps. A high-precision replica was digitalized using a 3D laser scanner, resulting in a cloud of high-density dots. This initial point cloud was imported into the reverse engineering software, where the model was cleaned, after which the initial surface model was obtained (Popov and Onuh 2009). Surface model of female hip bone was obtained by reverse engineering in Computer Aided Design (CAD) software through following steps: data acquisition from CT scanner and pre-processing, creating an initial polygonal model, healing and smoothing, identification and defining the anatomical and morphological characteristics which correspond to the Referential Geometric Entities (RGEs), creating sets of B-curves and splines, and creating parts of the surface model using loft and blend function. These parts were further merged into complete surface model of the hip bone (Tufegdžić et al. 2013).

5.1.2 Rationale for Developing a New Method

Reconstruction of medical images in 3D today is an integral part of biomedical research. Registration of multiple cross-sections is of great importance for correct 3D visualization and morphometric analysis of structures (Angelopoulou et al. 2015). CT and MRI are often used in clinical diagnosis and surgery planning, but their use as an imaging modality in interventions is limited due to lack of space in operating rooms and requirements for real-time operating procedures (Yaoa and Taylor 2012). Typical tomodensitometry methods enable obtaining exact 3D information about the human body anatomy, but high radiation doses which are harmful to the patient, large amount of information which should be collected and processed, as well as their price make them less functional (Benameur et al. 2001; Fattah 2013). X-ray radiography is the golden standard for obtaining medical images in orthopedic diagnostics, and radiographic projections still play an important role in diagnosis, surgery, and planning therapeutic procedures (Benameur et al. 2001; Fattah 2013; Lamecker et al. 2006). Belonging to the group of diagnostic methods that is characterized by low cost, mobility, uniform imaging speed and low doses of ionizing radiation (compared to CT), it bears no risk for patients who have ferromagnetic implants (compared to classic MRI machines). The evaluation of orthopedic trauma in traditional surgery planning is based on a small number of 2D radiographic projections in vast number of cases (Fattah 2013; Ehlke et al. 2013).

A number of open source or commercial software packages have been developed to visualize volume data and obtain 3D polygonal mesh bone models and export them to STereoLithography (STL) format, from medical CT images recorded in DICOM (Digital Imaging and Communications in Medicine) format. Some examples are 3D Slicer, 3D-DOCTOR, Amira, democratiz3D, ImageVis3D, MeVisLab, Mimics, OsiriX, etc. But, regardless of the program, the construction of a 3D polygonal hip bone model must be carried out through the following phases: data collection, image segmentation and surface generation. In cases when the volumetric images of the bones are complete and of high quality, their polygonal model will be meaningful and sophisticated. However, in a large number of cases, when due to the poor quality of the image the boundaries of the bones are insufficiently clear, it is necessary to conduct the so-called model healing. This process takes a long time and requires a lot of effort.

The first step is always collecting CT data which means that the patient must be exposed to radiation doses that are significantly higher than those during imaging by other conventional methods, such as radiography. In many cases, the patient has already been exposed to certain doses of radiation in the previous period and it is not possible to take another CT image. In addition, in case of a high degree of osteoporosis, the quality of the CT image is such that it prevents obtaining clouds of points of the entire bone volume. Sometimes, due to great trauma or bone disease, some parts of the bones no longer physically exist, so it is not possible to obtain data on that part based on the images. In such cases, reconstructing the required 3D bone model is impossible.

Therefore, it was necessary to develop a new method that enables obtaining a 3D surface model of the human hip bone, in the cases when the input data are incomplete and medical images do not contain all bone elements. This especially refers to situations when the only available data are 2D X-ray images in Anterior–Posterior (A-P) and lateral projection, which is of particular importance.

5.1.3 Reconstruction of 3D Models from 2D Images—State of Art

In order to form a 3D model for a specific patient from incomplete data obtained by ultrasound or X-ray imaging, reconstruction of surfaces is a good technology for preoperative planning or for navigation during operations (Yaoa and Taylor 2012). In recent years, methods for reconstructing a personalized bone shape from incomplete data using statistical shape modeling techniques are applied to a large extent. The main idea for shape reconstruction based on a statistical model is to find statistically probable values of model parameters that minimize the adjustment criteria between the initial model and the available information, which is patient specific. The type of information used for reconstruction is common to all methods. The information contains data on explicit morphological characteristics, such as parts of surfaces, contours or points. These methods are mainly based on multilinear regression (Blanc et al. 2012).

Some problems may arise when reconstructing pathological deformities or missing anatomical structures, when the normal natural appearance is unknown. In a large number of cases, objective criteria for guiding the remodeling and reshaping processes are lacking, and operators are guided by subjective assessment (e.g., aesthetics) (Lamecker 2008). Another group of methods use constraints based on nonlinear functions of point positions, but only explicit landmarks can be treated (Blanc et al. 2012).

Reconstruction of 3D unknown object geometry from 2D images is a problem that needs special attention, since it is necessary to generate a model with only a few (2 or more) radiographic projections (Benameur et al. 2001; Fattah 2013; Lamecker et al. 2006). The lack of information due to the small number of images can be compensated by the inclusion of prior knowledge, formulated to represent the shape of the bones in a way that allows deformation of the model based on the entities taken from the image. Assuming that the entities taken from the image, together with the information from the previously defined form (template), provide sufficient information, the patient's anatomy could be obtained, with the required accuracy. The template model implies information that is specific to a given bone, and is actually an estimate of the initial shape, in the form of a Statistical Shape Model (SSM) (Fattah 2013).

3D shape reconstruction from a set of incomplete 2D projection images is important for a large number of medical applications. Image-guided intervention systems require a personalized 3D anatomical model, which should be connected to the intra-operating system. Some alternatives suggest 3D model generation from calibrated radiographic projections, but it is necessary to integrate previous knowledge for a successful 3D reconstruction, e.g., using a statistical model shape. In the case of incomplete data, two groups of procedures are applied for the reconstruction of the precise anatomical shape of the bones: statistical deformation model and PDM (Baka et al. 2010).

Hybrid 2D-3D deformable registration was performed by combining a landmark registration from one A-P projection of the hip one with SSM based on a 2D-3D reconstruction scheme. Landmark registration was used to find the initial scale and initial rigid transformation between A-P projection and SSM (Zheng 2009). Similarity criteria, based on surface normal and distance was used for determining landmarks in the process of 3D reconstruction (Baka et al. 2010).

The statistical model of the pelvis was made from a collection of CT images, and a simulation of X-rays (known as Digitally Reconstructed Radiographs—DRRs) from CT data for a specific patient. The model was presented in the form of a network of tetrahedrons. These nets have great flexibility and can adapt to the anatomical shape (Yaoa and Taylor 2012).

5.2 Parameter-Based Patient Specific 3D Model

Due to the fact that CT became the golden standard for generating 3D geometrical bone models with the high accuracy, we used a sample of 38 male CT scans of the right hip bone, obtained with Toshiba MSCT scanner Aquillion 64 (120 kV, 150 mA, thickness 1 mm, in-plane resolution 0.781 × 0.781 mm (pixel size), acquisition matrix 512 × 512, field of view (FOV) 400 × 400 mm). The bones affected by pathological changes, fractures and deformities are excluded from the sample, so it has been reduced to 32 healthy bones, aged from 20 to 83 years (average 64 years).

Data from CT scans, written in DICOM format are converted to STL format and exported to CAD program with the aim to obtain polygonal models of bones. For some models it was necessary to reconstruct and heal the surfaces, eliminate errors and smooth sharp edges.

Research is conducted through a few steps, similar to those presented in Trajanovic et al. (2018) and Tufegdzic et al. (2015):

- Processing CT scans and generating 3D models from DICOM images
- Model reconstruction in CAD program and obtaining polygonal models
- Determining landmarks and parameters
- Measuring parameter values
- Statistical analysis of data and calculating statistical values
- Determining the correlations between parameters
- Choosing, testing and establishing proper regression models for parameters, and selecting of the proper regression model, according to statistical indicators such as the level of statistical significance and the highest value of variance.

At each polygonal model of the human hip bone, a sufficient number of anatomical points in the form of bilateral landmarks is separated in order to capture the shape of all constitutive bones. These 34 bilateral landmarks, presented on the right and left ilium, ischium and pubic bones, are easily identified and recognized on radiographic projections.

Bilateral landmarks defined and separated at the wing of ilium bone are (Trajanovic et al. 2018; Tufegdzic et al. 2015):

1. The most superior point on the iliac crest
2. The most lateral iliac crest point
3. Anterior superior iliac spine (ASIS)
4. Anterior inferior iliac spine (AIIS)
5. Posterior superior iliac spine (PSIS)
6. Posterior inferior iliac spine (PIIS)
7. The most superior point at the acetabular limbus

8. The deepest point at greater sciatic notch
9. The superior point at the sacroiliac joint
10. The inferior point at the sacroiliac joint.

ZS—the point of intersection between the posterior gluteal line with the outer lip of the iliac crest.
DS—the point of intersection between the inferior gluteal line with anterior edge of the iliac crest.
PS—the point of intersection between the anterior gluteal line with anterior end of the iliac crest (at the superior edge of the hip bone).
NISUA—the deepest point at the anterior iliac notch at the anterior edge.
NISUP—the deepest point at the anterior iliac notch at the posterior edge.

At the ischium and pubic bone the following bilateral landmarks are defined and separated:

11. The deepest point in acetabular fossa (Ruiz 2005; Lubovsky et al. 2010)
12. Point at the acetabular rim where ilium and ischium bone are connected (Betti et al. 2013; Ruiz 2005; Lubovsky et al. 2010)
13. Point at the acetabular rim where ilium and superior pubis ramus are connected (Betti et al. 2013; Ruiz 2005; Lubovsky et al. 2010)
14. The most inferior point of the posterior end of the lunate surface of the acetabulum (Betti et al. 2013; Lubovsky et al. 2010)
15. The tip of the ischium spine (Betti et al. 2013; Decker 2010; Margam et al. 2013; O'Connell 2004)
16. The deepest point at the lesser sciatic notch
17. The most prominent point at the upper part of the ischial tuberosity (Betti et al. 2013; Ruiz 2005; Margam et al. 2013; O'Connell 2004)
18. The most lateral point at the posterior edge of the ischial tuberosity (Betti et al. 2013; Ruiz 2005)
19. The tip of the ischial tuberosity, the most prominent point at the anterior edge of the ischial tuberosity (Betti et al. 2013)
20. The most inferior point at the ischial tuberosity (Betti et al. 2013)
21. The most posterior point of the obturator foramen (Betti et al. 2013; Ruiz 2005; O'Connell 2004)
22. The most anterior point of the obturator foramen (Ruiz 2005; O'Connell 2004)
23. The lowest point at the ischiopubic ramus (Ruiz 2005; Decker 2010; O'Connell 2004; Dhindsa et al. 2013)
24. The most superior point of the obturator foramen (Betti et al. 2013; Ruiz 2005; O'Connell 2004)
25. The most inferior point where inferior pubis ramus and ischium ramus are connected (Ruiz 2005; O'Connell 2004)
26. The most inferior point of the anterior end of the lunate surface of the acetabulum (Betti et al. 2013)
27. Pubic tubercle, as the most anterior point at the pubic tubercle (Betti et al. 2013; Lubovsky et al. 2010; Decker 2010)

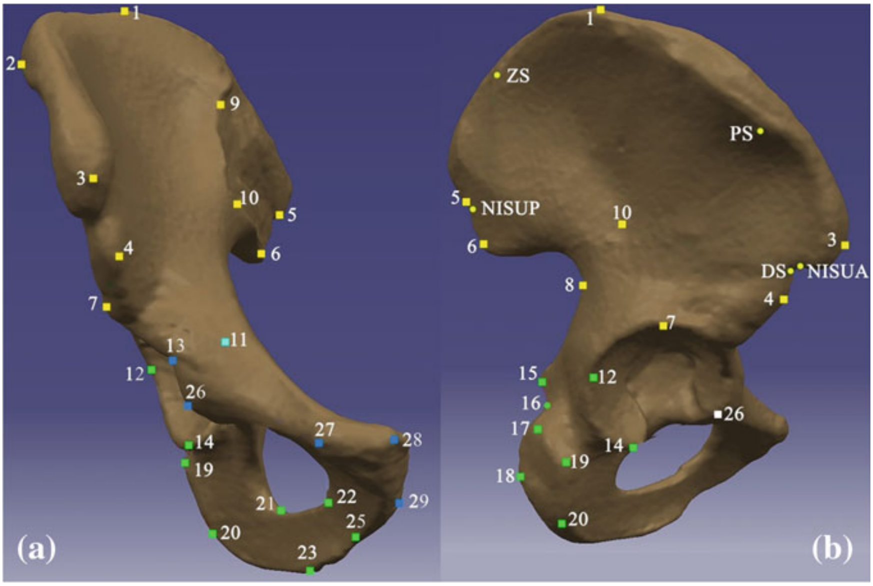

Fig. 5.1 Bilateral landmarks at the ilium, ischium and pubic bone **a** A-P projection, **b** lateral projection

28. The most superior point on the superior edge of the medial aspect of the pubic symphysis (Betti et al. 2013; Ruiz 2005; O'Connell 2004)
29. The most inferior point on the inferior edge of the medial aspect of the pubic symphysis (Betti et al. 2013; Ruiz 2005; O'Connell 2004).

Bilateral landmarks in A-P and lateral projection at the ilium, ischium and pubic bone are presented in Fig. 5.1.

Anatomical landmarks on ilium, ischium and pubic bone are interconnected by straight lines. These lines, defined by linear distance between chosen anatomical landmarks, represent parameters. From the points listed above, it is possible to create 105 parameters at the wing of ilium bone, and 406 parameters at the ischium and pubic bone. In our research we have used 58 parameters at the hip bone, because that number of parameters is sufficient to fully morphologically define the complex form of the human ilium, ischium and pubic bones. For better preview, the parameters will be listed depending on which bone they belong (26 at the ilium bone, 19 at the ischium bone, and 13 at the pubic bone). This will also make it easier for their practical implementation. Parameters at the ilium bone are presented and described in Table 5.1.

Selected parameters of the human ilium bone are presented in Fig. 5.2.

At the ischium bone, 18 parameters are separated. One additional parameter is also separated, labeled as d_{27} and considered common for ilium and ischium bone due to the fact that it connects landmark 8 (as the deepest point at greater sciatic notch) and landmark 12 from different bones. At the pubic bone 10 parameters are separated,

Table 5.1 Parameters at the wing of ilium bone (Trajanovic et al. 2018)

No.	Parameter	Label	Points
1	Distance between anterior and posterior superior iliac spines	d_1	3–5
2	Distance between anterior and posterior inferior iliac spines	d_2	4–6
3	Distance between anterior superior and posterior inferior iliac spines	d_3	3–6
4	Distance between the most lateral iliac crest point and the superior point at the sacroiliac joint	d_4	2–9
5	Distance between the point of intersection between the inferior gluteal line with anterior edge of the iliac crest and the inferior point at the sacroiliac joint	d_5	DS–10
6	Distance between the deepest points at anterior–posterior iliac notches	d_6	NISUA–NISUP
7	Distance between the point of intersection between the anterior gluteal line with anterior end of the iliac crest and the point of intersection between the posterior gluteal line with the outer lip of the iliac crest	d_7	PS–ZS
8	Distance between anterior inferior iliac spine and the deepest point at greater sciatic notch	d_8	4–8
9	Distance between the most superior point on the iliac crest and the deepest point at greater sciatic notch	d_9	1–8
10	Distance between the posterior inferior iliac spine and the point of intersection between the posterior gluteal line with the outer lip of the iliac crest	d_{10}	6–ZS
11	Distance between the most superior point on the iliac crest and the most superior point at the acetabular limbus	d_{11}	1–7
12	Distance between posterior inferior iliac spine and the deepest point at the iliac notch at the posterior edge	d_{12}	6–NISUP
13	Distance between the most lateral iliac crest point and anterior superior iliac spine	d_{13}	2–3
14	Distance between posterior superior iliac spine and the point of intersection between the posterior gluteal line with the outer lip of the iliac crest	d_{14}	5–ZS
15	Distance between the most superior point on the iliac crest and posterior superior iliac spine	d_{15}	1–5
16	Distance between the most superior point on the iliac crest and anterior superior iliac spine	d_{16}	1–3
17	Distance between the most superior point on the iliac crest and posterior inferior iliac spine	d_{17}	1–6
18	Distance between the most superior point on the iliac crest and posterior inferior iliac spine	d_{18}	1–4
19	Distance between the most superior point on the iliac crest and the point of intersection between the posterior gluteal line with the outer lip of the iliac crest	d_{19}	1–ZS

(continued)

Table 5.1 (continued)

No.	Parameter	Label	Points
20	Distance between the most superior point on the iliac crest and the most lateral iliac crest point	d_{20}	1–2
21	Distance between anterior superior iliac spine and the deepest point at the anterior iliac notch at the anterior edge	d_{21}	3–NISUA
22	Distance between the superior and the inferior point at the sacroiliac joint	d_{22}	9–10
23	Distance between anterior inferior iliac spine and the deepest point on the anterior iliac incisures at the anterior edge	d_{23}	4–NISUA
24	Distance between posterior superior iliac spine and the deepest point on the posterior iliac notch at the posterior edge	d_{24}	5–NISUP
25	Distance between the most superior point at the acetabular limbus and the deepest point at greater sciatic notch	d_{25}	7–8
26	Distance between the most superior point at acetabular limbus and anterior inferior iliac spine	d_{26}	7–4

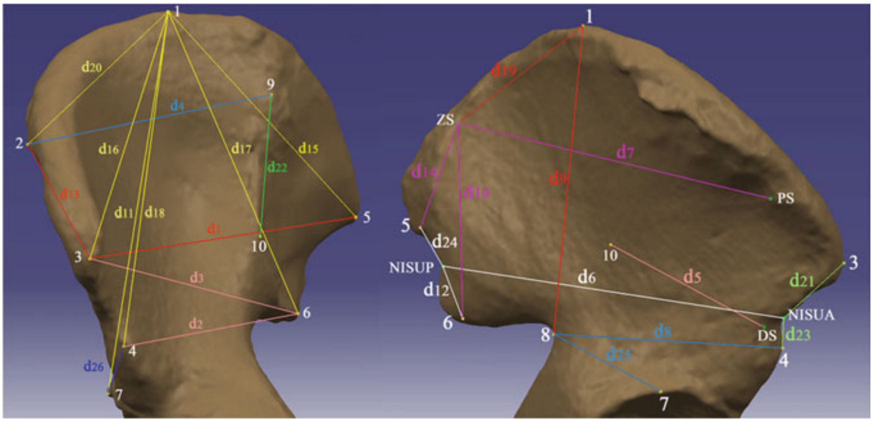

Fig. 5.2 Parameters at the ilium bone. Modified from Trajanovic et al. (2018)

as well as 3 additional parameters (d_{53}, d_{57} and d_{58}) that connect landmarks from different bones (26–14, 11–4 and 13–4, respectively). These parameters are presented and described in Table 5.2.

Selected bilateral landmarks and parameters are presented in Fig. 5.3 in A-P and lateral projection of the human ischium and pubic bone. Parameters at the ischium bone are displayed with cyan lines and parameters at the pubic bone with yellow lines. Parameters belonging to different bones appear as dash-dot lines (blue, green and white).

At each of the constitutive bones, parameters are divided into 2 groups. Parameters which can be easily measured in A-P and lateral projections of the hip bone are

Table 5.2 Parameters at the ischium and pubic bone

No.	Parameter	Label	Points
1	Distance between the point of maximum curvature (the deepest point) at greater sciatic notch and the point at the acetabular rim where ilium and ischium bone are connected	d_{27}	8–12
2	Distance between the tip of the ischium spine and the point at the acetabular rim where ilium and ischium bone are connected	d_{28}	15–12
3	Distance between the tip of the ischium spine and the deepest point at the lesser sciatic notch	d_{29}	15–16
4	Distance between the deepest point at the lesser sciatic notch and the point at the acetabular rim where ilium and ischium bone meet	d_{30}	16–12
5	Distance between the most prominent point at the upper part of the ischial tuberosity and the point at the acetabular rim where ilium and ischium bone are connected	d_{31}	17–12
6	Distance between the most lateral point at the posterior edge of the ischial tuberosity and the point at the acetabular rim where ilium and ischium bone are connected	d_{32}	18–12
7	Distance between the most prominent point at the upper part of the ischial tuberosity and the most lateral point at the posterior edge of the ischial tuberosity	d_{33}	17–18
8	Distance between the most lateral point at the posterior edge of the ischial tuberosity and the most prominent point at the anterior edge of the ischial tuberosity	d_{34}	18–19
9	Distance between the most lateral point at the posterior edge of the ischial tuberosity and the most inferior point at the ischial tuberosity	d_{35}	18–20
10	Distance between the most prominent point at the anterior edge of the ischial tuberosity and the point at the acetabular rim where ilium and ischium bone are connected	d_{36}	19–12
11	Distance between the most prominent point at the anterior edge of the ischial tuberosity and the most inferior point of the posterior end of the lunate surface of the acetabulum	d_{37}	19–14
12	Distance between the most prominent point at the anterior edge of the ischial tuberosity and the most inferior point at the ischial tuberosity	d_{38}	19–20
13	Distance between the most inferior point of the posterior end of the lunate surface of the acetabulum and the most inferior point at the ischial tuberosity	d_{39}	14–20
14	Distance between the most inferior point at the ischial tuberosity and the most posterior point of the obturator foramen	d_{40}	20–21
15	Distance between the most inferior point at the ischial tuberosity and the lowest point at the ischiopubic ramus	d_{41}	20–23
16	Distance between the most posterior point of the obturator foramen and the lowest point at the ischiopubic ramus	d_{42}	21–23
17	Distance between the most anterior point of the obturator foramen and the lowest point at the ischiopubic ramus	d_{43}	22–23

(continued)

Table 5.2 (continued)

No.	Parameter	Label	Points
18	Distance between the lowest point at the ischiopubic ramus and the most inferior point where inferior pubis ramus and ischium ramus are connected	d_{44}	23–25
19	Distance between the most anterior point of the obturator foramen and the most inferior point where inferior pubis ramus and ischium ramus are connected (O'Connell 2004)	d_{45}	22–25
20	Distance between the most inferior point where inferior pubic ramus and ischium ramus are connected and the most inferior point on the inferior edge of the medial aspect of the pubic symphysis (O'Connell 2004)	d_{46}	25–29
21	Distance between the most anterior point of the obturator foramen and the most inferior point on the inferior edge of the medial aspect of the pubic symphysis (Gupta et al. 2014)	d_{47}	22–29
22	Distance between the most superior point on the superior edge of the medial aspect of the pubic symphysis and the most inferior point on the inferior edge of the medial aspect of the pubic symphysis (Betti et al. 2013; Decker 2010; O'Connell 2004; Boulay et al. 2006)	d_{48}	28–29
23	Distance between the most anterior point of the obturator foramen and the most superior point on the superior edge of the medial aspect of the pubic symphysis	d_{49}	22–28
24	Distance between pubic tubercle and the most superior point on the superior edge of the medial aspect of the pubic symphysis (Betti et al. 2013)	d_{50}	27–28
25	Distance between pubic tubercle the most anterior point of the obturator foramen	d_{51}	27–22
26	Distance between pubic tubercle and most inferior point of the anterior end of the lunate surface of the acetabulum	d_{52}	27–26
27	Distance between most inferior point of the anterior end of the lunate surface of the acetabulum and the most inferior point of the posterior end of the lunate surface of the acetabulum	d_{53}	26–14
28	Distance between pubic tubercle and the point at the acetabular rim where ilium and superior pubis ramus meet (Sharma and Vijayvergiya 2013)	d_{54}	27–13
29	Distance between pubic tubercle and the deepest point in acetabular fossa (O'Connell 2004; Okoseimiema and Udoaka 2013)	d_{55}	27–11
30	Distance between the point at the acetabular rim where ilium and superior pubis ramus are connected and the deepest point in acetabular fossa	d_{56}	13–11
31	Distance between the deepest point in acetabular fossa and anterior inferior iliac spine (Boulay et al. 2006)	d_{57}	11–4
32	Distance between the point at the acetabular rim where ilium and superior pubis ramus are connected and the deepest point in acetabular fossa	d_{58}	13–4

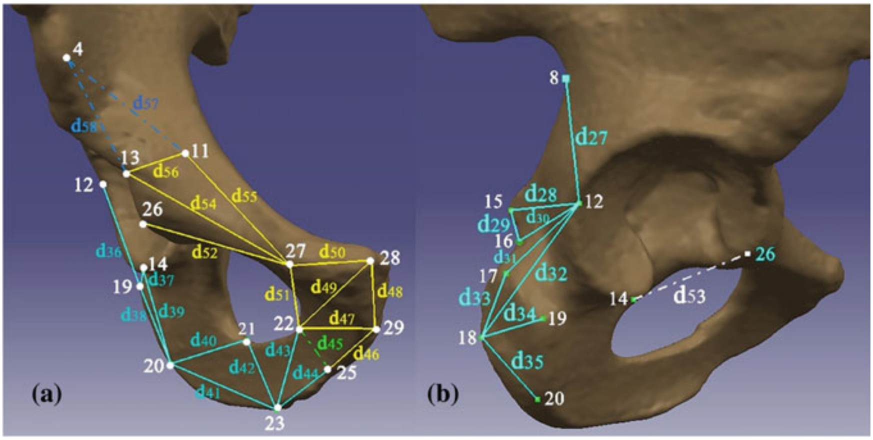

Fig. 5.3 Selected parameters at the ischium and pubic bone **a** A-P projection, **b** lateral projection

treated as independent variables and classified in the first group. The second group of parameters includes dependent variables, with the possibility to set up regression equations (Trajanovic et al. 2018).

Independent variables are:

1. At the ilium bone: d_1, d_2, d_3, d_4, d_8, d_9, d_{15}, d_{16}, d_{17} and d_{22} (10 parameters) (Trajanovic et al. 2018)
2. At the ischium bone: d_{27}, d_{32}, d_{38}, d_{40}, d_{41}, d_{42} and d_{45} (7 parameters)
3. At the pubic bone: d_{47}, d_{48}, d_{49} and d_{57} (4 parameters).

Dependent variables are:

1. At the ilium bone: d_5, d_6, d_7, d_{10}, d_{11}, d_{12}, d_{13}, d_{14}, d_{18}, d_{19}, d_{20}, d_{21}, d_{23}, d_{24}, d_{25} and d_{26} (16 parameters) (Trajanovic et al. 2018)
2. At the ischium bone: d_{28}, d_{29}, d_{30}, d_{31}, d_{33}, d_{34}, d_{35}, d_{36}, d_{37}, d_{39}, d_{43} and d_{44} (12 parameters)
3. At the pubic bone: d_{46}, d_{50}, d_{51}, d_{52}, d_{53}, d_{54}, d_{55}, d_{56} and d_{58} (9 parameters).

All parameters' values are measured over the whole sample and values for descriptive statistics are calculated. Correlation coefficients between parameters from independent and dependent groups are calculated with the aim to determine dependencies between variables. For each of the parameters from the second group, choosing regression models for testing was done by using scatter plots. Linear ($d_j = a + b \cdot d_i$), squared ($d_j = a \cdot d_i^2, d_j = a + b \cdot d_i^2, d_j = a + b \cdot d_i + c \cdot d_i^2$), third-degree polynomial ($d_j = a + b \cdot d_i + c \cdot d_i^2 + d \cdot d_i^3$), logarithmic ($d_j = a \cdot \ln(d_i)$, $d_j = a + b \cdot \ln(d_i)$), and exponential ($d_j = a \cdot e^{b \cdot d_i}$) models proved to be the best fitted models. Regression coefficients a, b, c and d in regression equation are calculated using least square method, while d_j stands for dependent variable, and d_i stands for independent variable.

The basic condition for the acceptance of the model is established in such way that the value of statistical significance (p-value) must be less than 0.01 for all parameters a, b, c and d. Value of variance R^2 is also determined. From all the models which satisfy the set condition, the one with the highest R^2 is selected according to methodology described in Trajanovic et al. (2018) and Tufegdzic et al. (2015).

Adopted regression models for ilium, ischium and pubic bone, so as the values for R^2 are presented in Table 5.3.

An exception was made when determining the regression model for the parameter d_{25}, where the correlation coefficient had a higher value for the parameter d_{11}, in relation to the correlation coefficient for the parameter d_2. The values of R^2 are significantly higher in the case of dependence between the parameters d_{25} and d_{11} than in the case of dependence from d_{25} on d_2. However, due to the fact that the value of the parameter d_{11} is obtained from the regression equation, which would increase the computational error, a model in which the parameter d_{25} is calculated as a function of d_2 has been adopted.

Various models presented in Table 5.3 may be associated with the complex shape of the human hip bone. Only non-linear regression is suitable for describing the proper dependencies between the parameters at the bones, such as 11 quadratic, 13 exponential, and 13 logarithmic. For example, at the ilium bone 3 quadratics, 8 exponential and 5 logarithmic, at the ischium bone 6 quadratics, 3 logarithmic and 3 exponential, and at the pubic bone 2 quadratic, 5 logarithmic and 2 exponential models, are adopted.

On the other hand, all regression models can be considered statistically significant based on the values of variance R^2. The only exception is the parameter d_{21}, since it is difficult to choose the appropriate model because the level of statistical significance for all tested models is greater than 0.01. However, there are few regression models for discussion according to the values of variance R^2. Some examples are d_{10}, d_{12} and d_{14} at the ilium bone, d_{33} and d_{37} at the ischium bone, so as d_{50} at the pubic bone (Table 5.3). Some improvements should be made by increasing the number of bones in the sample. Additional issues to be taken into consideration are the regression models for the parameter d_{35} at the ischium bone and the parameter d_{53} at the pubic bone because their values of variance R^2 are significantly smaller compared to the other value.

There are some interesting conclusions to be drawn, such as dependencies for parameters at the ischium and pubic bone. Parameters like d_{28} and d_{33} at the ischium bone are dependent from parameters d_8 and d_{17}, at the ilium bone respectively, while parameters at the pubic bone d_{54} and d_{55} show dependencies from parameters d_2 and d_1 respectively, also at the ilium bone.

In order to test the obtained and adopted models, all parameters from both groups are measured at one randomly chosen right male hip bone. Predicted values for dependent values are calculated, according to regression equations from Table 5.3. The differences between the measured and prediction values were calculated and presented in the form of absolute errors. For the purpose of additional comparison, considering the fact that the range of values of the measured parameters is large—from 11.185 to 126.074 mm at the ilium bone, from 11.488 to 87.543 mm at the

Table 5.3 Regression models for the parameters at the ilium, ischium and pubic bone. Expanded from Tufegdzic et al. (2015)

No.	Parameter	Adopted model	R^2
1	d_5	$d_5 = 45.99044 + 0.00510 \cdot d_8^2$	0.5179
2	d_6	$d_6 = 48.68143 \cdot e^{0.00623 \cdot d_1}$	0.6679
3	d_7	$d_7 = 41.51965 \cdot e^{0.00974 \cdot d_9}$	0.4326
4	d_{10}	$d_{10} = 39.82035 + 0.00249 \cdot d_{17}^2$	0.1739
5	d_{11}	$d_{11} = -236.556 + 77.831 \cdot \ln(d_9)$	0.4889
6	d_{12}	$d_{12} = 0.001189 \cdot d_{17}^2$	0.0956
7	d_{13}	$d_{13} = 9.1589 \cdot e^{0.015011 \cdot d_{16}}$	0.4364
8	d_{14}	$d_{14} = 10.47298 \cdot \ln(d_{15})$	0.0451
9	d_{18}	$d_{18} = 89.80292 \cdot e^{0.00312 \cdot d_2}$	0.2707
10	d_{19}	$d_{19} = -523.964 + 124.585 \cdot \ln(d_9)$	0.3477
11	d_{20}	$d_{20} = 38.09926 \cdot e^{0.00754 \cdot d_4}$	0.3467
12	d_{21}	$d_{21} = 64.25015 \cdot e^{-0.00746 \cdot d_{16}}$	0.1185
13	d_{23}	$d_{23} = 4.985783 \cdot \ln(d_{16})$	0
14	d_{24}	$d_{24} = 3.758796 \cdot \ln(d_{17})$	0
15	d_{25}	$d_{25} = 33.12012 \cdot e^{0.00408 \cdot d_2}$	0.2198
16	d_{26}	$d_{26} = 2.52512 \cdot e^{0.01479 \cdot d_8}$	0.5049
17	d_{28}	$d_{28} = 30.49856 + 0.00316 \cdot d_8^2$	0.4510
18	d_{29}	$d_{29} = 13.22304 + 0.00355 \cdot d_{42}^2$	0.2205
19	d_{30}	$d_{30} = 27.09725 + 0.00442 \cdot d_{32}^2$	0.4281
20	d_{31}	$d_{31} = 7.107463 \cdot e^{0.026285 \cdot d_{32}}$	0.7269
21	d_{33}	$d_{33} = 6.843322 \cdot \ln(d_{17})$	0
22	d_{34}	$d_{34} = 2.49362 + 0.00876 \cdot d_{38}^2$	0.4147
23	d_{35}	$d_{35} = 6.083382 \cdot \ln(d_{42})$	0.1468
24	d_{36}	$d_{36} = 13.27352 + 0.00713 \cdot d_{32}^2$	0.5765
25	d_{37}	$d_{37} = 72.4284 - 12.0838 \cdot \ln(d_{38})$	0.1972
26	d_{39}	$d_{39} = 29.69258 \cdot e^{0.01535 \cdot d_{32}}$	0.2034
27	d_{43}	$d_{43} = 109.3173 - 2.3663 \cdot d_{41} + 0.00161 \cdot d_{41}^2$	0.6699
28	d_{44}	$d_{44} = 126.0179 \cdot e^{-0.0254 \cdot d_{41}}$	0.6537
29	d_{46}	$d_{46} = -46.4303 + 18.9263 \cdot \ln(d_{47})$	0.5187
30	d_{50}	$d_{50} = 6.955778 \cdot \ln(d_{42})$	0.1252
31	d_{51}	$d_{51} = -98.9599 + 37.3463 \cdot \ln(d_{49})$	0.4869
32	d_{52}	$d_{52} = 34.32717 \cdot e^{0.00905 \cdot d_{49}}$	0.2256
33	d_{53}*	$d_{53} = 7.368643 \cdot \ln(d_{57})$	0.1097
34	d_{54}	$d_{54} = -142.760 + 43.089 \cdot \ln(d_2)$	0.3809
35	d_{55}	$d_{55} = 36.4147 \cdot e^{0.00436 \cdot d_1}$	0.3079
36	d_{56}	$d_{56} = 24.10751 + 0.00281 \cdot d_{57}^2$	0.3626

(continued)

Table 5.3 (continued)

No.	Parameter	Adopted model	R^2
37	d_{58}	$d_{58} = 14.90829 + 0.00560 \cdot d_{57}^2$	0.5134

*A logarithmic model was adopted for parameter d_{53}, although the value of R^2 (0.466) for the third-degree polynomial model is significantly higher, due the fact that the calculated parameter value had showed a significantly higher absolute error value compared to the adopted model, as well as to simplify calculation

Table 5.4 Average values of absolute and relative errors for the ilium, ischium, pubic and hip bone

	Bone			
	Ilium	Ischium	Pubic	Hip
Average values of absolute error (mm)	2.881	2.309	1.291	2.161
Average values of relative error (mm)	0.058	0.088	0.042	0.062

ischium bone, and 10.584 to 87.331 mm at the pubic bone, the values of relative errors were also calculated.

The values for errors, especially relative errors, could be considered in correlation with some statistical indicators, such as minimum and maximum values for measured parameters, values for variation and in particular, values for standard deviation over the sample. Increasing the number of samples will lead to further improvements.

For the purpose of comparative analysis of the obtained results, the average values of absolute and relative errors are calculated for the entities from which the hip bone is constituted as well as for the complete bone. The results are shown in Table 5.4.

The average value of the absolute error between the predictive and measured values of the parameters is the highest for the ilium, and the lowest for the pubic bone. This is understandable because the average values of the measured parameters are the smallest for the pubic bone. The average relative error is the largest for the ischium and the smallest for the pubic bone, while the average value of the relative error for the complete bone is in fact closest to the average value of the relative error for the ilium bone, which is the most complex geometric entity on the human hip bone.

5.3 Method of Parametric Regions

The process of geometric reconstruction during which polygonal models of human hip bones are formed from point clouds, included in the sample, represents the initial phase in the Method of parametric regions. After healing and smoothing, anatomical landmarks were determined on each of the polygonal models. Parameters were defined as linear distances between the landmarks. After establishing correlations between the measured parameter values, appropriate regression models were tested and selected using tools for mathematical (statistical) modeling.

In order to unambiguously determine the position of anatomical landmarks and all points on the surface of the bones whose coordinates need to be measured, an anatomical coordinate system of the pelvic bone was formed on the basis of anatomical landmarks. The Method of Anatomical Features (described in Chap. 2) applied in this phase of research has been extended and adapted to the complex hip bone anatomy needs, in Geometric morphometry process.

Cutting polygonal models with planes determined by the given parameters, using Quick Plane definition function in CATIA Shape module, results in the set of 26 intersection curves. Another set of intersection curves is obtained by cutting the polygonal models with planes at equal distances of 4 mm. These planes are perpendicular to the given parameters. The intersections of these two sets of curves represent points, whose values of coordinates (X, Y and Z) are measured in right-handed orientation anatomical coordinate system of the hip bone (Trajanovic et al. 2018). These values are taken as the input values for the statistical program. After establishing correlations between coordinates' and parameters' values, different linear and nonlinear regression models (quadratic, logarithmic and exponential) are tested for 1195 intersection points. Proper regression models are established using the criteria for the level of statistical significance ($p < 0.01$) and the highest value for the coefficient of determination (R^2) described in Trajanovic et al. (2018).

Based on the obtained results some conclusions should be drawn. The largest number of obtained regression models is nonlinear, for X coordinate is 98.83%, for Y coordinate is 99.58%, and for Z coordinate is 96.47%, from overall number of equations. The number of linear models is for X coordinate 1.14% and for Y coordinate 0.42%. These values should be considered as statistical errors, and logarithmic models should be chosen as proper regression models. In the group of nonlinear models, the most common ones are logarithmic models, especially at the Z coordinate (93.00%). The greatest variability is shown for X coordinate, given the fact that the positions of the points, e.g., the values of these coordinates, follow the complex geometry of the hip bone to a great extent.

For polygonal model parts that correspond to the edges of the hip bone (the superior edge and the parts of the anterior and posterior edge), the points are defined in such manner that the surfaces which correspond to the edges are fully described. The superior edge of the hip bone which extends from point 3 (ASIS) to point 5 (PSIS) is described by the parts of the polygonal model above the parameters d_{13}, d_{20}, d_{19} and d_{14}. At curves obtained by intersecting the polygonal model with the planes perpendicular to the aforementioned parameters, additional points are defined at distances of 5 mm from the intersection points on the curves through the given parameters at both sides of the hip bone (outer and inner). The part of the anterior edge of the hip bones that extends between anterior iliac spines (points 3 and 4) is described by parts of the polygonal model below the parameter d_{21} and right from the parameter d_{23}. Additional points were obtained in the same way as with the superior edge, at the curves that are perpendicular to the parameters d_{21} and d_{23}.

The part of the posterior edge of the hip bone between posterior iliac spines (points 5 and 6) was described by the parts of polygonal model left from the parameters d_{24} and d_{12}. For describing the part of the edge which extends from PIIS (point 6) to the deepest point at greater sciatic notch (point 8), one more measure is introduced. In order to describe the geometry of this part of the posterior edge, it is necessary to measure the distance between point 6 and the point obtained at the intersection of parameters d_3 and d_9 in the plane projection. Based on this distance it is possible to calculate the required number of intersection curves using the expression for the number of curves N_c presented in Trajanovic et al. (2018), where mean value of the measured distance d_{3x} is used as the average value of the parameters d_{sr}.

After measuring the values of the coordinates of all selected points on the edges of the hip bone, the methodology used for choosing proper regression models for points at the curves through the parameters was applied. The corresponding mathematical models for the point's coordinates in function of the respective parameter are obtained. The number of points on the curves was chosen so that a particular point covers the coordinate values in at least one half of the sample ($N \geq 16$).

For describing the geometry of the edges, e.g., the parts of the edges at the wing of ilium bones, it was necessary to define a total of 454 points. Linear dependences for the point's coordinates of on the values of parameters cannot describe the geometry on these parts of the hip bone. At the parts of the anterior and posterior edge all regression models for X coordinate are logarithmic, as well as for the Z coordinate at the posterior part of the edge. Variability in regression models is the greatest for the X coordinate at the superior edge of the hip bone bone (82.96% is logarithmic, 15.82% is square), for Y coordinates at the part of the posterior edge (31.52% is square and logarithmic, while 36.96% is exponential), and for Z coordinates at the part of the anterior edge (40.74% is logarithmic, 51.85% is exponential). The variability for the Y coordinates at the part of the posterior edge results from geometric shapes that appear on the part of the edge below the parameter d_3.

The predictive values of the X, Y and Z coordinates of all these points were calculated in the first iteration, and a polygonal model of the wing of ilium bone was constructed. Some additional operations like optimization, smoothing and increasing the neighbor value lead to improving the model, but the surface 3D model's geometry was disturbed. Bearing in mind that the obtained model has a certain number of holes that have to be filled in the areas between neighboring parameters, some additional points were defined. After thorough analysis, ten parametric regions were defined. Parametric regions are actually the areas between two neighboring parameters. At the wing of ilium bone, ten parametric regions were separated: parametric region d_{14}–d_{15}, parametric region d_{15}–d_{19}, parametric region d_{17}–d_{15}, parametric region d_{17}–d_9, parametric region d_9–d_{11}, parametric region d_{11}–d_{18}, parametric region d_{18}–d_{16}, parametric region d_{16}–d_{20}, parametric region d_{16}–d_{13} and parametric region d_8–d_{25}–d_{26}. Labels for parametric regions were assigned according to parameters that represent boundaries for the given region (Trajanovic et al. 2018). Parametric regions and the parts of the edges (colored in yellow) at the wing of ilium bone are presented in Fig. 5.4.

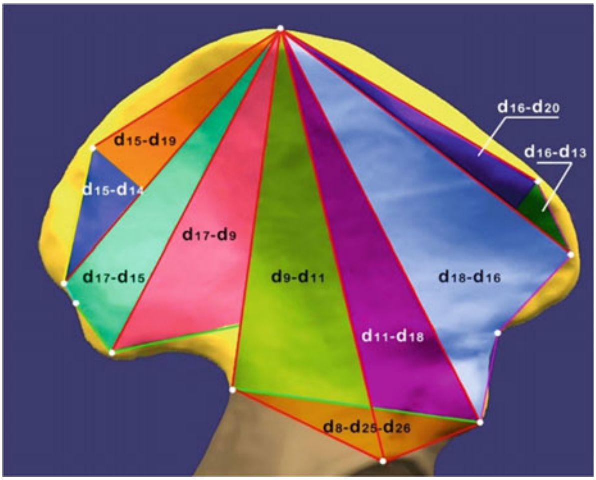

Fig. 5.4 Parametric regions at the wing of ilium bone

In each parametric region, additional points on the curves perpendicular to the corresponding parameters were defined. Points were defined at equal distances of 5 mm, starting from the intersection points, at curves obtained by cutting the polygonal model with planes determined by 26 parameters, at the outer and inner side of the bone surface.

To determine additional points in parametric regions the following curves were used:

1. For parametric region d_{15}–d_{14}—curves that are perpendicular to d_{14}
2. For parametric region d_{15}–d_{19}—curves that are perpendicular to d_{19}
3. For parametric region d_{17}–d_{15}—curves that are perpendicular to d_{15}
4. For parametric region d_{17}–d_{9}—curves that are perpendicular to d_{9}
5. For parametric region d_{9}–d_{11}—curves that are perpendicular to d_{11}
6. For parametric region d_{11}–d_{18}—curves that are perpendicular to d_{18}
7. For parametric region d_{18}–d_{16}—curves that are perpendicular to d_{16}
8. For parametric region d_{16}–d_{20}—curves that are perpendicular to d_{20}
9. For parametric region d_{16}–d_{13}—curves that are perpendicular to d_{13}
10. For parametric region d_{8}–d_{25}–d_{26}—curves that are perpendicular to d_{8}.

Coordinate values regression models of points were obtained using the same methodology as in the cases of points at intersection curves at parameters and points which belong to parts of the surface that correspond to the edges. In order to obtain a regression model for any of the points in the regions, it was necessary to measure the coordinates of the given point in at least one half of the sample ($N \geq 16$). The number of additional points depends of the total surface of the region. The number of selected points is directly related to the size of the parametric region, which is limited by the given parameters, e.g., the area of the bone surface that is covered by the given region. For example, for the region d_{11}–d_{18}, number of points was 269, while in the region d_{16}–d_{13} was only 15 points. The total number of points was 1310, after eliminating the points whose statistically significant results could not be obtained due to insufficient data. Thus, 3930 regression equations for the point's coordinates *X*, *Y* and *Z* in parametric regions were obtained. All obtained equations are logarithmic, because it was the only possible model with statistically significant results which satisfy the set criteria ($p < 0.01$).

Analyzing results on the number of obtained regression models leads to several conclusions. For building 3D surface model of the wing of the ilium bone it was necessary to choose 8869 regression equations for 2959 point's coordinates *X*, *Y* and *Z*, mostly logarithmic (7693) (Trajanovic et al. 2018). This fact could be explained by the complex surface to be created, with convex gluteal surface at the outer side, and concave iliac fossa and sacropelvic surface at the inner side. Additionally, gluteal surface, which extends from iliac crest to acetabular rim, is divided by gluteal lines to three unequal surfaces, while iliac crest which represents the superior edge is concave in front, rounding inward, and convex in back, rounding outward. These are the main reasons for small number of linear dependences for all coordinates (only 61).

The calculated predictive values of the coordinates for all points for one arbitrarily selected hip bone were used to construct the polygonal model with better quality in the second iteration. In need to manipulate a large amount of data, the implementation of equations for predicting the values of point coordinates at the surface of the wing of ilium and linking to the CAD program was automated. Therefore, during the research, three VBA (Visual Basic for Applications) short macro programs were developed: for entering the measured values of parameters and correction factors depending on the size of the X-ray, for selecting the range of points and for selecting a group of points from outer or from inner side of the bone to be exported to the CAD program. Separate sheets in Excel file for each of the predicted parameters is provided, so as for the each of the parametric regions.

Verification, done through comparative deviation and distance analysis between the initial and obtained polygonal models, confirmed significant improvement of the model. Although the method is developed for the right hip bone, it can be applied on the left ilium bone as well (Trajanovic et al. 2018).

5.3.1 Creating 3D Surface Model by Combining Parametric Regions

The method of parametric regions is flexible, because individual regions can be combined (enlarged), or divided into smaller regions, called sub-regions, depending on the needs and parts of the polygonal model of the wing of ilium bone that need to be constructed. By constructing all regions, it is possible to obtain a complete polygonal model of the wing of ilium bone.

For this purpose, individual parametric regions are aggregated with each other, and the result is then aggregated with parts of the edges, so that their polygonal models are constructed. This procedure was preceded by calculating the coordinate's predictive values for the intersection points on the curves through the parameters, the points on the selected parts of the edges of the hip bone and the points in the selected parametric regions. The selected values were exported to a CAD program and converted into point clouds, from which polygonal models were constructed.

For example, the following individual polygonal models were obtained (shown in Fig. 5.5a, where the red dots show the boundaries of the resulting polygonal models corresponding to the curves through parameters):

1. Polygonal model d_{14}–d_{15}–$d_{19} + Ed_{14} + Ed_{19}$—created by merging the regions d_{15}–d_{14} and d_{15}–d_{19} with the parts which represent the edge above curves through parameters d_{14} and d_{19}
2. Polygonal model d_{17}–$d_{15} + Ed_{24} + Ed_{12}$—created by merging the regions d_{17}–d_{15} with the parts which represent the part of the posterior edge left from d_{24} and left from d_{12}
3. Polygonal model d_{17}–$d_9 + Ed_3$—created by merging the regions d_{17}–d_9 with part of the posterior edge below d_3
4. Polygonal model d_9–d_{11}–d_{25}—created by merging the regions d_9–d_{11} with part of the parametric region d_8–d_{25}–d_{26} (part above d_{25})
5. Polygonal model d_{11}–d_{18}–d_{26}—created by merging the regions d_9–d_{11} with part of the parametric region d_8–d_{25}–d_{26} (part above d_{26})
6. Polygonal model d_{18}–$d_{16} + Ed_{23} + Ed_{21}$—created by merging the regions d_{18}–d_{16} with parts of the anterior edge right from d_{23} and below d_{21}
7. Polygonal model d_{16}–d_{20}–$d_{13} + Ed_{20} + Ed_{13}$—created by merging the regions d_{16}–d_{20} and d_{16}–d_{13} with parts of the anterior edge above d_{20} and above d_{13}.

A similar methodology for aggregating was applied on the inner side of the wing of ilium bone, except for the regions that are near the edges. Instead of polygonal model d_{14}–d_{15}–$d_{19} + Ed_{14} + Ed_{19}$, polygonal model d_{14}–d_{15}–d_{19} is created, and instead of

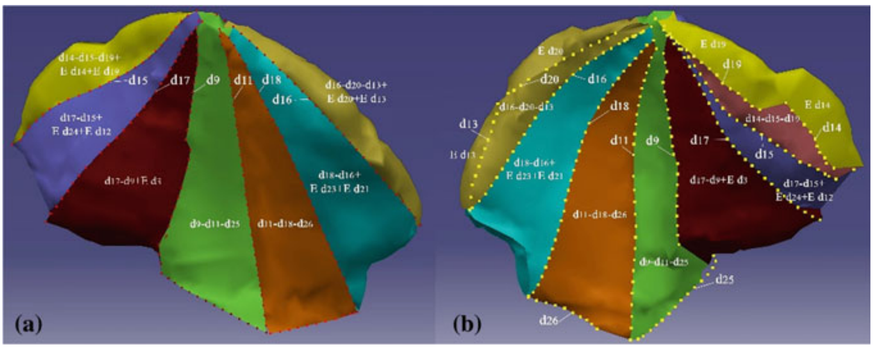

Fig. 5.5 Polygonal models obtained by aggregating parametric regions and parts of edges **a** outer side, **b** inner side

polygonal model d_{16}–d_{20}–d_{13} + Ed_{20} + Ed_{13} polygonal model d_{16}–d_{20}–d_{13}, since the parts which describe the upper edge of the hip bone were constructed in the previous step. Aggregated regions at the inner side are presented in Fig. 5.5b where the yellow dots show the boundaries of the resulting polygonal models corresponding to the curves through parameters.

Individual polygonal models of aggregated regions were merged into a single polygonal model, which required some additional improvement near the most superior point on the iliac crest (point 1). After cleaning (editing convex and concave triangles, detecting and editing collision triangles) and smoothing, the optimization of the polygonal model was performed. The analysis of the model was performed by comparing the initial polygonal model of the ilium wing (obtained from CT images) with the obtained model, where the deviation and distances were measured.

Deviations were measured between the initial polygonal model (reference model) and the model obtained by aggregating regions and parts of the edges (the model to measure). Maximal positive deviation was 10 mm, maximal negative deviation was −9.97 mm, expressed in the area around the posterior superior iliac spine (PSIS), around the posterior gluteal line (in her upper part) and just above parameter d_{26}, while 88.69% of the model surface had the deviations in the amount from −6.65 to 6.67 mm. Deviation analysis is presented in Fig. 5.6.

Distance analysis between the initial polygonal model, obtained from CT images (Source) and the polygonal model obtained by aggregating of the regions (Target)

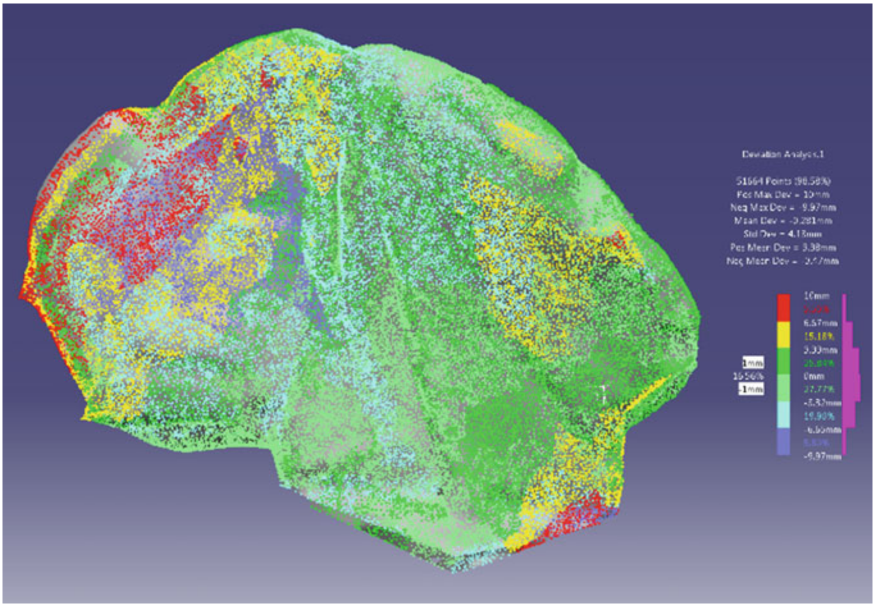

Fig. 5.6 Analysis of deviations between the initial and polygonal model obtained by aggregating regions

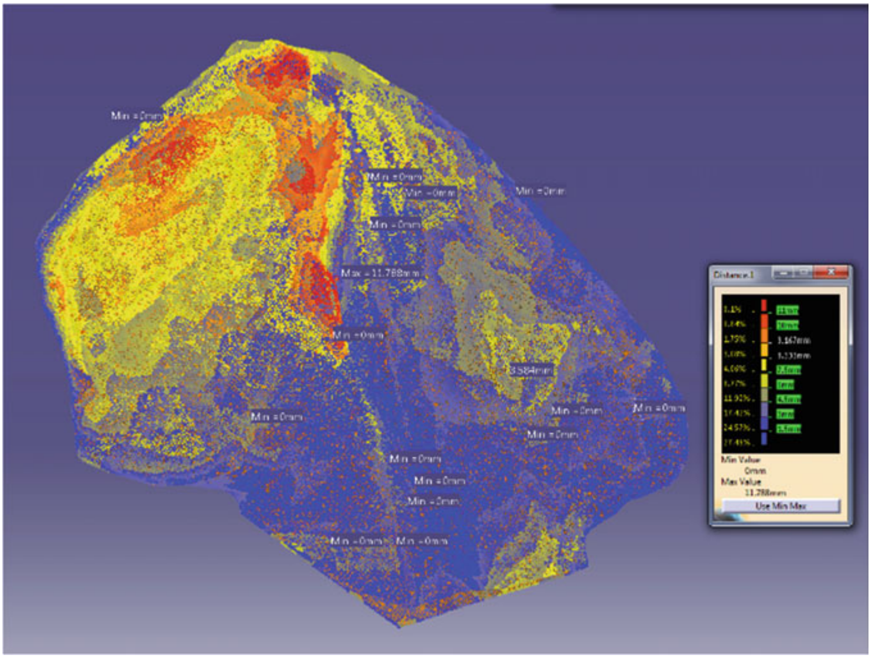

Fig. 5.7 Distance analysis between the outer sides of initial polygonal model and the polygonal model obtained by aggregating parametric regions

was performed with an accuracy of 0.001 mm and shown in the form of a color coded map in Fig. 5.7 and 5.8. Normal distances were taken for measurement direction. At the outer side of the bone maximum distance was pronounced in the middle part of the wing (below point 1), above parameter d_{11} (presented by red color in Fig. 5.7), with the value of 11.788 mm.

At the inner side maximal distance was just below the superior edge, at the auricular surface and in the area which is located left from auricular surface (presented by red color in Fig. 5.8).

5.3.2 Comparative Analysis of the Obtained Models

The comparison of the obtained polygonal models was performed based on the results acquired by the analysis of geometry, deviations and distances (deviations) between the initial and the obtained models. The first model was created without using the method of parametric regions, the second involved using method of parametric regions and the third using the method of parametric regions with aggregating regions.

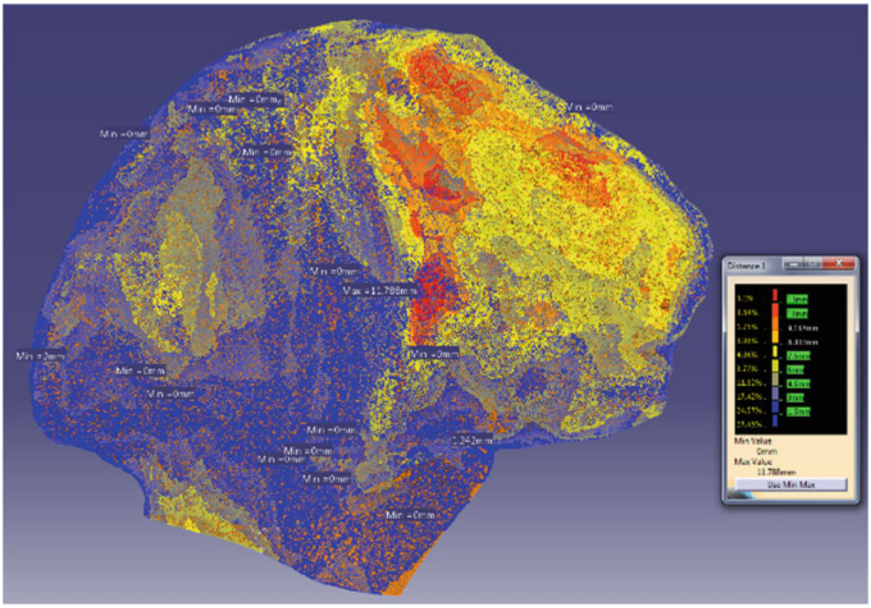

Fig. 5.8 Distance analysis between the inner sides of initial polygonal model and the polygonal model obtained by aggregating parametric regions

The parameters chosen for geometry analysis are Neighborhood values (the maximal edge length of the triangles displayed) before and after model optimization, statistical indicators such as number of points and triangles, the need for editing triangles and the existence of holes which need to be filled. In order to compare the models, optimization was conducted using the same parameter's values in all cases (minimal length 0.5 mm, maximal length 1 mm and the values of dihedral angle 30°). Comparative geometry analysis according to chosen parameters is presented in Table 5.5, where PM stands for polygonal model.

The second polygonal model gives the best results considering the need for editing triangles and filling holes. This model is the easiest to optimize in one step with the ratio of optimization of 6.067, calculated as the ratio of the maximal edge lengths

Table 5.5 Comparative geometry analysis. Expanded from Trajanovic et al. (2018)

Polygonal model parameters	The first PM	The second PM	The third PM
Neighborhood before optimization (mm)	18.599	11.394	9.921
Neighborhood after optimization (mm)	2.41	1.878	3.105
Number of points	1354	2421	2220
Number of triangles	2610	4808	3721
Triangles editing	Yes	No	Yes
Holes existence	Yes	No	Yes

Table 5.6 Comparative analysis for deviation parameters. Expanded from Trajanovic et al. (2018)

Deviation parameters	The first PM	The second PM	The third PM
Positive maximal deviation (mm)	11.7	12	10
Negative maximal deviation (mm)	−10.7	−10.1	−9.97
Mean deviation (mm)	0.567	−0.276	−0.281
Standard deviation (mm)	4.03	4.29	4.13
Positive mean deviation (mm)	3.58	3.49	3.38
Negative mean deviation (mm)	−2.76	−3.54	−3.47
Part of model surface with deviation values from −1 to 1 mm (%)	22.69	16.98	16.56

of the triangles, and very low neighborhood value, which sequentially leads to the largest number of triangles, comparing with the first and the third polygonal model.

The values of positive maximal and negative deviation, mean and standard deviation, positive and negative mean deviation, expressed in millimeters are taken into account for deviation analysis. The part of the model surface expressed in % where the value of deviation is in the range from −1 to 1 mm, used as the common denominator for all three analyzes, is also presented. The above values are presented in Table 5.6, where PM stands for polygonal model.

The third model has the smallest deviation regarding the initial polygonal model, if we consider the values for positive maximum and minimum deviation and positive mean deviation. On the other side, the mean deviation is the lowest in the second model, while the first model shows the best characteristics based on the values of the negative mean deviation and the area of the model that has a small value of deviations.

Statistical data from color coded maps with the same scale gradients were used for comparative distance analysis between the initial polygonal model and obtained polygonal model. Distance values were ranged in four classes and the cumulative values for the parts of the surface model expressed in %, found within the appropriate tolerance limits are presented in Table 5.7 (PM stands for polygonal model).

Table 5.7 Comparative analysis for distance values. Expanded from Trajanovic et al. (2018)

Distance values (mm)	The first PM	The second PM	The third PM
	Model surface (%)		
0–3	51.75	50.41	52.06
0–4.5	69.46	68.77	69.48
0–6	81.12	79.42	81.40
0–10	96.76	98.34	99.06
	Maximum distance (mm)		
	14.238	12.243	11.788

Taking into account the values shown in Table 5.6 by the criteria of deviation values for the given ranges, as well as for the maximum deviation value, the third model should be preferred over the previous two because the values for the model area expressed in % are the largest for all ranges given in Table 5.7. This statement, along with the fact that the third model has the smallest deviation value, leads to the conclusion that the third model is actually the one that deviates the least from the initial model.

Considering the results of comparative analyses of geometry, deviations and distances, and especially taking into account the fact that the second model is the only one that does not require additional editing of the obtained surfaces, has the best mean deviation, and that the difference in surfaces is in the range of 0–10 mm insignificant in relation to the third model (0.72%), as well as the difference in the maximum deviation values between the second and third model 0.635 mm, the second model should be chosen for the construction of the polygonal model of the complete wing of ilium. Additional argument for this is the fact that the difference in the areas of the model where the deviations range from -1 to 1 mm is only 0.42% in favor of the third model, but the time required to obtain the second model is significantly shorter. But, in the cases where there is a need to create some of the individual parts of the wing of ilium the third model should be used as a better solution.

5.3.3 Application of the Method of Parametric Regions for Implant Creation

An additional aspect of the application of the method of parametric regions lies in the fact that individual regions can be divided into subregions, in accordance with the needs, i.e., the parts of the bone for which it is necessary to make an personalized implant.

These implants can be made of artificial materials (substitutes for bone material) or natural bone in the form of an allograph obtained from a donor or in the form of an autograph of bone taken from a healthy part of the bone or from the patient's skeletal system. Thanks to the development of biomaterials, a large number of different materials, such as metals, polymers, ceramics and composites are successfully used for bone repair. In any case, there are always problems when creating an implant of the appropriate shape from the chosen material. In orthopedics, the geometry of a personalized implant is hand-drawn, and such implants can have geometric errors that make them less effective for a longer period of time. With the development of CAD, CAE (Computer Aided Engineering), CAD/CAM (Computer Aided Design/Computer Aided Manufacturing), new trends in medical technology are emerging that lead to a personalized approach, i.e., enable the construction and production of personalized implants at an affordable price and within a reasonable time (Trajanovic and Tufegdzic 2018).

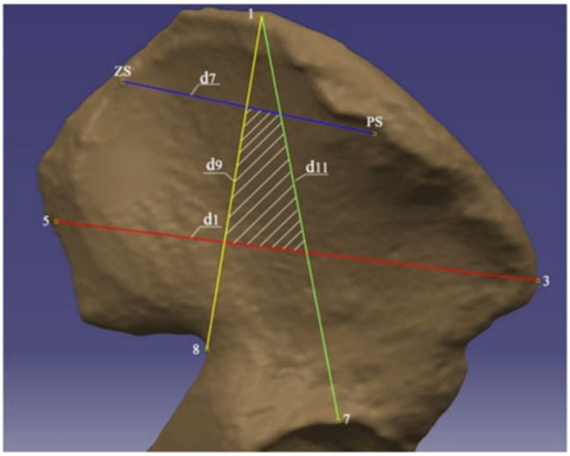

Fig. 5.9 Part of the parametric region d_9–d_{11}

In the example of applying the method of parametric regions it will be assumed that the bone damage is in the area at the outer side of the wing of ilium, in the parametric region d_9–d_{11}, bounded by parameters d_7 and d_1, which corresponds to the hatched area in Fig. 5.9. The first step was to determine anatomical landmarks 1, 3, 5 and 8, since the values for the parameters d_1 and d_9 need to be measured and inserted into Excel sheet, while the values for the parameters d_7 and d_{11} were calculated according to the formulas in Table 5.3 (which already exist in the Excel file). Points at the parameters d_1, d_9, d_7 and d_{11} were selected from special sheets. Point coordinates were calculated according to the algorithm used for the ilium bone, based on the regression equations which also exist in the Excel file, and selected by running a macro for point selection. The selected point coordinates must satisfy the condition from expression for N_c. In this case, only the points at the outer side should be selected (indexed with $d_{i\text{-}j\text{-}01}$). This procedure is repeated after selecting the required region, in this case d_9–d_{11}.

The values for the point coordinates are exported to the CAD program. Points that do not belong to the target area should be removed manually. These are all points outside the area bound by the points at the parameters d_7 and d_1, as well as the points at d_9 and d_{11}. After removing the unnecessary points, the remaining points are converted into a point cloud, and finally the desired subregion polygonal surface is created.

In order to conduct the analysis of deviations and distances the initial subregion polygonal surface is created by cutting the initial polygonal model of wing of ilium, obtained from CT images. Deviations were measured between the initial subregion polygonal model and the obtained subregion polygonal surface. Most of the obtained polygonal surface (71.73%) has deviations from the initial model in the range of −3.31 to 2.67 mm. The value for maximal positive deviation is 4 mm and the maximal negative deviation is −4.96 mm.

A slight maximum deviation of the constructed polygonal surface is noticeable, i.e., 1.36%. Maximal distance value is 4.649 mm. Most of the obtained subregion polygonal surface (89.22%) is within the tolerance limits from 0 to 2.905 mm. The obtained surface can be additionally adjusted in the procedures of successive iterations, which imply the possibility of removing additional points or small corrections of coordinate values.

Methodology applied in creating the part of the area bound by parameters can be applied to each of the regions or subregions. Subregions can be selected depending on the part of the bone that needs to be created, grouped or further divided. It is necessary to determine only the landmarks used to define the parameters whose values are to be measured, from two planar X-ray projections. Created subregions polygonal models can be increased or decreased using the offset function in CAD program.

The required subregion can also be constructed by intersecting a given parametric region. In the presented example, it is necessary to construct a complete parametric region d_9–d_{11} first, which is further intersected by the curves obtained by cutting polygonal models with planes determined by the given parameters d_7 and d_1.

The results of the deviation analysis between initial subregion polygonal model and obtained subregion polygonal model show that 67.37% of the subregion surface area of the obtained model is in the range of deviations −2.99 to 2.76 mm. On the other hand, the distance analysis gives better results compared to the method of separating points in the area of interest, because 91.39% of the obtained model surface is within the tolerance limits from 0 to 0.512 mm, and the value of the maximum deviation is reduced to 4.092 mm.

The methodology can also be applied to obtain polygonal models with completely arbitrary shape, but it is necessary to have a CT image since the target areas cannot be localized with sufficient accuracy from two plane X-ray projections.

5.3.4 Parametric Regions at the Ischium and Pubic Bone

The parametric region separation method described above at the example at the wing of ilium bone can be used to create 3D models of the ischium and pubic bones, or its parts. In some areas, it is necessary to use some of the parameters that are previously defined at the ilium bone, such as d_{25} and d_{26} (Fig. 5.2), and some of the anatomical landmarks defined for the wing of ilium, 4, 7 and 8 (Fig. 5.1). In such manner, a connection between constitutive entities of the hip bone is established, which ultimately provides complete coverage of the hip bone surface.

Input data in the form of parameters were also acquired from A-P and lateral X-ray projection of the hip bones. From the ischium bone the values for 7 parameters (d_{27}, d_{32}, d_{38}, d_{40}, d_{41}, d_{42} and d_{45}) and from pubic bone the values for 4 parameters (d_{47}, d_{48}, d_{49} and d_{57}) were taken. Predicted parameters' values were calculated using regression equations presented in Table 5.3. Parameters are used to obtain intersections with polygonal bone models from the sample using Quick Plane

Definition function in CATIA module. To determine the points at the intersection curves, cross-sections of polygonal models with planes at distances of 4 mm that are perpendicular to the parameters should be used. Two cross-sectional points are to be found on each of these curves. The notation for these points should be the same as in the case of ilium bone, $d_{i\text{-}j\text{-}01}$ and $d_{i\text{-}j\text{-}02}$ (index i refers the number of parameter, index j refers to the ordinal number of the curve obtained by intersecting with the plane perpendicular to the parameter, index 01 shows that the point is on the outer side, index 02 shows that the point is at the inner side of the hip bone). After measuring points' coordinates, values will be statistically processed. Testing and regression models will be selected for each of the points in the manner described for the points at the surface of the wing of ilium bone.

After that, the regionalization of the surfaces which describe the body of the ischium bone and the ramus of ischium, as well as the body and superior and inferior ramus of the pubic bone should be done, assigning the same notation for the labels according to parameters that represent boundaries for given region, as it was in the case of parametric regions at the wing of ilium bone.

At the ischium bone it is necessary to separate the following parametric regions:

1. Parametric region d_{27}–d_{28}—region outlined by the parameters d_{27}, d_{28} and with the part of the posterior edge between the points 8 and 15
2. Parametric region d_{28}–d_{29}–d_{30}—region whose boundaries are parameters d_{28}, d_{29} and d_{30}
3. Parametric region d_{30}–d_{31}—region outlined by the parameters d_{30}, d_{31} and with a part of the posterior edge between points 16 and 17
4. Parametric region d_{31}–d_{32}–d_{33}—region whose boundaries are parameters d_{31}, d_{32} and d_{33}
5. Parametric region d_{32}–d_{34}–d_{36}—region whose boundaries are parameters d_{32}, d_{34} and d_{36}
6. Parametric region d_{36}–d_{37}–$LAc_{12\text{–}14}$—region outlined by the parameters d_{36}, d_{37}, and with part of acetabular rim between points 12 and 14
7. Parametric region d_{34}–d_{35}–d_{38}—region whose boundaries are parameters d_{34}, d_{35} and d_{38}
8. Parametric region d_{37}–d_{38}–d_{39}—region whose boundaries are parameters d_{37}, d_{38} and d_{39}
9. Parametric region d_{39}–d_{40}—region outlined by the parameters d_{39}, d_{40}, and with the part of the rim of the obturator foramen, between the projections of point 14 on the rim of the obturator foramen and point 21
10. Parametric region d_{40}–d_{41}–d_{42}—region whose boundaries are parameters d_{40}, d_{41} and d_{42}
11. Parametric region d_{42}–d_{43}—region outlined by the parameters d_{42}, d_{43}, and with the part of rim of the obturator foramen, between the points 21 and 22
12. Parametric region d_{43}–d_{44}–d_{45}—region whose boundaries are parameters d_{43}, d_{44} and d_{45}.

For a detailed description of the ischium bone geometry, it is necessary to define the parts of the polygonal model that describe the edges and part of the ischial

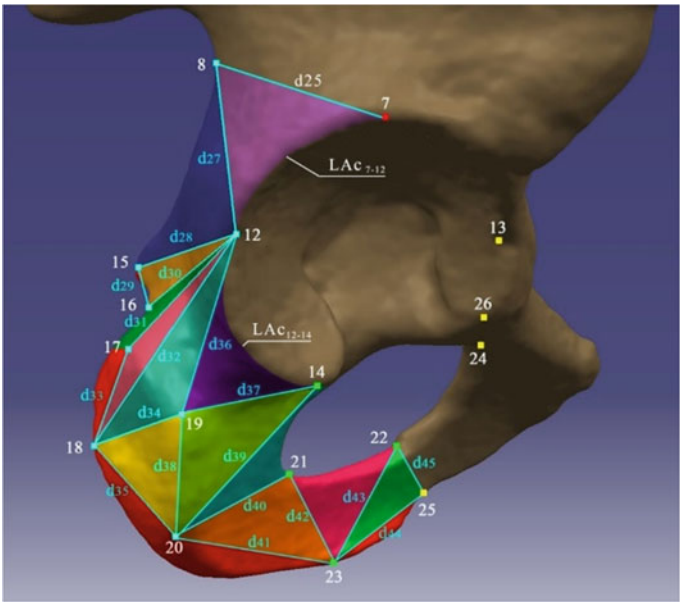

Fig. 5.10 Parametric regions and the parts of the hip bone edges at the ischium bone

tuberosity. The part of the posterior edge which is not covered by above regions is described by the part of the polygonal model left of the parameter d_{29}. The parts of the ischial tuberosity are described by the parts of the polygonal model left from the parameter d_{33} and left and below the parameter d_{35}, while the part of the inferior edge of the hip bone is described by the parts of the polygonal model below the parameters d_{41} and d_{44}. These parts are represented by the red color in Fig. 5.10 together with parametric regions at the ischium bone. To determine and predict the coordinates of the points on these parts of the polygonal model, the methodology described for the wing of ilium bone will be used, where the parts of the polygonal model are intersected by curves that are perpendicular to the aforementioned parameters.

Since the methodology for creating a surface model of the pubic bone is exactly the same, the parametric regions will be listed below. In order to fully describe the pubic bone geometry, the parts of the polygonal model which correspond to the superior and inferior edge parts will also be presented.

The selected parametric regions at the pubic bone (see Fig. 5.11) are:

1. Parametric region d_{45}–d_{46}–d_{47}, region whose boundaries are parameters d_{45}, d_{46} and d_{47}
2. Parametric region d_{47}–d_{48}–d_{49}, region whose boundaries are parameters d_{47}, d_{48} and d_{49}
3. Parametric region d_{49}–d_{50}–d_{51}, region whose boundaries are parameters d_{49}, d_{50} and d_{51}

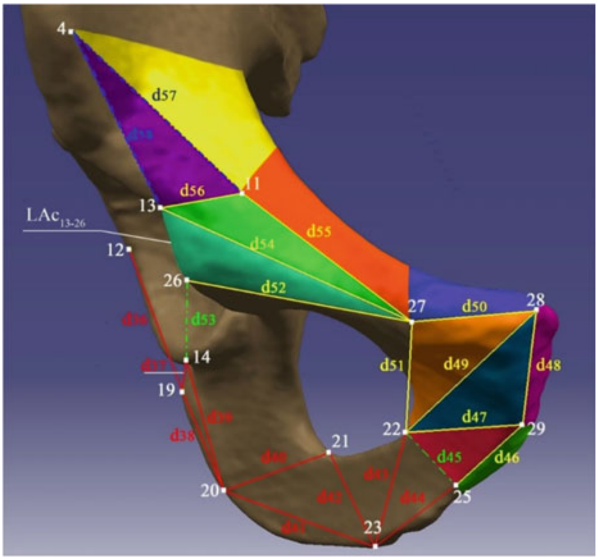

Fig. 5.11 Parametric regions and the parts of the hip bone edges at the pubic bone

4. Parametric region d_{52}–d_{54}—$LAc_{13–26}$, region outlined by the parameters d_{52}, d_{54} and with part of acetabular rim between points 13 and 26
5. Parametric region d_{54}–d_{55}–d_{56}—region outlined by the parameters d_{54}, d_{55} and d_{56}.

The parts of the inferior edge that are included in following parts of the polygonal model are located below and right from the parameter d_{46}, right from the parameter d_{48} and above the parameter d_{50}. The surfaces at the part of the superior pubic ramus, so as the part of the corresponding superior edge are described by the points constructed on curves that are perpendicular to the parameter d_{55}. The part of the anterior edge towards point 4, as well as part of the body of the ilium bone, is characterized by the points which belong to the set of curves perpendicular to the parameter d_{58}. At the surface which corresponds to the part of the edge of the obturator foramen, from point 22 toward the superior pubic ramus, it is necessary to use the points situated at the set of curves which are perpendicular to the parameter d_{51}. The surface which corresponds to the part of the edge of the obturator foramen below the acetabular notch is presented by the points at the curves that are perpendicular to the parameter d_{53}. These parts are shown in dark green, blue, orange and yellow in Fig. 5.11.

Beside the parametric regions that include parts of different bones (so called common parametric regions) mentioned and presented above d_{25}–d_{27}–$LAc_{7–12}$ (see Fig. 5.10) and d_{26}–d_{58}–$Lac_{13–26}$ (see Fig. 5.11 for $Lac_{13–26}$), it is necessary to point out the parametric region d_{56}–d_{57}–d_{58}. It is a region outlined by the parameters d_{56}, d_{57}, and d_{58} and curves perpendicular to the parameter d_{57} will be used to obtain additional points.

5.4 Conclusion

The method of parametric regions enables reverse engineering of the hip bone, with sufficient accuracy, in a short time. The method can be applied in case of complete or incomplete volumetric data, which can occur due to trauma, osteoporosis or tumors, but also in cases when the only data sources are 2D X-rays in the A-P and lateral projection. The implementation of parameter-based approach allows subject specific morphometry of the hip bone, using 34 anatomical landmarks, interconnected by 58 straight lines which represent parameters. On the other hand, complete morphometry is provided by 21 measured values of the parameters from 2D X-rays, due to developed statistical regression models which establish proper dependencies between parameters.

Measured and calculated parameters' values are used to predict numerical values for coordinates of the points on the surface at the wing of ilium bone, based on mathematical models. These points are defined for each of the 10 parametric regions, as well as for the corresponding edges. By selecting all points in the region, or some of them, it is possible to construct a polygonal model of the whole region or its parts. Depending on the needs and parts of the polygonal model of the wing of ilium bone that need to be constructed, it is possible to combine and merge individual parameter regions and parts of the edges, only at the outer or at the inner side of the bone, or on both sides at the same time.

Parametric regions are separated at the other constitutive bones, such as 12 regions at the ischium bone, 5 regions at the pubic bone and 3 common regions, since they are outlined by parameters which connect landmarks at different bones. The parts of the polygonal model which describe corresponding edges, the part of the ischial tuberosity and the part of the pubic body, are also defined. These regions and parts of the bones impose certain directions of further research in order to find the regression equations of the coordinates of points on the parameters, edges and parametric regions.

References

Aguirre MR, Linguraru MG, Ballester MAG (2007) Statistical bone shape analysis for image free surgery. Acta Univ Cibiniensis Tech Ser LV:121–129. https://doi.org/10.7892/boris.61086

Angelopoulou A, Psarrou A, Rodríguez JG et al (2015) 3D reconstruction of medical images from slices automatically landmarked with growing neural models. Neurocomputing 150(A):16–25. https://doi.org/10.1016/j.neucom.2014.03.078

Baka N, Niessen WJ, Kaptein BL et al (2010) Correspondence free 3D statistical shape model fitting to sparse X-ray projections. In: Davant BM, Haynor DR (eds) Proceedings of SPIE 7623. Medical imaging 2010: image processing, vol 7623. San Diego, California, United States, 76230D-1. https://doi.org/10.1117/12.840935

Benameur S, Mignotte M, Parent S et al (2001) 3D biplanar reconstruction of scoliotic vertebrae using statistical models. In: Proceedings of the 2001 IEEE computer society conference on computer vision and pattern recognition, CVPR 2001, vol 2. Kauai, HI, USA, pp 577–582. https://doi.org/10.1109/CVPR.2001.991014

Besbes A (2010) Image segmentation using MRFs and statistical shape modeling. Dissertation, Ecole Centrale Paris, Paris

Betti L, Cramon-Taubadel N, Manica A et al (2013) Global geometric morphometric analyses of the human pelvis reveal substantial neutral population history effects, even across sexes. PLoS ONE 8(2):e55909. https://doi.org/10.1371/journal.pone.0055909

Blanc R, Seiler C, Székely G et al (2012) Statistical model based shape prediction from a combination of direct observations and various surrogates: application to orthopaedic research. Med Image Anal 16(6):1156–1166. https://doi.org/10.1016/j.media.2012.04.004

Boulay C, Tardieu C, Benaim C et al (2006) Three-dimensional study of pelvic asymmetry on anatomical specimens and its clinical perspectives. J Anat 208(1):21–33. https://doi.org/10.1111/j.1469-7580.2006.00513.x

Chen JH, Shapiro LG (2009) 3D point correspondence by minimum description length with 2DPCA. In: Proceedings of annual international conference of the IEEE, 3–6 Sept 2009. Engineering in Medicine and Biology Society, Minneapolis, MN, USA, pp 5657–5660. https://doi.org/10.1109/IEMBS.2009.5333769

Chintalapani G, Ellingsen LM, Sadowsky O et al (2007) Statistical atlases of bone anatomy: construction, iterative improvement and validation. In: Ayache N, Ourselin S, Maeder A (eds) Medical image computing and computer-assisted intervention—MICCAI 2007. MICCAI 2007. Lecture notes in computer science, vol 4791. Springer, Berlin, Heidelberg. pp 499–506. https://doi.org/10.1007/978-3-540-75757-3_61

Decker S (2010) The human in 3D: advanced morphometric analysis of high-resolution anatomically accurate computed models. Dissertation, College of Medicine, University of South Florida, Tampa, USA

Dhindsa G, Singh P, Singh Z (2013) Morphometry of the adult human dry hip bone. Int J Pharm Pharm Sci 5(2):505–507

Ehlke M, Ramm H, Lamecker H et al (2013) Fast generation of virtual X-ray images for reconstruction of 3D anatomy. IEEE Trans vis Comput Graph 19(12):2673–2682. https://doi.org/10.1109/TVCG.2013.159

Fattah EDHAA (2013) Reconstruction of patient-specific bone models from X-ray radiography. Dissertation, University of Tennessee, Knoxville

Gupta S, Vaghela B, Dave M (2014) Morphometric analysis of pubic bone in sex dimorphism. Int J Sci Res 3(1):381–383. https://doi.org/10.36106/ijsr

Kirschner M (2013) The probabilistic active shape model: from model construction to flexible medical image segmentation. Dissertation, Fachbereich Informatik der Technischen Universität, Darmstadt

Lamecker H, Seebass M, Hege HC et al (2004) A 3D statistical shape model of the pelvis bone for segmentation. In: Fitzpatrick JM, Sonka M (eds) Proceedings of SPIE 5370. Medical imaging 2004: image processing, vol 5370. San Diego, California, United States, pp 1341–1351. https://doi.org/10.1117/12.534145

Lamecker H, Wenckebach TH, Hege HC (2006) Atlas-based 3D-shape reconstruction from X-ray images. In: Proceedings of the International Conference of Pattern Recognition, vol. I. IEEE Computer Society, Hong Kong, China, pp 371–374. https://doi.org/10.1109/ICPR.2006.279

Lamecker H (2008) Variational and statistical shape modeling for 3D geometry reconstruction. Dissertation, Fachbereich Mathematik und Informatik der Freien Universität Berlin, Berlin

Lubovsky O, Peleg E, Joskowicz L et al (2010) Acetabular orientation variability and symmetry based on CT scans of adults. Int J Comput Assist Radiol Surg 5(5):449–454. https://doi.org/10.1007/s11548-010-0521-9

Margam S, Doshi M, Jadhav S et al (2013) Sex and side determination of human hip bone by metric parameters of its posterior border. Natl J Clin Anat 2(1):16–21

O'Connell L (2004) An initial evaluation of the relationship between human pelvic size and shape and the distribution, type and severity of vertebral degenerative disease in archaeological material (Volume 1). Disseratation, Bournemouth University, Bournemouth, United Kingdom

Okoseimiema A, Udoaka A (2013) Radiologic determination of ischiopubic index in South-South Nigerian population. Asian J Med Sci 5(5):96–100. https://doi.org/10.19026/ajms.5.5361

Phillips ATM, Pankaj P, Howie CR et al (2007) Finite element modelling of the pelvis: inclusion of muscular and ligamentous boundary conditions. Med Eng Phys 29(7):739–748. https://doi.org/10.1016/j.medengphy.2006.08.010

Popov I, Onuh SO (2009) Reverse engineering of pelvic bone for hip joint replacement. J Med Eng Technol 33(6):454–459. https://doi.org/10.1080/03091900902952634

Ruiz LMA (2005) Reconstruction 3D du bassin humain à partir d'images médicales multimodales incomplètes. Application à l'assistance de la chirurgie de la prothèse totale de la hanche (PTH). Dissertation, Institut National Polytechnique de Grenoble—INPG, Français

Seim H, Kainmueller D, Heller M et al (2008) Automatic segmentation of the pelvic bones from CT data based on a statistical shape model. In: Botha CP, Kindlmann G, Niessen WJ et al (eds) EG VCBM'08: Proceedings of the first Eurographics conference on visual computing for biomedicine, Eurographics workshop on visual computing for biomedicine, 6–7 October 2008. Eurographics Association, Delft, Netherlands, pp 93–100

Sharma G, Vijayvergiya T (2013) Evaluation the various criteria of sex determination of hip bone of Jhalawar region of Rajasthan. J Pharm Biomed Sci 26(26):330–335

Shim VB, Pitto RP, Streicher RM et al (2007) The use of sparse CT datasets for auto-generating accurate FE models of the femur and pelvis. J Biomech 40(1):26–35. https://doi.org/10.1016/j.jbiomech.2005.11.018

Sierra R, Zsemlye G, Székely G et al (2006) Generation of variable anatomical models for surgical training simulators. Med Image Anal 10:275–285. https://doi.org/10.1016/j.media.2005.11.003

Styner MA, Rajamani KT, Nolte LP et al (2003) Evaluation of 3D correspondence methods for model building. In: Taylor C, Noble JA (eds) Information processing in medical imaging. IPMI 2003. Lecture notes in computer science, vol 2732. Springer, Berlin, Heidelberg, pp 63–75. https://doi.org/10.1007/978-3-540-45087-0_6

Su GM, Lai YC, Kwasinski A et al (2013) 3D visual communications. Wiley, Chichester West, United Kingdom

Trajanovic M, Tufegdzic M, Arsic S (2018) Obtaining patient-specific point model of the human ilium bone in the case of incomplete volumetric data using the method of parametric regions. Australas Phys Eng Sci Med 41:931–944. https://doi.org/10.1007/s13246-018-0689-9

Trajanovic M, Tufegdzic M (2018) Trends in producing personalized bone implants using additive manufacturing. In: Doroslovački R (ed) Proceedings of 13th international scientific conference. MMA 2018, September 28–29, 2018. Flexible Technologies, Novi Sad, Serbia, pp 371–373

Tufegdžić M, Trajanović M, Arsić S et al (2013) Toward reverse engineering of the hip bone. In: Proceedings of the 35th International conference on production Engineering, ICPE 2013. Faculty of Mechanical and Civil Engineering in Kraljevo, Department of Production Technologies, Kraljevo-Kopaonik, Serbia, September 25–28, 2013, pp 319–324

Tufegdzic M, Arsic S, Trajanovic M (2015) Parameter-based morphometry of the wing of ilium. J Anat Soc India 64(2):129–135. https://doi.org/10.1016/j.jasi.2015.10.008

Yaoa J, Taylor R (2012) Deformable 2D–3D medical image registration using a statistical model: accuracy factor assessment. Am J Sci Eng 1(2):1–13

Zheng G (2009) Statistical deformable model-based reconstruction of a patient-specific surface model from single standard X-ray radiograph. Comput Anal Images Patterns 57(2):672–679. https://doi.org/10.1118/1.3327453

Zsemlye G (2005) Shape prediction from partial information. Dissertation, Swiss Federal Institute of Technology, Zurich

Part III
Personalized Implants

Chapter 6
Design and Manufacturing of the Personalized Plate Implants

Miodrag Manic, Nikola Vitković, and Jelena Mitic

6.1 Introduction

CAOS (Computer Assisted Orthopedic Surgery) is a discipline where computer technology is applied to treat patients. CAOS includes various fields of science and technology, like medicine, engineering, mathematics, robotics, computer vision, information systems, and others (Zheng et al. 2015; Picard et al. 2019). The main requirement of CAOS is to provide the best medical treatment for the patient. Therefore, it includes all the stages of the treatment: pre-, intra- and post-operative procedures. Geometrical models of human bones and their geometrical accuracy, anatomical and morphological correctness are elements that greatly influence the outcome of applied CAOS procedures. With these models, it is possible to perform pre-operative procedures or conduct intra-operative tasks with greater accuracy. Also, such models enable the creation of customized bone implants and fixators using additive and/or other manufacturing technologies (Vitkovic et al. 2013; Ghyar et al. 2013).

In the field of orthopedic surgery, the main goal is to find the best treatment for the person with some bone fracture or some other trauma. In the treatment of bone fractures, orthopedic surgeons apply techniques of *internal* and *external* fixation. External fixation is a surgical technique used for the stabilization of bone fragments with the fixator frame positioned outside of the human body (only pins are being partially inside the body) (Fragomen et al. 2007). While performing fracture reduction intraoperatively, orthopedic surgeon sets the external fixator frame in an optimal position. Internal fixation presumes the use of osteosynthesis material (screws, pins, plates, other implants) inside the human body, to stabilize the bone fracture (Grewal et al. 2011; Musuvathy et al. 2011; Uhthoff et al. 2006; Bacon et al. 2008). Both

M. Manic (✉) · N. Vitković
Faculty of Mechanical Engineering, University of Nis, Nis, Serbia
e-mail: miodrag.manic@masfak.ni.ac.rs

J. Mitic
Faculty of Sciences and Mathematics, University of Nis, Nis, Serbia

O. Canciglieri Junior and M. D. Trajanovic (eds.), *Personalized Orthopedics*,
https://doi.org/10.1007/978-3-030-98279-9_6

internal and external fixation can be used in bone fracture treatment. Internal fixation is mostly used, but external fixation is the treatment of choice in some conditions—open fracture, local infection, significant damage of local soft tissues, etc. (Grewal et al. 2011).

There are two types of internal fixation—intramedullary fixation and extramedullary fixation. Intramedullary fixation is performed on long bones (e.g., tibia) by intramedullary nails. They are inserted into the medullary canal of the bone, and the screw bolts are inserted through the bone and through transverse holes of the nail. The main purpose of any fracture fixation method is to maintain the fracture healing in a proper position. Longitudinal bone fracture alignment can be easily achieved using an intramedullary fixation in some long bone shaft fracture types x(http://www.synthes.com 2015).

Extramedullary fixation is performed by various implants: screw bolts, plates, and other implants (e.g., internal fixators according to Mitkovic, presented in the Fig. 6.1) of different shapes and dimensions. The stem (body) of extramedullary fixation implants is placed on an external surface of the fractured bone (Mitkovic et al. 2012). The system of screw bolts is inserted through the holes on the implant body. In this way, fractured bone fragments are connected into a whole after bone fracture reduction, i.e.~~,~~ placement of bone fracture fragments in the correct position. It is recommended to ensure extramedullary implants to follow bone contour for some types of fractures as much as possible. In other cases, the direct contact between implant surface and bone outer surface should be avoided since the pressure between implant contact surface and a bone can damage the periosteum, which covers the bone surface and gives important bone nutrition through the periosteal blood vessels.

Plates are the most used internal fixation implants for the surgical treatments of bone fractures. They are made in various sizes and shapes, to be used for different fracture types (Uhthoff et al. 2006). However, the application of such implants for the treatment of a certain patient may be the problem because the bone and the plate may be significantly different in size and shape. In such cases it is hard to find the proper position of the plate, thus, the fracture healing process may be obstructed, etc.

The problem can be reduced if personalized implants (PPIs) are used. The geometry and shape of PPIs are customized to the anatomy and bone morphology of the patient (Majstorovic et al. 2013; Vitkovic et al. 2015b; Manic et al. 2015a). In this

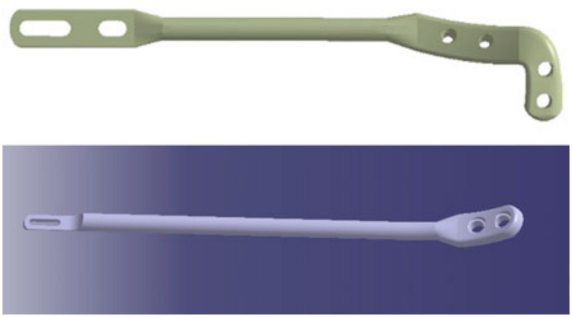

Fig. 6.1 Internal fixator for tibia according to Mitkovic. (Reproduced from Manic et al. 2015c)

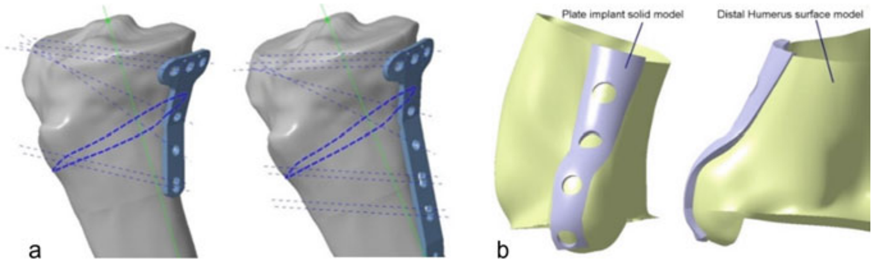

Fig. 6.2 **a** Insertion of a plate for upper part of tibia, **b** Plate for distal humerus. (Reproduced from Manic et al. 2015a; Rashid et al. 2017)

way, there is a need for pre-operative planning. In addition, PPIs are used in situations when both intra-operative and post-operative complications are expected to occur if the predefined (standard) implants are used.

Plates are fixed to the bone with screws (Fig. 6.2a). Plates are placed on the external surface of the bone (Fig. 6.2b). In this way, fractured bone fragments are connected into a whole after fracture reduction.

Compression plates are used in various designs and provide compression between bone fragments (Lai et al. 2012). There are Dynamic Compression Plates (DCP) having oval holes. Oval holes are used to provide interfragmentary compression by screw tightening. These specially designed oval holes are described in Lai et al. (2012). The benefits of DCP are lower incidence of malunion, stable internal fixation, and less frequent need for post-operative external immobilization with the splint, providing immediate movement of adjacent joints (Gardner et al. 2004). To provide adequate stability and functional requirements of the bone, DCPs must be placed onto the periosteum (the tissue covering the outer surface of the bones) and should be pressed onto the bone. On the other hand, the excessive pressure surface on the periosteum can obstruct bone vascularization from periosteal vessels, resulting in cortical bone weakness. There are some questions since this problem was reported (Berkin et al. 1972; Perren et al. 1988). Refracture after plate removal was another possible complication of fracture treatment with DCPs. To prevent refracture it was highly recommended that the plate should not be taken out at least 15–18 months after surgery, to have enough time for completely new bone maturing in the fracture gap between bone fragments. Different studies analyzed the reasons inducing a refracture~~,~~ and the conclusion was that refracture was an effect of cortical necrosis (Takigami et al. 2010; Jain et al. 1999). The new plate was designed to reduce plate's contact surface with the periosteum and decrease cortical porosity. The construction was named the Limited Contact-Dynamic Compression Plate (LC-DCP). LC-DCP makes less surface-to-surface contact with the periosteum of the bone in comparison to DCP. In this way necrosis of cortical bone and weakness of the bone under the plate was reduced. Also, LC-DCP is constructed with plate-hole symmetry, providing dynamic compression from either side of the hole (Lai et al. 2012). Otherwise, some studies

(Uhthoff et al. 2006) referred that LC-DCP does not improve either blood flow to the bone and biomechanical properties of the bone-implant assembly.

Today, nearly all the mentioned plates were substituted with plates being capable of both locking and unlocking functions, such as Locking Compression Plates (LCP). It is possible to use both locking and unlocking screwing techniques depending on the situation (Lai et al. 2012; Gardner et al. 2004; Perren et al. 1988). LCP gives better fixation, and they can bear more load than DCP plates (Walsha et al. 2006). To choose the best fixation for the certain patient it is necessary to evaluate the condition of the fractured bone, quality of surrounding soft tissues and the patients' overall health because it has an impact on the final outcome. DCP and LCP fixation methods are based on anatomically pre-contoured plates, reducing or eliminating the need for intra-operative (in-situ) plate modification (bending by the surgeon). LCP does not require precise contouring because these plates do not touch the bone with all its surface. However, greater distance between the plate and the bone can cause a problem (Walsha et al. 2006; Rose et al. 2006; Sanders et al. 2007).

Reconstruction plates are constructed with deep notches among the holes, and they can be contoured (bent) in three planes to fit complex surfaces. Reconstruction plates are a bit thicker and stiffer than previously described plates. Their screw holes are oval, like in compression plates, and they provide potentially limited compression (Koonce et al. 2012). More about this type of plates is presented in https://www.aofoundation.org.

The new objective in plates design and production is to achieve maximal stabilization with minimal damage to the blood supply during the fracture healing process. The initial part of that process requires fully rigid fixation, while it can be less rigid in the latter part.

There are only a few papers in the literature describing the methods for creating an anatomically adjusted 3D model of implants. In general, these studies are based on 3D bone models, made from bone CT scans, and standard reverse engineering procedures for 3D plate modeling. Applied methods included CAD software to design implants and it was based on ideas of orthopedic surgeons and engineers. These researchers constantly seek for new methods and techniques in designing and producing implants that could improve fracture healing. The basis for an implant 3D geometrical model creation is its contour defined in relation to the bone surface. After modeling the implant contact surface, holes for screws are made on the implant's surface. In Matthys et al. (2009), an example of an implant design process is presented (Fig. 6.3a), as well as the design process for the hip sliding screw (Nooshin et al. 2011) (Fig. 6.3b).

In Amone et al. (2011) the method and procedure of designing a plate-shaped implant called "Medially Locking Plate" (MLP) are described, referring to the treatment of femoral fractures by implants on its lateral side. The position of a plate related to the femur is defined by creating a datum plane. A medial sketch of the MLP was created on the sagittal plane. The sketch was then extruded in both normal directions. The inner side of the implant is approximated by polygons to the bone surface. A 3D model of the femur is used in this designing process. The datum planes were positioned in such way that the sagittal plane was parallel to a planar

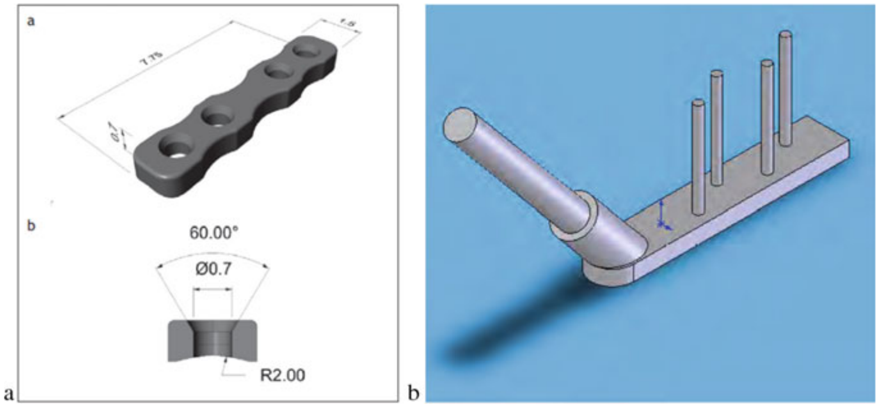

Fig. 6.3 Plate modelling **a** plate modeling. (Reproduced from Matthys et al. 2009), **b** designing of a plate with sliding screw for hip and with four standard screws.
(Reproduced from Nooshin et al. 2011)

approximation of the medial epicondylar surface and approximately tangent to the diaphyseal (bone shaft) surface. The coronal plane was then positioned at 90° to the sagittal plane rotated around a linear approximation of the diaphyseal axis (Fig. 6.4a). Morphometric values for the specific bone are presented in Fig. 6.4b.

Next, a medial sketch of the MLP was created on the sagittal plane, thus sketch matched the femur 3D model with average dimensions (Fig. 6.5a). The medial sketch was then extruded in both normal directions; thus, the extrusion intersected the femur at all points within the cross-section and extended at least 1 cm beyond the most medial point on the medial epicondylar surface (Fig. 6.5b).

A sketch of the anterior profile (with an initial plate thickness of 5.0 mm) was then created on the coronal plane with a contour matching the average femur model.

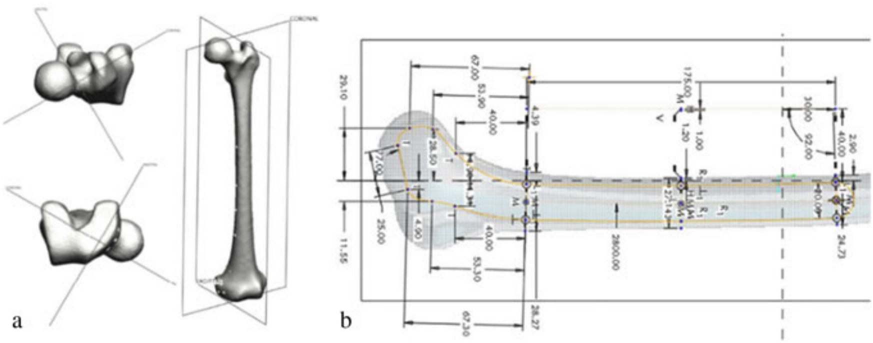

Fig. 6.4 The method and procedure of designing a plate-shaped implant MLP **a** creating a plane for drawing on a bone, **b** contour of an implant. (Reproduced from Arnone et al. 2011)

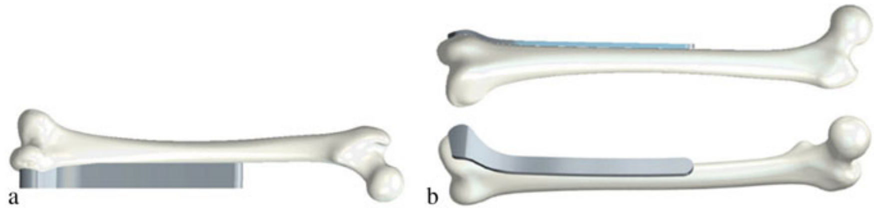

Fig. 6.5 The method and procedure of designing a plate-shaped implant MLP **a** extruding the contour of an implant, **b** extrusion cutting of the anterior profile. (Reproduced from Amone et al. 2011)

The sketch was then infinitely extruded in both directions, removing material where it intersected the initial, medial/lateral extrusion (Fig. 6.4b).

Finally, the locations of the threaded holes for screws were sketched and extruded (removing material when intersecting the concept model) from the sagittal plane (Fig. 6.6a). The final model of a plate optimized for structural integration is shown in Fig. 6.6b.

In Vitkovic et al. (2012), Stevanovic et al. (2013) and Manic et al. (2015c) the novel method was used to design Tibia-Plato-Lateral (TPL) internal fixator according to Mitkovic. The suggested method is based on the application of Method of Anatomical Features (MAF), and newly developed techniques for designing fixation supporting surfaces. The result of the method application is the parametrical fixator model which shape and geometry can be changed by changing parameters values. It was possible to change the implant's shape and adjust it to the patient's bone shape, in this case—the tibia, based on dimensions from X-ray or CT scans. The case related to reverse engineering of the sternum (chest bone), presented in the paper (Stojkovic et al. 2010), and describes a method of customized implant creation. Bone defect of the sternum, caused by cancer, was compensated by the implant design. Custom

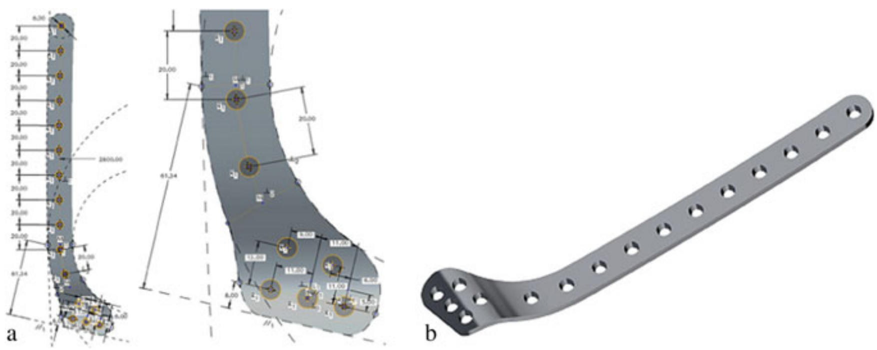

Fig. 6.6 The method and procedure of designing a plate-shaped implant MLP **a** creating the holes for screws, **b** final model of MLP. (Reproduced from Amone et al. 2011)

implant shape and geometry were created according to the sternum's virtual model, corresponding to a similar healthy sternum.

6.2 Design Process of Customized Implants

The general engineering techniques for design, analysis, and manufacturing of customized implants include several tasks (Manic et al. 2018) (Fig. 6.7):

- creating a 3D parametric model of bone,
- creating a 3D parametric model of the fracture using a patient's bone CT scan,
- selecting the place on the bone where the implant will be positioned,
- adjusting the geometry of the implant according to the requirements of the surgeon,
- creating a customized 3D model of the implant,
- simulation of implant placement to the bone,
- analysis and optimization of the implant's shape and dimensions,
- implant manufacturing.

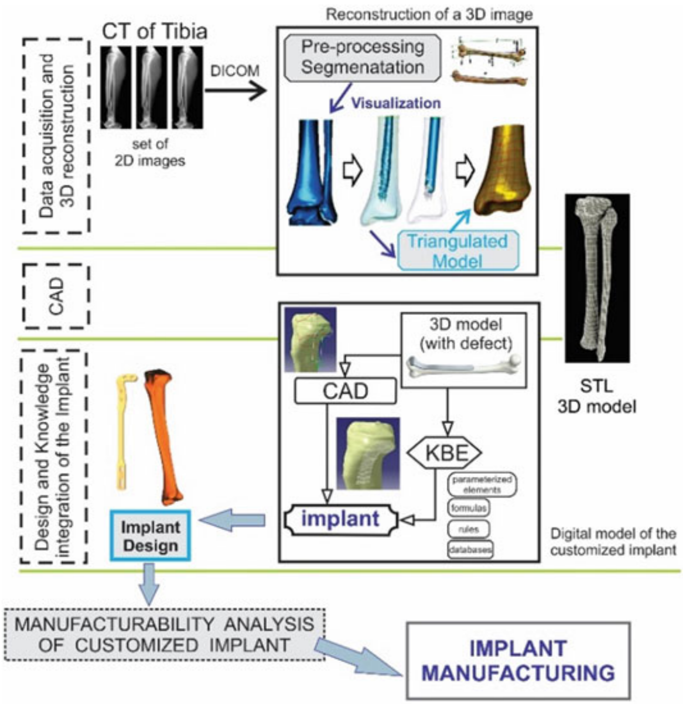

Fig. 6.7 Phases in designing and manufacturing of customized implants. (Reproduced from Manic et al. 2015a)

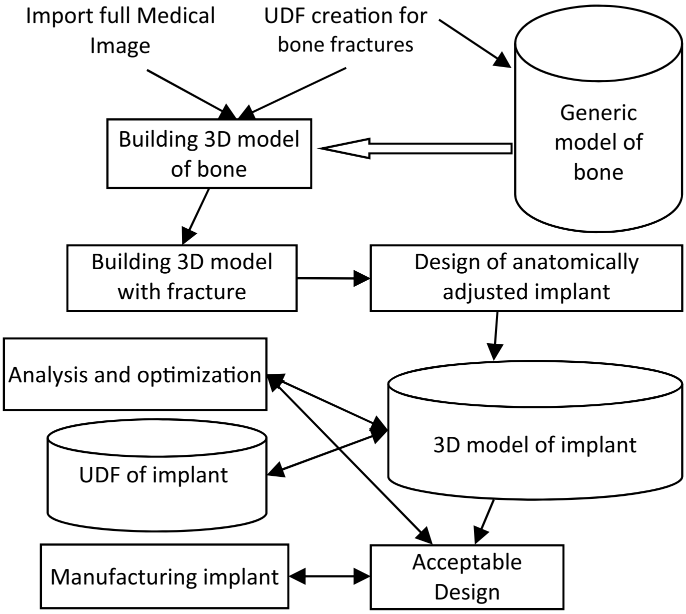

Fig. 6.8 Typical design process of anatomically adjusted customized implant. (Reproduced from Manic et al. 2018)

The creation of geometrically anatomical 3D models of human bones utilizes a number of different techniques and presents a unique challenge, because their geometry and form are very complex. These shapes can be modelled by using surface patches represented by Bezier or B-spline surfaces, or using NURBS patches, which are commonly used in traditional CAD applications, e.g., CATIA (Vitkovic et al. 2013).

The creation of a customized implant 3D model is based on the parametric 3D model of the patient's bone and the fracture. The design process of anatomically adjusted customized implants is shown in Fig. 6.8. For this purpose, the first step is to create a 3D model of a bone. To enable potential fast manufacturing, STL (Stereolithography) file from CATIA can be created, thus, allowing it to be directly transferred into Rapid Prototyping (RP) machine or Computer Aided Manufacturing (CAM) software to generate the code for Computer Numerical Control (CNC) machine tools.

6.2.1 Creating 3D Parametric Model of Fractured Bones

Within the project VIHOS (Virtual human osteoarticular system and its application in preclinical and clinical practice) (Vihos project web site, 2019) taking the place at Faculty of Mechanical Engineering and Faculty of Medicine of University of Nis (Nis, Serbia), the 3D parameterized geometrical bone models were developed. For the creation of such models, MAF was developed and tested trough many studies (Vitkovic et al. 2015a, 2018).

One of this method's goals is to find the best solution to create a parametric point model of the human bone. MAF enables the creation of patient-specific geometrical (polygonal, surface, and solid) and parametric models of the human bones. Parametric models enable the creation of geometrical models even in cases when the geometrical data about specific bone is incomplete (e.g., bone fractures or diseases). In these situations, geometrical models are created by applying the values of parameters measured in the medical images. A more detailed description of the MAF and its various applications are presented in Majstorovic et al. (2013), Vitkovic et al. (2012, 2013), Vitkovic et al. (2015a) and Vitkovic et al. (2018). MAF consists of several procedures which enable the creation of geometrically accurate and anatomically correct 3D models of the human bones:

- importing and editing of point cloud acquired from a medical imaging device,
- tessellation of point cloud and creation of polygonal model (mesh),
- anatomical and morphological analyses of a selected bone,
- identification of RGEs (Referential Geometrical Entities), which are based on the anatomical and morphological characteristics of a selected bone (points, directions, planes, and views)
- creating and editing the curves on a polygonal model of the selected bone, according to the RGEs,
- creating and editing the surface model of the selected bone's outer surface by sweeping, lofting, blending and trimming the curves.

The described method can be useful in different ways in medicine and technology. The most essential characteristic of the created parametric model is its ability to adapt to the particular dimensions of the bone, having a significant role in pre-operative planning, creation of a solid model for structural analysis by Finite Element Analysis (FEA), manufacturing of implant prototypes, manufacturing of bone models for orthopedic education courses, etc.

The bone models are used as starting point for the creation of fracture models. Fracture models are created by using an X-ray or CT scan of the patient's bone. Characteristic points of the fracture are determined by consulting an orthopedic surgeon. After the definition of the points, they are constructed on the 3D model of healthy bone in CAD software. The outside contour of the fracture is created by using defined points. Finally, the complete fracture model is created using adequate engineering techniques for free form surfaces and spline modeling. For this purpose, AO/OTA fractures classification (AO Foundation 2021, Ruedi et al. 2007) can be used to create a 3D model of each fracture type. Some examples of created tibia fracture 3D models are shown in Fig. 6.9.

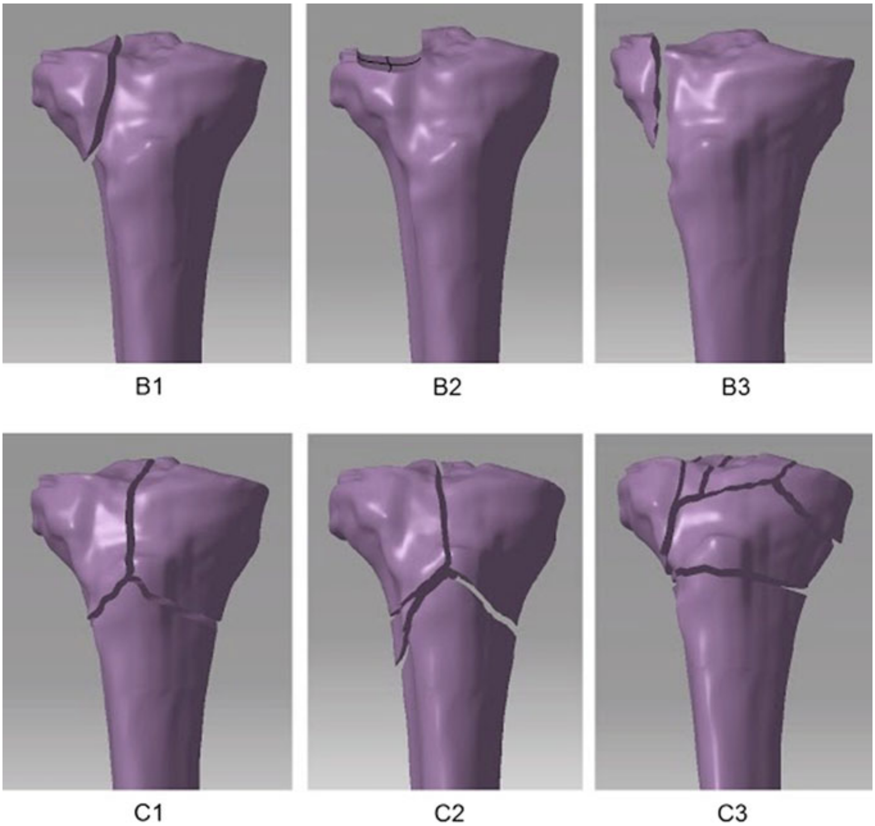

Fig. 6.9 3D models of tibia upper part fractures. (Reproduced from Manic et al. 2015a)

6.3 Design of Anatomically Customized Implants

Designing customized implants requires CAD software, and these methods are based on the ideas coming from orthopedic surgeons and engineers. The basis for 3D geometrical model implant creation is an outline of its contour defined in a suitable position to the bone surface. In the process of implant insertion, it is of the highest importance to create minimal direct contact between the fixation and the bone surface while ensuring that the implant follows the bone contours. The large implant-bone contact surface should be avoided since it can damage the periosteum, covering the bone and providing bone nutrition through the periosteal blood vessels. Different types of customized implants are shown in Fig. 6.10. The design method for a scaffold is presented in Stojkovic et al. (2016). Other types of personalized implants will be described in the following sections.

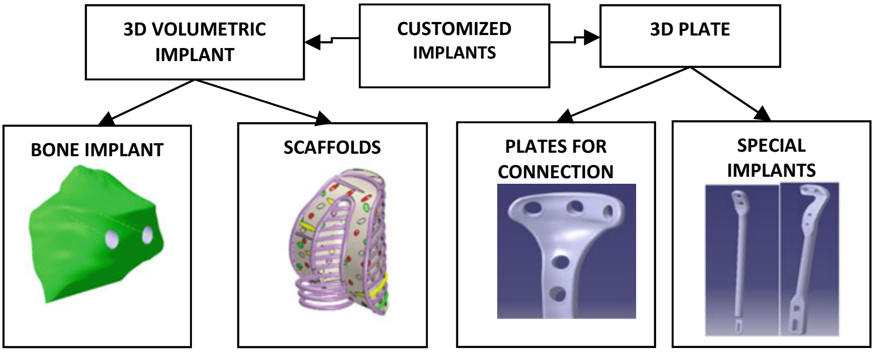

Fig. 6.10 Different types of customized implants. (Reproduced from Manic et al. 2015a)

6.3.1 Designing Technique of an Anatomically Adjusted 3D Volumetric Implants

The process of implant designing begins with a 3D bone model, as explained before in this Chapter. Then a 3D model of the fracture is generated based on the fracture images (X-ray or CT scan). These are the basics of designing customized implants.

According to the radiological image of a fracture and the surgeon's suggestions, a 3D fracture model is created, using adequate engineering techniques for free form surfaces and spline modeling (Fig. 6.11a) (Manic et al. 2015a).

When the 3D fracture model is created, and its form satisfies surgeons' needs, healthy bone fragments not belonging to the implant are removed. The initial model of

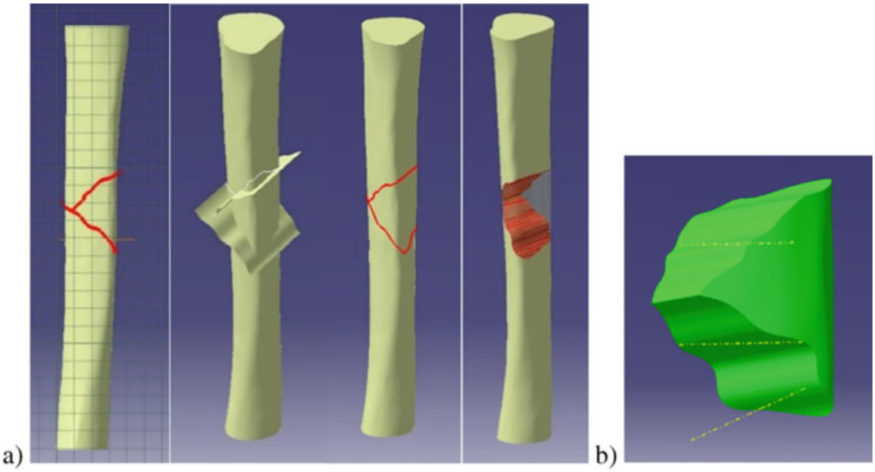

Fig. 6.11 3D fracture model creation process: **a** 3D modeling of the bone fracture, **b** basic 3D model of volumetric implant. (Reproduced from Manic et al. 2015a)

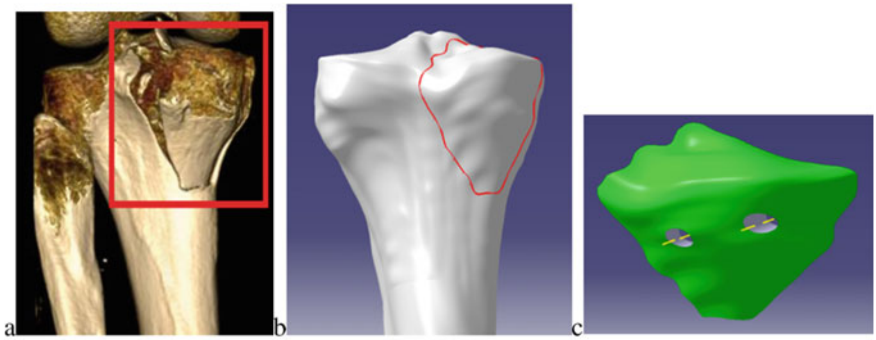

Fig. 6.12 Creation of tibia bone implant: **a** CT scan of the fractured bone, **b** bone model in CATIA, **c** created model of implant

an implant can be created and modified to follow surgeon and manufacturing requirements (Fig. 6.11b). For instance, bevels, rounding, and additional screw holes can be added, and other details are required for implant production and implementation. The practical application of this method can be seen in the example from Fig. 6.12, where a CT scan of a bone fracture obtained at the Clinical Center Nis (Nis, Serbia) was used.

6.3.2 Designing Technique of an Anatomically Adjusted Plate Formed Implants

Designing procedures are very similar to previously described for 3D volumetric implants, especially in the initial phase of implant creation (Manic et al. 2015a). The first step is creating a model of the fracture. (Fig. 6.13a).

Next, the datum plane, not far from the lateral surface of the bone, is created and placed opposite to the contour of the fracture (Fig. 6.13b). The surgeon suggests and defines the position and orientation of this plane. Inside it, the outline (contour) of the proximal part of the plate is drawn. Following that, the contour extrusion in the direction of the lateral bone side is performed to ensure that extruded contour surface penetrates the bone surface (Fig. 6.14a).

The intersected closed contour of the plate's internal side oriented to the bone is created by using an intersection between extrusion and bone model. After this step, all the surfaces are removed, and the only surface left is the one presenting the internal side of the plate (facing to the bone) (Fig. 6.14b).

The final step is to create a volume model of the patient-adapted plate by using the thickness feature of CATIA (2 mm thickness).

The remaining plate features are constructed by using standard technical elements. According to the orthopedist's request, the screw holes on the side of the plate are created next (Fig. 6.15a). The process of screw holes creation is based on projection

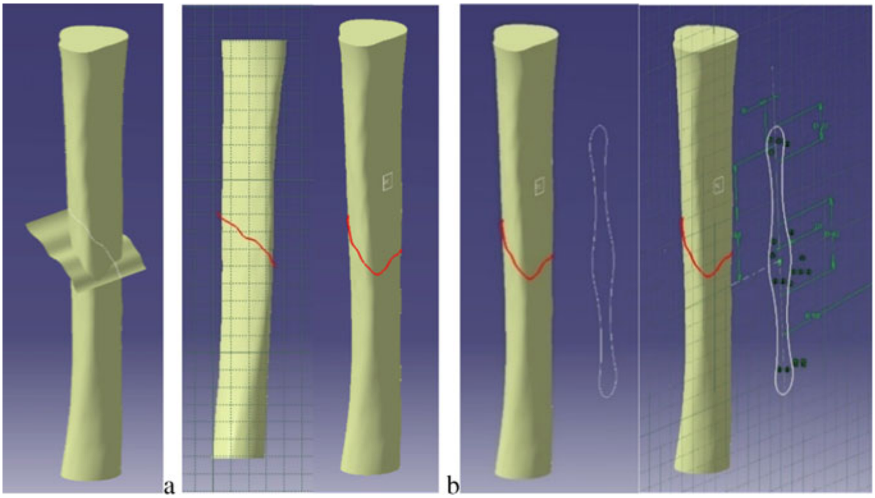

Fig. 6.13 **a** Creating the model of the fracture, **b** creating of plane for contour drawing and creating the contour of the proximal part of the plate. (Reproduced from Manic et al. 2015a)

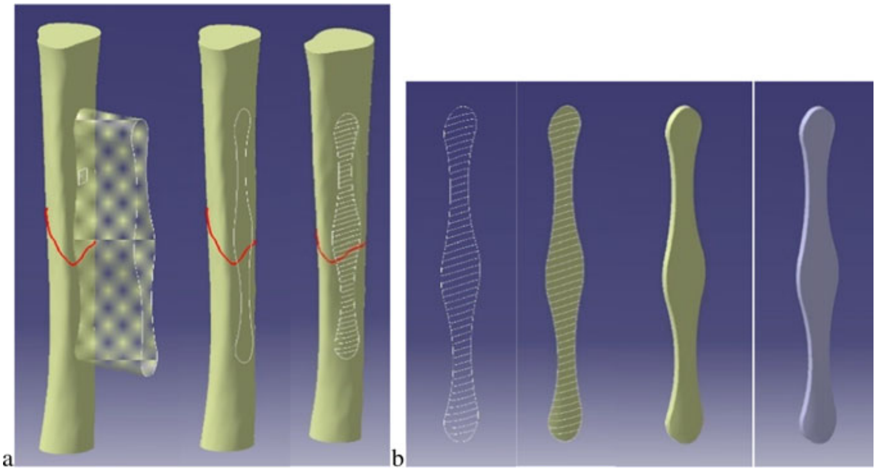

Fig. 6.14 **a** Extrusion of the contour and its penetration through the bone, **b** base plate design. (Reproduced from Manic et al. 2015a)

points and created tangent planes, and it is performed on the part of the plate surface. The final model is presented in (Fig. 6.15b).

The assembly module of the CAD system can be used to check whether the plate model has created accurately (Fig. 6.16). In this way, the model, seating, the number of necessary screws, etc., can be checked. Furthermore, this 3D model of an assembly can be used for FEM analysis and dimension and shape optimization.

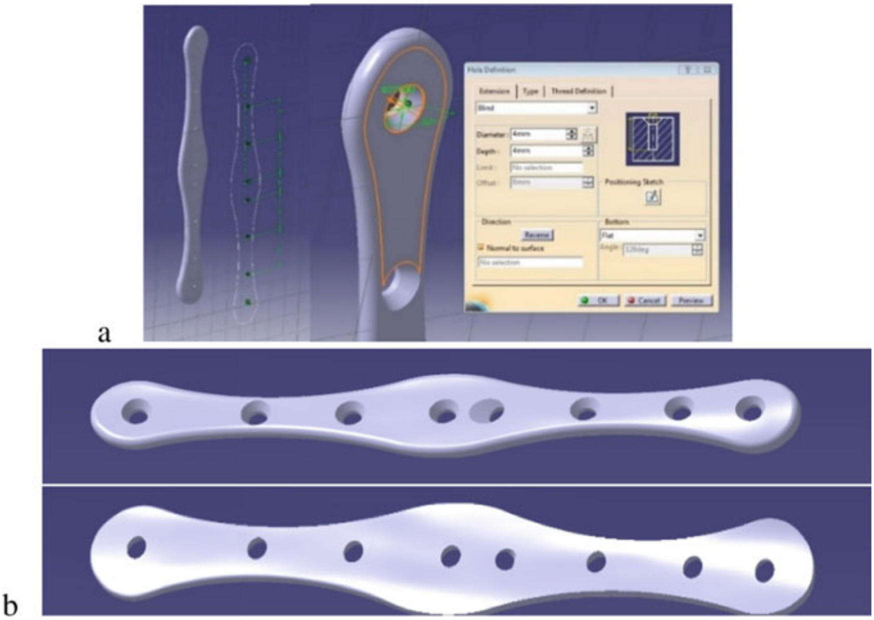

Fig. 6.15 Creating a plate solid model: **a** design of additional features, **b** final solid model. (Reproduced from Manic et al. 2015a)

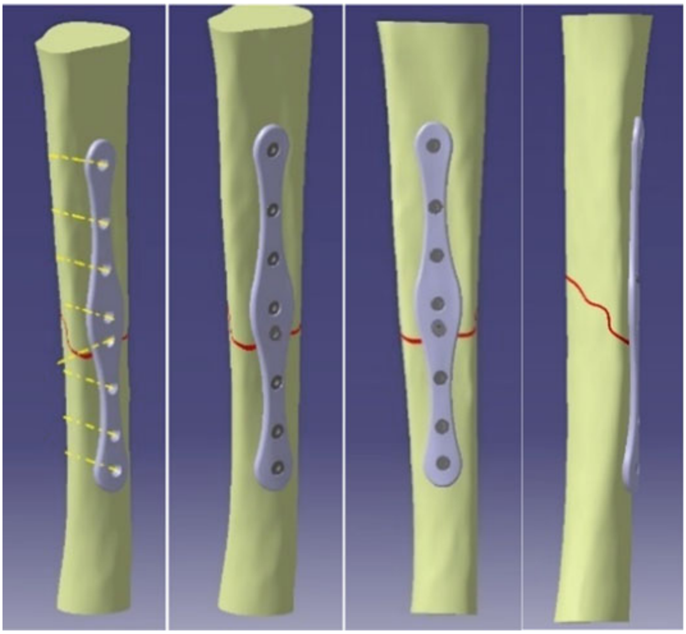

Fig. 6.16 Bone and plate assembly. (Reproduced from Manic et al. 2015a)

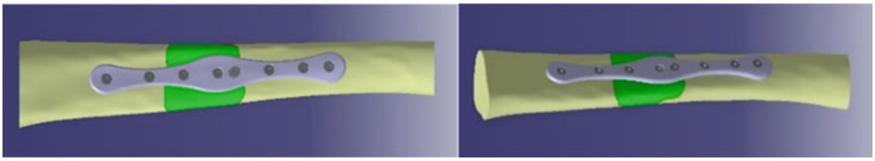

Fig. 6.17 Assembly of bone-volumetric implant-fixation plate. (Reproduced from Manic et al. 2015a)

Combining two previously described techniques a 3D volumetric implant and a plate for its fixation can also be made. Moreover, an assembly of the bone-volumetric implant plate-bonding elements can be designed. This assembly is presented in Fig. 6.17.

6.3.2.1 Case One—Tibia with Multiple Fractures

An example of designing a personalized implant for a tibia with multiple fractures will be described (Manic et al. 2018). After creating a 3D model of bone, or importing this model from a database, the creation of a personalized plate follows.

The first step is to create plate contour, followed by plate solid model created by using the same approach as in the previous section (Fig. 6.18a).

With this process completed, we get a full 3D model of a plate that is completely anatomically adjusted to the surface of the proximal part of the tibial bone (Fig. 6.18b).

The assembly module of the CAD system can be used to check whether the implant model plate is appropriate by creating an assembly of a bone, plate, and other fixation elements (Fig. 6.19). In this way, we can check the model, seating, the number of necessary screws, etc.

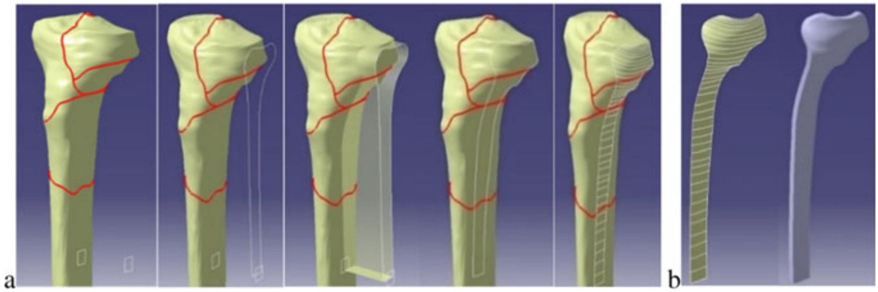

Fig. 6.18 **a** creation plate contour, **b** plate contact surface creation. (Reproduced from Manic et al. 2018)

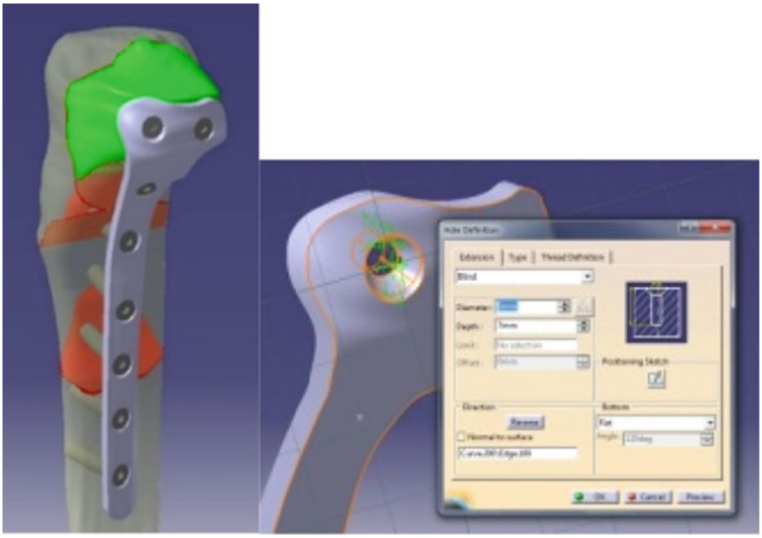

Fig. 6.19 Plate implant solid model. (Reproduced from Manic et al. 2018)

6.3.2.2 Case Two—Anatomically Adjusted Internal Fixator of Tibia According to Mitkovic Type TPL

In this example, the process of designing an anatomically adjusted dynamic internal fixation of tibia according to Mitkovic type TPL, using the CATIA V5 software package is presented (Manic et al. 2015c). Firstly, the parametrical 3D geometrical model of tibia based on the patient's CT scan is used for the creation of a patient-adapted tibia surface model (Vitkovic et al. 2015b). Next, the already described procedure for plate contour creation is applied (Fig. 6.20).

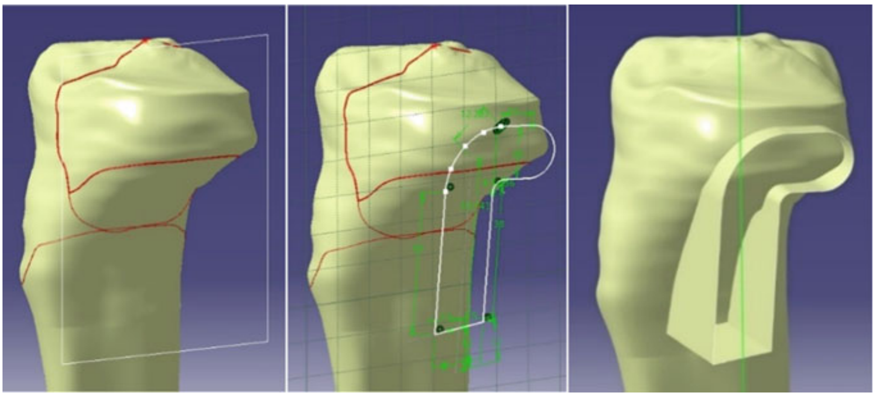

Fig. 6.20 Contour of the proximal part of the plate. (Reproduced from Manic et al. 2015c)

Following that, contour extrusion in the direction of the lateral tibia side is performed to ensure that extruded contour surface penetrates the bone surface. The intersected closed contour of the fixator's inner side is created (Fig. 6.21a) and 3D splines that follow the bone contour are constructed (Fig. 6.21b).

After this step, all the surfaces are removed, and the only surface left is the one that presents the internal side that is faced directly to the bone (Fig. 6.22a). This surface is extruded to create a full model. With this process completed, we get a full 3D model of a proximal part of the fixator that is completely anatomically adjusted to the surface of the proximal part of the tibia (Fig. 6.22b).

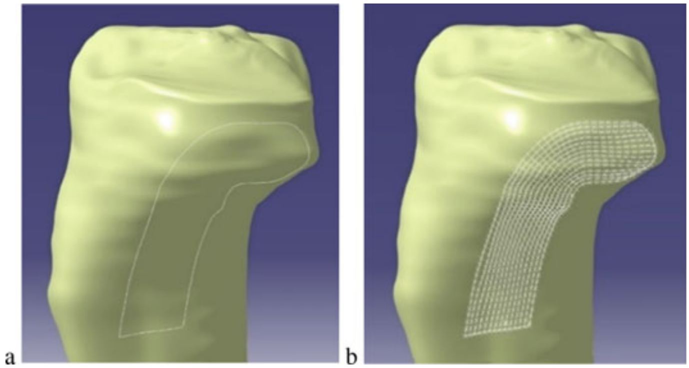

Fig. 6.21 Plate inner geometry creation process: **a** contour curve, **b** 3D splines inside the contour. (Reproduced from Manic et al. 2015c)

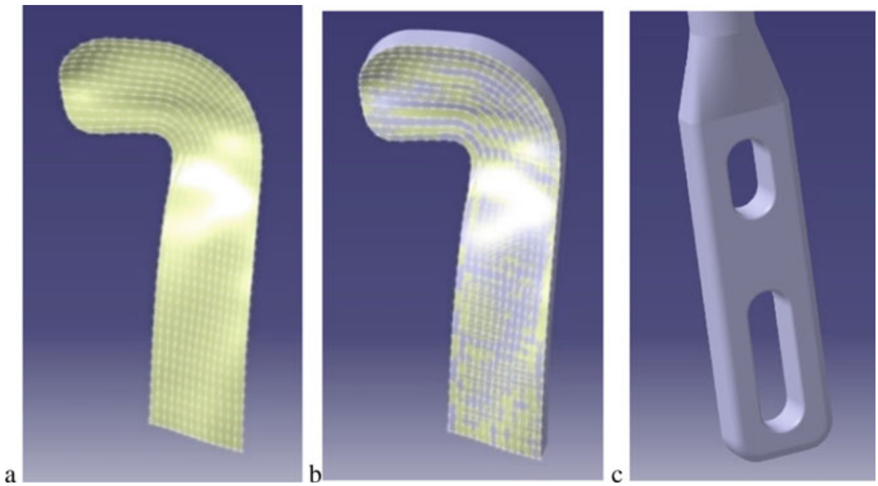

Fig. 6.22 Construction of the plate implant: **a** creating a 3D surface; **b** creating a full model of proximal part of the fixator, **c** distal part of the fixator with the grooves for dynamization. (Reproduced from Manic et al. 2015c)

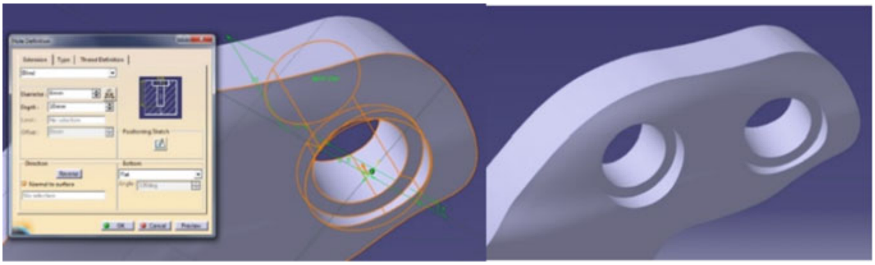

Fig. 6.23 Creation an additional scheme with points for screw holes. (Reproduced from Manic et al. 2015c)

The remaining parts of the internal dynamic fixator according to Mitkovic are made with the use of standard technical elements. It is important to mention that in the distal part of the plate fixator, two groves were created. These groves are used for conducting the process of dynamization (Fig. 6.22c).

The fact, the process of dynamization can be performed by using the lower groove for the screw bolts, i.e., when the screw bolt from the upper groove, blocking the dynamization process, is removed. In this way, a direct contact between bone fractured fragments is achieved, which enables forming of a new bone tissue and supports the bone healing process. After the internal fixator has been shaped, the construction of screw holes on the proximal part of the fixator is performed, according to the orthopedist's request. The process of screw holes creation is based on projection points and created tangent planes and is performed on the part of the fixator's surface (Fig. 6.23).

The final model of the internal dynamic fixator for tibia according to Mitkovic is shown in Fig. 6.24.

Physical models, used in educational courses for orthopedic surgeons (organized by "Mitkovic School"), are shown in Fig. 6.25 (http://www.mitkovic.net/index.html).

6.3.2.3 Case Three—Creation of Human Humerus Plate Implants

In this example, the design process for the creation of geometrical models of two plate implants (cloverleaf plate and personalized reconstruction plate) will be shown. The geometry and shape of these implants are personalized for the specific patient.

To create the parametric models of plates, CT scans of two human upper arms were used. The first scan was used as a sample scan and the second scan was considered as a test scan, to test the method. Both scans were taken from the men who were the same age (50-year-old), and they were almost the same height and weight. CT scanning was performed at Clinical Center Nis (Nis, Serbia) by Toshiba 64 slice scanner.

Scanning parameters were defined according to the standard protocol: radiation of 120 kVp, current of 150 mA, rotation time of 0.5 s, exposure time of 500 ms,

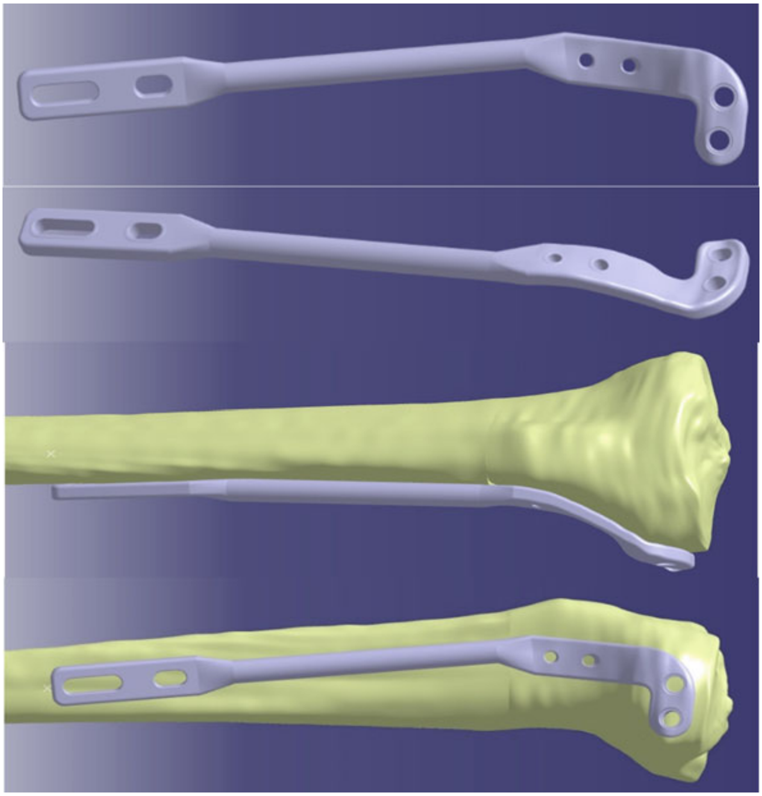

Fig. 6.24 Final model of dynamic fixator according to Mitkovic. (Reproduced from Manic et al. 2015c)

rotation time 0.5 s, slice thickness of 0.5 mm, image resolution 512 × 512 px, pixel size about 0.38 mm for sample scan and 0.40 for test scan, 16 bits allocated and stored.

Patient-Adapted Cloverleaf Plate Implant

The fracture of proximal part of humerus (the bone above the elbow, which connects arm to the shoulder) was present on the sample scan. The applied fixation implant for the treatment of this fracture was a modified cloverleaf plate (Bacon et al. 2008; Uhthoff et al. 2006). The universal procedure for the creation of a personalized cloverleaf plate implant is presented in Fig. 6.26. The procedure contains several processes/sub-procedures (Rashid 2018):

- **Diagnostic procedure**—Analysis of patient medical data. It is possible to analyze them using computer software (e.g., Materialise Mimics) or an analog X-ray device.

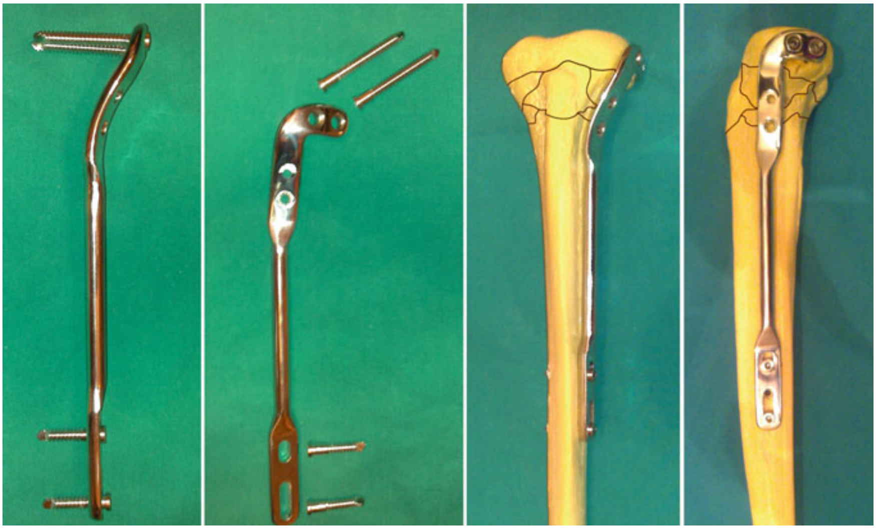

Fig. 6.25 Physical model of dynamic fixator according to Mitkovic. (http://www.mitkovic.net/index.html)

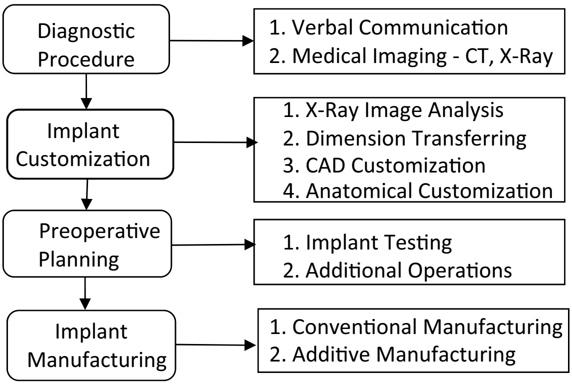

Fig. 6.26 Scheme of the process (surgical case). (Reproduced from Rashid 2018)

- **Implant Customization**—The creation of a prototype 3D model of the customized fixation implant for the particular patient. The detailed description will be found in the further text.
- **Process before operation**—After the creation of the geometrical model of the implant, orthopedic intervention is planned and stimulated by orthopedic surgeon. The crucial point is to plan all surgical intervention steps to provide the best possible treatment which can be very complex. Therefore, it is recommended that this process should be connected with the previously mentioned one. In that way, 3D implant model (geometry and topology) will be optimally customized to the

patient needs and surgeon's requirements. Many different computer software can be used for this purpose (e.g., Vitrea, Mimics, etc.) (Picard et al. 2019).

- **Manufacturing of the implant**—The last step is manufacturing of the geometrical prototype of the customized implant. Conventional manufacturing can be used for this purpose, or some other production technologies (e.g.~~,~~ based on additive technologies. Since the implant's shape is very complex (free form surface), it is advisable to use additive technologies. If we use biocompatible material, the result is a physical model of the customized implant.

Design Process of the Cloverleaf Plate Parametric Model

During this process we create the geometrical model of the customized plate for a particular patient. We define parameters according to the dimensions measured on the 3D model of the sample humerus model. The measured dimensions are shown in the Fig. 6.27a, in AP plane. Two crucial dimensions must be defined: distal part of the plate (RDmax) and proximal part of the plate (RPmax). RDmax and RPmax are maximal distances from the humeral body anatomical axis to the outer bone surface. These two dimensions combined with other defined radiuses, make it possible to create the profile curves. These profile curves are used to develop an initial plate surface model with the multisection feature in CATIA.

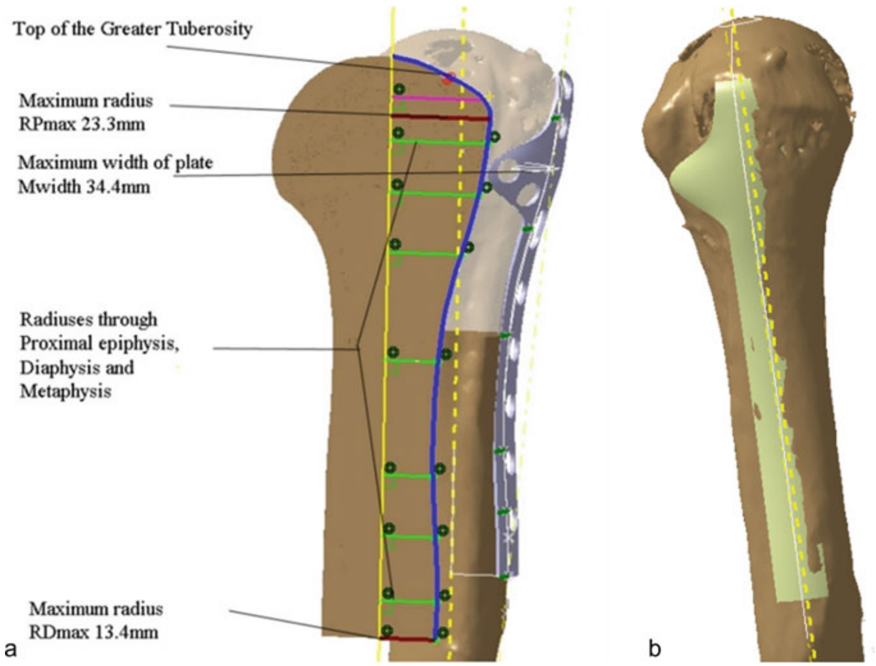

Fig. 6.27 **a** Defined dimensions (parameters) of the humerus bone presented in AP plane, **b** surface model of the plate contact surface. (Reproduced from Rashid et al. 2017)

Profile curves are created as circle arcs. Their limits are determined as the values of both RPmax and RDmax. To define the widest part of the proximal plate part, new parameter Mwidth was set. Mwidth is define as radius in AP plane. It represents a circle chord which defines how wide plate envelops the proximal humerus outer surface. The predefined values value is 34 mm. Using profile curves and values measured from sample model, geometrical model of the contact surface was created. To create solid model of the plate it is necessary to add thickness to the surface (Fig. 6.27b).

We can consider the defined dimensions as parameters and their values are changed due to the measurements obtained from radiological images. Accordingly, that prototype can be considered as a parametric prototype. To test the parameters, test humerus model was used. Dimensions were defined and measurements were performed. Maximal values were: 21.2 (RPmax), 11.5 (RDmax), and 30.3 (Mwidth). There was an overlapping between humerus polygonal model and the plate surface, thus the appropriate transformation of the plate location had to be applied. Plate surface was translated normally from the Lateral—Medial (Sagital) plane for 1 mm and rotated around its axis (Lateral—Medial Angle—LMA) for about 11°. The line between middle point of the widest part (Mwidth) of the proximal section of the plate and the middle point at the RDmax location (distal end of the plate) is defined as the plate axis, and it is located in the LM (Lateral—Medial) plane of the humerus (Fig. 6.28a).

One more rotation about the axis positioned in the Transverse (Axial) plane of humerus, positioned just below the metaphysis, was performed. This axis passes through the point on anatomical axis and it is normal to AP plane. Transverse Angle (TA) is the angle of rotation, and it equals 0.5° (Fig. 6.28b). To create solid model of the plate thickness of 2 mm was added to the surface model.

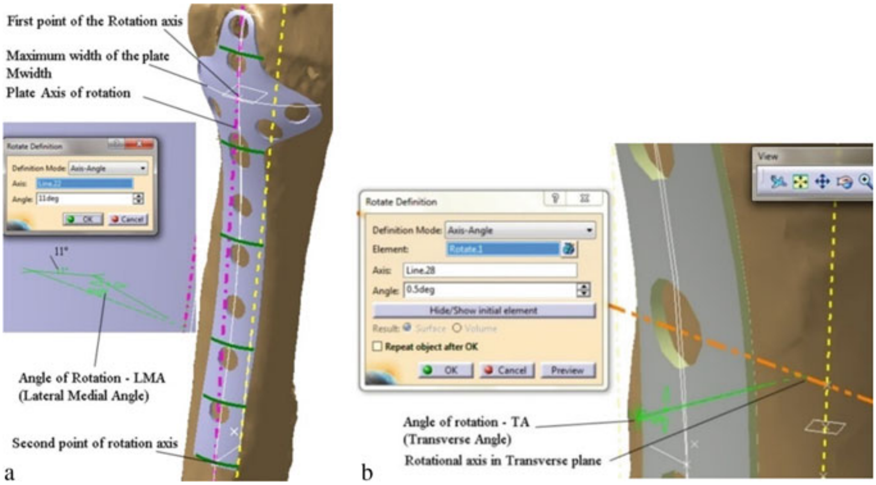

Fig. 6.28 Parameters definition for cloverleaf plate: **a** Mwidth and LMA angle definition, **b** TA angle definition. (Reproduced from Rashid et al. 2017)

Fig. 6.29 Assembly of the customized plate solid model and surface model of the humerus. (Reproduced from Rashid 2018)

Finally, the customized plate solid model was created, and assembly with the bone was set up (Fig. 6.29). There were no intersections between models indicating that the additional parameters were adequately chosen. If there is a requirement, it is possible to adjust the plate surface geometry by changing the values of the parameters.

There were some deviations between the intersections of the AP plane and the plate. This maximum deviation was 2.267 mm in the proximal epiphysis section and the one which was observed in the proximal diaphysis section was 2.44 mm.

The orthopedic surgeons who took part in this research found that these two deviations, which were located on the top and bottom area of the plate, were acceptable. About 89% of the plate contact surface is under 1 mm distance from the periosteum surface of the treated bone, which is quite acceptable as stated by orthopedic surgeons.

We can state that the current parametric model is suitable for DCP and LCP fixation. The form of the plate was appropriately defined, and the described method can be applied. There is still a need for additional verification, which will be performed by using more bone samples and possibly additional parameters.

Creation of Plate Implant Geometrical Model for Distal Humerus

Reconstruction plates are used as a repairing solution for various clinical indications, such as different bone fractures and traumas. For humerus bone, specifically for the distal humerus, reconstruction plates are used for the fixation on the lateral and medial side (Bacon et al. 2008). On the lateral side, the plate can be placed distally onto the posterior aspect of the humeral capitellum. On the medial side, the plate is usually bent around the medial humeral epicondyle.

This research is focused on developing a new method for creating a specific type of medial reconstruction plate. MAF was used for the construction of the plate geometrical model. Curves used in the construction of the distal humerus surface model were used to construct the parametric prototype model of the reconstruction plate. Four radiuses were defined, and one medial curve was created as a helper curve for surface orientation. Radiuses were defined on spline curves which were applied for the construction of the distal humerus surface model. Each radius defines one arc of adequate length. Arc length is a changeable parameter, and it defines the width of the plate (it can be constant). Each arc length is defined by four corresponding arc angles. One more parameter was defined, and that was the angle of bending in the lower part of the medial plate. Defined radiuses (R1…R4), angles (α1…α4), medial curve, and bending angle (Bending Angle) are presented in Fig. 6.30a. The values of parameters

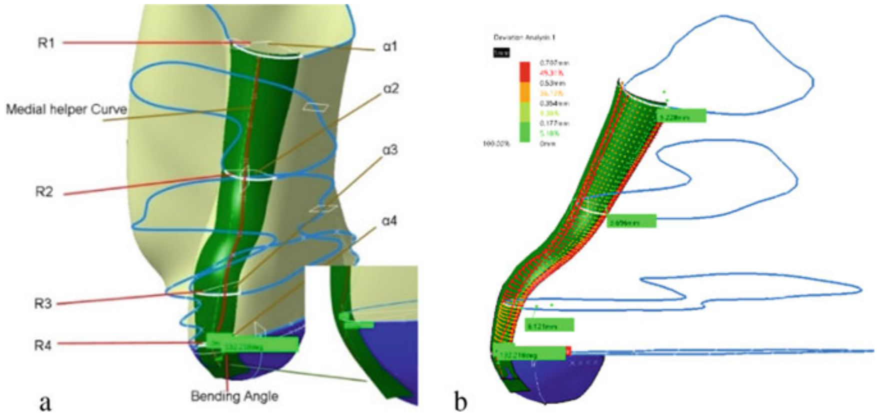

Fig. 6.30 Parameters and analysis of the reconstruction plate contact surface **a** defined parameters and surface model of the bone-plate contact surface, **b** deviation analysis between plate contact surface and bone surface. (Reproduced from Rashid 2018)

Table 6.1 Values parameters measured for the specific patient

R1 [mm]	R2 [mm]	R3 [mm]	R4 [mm]	Bending angle [°]
5.3	3.7	6.1	5.7	132.2°
α1 [°]	α2 [°]	α3 [°]	α4 [°]	
109.2	126.6	58.6	54.5	

for this specific patient are presented in Table 6.1. These values of parameters were applied for the construction of the plate contact surface prototype model. That surface was at the right distance from the bone surface, and the intersection with the surface of the bone was minimal and only at the end of the bent part.

Deviation analysis between the surface model of the distal humerus and the plate contact surface is shown in Fig. 6.30b. It can be concluded that maximal deviation is 0.707 mm, in the outer region of the plate surface—closer to the edges. The deviation range is from 0.177 mm to 0.707 mm, which is pretty accurate concerning the requirement that the plate contact surface should correspond to the bone outer surface as maximal as possible (Perren et al. 1988). Analysis confirms that nine parameters were enough for the definition of implant surface shape with respect to the defined requirement.

There should be mentioned that during the real surgical intervention, a surgeon can manipulate the plate. The surgeon can rotate, move, and perform additional bending (the amount of applied bending would be much smaller) to adapt the plate to the bone.

The solid prototype model of the reconstruction plate was constructed applying the thick surface feature in CATIA (thickness was defined as 3 mm) and it is presented in Fig. 6.31.

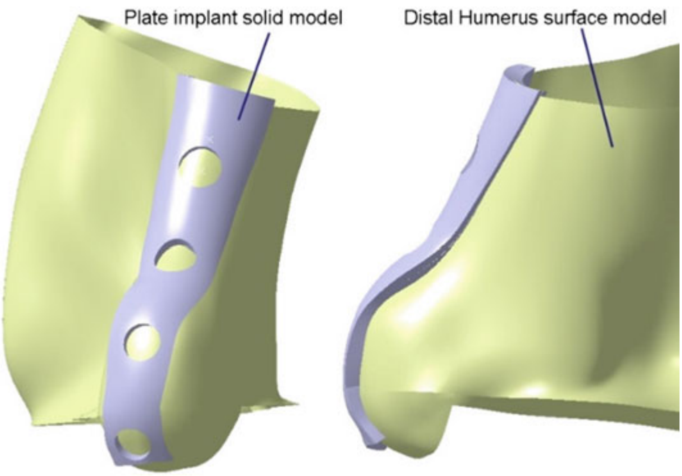

Fig. 6.31 Assembly of the plate implant solid model and bone surface model. (Reproduced from Rashid 2018)

6.3.2.4 Case Four—Customized Anatomically Adjusted Plate for Fixation of Mandible Fractures

Mandible fractures are a common injury due to the mandible's lack of structural support. Various fixation elements are used in the treatment of such injuries. To improve the quality of the orthodontists' interventions, anatomically correct and geometrically accurate customized implants are desirable. The side of the implant, being in contact with the periosteum covering the outer surface of the mandible, is fully aligned with the shape of the mandible outer surface near the fracture. The MAF was used for the creation of human mandible surface models (Majstorovic et al. 2013). The steps used for the creation of mandible surface model by MAF were described in (Mitic et al. 2020).

The same procedure, presented in the previous sections, was applied for the creation of 3D model of simple fracture. This model was created on the surface model of the mandible (Fig. 6.32a) with the assistance of the medical practitioner involved in this research (Fig. 6.32b, c).

Close to the model of the fracture, a datum plane, not far from the surface of mandible, was created (Fig. 6.33a). The surgeon suggests and defines the position and orientation of this plane. The contour of the customized implant is drawn inside this plane (Fig. 6.33b). Eighteen spline curves were created in the area limited by the created contour. Each of the spline curves follows the shape of the mandible surface model as presented in Fig. 6.33c.

The surface which represents the internal side of the plate implant was created by the application of these curves. After this step, all the surfaces are removed, and the only surface left is the one that presents the internal side of the plate leaning on the bone. The volume model of the fixation plate is created by the extrusion of the

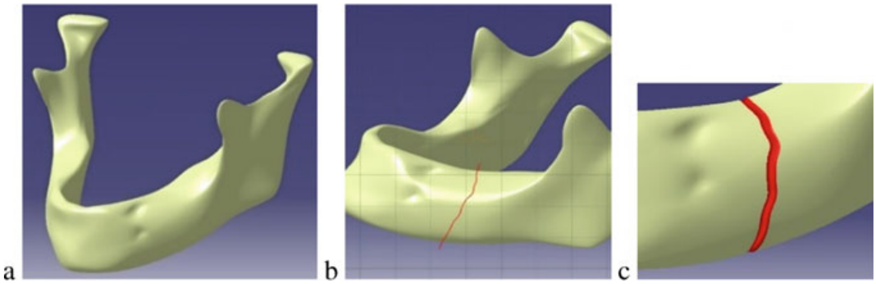

Fig. 6.32 Mandible with the fracture: **a** mandible surface model, **b** fracture position, **c** Fracture model. (Reproduced from Manic et al. 2015b)

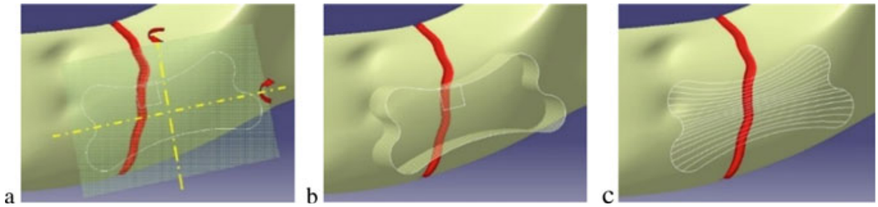

Fig. 6.33 Implant profile creation procedure: **a** datum plane, **b** plate contour, **c** Contour spline curves. (Reproduced from Manic et al. 2015b)

surface normal to the created datum plane. On the volume model, screw holes were created and the model was finalized (Fig. 6.34a). As the last step, assembly of the created models was constructed, as presented in Fig. 6.34b.

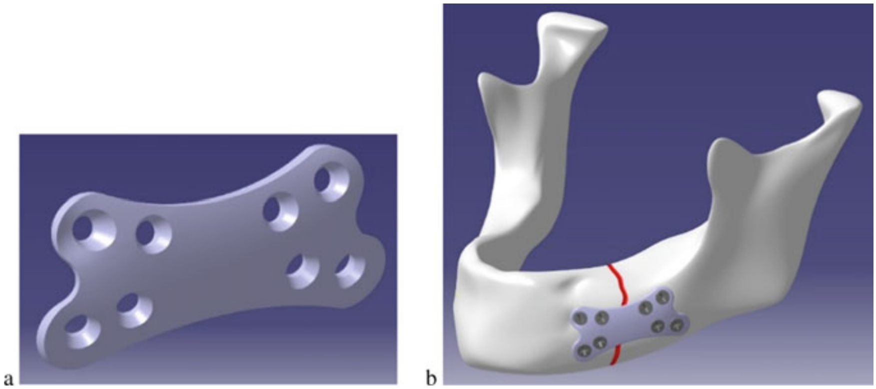

Fig. 6.34 The Final 3D volume model of the customized plate: **a** plate solid model, **b** assembly of plate and mandible models. (Reproduced from Manic et al. 2015b)

6.3.2.5 Case Five—Creation of Personalized Implant for a Patient with Congenital Malocclusion Class III

Progeny is characterized by an overdeveloped lower jaw in all directions and the goal of surgery is to shorten the length of the lower jaw. The most common surgery used for this purpose is a bilateral mandibular split osteotomy.

There are two fixation techniques: non-rigid and rigid fixation. Intermaxillary non-rigid fixation showed a significant tendency to relapse. Another technique, rigid fixation at three points with implants (screws) or fixation with plates indicates the mentioned technique gives quite good and stable results even if there is a certain degree of recurrence (Epker 1977). This way of fixation has become the gold standard in the care of such patients because it enables a comfortable and faster recovery of the patient. The main disadvantage of this technique is that the fixation plates are uniform and factory-produced, thus it is necessary to adjust them anatomically to the bone surface prolonging the duration of already complicated surgical intervention.

During the surgery of progeny, it is important to remain the exact position of the condyle as before the intervention. However, condylar displacement in relation to the pre-operative position can cause several complications (increased risk of temporomandibular dysfunction), and therefore, additional attention is focused on the choice of fixation. The solution for the problem solving is to make personalized plates that would completely correspond to the planned position of the bone fragments after osteotomy. The geometry and topology of the personalized plates correspond to the shape of the patient's bone, thus enabling adequate stability of the broken fragments. The steps used to create 3D model of a customized plate were presented in Mitic et al. (2019):

- Patient scanning on X-ray and Sirona SL Orthophos scanners
- Anatomical feature recognition
- Definition of the Referential Geometrical Entities on 2D medical image
- Importing the scanned model into the CATIA application
- Determination of the rotation axis of the temporomandibular joint on a 3D polygonal model of the mandible
- Creation of the geometrical model of the fracture
- Selecting the location on the mandible where the customized plate will be placed
- Adjusting the geometry of the customized plate according to the requirements of the surgeon
- Creating a customized 3D model of the plate
- 3D printing of customized plates.

In accordance with the bone anatomical and morphological characteristics, two anatomical reference points are defined in the 2D medical image: Menton (Me) and Gonion (Go). Menton is the lowest point on the mandibular symphysis and Gonion is the lowest inferior point on the corner of the mandible. The horizontal (mandibular) line was obtained by connecting two anatomical points.

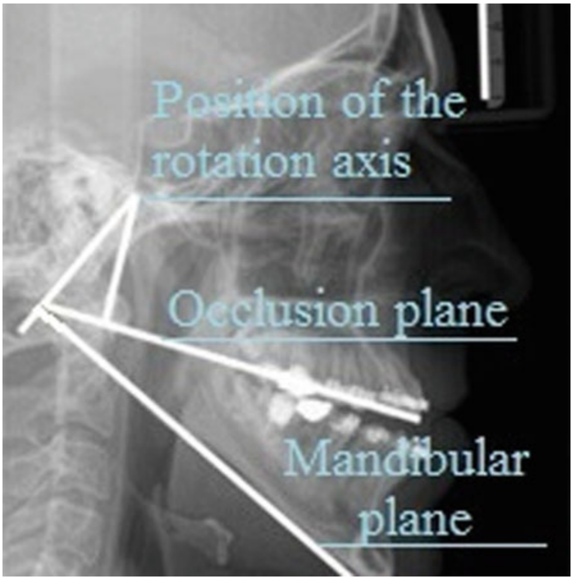

Fig. 6.35 Reference geometric entities in a 2D medical image. (Reproduced from Mitic 2019)

The next step is to determine the occlusal line. The occlusal line is an imaginary line that theoretically implies the contact of the occlusal surfaces of the teeth at the basic positions and movements of the lower jaw.

The following step is to determine the position of the temporomandibular joint rotational axis (point) on a 2D medical image. Through the point (representing the position of the temporomandibular joint rotational axis) at a right angle, the distances concerning the line of the mandible and occlusion are determined (Fig. 6.35). The measured distance values were used to determine the position of the axis of rotation on the 3D scanned model.

The same referential anatomical points were used for the 3D polygonal model of the patient mandible. By connecting the referential anatomical points, planes are created: mandibular and occlusal (Fig. 6.36a). The position of the temporomandibular joint axis of rotation is determined in the cross-section of the defined normal planes (orthogonal to occlusion and mandibular planes) (Fig. 6.36b).

The most important step is to create a model of fracture (the cut line). In cooperation with maxillofacial surgeons, the cut line was determined on the bone surface of the polygonal model and was placed in front of the seventh tooth on the left and right sides. After cutting the polygonal model along the cut line on the left and right sides, the rotation and movement of the lower jaw are performed in relation to the rotational axis of the joint. After rotating and moving, the lower jaw is brought into the appropriate position, in which a satisfactory aesthetic form of the face was achieved. Finally, the most important goal was achieved—a good occlusion.

After moving and rotating, the parts of the lower jaw are brought to the appropriate position and the size of the bone tissue that must be removed is determined. In this way, maxillofacial surgeons are informed about the overall outcome of the

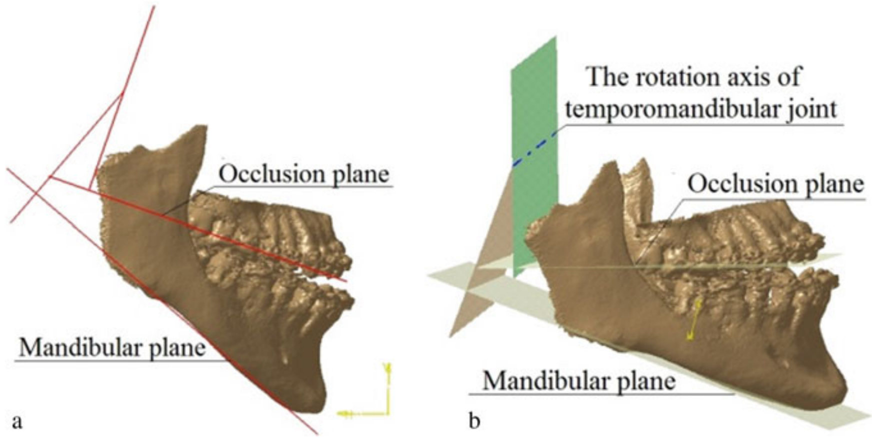

Fig. 6.36 The process of determining the position of the axis of rotation on a 3D polygonal model **a** determination of the mandibular and occlusal planes, **b** intersection of normal planes. (Reproduced from Mitic 2019)

surgery, before performing it (Fig. 6.37a). Newly formed occlusive relationships can be analyzed and indicate possible changes in the operative plan or may indicate the need for pre-operative orthodontic treatment.

Around the referential line on the polygonal model of the lower jaw (Fig. 6.37b), spline curves were created on the extracted surface, which are later going to be used to generate the inner side of the personalized plate (Fig. 6.38). In this way, the geometry and topology of the personalized plate are fully adapted to the patient's bone shape. The personalized plate surface 3D model was created by extruding the surfaces.

The process of creating the personalized plate shape is repeated on the right side of the lower jaw. For easier recognition, the corners at the bottom of the personalized plates are cut. In this way, the maxillofacial surgeon can easily orient in recognizing the left and right personalized plates. The personalized plate on the left and right is shown in Fig. 6.39.

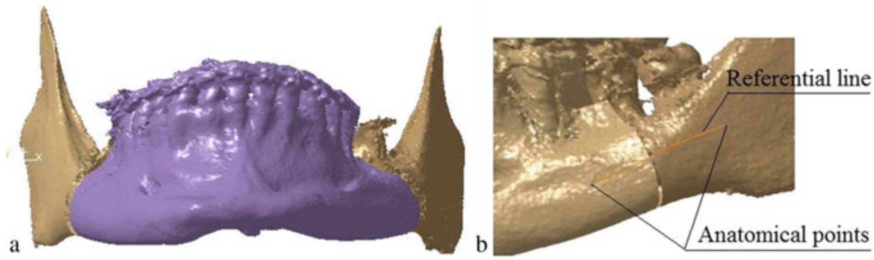

Fig. 6.37 **a** solid model of the adapted part of the lower jaw, **b** cut line of the lower jaw. (Reproduced from Mitic 2019)

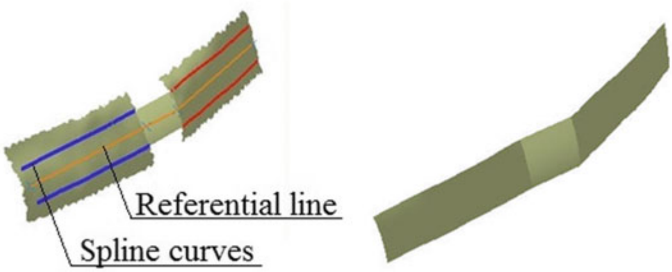

Fig. 6.38 Personalized plate surface model. (Reproduced from Mitic 2019)

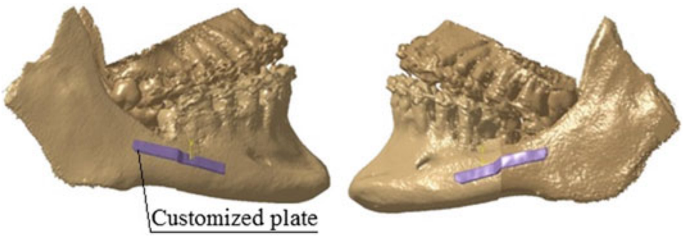

Fig. 6.39 Personalized implant on a 3D polygonal model of the lower jaw and printed model. (Reproduced from Mitic 2019)

6.4 Personalized Implant Manufacturing

In this chapter manufacturing technologies used to produce plate implants will be presented.

6.4.1 CNC Machining (Milling)

In the fabrication of implants made of titanium alloys conventional machining processes (turning, milling, drilling, high-speed cutting), forming processes (cold and hot forming, hydroforming, forging), substitutional machining processes (laser cutting, water-jet cutting, direct metal laser sintering, targets metal deposition technology) are applied. Those technics are very challenging since titanium alloys have very high tensile strength, low ductile yield, 50% lower modulus of electricity (104 Gpa), and about 80% lower thermal conductivity than alloys made of steel. Greater “spring back “may be caused by the lower modulus of elasticity and deflation of the process object. That means that the tools of greater clearness and more rigid setups should be used. In the zones of the tool contact high temperatures and pressures can arise (the tool-to-workpiece interface). Laminar chips can remove no more than 25% of the heat and the rest is eliminated through the tools. Conditioned by this phenomenon, it is possible to treat titanium alloys at relatively low cutting speeds. If titanium alloys are treated at higher temperatures which are caused by friction, titanium is more chemically reactive, and it can “weld “to the tool parts during the process. If the surface becomes over-heated, the interstitial pickup of oxygen and nitrogen can occur. The result of this is the production of a hard and brittle alpha case. For cutting titanium during this operation, it is advisable to use carbides with high WC–Co content (K-grades) and high-speed steels with high cobalt content. Cutting depths of turning operations should be as large as possible, speed of cutting Vc from 12 to 80 m/mm and almost 50% lower than the tools of High-Speed Steel (HSS) are used. Large volumes of cooling lubricants should be used to remove the generated heat. In the presence of chlorine, titanium can be susceptible to stress corrosion failures, so it is better not to use chlorinated cutting fluids. Since the titanium is very reactive at high temperatures, any kind of hot working or forging operation should not be performed above 925 ºC (Balazic et al. 2007).

6.4.2 Metal Forming

Many factors affect titanium alloys in terms of deformability. These factors can be temperature, structure, chemical composition, and strain velocity. One of these factors is a way of deformation. The main reasons why plastic work on titanium alloys is considered to be difficult are susceptibility to the creation of the build-ups on the tools (adhesive wear), and low thermal conductivity, high friction coefficient, and high reactivity with gases (oxygen, nitrogen, hydrogen), especially in higher temperature. This means that these parameters of deformation should be chosen according to the process specificity (Adamus 2007).

6.4.3 Forging

Forging titanium and its alloys is the most frequent applied plastic working process in implant production. Different kinds of endoprosthesis stems are produced by forging. These stems are mainly presented in endoprosthesis of knee, elbow, or hip joint. Stem is the basic element of each joint endoprosthesis. Endoprosthesis stem transfers complex, variable in cycles mechanical loads for 10–15 years. Nowadays only forged stems are used because there was a very negative experience with the casting stems for many years. The forging process of Ti6Al4V titanium alloy is performed in the span of temperature 1000–800 ºC. The main influences on the properties of the forged elements have temperature and strain velocity. Due to the high sensitivity to strain velocity, it is more appropriate to use hydraulic presses than hammers for the forging titanium. If hydraulic presses have used the alloys’ formability increases by about 10–12%. Since titanium has low thermal conductivity and due to the high coefficient of friction between the deformed metal and tool, strain heterogeneity may occur.

The result is structure and properties heterogeneity. There are some problems and obstacles in the hot forging of titanium alloys because of the strong affinity with hydrogen, oxygen, and nitrogen. Gaseous diffusion causes some changes on the top layer of the product in both microstructure and chemical constitution. These changes are not acceptable when we talk about endoprosthesis stems, so there is a need to overcome that. It is possible if we overcome three “technological barriers”. These obstacles are: to protect forging surface against gaseous diffusion while it is being heated till the forging temperature is reached; between the deformed metal and the tool is fractional resistance which needs to be decreased; the third “barrier” is proper heat treatment (homogenizing treatment) after the process of forging. This implies that an adequate protective atmosphere must be provided while the slug forging (rods) is being heated. At the same time, it is necessary to use adequate technological lubricant. These lubricants have double role: lubricating and protection (Adamus 2007).

6.4.4 Stamping of Titanium Alloys

To produce some elements for the knee endoprosthesis (e.g.~~,~~ clamping plates of the polyethylene inserts, condyle elements of the sled endoprostheses) the process which is used is stamping. Stamping technology is used in some other productions such as different kinds of castings: for the artificial heart chamber, endoprosthesis accelerator cups. Some tools, e.g., forceps, are produced by stamping etc.

The adequate plastic properties (annealed state) and microstructure are necessary at the titanium sheets which are applied for draw-parts. It is possible to perform the forming process of titanium sheets in room and higher temperature (semi-hot forming). Semi-hot stamping requires a temperature of 350–400 °C. Decreasing the numbers of operations and increasing the accuracy of the work sheet-titanium forming in higher temperature is performed. It is considered that it is much more difficult to perform sheet-titanium forming process, especially of Ti6A14V alloy than performing the process of the sheet-steel forming. The difficulty results from high strain hardening, high yield point, tensile strength, and susceptibility to the creation of the titanium “build ups” on the surface of the steel tools and high frictional resistance, high value of the Re/Rm. Applying the intermediate annealing must be in the cold stamping process. Stress relief annealing must be applied to the final products to remove internal stresses. Both annealing’s: intermediate and stress relief annealing must be performed in the atmosphere which is protective. The criteria for determination sheet ability to deep drawing operation is limit drawing coefficient $m = d/D$. When the cold stamp process of Ti6A14V titanium alloy is applied $m = 0.83/0.76$ and during the hot stamp process $m = 0.83/0.63$. The main impact on the process of forming sheet-titanium has strain velocity, so it is preferable to apply the use of the hydraulic press for titanium sheets forming with a velocity lower than 0.25 m/s.

6.4.5 Die Shearing, Re-Striking

The die shearing process is the process that is mainly used in the production of surgical instrumentation and implants. The starting material in this production is cold-rolled annealed titanium sheets. The next stage is shaping the blanks applying restriking (to get work hardening in the surface layer) and machining (holes are drilled and milled). Next, after restriking and machining, the next stage of the process is polishing the implant surface with the aim to get adequate quality of the surface. Die shearing restriking and milling are used in the production of different precise surgical tools (e.g., tweezers).

Titanium sheet cutting is often performed by some conventional methods (a guillotine or a blanking tool).

6.5 Conclusion

The presented method for implants creation is based on the application of regular and parametric 3D bone models. After the initial design, further model adjustments to the bone and manufacturing methods can be performed. This method can be used for various types of internal fixation implants, that can further be directly attached to any bone surface. The inner surfaces lying on the bone are fully aligned with the bone surface. In this way, it fits the bone ideally. This method provides the possibility to create a 3D model of positioning and insertion of the implant and tiles, hence~~,~~ it can be used as a simulation model in pre-operative planning. Furthermore, a full analysis and shape and dimension optimization of fixation material can be performed, thus it can be applied to other tile type implants and for any human bone. The requirement that must be met is to have a 3D bone model with a fracture model.

This method has significantly improved the technique for the design and production of anatomically adjusted internal fixation implants and offers the possibility of their production by 3D printing or by CNC machine.

References

Adamus J (2007) Forming of the titanium implants and medical tools by metal working. Arch Mater Sci Eng 28(5):313–316

AO Foundation (2021) Plate fixation. https://www.aofoundation.org/. Accessed 10 May 2021

Arnone JA (2011) Comprehensive simulation-based methodology for the design and optimization of orthopedic internal fixation implants. Dissertation, University of Missouri, Columbia

Bacon S, Smith WR, Morgan SJ et al (2008) A retrospective analysis of comminuted intra-articular fractures of the tibial plafond: open reduction and internal fixation versus external Ilizarov fixation. Injury 39(2):196–202

Balazic M, Kopac J (2007) Improvements of medical implants based on modern materials and new technologies. J Achiev Mater Manuf Eng 25(2):31–34

Berkin CR, Marshal DV (1972) Three-sided plate fixation for fractures of the tibial and femoral shafts: a follow-up note. J Bone Joint Surg Am 54(5):1105–1113

Epker BN (1977) Modifications in the sagittal osteotomy of the mandible. J Oral Maxillofac Surg 35(2):157–159

Fragomen AT, Rozbruch SR (2007) The mechanics of external fixation. HSS J 3(1):13–29

Gardner MJ, Helfet DL, Lorich DG (2004) Has locked plating completely replaced conventional plating? Am J Orthop (belle Mead NJ) 33(9):440–446

Ghyar R, Subburaj K, Ravi B et al (2013) Adaptive probabilistic approach for selecting tumour knee prosthesis. Comput Sci Inf Syst 10(3):1407–1428

Grewal R, MacDermid JC, King GJ et al (2011) Open reduction internal fixation versus percutaneous pinning with external fixation of distal radius fractures: a prospective, randomized clinical trial. J Hand Surg Am 36(12):1899–1906

http://www.synthes.com/MediaBin/International%20DATA/036.000.380.pdf. Accessed 9 Jan 2015.

Jain R, Podworny N, Hupel TM et al (1999) Influence of plate design n cortical bone perfusion and fracture healing in canine segmental tibial fractures. J Orthop Trauma 13(3):178–186

Koonce RC, Baldini TH, Morgan SJ (2012) Are conventional reconstruction plates equivalent to precontoured locking plates for distal humerus fracture fixation?a biomechanics cadaver study. Clin Biomech (bristol, Avon) 27(7):697–701

Lai YC, Tarng YW, Hsu CJ et al (2012) Comparison of dynamic and locked compression plates for treating midshaft clavicle fractures. Orthopedics 35(5):697–702

Majstorovic M, Trajanovic M, Vitkovic N et al (2013) Reverse engineering of human bones by using method of anatomical features. CIRP Ann 62(1):167–170

Manic M, Stamenkovic Z, Mitković M et al (2015a) Design of 3D model of customized anatomically adjusted implants. Facta Univ Ser Mech Eng 13(3):269–282

Manic M, Vitkovic N, Stamenkovic Z et al. (2015b) Customized anatomically adjusted plate for fixation of mandible internal fractures. Paper presented at BIBE International conference on bioinformatics and bioengineering Belgrade, Serbia

Manic M, Mitkovic M, Stamenkovic Z et al. (2015c) Designing of internal dynamic tibia fixation 3D model according to mitkovic type TPL. ICIST 5th international conference on information society and technology, proceedings, issued in Belgrade, Serbia, pp 223–229.

Manic M, Vitkovic N, Stojkovic M et al. (2018) Design of customized anatomically adjusted implants. Invited paper at 13th international scientific conference, Novi Sad, Serbia

Matthys R, Perren SM (2009) Internal fixator for use in the mouse. Injury Int J Care Injured 4:103–109

Mitic J (2019) Creating a 3D parametric model of human mandible using artificial intelligence techniques. Dissertation, University of Nis, Serbia

Mitic J, Vitkovic N, Manic M et al (2020) Reverse modeling of the human mandible 3D geometric model. Vojnosanit Pregl 77(3):262–270

Mitkovic M, Milenkovic S, Micic I et al (2012) Results of the femur fractures treated with the new selfdynamisable internal fixator (SIF). Eur J Trauma Emerg Surg 38(2):191–200

Musuvathy S, Azernikov S, Fang T (2011) Semi-automatic customization of internal fracture fixation plates. Engineering in medicine and biology society, EMBC, annual international conference of the IEEE, Boston MA, pp 595–598

Nooshin ST (2011) Modelling and analysis of a dynamic hip screw: biomechanical analysis of a dynamic hip screw under different load conditions. Dissertation, Swinburne University of Technology, Australia

Perren SM, Cordey J, Rahn BA et al (1988) Early temporary porosis of bone induced by internal fixation implants: a reaction to necrosis, not to stress protection? Clin Orthop 232:139–151

Picard F, Deakin AH, Riches PE et al (2019) Computer assisted orthopedic surgery: past, present and future. Med Eng Phys 72:55–65

Rashid M (2018) Parametric models of the plate implants for humerus bone. Dissertation, University of Nis Ph. D thesis, Mechanical Engineering Faculty, University of Nis, Serbia

Rashid MM, Husain KN, Vitkovic N et al (2017) Geometrical model creation methods for human humerus bone and modified cloverleaf plate. J Sci Ind Res 76:631–639
Rose PS, Adams CR, Torchia ME et al (2006) Locking plate fixation for proximal humeral fractures: initial results with a new implant. J Shoulder Elbow Surg 16(2):202–209
Ruedi TP, Buckley RE, Moran CG (2007) AO principles of fracture management, vol 2, Specific fractures, 4th ed. Thieme, Stuttgart
Sanders BS, Bullington AB, McGillivary GR et al (2007) Biomechanical evaluation of locked plating in proximal humeral fractures. J Shoulder Elbow Surg 16(2):229–234
Stevanovic D, Vitkovic N, Veselinovic M et al (2013) Parametrization of internal fixator by Mitkovic. Paper presented at international working conference" total quality management—advanced and intelligent approaches", Belgrade, Serbia, 4–7 June 2013.
Stojkovic M, Milovanovic J, Vitkovic N et al (2010) Reverse modeling and solid free-form fabrication of sternum implant. Australas Phys Eng Sci Med 33:243–250
Stojkovic M, Korunovic N, Trajanovic M et al (2016) Design study of anatomically shaped latticed scaffolds for the bone tissue recovery. Paper presented at III South-East European conference on computational mechanics-SEECCM III, KOS, Greece
Takigami H, Sakano H, Saito T (2010) Internal fixation with the low-profile plate system compared with Kirschner wire fixation: clinical results of treatment for metacarpal and phalangeal fractures. Hand Surg 15(1):1–6
Uhthoff HK, Poitras P, Backman D (2006) Internal plate fixation of fractures: short history and recent developments. J Orthop Sci 11(2):118–126
VIHOS projekat Vihos project web site. http://vihos.masfak.ni.ac.rs. Accessed 30 Mar 2019
Vitkovic N, Milovanovic J, Korunovic N et al (2013) Software system for creation of human femur customized polygonal models. Comput Sci Inf Syst 10:1473–1497
Vitkovic N, Mitic J, Manic M et al (2015a) The parametric model of the human mandible coronoid process created by method of anatomical features. Comput Math Methods Med 3:1–10
Vitkovic N, Mitkovic MM, Mitkovic BM et al (2015b) Reverse engineering of the Mitkovic type internal fixator for lateral tibial plateau. Facta Univ Ser Mech Eng 13(3):259–268
Vitkovic N, Mladenovic S, Trifunovic M et al (2018) Software framework for the creation and application of personalized bone and plate implant geometrical models. J Healthc Eng 2018:1–11
Vitkovic N, Veselinovic M, Misic D et al (2012) Geometrical models of human bones and implants, and their usage in application for pre-operative planning in orthopedics. Paper presented at 11th international scientific conference MMA 2012—advanced production technologies, Novi Sad, Serbia, 20–21 September 2012.
Walsha S, Reindla R, Harveya E et al (2006) Biomechanical comparison of a unique locking plate versus a standard plate for internal fixation of proximal humerus fractures in a cadaveric model. Clin Biomech 21(10):1027–1031
Zheng G, Nolte LP (2015) Computer-assisted orthopedic surgery: current state and future perspective. Front Surg 2:1–14

Chapter 7
Method to Support Dental Implant Process Based on Image Processing

Sabrina Tinfer, Anderson Luis Szejka, and Osiris Canciglieri Junior

7.1 Introduction

The continuous evolution of the processing capacity of computerised systems combined with image processing techniques, artificial intelligence and reengineering has enabled the conception of expert systems capable of developing activities in an automatic manner, helping people in complex tasks or providing support for decision making.

In parallel with this evolution, computed tomography, created in the 1970s by Hounsfield (1973), revolutionised diagnosis by images, allowing the use of image processing algorithms in data extraction, three-dimensional reconstruction and in intelligent fault reconstruction systems (Canciglieri Jr. et al. 2010). However, although some areas already use these systems, others, such as implant dentistry, rely on the experience of the dental surgeon to define the implant and the prosthesis to be used.

These definitions occur through visual analysis of computerized tomography or magnetic resonance imaging, where the dental surgeon identifies the dental fault and analyses the region to be implanted, checking bone volume, nerve location, bone and tooth boundaries.

Based on this context, this chapter presents the study of the conceptual proposal of an expert system of design oriented to the process of dental implantation, whose objective is to seek from the concepts and techniques of image processing and dental implantation, to formulate a conceptual model that provides support for decision making through an expert system. This model has inference mechanisms that are

S. Tinfer · A. L. Szejka · O. Canciglieri Junior (✉)
Industrial and Systems Engineering Graduate Program, Pontifical Catholic University of Paraná, Curitiba, Paraná, Brazil
e-mail: osiris.canciglieri@pucpr.br

A. L. Szejka
e-mail: Anderson.szejka@pucpr.br

O. Canciglieri Junior and M. D. Trajanovic (eds.), *Personalized Orthopedics*,
https://doi.org/10.1007/978-3-030-98279-9_7

able to capture information contained in a representation, convert them, translate them and/or share them with other representations, offering subsidies to the dentist in choosing the most appropriate dental implant.

As main contributions of this research we can highlight: (i) improvement of the dental implant process based on analysis of precise information of the patient's dental arch extracted from CT images; (ii) reduction of the surgical procedure time, due to a previous planning of the dental implant process as well as the reduction in the dental implant absorption time due to trauma reductions; (iii) reduction of the dental implant rejection risks.

7.2 Research Methodology

This research is considered of applied nature, because according to Lacerda et al. (2013) seeks to understand, explain and produce knowledge for practical application, directed to the solution of specific problems, through theories already formulated. According to Collis and Hussey (2005), the applied research aims to find ways of applying the process to solve a problem, characterizing as exploratory, because it aims to provide insight into the subject and then propose a conceptual method. Regarding the approach, it is qualitative, because it seeks a deep understanding of a specific phenomenon through de-descriptions, comparisons and exploratory interpretations, in order to provide greater familiarity with the problem, according to Berto and Nakano (2000), researches of qualitative nature seek to unite the theories of facts, whether through the description and interpretation of conditions or events, generating knowledge through the relationships between the context and the actions of the process, generating particularized results based on phenomenological analysis of the researcher. This approach, according to Miguel et al. (2018), houses a series of interpretation techniques that seek to describe, decode, translate any other term related to the understanding and not to the frequency of occurrence of the variables of a given phenomenon.

The scientific objectives of this research are exploratory, as they propose a greater knowledge of the phenomenon whose definition or problematic are not yet completely explicit, as new variables need to be assessed in order to understand the impact they cause in the solution of the problem. The technical procedures adopted in this research are bibliographic and experimental. Bibliographical, because based on the bibliographical revision the knowledge to develop the conceptual model of the expert system of design oriented to the dental implant process was built. It is experimental, because initially it is necessary to determine the object of study and de-define the variables that influence the process, being possible, in this way, to control the object under study, differing from a case study, according to Souza et al. (2013), aims at the materialization of a product or service and/or the feasibility study of this, as in the case of the development of a decision support method.

7.3 Background Technologies

The evolution of computerized systems has made it possible to develop increasingly complex algorithms that perform processing almost instantly, being used increasingly in biological areas and helping the planning of diagnoses and treatments (Grauer et al. 2009). These diagnoses are often obtained by means of CT and MRI images in DICOM standard, allowing the extraction of characteristics or patient information.

Computed tomography is a method of image acquisition and reconstruction of a cross section based on attenuation measurements, as compared to conventional radiographs. These images are free of tissue overlapping, allowing the generation of a better-defined contrast, due to the elimination of scattering (Silva 2018).

The DICOM standard allows the evolution of image processing algorithms, since the information that is obtained, regardless of the manufacturer, are equal, allowing efforts to be focused on the development of systems in order to support doctors, dentists and nurses in their activities. Moreover DICOM image files, as shown in Fig. 7.1 detail “A”, can be converted into different formats, allowing them to be viewed on computers without dedicated applications and with the aim of compressing the size of the image file, allowing them to be sent over the network to remote computers (Graham et al. 2005). However, depending on the choice of format there may be considerable loss of important information for the analysis of this image (Wiggins et al. 2001).

In the case of implant dentistry, a branch of dentistry aimed at treating edentulous patients with dental implant rehabilitation, there has been an increase in the use of such equipment, especially in the area of 3D image reconstruction by means of computed tomography, providing a better visualization of the patient’s bone structure to the dental surgeon (Greboge, Canciglieri and Rudek 2010). This approach overcame some of the limitations found in conventional dental implant treatment

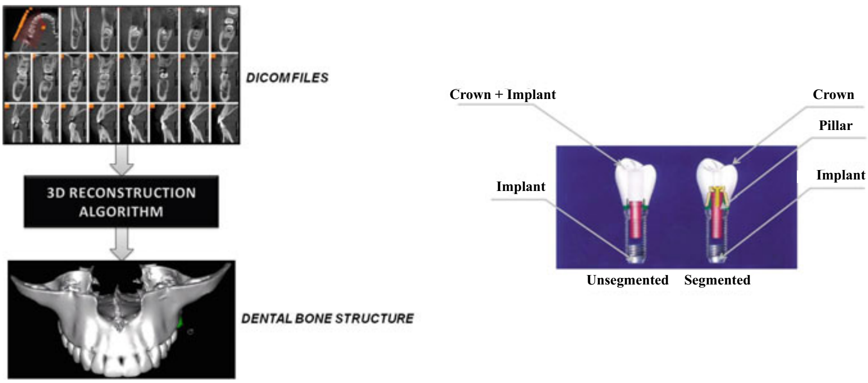

(A) 3D virtual reconstruction (B) Dental Implant

Fig. 7.1 Dental reconstruction and implant framework planning, especially in the pre-implantation stages, where it was based on 2D data obtained by MRI. Moreover, in this multi-view graphic environment, it provides image reconstruction, increasing the interactivity of the dental surgeon with surgical planning (Grauer et al. 2005).

An important point to be considered is also the advantage of using fixed prostheses (screwed), because according to Misch (2006), it is the longevity that these prostheses have when compared with partially fixed prostheses (screwed and cemented). The use of screw-retained prostheses reduces the risk of caries, improves hygiene, reduces the risk of sensitivity and contact with the root of existing teeth, improves the aesthetics of the prosthetic pillars, the hygiene of the bone in the edentulous space, reduces the risk of tooth loss of the prosthesis, and also the psychological aspect. The disadvantages are the high cost, long treatment time and the possibility of implant insertion failure due to inadequate planning and execution. Bottino et al. (2006) report as an advantage the non-occurrence of the re-absorption process of the bone structures that surround the missing dental element, as there is no absorption of the soft bone present in this region.

The implanted fixed prosthesis can be divided into segmented and non-segmented prosthesis, as illustrated in Fig. 7.1 detail "B". The segmented prosthesis consists of three distinct parts: implant, abutment and crown, whereas the non-segmented prosthesis consists of only two parts: implant and crown (built from an abutment connected to the prosthesis) facilitating the aesthetic result (Ochiai et al. 2003; Lewis et al. 1995; Breeding et al. 1995).

The use of computed tomography in the process of dental implantation has made the procedure increasingly safer, as is the case in other areas that already use these images in three-dimensional (3D) modeling, such as cranial reconstruction (Greboge et al. 2010), where it is possible to geometrically reconstruct the bone and virtually correct any flaws that may exist in the bone. These virtual reality technologies have been widely disseminated, improving the interpretation of patients' tomographic images in order to improve performance in the planned treatment and reduce recovery time.

7.4 Design for Dental Implant—*DFDImplant*

In dental implant processes, the dental surgeon specialist must determine which implant should best adapt to the patient, always taking into consideration the patient's dental structure through images obtained by computerized tomography. However, analysis based only on images is not deterministic and data such as bone density, area, bone volume, geometry of nerves, among other variables, are important to define the most suitable implant should be used. These variables are not found directly on the images, leaving it up to the experience of the dentist (oral and facial surgeon) to define the best implant, and in many cases, this ends up occurring during the surgical procedure without adequate planning. The inaccurate and reduced information makes the definition of the dental implant difficult and imprecise, and may cause its premature failure, bone loss, implant rejection and infections, compromising the treatment of partial and/or total edentulousness (Pye et al. 2009; Li et al. 2010).

The existing computer systems only provide the dentist with the process of three-dimensional reconstruction of the dental arch (Galanis et al. 2006), but these systems do not offer the subsidies or interactivity that the dentists need in their decision-making to determine the implant, as occurs in computer-aided diagnosis systems. These systems are important tools used and accepted in the medical field, as they provide support to the specialist based on knowledge already tested by specialists' dentists in their diagnoses. However, in the literature review (Tinfer et al. 2020), the use of this type of system in the dental implant planning process was not identified. However, it was found that it is possible to design a system of this level meeting this need, based on the processing of images obtained by computerized tomography. This system must be capable of analysing these images and selecting, based on the characteristics obtained, the set of implants and abutments which best suit the patient, supporting and corroborating the decision of the specialist dentist, contributing to a more suitable surgical planning.

The selection of the dental implant is a process of simultaneous and independent analysis of aspects such as bone structure, nerve positioning, geometry of the mouth and dental arch. Thus, the Design for Dental Implant Systems—***DFDImplant*** must provide support to multiple processes by performing a simultaneous and automatic analysis of the images searching for features that fulfill these issues, providing enough information to subsidize the selection of the set of implants that best fit each patient. Figure 7.2 illustrates the proposed conceptual framework of the ***Design for Dental Implant Systems—DFDImplant*** that is based on the concepts of product and manufacturing models. The question marks "?" (Fig. 7.2a) represent the existing interactions between the different representations within the Product Model and the existing interactions between the *DFDImplant* functions and the existing information in the Manufacturing Model.

The ***Product Model*** must be responsible for storing the requirements and information specifications needed to support the functions that compose DFDImplant. Each of these representations contains the information related to the product and to the dental implant procedures or techniques, such as the DICOM representation, which contains the tomographic files and patient information. Figure 7.2b illustrates the generic hierarchical structure of the Product Model consisting of DICOM, Dental Implant (Fig. 7.2c) and Guide Mask Representations respectively. Figure 7.2d illustrates a set of tomographic slices highlighting the region of interest where one or more of the patient's teeth are missing.

The ***Manufacturing Model*** should be responsible for storing the information regarding the manufacturing processes required during the stages of the surgical process. The Manufacturing Model contains the manufacturing technologies and knowledge that may help the dental surgeon during the procedure of implant insertion in the patient, such as drills, tools for tapping, torque wrenches, among others. However, the issues involved between the existing representations in this model will not be addressed in the research reported in this chapter.

The ***Design for Dental Implant Functions*** (***DFDImplant***) must be responsible for the definition of the inference mechanisms between one representation and another for the *conversion*, *translation* and *sharing* of information. These functions determine the selection of the most suitable dental implants for each case, taking into account the information from DICOM representations, Dental Implant and Mask representations in the product model, associating it with the most suitable manufacturing process contained in the representations in the manufacturing model (manufacturing

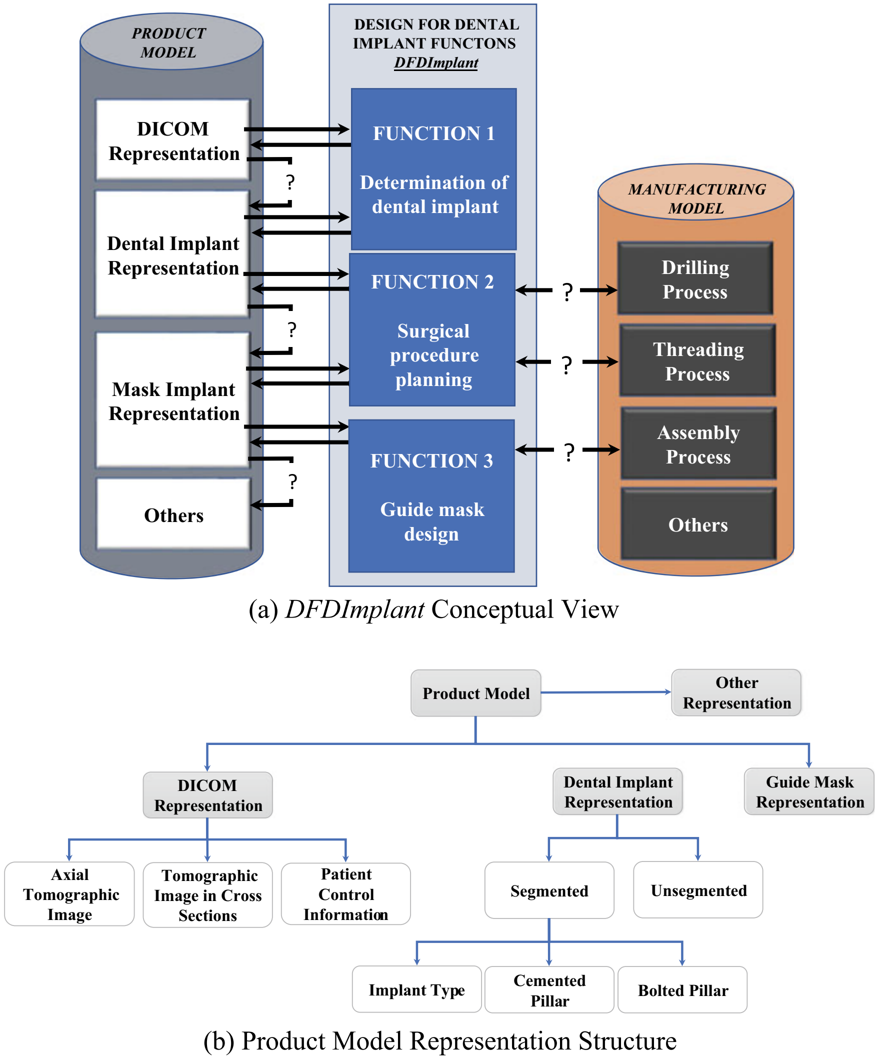

Fig. 7.2 DFD implant conceptual structure

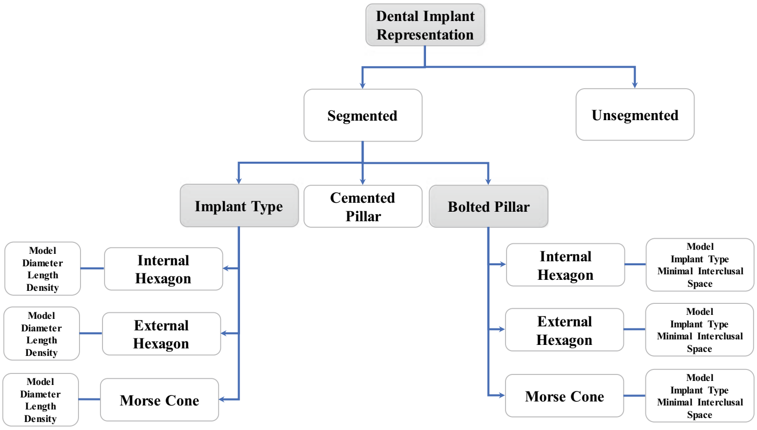

(c) Dental Implant Representation Structure

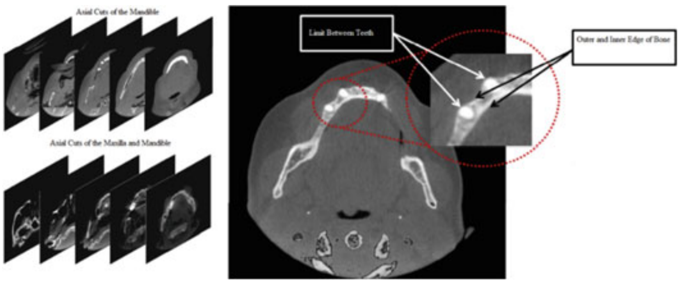

(d) CT sections and interest area in DICOM format

Fig. 7.2 (continued)

requirements, characteristics, machining tools, constraints, materials, among others) in an integrated way.

7.5 Product Model

The product model was structured to support the DFDImplant System in the process of conversion, translation and sharing of information between DICOM, Dental Implant and Mask Implant representations. Between DICOM and Dental Implant representations the information must be converted or translated in order to support the “Function 1”, and between Dental Implant and Mask Implant the information must be shared in order to Support the “Function 2”. This way, the system works with multiple representations, and for this it is necessary to understand how the information contained in one representation will be represented in another representation. With this reasoning, the product model contains the informational requirements necessary for DFDImplant functions, in a structured way. The DICOM representation holds information directly extracted from the computed tomography in the DICOM 3.0 standard, which are:

(i) **Control parameters—**it is the information contained in the tomographic file header obtained in the DICOM standard (Fig. 7.3a—physiological data of the patient, as well as data from the tomographer who performed the acquisition and the parameters of how the images are conditioned in the DICOM standard). For this research, the parameters *Width, Height, PixelSpacing, SliceThickness, Colortype and BitDepth* were used because they guide the system during processing, conversion and translation of the images into information that will be used to analyze the definition of the dental implant;

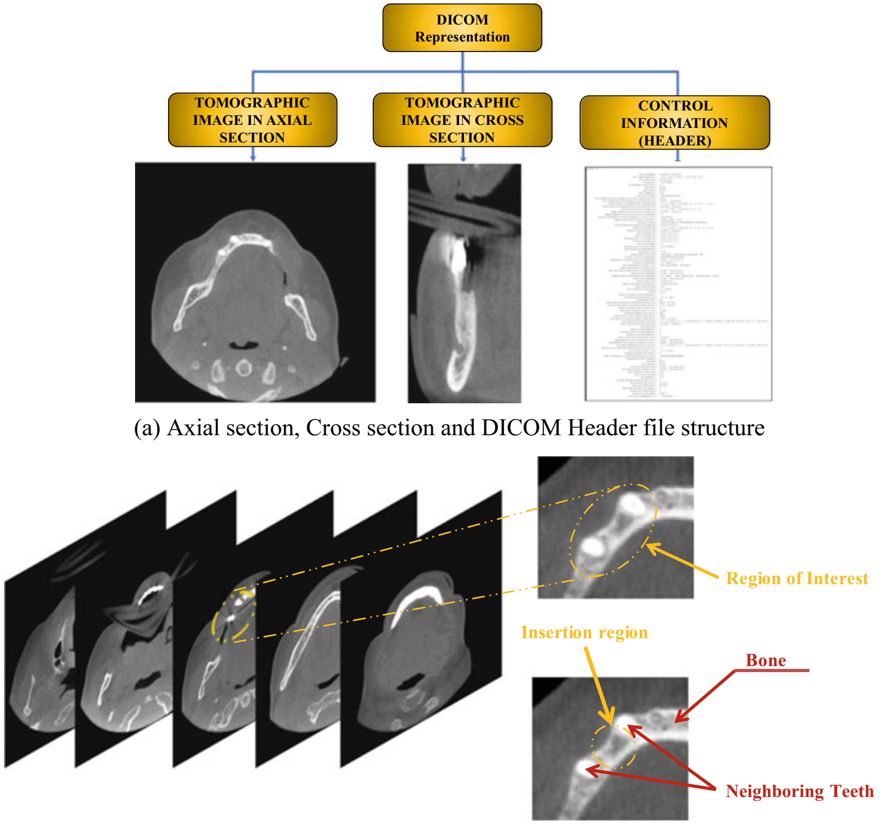

(a) Axial section, Cross section and DICOM Header file structure

(b) DICOM sections examples

Fig. 7.3 DICOM representation (product model)

(ii) **Tomographic images in axial section—**the information contained in the axial sections guide the delineation of the bone geometry, showing the limits between teeth and between the external bone border and the internal bone border, as can be seen in Fig. 7.3a. With this data it is possible to identify the location of the region for implant insertion and calculate the diameter of the implant that will fit this region. In addition to this information, it is possible, with the delineation obtained by the axial section and the region of insertion of the implant, to generate a transverse section, through the inference conversion mechanism, extracting new parameters from this new image;

(iii) **Cross-sectional CT images—**the cross-section is a section perpendicular to the axial section as illustrated in Fig. 7.3a, generated from a midline between teeth or auxiliary axes created by the dentist in the system for generating the cross-section. The detail of this process is contained in the deduction of the inference mechanisms for determining the cross section. By processing the cross-sectional image, it is possible to determine information such as the length of the dental implant, bone density, location of nerves and check the information of the diameter, obtained when processing images in axial sections.

The representation of the Dental Implant contains the information inherent to the dental implant models (types, diameters, length, among others), which will form the database. In this research, it is being addressed the screwed and segmented dental implant which is composed of 3 parts: (i) prosthesis; (ii) abutment; and (iii) body. The study is focused on the application of the abutment and the implant body, and the handling of the prosthesis will be addressed in future studies. With the information of diameter, length and bone density will be obtained by the inference mechanisms that process the DICOM representation, together with information of the interocclusal region. In this context, Fig. 7.2c presents the conceptual structure for the database of the dental implant representation, to which the expert system, based on the information obtained from CT scans, will select the appropriate group of implants that can satisfy the requirements imposed in each case. This structure presents characteristics of the dental implants such as diameter, length, bone density in which the implants are applicable, besides containing the type and model that are used in the definition of the implant body. Besides this information, this base presents data of the pi-lar, which will fix the prosthesis to the implant body, with its models, type of implant for which they are intended and the minimum interocclusal space necessary for its fixation.

Regarding the type of dental implant, the classification proposed by Misch (2000) was used. From the information extracted from the manufacturer's catalogue, the most important for implant selection are the bone density for which they are indicated, the diameter and the length. Although Misch's classification (2000) presents several models, for this study the internal hexagon, external hexagon and morse cone types were adopted.

The abutment is the element that makes the connection between the implant body, which is fixed on the bone, and the prosthesis located on the surface of the gum tissue.

The selection of the pillar is conditioned by three basic requirements: (i) minimum interocclusal space; (ii) style of prosthesis (single or double); and (iii) type of implant.

7.6 Inference Mechanisms

Inference mechanisms are the elements of an expert system capable of seeking the necessary rules to be evaluated and ordered in a logical way and from there, direct the inference heuristic process (Couto et al. 2007). Thus, the method most applied by this technique is the evaluation of rules, where these must be the knowledge base so that there is the translation, conversion or sharing of information in support of the deployment process. In order to perform the translations, conversions or information sharing information between DICOM, Dental Implant and Guide Mask representations, these mechanisms were structured in three basic functions: (i) Determination of the Dental Implant (Function 1—Fig. 7.4a); (ii) Planning of the Dental Implantation Process (Function 2—Fig. 7.4b); and (iii) Guide Mask Design (Function 3—Fig. 7.4c), as illustrated in the conceptual model (Fig. 7.2a). It should be noted that in this chapter only the exploration of the inference mechanisms related to "Function 1" of *DFDImplant* will be documented.

7.6.1 Inference Mechanisms for Determining the Dental Implant—Function 01

Function 01 has inference mechanisms capable of determining the most suitable set of dental implants based on the extraction or capture of information contained in the patient's DICOM Representation. This information is fundamental for determining: (i) the adequate diameter of the implant; (ii) the adequate length of the implant; and (iii) the bone density for determining the type of thread of the implant. The mechanisms were divided into two parts: (i) determining the body of the dental implant, and (ii) determining the abutment.

7.6.1.1 Determination of Adequate Implant Diameter

The implant diameter is calculated from the geometric information of the symmetry axis S(x), the reference lines PR1(x) and PR2(x) and the bone and teeth borders. For edentulous patients, only the bone thickness existing in the region where the implant is inserted is considered, whereas for partial edentulous patients it is necessary to evaluate bone thickness and the distance between teeth, using the smallest measure obtained between these two parameters. The bone thickness is determined by means of two points obtained between the intersection of the symmetry axis and the external

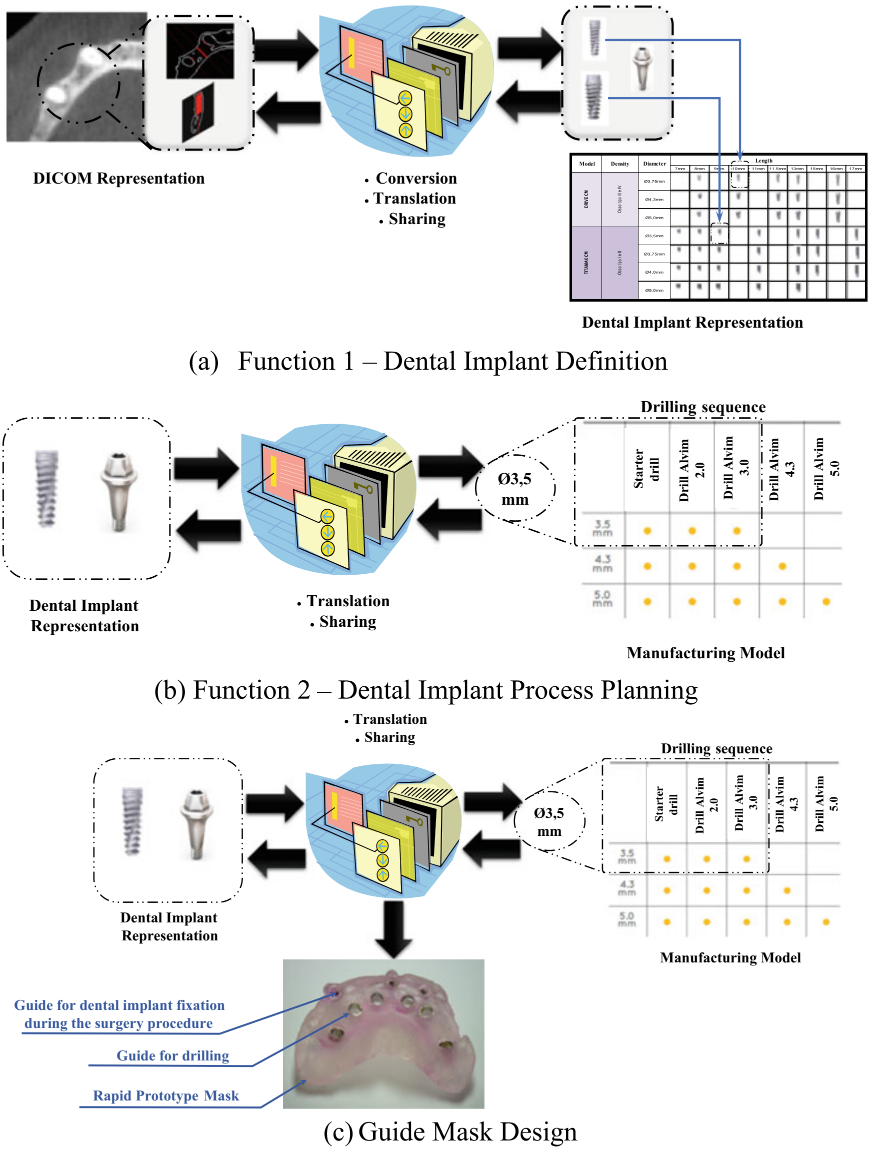

Fig. 7.4 Inference mechanisms

and internal borders of the bone PI1(x,y) and PI2(x,y) as illustrated in Fig. 7.5a and applied to Eqs. 7.1 and 7.2 respectively, obtaining the values in mm.

$$thickness = \sqrt{(PI2x - PI1x)^2 + (PI2y - PI1y)^2}(pixel) \qquad (7.1)$$

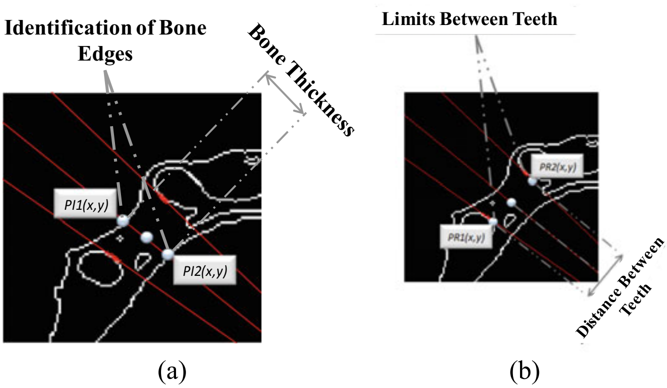

Fig. 7.5 Expert system calculation and plotting for single implant cases

where, PI1x and PI1y are the first points where the line intersects the bone and PI2x and PI2y are the last points where the line intersects the bone and thickness is the bone thickness.

$$ESm = (ESp * PixelSpacing)(\text{mm}) \tag{7.2}$$

where, Pixel Spacing is the measure in mm/pixel of how much the distance of each pixel is worth and thickness in mm is the bone thickness in mm, *ESm* is thickness in millimetres and *ESp* is thickness in pixels.

In the case of partial edentulous cases where there is a need to investigate the distance between neighbouring teeth, the auxiliary straight lines (PR1(x) and PR2(x)) are used to determine the distance that the centre of the insertion is in relation to the neighbouring teeth, i.e., how far the centre of the insertion is from the auxiliary straight lines. Thus the distance between teeth can be obtained by means of a straight line perpendicular to the symmetry axis, according to Eq. 7.3, at the insertion point of the implant, whose straight line will intersect the reference straight lines PR1(x) and PR2(x) as illustrated in Fig. 7.5b

$$SP(x) = mx + (y_0 - mx_0), \text{onde para ser perpendicular m} = \frac{-1}{\text{b}} \tag{7.3}$$

With the straight line perpendicular to the axis of symmetry, its intersection with the reference straight lines PR1(x) and PR2(x) is verified. By solving a linear system of equations obtained by SP(x) and PR1(x), Eq. 7.4, and SP(x) and PR2(x), Eq. 7.5, the points of intersection × 1,y1 and × 2,y2 are obtained, enabling the calculation of the distance between teeth.

$$\begin{cases} (y_0 - mx_0) + mx = SP(x) \\ a + bx = PR1(x) \end{cases} \tag{7.4}$$

$$\begin{cases} (y_0 - mx_0) + mx = SP(x) \\ a + bx = PR2(x) \end{cases} \tag{7.5}$$

where, SP(x) is the equation of the line perpendicular to the symmetry axis and PR1(x) and PR2(x) are the reference lines to the symmetry axis and through Eq. 7.6 it is possible to obtain the distance in pixel between the teeth.

$$\begin{aligned} DDp &= \sqrt{(x2 - x1)^2 + (y2 - y1)^2}(pixel) \\ DDm &= DDp * PixelSpacing(\mathrm{mm}) \end{aligned} \tag{7.6}$$

where, *DDp* is the distance between teeth in pixel and *DDm* is the distance between teeth in millimetres. From the bone thickness and the distance between teeth it is possible to determine the diameter of the implant to be used.

If the bone thickness is smaller than the distance between teeth, the thickness will be used as a parameter to determine the implant, but if the distance between teeth is smaller, the distance between teeth will be used, as shown Fig. in 7.4. The diameter will be determined by the bone thickness or the distance between teeth minus 2 mm, because according to Brink et al. (2007), Lee et al. (2005) and Mahon et al. (2000), the implant should be wrapped with at least 1 mm of surface around it.

7.6.1.2 Determination of Adequate Implant Length

The inference mechanism for the length calculation must analyze and translate the information contained in the cross-section by analyzing the bone depth. This calculation determines the length of the body of the dental implant based on the geometry of the bone and on the location of the nerves when necessary. The location of the nerves is fundamental, as any sizing error can cause irreversible lesions. As in the definition of the bone geometry in the axial section, the bone contour in the cross section follows the same thresholding procedure, where the image is thresholded to a band and unnecessary information is excluded, obtaining only the detail of the bone, as illustrated in Fig. 7.6.

However, although the thresholding extracts information from the bone (Fig. 7.6a), it is also possible to obtain information from the nerve, because according to Table 7.1 (next item) of the Hounsfield scale, the nerve can range from 20 to 40Hu, and in this range the value obtained in the thresholding will be 0 (null), i.e., black, meaning that the nerve is located within the bone and preventing the implant from intercepting the nerve (Fig. 7.6b).

From the image illustrated in Fig. 7.6c (x,z), when applying the edge detection technique using the mathematical simplification model proposed by Sobel, the bone contour and the nerve contour are extracted from the image, which will allow determining the maximum length allowed for the implant. With the outlined bone contour

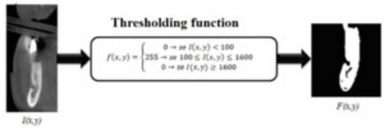

(a) Thresholding function

(b) image with nerves location

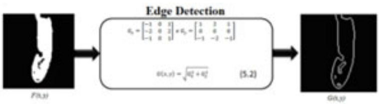

(c) Bone edge determination

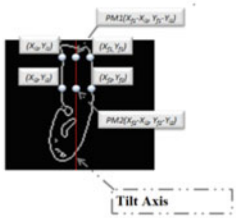

(d) Determination of the axis for implant positioning

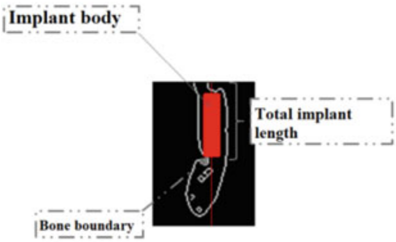

(e) Determination of the maximum implant length

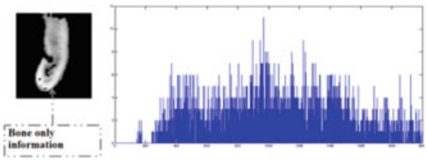

(f) Cross-section and bone density graph

Fig. 7.6 Information for calculating the implant length

Table 7.1 Bone density classification

Bone	Density
D1	>1250 HU—Dense cortical bone
D2	= 850 to 1250 HU—Thick cortical bone, dense to porous at the ridge of the ridge and thin trabecular bone inside
D3	= 350 to 850 HU—Thin porous cortical bone at the rim involving thin trabecular bone
D4	= 150 to 350 HU—Thin trabecular bone
D5	<150—Non-mineralized immature bone

and the highlighted nerves it is possible to safely determine the length of the implant that can be inserted in the region, but for this to occur it is necessary to create an axis of orientation or inclination of the implant, which will be the midpoint between the edges of the bone. This axis is represented by a straight line, named EI(x), obtained by two midpoints PM1(x,z) and PM2(x,z), allowing the construction of the inclination axis, as illustrated in Fig. 7.6d.

The axis of inclination axis will be used as a reference to determine the length of the implant, because when traversing the straight line $EI(x) = a + bx$ with the im-plant diameter in the Z-axis, from 1 to the limit of the Z-axis, it is possible to visually check that the implant does not exceed the bone border or intercept the nerve (Fig. 7.6e). Should one of these conditions occur, the implant body length will assume the current Z-axis position. After converting the pixel unit to millimetres (Eq. 7.7), 1 mm should be deducted due to the osseointegration process, as recommended in the literature (Brink et al. 2007; Lee et al. 2005; Mahon, Norling and Phoenix 2000).

$$\mathrm{Cm} = (\mathrm{Cp} * \mathrm{Slice\ Thickness}) - 1\mathrm{mm} \tag{7.7}$$

where Cm is the length in millimetres of the implant, Cp is the compression in pixels and Slice Thickness is the ratio between the distance between the pixel in millimeters.

7.6.1.3 Inference Mechanism to Determine the Transversal Section

For the determination of the implant body it is necessary to obtain from the DICOM representation the diameter, the length and the density. The diameter is obtained through the geometry of the bone by axial sectioning. As it is not possible to obtain the length and bone density of the insertion region using only the axial section, in this particular case an auxiliary section is needed, the cross-sectional section, which enables the extraction of this information. To determine the cross-section, the straight line of the symmetry axis is used to generate a plane named WZ, where W is formed by the equation of the straight line of the symmetry axis and Z is formed by the axial sections (varying from 1 to Z), as illustrated in Fig. 7.7. From this plane, information from the tomographic image will be extracted to compose the image of the transverse section named f(x,z). The limits of the axial section image are obtained in the control information (header) in the variable width (X) and height (Y) and in the filename is obtained the number of existing axial sections (Z).

7.6.1.4 Determination of Bone Density

Bone density calculation is the inference mechanism that identifies the type of dental implant appropriate for the bone where the implant body will be inserted. The density is obtained using the histogram of the bone H(x), which for-names the frequency that each intensity value appears in the image. In this research the intensity level followed

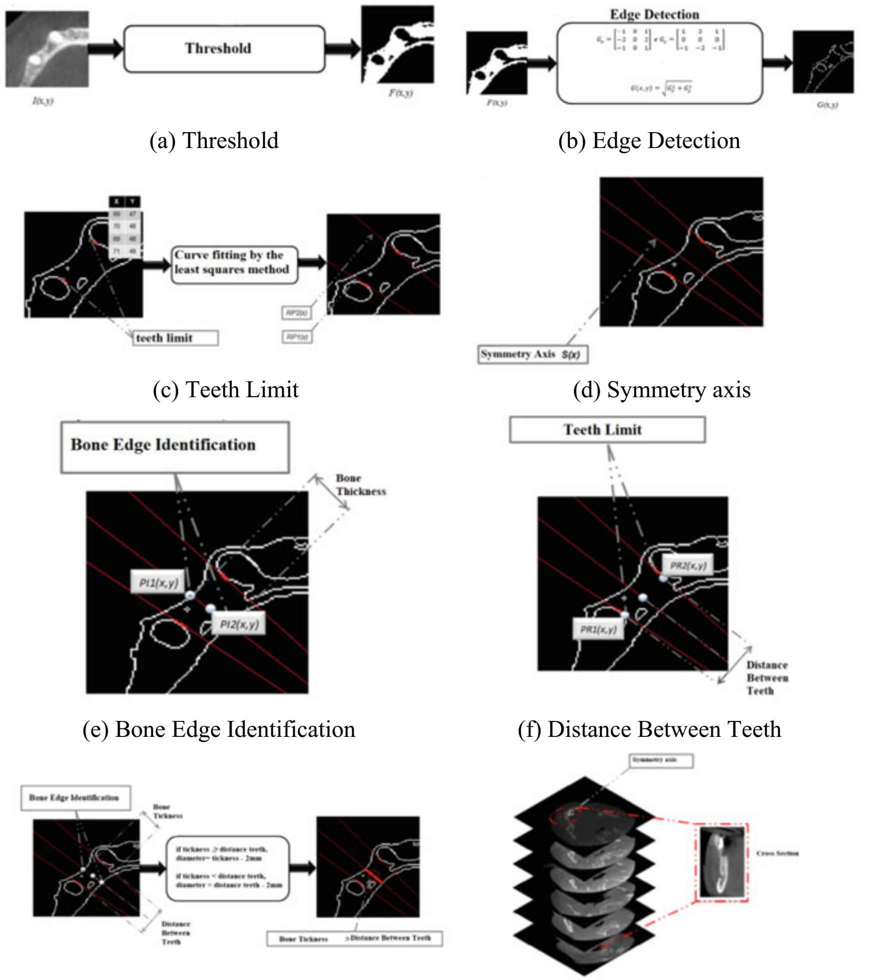

(a) Threshold (b) Edge Detection

(c) Teeth Limit (d) Symmetry axis

(e) Bone Edge Identification (f) Distance Between Teeth

(g) Bone Edge Identification (h) Symmetry Axis

Fig. 7.7 Expert system calculation and plotting for single implant cases

the scale proposed by Hounsfield, and based on Table 7.1, which presents the intensity ranges that each type of bone fits into, it is possible to obtain the bone density of the image.

In order to apply the histogram it is necessary to extract from the original image I(x,y) only the bone information, thus similar to the bone geometry detection procedure, when performing the thresholding process, from the original image f0(x,y), the information which fits in the bone range is searched (Table 7.1). Thus, a new image named Iosso(x,y) is obtained, whose values fit only the bone range. This way, the other information is excluded from the image, allowing the histogram H(x) process of this image, as illustrated in Fig. 7.6f.

After applying the histogram technique it is possible to calculate the bone density through the summation of the intensities that are in the range of each bone type (Table 7.1) and Eq. 7.8, where the bone type that presents the highest summation value is the predominant bone type with its respective calculated density.

Adapted from Misch (2000).

$$
\begin{aligned}
D1 &= \sum_{i=1250}^{1600} H(i), \\
D2 &= \sum_{i=850}^{1249} H(i), \\
D3 &= \sum_{i=350}^{849} H(i), \\
D4 &= \sum_{i=150}^{349} H(i), \\
D5 &= \sum_{i=0}^{149} H(i),
\end{aligned} \tag{7.8}
$$

where the equations described in Eq. 7.8 are the rules for determining bone density levels, corresponding to the classification proposed in Table 7.1.

7.6.1.5 Mechanism for Determining the Implant Abutment

The definition of the implant abutment is based on an inferred comparison mechanism, since the information required for determining the abutment (interocclusal region, implant type and implant modality—single or multiple) is obtained from previous processes or provided by the oral and facial surgeon. Therefore, the selection of the implant abutment is basically a search on the dental implant representation, whose implant abutment models must meet the stipulated requirements (Fig. 7.4). In the case of the interocclusal region, it is not possible to define the implant by direct comparison, since the implant body and abutment supplier requires a minimum space for fixation in the patient's bone structure.

7.7 Double Failure Dental Implants

The Systematic Literature Review (SLR) and Content Analysis (CA) conducted by Tinfer et al. (2020) identified that there are studies addressing the decision support process. However, most of these studies focus on the solution of cases in an individualized manner, and with this, pointing to the need to develop methods or conceptual approaches for decision support in the process of dental implants with multiple failures. To this end, it is necessary to take into consideration the size of the failure, the bone structure, and the location in the lower nerves by means of computerized tomography image processing, providing the dental surgeon with a better basis for performing the implantation process. Basically, in the RSL and CA showed that: (i) product models are inserted in 75% of the articles considered relevant; and (ii) digital image processing proved important, as 81.25% if was based on the surgeon's decision using the CT scan analyses and the clinical condition variables.

The process variables were defined on the basis of the characteristics found in the definition of the state of the art, where it was possible to identify variables relevant to the process: (i) the diameter and length of the implant as significant variables in the process, because it is through these that it is possible to identify the spacing between teeth and thus calculate the size of missing teeth in the development of a systematic protocol to support the surgeon in the implantation process (Lin et al. 2010); and (ii) bone density, to determine the type of bone, as it is through the analysis of the patient's bone structure that it is possible to identify which are the options for fixing the dental implant and consequently the implant stability. In the state of the art it was possible to identify that 43.75% of the resulting studies took this variable into account. Ribeiro Rotta et al. (2011) worked with the definition of bone tissue characteristics and methods of planning and placement of the implant, whereas Luangchana et al. (2015) proposed a software bone analysis to better support the surgeon's decision in the process.

Based on content analysis and conceptual proposal it was possible to identify that the authors address issues of product model, the information is used by surgeons to assist in the process and how the concept is explicit in the method. It was possible to identify that none of the articles addressed all the processes simultaneously and, therefore, the need arose to develop a conceptual method to support the process of dental implants.

7.7.1 Calculating Symmetry Through Lines

To determine the straight line of the bone edge, mathematical concepts were used, as the straight lines in a plane present their algebraic form in relatively simple equations, being deduced from their angular coefficient. To determine the equation of the line that passes through the points marked on the edge of the bone, the angular and linear coefficients of the line must first be calculated.

For the determination of the linear coefficient the system identifies the coordinates of the points (start and end), identifying a line segment. The horizontal distance between points "A" and "B" is called step (Fig. 7.8a) and the vertical distance between the points is called elevation (Fig. 7.8a). The ratio of elevation to step is the determination of the angular coefficient of the line (Fig. 7.8b), traditionally called m,

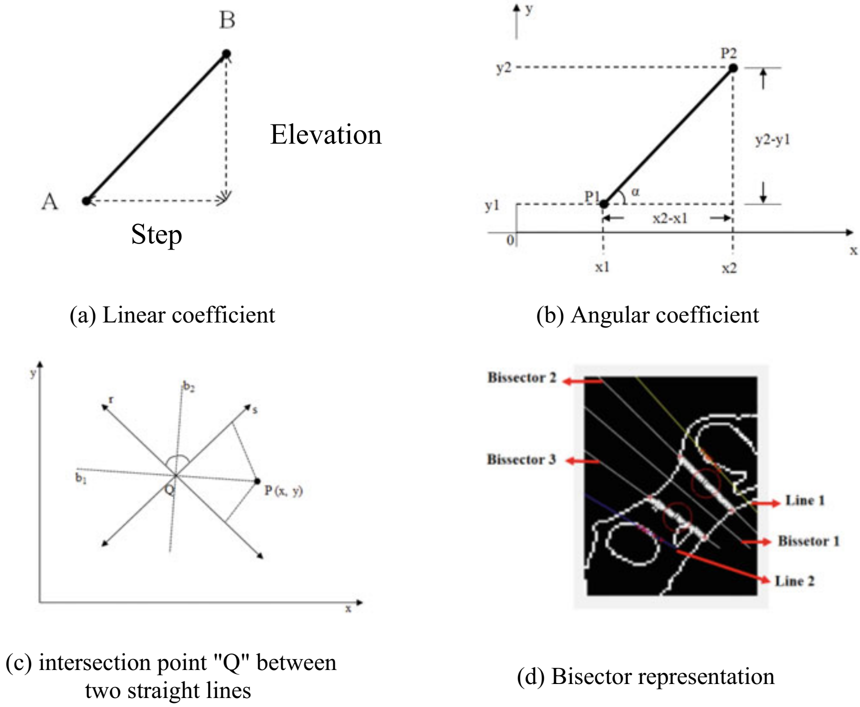

Fig. 7.8 Bisector calculation

therefore by definition the coefficient of the line present in the image and the plotted points is calculated by calculating Eq. 7.9 (Angular Coefficient).

$$\text{Angular coefficient} = \text{m} = \frac{\text{elevation}}{\text{step}} \tag{7.9}$$

Therefore within the Cartesian system and the line segment plotted by the points we have the points P1 (×1, y1), P2 (×2, y2) and so on with de-more points as illustrated in Fig. 7.8b. In trigonometric language "**α**" is the angle of inclination that the line makes with any horizontal axis measured counterclockwise and "**m**" is the trigonometric tangent of this angle to calculate the linear coefficient of the line (Eq. 7.10).

$$\text{m} = \tan \propto \tag{7.10}$$

Thus, the system will calculate the angular coefficient of the line based on the ratio of the variation of y by the variation of x. With the coordinates of the plotted points, using two points for calculation, by the property of calculating the angular coefficient arrived at the Eq. 7.11.

$$\frac{y - y_1}{x - x_1} = \frac{y_2 - y_1}{x_2 - x_1} \therefore y - y_1 = \frac{y_2 - y_1}{x_2 - x_1} * (x - x_1) \tag{7.11}$$

As we first identified the slope m and the plotted point of the line, we arrived at the following result shown in Eq. 7.12. Then substituting the point, we arrived at the angular equation of the line, and organizing mathematically we arrived at the reduced equation of the line 7.13.

$$y - y_1 = m * (x - x_1) \tag{7.12}$$

$$y = ax + b \tag{7.13}$$

Thus, the system identifies the coordinates of each plotted point, calculates the angular and linear coefficient and stores the straight line functional, repeating the process with the points plotted on the other tooth edge and calculating the angular and linear coefficient and storing the straight-line function 2.

7.7.2 Intersection Point of the Lines

To identify the point of intersection of the lines, the expert system determines the point of intersection using the equation of each line identified in the previous step, solving the system formed by the two equations (e.g., the lines r: 2x + y-4 = 0 and s: x–y + 1 = 0), gives the solution of the system according to Eq. 7.14. Therefore, the point of intersection of the lines used in this example is P (1,2), so the software calculates the point of intersection of the two plotted lines. To divide the dental gap and ensure the symmetry of the patient's mouth, the software separates the section according to the bisector calculation. To calculate the intersection point, it is necessary to calculate the bisector line to identify each area destined for each implant (Fig. 7.8c).

$$\begin{aligned} &\begin{cases} 2x + y - 4 = 0 \\ x - y + 1 = 0 \end{cases} ; \begin{cases} 2x + y = 4 \\ x - y = -1 \end{cases} \\ &3x = 3 \therefore x = 1 \\ &1 - y = -1 \therefore y = 2 \end{aligned} \tag{7.14}$$

Conceptually, consider two competing straight lines *r: a1x + b1y + c1 = 0* and *s: a2x + b2y + c2 = 0*, which intersect at a point Q. If any point P (x, y), P ≠ Q, equidistant from r and s, then p belongs to the bisector of the angle formed by the lines r and s (Fig. 7.8d). Considering the positive sign, we obtain the bisector and considering the negative sign we obtain the other bisector which are perpendicular to each other. The software calculates the first bisector to divide the failure environment into mathematically correct spaces and then repeats the process in each section to find the centre of each implant, plotting the bisector to the user.

7.7.3 Implant Determination (Diameter, Length, Density and Cross Section)

To determine the diameters, lengths, densities and cross-sections of the implants, for double failure, they are calculated individually using the same calculations used for single failure. From the point of view for determining the implant diameter, the system first calculates using the parameters of line space1, bisector1, bisector2, taking into account the central axis of the implant and the tooth thickness, discounting 1 mm on each side to consider the osseointegration of the first implant. Then, the process is repeated for the second implant, using line2, bisector1, and bisector3, also discounting 1 mm on each side to consider osseointegration of the second implant.

The cross-section is calculated based on bisector lines 2 and 3, presenting complementary information to that identified in the axial section of the image. The system calculates by repeating on bisector axis 2 for implant 1 and then on bisector axis 3 for implant 2.

To determine the length of each dental implant, the system considers the cross-section generated in the previous section, first for implant 1, repeating the process for implant 2, identifying whether the diameter of each implant intersects any inferior nerve or the length of the bone of each implant.

To calculate the bone density, the system performs the independent calculations for each implant defining the bone geometry and classifying the bone type, repeating the process for each implant location to be implanted and determining the bone density according to the classification presented by Misch (2000).

7.8 Case Studies

For the test and evaluation of the method, a prototype computer application (software) was developed on the *Matlab* platform from *Mathworks* (Fig. 7.9a), where the conceptual models were converted and programmed in this interface, with the intention of validating the inference models obtained. This system links the classes and subclasses of the product model to the inference mechanisms through functions and connections (in the case of the connection, with Oracle's *MySQL* database), supporting the whole process of translation, conversion and sharing for the determination of the dental implant. In this section the application of the method in three real cases is being presented: (i) the first case is a partial edentulous patient with a single failure in the mandible in the region of the canine; (ii) the second case is a total edentulous patient with a failure in the region of the maxilla; (iii) the third case is a patient with a double failure in the maxilla.

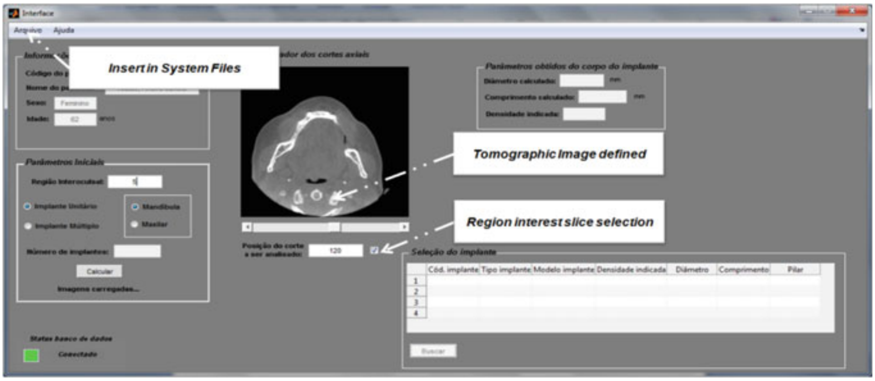

(a) Experimental systems developed (software)

(b) Single failure

Fig. 7.9 Experimental systems and CT emphasizing a single dental fault

7.8.1 Experimental Case I—Single Mandibular Dental Implant

In test case 1, the patient has a partial mandibular dental defect in the left canine region as illustrated in Fig. 7.9b. With the aid of the dental implant process-oriented design system, it is desired to determine the set of implants (body + abutment) that best suits this patient.

The tomographic images obtained from the patient were inserted into the prototype software, where initially the image that best represented the region of the implant to be inserted was located. Figure 7.10 shows the steps for determining the dental implant, identifying the region of interest and defining the points that outline the edge of the teeth surrounding the region of implant insertion, detail A. From this information the symmetry axis is generated, which allows defining the insertion point of the implant and its diameter, presenting the cross-sectional image generated from the axial slice images, thus allowing analysing the image from another perspective and

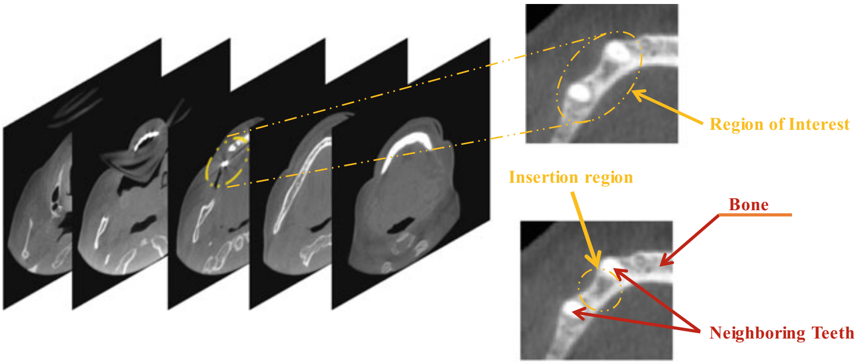

(a) Tomographic sections and region of interest

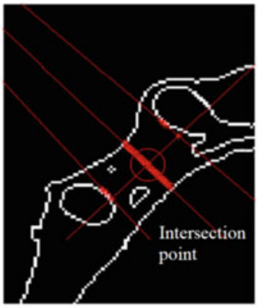

(b) Symmetry axis and implant diameter

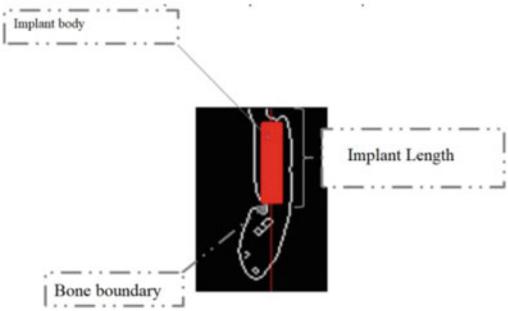

(c) Implant length

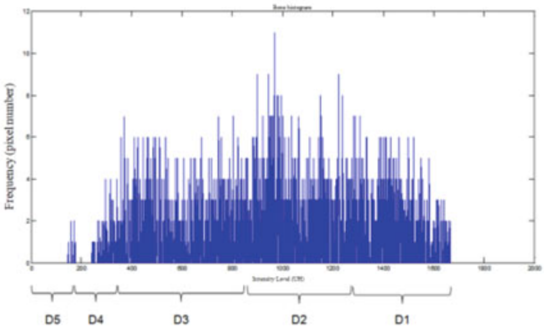

(d) Histogram for determining bone density

Fig. 7.10 Logic for determining the dental implant determining the length of the dental implant. Finally, the bone density is presented by the histogram method and the identification of the type of bone this patient presents, as shown in Fig. 7.10d.

By running the models through the expert system prototype, the following results were obtained on the tomographic image inserted into the system:

- Implant body diameter: 3.85 mm
- Length of the implant body: 13.5 mm
- Bone density of the region: D2.

From these parameters obtained in a calculated way, it selected in a database, built from data extracted from a manufacturer, the implants that best fit these characteristics. The expert system is able to create an axis of symmetry between the two teeth through interaction with the user (Fig. 7.10b). This axis is precisely generated as it is based directly on the image, which has an uncertainty of 0.25 mm, which can be considered insignificant from an implantology point of view. Furthermore, this system is capable of defining the implant diameter based on bone thickness or on the distance between teeth, i.e., it uses the smallest distance obtained by these two units to calculate the diameter (Fig. 7.10b).

To determine the length of the implant (Fig. 7.10c) the system uses the contour of the lower bone when it is the mandible and the upper bone when it is the maxilla, as well as the positioning of the nerves, because these limit the measurement of the depth of the hole where the implant will be inserted. For this case where the dental fault has the space for a single tooth, the system calculates the position, diameter, depth and density appropriately (Fig. 7.10b, c). This will not be true when the gap has space for two or more implants. By the rules currently implemented in the system presented as a result **eight** possible implants for this specific case as described in Table 7.2. However, it is believed that if the basis of the criteria for choosing the implant is improved in terms of accuracy, these options will tend to be reduced.

7.8.2 Experimental Case II—Maxillary Dental Implant

In the experimental case II, the patient has total edentulousness of the jaw and it is desired to determine the dental implant for the region of the left lateral incisor with the help of the design system oriented to the dental implant process. This experimental case differs from the previous one, since the patient is edentulous and the expert dental implant-oriented design system uses the teeth as reference, it is up to the dentist-surgeon in this situation to determine the region of insertion of the dental implant. The region of interest was identified and the points that outline the edge of the teeth surrounding the region of insertion of the implant were defined. From this information is generated the symmetry axis that allows calculating the insertion point of the implant and the diameter that it can have after analysing the bone distance and the distance between teeth. With the execution of the models through the prototype

Table 7.2 Implants selected by the specialist system—case I

manufacturer code	Implant body type	Implant body model	Bone Density	Implant body diameter	Implant body length	Implant pillar model
109.616	Morse cone	Titamax CM	2	3.5	11	Pillar cm
109.617	Morse cone	Titamax CM	2	3.5	13	Pillar cm
109.609	Morse cone	Titamax CM	2	3.75	11	Pillar cm
109.610	Morse cone	Titamax CM	2	3.75	13	Pillar cm
109.633	Morse cone	Titamax CM	2	4.0	11	Pillar cm
109.620	Morse cone	Titamax CM	2	4.0	13	Pillar cm
109.464	Internal Hexagon	Titamax IIPlus	2	3.75	11	Mini conical pillar II Plus
109.465	Internal Hexagon	Titamax IIPlus	2	3.75	13	Mini conical pillar II Plus

of the expert system, the following results on the tomographic image inserted in the system were obtained:

- Diameter of the implant body: **3.66 mm**
- Length of the implant body: **17 mm**
- Bone density of the region: **D4**.

From these parameters obtained in a calculated way, a database was selected, built from data extracted from a manufacturer, the implants that best adapt to these characteristics, obtaining Table 7.3.

The expert system can create the symmetry axis based on two planes defined by the system user. The implant diameter is conditioned to the distance between the two

Table 7.3 Implants selected by the specialist system—case II

Manufacturer code	Implant body type	Implant body model	Bone density	Implant body diameter	Implant body length	Implant pillar model
109.684	Morse cone	Drive CM	4	3.5	16	Pillar cm
109.629	Morse cone	Drive CM	4	3.5	16	Pillar cm
109.664	Morse cone	Titamax EX	4	3.5	15	Pillar cm
109.665	Morse cone	Titamax EX	4	3.5	17	Pillar cm
109.669	Morse cone	Titamax EX	4	3.75	15	Pillar cm
109.670	Morse cone	Titamax EX	4	3.75	17	Pillar cm
109.660	Morse cone	Alvim CM	4	3.5	16	Pillar cm

planes when this is less than the bone thickness. In this case, the uncertainty remains the same as in the previous case, being 0.25 mm. The depth also follows the same criteria of the previous case. The only difference is that for this study the system needs the user's knowledge to position the planes and determine the insertion position of the implant. It is not possible to generate the positioning of multiple implants, which is a limitation in this specific case.

7.8.3 Experimental Case III—Implante Dentário Duplo no Maxilar

For the case of failure where more than one implant (doubles) will be needed, a case study was carried out with a 70-year-old female patient who presented double tooth failure in the mandible region, as illustrated in the Fig. 7.11a.

The system loads the image in DICOM format through the File/Open buttons, then the user must choose the image slice to be analyzed, select and click on the calculate button. By clicking on calculate, the system processes the image and the user defines the region of interest, that is, the user limits the processing exclusively to the region of tooth failure, as shown in Fig. 7.11a. When selecting the region of interest, the system asks the user to identify at four points the edge of the tooth existing in the two neighbors of the existing fault as in Figs. 7.11c–d. Then the system returns with the calculation of the straight lines, the bisector, then the bisector of each implant, plotting the implant on the screen for the user as shown in Fig. 7.11e. The system in each central bisector of the implant will identify the plane for the cross section as shown in the Figs. 7.12a, b, e.

The system returns and calculates the implant length by returning the length plot as shown in Figs. 7.12c–d, later, the system performs the histogram calculation to define the bone type as shown in Fig. 7.12e and finally, the system returns the information to the user, so that it can be compared with the manufacturer's catalog, as shown in Fig. 7.12f and Table 7.4.

7.9 Conclusion

This research presented a proposal for a conceptual model of an expert system oriented to the dental implant process that helps the decisions that the oral facial surgeon needs to take to define the implant that best suits the patient, as in the traditional processes of dental implant the information available for consultation does not provide sufficient support for the correct determination of the implant. This failure in the decision leads to premature fatigue of the implants, prolonged surgical procedures with high trauma and in some situations, the incorrect sizing of the implant

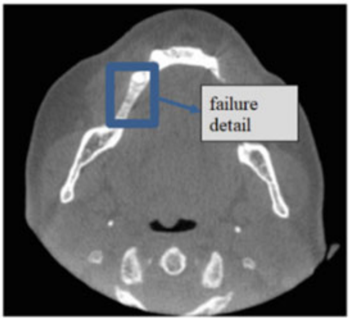

(a) tomography with the region of interest (failure)

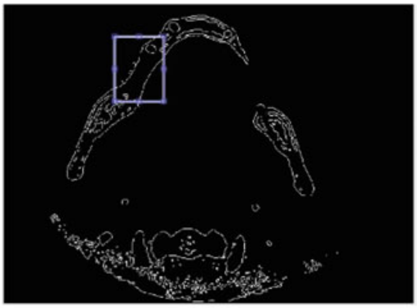

(b) edges of the region of interest

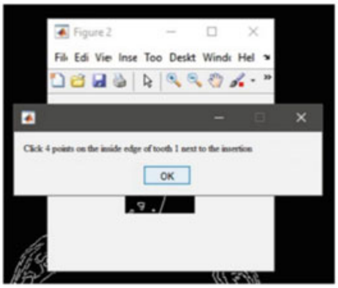

(c) User interface

(d) User interface

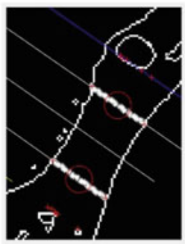

(e) Plot of Bisectors and Diameters

Fig. 7.11 Calculation of double implant

body, causing the disruption of the nerves that can cause anything from a partial stoppage of the mouth for a certain time to stoppage total indefinitely.

Thus, we searched through the concepts and techniques in the area of simultaneous engineering, image processing (threshold, edge detection, histogram, arithmetic and algebraic processes) and dental implant (segmented prostheses, two-stage protocol, definitions of implant body and abutment applications) formulate a conceptual design model oriented to the dental implant process, with a product model and inference mechanisms, where the first provides information to the second, which performs the conversion, translation and sharing information in order to determine the implant

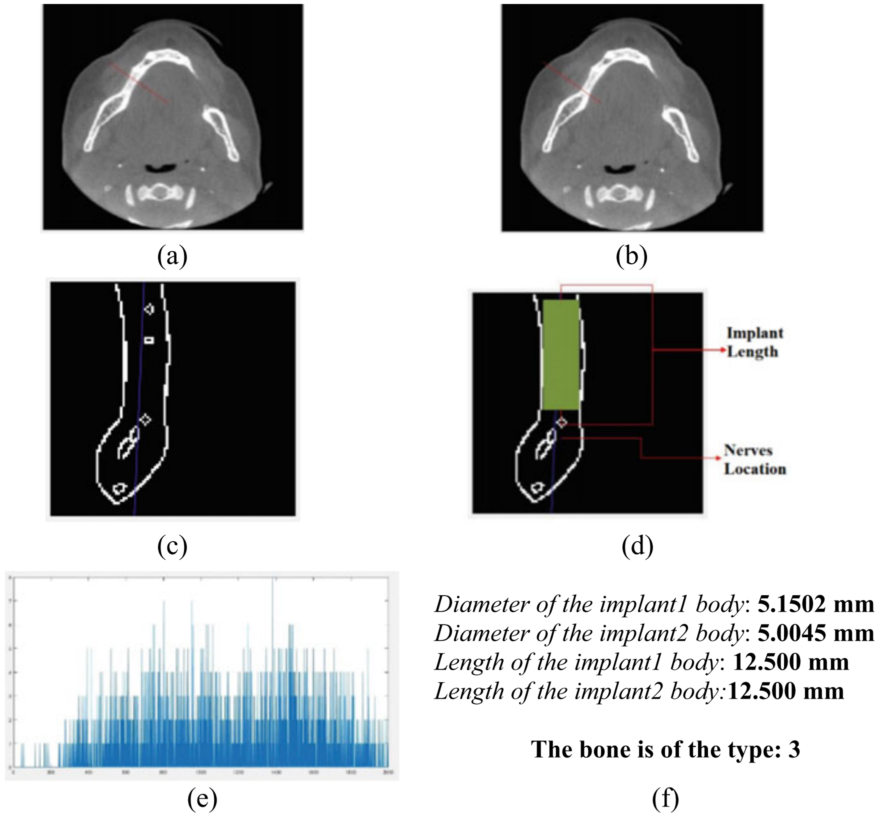

Fig. 7.12 Logic for determining the dental implant

Table 7.4 Implants selected by the specialist system—case III

Manufacturer code	Implant body type	Implant body model	Bone density	Implant body diameter	Implant body length	Implant pillar model
140.953	Morse cone	HelixGM	3	5.0	8	Screwed
140.954	Morse cone	HelixGM	3	5.0	10	Screwed
140.955	Morse cone	HelixGM	3	5.0	11,5	Screwed

that fits the patient's requirements. This conceptual model was implemented in a computer system, resulting in an expert system that presents interactivity with the user and provides, at the end of the inference mechanisms procedures, the indication of a group of sets of dental implants (implant body and abutment) and information subsidy (diameter, length, density, geometry, location of nerves) so that the oral and facial surgeon can choose the most suitable one among these implants. its implementation was developed in a *Mathworks Matlab* environment that allowed the development of the conceptual prototype of the system. Although this implementation presents a user-friendly interface, it is not recommended for professional development, as this research was concerned only with the conceptual side of the models, leaving the interface and the processing time of this system in the background.

Three cases were applied in the specialist system, the first presented a dental failure between two teeth, the second a failure in an edentulous patient and the third was a case of partial edentulous. For all cases, the dimensional uncertainty was in the order of 0.25 mm and this value is not significant from the perspective of implantology. Although the results presented were mostly positive, it is noted that there is a long way to go in order for the system to be able to carry out more complex analyzes than simply a single failure and this should be the object of future research study.

Acknowledgements The authors would like to thank the Pontifical Catholic University of Parana (PUCPR) for financial support to the development of this research.

References

Berto RMVS, Nakano DN (2000) Scientific Production in the Annals of the National Meeting of Production Engineering: A Survey of Methods and Types of Research. ABEPRO 9(2):65–76. https://doi.org/10.1590/S0103-65131999000200005

Bottino MA, Itinoche MK, Buso L, Faria R (2006) Aesthetics with implants in previous region. J Implant News 3(6):560–568

Breeding LC, Dixon DL, Sadler JP, Mckay ML (1995) Mechanical consideration for the implant tooth-supported fixed partial denture. J Prosthet Dent 74(5):487–492

Brink J, Meraw SJ, Sarment DP (2007) Influence of implant diameter on surrounding bone. Clinical Oral Implantology Res 18(1):563–568

Canciglieri Junior O, Rudek M, Souza TM, Francesconi T (2010) A geometric modelling in the CAD system from the medical images to support prosthesis design. In: 17th ISPE international conference on concurrent engineering, 2010, Cracow, pp 431–441

Collis J, Hussey R (2005) Research in administration: a practical guide for students of undergraduate and graduate. 2nd ed, Porto Alegre, Bookman

Couto Filho MB, Souza JC, Stacchini SMT (2007) On the problem of widespread data integration. Control Autom J 18(1):24–43

Galanis CG, Sfantsikopoulos MM, Koidis PT, Kafantaris NM, Mpikos PG (2006) Computer methods for automating preoperative dental implant planning: Implant positioning and size assignment. Comput Methods Programs Biomed 86:30–38. https://doi.org/10.1016/j.cmpb.2006.12.010

Graham RNJ, Periss RW, Scarsbrook AF (2005) DICOM demystified: a review of digital file formats and their use in radiological practice. Clin Radiol 60(1):1133–1140

Grauer D, Cevidanes LS, Styner MA, Ackerman JL, Proffit WR (2009) Pharyngeal airway volume and shape from cone-beam computed tomography: relationship to facial morphology. Am J Orthod Dentofacial Orthop 136:805–814

Grauer JN, Shafi B, Hilibrand AS, Harrop JS, Kwon BK, Beiner JM, Albert TJ, Fehlings MG, Vaccaro AR. Proposal of a modified, treatment-oriented classification of odontoid fractures. Spine J. 2005 5(2):123–9. https://doi.org/10.1016/j.spinee.2004.09.014. PMID: 15749611

Greboge T, Canciglieri Junior O, Rudek M (2010) 3D prosthesis modeling based on computed tomography images. XVII symposium on production engineering SIMPEP, Bauru, SP, Brazil

Hounsfield GN (1973) Computed transverse axial scanning (tomography): part I. Description Syst Br J Radiol 46(552):1016–1022
Lacerda DP, Dresch A, Proença A, Antunes Júnior JAV (2013) Design science research: a research method to production engineering. Gest Prod 20(4):741–761
Luangchana P, Pornprasertsuk-Damrongsri S, Kiattavorncharoen S, Jirajariyavej B (2015) Accuracy of linear measurements using cone beam computed tomography and panoramic radiography in dental implant treatment planning. Int J Oral Maxillofac Implants 30(6):1287–1294. https://doi.org/10.11607/jomi.4073
Lee JH, Frias V, Lee KW, Wright RF (2005) Effect of implant size and shape on implant success rates: a literature review. J Prosthet Dent 94(1):377–381
Lewis S (1995) Anterior single-tooth implant restorations. Int J Periodontics Restorative Dentistry 15(1):31–41
Li T, Kaijin H, Cheng L, Ding Y, Ding Y, Shao J, Kong L (2010) Optimum selection of the dental implant diameter and length in the posterior mandible with poor bone quality—a 3D finite element analysis. Appl Math Model 35:446–456. https://doi.org/10.1016/j.apm.2010.07.008
Lin D, Li Q, Li W, Duckmanton N, Swain M (2010) Mandibular bone remodeling induced by dental implant. J Biomech 43(2):287–293. https://doi.org/10.1016/j.jbiomech.2009.08.024
Mahon JM, Norling BK, Phoenix RD (2000) Effect of varying fixture width on stress and strain distribution associated with an implant stack system. Implant Dent 9(1):310–320
Miguel PAC, Fleury A, Mello CHP, Nakano DN, Lima EP, Turrioni JB, Ho LL, Morabito R, Martins RA, Sousa R, Costa SEG, Pureza V (2018) Research methodology in production engineering and operations management, 3rd edn. Elsevier, Rio de Janeiro
Misch CE (2000) Contemporary dental implants, 2nd edn. Santos Bookstore Publishing, São Paulo, pp 210–240
Misch CE (2006) Implant prosthesis, 3rd edn. Santos Bookstore Publishing, São Paulo, pp 353–366
Ochiai K, Ozawa S, Caputo AA, Nishimura RD (2003) Photoelastic stress analysis of implant-tooth connected prostheses with segmented and nonsegmented abutments. J Prosthet Dent 89(5):495–502
Pye AD, Lockhart DEA, Dawson MP, Murray CA, Smith AJ (2009) A review of dental implants and infection. J Hosp Infect 72(2):104–110
Ribeiro-Rotta RF, Lindh C, Pereira AC, Rohlin M (2011) Ambiguity in bone tissue characteristics as presented in studies on dental implant planning and placement: a systematic review. Clin Oral Implant Res 22(8):789–801. https://doi.org/10.1111/j.1600-0501.2010.02041.x
Silva LA (2018) FUNARI, Pedro Paulo Abreu. Paulo de Tarso: um apóstolo para as nações. São Paulo, Paulus, 2013. ISBN:9788534936293. Heródoto, 3(1):610–614. https://doi.org/10.31669/herodoto.v3i1.372
Souza DI, Muller DS, Fracassi MAT, Romeiro SBB (2013) Guidelines for research projects. Liberato Salzano Vieira da Cunha Technical School Foundation. New Hamburg
Tinfer S, Canciglieri Junior O, Szejka AL, Rudek M (2020) Support the decision-making in the process of dental implant: a review and content analysis. Revista SODEBRAS 15(172):27–36. https://doi.org/10.29367/issn.1809-3957.15.2020.172.27
Wiggins RH, Davidson HC, Harnsberger HR, Lauman JR, Goede PA (2001) Image file formats: past, present, and future. Radiographics 21(2):789–798

Chapter 8
Application of Artificial Materials in Thoracic Surgery

Slobodan Milisavljevic and Ana Lukovic

8.1 Introduction

Today, numerous biological and synthetic materials are used for the reconstruction of the chest wall. Biological materials may be autologous, such as: fascia lata, bone grafts (ribs, tibia, fibula, iliac crest, dura mater, pericardium) or heterologous (dura mater, pericardium, fascia). The expanded use of synthetic materials for the reconstruction of the chest wall encourages their diversity, availability, inert nature, and ease of use. It should be kept in mind that no material is absolutely inert and that the human body reacts to the presence of a foreign body by inflammation and the formation of pseudocapsules. Synthetic materials are rigid and fragile and can migrate into tissue, which can sometimes lead to serious injury to internal organs (i.e., lungs). Most of the synthetic materials used for implantation are produced in the form of plates, supporters or meshes. The plates can be made of metal or fiberglass, while meshes are fabricated from Teflon (polytetrafluoroethylene), nylon, polypropylene, prolene or vicryl. Also, today there are synthetic prostheses such as those consisted of acrylic derivatives or Teflon, as well as those made of composite materials. Nowadays, composite protective products made of methacrylate and marble meshes are increasingly being applied. In difference to synthetic woven meshes, the composite protective products made of methacrylate and marble meshes are increasingly being used due to their ability to fully cover massive chest wall defects, preclude paradoxical respirations, and avoid the development of chest malformations (Tamburini et al. 2019). As part of the preparation of the surgical intervention, the size of the chest wall defect that remains after radical resection is being assessed, and after that, a methyl

S. Milisavljevic (✉) · A. Lukovic
Department of Surgery, Faculty of Medical Sciences, University of Kragujevac, Kragujevac, Serbia
e-mail: s.milisavljevic65@gmail.com

A. Lukovic
e-mail: analukovic91@gmail.com

O. Canciglieri Junior and M. D. Trajanovic (eds.), *Personalized Orthopedics*,
https://doi.org/10.1007/978-3-030-98279-9_8

acrylate implant is being created by 3D printing to be finally incorporated into the defect site between the two layers of the Marlex mesh. In addition to their hardness, these protheses maintain the physiological curvature of the chest wall, they are easily fixed to the chest wall, and, above all, they are fairly inexpensive (Goldsmith et al. 2020). In the process of their production, experts of various specialties (surgeons, bioengineers, immunologists, etc.) are involved, which in the future can lead to the application of biodegradable scaffolds with implantation of stem cells in order to gain the artificial bones to be applied in various areas of surgery such as orthopedics, maxillofacial, thoracic surgery and neurosurgery.

8.2 Historical Aspects of Implantable Materials for Chest Wall Reconstruction

The first relevant attempt to reconstruct the chest wall dates to the early twentieth century when Tansini used latissimus dorsi myocutaneous flap for closuring the soft-tissue defect after radical mastectomy (Maxwell 1980). About 60 years later, chest wall reconstruction techniques were first introduced. In the 1940s Watson and James described the use of fascia lata grafts for closure of chest wall defects (Watson and James 1947). Bisgard and Swenson were the first to use rib grafts as horizontal struts for reconstruction after sternal resection (Bisgard and Swenson 1948). The main drawback associated with these methods of autotransplantation refers to the lack of available tissues and harm of place from which the donor tissue was taken, especially after an extensive resection had been performed. Therefore, although Gangolphe initially published the insertion of a metal prosthesis about 110 years ago (Gangolphe 1909).

In the fifties of the last century began the implantation of artificial prosthetic materials sporadically, with the intensive development of surgical techniques and materials in the coming years. Initially, woven, and soft synthetic types of prosthetics were being used, such as meshes made of polypropylene or polyester or polytetrafluoroethylene, but their inability to provide the full protection of inner thoracic organs from the effects of external factors led to subsequent introduction of rigid materials, e.g., sandwich-like composite material made of methyl methacrylate and polypropylene mesh. The introduction of the latter improved the stability and protection of the thoracic wall, but also reduced its flexibility during breathing movements, which could lead to potential impairment of respiratory rhythm and plasticity in such patients. Besides, albeit to a significantly lesser extent, this procedure could also result to abrasion of attached subjacent anatomical structures, implant rejections and infections.

Several years ago, based on the previous positive experience in other surgical branches, reinforced prostheses with titanium plates or meshes were proposed as the best possible artificial material for the reconstruction of the chest wall because it provides adequate rigidity of the thoracic cage, as well as prevents injuries and infections of the internal thoracic organs to a significant extent most likely due to the high degree of biological inertia and biocompatibility, which in turn leads to better tolerance of patients compared to the above mentioned synthetic meshes. Another potentially fascinating approach involves the transplantation of cryopreserved bone allografts, bearing in mind its superiority in relation to autotransplantations and implantation of synthetic materials in terms of relatively easier, safer, and cheaper procurement of implantable materials, as well as unlimited number of bones collected in the bone banks. Although the first bone bank was established more than 70 years ago, the first allograft transplantation of chest wall bone was awaited until 1993, when Cara et al. reported on reconstruction of sternum using iliac bone and musculocutaneous flaps (Cara et al. 1993). Subsequently, the other authors are also reported on successful combination of iliac bone allografts with other biological or synthetic materials to cover massive thoracic defects, highlighting another advantage of bone allograft versus systemic reflected in the greater ability to fully incorporate into the host organism and become its essential component over time. In accordance with the current achievements in the process of improving the production and quality of synthetic implantable materials, in the future it is much expected from the application of biodegradable scaffolds with implantation of stem cells in order to get the artificial bones for the complete closure of the large defects in various areas of surgery (i.e., orthopedics, maxillofacial, chest and neurosurgery, etc.), which would be an important step forward when it comes to all types of implant procedures. Finally, it is important to emphasize that until now the selection of the most suitable artificial material for the reconstruction of bone structures of the chest has not yet been clearly established, unlike biological, especially autogenous grafts that are widely being used to restore soft tissue defects.

8.3 Applications of Biodegradable Synthetic Materials in Thoracic Surgery

Biocompatible artificial or synthetic materials have wide application in chest surgery and surgery in general today. In the field of chest surgery, they are being used to reconstruct chest wall defects after extensive resection due to primary or secondary neoplasm, congenital anomalies, infections, radiation injuries and trauma. After extensive wall resections, large defects of soft tissue and bone structures (sternum and ribs) can remain and requires carefully planned and extensive reconstruction of such defects. Reconstruction of the chest wall after such extensive resections is a procedure aimed at stabilizing the bone wall and reconstructing the soft tissues. When planning resection of the chest wall due to neoplasm, a particular attention must be paid to the general condition of the patient as well as to the size and the localization of the tumor, since the defects extending from 5 to 7 cm in the largest diameter rarely require stabilization, while larger defects mostly require some type of stabilization procedures in order to preserve the normal lung function. Also, localization of resection is very important. For example, the resection covering the area of the scapula, or the area of the large chest muscles, rarely requires stabilization of the chest wall, while on the other hand, those involving the lateral or the lower part of anterior portion of the thoracic wall should always be subjected to the stabilization procedure (Sanna et al. 2017).

The chest wall has both a structural and a functional role. The structural role is reflected in the fact that it protects the internal vital organs (heart, lungs, liver, etc.). It also provides a flexible skeletal frame to stabilize shoulder and arm function. The inspiratory and expiratory muscles of the chest wall work in a precisely coordinated movement to execute a functional breath (Clemens et al. 2011).

Careful preoperative evaluation, meticulous surgical technique, and active postoperative treatment are important for any chest wall reconstruction. The choice of reconstruction is individual and is based on the nature, size and location of the defect, as well as on the general health condition of the patient and the prognosis. The goals of reconstruction are to provide the structural and functional role of the chest (Tukiainen 2013).

As described earlier, different types of synthetic, biological and metallic materials are available for the reconstruction of chest wall defects. Each prosthetic material has its advantages and disadvantages, and none has proven to be ideal (Weyant et al. 2006).

The main potential disadvantages of this prosthesis seem to be its negligible permeability to fluid that can lead to exacerbation of preexisting painful condition and enhanced rigidity of the chest wall. Rarely, the occurrence of methacrylate fractures usually followed by an infection, when the implant must be removed immediately. Owing to its outstanding inertness, low density, and resistance to weakening by rusting and stretching, the plates or meshes with titanium provide a certain advantage over other synthetic materials. Besides, these are materials repelled by a magnetic field thus they can be used without any restriction when magnetic resonance imaging scan is being performed. Although insertion of titanium implants is rarely associated with early and delayed respiratory and infective complications only a couple of them were noticed, such as fracture and/or dislocation of system's components as well as severe chest pain. Isolated implantation of titanium plates is particularly useful for reconstructing the chest wall after resection due to traumatic events (e.g., reconstruction of sternum after partial or total sternectomy needed to maintain thoracic wall stable), while titanium meshes are usually used in conjunction with plates and some other biological materials to cover large, fully thickened defects after radical, mutilating surgery due to locally advanced tumors (Thomas and Brouchet 2010).

In cases of a full-thickness chest wall defect, many rigid implants may be used. Modern titanium devices are rigid, corrosion-free, chemically inert implants that are quickly and precisely adaptable to the shape of the thoracic wall. Moreover, titanium can safely be imaged with both computer tomography (CT) and magnetic resonance imaging, and therefore it does not affect the follow-up. Traditionally, most of the available chest wall prosthesis materials are evolved from implanted devices used in other fields such as abdominal repair. A common feature of these materials is their biological “inertness,” nonreactivity, and durability. According to these principles, several meshes, such as Prolene and Marlex meshes, have gained acceptance. However, the use of these materials may lead to an infection. Chronic and persistent pain, erosion, bleeding, hematoma, and pulmonary restrictive disease may occur due to inadequate incorporation, mesh shrinkage, and migration. In such circumstances, most of the prostheses must be removed. In cases of the sternal, chest wall, and diaphragm reconstruction, Composix Mesh™, titanium mesh, and Marlex mesh as well as methyl methacrylate were also successfully used. Although resection of tumors in this region with sufficient margins may lead to a large chest wall defect, primary closure of these defects can be satisfactorily achieved in most cases (Khalil et al. 2010). As far as our knowledge is concerned, this seems to be the very first attempt to produce anatomical design of sternal defect. The ideal prosthetic material characteristics should be:

1. strong enough to withstand physiologic stresses over a long period.
2. conform to the chest wall.
3. promote strong host tissue ingrowth, which mimics normal tissue healing and ensuring wall incorporation.
4. resist erosions into surrounding tissue and visceral structures.
5. not induce allergic or adverse foreign body reactions.
6. resist infection.
7. be easy to use.

Successful reconstruction of the chest wall after extensive surgical resections plays a key role in the proper functioning of vital thoracic organs as well as the whole organism. As a matter of fact, the loss of completeness of the full thickness of thoracic wall layers inevitably leads to respiratory failure, which significantly increases the risk of death in such patients. In recent decades many and various biodegradable materials are being used in thoracic surgery in order to repair either acquired or congenital large chest wall defects and ensure the stability of thoracic cage. The choice of an adequate materials and surgical techniques used for such indispensable procedure should be always based on multidisciplinary approach, with inclusion of different clinicians (e.g., thoracic surgeons, plastic surgeons, neurosurgeons, orthopedists, radiologists, oncologists, pediatricians), but also the other experts, such as biomedical engineers, chemists, physicists, microbiologists, immunologists, pharmacologists, etc. Materials used to reconstruct chest wall can be of biological (xeno-, allo- and auto-grafts), synthetic and metallic origin, whereby the implantation of any of them has certain benefits and drawbacks, without proven dominance over others. Such pros and cons should be taken into account when deciding to apply each of them rationally in a particular situation according to the needs of an individual patient. In fact, to achieve a successful clinical outcome all potential benefits to a patient must be carefully balanced over the possibility of early and delayed surgical and non-surgical complications after the insertion of these prosthetic materials, on an individual basis. Today, the implantation of modern biomaterials, such as particularly hybrid human tissue-engineered products containing proteins, stem cells and/or other biological ingredients, implies a rather promising approach to optimize risk/benefit ratio (e.g., the emergence of infections versus favorable effects referring to structural and functional stability), wherever possible.

The expanded use of various synthetic materials for the reconstruction of the chest wall is supported by their diversity, availability, relatively inert nature, and apparent simplicity of use. However, considering no material is absolutely inert, the human body usually responds to insertion of prostheses by inflammation (displaying both types of immune response) and subsequent irregular formation of fibrous tissue containing numerous immune and foreign body giant cells that surround such an implant. Hence, since the organism can have relevant biological and physical-chemical influence on the implanted material in terms of its absorption, degradation, calcification, abrasion, oxidation, etc., on the other hand the implant can also demonstrate local and systemic effects to entire organism that are clinically manifested with occurrence of infection, toxic and allergic reactions, carcinogenesis, etc. In this way, due to the variable bidirectional interactions between implants and tissues in a particular environment the materials used in different tissues are expected also to cause the different responses, which is essential for their development and usage. Besides, synthetic materials are rigid and fragile enough, and also have the possibility to migrate deep into tissues, which can sometimes lead to serious injury to internal organs (i.e., heart, lungs, blood vessels, etc.) (Hayashi et al. 2019).

Regardless of its origin, the characteristics of implantable materials used to reconstruct the chest are more or less approaching the optimal material in the sense that they provide sufficient stiffness of the chest wall necessary to preclude paradoxical movements, while enabling the proper adaptation of the chest wall during breathing; in addition, they are also sufficiently inert to harmonize the growth of fibrous tissue around the implants and the risk of developing the infection, while at the same time, the monitoring and detection of potential local tumor recurrences are facilitated when these materials are used since they are often shown as radiolucent (hypodense) regions on radiographic imaging procedures making an anatomic landmark of separation (Weyant et al. 2006).

8.4 Chest Wall Resection and Reconstruction with Methacrylate Implant

The human musculoskeletal system is prone to injuries and various diseases such as tumors. In addition to the division into primary and secondary, benign, and malignant, all chest wall tumors are divided into soft tissue tumors and tumors of the bone structures of the chest wall. Surgery with resection has shown to be the best option for primary tumors and a selection of secondary tumors of the chest wall and may even be curative. In the surgical treatment of tumors, it is necessary to consider the localization, size and depth of the tumor tissue, the condition of the local tissue, the general condition of the patient, the expected survival and prognosis. Planning and preparation of operations are a key factor for the success of a surgical intervention.

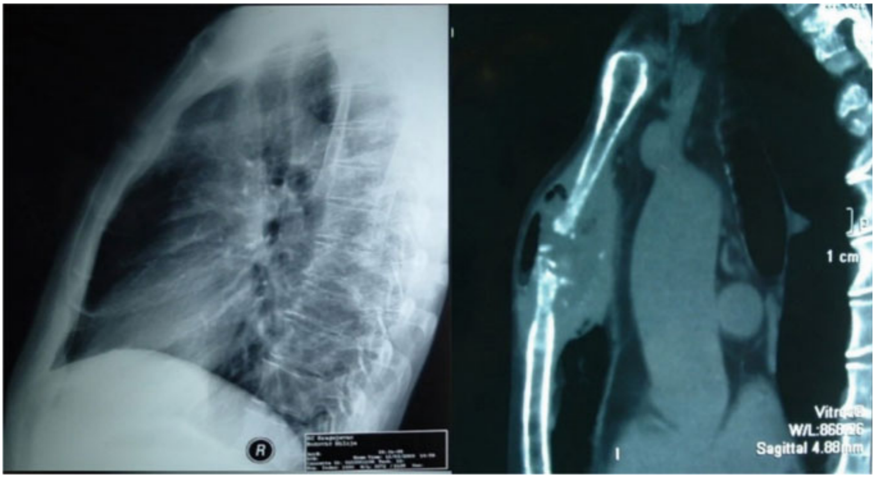

Fig. 8.1 Malignant tumor of the sternum—chondrosarcoma X-ray

Chest wall reconstruction depends primarily on the size and localization of the tumor. The implant that will replace the bone or part of the bone must match the shape and function of the replaced bone, and the manufacturing technology used should save time and costs.

Chest wall sarcomas is usually formed in the cartilage, soft tissues, and bones of the thoracic cavity, including chondrosarcomas, osteosarcomas, rhabdomyosarcomas, plasmacytomas, malignant fibrous histiocytomas, and Ewing sarcomas.

The chondrosarcoma is the most common primary malignant tumor of the chest wall and accounts for about 95% of all malignant tumors of the bone structures of the chest wall. It occurs as a slow-growing mass on the costochondral joints and most often occurs in the third and fourth decades of life. It is more common in men than in women. The chondrosarcoma is treated exclusively surgically because it is resistant to chemo and radiotherapy. Adequate surgical procedure with removal to a healthy length of about 5 cm is a surgical position that should always be followed (Bajaj and Aboeed 2021). Chondrosarcoma of the sternum is extremely rare and often untreatable. Removal of the sternum due to a malignant tumor leads to large defects of the bones and soft tissue, which leads to deformities and paradoxical movements of the chest wall and makes the recontruction of the chest wall very important (Fig. 8.1). If possible, it is necessary to preserve the manubrium of the sternum in order to maintain the stability of the thorax (Haraguchi et al. 2006).

CT scans of the affected bones and images of healthy bones are used for geometric analysis of bones and further processed in a 3D medical image processing software package for three-dimensional design and modeling (Stojkovic et al. 2010).

Based on the 3D model created in Dassault Catia software, the export in STL format results in a model suitable for 3D printing. Due to the specifics of subsequent processing, another additional model is made, which in addition to the main geometry includes a partial surface (which also has a thickness of about 2 mm), in order of forming mold easy. These models are then read in the dedicated ZPrint software specialized for 3D printing by ZCorporation ZPrinter 310 System. The loaded model and the device on which the output is performed are shown in Figs. 8.2 and 8.3.

The core prototype (core cavity of the mold) was used for the fabrication of the casting mold for the sternum implant manufacturing, while the sternum implant prototype was used for visualization in preoperative treatment planning. Before starting of development, it is necessary to determine the printing parameters. This specifically refers to the choice of working material and binder (in this case the powder was ZP130, and the binder ZB58), as well as the layer thickness that affects the surface quality. Since the printed part is the original molds for production, it is of the great importance that the quality of the surface is as good as possible, for the

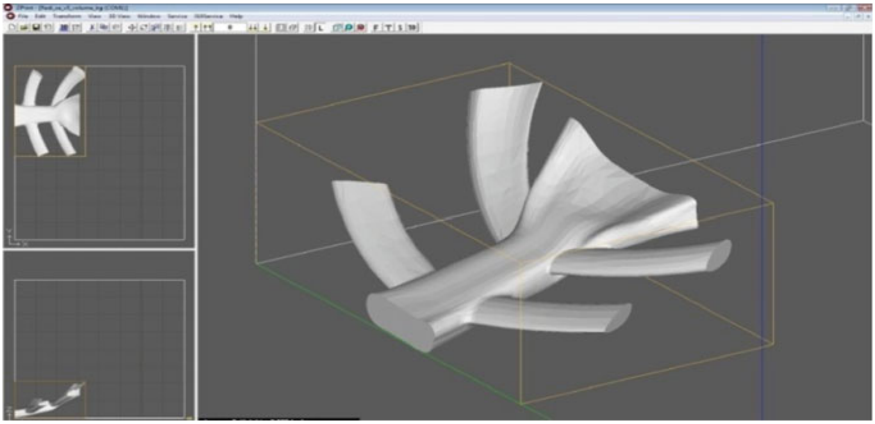

Fig. 8.2 3D geometrical model of a part of sternum implant in the ZPrint software

Fig. 8.3 ZCorporation ZPrinter 310 System

Fig. 8.4 The process of making the original mold

purpose of easier making and separation of the mold. Printing time depends on these parameters, so if a thicker layer is selected for fabrication, more time is required. In addition, the models are positioned in the working volume in a way that maximizes the surface quality and strength of the finished parts. The production process and the printed original are shown in Fig. 8.4.

The printing process itself takes about 2 h, and then the parts are left to harden for another 45 min before being removed from the powder. After the parts are removed from the powder, the excess powder is removed with compressed air. In order to achieve the best possible mechanical characteristics and shorten the drying time, the parts are placed in an oven at 100 °C for 90 min. Only after this operation the sternum implant prototypes for making the mold are obtained (Fig. 8.5).

Since the original mold are not safe for direct use for prosthetic purposes, it is necessary to make a mold which would have implants from medically tested prosthetic material. A special type of polyurethane plastic is used to make the mold, which has the hardness required for casting acrylates, which make up the largest

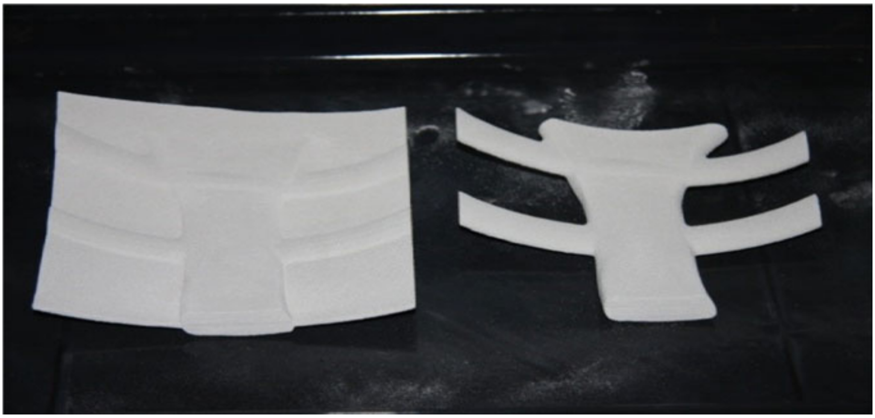

Fig. 8.5 Finished original mold obtained by 3D printing process

percentage of the mentioned material (75% methyl methacrylate–styrene-copolymer and 15% polymethylmethacrylate). First, the lower part of the mold is poured into the box, using an auxiliary model with a “cloak”, and then the upper part of the mold is made using the original. The auxiliary model is destroyed in the process of making the mold, while the original remains undamaged, and can be reused if the need arises. The result of this procedure is given in Fig. 8.6, as well as the procedure of filling the mold with prosthetic material.

The prepared prosthetic material is applied to the cavities of the mold and, after the expansion, it completely fills the mold. After the time allowed for the prosthetic material to harden, the implant is removed from the mold, as shown in Fig. 8.7.

This is followed by mechanical processing of the material, cutting and grinding, and finally the implant is sterilized.

In the case of chondrosarcoma of the sternum shown above and the intraoperative finding shown in Fig. 8.8, after the preparation of an adequate, patient- adapted implant, a specified surgical method is performed in accordance with the preoperative plan. The resection of the sternum in the length of 100 mm and the cartilages of the second and third ribs on both sides including cuneiform resection of the anterior segment of right superior lobe was done (Fig. 8.9). The implant of sternum is fixed to the proximal fragment of the manubrium and distal part of the body of sternum with K-wires. In addition, artificial costal cartilages of the implant are matched and connected to the patient’s second and third thoracic rib with K-wires. Mesh wire is placed above the implant which is sutured to the chest wall using PROLEN 0 (Fig. 8.10). After that, the chest wall was closed (Milisavljevic et al. 2013). A control CT of the chest was performed with a recontruction that shows the correct position of the sternum implant. (Fig. 8.11).

The pleomorphic Sarcoma of Bone, formerly known as Malignant Fibrous Histiocytoma, are rare malignant histiocytic lesions of bone. Treatment is the same

Fig. 8.6 Mold obtained on the basis of the original (left) and filling of the mold with prosthetic material (right)

Fig. 8.7 Implant cast in a mold before removing from the mold

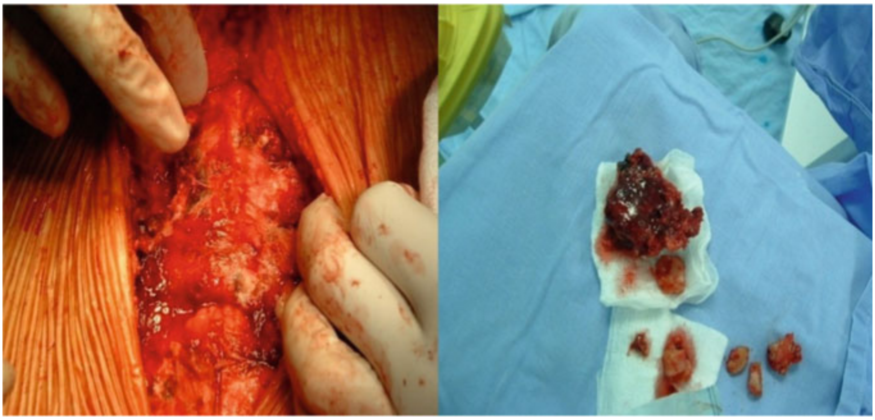

Fig. 8.8 Chondrosarcoma of the sternum—intraoperative finding

as conventional osteosarcoma, including pre- and postoperative chemotherapy and surgical resection (Malik et al. 2020).

Below is an example of Malignant Fibrous Histiocytoma localized at the posterior end of the 8th rib on the left side (Fig. 8.12). The 8th rib on the left side was resected and replaced with a methyl acrylate implant created by 3D printing, and the reconstruction of the chest wall was supplemented with mesh wire in order to improve the stability of the chest wall (Fig. 8.13).

Not only the tumors of the chest wall require surgical resection and reconstruction of the chest wall, but also the rarely tumors originating from the breast can also lead to infiltration of the chest wall. An extreme example of a phylloid breast tumor with

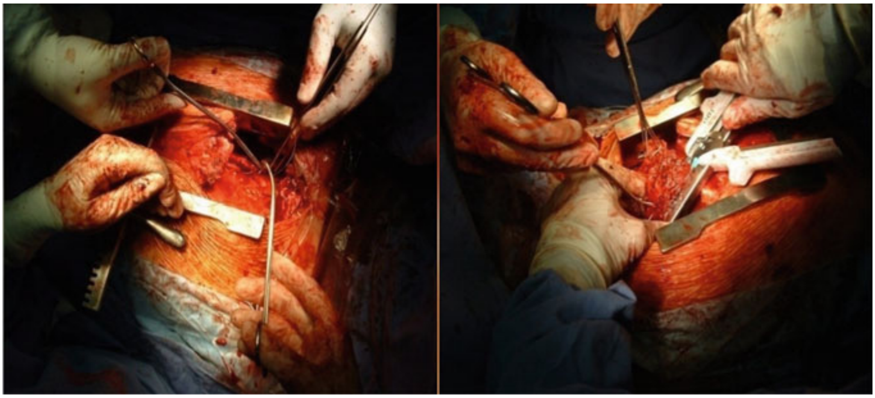

Fig. 8.9 The resection of the sternum in the length and the cartilage of the second and third ribs on both sides; cuneiform resection of the anterior segment of the right superior lobe of right lung

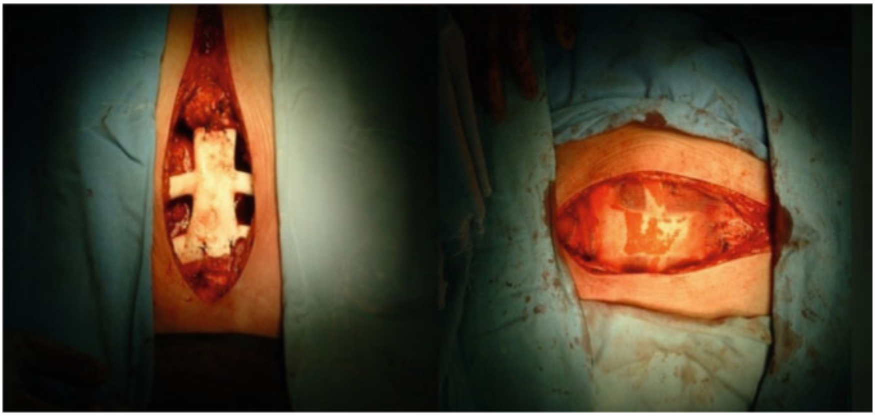

Fig. 8.10 Matched implant of sternum and the mesh wire placed above

infiltration of all layers of the chest wall, including bone structures, i.e., ribs is present on (Fig. 8.14).

The phylloid breast tumor was excised and the chest wall was resected, including three ribs (the 4, 5 and 6th ribs on the left side) (Fig. 8.15). The implant is fixed with K-wires and mesh wire is placed above the implant. Chest wall was then closed. The defect was additionally reconstructed with omentoplasty and skin flap (Fig. 8.16).

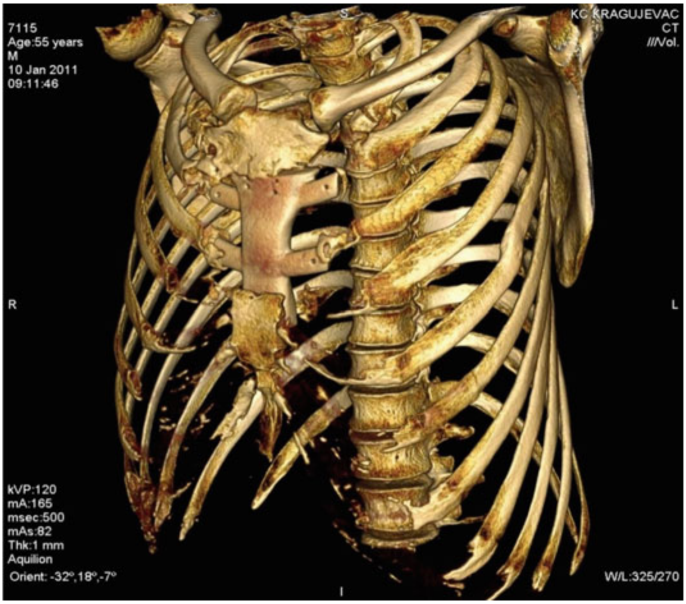

Fig. 8.11 Postoperative status—CT reconstruction of chest wall with sternum implant

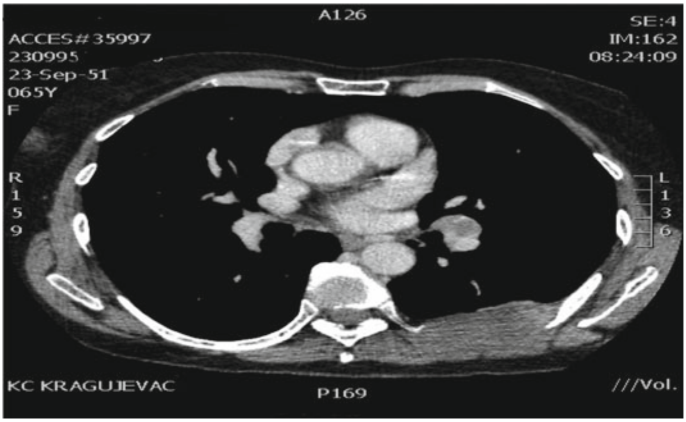

Fig. 8.12 CT scan—Malignant Fibrous Histiocytoma of the 8th rib on the left side

8.5 Conclusion

After an extensive wall resection, complex chest wall defects, which includes large defects of the soft tissue and bone structures, can be some of the most challenging problems that thoracic surgeons must face. Successful reconstruction after extensive surgical resections of the chest wall plays a key role in the proper functioning of

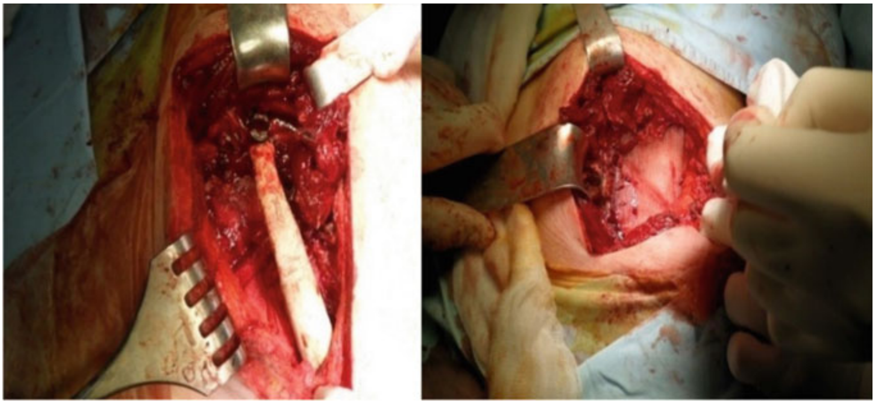

Fig. 8.13 Reconstruction of the chest wall with a methyl acrylate implant and mech wire

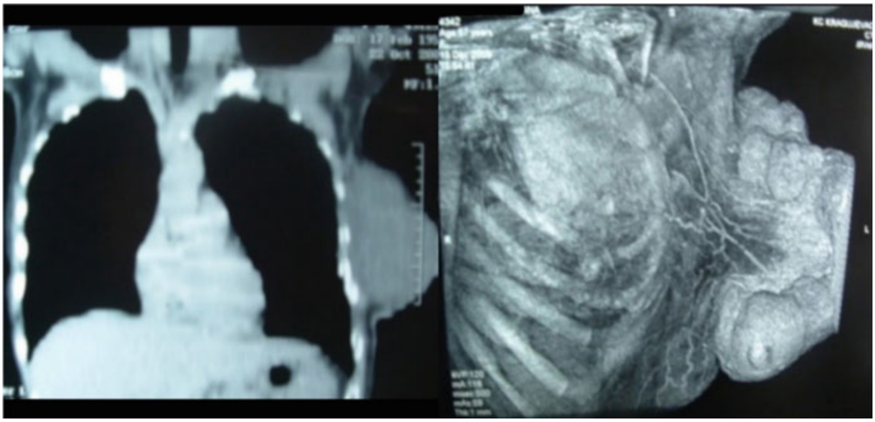

Fig. 8.14 Phylloid breast tumor with infiltration of all layers of the chest wall

vital thoracic organs as well as the whole organism. The length of postoperative recovery is related to the size of the defect and the choice of appropriate materials and surgical techniques. Each case requires an individual plan, approach, selection of appropriate material and surgical techniques. The choice of an adequate materials and surgical techniques should be always based on multidisciplinary approach. The use of synthetic materials for chest reconstruction is supported by their diversity, availability, relatively inert nature and ease of use. Chest reconstruction with biocompatible artificial or synthetic materials is safe and effective in most defects. It also expands the indications for resection and reconstruction of the chest wall and reduces overall costs. It is important to emphasize that until now, the selection of the most suitable artificial material for the reconstruction of structures of the chest

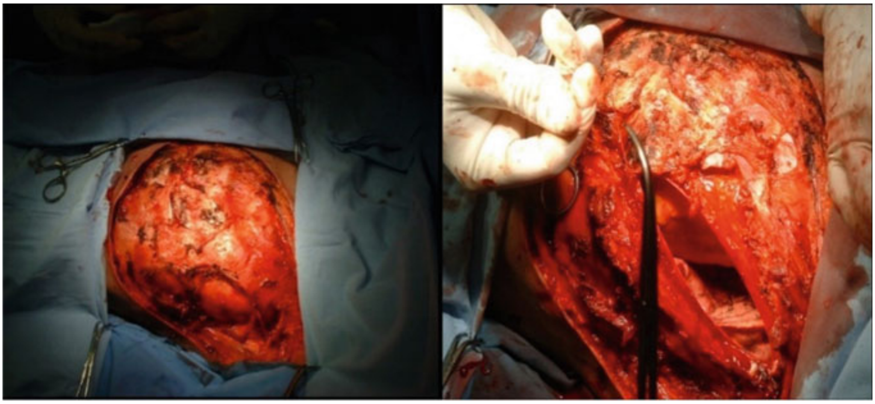

Fig. 8.15 Resection of phylloid breast tumor and the chest wall

Fig. 8.16 Reseconstruction of chest wall with implant (left) and omentoplasty (right)

wall has not yet been clearly established. The implantation of the modern biomaterials (particularly hybrid human tissue-engineered products containing proteins, stem cells and/or other biological ingredients) implies a rather promising approach to optimize risk/benefit ratio.

References

Bajaj T, Aboeed A (2021) Chest wall tumors. In: StatPearls (Internet). Treasure Island (FL). StatPearls Publishing

Bisgard JD, Swenson SA Jr (1948) Tumors of the sternum; report of a case with special operative technic. Arch Surg 56(5):570–578

Cara JA, Lacleriga AF, Cañadell J (1993) Iliac allograft used for sternal reconstruction after resection of a chondrosarcoma. Int Orthop 17(5):297–299

Clemens MW, Evans KK, Mardini S, Arnold PG (2011) Introduction to chest wall reconstruction: anatomy and physiology of the chest and indications for chest wall reconstruction. Semin Plast Surg 25(1):5–15

Gangolphe L (1909) Enorme enchondrome de la fourchette sternale. Lyon Chir 2:112

Goldsmith I, Evans PL, Goodrum H, Warbrick-Smith J, Bragg T (2020) Chest wall reconstruction with an anatomically designed 3-D printed titanium ribs and hemi-sternum implant. 3D Print Med 6(1):26

Haraguchi S, Hioki M, Hisayoshi T, Yamashita K, Yamashita Y, Kawamura J, Hirata T, Yamagishi S, Koizumi K, Shimizu K (2006) Resection of sternal tumors and reconstruction of the thorax: a review of 15 patients. Surg Today 36(3):225–229

Hayashi T, Sakakura N, Ishimura D, Kozawa E, Yoshida M, Sakao Y, Yamada H, Tsuku-shi S (2019) Surgical complication and postoperative pulmonary function in patients undergoing tumor surgery with thoracic wall resection. Oncol Lett 17(3):3446–3456

Khalil el-SA, El-Zohairy MA, Bukhari M (2010) Reconstruction of large full thickness chest wall defects following resection of malignant tumors. J Egypt Natl Canc Inst 22(1):19-27

Malik AT, Baek J, Alexander JH, Voskuil RT, Khan SN, Scharschmidt TJ (2020) Malignant fibrous histiocytoma of bone: a survival analysis from the National Cancer Database. J Surg Oncol 121(7):1097–1103

Maxwell GP (1980) Iginio Tansini and the origin of the latissimus dorsi musculocutaneous flap. Plast Reconstr Surg 65(5):686–692

Milisavljevic S, Grujovic NN, Mrvic S, Stojkovic D, Arsenijevic M, Jeremic B (2013) Sternum resection and chest wall reconstruction with metaacrilate implant in tuberculosis. Indian J Surg 75(Suppl 1):257–260

Sanna S, Brandolini J, Pardolesi A, Argnani D, Mengozzi M, Dell'Amore A, Solli P (2017) Materials and techniques in chest wall reconstruction: a review. J Vis Surg 3:95

Stojkovic M, Milovanovic J, Vitkovic N, Trajanovic M, Grujovic N, Milivojevic V, Milisavljevic S, Mrvic S (2010) Reverse modeling and solid free-form fabrication of sternum implant. Australas Phys Eng Sci Med 33(3):243–250

Tamburini N, Grossi W, Sanna S, Campisi A, Londero F, Maniscalco P, Dolci G, Quaran-totto F, Daddi N, Morelli A, Cavallesco G, Dell'Amore A (2019) Chest wall reconstruction using a new titanium mesh: a multicenters experience. J Thorac Dis 11(8):3459–3466

Thomas PA, Brouchet L (2010) Prosthetic reconstruction of the chest wall. Thorac Surg Clin 20(4):551–558

Tukiainen E (2013) Chest wall reconstruction after oncological resections. Scand J Surg SJS Official Organ Finnish Surg Soc Scand Surg Soc 102(1):9–13

Watson WL, James AG (1947) Fascia lata grafts for chest wall defects. J Thorac Surg 16(4):399–406

Weyant MJ, Bains MS, Venkatraman E, Downey RJ, Park BJ, Flores RM, Rizk N, Rusch VW (2006) Results of chest wall resection and reconstruction with and without rigid prosthesis. Ann Thorac Surg 81(1):279–285

Chapter 9
Implant Personalization Needs in Dynamic Internal Fixation of Bone Fractures

Milan M. Mitkovic

9.1 Bone Fractures

The main purpose of the human skeleton is to support and to protect the soft tissues. Being attached to the muscles by tendons, the human skeleton is essential to provide lever based articulated motions (Caon 2018; Fister et al. 2018; Shipman et al. 2013). Any painful condition or limiting deformity in osteoarticular system has an influence in meeting personal needs and wishes based on these motions, thus playing a significant role in the quality of human life. The skeleton functions also as a metabolic factor in the human body: the blood cells are mostly produced in the bone marrow (the soft tissue inside the bone cavity), and the bone tissue is a depot of calcium ions in the form of calcium-phosphate, being prepared to release these ions if the lack of calcium in blood is occurred (Peacock 2021). The bone tissue metabolic activity is followed by a permanent itself renewal—there are parallel activities of the bone resorption (osteolysis) and the bone formation (osteogenesis), thus the complete human skeleton is renewed in approximately 10 years (Welch and Hayhoe 2019). The bone union after bone fracture is a specific process of the bone tissue formation, defining some features necessary to be implemented in the bone fractures treatment.

There are four main forms of the human skeleton bones: long bones, short bones, flat bones, and irregular bones. Long bones are the main bone forms in human extremities, thus improving in their fracture treatment is going carefully in the orthopedic surgery science (Gilliland and Kernick 2021; Shen et al. 2019).

Bone tissue is presented in two types—*cancellous bone* (also called *woven bone* or *trabecular bone*) and *cortical bone* (also called *lamellar bone*). Cancellous bone is sponge formed bone and it is much more vascularized than a cortical bone. Cortical bone is more compact than cancellous bone, having the system of connected narrow

M. M. Mitkovic (✉)
Faculty of Medicine, University of Nis, Nis, Serbia
e-mail: milan.mitkovic@medfak.ni.ac.rs

Clinic for Orthopedics and Traumatology, University Clinical Center Nis, Nis, Serbia

O. Canciglieri Junior and M. D. Trajanovic (eds.), *Personalized Orthopedics*,
https://doi.org/10.1007/978-3-030-98279-9_9

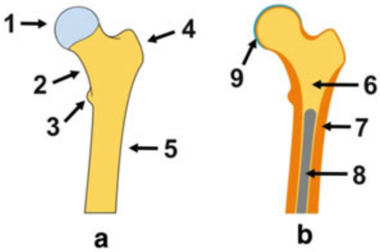

Fig. 9.1 Topographic (**a**) and structural (**b**) anatomy of the proximal part of the femur; femoral head (**1**), femoral neck (**2**), lesser trochanter (**3**), greater trochanter (**4**), femoral shaft (**5**), cancellous bone (**6**), cortical bone (**7**) medullary canal (**8**), cartilage (**9**)

channels for vessels and nerves. Every long bone has the mid, tube form part, called as *shaft* or *diaphysis*, dominated by a cortical bone, and the two peripheral parts (one proximal and one distal part), each of two consisting of *epiphysis*, lying the most peripherally, and *metaphysis*, lying between the epiphysis and the diaphysis. Peripheral part of the long bone is dominated by a cancellous bone. Shaft of a long bone contains *medullary canal* (longitudinal cavity inside the bone) and *cortex* (wall of the medullary canal) consisting of the cortical bone (Fig. 9.1) (Gilliland and Kernick 2021; Meinberg et al. 2018; Shipman et al. 2013).

Bone fractures are defined as loss of the bone tissue continuity and they can be classified into *simple fractures*, having two fracture fragments, and *comminuted fractures*, having three or more fragments. Based on the geometry of the fracture pattern, simple fractures can be classified into *transversal*, *oblique*, and *spiral fractures*, while comminuted fractures can be classified into *multifragmentary* and *fragmentary segmental fractures*. Fragmentary segmental fractures have multiple fracture lines without its crossing (in long bones these lines are at different levels) (Kim et al. 2021; Shipman et al. 2013).

Fixation of the fractures, as a surgical treatment method, has the role to support the bone healing process, to provide the bone union in an anatomically adequate position, to prevent the injury of local important vessels and nerves by the sharp edge of a mobile bone fracture fragment and to allow early mobilization of the injured limb, thus preventing the stiffness of adjacent joints. There are two types of bone fractures fixation—internal fixation and external fixation (Alhammoud et al. 2019; Baron et al. 2020; Fowler et al. 2019; Hak et al. 2018). Internal fixation is performed by the implants remaining entirely under the skin after surgery. External fixation is performed by a device having the pins and/or the wires, being attached to the bone, passed throw the soft tissues (including the skin) and attached to an external fixator frame outside the body. There are two main types of internal fixation—intramedullary and extramedullary fixation (Gajdobranski et al. 2014; Grubor et al. 2019; Hak et al. 2018; Mitkovic et al. 2020a, b). Intramedullary fixation is performed by the implants with the stem (implant body) being introduced into the medullary canal of a long bone. Extramedullary fixation is performed by the implants with the stem being leaned on the outside of the bone.

There are various commercial implants for bone fractures fixation, each adapted to the shape of an appropriate part of the bone. The need for a personalized implant (with a customized shape) in the treatment of a bone fracture is commonly associated by an obstruction in the bone healing process—delayed union or nonunion. Any of these problems regarding bone healing process are desired to be followed by the feature of dynamization in the bone fracture fixation method used (Fu et al. 2021; Kostic et al. 2015; Mitkovic et al. 2017, 2018, 2020a, b; Perumal et al. 2018).

9.2 Fracture Healing and the Dynamization

In some unstable fractures, especially where the less vascularized bone is present and where the cortical bone is predominant, it is desired to perform initially rigid fixation but to transform it into a dynamic mode after several weeks (Kostic et al. 2015; Milenkovic et al. 2017; Mitkovic et al. 2010, 2017, 2018, 2020a, b; Stojiljkovic et al. 2013; Stojiljkovic et al. 2015). Immature bone tissue formation at the fracture area, being there during the bone healing process, is called *callus*. The rigid fixation is desired while the soft callus is being formed in the fractured area. The process of a soft callus formation includes a capillary ingrowth from the bone fragments into the soft tissue formed at the fracture gap, being finished by a capillary bridging between the bone fracture sides. The fracture sides are being bridged by a hard callus after the soft callus calcification. This process requires sufficient bridging vascularization between bone fracture fragments. The further bone maturation in the fractured area is followed by a hard callus transforming into a cancellous bone (Ercin et al. 2017; Pountos and Giannoudis 2018). This type of a new cancellous bone is afterwards remodeling into a cortical bone at the cortical area of a fracture. The process of soft callus maturation is as more effective as the strains in the fracture area are lower. This could be considered as the reason for fixation of bone fractures to be initially rigid. Thus, the key factor in the soft callus maturation into the hard callus and into the mature bone afterwards is the vascular bridging with sufficient blood flow between bone fracture fragments.

The main causes for an insufficient vascular bridging between bone fracture fragments could be considered as:

- excessive distance between bone fracture fragments—this condition can result either from an inadequate intraoperative fracture reduction while performing the fixation surgery or from an osteolysis-osteogenesis imbalance at the initial period after surgery, followed by the osteolysis domination (excessive bone tissue resorption induce the appearance of an excessive space between fixed bone fragments), or both; excessive distance between bone fracture fragments can prevent enough vascular ingrowth at the fracture gap and hence disable the vascular bridging between bone fracture fragments,

- insufficient contact surface area between bone fracture fragments—the causal factors for insufficient vascular bridging here are the same as written above regarding reduced capillary bridging,
- insufficient vascular bridging despite sufficient contact between bone fracture fragments—this condition can result either from reduced stimulation of local capillary ingrowth or from too narrow bridging capillaries resulting in its insufficient blood flow.

In addition to the bridging vascularization, an important factor in a new bone tissue maturing at the bone fracture area is the pressure (compression) between bone fragments after the fracture fixation (Ganadhiepan et al. 2019; Ghimire et al. 2018). This pressure results in hard callus transforming into the mature bone tissue with a morphological structure that is the most resistant to the local biomechanical forces. Thus, reduced contact between the bone fracture fragments results in reduced surface of that pressure, obstructing desired mature process of the new bone in the fractured area.

While the contact between bone fracture fragments is absent after the fracture fixation, then the whole biomechanical load transmission from one bone fracture fragment to another is occurring throw the implant used (Mitkovic et al. 2018, 2020a, b; Ruedi et al. 2007). The implant is high loaded in such conditions, but when the hard callus is starting to be formed between the bone fracture fragments then the biomechanical load is being shared between the bone and the implant. Finally, when the contact between adjacent bone fracture fragments is fully performed by a hard tissue, almost the whole local biomechanical load is passing throw the bone, relieving the implant from high loads. If the absence of the contact between bone fracture fragments (without the biomechanical pressure between) is lasting too long, the material fatigue effect will induce the implant breakage, leading to the need for a new surgery.

Dynamization of a fixed bone fracture could be considered as a factor giving conditions that can solve the problems regarding vascular bridging obstruction and absence of the biomechanical pressure. Dynamization is in orthopedic science defined as any controlled movement between two fracture fragments promoting the process of bone union there (Mitkovic et al. 2020a, b). In this way, dynamization mostly refers to an axial translation of a bone fracture fragment inducing the fracture gap closing and the compression between adjacent fragments. This controlled translation of a fixed bone fracture fragments can be realized only by the implants having a feature of translational movement between some implant parts. Performing the dynamization, it is desired to maintain correct angular relations between bone fracture fragments achieved intraoperatively and just to enable the compression at the fracture area. Thus, the part of the implant where the translational movements are performed has to have a straight form.

Benefits of a dynamization in a bone fracture area could be considered as:

- reducing enough or losing the distance between the bone fracture fragments, thus providing better conditions for vascular ingrowth and for bridging capillaries formation,

- further stabilization of the fracture resulting in larger surface of the fracture fragments contact, thus giving the chance for more bridging capillaries between bone fracture fragments,
- reducing the distance between bone fragments can result in relaxation of previously formed soft callus bridging capillaries, thus inducing higher blood flow throw them and hence higher local calcification of the adjacent soft callus, promoting a more effective hard callus forming; furthermore, higher blood flow throw the bridging capillaries provides higher inflammation mediators level in the fracture area, giving more stimulation in local new vascular ingrowth, resulting in more bridging capillaries forming,
- achieving of previously loosed or making larger contact between bone fracture fragments can promote the local biomechanical compression at the fracture area, contributing to the process of a local new bone maturing into the form with the most resistance regarding local biomechanical loads,
- achieving of previously loosed or making larger contact between bone fracture fragments gives a relief to the implant by sharing the biomechanical load between implant and bone; implant breakage by the material fatigue effect is being prevented in this way.

There is still not possible to predict if a patient will have the need for the dynamization of the fixed fracture. In this reason, using the implants with dynamizing feature could be suggested as a principle, especially in cases where it seems to expect any problem with the bone fracture healing process (mostly in elderly population, where the osteoporosis is common, or in cases with complex fractures, etc.). There was explained in the text above why the fracture fixation should be initially rigid for most fracture types, but to have the feature to activate the dynamization later if needed. Many implants provide rigid initial fixation with the possibility to transform it into a dynamic mode by an additional surgery, in terms of its locking screw removal (intramedullary nails, Medoff plate, etc.). Selfdynamizable Internal Fixator (SIF) is the only internal fixation implant today having the feature to provide a delayed dynamization after an initially rigid fixation without the need for additional surgery.

Dynamization in long axis of a long bone is provided by different mechanisms in internal fixation implants. Using intramedullary nails, this type of the dynamization occurs by a bone fracture fragment telescopic movement around the nail inside the medullary canal. The medullary canal of the femur or tibia (bones of the lower extremity that most often need the dynamization) has to be reamed intraoperatively before the intramedullary nail is introduced inside the medullary canal. Dynamization in long direction of the bone is in Medoff plate, as an extramedullary implant, provided by sliding grooves between two parts of the implant stem (Arirachakaran et al. 2017). The construction of Selfdynamizable Internal Fixator includes the clamps pulled around a cylindrical part (bar) of the implant stem (Mitkovic et al. 2012, 2020a, b). The dynamization in long direction of the bone is in this implant provided by a sliding contact between clamps and the bar. Both in an intramedullary nail and in Selfdynamizable Internal Fixator, there is the locking screw passing throw the straight, longitudinally directed oblong hole (slot) in the implant body. This locking

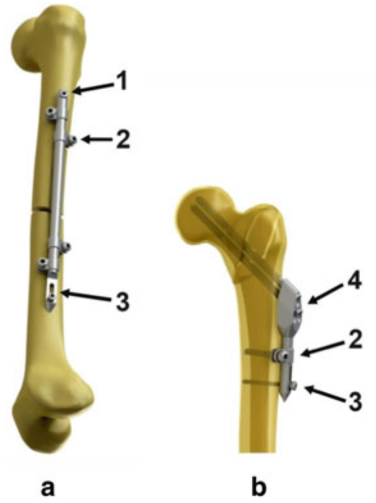

Fig. 9.2 Femoral shaft fracture (**a**) and pertrochanteric fracture (**b**) fixed by Selfdynamizable Internal Fixator; screw passing the simple hole of the bar (**1**), screw passing the clamp (**2**), screw passing the oblong hole of the bar (**3**), sliding screws passing the "trochanteric unit" of the implant stem (**4**) Reproduced from Mitkovic et al. (2020a)

screw prevents the torsion between the bone fracture fragments. If the locking screw is placed at the peripheral end of the slot intraoperatively then the dynamization can occur in direction of the slot, limited for the distance between screw and inner end of the slot (Fig. 9.2).

Using Medoff plates and intramedullary nails, transforming the fixation from rigid into dynamic form in the long direction of the bone is performed by removal of the locking screw passing the simple circular hole (not the oblong hole) in the implant stem. In intramedullary nails, other locking screw passing throw the oblong hole remains in place in this additional surgery, thus allowing the dynamization but still preventing the torsion between bone fracture fragments.

Using Selfdynamizable Internal Fixator, initially rigid fixation is achieved by tight screw-driving of the screws passing the hole of each clamp. Tight screw-driving of these screws results in both rigid contact of the clamp to the bone and in strong tightening of the clamp around the bar of the implant. The rigid fixation achieved in this way can be transformed into a dynamic mode spontaneously at the weeks after surgery, by spontaneous "unlocking" of some clamps, without additional surgery (Fig. 9.3). Such spontaneous activating of the dynamization in long direction of the bone (in axis of the implant bar) has been clinically approved (Mitkovic et al. 2012). This unique feature of the implant could be explained by several possible reasons that follow a prolonged absence of the stable contact between bone fracture fragments:

- longer high load of the clamps resulting from local biomechanical forces leads to a slightly clamp dilatation, enough to provide sliding of the clamp around the implant bar,
- longer repetitive loads of the screw passing throw the clamps resulting from local biomechanical forces, could induce its slightly unscrewing, leading to a

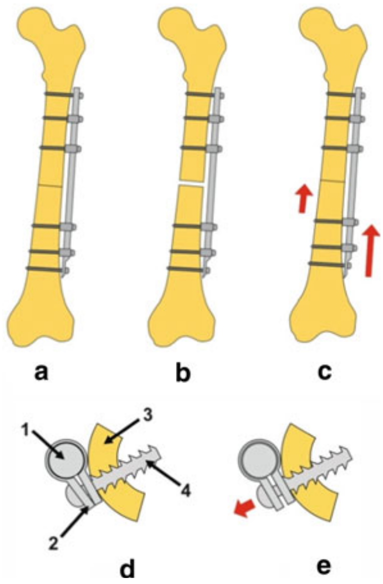

Fig. 9.3 Dynamization of a femoral shaft fracture fixed by Selfdynamizable Internal Fixator and the mechanism of spontaneous clamp unlocking; intraoperative fracture reduction and fixation (**a**); loss of the contact between fixed bone fracture fragments in weeks after surgery (**b**); dynamization of the fracture achieved by delayed spontaneous clamps unlocking, reestablishing the contact between bone fracture fragments (**c**); bar (**1**), clamp (**2**), bone (**3**), screw (**4**); locked clamp (**d**), unlocked clamp (**e**)

less strength contact between the clamp and the implant bar, enough to provide a sliding contact there (Fig. 9.3),

- longer repetitive loads of the screw passing the clamps resulting from local biomechanical forces, could induce a slight osteolysis around the screw, leading to a less strength contact between the clamp and the implant bar, enough to provide a sliding contact there.

9.3 Personalization Needs in the Use of Clamps

There could be considered the initiating of longitudinal dynamization in a femoral shaft fracture fixed by Selfdynamizable Internal Fixator depends on the number of clamps used, on the screwing intensity of the screws for clamps, and, possible, on the vertical level of each clamp. If a large number of clamps with strongly screwed screws were used, this could result in an impossibility of dynamization initiating, because local biomechanical forces, significantly depending on the body weight, would not be sufficient to “unlock” all these strongly tightened clamps (Mitkovic et al. 2012, 2020a, b; Mitkovic 2020; Stojiljkovic et al. 2013). Based on this, further investigations would be desirable to define recommended number of clamps and screwing banding moment for each screw for clamp, relating to the patient’s body weight, length of broken bone, patient’s height, length of the implant used, vertical level and shape of the fracture, and each clamp vertical level on the implant stem, to provide dynamization initiating in a certain patient. This type of analysis could even define the expected time of dynamization initiating. There are not many data in the literature regarding suggestions for optimal time to start with the fixed bone fracture dynamization. In some data twelve weeks after surgery are referred as the suggested time for a locking screw removal in intramedullary nailing, while other sources state a successful bone fracture union when the dynamization is activated 6–8 weeks after surgery (Mitkovic et al. 2012; Perumal et al. 2018). If there would be desirable to initiate the dynamization with a greater delay, then a larger screwing banding moment of the screws passing the clamps would be recommended, as well as a larger number of clamps. This refers to the clamps for the bone fracture fragment into which is screwed the locking screw passing through the oblong hole. The screwing intensity of the screws passing the clamps for the other bone fracture fragment (bone fracture fragment into which is screwed the locking screw passing the simple circular hole in the implant stem) should not be considered as significantly relevant in the dynamization initiating.

Since the part of the Selfdynamizable Internal Fixator where the clamps relevant in the dynamization are being attached on should have to have a straight form (the bar), there may sometimes be desirable for clamps to be personalized in order to maintain fixed fracture fragments in anatomical position for bones with unusually curved surface. Rigid fixation in the use of Selfdynamizable Internal Fixator is fully achieved by screws for clamps tightening if the screw head leans on one side of the clamp and the other side of the clamp leans on the bone. Each clamp is rotatory adjustable relative to the bar of the Selfdynamizable Internal Fixator. But since a screw for clamp should pass approximately through the center of the femoral shaft and the position of the Selfdynamizable Internal Fixator's stem is determined previously, then the standard clamp being passed through by the screw cannot sometimes be rotated enough around the bar to lean on the bone surface, preventing enough tightening of the clamp around the bar, i.e., preventing initially full rigid fixation. Hence there could be considered a need to use clamps with different dimensions than in the standard clamps for such situations. Tightening of the screw passing such personalized clamp provides one side of the clamp to lean on the screw head and the other side of the clamp to lean on the bone, maintaining adequate fracture position in an unusually curved bone. The use of X-ray or CT scan of the other uninjured leg could be useful to determine the personalized clamp dimensions (Rashid et al. 2017). Using standard clamps in some situations would result in a non-anatomical reduction of the bone fracture if all clamps are being in touch to the bone, because it can result in a side "opening" at the fracture gap, but this could be avoided by the use of personalized clamps described above (Fig. 9.4).

9.4 The Need for an Extramedullary Implant with Customized Shape

In the bone fracture treatment, the need for internal fixation implants stem personalization can be present if there would be an uncommon bone prominence at the side

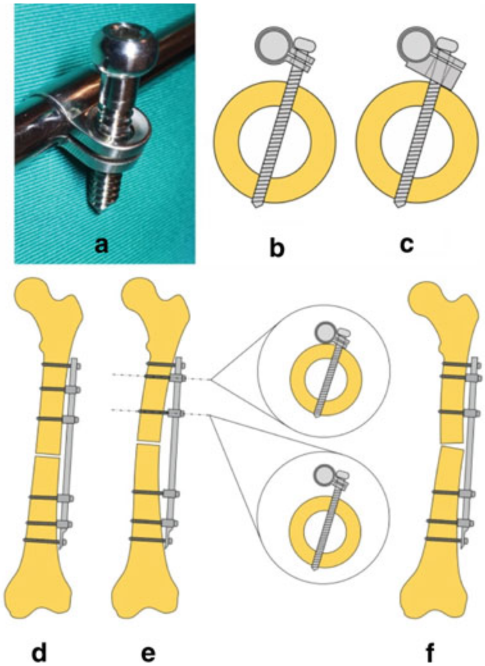

Fig. 9.4 The screw passing the standard clamp is in some extent angularly adjustable to the clamp due to the wider clamp hole than the screw diameter (**a**); the range of this adjustability is sometimes not enough to provide standard clamp to touch the bone (**b**), thus a personalized clamp should be used (**c**); Selfdynamizable Internal Fixator with standard clamps used in a shaft fracture fixation on the femur having standard anatomical shape, where all the clamps can be in touch to the bone (**d**), and on the femur having shaft more curved than normally, thus standard clamps somewhere cannot be in touch to the bone when the best fracture reduction is achieved (**e**) and where a lateral "opening" at the fracture gap will occur if all the standard clamps will be in touch to the bone (**f**)

for the implant placement. That prominence can be the result of a previous fracture union on the same bone. This problem can also be present in some fragmentary segmental fractures, where the fracture had healed (with bone union) at the level of lateral bone prominence, but the bone healing was not finished at the other level of the fragmentary segmental fracture. This condition of a not finished bone union process could be considered either as a delayed union or a nonunion. Furthermore, local bulging bone prominence can follow some bone tumor process, resulting in the bone shape which is not capable for conventional shapes of internal fixation implants. In some conditions, bone prominence could be osteotomized (removed by a chisel) to free up the space for an adequate placement of a conventional implant. But in some other conditions that prominence should not be osteotomized, to prevent the excessive bone weakness accompanied by the risk of repeated fracture. Also, in some fractures with the tumor process in other part of the same bone, tumorous changes can be expressed as a local bone bulging (ballooning bone changes) accompanied by thinned cortical bone and by reduced density of inner cancellous bone. Any surgical work on such bone changes, including osteotomy, could result both in weakness of the bone and in dissemination of malignant cells.

The fractures described above, regarding delayed union, nonunion or a tumor bone change at the same bone, are referred to an obstruction of the bone union process, thus requiring the fracture fixation with the implant having the feature of dynamization.

The presence of such bone prominence that is not desirable to be osteotomized imposes the need for use an extramedullary fixation implant with a customized shape, providing an implant "bypass" around the prominence. Clamps sliding feature, necessary to provide the dynamization of Seldynamizable Internal Fixator, cannot be achieved along this curved part of the implant stem thus sliding clamps should be placed at another part of the implant's stem, where it has a straight form. If the implant did not have a shape that was adapted to the bone prominence described above, then the implant stem would have to be moved laterally, making too much "free space" for screws between the implant stem and the bone, leading to a greater implant stress (greater lever arms of the screws loading) that could result in an implant breakage. Furthermore, too lateralized implant stem would interfere with the local muscles in the extent to obstruct the function of these muscles significantly. Thanks to the customized shape of the implant stem relating to the bone prominence, there would be possible to provide the stem not to be too far from the bone, reducing both implant load and local muscles mechanical irritation (Fig. 9.5).

In the situations from above, regarding the need for implants with a personalized shape of the stem, there would be presented a need for the use of previously described personalized clamps too, because the bone shape is often variable in such cases.

Fig. 9.5 Fragmentary segmental fracture of the femoral shaft followed by slightly rotational dislocation of the free fragment with bone union at the upper fracture gap and with nonunion at the lower fracture gap. Lateral bone prominence should not be osteotomized in such case, to prevent mechanical weakness of the bone, thus custom curved implant should be used in the fixation

9.5 Personalization Needs in the Use of Sliding Screws

Sliding screws are used in the internal fixation of pertrochanteric fractures. According to AO bone fractures classification, as one of the most applied classifications in orthopedic traumatology today, pertrochanteric fracture is defined as a fracture of the proximal (upper) part of the femur (thigh bone) extending obliquely from its upper-outer part to its lower-inner part of the proximal femur (Mattisson et al. 2018; Ruedi et al. 2007). In the upper-outer part, there is an anatomical eminence, called *greater trochanter*, while in the lower-inner part is a smaller anatomical eminence, called *lesser trochanter*, thus in pertrochanteric fractures a fracture line extends from the greater trochanter to the lesser trochanter (Fig. 9.1) (Caruso et al. 2017; Mori et al. 2018; Ruedi et al. 2007). These fractures are very common, and they have a great healing potential (potential for bone union) since the trochanteric region of the femur is rich in cancellous bone. In these reasons, the pertrochanteric fractures are not followed by significant damage of blood vessels responsible for the trochanteric region vascularization. Pertrochanteric fractures are unstable, thus their non-surgical treatment commonly results in malunion (bone union in a bad fracture position). The typical type of trochanteric fracture malunion is followed by shortening of injured leg (Mori et al. 2018; Prommik et al. 2021). Leg shortening further leads to a gait disorder reflecting both in hips condition and in the condition of a wider skeletal area (knees, spine). Surgical treatment of these fractures is desirable not only to prevent pertrochanteric fracture malunion and leg shortening, but also to enable patients to be mobilized as early as possible. Pertrochanteric fractures are the type of the so-called *osteoporotic fractures*, because they occur most often in the elderly population, older than age of 65 years. Continuous bed lying for a long time is very important to be avoided in elderly population, because it can be an inducing factor for various medical problems—myocardial infarction, pulmonary thromboembolism, pneumonia, pressure ulcers, and urinary tract infections (Chlebeck et al. 2019; Mori et al. 2018; Velez et al. 2020). These medical complications are the result of slowed blood flow in the circulation, slowed breathing (slowed air flow in airways), long pressure on the skin (inducing a blood flow obstruction in the small vessels at the pressured skin area), and slowed urine flow in the urinary tract—all due to reduced movements of the body during the long bed lying. In patients with a pertrochanteric fracture, even the slightest movement of the thigh is often very painful if the fracture is not stabilized by an implant. For these reasons, the treatment of pertrochanteric fractures is most often performed surgically by internal fixation using an intramedullary or extramedullary implant after the fracture reduction (the correct positioning of the bone fragments) (Chang et al. 2020; Gjertsen et al. 2017; Inui et al. 2021; Kumar Srivastava 2019; Shinoda et al. 2017; Zhu et al. 2017). Development of pertrochanteric fractures internal fixation had become intensive in the first half of twentieth century. At that time, there was considered that it is not enough to use only screws in the fixation of a pertrochanteric fracture, but it is necessary for the fixation implant to contain a body (stem) through which a screw or a wedge is inserted into the neck and head of the femur (Andersson et al. 1984; Koval Zuckerman 2000). This is the safest way in internal fixation to maintain the correct angle between femoral neck (femoral *column*) and femoral shaft (femoral *diaphysis*)—*collo-diaphyseal angle*. The bone union with a proper collo-diaphyseal angle of the femur is a very important factor in maintaining the correct length of the leg, but also in maintaining desirable biomechanical loads in the hip joint. First implants for pertrochanteric fractures fixation had rigid contact between the stem and the part introduced into the femoral neck and head. Afterwards, there has been confirmed that this rigidity was often followed by mechanical postoperative complications, such as the implant protrusion through the femoral head, implant bending with the consequent fracture malunion, implant breakage, etc. (Bartonicek and Rammelt 2014).

Further improvement of implants for pertrochanteric fractures internal fixation indicated that these postoperative complications were less common after introducing of sliding contact between the component for the femoral neck and head, and stem in the implant construction (Bartonicek and Rammelt 2014; Claes 2018; Waddell 2010). The sliding component, inserted into the femoral neck and head, is usually found as a *sliding screw*, although such sliding components are in some implants found as a *sliding nail* or a *sliding blade*. This sliding effect provides a postoperative compression between bone fracture fragments, thus making the fracture fixation more stable, with less implant load and less chance for a sliding screw tip to protrude the femoral head under the local biomechanical forces (including body weight). Lower prevalence of postoperative complications when using a sliding component indicates there is often a need for additional postoperative stabilization of pertrochanteric fractures, achieved by the dynamization. This need could be explained by the fact that the layer of a cortical bone is thin, and the cancellous bone, which is softer than cortical bone, is the most dominant in the trochanteric part of the femur. Thus, pertrochanteric fracture stabilization is mostly achieved when the fracture fragments are additionally impressed into each other by the biomechanical forces after surgery. Furthermore, the need for pertrochanteric fracture dynamization after surgery may be the result of an initial temporary osteolysis overcoming the simultaneous osteogenesis in the fracture area, making the fracture gap wider than intraoperatively. In this occurrence, the dynamization is desirable to re-establish necessary contact and further compression between bone fracture fragments, providing as better conditions for the fracture union as possible until the osteogenesis process overcome the osteolysis.

Experience in the treatment of pertrochanteric fractures treatment proved that their fixation is not necessary to be initially rigid (as is, for example, in femoral shaft fractures), thus no initial locking of the sliding screws is required and the sliding screws dynamization is being enabled all the time (Mitkovic et al. 2020a, b; Mitkovic 2020). Despite absence of initial sliding screws locking, the fixation of pertrochanteric fractures is proved as stable enough, due to the very strong and tightened muscles of the hip area. This tightness prevents the overspreading of the pertrochanteric fracture gap in extent which could obstruct the fracture healing process. Also, highly vascularized and dominant cancellous bone in the area of a pertrochanteric fracture make an eventual momentary distancing between bone fracture fragments not to be sufficient enough to obstruct the bone fracture healing process.

The compression between bone fracture fragments has a role both in faster fracture healing and in more efficient new bone maturing process. Body weight is a biomechanical factor causing the compression between pertrochanteric fracture fragments, especially in the moment of the full stance on the injured leg. In addition to the body weight, local biomechanical forces caused by tension and contractions of local muscles have the roll in compression between fracture fragments too. It is desirable to examine whether the sliding screws dynamization is always achievable or in some patients it can be blocked while fully standing on the leg with a fixed pertrochanteric fracture. This type of examination gives some suggestions in implants personalizing in order to avoid blocking of the sliding screws dynamization.

In the moment of the full stance on one leg during the gait, there is the hip load force acting on the femoral head, resulting from simultaneous body weight force and the hip abductor muscles contraction force (hip abductor muscles prevent the torso to lean to the opposite side in that moment). The direction of this resulting force is angled for 159° to the vertical, while the direction of sliding screws is less angled to the vertical (120°–130°) (Kotzar et al. 1991; Pauwels 1935). Due to the difference in these angles, there is a sliding screw bending force (as a component of the hip load force, being transversal to the sliding screw) while one-leg stance. In that moment, there are two supporting points between the sliding screw and the implant stem—on the lower part of the hole at the medial side and on the upper part of the hole at lateral side of the barrel for the sliding screw in the implant's stem. Sliding screw bending force is followed by reaction forces at the supporting points to the implant stem, resulting in friction forces too. The dynamization of a sliding screw can occur only if the sliding screw translational force (as a component of the hip load force, being parallel to the sliding screw) overcomes these friction forces (Loch et al. 1998; Mitkovic 2020). Bending moment of the sliding screw during the walk is defined by sliding screw bending force and sliding screw lever arm (distance from the tip of sliding screw to the implant stem medial hole supporting point). Friction forces are higher as the body weight is higher, as the femoral neck is longer (sliding screw have to be longer if the femoral neck is longer), and as the angle between sliding screw and the implant stem is smaller (Fig. 9.6).

There was research in the Laboratory for Intelligent Manufacturing Systems at the Faculty of Mechanical Engineering (University of Nis, Nis, Serbia) performed to measure the intensity of the force directed parallel to the sliding screws, required to initiate the dynamization of transversally loaded sliding screws. Based on the measured results, a mathematical model was defined, giving the possibility to predict value of the force required to initiate the sliding screw dynamization while standing on the operated leg during the gait, for certain body weight and for certain femoral neck length. Furthermore, this could be used in prediction whether the body weight will initiate the dynamization of sliding screws or this dynamization would be blocked and full compression between the fracture fragments wouldn't be achieved at the moment of the stance on the operated leg only.

The above noted research included a special construction made to avoid the use of heavy weights during the experiment. The construction included a wooden support and several components that were made in relatively simple way, using

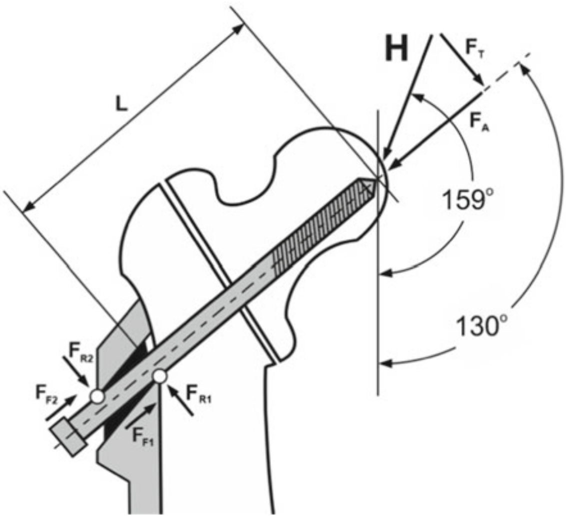

Fig. 9.6 Scheme of a sliding screw loads in the moment of one-leg stance during the gait; hip load force (H), transversal component of the hip load force (F_T) inducing the lag screw bending, sliding screw bending moment lever arm (L), reaction forces (F_{R1}, F_{R2}); sliding screw dynamization can be achieved if axial component of the hip load force (F_A) overcomes friction forces (F_{F1}, F_{F2}) Reproduced from Mitkovic (2020)

a lathe machine. In addition, 2 electronic dynamometers were used—electronic dynamometer no. 1 was used to control the sliding screw transversal load and the electronic dynamometer no. 2 was used to measure the friction force when pressing on the tip of the sliding screws (Fig. 9.7).

The force-time graph of the force measured by electronic dynamometer no. 2 had the initial steeper part, corresponding to the pressure on the sliding screw tip before the dynamizaton, and the terminal less steep part, corresponding to the pressure on the sliding screw tip during the dynamization. The value at the transition of these two parts of the graph is considered as the force required for dynamization initiating while the sliding screw is transversally loaded. In patients with a pertrochanteric fracture fixation, sliding screw transversal load mostly depends on body weight and on femoral neck length. There should be noted that the force required to initiate sliding screw dynamization also depends on implant parts dimensions, on angular relations in the implant and on the material from which it is made.

Forces required to initiate the dynamization were measured in this research using the third generation Gamma Nail and the Selfdynamizable Internal Fixator. The measured results indicate that higher body weight and longer femoral neck may be followed by a rigid contact between sliding screws and implant stem in the moment of the full stance on the leg with fixed pertrochanteric fractures during the gait. Therefore, nor the sliding screws dynamization, nor the desired full compression between bone fragments may be achievable in these conditions.

In patients who are expected not to have the dynamization of sliding screws while fully standing on the leg, due to a high bending moment of the lag screws, the fixation by personalized implants may be indicated in the treatment of a pertrochanteric fracture. Customization would, in this way, refer to the design of an implant with the angle between sliding screw and implant stem being large enough to enable

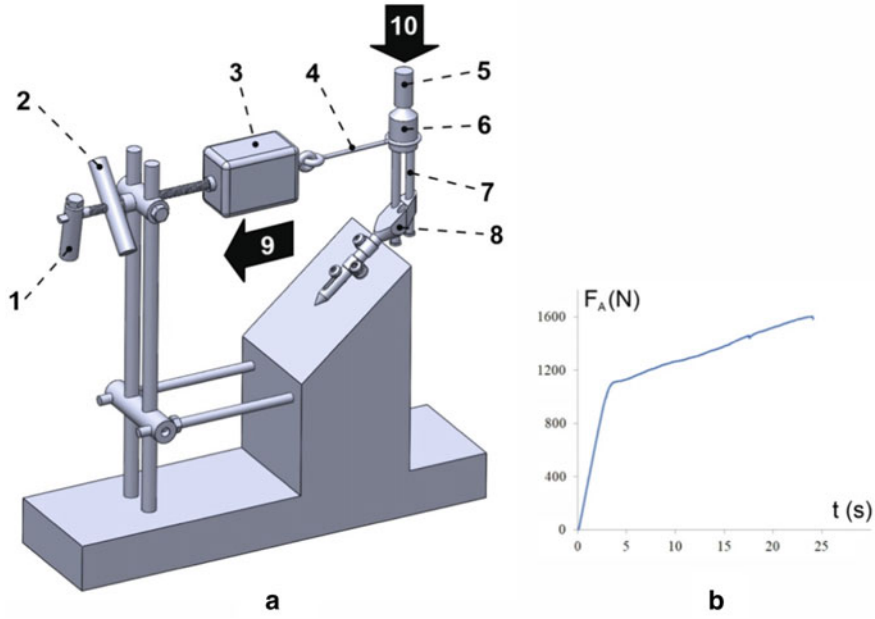

Fig. 9.7 The construction used in biomechanical investigation of forces required to initiate the dynamization of sliding screws with different bending moments (**a**): anti-rotation lever (**1**), clamping lever (**2**), electronic dynamometer no. 1 (**3**), connecting cable (**4**), electronic dynamometer no. 2 (**5**), cap for multiple sliding screws (**6**), sliding screw (**7**), examined implant (**8**), direction of bending moment force (**9**), direction of the force causing sliding screws dynamization (**10**); while holding anti-rotation lever, turning of the clamping lever results in connecting cable strengthening of the, controlled by electronic dynamometer no. 1; electronic dynamometer no. 2 measures the axial force acting on tip of the sliding screw (or on the cap used if implant contains multiple sliding screws); force-time graph of the axial force (F_A) measured during the pressure on tip of the sliding screw loaded by a bending moment (**b**); the transition point between initial part of the graph, which is steeper, and terminal part of the graph, which is less steep, marks the force required to initiate sliding screws dynamization Reproduced from Mitkovic (2020)

the dynamization during the full stance on the operated leg, but not too large, to avoid too steep sliding screw direction (if the sliding screw is too steep than its tip would be placed in the upper half of the femoral head, what has been proved as a significant risk factor for the failure of a pertrochanteric fracture fixation) (Herzog et al. 2019). In addition to defining an appropriate angle between sliding screw and implant stem, defining optimal sliding screw diameter for a certain patient should be another factor influencing implant customization activities aimed on the ability for sliding screws to dynamize in the moment of one leg stance during the gait. The method of biomechanical testing described above could be performed on implants with different values of sliding screws diameter. The mathematical models calculated after, regarding linear function of the sliding screw transversal load and the force required to initiate its dynamization, could be used to determine which sliding screw

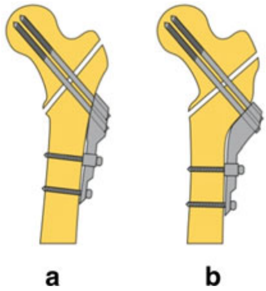

Fig. 9.8 Pertrochanteric fracture fixed by Selfdynamizable Internal Fixator with sliding screws—in femur with a standard anatomic (**a**) and in femur with the lateral bone prominence below the greater trochanter, being a consequence of the previous fracture malunion in that area (**b**); personalized implant should be used in the situation B, where the sliding screws will pass the "trochanteric unit" in different angle than usually

diameter should be the most desirable for a certain patient to achieve the dynamization during the gait.

The need for personalized extramedullary implants containing sliding screw could be desirable in patients with a pertrochanteric fracture and with malunion of previously suffered fracture at just below area—transverse trochanteric fracture (according to the AO bone fractures classification, transverse trochanteric fractures are different from pertrochanteric fractures; transverse trochanteric fractures extend from below greater trochanter laterally to the place of lesser trochanter medially). In such cases, there could be a bone prominence at the lateral femoral side just below the greater trochanter. Since the stem of an extramedullary fixation implant should not prominent too much into adjacent soft tissues, it is desirable for implant shape to follow the leaning bone surface as more as possible. Having this in mind in the situation from above (pertrochanteric fracture with associated malunion of a previous fracture just below), the part of a personalized extramedullary implant stem through which the sliding screws are being passed (it is "trochanteric unit" in Selfdynamizabe Internal Fixator) should be at the different angle to the lower part of the stem than usually (Fig. 9.8). Using the stem personalized in this way, the angle between sliding screws and the "trochanteric unit" will be different than usually, thus presenting an additional factor for ability of sliding screws dynamization in the moment of the injured leg full stance. Therefore, in order to examine the dynamization ability in such case, a biomechanical investigation with the construction described above should be recommended to perform.

Acknowledgements This chapter is part of the project "Virtual human osteoarticular system and its application in preclinical and clinical practice" (No. III41017) funded by the Ministry of Education, Science and Technological Development of Republic of Serbia.

References

Alhammoud A, Maaz B, Alhaneedi GA et al (2019) External fixation for primary and definitive management of open long bone fractures: the Syrian war experience. Int Orthop. https://doi.org/10.1007/s00264-019-04314-0

Andersson S, Herrlin K, Walloe A et al (1984) Complications after trochanteric fractures: a comparison between ender and nail-plate osteosynthesis. Acta Orthop Scand 55:187–191. https://doi.org/10.3109/17453678408992335

Arirachakaran A, Amphansap T, Thanindratarn P et al (2017) Comparative outcome of PFNA, gamma nails, PCCP, medoff plate, LISS and dynamic hip screws for fixation in elderly trochanteric fractures: a systematic review and network meta-analysis of randomized controlled trials. Eur J Orthop Surg Traumatol 27(7):937–952. https://doi.org/10.1007/s00590-017-1964-2

Baron MD, Cazan B, Agel J (2020) Similar patient reported outcomes at long-term follow-up after external fixation versus internal fixation of the anterior ring component of APC injuries. Injury. https://doi.org/10.1016/j.injury.2020.05.037

Bartonicek J, Rammelt S (2014) The history of internal fixation of proximal femur fractures Ernst Pohl—the genius behind. Int Orthop 38:2421–2426. https://doi.org/10.1007/s00264-014-2320-3

Caon M (2018) Skeleton and joints. Springer Nature Switzerland, Cham

Caruso G, Bonomo M, Valpiani G et al (2017) A six-year retrospective analysis of cut-out risk predictors in cephalomedullary nailing for pertrochanteric fractures. Bone Joint Res 6(8):481–488. https://doi.org/10.1302/2046-3758.68.BJR-2016-0299.R1

Chang SM, Hou ZY, Hu SJ et al (2020) Intertrochanteric femur fracture treatment in Asia: what we know and what the world can learn. Orthop Clin North Am 51(2):189–205. https://doi.org/10.1016/j.ocl.2019.11.011

Chlebeck JD, Birch CE, Blankstein M et al (2019) Nonoperative geriatric hip fracture treatment is associated with increased mortality: a matched cohort study. J Orthop Trauma 33(7):346–350. https://doi.org/10.1097/BOT.0000000000001460

Claes L (2018) Dynamization of fracture fixation: timing and methods. Unfallchirurg 121(1):3–9. https://doi.org/10.1007/s00113-017-0455-6

Ercin E, Hurmeydan OM, Karahan M et al (2017) Bone anatomy and the biologic healing process of a fracture. In: Gobbi A, Espregueira-Mendes J, Lane JG et al (eds) Bio-orthopaedics. Springer Nature Switzerland, Cham, pp 437–447

Fister I, Fister I Jr, Fister D (2018) Principles of human movement. Springer Nature Switzerland, Cham

Fowler T, Whitehouse M, Riddick A et al (2019) A retrospective comparative cohort study comparing temporary internal fixation to external fixation at the first stage debridement in the treatment of type IIIB open diaphyseal tibial fractures. J Orthop Trauma 33(3):125–130. https://doi.org/10.1097/BOT.0000000000001362

Fu R, Feng Y, Liu Y et al (2021) The combined effects of dynamization time and degree on bone healing. J Orthop Res. https://doi.org/10.1002/jor.25060

Gajdobranski D, Mitkovic MB, Vuckovic N et al (2014) Influence of different methods of internal bone fixation on characteristics of bone callus in experimental animals. Srp Arh Celok Lek 142(1–2):40–47. https://doi.org/10.2298/sarh1402040g

Ganadhiepan G, Miramini S, Patel M (2019) Bone fracture healing under Ilizarov fixator: influence of fixator configuration, fracture geometry and loading. Int J Numer Method Biomed Eng, 35(6):e3199. https://doi.org/10.1002/cnm.3199

Ghimire S, Miramini S, Richardson M (2018) Role of dynamic loading on early stage of bone fracture healing. Ann Biomed Eng 46(11):1768–1784. https://doi.org/10.1007/s10439-018-2083-x

Gilliland KO, Kernick ET (2021) Musculoskeletal tissues and anatomy. In: Esther RJ (ed) Clinical foundations of musculoskeletal medicine. Springer Nature Switzerland, Cham. pp 11–21

Gjertsen JE, Dybvik E, Furnes O et al (2017) Improved outcome after hip fracture surgery in Norway. Acta Orthop 88(5):505–511. https://doi.org/10.1080/17453674.2017.1344456

Grubor P, Mitkovic MB, Mitkovic MM et al (2019) Comparison of biomechanical stability of osteosynthesis materials in long bone fractures. Med Glas (zenica) 16(1):88–92. https://doi.org/10.17392/985-19

Hak DJ, Banegas R, Ipaktchi K et al (2018) Evolution of plate design and material composition. Injury 49(1):S8–S11. https://doi.org/10.1016/S0020-1383(18)30295-X

Herzog J, Wendlandt R, Hillbricht S (2019) Optimising the tip-apex-distance in trochanteric femoral fracture fixation using the ADAPT-navigated technique, a longitudinal matched cohort study. Injury 50(3):744–751. https://doi.org/10.1016/j.injury.2019.02.010

Inui T, Watanabe Y, Kurata Y et al (2021) Early postoperative Barthel index score and long-term walking ability in patients with trochanteric fractures walking independently before injury: a retrospective cohort study. Arch Orthop Trauma Surg 141(8):1283–1290. https://doi.org/10.1007/s00402-020-03548-7

Kim KE, Kim EJ, Park J et al (2021) Humeral shaft fracture and radial nerve palsy in Korean soliders: focus on arm wrestling related injury. BMJ Mil Health 167(2):80–83. https://doi.org/10.1136/bmjmilitary-2019-001373

Kostic I, Mitkovic MM, Mitkovic MB (2015) Treatment of stable and unstable intertrochanteric fractures with selfdynamisable internal fixator (concept of double dynamisation). Vojnosanit Pregl 72(7):576–582. https://doi.org/10.2298/vsp131025068k

Kotzar GM, Davy DT, Goldberg VM (1991) Telemeterized in vivo hip joint force data: a report on two patients after total hip surgery. J Orthop Res 9:621–633. https://doi.org/10.1002/jor.1100090502

Koval KJ, Zuckerman JD (2000) Hip fractures. A practical guide to management. Springer New York

Kumar CN, Srivastava MP (2019) Screw versus helical proximal femoral nail in the treatment of unstable trochanteric fractures in the elderly. J Clin Orthop Trauma 10(4):779–784. https://doi.org/10.1016/j.jcot.2018.07.012

Loch DA, Kyle RF, Bechtold JE (1998) Forces required to initiate sliding in second-generation intramedullary nails. J Bone Joint Surg 80:1626–1631. https://doi.org/10.2106/00004623-199811000-00009

Mattisson L, Bojan A, Enocson A (2018) Epidemiology, treatment and mortality of trochanteric and subtrochanteric hip fractures: data from the Swedish fracture register. BMC Musculoskelet Disord. https://doi.org/10.1186/s12891-018-2276-3

Meinberg EG, Agel J, Roberts CS (2018) Fracture and dislocation classification compendium—2018. J Orthop Trauma 32(1):S1–S170. https://doi.org/10.1097/BOT.0000000000001063

Milenkovic S, Mitkovic MB, Mitkovic MM (2017) Surgical treatment of osteoporotic fractures. Vojnosanit Pregl 74(9):878–883. 13.2298/VSP151205280M

Mitkovic MM, Milenkovic S, Micic I et al (2018) Operation time and intraoperative fluoroscopy time in different internal fixation methods for subtrochanteric fractures treatment. Srp Arh Celok Lek 146(9–10):543–548. https://doi.org/10.2298/SARH180220042M

Mitkovic MM, Milenkovic S, Micic I et al (2020a) Comparative analysis of operation time and intraoperative fluoroscopy time between intramedullary and extramedullary fixation in trochanteric fractures treatment. Vojnosanit Pregl. https://doi.org/10.2298/VSP200516094M

Mitkovic MM, Milenkovic S, Micic I et al (2020b) Hip function and health-related quality of life in intramedullary and extramedullary internal fixation of trochanteric fractures. Srp Arh Celok Lek 148(7–8):451–454. https://doi.org/10.2298/SARH200301029M

Mitkovic MB, Bumbasirevic M, Milenkovic S et al (2010) Fractures of the upper part of the femur treated with Mitkovic selfdynamisable internal fixator (SIF). Acta Chir Iug 57(4):103–107. https://doi.org/10.2298/aci1004103m

Mitkovic MB, Milenkovic S, Micic I et al (2012) Results of the femur fractures treated with the new selfdynamisable internal fixator (SIF). Eur J Trauma Emerg Surg 38(2):191–200. https://doi.org/10.1007/s00068-011-0157-7

Mitkovic MM, Milenkovic S, Micic I et al (2017) Application of the new selfdynamisable internal fixator in the tratment of femoral shaft fractures. Acta Fac Med Naiss 34(2):129–136. https://doi.org/10.1515/afmnai-2017-0014
Mitkovic MM (2020) Comparative analysis of clinical and biomechanical parameters of surgical treatment of trochanteric fractures using self-dynamisable internal fixator and gamma nail. Dissertation. University of Nis, Serbia
Mori CM, Vicenti G, Carrozzo M et al (2018) The fake unlocked femoral nail: a configuration to avoid in stable pertrochanteric femur fractures. Injury 49(3):S32–S36. https://doi.org/10.1016/j.injury.2018.09.057
Pauwels E (1935) Der schenkelhalsbruck ein mechanisches problem. grundlagen des heilungsvorganges prognose und kausale therapie. Ferdinand Enke, Stuttgart
Peacock M (2021) Phosphate metabolism in health and disease. Calcif Tissue Int 108(1):3–15. https://doi.org/10.1007/s00223-020-00686-3
Perumal R, Shankar V, Basha R et al (2018) Is nail dynamization beneficial after twelve weeks—an analysis of 37 cases. J Clin Orthop Trauma 9(4):322–326. https://doi.org/10.1016/j.jcot.2017.12.007
Pountos I, Giannoudis PV (2018) Fracture healing: back to basics and latest advances. In: Giannoudis PV (ed) Fracture reduction and fixation techniques. Springer Nature Switzerland, Cham, pp 3–17
Prommik P, Tootsi K, Saluse T et al (2021) Nonoperative hip fracture management practices and patient survival compared to surgical care: an analysis of Estonian population-wide data. Arch Osteoporos. https://doi.org/10.1007/s11657-021-00973-y
Rashid MM, Husain KN, Vitkovic N et al (2017) Geometrical model creation methods for human humerus bone and modified cloverleaf plate. J Sci Ind Res 76:631–639
Ruedi TP, Buckley RE, Moran CG (2007) AO principles of fracture management. vol 2: specific fractures, 4th edn. Thieme, Stuttgart
Shen R, Waisman H, Yosibash Z et al (2019) A novel phase field method for modeling the fracture of long bones. Int J Numer Method Biomed Eng 35(8):e3211. https://doi.org/10.1002/cnm.3211
Shinoda S, Mutsuzaki H, Watanable A et al (2017) Factors influencing period from surgery discharge in patients with femoral trochanteric fractures. J Phys Ther Sci 29(11):1976–1980. https://doi.org/10.1589/jpts.29.1976
Shipman P, Walker A, Bichell D (2013) The human skeleton. Harvard University Press, Cambridge
Stojiljkovic P, Micic I, Milenkovic S et al (2013) Minimally invasive treatment of bilateral femoral shaft fractures in polytrauma patient using selfdynamisable internal fixator. A case report. Acta Chir Iug 60(2):59–64. https://doi.org/10.2298/aci1302059s
Stojiljkovic P, Mitkovic MB, Golubovic Z et al (2015) Selfdynamisable internal fixator Mitkovic in treatment of periprosthetic supracondylar femoral fracture after total knee arthroplasty. Acta Chir Iug 62(1):49–55. https://doi.org/10.2298/ACI1501049S
Velez M, Palacios-Barahona U, Paredes-Laverde M et al (2020) Factors associated with mortality due to trochanteric fracture. A cross-sectional study. Orthop Traumatol Surg Res 106(1):135–136. https://doi.org/10.1016/j.otsr.2019.06.022
Waddell JP (2010) Fractures of the proximal femur: Improving outcomes. Elsevier, Philadelphia
Welch AA, Hayhoe RPG (2019) The relationship between dietary fat and sarcopenia, skeletal muscle loss, osteoporosis and risk of fractures in aging. In: Weaver CM, Bischoff-Ferrari H, Daly RM et al (eds) Nutritional influences on bone health. Springer Nature Switzerland, Cham. pp 211–225
Zhu Q, Xu X, Yang X et al (2017) Intramedullary nails versus sliding hip screws for AO/OTA 31–A2 trochanteric fractures in adults: a meta-analysis. Int J Surg 43:67–74. https://doi.org/10.1016/j.ijsu.2017.05.042

Part IV
Personalized Prothesis

Chapter 10
The Influence of Human Factors in the Functional Analysis of the Support Device for Users with Upper Limb Agenesis

Maria Lucia Miyake Okumura, Geane Aparecida Poteriko da Silva, and Osiris Canciglieri Junior

10.1 Contextualization

The Integrated Product Development Process (IPDP) oriented for Assistive Technology (AT) presents multidisciplinary and interdisciplinary aspects according to the design elaboration phases. The design phases use methods and tools that interact information and concepts between the different areas of knowledge to structure a design that investigates and analyses the user's specificity and the demand, understanding the requirements of the product under development. The users of assistive technology are people with disabilities and people with reduced mobility, that is, with physical, sensory or cognitive limitations, which can be temporary or permanent. These users make use of the support products and services to reach development, autonomy and, increase functionality and improve quality of life.

There are children with congenital hand agenesis among assistive technology users who use prosthetic support devices in rehabilitation and perform bimanual activities. According to Borg et al. (2011), the prosthetic support device is externally applied to replace fully or partially a missing part of the body or parts with alteration

M. L. M. Okumura (✉) · O. C. Junior
Industrial and Systems Engineering Graduate Program, Pontifical Catholic University of Paraná (PPGEPS/PUCPR), Curitiba, Paraná, Brazil
e-mail: luciamiyake@gmail.com

O. C. Junior
e-mail: osiris.canciglieri@pucpr.br

M. L. M. Okumura · G. A. P. da Silva · O. C. Junior
Product Development Research Center oriented to assistive technology of PPGEPS/PUCPR, Curitiba, Brazil

G. A. P. da Silva
Paraná State Department of Education, Curitiba, Brazil

O. Canciglieri Junior and M. D. Trajanovic (eds.), *Personalized Orthopedics*,
https://doi.org/10.1007/978-3-030-98279-9_10

in its structure, allowing the individual to return to the social structure and productive activities (Laferrier and Gailey 2010; Lazorski 2019).

Thus, methods and tools associated with IPDP are applied in the pre-design phase to elaborate a product-oriented towards assistive technology. Among the IPDP methods and tools, product ergonomics and usability are applied in the prosthetic support device design to contribute to the biomechanical structure, and human factor and are also integrated into various areas of knowledge highlighted in the activities of the development process in assistive technology (Back et al. 2008; Iida 2005; Browning 2010; Okumura and Canciglieri Junior 2019).

The main objective of the research is to present the functional analysis of a prosthetic support device, considering the development of the user with congenital hand agenesis during seven years and the human factors identified to improve the quality of AT product design and manufacturing. The research methodology is applied nature with a qualitative approach and exploratory scientific objective. The technical research procedures consist of field observational analysis, the applying of the IPDP that comprehend the elaboration of the design of the prosthetic support device and its production in additive manufacturing and a rehabilitation program to monitor the user's performance in tasks execution The results show the manufacture of eleven prosthetic support devices, one of which is currently in the manufacturing process. Also, the performed tasks and the functionality analysis involving aspects of safety, efficiency, comfort and fatigue according to the user's and even indirect users' difficulties are shown. Finally, the conclusion presents the contribution of the influences of human factors in the interaction between the user in IPDP of the prosthetic support device and the effective benefits of muscular stimulation of the upper limb with hand agenesis.

It is worth mentioning that this Chapter refers to the extended version of the research started in 2014 (Poteriko da Silva et al. 2020) comprising the human factors in the IPDP applied to ergonomics and usability in the design phases for the development of prosthetic support devices for the upper limb.

10.2 Bibliographic Review

10.2.1 Integrated Product Development Process-Oriented to Assisted Technology

The objective of the Integrated Product Development Process is to convert the customers' needs and requirements into information so that a product or technical (Okumura and Canciglieri Junior 2019) needs and the activity that will be performed are linked in this process that is oriented to Assistive Technology, proposing appropriate solutions, from design and at every stage of the product's life cycle, ensuring and attributing manufacturability, seeking quality, reduced cost and attractive price. Thus, the product's development environment comprises a variety of methods, tools and models. They emerged and were provided according to the expertise area and the need to adequately solve the gaps identified in the development process (Okumura and Canciglieri Junior 2019). In addition, other tools are included and are developed from existing ones by the implementation's occurrence.

In these terms, for the integrated products development, resources and other elements related to assistive technology, there is a need to seek adequate solutions to meet users with specific needs. These solutions strongly influence the theoretical, practical and social foundations and tend towards new product designs and processes (Okumura and Canciglieri Junior, 2019). Thus, social, environmental, political and economic aspects are considered, in addition to biological, psychological and other factors. In an integrated way, these aspects compound the human unity, which extends to the principles of multiple diversities. Thus, Back (1983) highlights the need to know the specific functions and specificities and detailed requirements, whose design must be executed to satisfy a human need, and always in the perspective of the most economical condition in order to constitute a product that is within reach of most people.

10.2.2 Concept of Ergonomic

According to the International Ergonomics Association (IEA 2000), ergonomics is the scientific discipline related to the understanding the interaction between humans and other elements of a system and a profession that applies theory, principles, data and methods to design to optimise human well-being. It also adds the importance of the contribution of professionals in ergonomics to the design and assessment of tasks, jobs, products, environments and systems to make them compatible with the people's needs, skills and limitations (IEA 2000). In this term, ergonomics seeks to improve human well-being and improve the production system favouring the sustainability of both organisations and society (Bitencourt and Okumura 2020).

According to Iida (2005), the main human functions that interest ergonomics influence the neuromuscular function, spine, metabolism, vision, hearing kinesthetics sense, and operational aspects. In neuromuscular function occurs the synapse, which is the connection of an axon with a dendrite of the following cell, with the following properties: (a) one-way signals; (b) fatigue due to frequently used signs; (c) signs with residual effect when quickly repeating the same stimulus; (d) development to signs with repeated and prolonged stimulation for several days (responsible for memory and learning); (e) acidity when the signal has increased alkaline content in the blood, increasing excitability and decreasing neuronal activity.

10.2.3 Usability

Usability is considered a requirement of work ergonomics and is defined as the "capacity that an interactive system offers to its user, in a given operating context, to perform tasks effectively, efficiently and pleasantly" (ISO 9241). Furthermore, in the ISO/IEC 9126 standard, the concept of usability is the "easiness that a user can learn to operate, prepare inputs for and to interpret the outputs of a system or component". In this aspect, usability is associated with the way of using the product, the suitability of the type of tasks or activities to be performed, and the suitability of the environment in which the product is used.

10.2.4 Human Factors

The human factor concept is linked to the human capabilities and limitations attributed to the workplace (ICAO 2003). Therefore, human interaction at work and living conditions are related: between people and the used machines and equipment, the written and verbal procedures, the rules that must be followed, the environmental conditions around and the interactions with other people, which influence the behaviour and work, to such an extent that can affect health and safety. Understanding human factors contribute to the best results in the relationship between people and their activities through a systematic application of the Human Sciences integrated with the concepts of Systems Engineering (Hawkins 1993). Thus, the human factor objectives guarantee the system's efficiency, including the safety, efficiency and well-being of the person involved in the activity. Human factors influence the interaction between the user and his tools, especially in assistive technology products, to be able to perform an activity. In this interaction, physiological, sensory, psychological and biomechanical aspects are involved, directly related to the performance of the device's design used by the person with a disability when performing a task. In the interaction between the user with upper limb agenesis and AT products, professionals of multidisciplinary areas are involved in the Integrated Product Development Process (IPDP) of prosthetic devices (Okumura and Canciglieri Junior 2019).

To Bitencourt and Okumura (2020), human factors contribute to increasing the quality of life and solutions to social and environmental issues, that is, they are involved in a generic and multidisciplinary dimension when it comes to quality of life. Thus, it is observed that the application of ergonomics enhances the analysis of human factors systemically and integrally, considering a view of socio-technical systems that lead to new technologies allied to human and social well-being and with greater overall performance in the systems.

According to WHOQOL Group (1997), the individual's quality of life is related to services that involve physical, psychological, social levels of independence, beliefs, device's biomechanical function, environmental and external factors, thus, comprising diversity, which has elements of domains categorised according to

Table 10.1 Category of elements of human factors domains

Domain elements	Faces and unfolding
Physical factor/physiological	Pain and physical fatigue with unfolding for discomfort, exertion, exhaustion, loss of energy, loss of speed, decreasing frequency
Psychological	Fear, negative thought, mental fatigue, indisposition
Level of independence	Autonomy, self-taught, learning
Social factors	Negative: Prejudice, discrimination, exclusion Positive: Incentives, motivation
Beliefs, spiritual aspects	Culture, religiosity
Biomechanical function (prosthetic support devices)	Operational functioning, maintenance and repair
External factors	Lack of laws and public policies, need to travel, lack of security
Environmental factors	Sound (noise), physical space, temperature

Source Adapted from WHOQOL Group (1995), Smets et al. (1995), Cella (1998), Ahsberg et al. (2009), Bitencourt and Okumura (2020)

specific characteristics that unfold and identify different faces, as illustrated in Table 10.1.

Domain elements in human factors influence the performance when executing a task and can result in low efficiency and reduced motivation and activity (Cella 1998; Smets et al. 1995).

In the domain that involves physical factors, Iida (2005) mentions muscular fatigue that unfolds the reduced strength caused by deficiency of blood supply to the muscle, which can be recovered after a period of rest. The lack of blood supply in muscle contraction is due to the lack of oxygen and results in the accumulation of lactic acid, potassium, increased heat, carbon dioxide and water generated during the metabolism. Thus, the stronger the muscle contraction, the greater the strangulation of blood circulation, reducing the time to maintain muscle contraction. According to Iida (2005), the time to maintain maximum muscle contraction may be from few seconds to up to a minute for half of the contraction. Muscle contraction cannot exceed 20% of the maximum contraction for an extended period as intense pain and discomfort begin to appear. Regarding comfort and discomfort, Iida (2005) mentions that subjective assessment should be considered and used when intending that the users evaluate a product.

10.2.5 Assistive Technology Users

Given Assistive Technology services and products, Okumura and Canciglieri Junior (2019) identify three types of users:

- *end-user*: it is the person who uses the support device;
- *secondary user*: it is the person who helps the end-user such as family members and caregivers;
- *indirect user*: it is the professional related to the end user's activity.

The end-user is the primary individual who uses the Assistive Technology products and services to perform functional activities and improve aspects of quality of life. Thus, human factors are associated according to the identification level of the user with the product (Kintsch et al. 2002; Okumura and Canciglieri Junior 2019), which are classified and identified as shown in Table 10.2.

10.2.6 Prosthetic Support Device

The diversity of prosthetic components has increased with the advance of technology, enabling people with limb differences to benefit from prostheses with more comfort, stability and responsiveness. In this aspect, the Integrated Product Development Process (IPDP) is defined as a set of actions that meet specificities of particular users, develop a product or service, integrating various areas of knowledge (Back et al. 2008). Regarding the processes involving people with disabilities, Okumura and Canciglieri Junior (2019) recommend applying the Design for Assistive Technology in the IPDP, as the design of the AT product requires a profound investigation of the product's function and information concerning the user's limitation and the environment of use.

The implementation of a product can fail due to a lack of innovation effectiveness to the ineffectiveness in the implementation process, which may include a lack of user participation and training. This failure is often represented by the abandonment of a device after successful development and adoption without the help of a prosthetic device (Chau et al. 2013; Lazoski 2018). According to Biddiss and Chau (2007, 2008), the reason for abandoning the prosthesis comes from factors related to discomfort and functional limitation, which leads to dissatisfaction and abandonment of the device. Other justifications for the abandonment referred to the durability, mechanical failure, weight, high cost and lack of movement and dexterity provided by the prosthesis (Resnik 2011). These data suggest that many prostheses on the market do not meet the expectations and needs of users. (Lazoski 2018).

Regarding prostheses for congenital malformations, Afonso et al. (2009) consider it important to start using the prosthesis between 3 and 9 months to contribute to the motor and psychological development, the bilateral use of the upper limbs and to assist in the development of the vertical position. In addition, it is important for the development of symmetry and integration of the prosthesis into the child's body scheme. The authors emphasise that using the prosthesis later, from 2 years onwards, results in higher levels of rejection, considering that, at this age, children have already

Table 10.2 Classification of user and AT factors

Level of user	Classification of user and AT factors	Identification
End-user	The direct user of assistive technology: he/she wants to improve what he/she is able to do; he/she has discipline and tolerance for frustration; he/she is proud to use the equipment; he/she wants to use AT in daily routine	The person with disability, the person with reduced functional mobility to perform a task
Secondary user	Family member, caregiver and professionals who helps and participates in the handling of AT products as they are closer to the end-user, following their day-to-day activities and helping to perform the task: he/she is dedicated to the effort of learning the AT use and its customisation; he/she helps the end-user in using the new tool and wants the changes that the equipment brings to the social dynamics; he/she understands that customisation is not instantaneous and may continue throughout the AT use period	Parents, close relatives, mediators, teachers, colleagues and caregivers
Indirect user	Professionals who provide AT services or professionals who establish methods, training/rehabilitation for the end-user: they have knowledge about AT; they learn about new tools that appear on the market; they facilitate the process of collaboration rather than prescription; they provide training and support for both adjustments and integration into activities; they are sensitive to family values and cultural differences	Designer, engineer, physician, physiotherapist, occupational therapist, psychologist, orthopaedist and others
	Manufacturer and Maintenance Services: professionals who manufacture or maintain AT: they have the understanding of the functional limitations; they develop customisable tools; they develop tools with simple adjustments; they develop durable tools; they offer aesthetic options to the user; they help the user with technical support and technical assistance	Technician, engineer, designer, repair and maintenance mechanical workshop

Source Okumura and Canciglieri Junior (2019), DePaula (2002) developed compensatory techniques. Therefore, psychological and motor development stages should guide the prescription of the upper limb prosthesis (Lazoski 2018; Xavier 2021).

According to Dabaghi-Richerand, Haces-García and Capdevilla-Leonori (2015), there is a significant difference between prosthesis use and the level of rejection when comparing people with congenital and acquired amputations. Kannemberg (2017) justifies this difference because early or immediate prosthetization does not allow the individual to experience using the residual limb in bimanual activities; therefore, they begin to appreciate the prosthesis use. To Dabaghi-Richerand, Haces-García and Capdevilla-Leonori (2015), the process must occur before 6 years of age so that the user discovers the benefits of using the prosthesis in daily activities. In cases where prosthetization started after this age, they concluded that rejection levels might increase (Lazoski 2018).

10.2.7 Additive Manufacture of Prosthetic Support Device

Additive manufacture has become widely used in recent years due to the reduction of machine costs combined with the dissemination of designs, such as the Open Source, that made available ready-made objects models and enable the modification of the project, whether for improvement or adaptation (Maia 2016).

Additive manufacture consists of printing objects through the deposition of a particular material in layers and has been gaining more applicability in the industry, whether in the aerospace, automotive or medical fields. The flexibility and ability to print complex geometries are two of the main characteristics of this technology, which has been present in the market since the late 1980s. However, it has gained prominence in recent years and provided a huge technological leap (Schubert et al. 2014). In addition, the launch of affordable, smaller-based printers for printing smaller objects enables new trends in design.

Material deposition manufacturing would be known as rapid prototyping, but in 2010, the American Society for Testing and Materials redefined the name for additive manufacturing, a broader term that includes the philosophy of manufacturing and the different technologies developed (Lazoski 2018). It has been used in healthcare since the 2000s, when it was first used to manufacture dental implants and prostheses (Cui et al. 2012; Gross et al. 2014). Currently, there is an increasing interface between engineering and health, with the use of technology to manufacture tissues and organs, surgical and orthopaedic prostheses, dental implants, bones, among others (Klein et al. 2013).

It can be considered a good resource for upper limb prostheses manufacturing, especially for children. For these audiences, additive manufacturing allows customisation, lightness and easy repair, considering the high probability of device damage. Besides that, children need to change prostheses with a certain frequency due to growth, and additive manufacturing allows this change to be realised at a lower cost when compared to other options on the market (Burn et al. 2016; Lazoski 2018).

Burn et al. (2016) state that the best candidates for the use of prostheses produced by additive manufacturing are children who are unilaterally amputated, whether by a traumatic or congenital amputation with low-level amputations, usually at wrist height. For even lower amputations, such as finger amputations, the authors report that these prostheses are rarely indicated because generally, these people are highly functional and only need the clamp function. However, for higher amputations, above wrist level, the author highlights that prosthetization presents an increased complexity, making it difficult but possible to use prostheses manufactured by additive manufacturing (Lazoski 2018).

10.3 Methodology

The research methodology is applied with a qualitative approach, exploratory scientific objective and field observation analysis. The research of exploratory objective approximates an initial contact of the topic familiarised with the problem phenomenon, relying on external resources to the situation to define the fact to be analysed (Fontelles et al. 2009). Regarding observational research, the same study highlights the spectator's encounter with facts and phenomena without interfering in the situation. However, amidst the facts, procedures for data collection can be carried out. Finally, the qualitative approach research is an appropriate method for understanding in-depth complex and specific phenomena used for themes from social and cultural universes, based on descriptions and interpretations (Fontelles et al. 2009).

In the technical procedure of the research, the method follows the phases of the IPDP oriented for assistive technology considering the structure of the Design for Assistive Technology that follows the stages of the: Informational Design, Conceptual Design, Preliminary Design and Detailed Design with requirements feedback for new devices with quality improvements (Okumura and Canciglieri Junior 2019).

The IPDP informational phase began with a literature review of the main research topics and the investigation of different characteristics of limb agenesis, limitations and specificity of people with disabilities, users of prostheses and support devices. Then, data collection was carried out in the field, observing the activities realised in a non-profit association related to supporting people with hand agenesis. The phases of Conceptual, Preliminary and Detailed Design of the IDPP were divided into three stages: (a) design prosthetic support devices using additive manufacturing resources; (b) monitor the functionality assessment; (c) monitor the development of the user with congenital hand agenesis in the rehabilitation session. The Association's team of academic professionals and volunteers participated in this research. Eleven prosthetic support devices were manufactured for a user, one of which is in the current manufacturing phase, during seven years. After each functionality assessment, the results were converted into product requirements that were fed back to the informational phase of the IPDP and consequently to the development of a new device with design improvements.

In this research, the prosthetic support devices were intended for a user with congenital hand agenesis. The user is referenced in the research with the codename “D.P.S”. The procedure of observing the user was to monitor the evolution and development for seven years, including the use of the prosthetic device from the age of 3 years onwards. Finally, the analysis and assessment of the functionality of the prosthetic support devices are presented in the obtained results containing the report of the rehabilitation sessions with aspects that involve human factors.

10.3.1 Presentation of the Support Network for People with Limb Agenesis

This research was carried out with a non-profit association, identified as a Civil Society Organization (CSO) that develops social works, headquartered in the Parana State countryside, Brazil. The CSO works as a support network for people with agenesis, dysgenesis and limb malformation disabilities, especially in the upper limbs. The partnership with the University started in 2014, even before the CSO constitution, with the Research Group of Products Oriented for AT of the Graduate Program in Production and Systems Engineering (Poteriko 2019; Associação Dar a Mão 2021). In this context, the research began by monitoring the user’s development, who was born in 2013. In 2016, the study monitored the user’s development using the first prosthetic support device and the participation in tests to improve the product quality and verify its functionality for performing some daily life activity. It is worth noting that CSO professionals provided all direct assistance to the user. Furthermore, the University participates in the design of prosthetic support devices and rehabilitation sessions monitoring using the information provided by health professionals and the CSO, without the user’s identification.

10.4 Results

In this research, the IPDP comprises the AT products and services; thus, professionals from different academic areas in partnership with the CSO members form a multidisciplinary and interdisciplinary team according to the design phases. Among the professionals stands out the participation of engineers, designers, orthopaedic doctors, physiotherapists, occupational therapists, psychologists, specialists in orthotics, prostheses and special materials (OPSM).

The user D.P.S., referred by the CSO, has right-hand congenital agenesis with a closed diagnosis due to amniotic band syndrome. Figure 10.1 shows the image and radiologic report of the right upper limb.

The amniotic band syndrome occurs approximately for one child of every 1500 births. Amniotic band syndrome occurs due to fibrous bands in the uterus that float

Radiological report of the right upper limb:
- Radio and ulna without radiographic changes;
- Phalangeal agenesis (hand).

(a) Radiological image of a 2-month-old patient.

Radiological report of the right upper limb:
- Phalangeal agenesis;
- Presents bone pigments (undeveloped phalanges).

(b) Radiological image of a 6-year-old patient.

Fig. 10.1 Radiological report of the patient with hand agenesis due to amniotic band syndrome

in the amniotic fluid along with the foetus, leading to the imprisonment of part of the foetus, such as arms, legs, fingers, among others. Subsequently, there will be foetal growth, but the parts affected by the "bands" will not, thus conceiving the constrictions that lead to reduced blood circulation, resulting in congenital anomalies, that is, the malformation of the upper and/or lower limbs. The deformities of the lesions are asymmetric, and when bilateral, there is concomitance of involvement in pododactile and feet. The highest impairment concentration in the upper limb is in the hands and are usually accompanied by brachydactyly and other anomalies in the hand without presenting a standard characteristic. In addition, there are other syndromes and rare diseases that can affect congenital malformations of the upper and/or lower limbs (Associação Dar a Mão 2021).

User D.P.S. has participated in physical and functional rehabilitation sessions since she was 2 years and 6 months. She was referred by an orthopaedist doctor in February 2016, through the "*Guia de Referência do Sistema Único de Saúde-SUS*" (Reference Guide of the Unified Health System) (Brasil 2013), requesting "occupational therapy" by reporting "patient with agenesis of the phalanges of the right upper limb", code ICD 10:Q74.

The CSO and the health professionals provided the Informed Consent Form documentation (ICF), authorization of images, and commitment declaration to carry out the rehabilitation sessions.

10.4.1 Design of Prosthetic Support Devices

The Conceptual and Detailed phases of the IPDP consider the procedure for designing devices, which comprises the following steps: measurement, selection of the device model, parameterisation, scaling, customisation with aesthetic design, manufacturing and assembly, customisation, delivery to the user, participation in the rehabilitation program for device use and functionality assessment.

Measurements are provided by healthcare professionals, following the anthropometric data instructions for parameterization of E-Nable (2021), as shown in Fig. 10.2 (Burn et al. 2016; Associação Dar a Mão 2021). Because each prosthetic support device has the user's specific measure, its reuse for other purposes is not feasible. In some cases, videos showing the movement of the residual limb with hand agenesis are also requested. Measurements are accompanied by prescriptions or statements from doctors, physiotherapists or occupational therapists saying that the patient is able to use the prosthetic support device and is participating in a rehabilitation program. Those professionals also participate in the selection of models and technical tests of the devices, as well as to the functionality assessment according to identified human factors.

Specialists in parameterization, scaling and from the area of OPSM and rehabilitation participate in selecting prosthetic support device models. The models selected for the CSO free distribution are Open Source. The device's movement occurs mechanically through elastic components that passively allow handgrip through elbow flexion and fingers relaxation.

The mechanical model Unlibited Arm was selected in this research (E-Nable 2021) with some adaptations made by the professional design according to the user's hand agenesis characteristic. The 3D printer was used to manufacture the device's parts, and then the parts were assembled. Customisations refer to the device's manufacturing filaments colours and the aesthetic finishing chosen by the users according to their favourite theme and are considered part of the use motivation. Ten devices were developed, manufactured and delivered to the user D.P.S. The next device numbered eleven, the "Kinect" model that is activated by flexing the wrist and hand, is currently in the manufacturing process as indicated by the occupational therapist. This device will strengthen the biceps and wrist. The devices and their characteristics are shown in Table10.3.

The devices were manufactured as instructed by the health professionals and technicians that accompany the rehabilitation session, and most justifications for switching were due to the natural physical growth of the user D.P.S. A new device was needed because of the user's physical development or due to its wear and breakage of some fragile parts.

The filament used in the 3D printer was the Polylactic Acid known as PLA, which has mechanical properties, good toughness and good resistance (Maia 2016). However, the smaller parts wear out quickly and have been replaced by metal screws. The nylon threads were renewed due to wear with the amount of the device's activation of the device.

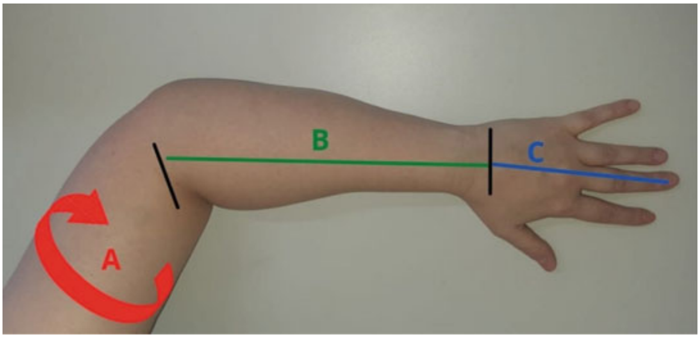

Anthropometric measurements (E-Nable, 2020).

Upper limb measurements.

Measurement (A).

Measurement (B) e (C).

Fig. 10.2 Anthropometric measurements of the user at 2 years and 6 months

10.4.2 Professionals in Services of Assistive Technology

Assistive Technology services comprise rehabilitation and psychology professionals in the assistance to the user D.P.S., which are listed in Table 10.4.

Table 10.3 Manufactured devices of the user D.P.S. in the period of 2016–2021

Year/Seq	User's measure (cm)	Model + adaptation	Situation	Mass (kg)	Customisation/filament colour	Tasks
2016/1	A = 16 B = 11 C = 3	Unlibited Arm, adapted connections	Delivered Used In disuse	0.080	Red (light)	Rehabilitation
2016/2	A = 16 B = 11.5 C = 3	Unlibited Arm, adapted connections	Delivered Used In disuse	0.095	"Monster High" doll theme/Pink	Rehabilitation
2017/3	A = 17 B = 12 C = 3.5	Unlibited Arm, with part adaptations	Delivered Used In disuse	0.120	Twilight theme/Light pink	Rehabilitation, ballet, bimanual activities
2017/4	A = 17 B = 12,5 C = 3.5	Unlibited Arm with part adaptations	Delivered Used In disuse	0.132	Lady Bug theme/Red and Black	Rehabilitation, ballet and bimanual activities at home and school
2018/5	A = 17 B = 13 C = 3.5	Unlibited Arm, reformed forearm exchange	Delivered Used In disuse	0.147	Wonder Woman theme/Blue and Red	Rehabilitation, ballet and bimanual activities
2018/6	A = 17 B = 13,5 C = 3.5	Unlibited Arm with part adaptations	Delivered Used In disuse	0.156	Light pink with customization	Rehabilitation, ballet and bimanual activities
2019/7	A = 17 B = 13.5 C = 4	Unlibited Arm with parts adaptations	Delivered Used In disuse	0.168	Descendants theme/Red and White	Rehabilitation, ballet and bimanual activities
2019/8	A = 17 B = 14 C = 4	Unlibited Arm with parts adaptations	Delivered Current use	0.165	Hello Kitty theme/Pink and White	Rehabilitation, ballet and bimanual activities at school
2020/9	A = 17 B = 14 C = 4.4	Unlibited Arm with parts adaptations	Delivered Current use	0.178	Yellow with customization	Rehabilitation, bimanual activities
2021/10	A = 17.3 B = 14.5 C = 4.5	Unlibited Arm with parts adaptations	Delivered Current use	0.180	Descendants II theme/Purple and Black	Rehabilitation, bimanual activities

(continued)

Table 10.3 (continued)

Year/Seq	User's measure (cm)	Model + adaptation	Situation	Mass (kg)	Customisation/filament colour	Tasks
2021/11	A = 17.3 B = 14.5 C = 4.7	Kinect with wrist trigger	In manufacturing process	0.188	Descendants III theme/Blue and Red	

Table 10.4 User D.P.S. in rehabilitation sessions and psychological appointment

Duration/period	Use of device	Programs/sessions
6 months 2 × a week	No	Rehabilitation: Muscular strengthening, stimulation of the limb with agenesis, postural correction in the development of daily tasks and functional training in manipulating objects
1 h 1 appointment	No	Appointment with a psychologist: psychological assessment to start the prosthetization process and use a prosthetic support device
1 × a week	Yes	Rehabilitation: Muscular strengthening, occupational activities with fine motor coordination, fun activities and diversified games
1 × a week	Yes	Rehabilitation: global child development, motor coordination, range of motion, sensory integration
Daily	Yes	Rehabilitation: insertion of the use of devices in daily activities

10.4.3 Monitoring of Activities with Motor Coordination

The user D.P.S. had monitoring activities with motor coordination since 2 months of age. Initially monitored by parents as indicated by the pediatrician. After 2 years of age with monitoring of rehabilitation and psychological services, which are listed in Table 10.5.

10.5 Discussion

The user D.P.S. started school activities at the age of 18 months at the Centro Municipal de Educação Infantil no Brasil—CMEI (Municipal Centre for Child Education), which is a public school for children from 0 to 5 years old, attending from nursery to preschool. The activities at CMEI are plays, games, works that include movements, arts, orality, literature and actions aimed at caring for children's food, safety and hygiene. Thus, children who attend school activities at CMEI have the opportunity to develop basic skills for daily life, such as walking, talking, expressing

Table 10.5 User D.P.S. in activities with motor coordination appointment

Duration/period	Use of device	Programs/sessions
6 months 2 × a week	No	Rehabilitation: Muscular strengthening, stimulation of the limb with agenesis, postural correction in the development of daily tasks and functional training in manipulating objects
1 h 1 appointment	No	Appointment with a psychologist: psychological assessment to start the prosthetization process and use a prosthetic support device
1 × a week	Yes	Rehabilitation: Muscular strengthening, occupational activities with fine motor coordination, fun activities and diversified games
1 × a week	Yes	Rehabilitation: global child development, motor coordination, range of motion, sensory integration
Daily	Yes	Rehabilitation: insertion of the use of devices in daily activities

their feelings, exploring their environment and social interaction, with the support of pedagogues and teachers. In this aspect, the child acquires the capacity for self-expression, interaction and playing both on their initiative and in response to external stimuli; the earlier the child starts school activities and has social contact, the greater the developmental benefits to the child and society (NCPI 2014).

At 2 years and 6 months, D.P.S. started activities at the ballet class. She took the prosthetic support device to the CMEI and the ballet class, using it according to the activity to be performed. The assessment of the device's functionality was carried out together with the activities realized in the rehabilitation sessions (Fig. 10.3e). In addition, other activities that the user D.P.S. participated in using the devices (Fig. 10.3a) include holding a ball, holding the bike handlebar (Fig. 10.3b), and manipulating toys with both hands.

Ballet class has the 5th basic position, in which the fingers of both hands must meet on top of the head, and D.P.S. looks to be happy observing at the device's fingertips meeting her left-hand fingers (Fig. 10.3c), accomplishing the position. Another occasion that brought satisfaction was to hold a closed umbrella with the device hand and open it with the other hand (Fig. 10.3d). The user prefers not to use the support device for activities such as finger painting (Fig. 10.3f) and washing the hands (Fig. 10.3g) or playing with plasticine, which has the perception of touch and domain of the task.

Table 10.6 is listed the D.P.S. preferences of using or not the prosthetic support device to perform activities and tasks and factors pointed out by the end-user and the indirect users.

D.P.S. affirms that the most relevant activity using the prosthetic support device was riding a bicycle, as it helps the balance when holding the handlebars with both hands. However, the user prefers not to use the device for activities that involve touches, such as using the hands to paint and use plasticine, as the device bothers and is uncomfortable when manipulating paint and dough. She prefers to use the device


(a) Prosthetic devices. (b) Riding a bicycle.


(c) Ballet step. (d) Holding an umbrella.


(e) Rehabilitation. (f) Painting with the fingers.


(g) Washing the hands. (h) Holding a 500ml bottle.

Fig. 10.3 Prosthetic support devices and the user

Table 10.6 Activities and preferences to perform with or without a prosthetic support device

Activities	Preference of the device	Indicated factors
Open the umbrella	Use	Functional and efficiency
Ride a bike	Use	Functional, security and balance
Support notebooks and sheets in writing during class	Use	Efficiency, social life
Play with ball	Use	Functional and efficiency
Play with plasticine	Do not use	Comfort and pleasure of touch
Play with paint	Do not use	Comfort and pleasure of touch
Play in the park	Do not use	Prefers the hands free to play
Put on shoes	Do not use	Has better control in manipulating with both hands
Eat	Do not use	Ease of eating without device
Run	Do not use	Feeling of being free
Dance ballet	Use	Functional and safety to complete ballet steps
Dance jazz/dance music	Do not use	Feeling of being free
Climb on toys in the park	Do not use	Has better control
Brush the teeth	Do not use	Has better control and manual domain
Browse and manipulate books	Do not use	Contact and manual domain
Interaction with other children	Use	Aesthetics and better social interaction
Play video game	Do not use	Freedom for controlling with both hands
Apply lipstick while holding a mirror	Use	Efficiency in combined function
Walk	Use	Aesthetics, pleasure to show the device
Brush the hair	Do not use	Manipulation with both hands domain
Hold dolls and toys	Use	Efficiency for manipulating with both hands
Hold cell phone	Do not use	Manipulation with both hands domain
Hold cup	Use	Efficiency and safety
Hold baby bottle	Do not use	Freedom sensation and easy manipulation
Social life situations	Use	Aesthetics and better social interaction
Dress up	Do not use	Efficiency and manipulation domain

in the case of thin, tall model glass or bottle as it allows her to lift up to 500 ml more easily. Further, she would rather not use a prosthetic support device during meals, preferring to use a fork, which she holds with the left hand and support the plate with the right hand. Food is cut by parents or family members because the user does not know how to handle the knife. At school, she uses her left hand to cutting paper and other materials with scissors.

The user mentioned the uncomfortable factor on very cold days, making it challenging to put on, adjust, and take off the prosthetic support device over a long-sleeved blouse, especially with denser fabrics.

The occurrence of fatigue or lack of interest is revealed when D.P.S. prefers not to use the prosthetic support device to perform a task, such as using the cell phone and playing games, in which she has mastery of operating with both hands without the need for support. The maximum time of continuous use of the device was two hours in places like churches, shopping malls and parks and in physiotherapy sessions was one hour.

In the first devices, objects used to slip, and silicone materials were added to the fingertips to improve the fixation. Thus, the functional assessment results established the requirements for the development of the new device and the research's continuity with the study of materials, biomechanical movement, design and aesthetic presentation.

The aesthetics of prosthetic devices was relevant, and customization with themes of interest to the child user motivates their use and psychologically helps understand that physical disability is not synonymous with incapacity. The possibility of choosing the theme and colors affects the end-user interest in the device's use or not, and depending on the activity, the user will feel more confident and secure to use the device. In addition, the user's motivation to use the device is taken into consideration, and even though a device is manufactured, its use depends on the user's interest in the activity. For example, in the D.P.S. case, a support device to play the guitar is already available, but she has not shown interest in using it.

In view of other testimonials provided by the CSO, physical and emotional improvements are immediately perceived in children using the support device. Furthermore, improvements were observed in the execution of basic daily activities with more independence, autonomy and security, which enabled the learning and training of hand manipulation functions.

The results analysis shows the benefits of the device's users regarding muscle stimulation, which are positive because the child exercises and stimulates the limb with agenesis more effectively.

Contributions are as follows:

- increase in the performance of physical development, muscle stimulation and the user's total range of motion;
- reduction of the user's muscle atrophy;
- increased motivation and self-esteem: themes of interest about superheroes or various characters were chosen for customization;
- facility to use the prosthetic support device, from the user's position;

- contribution to bilateral orientation and body symmetry.

10.6 Conclusions

The IPDP oriented to Assistive Technology provides greater integration between the areas of knowledge involved in developing prosthetic support devices. In this research, professionals from different areas participated in the development of the devices and in the rehabilitation sessions to monitor the assessment of functionality and the user's evolution. Eleven devices were manufactured, which showed effective benefits to the user with muscle stimulation of the upper limb.

It was observed that there is a need to change the prosthetic support device with frequency due to the child's natural physical growth or according to the material wear. Thus, additive manufacturing allows this change to be carried out at a lower cost than other market options.

Secondary users and indirect users noted that the end user's participation during the prosthetic support device manufacturing led to a considerable motivation for its use, resulting in higher efficiency.

The device currently being manufactured is the "Kinect" model, which uses wrist flexion to open and close the prosthetic hand. It allows the assignment of differentiated exercises to strengthen parts of the skeletal muscle of the arm in the rehabilitation program. Therefore, each model of prosthetic support device has different instrumental functions that depend on the user's use. Each model considers age and functional activity factors to improve the individual's perception of participation and the cultural and social environment that influence motivation issues.

This research will continue to follow the user D.P.S. evolution with the prosthetic support device and intends to add other users. Besides, it will continue the study of the functionality involving important human factors and add to the AT design-oriented requirements.

Acknowledgements The authors would like to thank the Postgraduate Program in Production and Systems Engineering at the Pontifical Catholic University of Paraná (PPGEPS/PUCPR) and the Associação Dar a Mão with its team of professionals and volunteers for supporting the research.

References

Afonso C, Coelho JP, Cadete A, Lopes A, Vasconcelos A, Batalha I (2009) Congenital skeletal deficiencies in upper limb in a pediatric population: 27 years Revision. Revista Da Sociedade Portuguesa De Medicina Física e De Reabilitação 17(1):26–29

Åhsberg E, Kecklund G, Åkerstedt T, Gamberale F (2000) Shiftwork and different dimensions of fatigue. Int J Ind Ergon 26:457–465

Back N (1983) Metodologia de projeto de produtos industriais. Editora Guanabara Dois, Rio de Janeiro

Back N, Ogliari A, Silva J Da, Dias A (2008) Projeto integrado de produtos: planejamento, concepção e modelagem. Barueri, São Paulo, Manole
Biddiss EA, Chau TT (2007) Upper limb prosthesis use and abandonment: a survey of the last 25 years. Prosthet Orthot Int 31(3):236–257
Biddiss EA, Chau TT (2008) Multivariate prediction of upper limb prosthesis acceptance or rejection. Disabil Rehabil Assist Technol 3(4):181–192
Bitencourt RS, Okumura MLM (2020) Um panorama da Indústria 5.0: o resgate do fator humano. Anais do XX Congresso Brasileiro de Ergonomia, 23 a 27 nov 2020. Rio de Janeiro, Abergo
Borg J, Lindström A, Larsson S (2011) Assistive technology in developing countries: a review from the perspective of the Convention on the Rights of Persons with Disabilities. Prosthet Orthot Int 35(1):20–29
Brasil (2013) Ministério da Saúde. E-SUS: Manual de preenchimento de fichas. Secretaria de Atenção à Saúde. Departamento de Atenção Básica. Brasília, Editora do Ministério da Saúde
Browning TR (2010) On the alignment of the purposes and views of process models in Project management. JOper Manage 28(4):316–332. https://www.sciencedirect.com/science/article/pii/S0272696309000862
Burn MB, Ta A, Gogola GR (2016) Three-dimensional printing of prosthetic hands for children. J Hand Surg 41:103–109
Cella D (1998) Progress toward guidelines for the management of fatigue. Oncology (williston Park) 12(11A):369–377
Chau T, Moghimi S, Popovic MR (2013) Knowledge translation in rehabilitation engineering research and development: a knowledge ecosystem framework. Arch Phys Med Rehabil 94(1 Suppl):S9–S19
Comitê Científico do Núcleo Ciência pela Infância – NCPI (2014). Estudo nº 1: O Impacto do Desenvolvimento na Primeira Infância sobre a Aprendizagem. https://www.mds.gov.br/webarquivos/arquivo/crianca_feliz/Treinamento_Multiplicadores_Coordenadores/impacto_desenvolvimento_primeira%20infancia_sobre_aprendizagem.pdf
Cui X, Boland T, D'lima DD, Lotz MK (2012) Thermal inkjet printing in tissue engineering and regenerative medicine. Recent Pat Drug Deliv Formul 6(2):149–155
Dabaghi-Richerand A, Haces-Garcia F, Capdevilla-Leonori R (2015) Prognostic factors of a satisfactory functional result in patients with unilateral amputations of the upper limb above the wrist that use an upper limb prosthesis. Revista Española de Cirugía Ortopédica y Traumatología. (English Edition), 59(5):343–347. https://www.sciencedirect.com/science/article/pii/S1988885615000541
Associação Dar a Mão. Uma rede de apoio à diferença de membros (2021). www.daramao.org
E-Nable (2021) e-Nable community: enabling the future. http://enablingthefuture.org
Fontelles MJ, Simões MG, Farias SH, Fontelles RGS (2009) Metodologia da Pesquisa Científica: Diretrizes para a Elaboração de um Protocolo de Pesquisa. Núcleo de Bioestática Aplicado à pesquisa da Universidade da Amazônia – UNAMA. Belém, PA
Franca Bisneto EN (2012) Deformidades congênitas dos membros superiores: parte I: falhas de formação. Rev Bras Ortop 47(5):545–552
Gross BC, Erkal JL, Lockwood SY (2014) Evaluation of 3D printing and its potential impact on biotechnology and the chemical sciences. Anal Chem 86(7):3240–3253
Hawkins FH (1993) Human factors in flight. Ashgate, Aldershot
Iida I (2005) Ergonomia: projeto e produção. 2nd ed. revista e ampliada. São Paulo, Edgard Blücher
International Civil Aviation Organization - ICAO. Human Factors Guidelines for Aircraft Maintenance Manual (Doc 9824). Montreal, Canadá: ICAO, 2003. https://store.icao.int/en/human-factors-guidelines-for-aircraft-maintenance-manual-doc-9824
International Ergonomics Association—IEA (2000) Ergonomics International News and Information August, 2000. Marshall Associates, London
ISO 9241-11(1998) Ergonomic requirements for office work with visual display terminals (VDTs) Part 11: Guidance on usability 1998. http://www.it.uu.se/edu/course/homepage/acsd/vt09/ISO9241part11.pdf

ISO/IEC 9126 (1999) Information technology—software product quality- part 1: quality model (FDIS)
Kannenberg AMD (2017) Active upper-limb prostheses: the international perspective. J Prosthet Orthot 29(4S):P57–P62
Kintsch A, DePaula R (2002) A framework for the adoption of assistive technology. In: Supporting learning through assistive technology—SWAAAC, 2002. Winter Park, CO, USA. http://l3d.cs.colorado.edu/clever/assets/pdf/ak-SWAAAC02.pdf
Klein GT, Lu Y, Wang MY (2013) 3D printing and neurosurgery—ready for prime time? World Neurosurg 80(3–4):233–235
Kottke FJ, Stillwell GK, Lehmann JF (1984) Tratado de Medicina Física e Reabilitação de Krusen. 3rd ed. São Paulo, Editora Manole
Laferrier JZ, Gailey R (2010) Advances in lower-limb prosthetic technology, vol 21. Physical Medicine and Rehabilitation Clinics of North America Publications, pp 87–110
Lazoski VCS (2018) Método conceitual para o desenvolvimento integrado de produto orientado a próteses. Dissertação de mestrado, Programa de Pós-graduação em Engenharia de Produção e Sistemas, Pontifícia Universidade Católica do Paraná, Curitiba, Paraná, Brasil
Lei Nº 8.069, 13 Jul 1990 Dispõe sobre o Estatuto da Criança e do Adolescente e dá outras providências. Diário Oficial da República Federativa do Brasil. Brasília, DF, 16 jul. 1990. http://www.mp.go.gov.br/portalweb/hp/10/docs/lei_n._8.069_de_1990.pdf
Maia BA (2016) Parametrização dimensional, por modelo de regressão, de próteses de mão para crianças, confeccionadas por manufatura aditiva. Catalão, UFG
Mcgimpsey G, Bradford T (2010) Limb prosthetics services and devices, critical unmet need: market analysis. Worcester, Bioengineering Institute Center for Neuroprosthetics
Okumura MLM, Canciglieri Junior O (2019) Modelo Conceitual de Projeto Orientado para Tecnologia Assistiva: Design for Assistive Technology – DFAT. Mauritius, Novas Edições Acadêmicas, OmniScriptum
Poteriko da Silva GA, Okumura ML, Canciglieri Junior O (2020) Dispositivo de Apoio Protético: Avaliação Funcional e a Contribuição da Reabilitação na Infância. Anais do Congresso Brasileiro de Tecnologia Assistiva (CBTA/2020), Caxias do Sul/RS
Poteriko G (2019) Joia Rara: Agenesia de membros. Sinergia, Maringá
Resnik L (2011) Development and testing of new upper-limb prosthetic devices: Research designs for usability testing. J Rehabil Res Dev 48(6):697–706. https://www.rehab.research.va.gov/jour/11/486/resnik1486.html
Schubert C, Van Langeveld MC, Donoso LA (2014) Innovations in 3D printing: a 3D overview from optics to organs. Br J Ophthalmol 98:159–161
Smets EM, Garssen B, Bonke B, De Haes JC (1995) The multidimensional fatigue inventory (MFI): psychometric qualities of an instrument to assess fatigue. J Psychosom Res 39(3):315–325
Smith DW (2002) Introducing EDG students to the design process. In: Proceedings of the 2002 annual midyear meeting of the engineering design graphics division of the american society for engineering education, Berkeley
World Health Organization—WHO (1997) Measuring quality of life: the world health sorganisation quality of life instruments
World Health Organization—WHO (2019) International Statistical Classification of Diseases and Related Health Problems. 10th Revision (ICD-10)-WHO Version for 2019
Xavier D (2021) A fisioterapia na reabilitação da criança com necessidades especiais. http://andanenem.com.br/importancia-da-fisioterapia-na-reabilitacao-da-crianca-com-necessidades-especiais

Chapter 11
Modelling of the Personalized Skull Prosthesis Based on Artificial Intelligence

Luiz Gustavo Schitz da Rocha, Yohan Boneski Gumiel, and Marcelo Rudek

11.1 Introduction

The recent evolutions in the Artificial Intelligence (AI) field have introduced innovative approaches in the many medicals processes. Nowadays, the same pillars of industry 4.0 revolution, as the Internet of Things (IoT) or IoHT to "health things" in the medical area), Cloud Computing and Cyber-Physical Systems (CPS) have made some relevant contributions to solve the problems in medicine with a focus on processes optimization. Inside these innovative concepts, the data based on medical images analysis are essential to support different processes.

From images, those processes that require 3D reconstruction depend on a wide set of data, and from the engineering's viewpoint, require a high computational processing level.

Medical images from computed tomography (CT) or magnetic resonance imaging (MRI) are frequently used to model the existing bones structures, improve visualization and clinical interpretation, and used in the surgical preparation of implants, construction of molds, and virtual models for prosthetics pieces.

Virtual bone modeling is a challenging process due to the complexity of the geometry and because sometimes we do not have enough information to build a model.

L. G. S. da Rocha
Control and Automation Engineering, Pontifical Catholic University of Paraná (PUCPR), Curitiba, Brazil
e-mail: luiz.schitz@pucpr.edu.br

Y. B. Gumiel
Health Technology Graduate Program (PPGTS), Pontifical Catholic University of Paraná (PUCPR), Curitiba, Brazil
e-mail: yohan.gumiel@pucpr.br

M. Rudek (✉)
Production and System Engineering Graduate Program—PPGEPS, Pontifical Catholic University of Parana - PUCPR, Curitiba, Brazil
e-mail: marcelo.rudek@pucpr.br

O. Canciglieri Junior and M. D. Trajanovic (eds.), *Personalized Orthopedics*,
https://doi.org/10.1007/978-3-030-98279-9_11

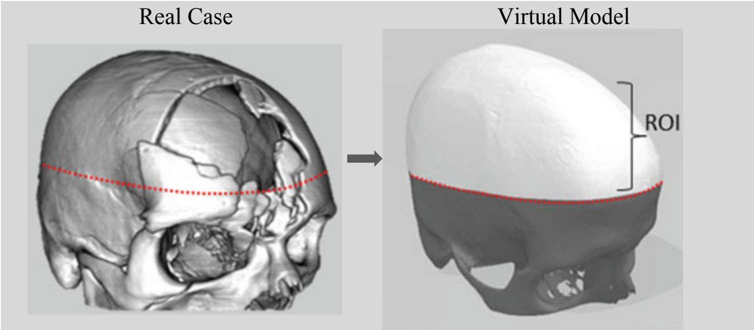

(a) Skull with frontal fractures (VISUALDATA 2021).

(b) Region of interest (white part).

Fig. 11.1 The problem interpretation for skull modeling

In this context, the skull prosthesis modeling has the same challenge, mainly for non-symmetric fractures, because mirroring techniques are ineffective, for example, as in Fig. 11.1a (VISUALDATA 2021). The conceptual basis for a personalized reconstruction is to look for the image parameters from knowing data. In this way, as in Fig. 11.1b, a virtual model can rebuild a complete skull, and an estimative of a prosthesis piece can be calculated to fill the gaps in the bone. The region of interest (ROI) addressed in this research is the calvaria region.

Following the concept presented in Fig. 11.1, some techniques were experimented by the PPGEPS (Industrial and Systems Engineering Program) team during last years based on optimization techniques and AI tools and made some different approaches to virtual model creation as (i) Adjusted Ellipses and Super-Ellipses concept, (ii) PSO (Particle Swarm Optimization), (iii) Splines and Bezier Curves, (iv) Data Mining, (v) Content-Based Retrieval, (vi) Neural Networks, (vii) CNNs (Convolutional Neural Networks) and Deep learning, and (viii) Semantic Segmentation; all of them aligned with virtual design systems integration. The unfolding from these initial experiments using more advanced approaches as Variational AutoEncoder (VAE) has been analyzed here. Thus, the objective is to show the advances in prosthesis modeling by investigating the most recent research studies and propose a suitable solution for the anatomic prosthesis.

11.2 The State of the Art for the Skull Modelling

Several approaches have been used over the years to address the task of skull reconstruction. We reviewed these approaches by searching for articles related to skull reconstruction in PubMed, Science Direct, and Google Academic as in the method of (Reche et al. 2020). We considered all articles, with no restriction towards the publication year. After our article selection step, we selected 34 articles that are summarized and analyzed over this section. All selected articles are summarized in Table 11.1; we provide information regarding the dataset, the approach, the dataset size, and the obtained results. Some of the articles evaluated their results visually, others with knowing metrics, for instance, applying the Dice Similarity Coefficient (DSC) and Hausdorff distance (HD).

Among the methods for skull modeling, there are approaches based on mirroring. Mirroring uses the reflection of the healthy half of the skull onto the defective one, using the patient's data as a template for the implant (Marzola et al. 2019). Unilateral defects can be solved with mirroring, either with minimal manual effort or automatically (Mainprize et al. 2020).

Preliminary studies from Lee et al. (2002) and Hieu et al. (2003) from the 2000s. Both used mirroring and an additional manual adjustment step. The approaches from Gall et al. (2016) and Egger et al. (2017) also used mirroring and manual adjustment. The adjustment was based on Laplacian smoothing followed by a Delaunay triangulation. The mirroring provided an initial design, while the smoothing and triangulation provided an aesthetic-looking and well-fitting outcome (Egger et al. 2017). The approach from Rudek et al. (2015b) also applied symmetric mirroring. Further, Chen et al. (2017) developed a mirroring, contour clipping, and surface fitting method. Marzola et al. (2019) developed a mirroring and surface interpolation method for unilateral and quasi-unilateral defects.

However, just mirroring may not be enough for an implant, as human heads are generally too asymmetric (Gall et al. 2016). Further, mirroring can only be applied to unilateral defects, not to defects that cross the symmetry plane (Shi and Chen 2020; Marzola et al. 2019).

An alternative is using slice-based techniques, where 2D images (generally CT images) are used to fit curves to the bone contours (Marzola et al. 2019). The information from the healthy part is usually used as a boundary to the curve optimization algorithms and functions.

Among the techniques, Rudek et al. (2018), Rudek et al. (2016), and Rudek et al. (2015a) generated control points for each CT slice with Cubic Bezier Curves and the ABC algorithm to optimize the curve. Afterward, they compared control points of the defective slices with healthy slices, selecting the healthy slice with the smallest error to fulfill the missing part. Mohamed et al. (2015) also used Bezier Curves; they combined C1 Rational Bezier Curves with Harmony Search (HS) to complete the missing piece on every slice with a defect.

The approaches of Lin et al. (2017) and Chang and Cheng (2018) used methods based on active contour models. Lin et al. (2017) developed a self-adjusting method based on active contour models, optimizing the shape for every slice and then combining the results for each slice. While Chang and Cheng (2018) developed a self-adjusting method based on active contour models, using the Adaptive Balloon Force Active Surface Model.

Further, Rudek et al. (2013) and Lin et al. (2016) used methods based on Superellipses. Rudek et al. (2013) adjusted Superellipses to the missing part. The Superllipses parameters were optimized by Particle Swarm Optimization (PSO). Lin et al. (2016)

Table 11.1 Articles regarding the reconstruction of skulls

Article	Dataset	Approach	Dataset	Results
Ellis and Aizenberg (2020)	CQ500 Dataset	Data augmentation + Unet	210 complete skulls (630 files)	Mean DSC: Test case (100) 0.944, Test case (10) 0.932, Overall (110) 0.942; Mean HD: Test case (100) 3.564, Test case (10) 3.934, Overall (110) 3.598
Kodym et al. (2020a)	CQ500 Dataset	CNN + 2 Unet	210 complete skulls (630 files)	Mean DSC: Test case (100) 0.920, Test case (10) 0.910, Overall (110) 0.919; Mean HD: Test case (100) 4.137, Test case (10) 4.707, Overall (110) 4.189
Mainprize et al. (2020)	CQ500 Dataset	Data augmentation + U-net + post-processing	210 complete skulls (630 files)	Mean DSC: Test case (100) 0.907, Test case (10) 0.87, Overall (110) 0.904; Mean HD: Test case (100) 4.18, Test case (10) 4.76, Overall (110) 4.23
Bayat et al. (2020)	CQ500 Dataset	2 CNN (2D CNN + 3D CNN)	210 complete skulls (630 files)	Mean DSC: Test case (100) 0.8957; Mean HD: Test case (100) 4.6019
Wang et al. (2020)	CQ500 Dataset	RDU-Net	210 complete skulls (630 files)	Mean DSC: Test case (100) 0.8910, Test case (10) 0.4729, Overall (110) 0.8530; Mean HD: Test case (100) 6.9091, Test case (10) 21.0492, Overall (110) 8.1946

(continued)

Table 11.1 (continued)

Article	Dataset	Approach	Dataset	Results
Jin, Li, and Egger (2020)	CQ500 Dataset	V-net + image partitioning	210 complete skulls (630 files)	Mean DSC: Test case (100) 0.8887; Mean HD: Test case (100) 5.5339
Eder, Li and Egger (2020)	CQ500 Dataset	2 U-Net + post-processing	210 complete skulls (630 files)	Mean DSC: Test case (100) 0.889; Mean HD: Test case (100) 5.534
Kodym et al. (2020b)	CQ500 Dataset	2 U-net	189 complete skulls (945 defective skulls)	Syntectic defects average surface error: 0.56 mm; real defects average surface errors: 0.69 mm
Lin et al. (2017)	–	Active contour models	–	Only visual evaluation
Chang and Cheng (2018)	–	Active contour models	–	Only visual evaluation
Chang et al. (2021)	DICOM images from the Department of Neurosurgery	CNN	Seventy-three complete skulls sets (7,154 augmented sets)	–
Lin et al. (2016)	–	Superellipse	–	Fitness of 0.26 (0.06) for the outer border and 0.25 (0.05) for the inner border
Hsu and Tseng (2001)	–	orthogonal NN	–	–
Rudek et al. (2018)		Cubic Bezier Curves	One skull (7 artificially created defective slices)	Maximum error of 1.7087 mm in comparison to the real skull
Hsu and Tseng (2000)	–	orthogonal NN	One defective skull	–
Li et al. (2020)	CQ500 Dataset	2 encoder-decoder network + bounding box	210 complete skulls (630 files)	N1: DSC 0.8097, HD (mm) 5.4404, RE (%) 0.20; N2: DSC 0.8555, HD (mm) 5.1825, RE (%) 0.15;

(continued)

Table 11.1 (continued)

Article	Dataset	Approach	Dataset	Results
Matzkin et al. (2020a)	Division of Anesthesia of the University of Cambridge	U-net	98 CT images	Superior results with U-Net and direct estimation of the bone flap
Rudek et al. (2013)	–	Superellipse	–	Only visual evaluation
Rudek et al. (2016)	–	Cubic Bezier Curves	One skull (15 artificially created defective slices)	Maximum error of 1.7087 mm in comparison to the real skull
Da Rocha et al. (2020)	CQ500 Dataset	Cubic Bezier Curves + NN	90 skulls (the dataset contains 491 skulls)	An error of 2.184% of the volume
Rudek et al. (2015a)	–	Cubic Bezier Curves	One skull (25 artificially created defective slices)	Only visual evaluation
Rudek et al. (2015b)	–	Mirroring	One skull	Only visual evaluation
Marzola et al. (2019)	–	Mirroring + surface interpolation	–	The tests cases proved the effectiveness of the method
Morais, Egger and Alves (2019)	1200 Subjects Release (S1200)	Volumetric Convolutional Denoising Autoencoder	113 MRI scans	Average reconstruction errors lower than 4%
Chen et al. (2017)	–	Mirroring + contour clipping + surface fitting	–	Intra-rater reability of 87.07 + - 1.6% and inter-rater reability of 87.73 + -1.4%
Gall et al. (2016)	–	Mirroring + manual fitting	–	The tool can enable surgeons to generate implants in several minutes
Lee et al. (2002)	–	Mirroring + manual fitting	–	The custom implant reduced the operation time
Hieu et al. (2003)	–	Mirroring + manual fitting	–	Reduced design time and required design skills

(continued)

Table 11.1 (continued)

Article	Dataset	Approach	Dataset	Results
Mohamed et al. (2015)	–	C1 Rational Bezier Curves	2 CT images	According to the author, the method might be effective in real clinical practice
Egger et al. (2017)	–	Mirroring + manual fitting	–	The software was successful in planning and reconstructing
Fuessinger et al. (2018)	–	SSM + GM	–	Precise and straightforward tool to reconstruction, showing higher precision in comparison to mirroring

developed a self-adjusting method based on Superellipse combined with Differential Evolution for the Superellipse parameter optimization.

The downside of Curve optimization methods is that they work only at slice-level and only consider information about that specific slice for which the curve is being optimized. Hence, the lack of information about the missing area (all slices that have a defect) could affect the reconstruction (Marzola et al. 2019). Further, methods trained over several images have a better chance of "learning" the characteristics of missing parts in general and better designing more realistic implants.

Over time deep learning models have become an alternative to traditional machine algorithms traditionally used in medical imaging (Singh et al. 2020). Convolution neural networks (CNNs) are widely used in medical imaging, considering 2D or 3D images. Additionally, classification problems involving 3D images, such as CT images, can always be downgraded to 2D-level. The drawbacks of developing deep learning for 3D images are the limited available data to the algorithms and computational cost (Singh et al. 2020). However, data augmentation techniques and more powerful GPUs mitigate these issues (Singh et al. 2020).

Over the literature, we verified a predominance of publications involving CNN-based models in the latest years, especially in 2020 and 2021. Most of the publications were related to the AutoImplant 2020 shared task,[1] with 210 complete skulls from the CQ500 dataset[2] with their corresponding defective skulls and the implants (Li and Egger 2020a, b).

The approaches used for the AutoImplant 2020 challenge are detailed below. Pimentel et al. (2020) adjusted a 3D statistical shape model (SSM) to locate and

[1] (https://autoimplant.grand-challenge.org/).

[2] (http://headctstudy.qure.ai/dataset).

correct the defect, followed by a 2D generative adversarial network (GAN) to make corrections and better fit the design. Shi and Chen (2020) decomposed into slices for each axis (2D level), applying three 2D CNNs (one for each axis) and then combining the results from all axes. Further, Bayat et al. (2020) approached was based on CNNs, with a 3D encoder-decoder to complete the downsampled defected followed by a 2D upsampler to upsample the shape. Downsampling turned the approach more feasible for commonly available GPUs. Li et al. (2020) developed a baseline approach for the AutoImplant 2020 shared task. The approach was based on an encoder-decoder network that predicted a downsampled coarse implant; afterward, the data is upsampled, a bounding box is applied to locate the defected region on the high-resolution volume, and the data passes by another encoder/decoder network that generated an implant from the bounded region.

Several of the papers used models based on U-net (Ronneberger et al. 2015). As highlighted by (Ronneberger et al. 2015), the U-net model has the advantage of being trained end-to-end from very few images, achieving excellent results while the training is fast.

The papers that used models based on U-net are detailed further below. Ellis and Aizenberg (2020) augmented the dataset with data transformations that added different shapes and orientations (9903 additional images—significant augmentation) and used a U-Net model with residual connections. Kodym et al. (2020a)'s approach was based on skull alignment with landmark detection with 3D CNN and two 3D U-net models for the reconstruction. They also applied shape pros-processing steps. Mainprize et al. (2020) predicted the skull with a U-Net model and data augmentation, subtracted from the original skull to obtain the prosthesis, and added further post-processing. The data augmentation occurred by adding cubic and spherical defects. Eder et al. (2020)'s framework used 2 U-Net models, the first one was used to reconstruct the skull with low-resolution data, and the other was used to up-sample the low-resolution data. Also, they applied some post-processing filters to provide specific corrections. Kodym et al. (2020b) predicted the implant with two U-net models, testing discriminative and generative models. Additionally, provided tests with synthetic data.

Further, Matzkin et al. (2020b) adapted the model from Matzkin et al. (2020a) to consider flaps similar to the ones for the challenge dataset, tested two methods: (1) using a 3D DE-UNet model and (2) DE-UnET model with data augmentation from additional input from shape priors. Wang et al. (2020) predicted the complete skull with a Residual Dense U-net (RDU-Net) model with the encoder of the Variational Auto-encoder (VAE) model being added as the U-net regulation term, later subtracted the defective skull to delimiter the implant. Jin et al. (2020) approach was based on a V-net model, an adaptation of the U-Net model proposed by Milletari et al. (2016). To address the problem of high-resolution input images to neural networks tested two methods: resizing the images and partitioning the images.

Among the papers related to the AutoImplant 2020 shared task, we highlight the approach of Ellis and Aizenberg (2020), in which the augmentation of training data with registration directly improved the classifier results. Further, for Matzkin et al. (2020b), data augmentation was helpful for out-of-distribution cases, in which the defects did not follow the distribution from the training data, where the network tended to fail. Thus, data augmentation can provide additional data for the network's training with the cost of computational power. Generally, deep learning models tend to achieve superior performance by providing additional data.

Outside of the AutoImplant 2020 shared task dataset, some papers used neural networks. Hsu and Tseng (2000) and Hsu and Tseng (2001) are preliminary studies that addressed that used models based on 3D orthogonal neural networks. Further, Rocha et al. (2020) used a Generative Adversarial Network (GAN) model to predict the missing part of each slice. Additionally, the Morais et al. (2019) approach was based on the Volumetric Convolutional Denoising Autoencoder model that Sharma et al. (2016) proposed with some adaptions. Further, they used MRI images, not CT images. Fuessinger et al. (2018)'s approach used a statistical shape model (SSM) based on 131 CT scans combined with geometric morphometrics (GM) methods, comparing the results with the mirroring technique (only for unilateral defects).

Further, (Chang et al. 2021) used a CNN-based deep learning network with 12 layers and data augmentation to complete the defect, subtracting the completed skull from the incomplete skull to obtain the implant. In the approach proposed by Matzkin et al. (2020a), the images passed by registration, resampling, and thresholding being fed into a U-Net that directly predicted the implant. Tested several architectures and reconstruction strategies (direct estimation and reconstruct and subtract), achieving superior results with U-Net and direct estimation of the implant.

Hence, in general, we verified that most of the preliminary studies addressed the reconstruction task with mirroring or slice-based techniques. With the advances in deep learning models, especially CNNs and their variants (U-net), deep learning-based models became the primary approach. Further, techniques that relieve the computational cost of the training, such as the usage of downsampling combined with upsampling techniques and data augmentation techniques that provide additional images to the training step, are relevant to the research theme.

Among the techniques that were used to address skull reconstruction, VAE models have addressed the task well. Hence, in the next section, we detail some of our experiments of skull reconstruction with a VAE-based model. The following section provides details about our proposed method with its results. Additionally, we provide details about standard evaluation metrics and several images to give the viewer a better understanding of the whole process.

11.3 Background

11.3.1 The VAE Neural Network

The Variational AutoEncoder (VAE), as presented in Fig. 11.2, is a neural network that encodes and decodes data. In the encoding part, the data is compressed into a regularized latent space. In the decoding part, the data is decompressed from this

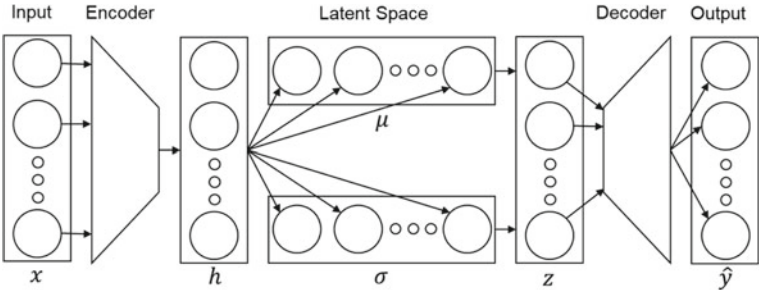

Fig. 11.2 The VAE architecture

space. The regularization of the latent space is made by minimizing the Kullback and Leibler Divergence (KL divergence), this makes the VAE a generative model.

Figure 11.2 represents the VAE architecture where x represents the input data, h represents the coded data, σ represents the measure of the standard deviation of h, μ represents the measure of the mean of h, z represents the sampled data of the probability distribution $\mu + p(0, 1)*\sigma^2$ and ŷ represents the classification of decoding data.

11.3.2 Evaluation Criteria

The VAE neural network (Patterson and Gibson 2017) is a generative model that encodes the input into a latent space close to the uniform distribution using KL loss and decodes the latent space into a classification problem measured using reconstruction loss, additional methods like dice similarity coefficient and Hausdorff distance are used to compare results between proposed method and results in (Li and Egger 2020a, b), assuming y is the removed part of skull and ỹ is 1 where ŷ > 0.5 and 0 otherwise. The measuring methods are described below.

11.3.2.1 The Dice Similarity Coefficient

As presented by Taha and Habury (2015), the Dice Similarity Coefficient (DSC) measures the difference between an y and an ỹ. Both images are required to have the same size and pixels values should be 0 or 1. The formula uses the sum of pixels and the intersection between both images, according to Eq. 11.1.

$$DSC = \frac{2 * sum(\mathrm{y} * \tilde{\mathrm{y}})}{sum(\mathrm{y}) + sum(\tilde{\mathrm{y}})} \tag{11.1}$$

11.3.2.2 The Hausdorff Distance

According to Taha and Habury (2015), the Hausdorff Distance (HD) is a way of measuring the difference between two images based on the maximum distance between a pixel in y and a pixel in ỹ, according to Eq. 11.2.

$$HD = \max_{a \epsilon y} \min_{b \epsilon \tilde{y}} \|a - b\| \tag{11.2}$$

11.3.2.3 The Kullback and Leibler Divergence

From Bonaccorso (2018), the Kullback and Leibler divergence (KL divergence) is used to compare two distributions, where the KL loss is the comparison between a p(μ, σ) distribution and a normal distribution p(0,1), with μ the measured mean and σ the measured standard deviation, according to Eq. 11.3.

$$KLloss = \sum\nolimits_{i}^{N} \frac{{\mu_i}^2 + e^{{\sigma_i}^2} - 1 - {\sigma_i}^2}{2} \tag{11.3}$$

11.3.2.4 The Reconstruction Loss

As presented in Bonaccorso (2018), the Reconstruction loss measures a classification using a reference binary image and a classification image with values between 0 and 1, according to Eq. 11.4.

$$Reconstructionloss = -\sum_{i}^{N} y_i * ln(\hat{y}_i) + (1 - y_i) * ln(1 - \hat{y}_i) \tag{11.4}$$

11.4 Proposed Method

The method uses a Variational AutoEncoder (VAE) neural network (Patterson and Gibson 2017) to generate each layer of the prosthesis. The method was separated into four main steps: (i) image selection, (ii) image segmentation, (iii) neural network training, and (iv) reconstruction, as in Fig. 11.3.

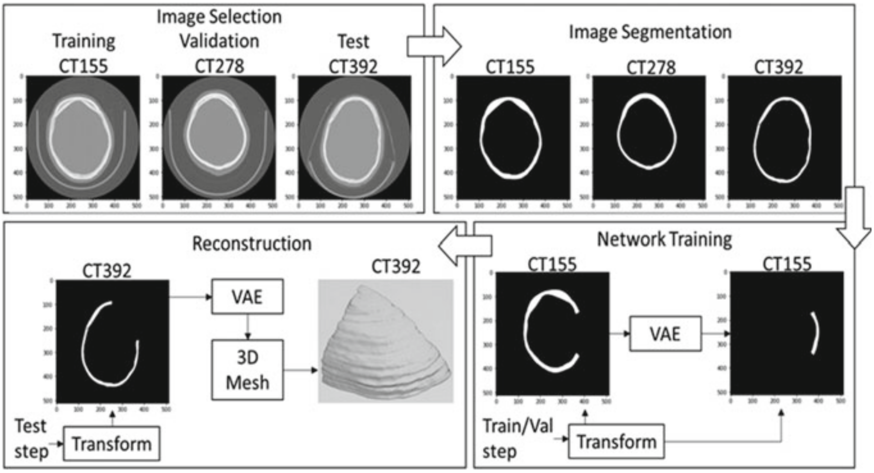

Fig. 11.3 The step sequence of the proposed method

11.4.1 Step 1—Image Selection

The creation of the training, validation and test sets separated some files of skulls without fracture identification. The fracture identification was performed by three specialists and noted in an auxiliary dataset as in Table 11.2. The skulls without any indication of fracture were selected. The images size is 512 × 512 pixels, with voxel dimensions from 0.441 × 0.441 × 0.625 mm to 0.488 × 0.488 × 0.625 mm. Also, each exam having from 233 to 256 image slices of the upper skull region (calvaria region). The selection resulted in 123 skulls, where 80% of them were used for training, 10% for validation, and 10% for the test.

Table 11.3 represents the voxel height statistics considering those images without fracture, with a dimension of 512 × 512 pixels and a voxel depth of 0.625 mm.

Table 11.2 Discrepancy on Fracture indications from experts' observation

CT number	Expert #1	Expert #2	Expert #3
CQ500-CT-109	Yes	No	No
CQ500-CT-167	No	No	No
CQ500-CT-449	Yes	Yes	No
CQ500-CT-417	Yes	Yes	Yes
CQ500-CT-240	No	Yes	No

Table 11.3 Voxel height

Metric	Mean	Std	Min	25%	50%	75%	Max
value (mm)	0.471	0.061	0.213	0.411	0.473	0.488	0.877

Table 11.4 Number of layers

Metric	Mean	Std	Min	25%	50%	75%	Max
Value	225.269	77.0245	1	233	250	256	413

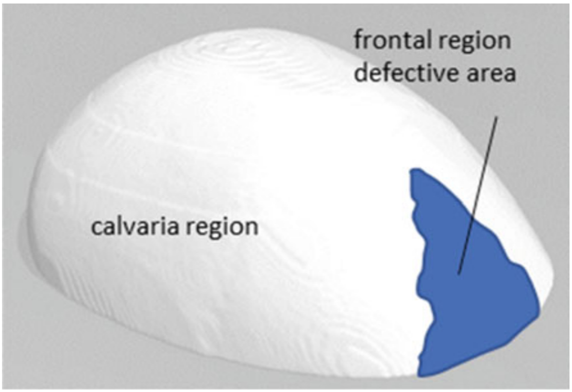

Fig. 11.4 Region of interest in skull calvaria

Table 11.4 shows the statistics of the number of layers after voxel selection between 25 and 75%.

The region of interest was selected as 40% of the upper layers, as presented in Fig. 11.4. We can simulate a frontal defect area in this region by removing the data from a one-by-one 2D CT slicing.

11.4.2 Step 2—Image Segmentation

Bone tissue was identified using the Hounsfield scale in the image sets. The value of 500HU was found based on segmentation tests and histogram comparison. After, for each skull, a volume was created with the CT slices overlapping operation. Finally, identifying connected pixels and selection of the largest connected group, removing unwanted objects presented in Fig. 11.5.

11.4.3 Step 3—Neural Network Training

The training set and the validation set of CT images were used to train and validate the neural network. The total number of skull images was augmented by changes in position and size to increase the number of data samples. From each skull file, the image is transformed by: a vertical inversion with a 50% change, rotated between –45° and 45°, scaled between 90 and 110%, and finally translocated between –16 and

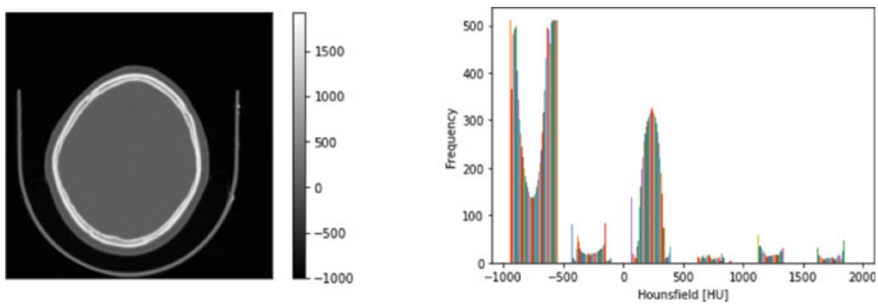

(a) CT image. (b) Histogram.

Fig. 11.5 CT image sample and its respective Hounsfield scale histogram

16 pixels. After the transformation, up to 25% of the image is removed and used as the neural network's output. Further, the image complement is used as the input of the neural network. Figure 11.6 represents an example of each type of transformation.

The VAE neural network architecture was used with input and output of 512 $\times$ 512 $\times$ 1, six layers of convolution and deconvolution with 2layer filters, latent space with two layers of 4096 and samples among the latent space. The ReLu was used as the activation function in the convolution and deconvolution layers. The Linear activation function was applied in the latent space layers, and the Sigmoid activation function was used in the output of the neural network. Figure 11.7 represents the

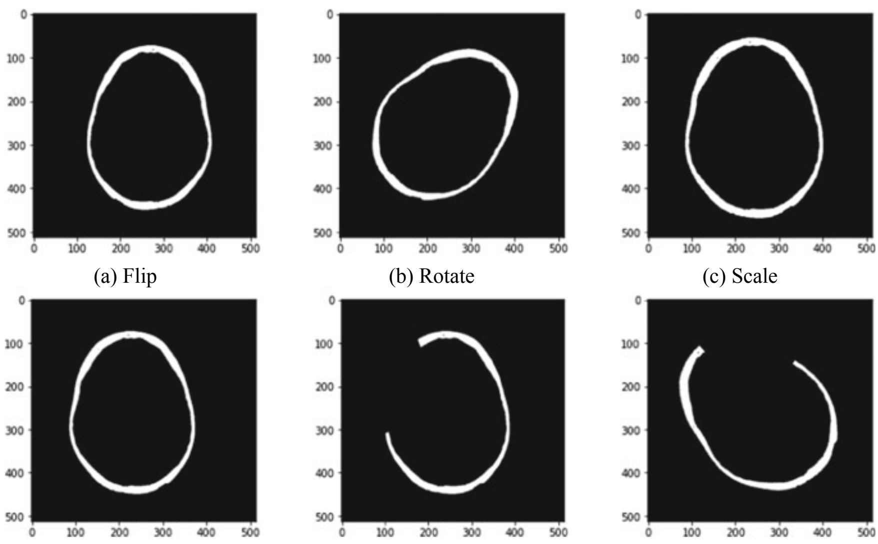

(a) Flip (b) Rotate (c) Scale

(d) Translation (e) Remove (f) Aug. and remove

Fig. 11.6 Transformation examples performed for each skull from the dataset

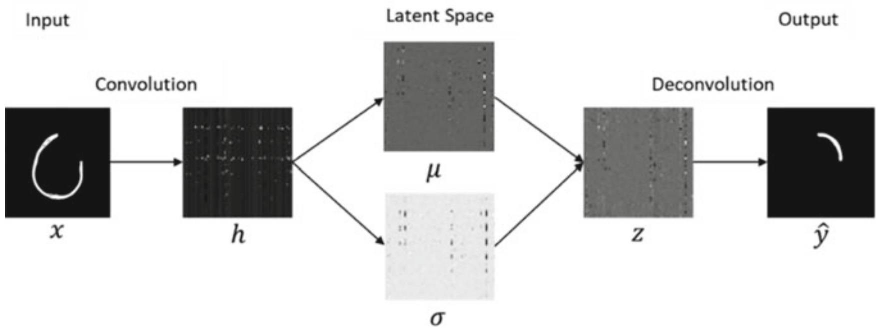

Fig. 11.7 The pipeline for generation of a virtual prosthesis layer

generation of a prosthesis layer, going through the stages of convolution, parameter estimation, sampling, and deconvolution.

The sum of Reconstruction Loss with KL Loss was used as the loss function. The Reconstruction Loss was calculated between ŷ and y. The KL Loss was calculated between μ and σ. The DSC and HD metrics were calculated between y and ỹ, these metrics were used only for visualization and did not interfere with learning. The ADAM optimizer (Bonaccorso 2018) was used for training. Figure 11.8 represent the metrics in respective scale.

11.4.4 Step 4—Reconstruction

The test set without transformation and with removed skull parts was used to create the three-dimensional models, where the interference between x and ỹ was removed. The marching cubes (Lorensen and Cline 1987) method was used to obtain the vertices and faces of the triangles obtained on the surface of the prosthesis (superimposition of layers), using the voxel dimensions as a reference. The Laplacian smoothing (Vollmer et al. 1999) method was used to reduce the sharp surface differences. Figure 11.9 represents the reconstruction process.

11.5 Application Example

The dataset provided by the Center for Advanced Research in Imaging, Neurosciences, and Genomics (CARING) (VISUALDATA 2021) was used in the simulations. It contains 491 skulls with and without fractures, and each skull is composed of different data collections where the number of files and the dimensions of the voxel (Height, Width, Depth) may vary. The absolute path, study name, fracture identification, image size, image position, and voxel dimensions (HxWxD) were mapped

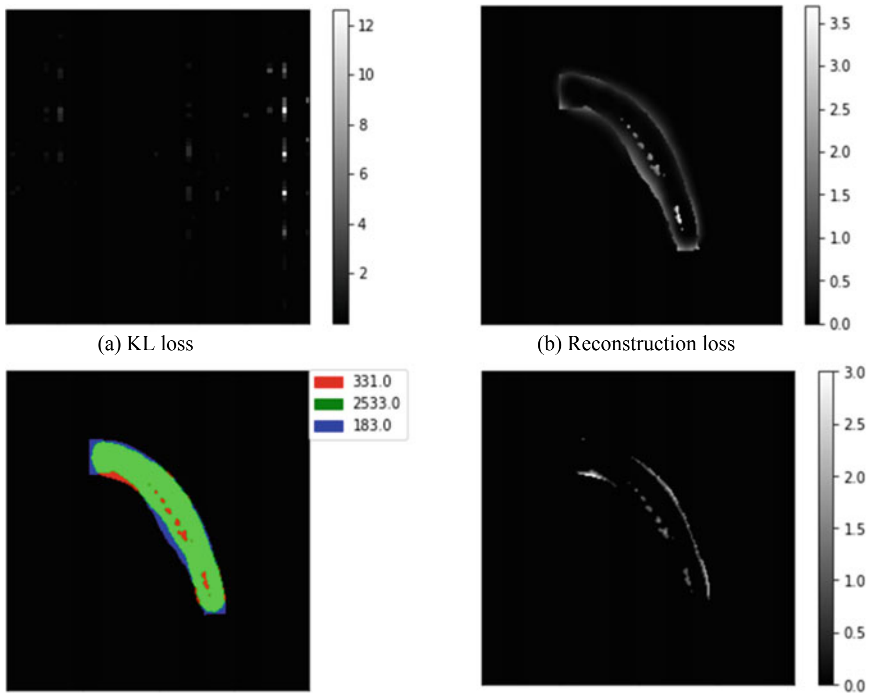

(a) KL loss (b) Reconstruction loss

(c) DSC (d) HD

Fig. 11.8 The metrics of reconstructed piece evaluation

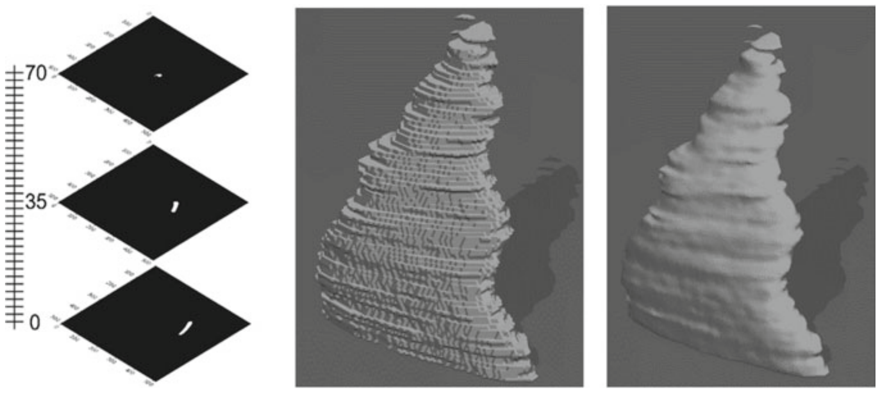

(a) CT slices stack. (b) Marching Cubes. (c) Laplacian Smoothing.

Fig. 11.9 The reconstruction process slice by slice superimposed and surface enhancement to each file. A machine with AMD Ryzen 5 3600X Hexa-core processor, NVIDIA Graphics Card, was used for neural network training and 3D mesh generation. An RTX 2060 super 8 GB VRAM, 32 GB RAM, and Windows 11 operating system. Python programming language was used for software development.

Figure 11.10 shows the synthetic cut artificially created in (a) by removing 25% of the skull and the generated prosthesis in (b). The colors scale in (b) represents the distance between the prosthesis and the original removed part of the skull. See Fig. 11.11 about color scale and respective metrics.

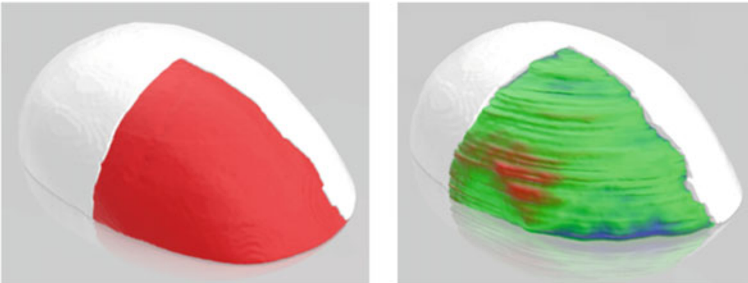

(a) external view (synthetic). (b) adjusted piece from VAE.

Fig. 11.10 The synthetic removed piece from skull and its respective virtual model

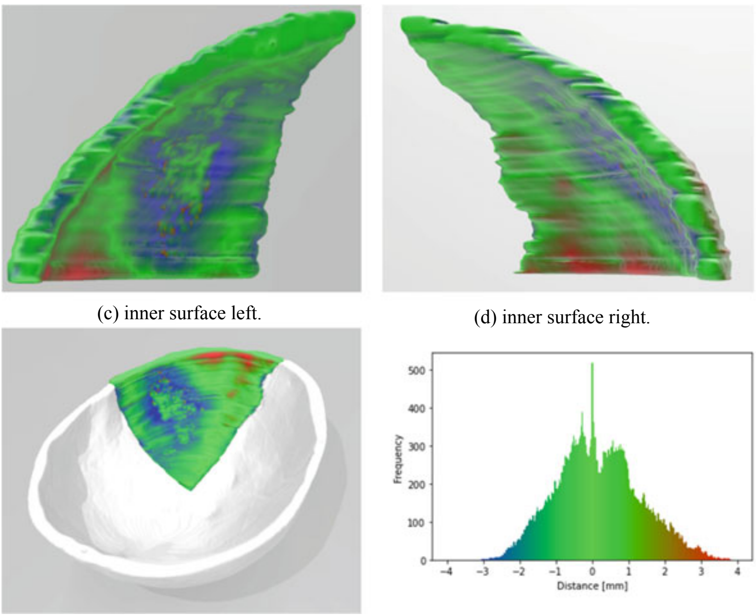

(c) inner surface left. (d) inner surface right.

(e) inner view. (f) error scale legend.

Fig. 11.11 Sample of Model of the generated prosthesis

Table 11.5 The metrics obtained from simulated cut as in Fig. 11.10a

Metric	Value
Quantity of Images	87
Voxel dimensions	0.488 × 0.488 × 0.625 mm
Mean Reconstruction loss	2202.046
Mean KL loss	167.175
Mean HD	5.587 pixels (2.726 mm)
Mean DSC	0.792
Sampled vertices	77,682
Min Distance (inner surface)	–3.073 mm
Max Distance (outer surface)	3.786 mm
Mean Distance	0.150 mm
Standard Deviation	1.134

Figure 11.10b shows differences in the prosthesis boundary connected with the original removed piece, with measures differences around 2 mm as indicated by the green representation. Table 11.5 represents the metrics obtained from removed part of the skull (piece cut as in Fig. 11.10a). The (+) and (–) signals represent if the difference is on outer or inner surface respectively by comparing with the real bone.

The other view of the generated prosthesis is presented in Fig. 11.11. From colored scale, in green the distances are between –2 and 2 mm; in red, the distances are greater than 2 mm; and in blue, the distances are smaller than -2 mm.

11.6 Conclusion

The research presented the advances to skull prosthesis modeling based on a literature review and respective content analysis. A set of 35 papers were selected to demonstrate the techniques addressed in recent years. The CNN-based techniques are proved as the best way to find missing information on CT/MRI images with efficiency validated by the metrics Mean DSC and Mean HD.

We observed that the virtual skull repairing based on Variational Auto-encoder (VAE) model presented in literature looks like promisor and we investigated its application for own method. As presented in example, the best result for our method was 0.792 to Mean DSC and 5.587 to Mean HD.

The performance achieved by the proposed method according to the metrics: Mean HD and Mean DSC, present important improvement by comparison of the previous explored methods if compared with PSO, Superellipse, ABC and other previously studied by the authors. However, the metrics indicates that we do not get similar results as found in literature.

The next step is improving HD and DSC by testing addicting 3D CNN, more filters in convolution/deconvolution or more neurons in latent space.

References

Bayat A, Shit S, Kilian A et al (2020) Cranial implant prediction using low-resolution 3D shape completion and high-resolution 2D refinement In: Cranial implant design challenge, pp 77–84

Bonaccorso G (2018) Mastering machine learning algorithms: expert techniques to implement popular machine learning algorithms and fine-tune your models. Packt Publishing Ltd

Chang CC, Cheng CY (2018) The adaptive balloon forces for active surface models in skull repair technique. In: 2018 International conference on engineering, applied sciences, and technology (ICEAST), pp 1–5

Chang YZ, Wu CT, Yang YH (2021) Three-dimensional deep learning to automatically generate cranial implant geometry

Chen X, Xu L, Li X et al (2017) Computer-aided implant design for the restoration of cranial defects. Sci Rep 7(1):1–10

Eder M, Li J, Egger J (2020) Learning volumetric shape super-resolution for cranial implant design. In: Cranial implant design challenge, pp 104–113

Egger J, Gall M, Tax A et al (2017) Interactive reconstructions of cranial 3D implants under MeVisLab as an alternative to commercial planning software. PLoS One 12(3):e0172694

Ellis DG, Aizenberg MR (2020) Deep learning using augmentation via registration: 1st place solution to the autoimplant 2020 challenge. In: Cranial implant design challenge, pp 47–55

Fuessinger MA, Schwarz S, Cornelius CP et al (2018) Planning of skull reconstruction based on a statistical shape model combined with geometric morphometrics. Int J Comput Assist Radiol Surg 13(4):519–529

Gall M, Li X, Chen X et al (2016) Computer-aided planning and reconstruction of cranial 3D implants. In: 2016 38th annual international conference of the IEEE engineering in medicine and biology society (EMBC), pp 1179–1183

Hieu LC, Bohez E, Vander et al (2003) Design for medical rapid prototyping of cranioplasty implants. Rapid Prototyping J 9(3):175–186

Hsu JH, Tseng CS (2000) Application of orthogonal neural network to craniomaxillary reconstruction. J Med Eng Technol 24(6):262–266

Hsu JH, Tseng CS (2001) Application of three-dimensional orthogonal neural network to craniomaxillary reconstruction. Comput Med Imaging Graph 25(6):477–482

Jin Y, Li J, Egger J (2020) High-resolution cranial implant prediction via patch-wise training. In: Cranial implant design challenge, pp 94–103

Kodym O, Spanel M, Herout A (2020a) Cranial defect reconstruction using cascaded CNN with alignment. In: Cranial implant design challenge, pp 56–64

Kodym O, Spanel M, Herout A (2020b) Skull shape reconstruction using cascaded convolutional networks. Comput Biol Med 123:103886

Lee MY, Chang CC, Lin CC et al (2002) Custom implant design for patients with cranial defects. IEEE Eng Med Biol Mag 21(2):38–44

Li J, Egger J (2020a) Dataset descriptor for the autoimplant cranial implant design challenge. In: Cranial implant design challenge, pp 10–15

Li J, Egger J (2020b) Towards the automatization of cranial implant design in cranioplasty. Springer, Cham

Li J, Pepe A, Gsaxner C et al (2020) A baseline approach for autoimplant: the miccai 2020 cranial implant design challenge. In: Multimodal learning for clinical decision support and clinical image-based procedures, pp 75–84

Lin Y, Cheng C, Cheng Y et al (2017) Skull repair using active contour models. Procedia Manufact 11:2164–2169

Lin YC, Cheng CY, Cheng YW et al (2016) Using differential evolution in skull prosthesis modelling by superellipse

Lorensen WE, Cline HE (1987) Marching cubes: a high resolution 3D surface construction algorithm. Comput Graph 21(4)

Mainprize JG, Fishman Z, Hardisty MR (2020) Shape completion by U-Net: an approach to the autoimplant MICCAI cranial implant design challenge. In: Cranial implant design challenge, pp 65–76

Marzola A, Governi L, Genitori L et al (2019) A semi-automatic hybrid approach for defective skulls reconstruction. Comput-Aided Des Appl 17:190–204

Matzkin F, Newcombe V, Glocker B et al (2020b) Cranial implant design via virtual craniectomy with shape priors. In: Cranial implant design challenge, pp 37–46

Matzkin F, Newcome V, Stevenson S et al (2020a) Self-supervised skull reconstruction in brain CT images with decompressive craniectomy. In: International conference on medical image computing and computer-assisted intervention, pp 390–399

Millletari F, Navab N, Ahmadi AS (2016) V-Net: fully convolutional neural networks for volumetric medical image segmentation. In: 2016 fourth international conference on 3D vision (3DV), pp 565–571

Mohamed N, Majid AA, Piah ARM et al (2015) Designing of skull defect implants using C1 rational cubic Bezier and offset curves. In: AIP conference proceedings, p 050003

Morais A, Egger J, Alves V (2019) Automated computer-aided design of cranial implants using a deep volumetric convolutional denoising autoencoder. In: World conference on information systems and technologies, pp 151–160

Patterson J, Gibson A (2017) Deep learning: a practitioner's approach. O'Reilly Media, Inc.

Pimentel P, Szengel A, Ehlke M et al (2020) Automated virtual reconstruction of large skull defects using statistical shape models and generative adversarial networks. In: Cranial implant design challenge, pp 16–27

Reche AYU, Canciglieri Junior O, Estorilio CCA et al (2020) Integrated product development process and green supply chain management: contributions, limitations and applications. J Clean Prod 249:119429–1194459

Rocha LGS, Rudek JVL, Rudek M (2020) Extraction of geometric attributes based on GAN for anatomic prosthesis modeling. In: ICIST 2020 proceedings, pp 64–67

Ronneberger O, Fischer P, Brox T (2015) U-Net: convolutional networks for biomedical image segmentation. In: International conference on medical image computing and computer-assisted intervention, pp 234–241

Rudek M, Gumiel YB, Canciglieri Junior O et al (2018) A cad-based conceptual method for skull prosthesis modelling. Facta Univ Ser: Mech Eng 16(3):285–296

Rudek M, Canciglieri Junior O, Jahnen A et al (2013) CT slice retrieval by shape ellipses descriptors for skull repairing. In: 2013 IEEE international conference on image processing, pp 761–764

Rudek M, Gumiel YB, Canciglieri Junior O et al (2015a) Optimized CT skull slices retrieval based on cubic bezier curves descriptors. In: CIE45—the 45th international conference on computers & industrial engineering

Rudek M, Mendes GC, Canciglieri Junior O et al (2015b) Skull failure-correction modelling method by symmetry mirroring. In: CIE45—the 45th international conference on computers & industrial engineering

Rudek M, Gumiel YB, Canciglieri Junior O et al (2016) Optimized CT skull slices retrieval based on cubic Bezier curves descriptors. In: 6th international conference on information society and technology ICIST 2016, pp 75–79

Sharma A, Grau O, Fritz M (2016) Vconv-dae: Deep volumetric shape learning without object labels In: European conference on computer vision, pp 236–250

Shi H, Chen X (2020) Cranial implant design through multiaxial slice inpainting using deep learning. In: Cranial implant design challenge, pp 28–36

Singh SP, Wang L, Gupta S et al (2020) 3D deep learning on medical images: a review. Sensors 20(18):5097

Taha AA, Habury A (2015) Metrics for evaluating 3D medical image segmentation: analysis, selection, and tool. BMC Med Imaging 15(1):1–28

VISUALDATA (2021) CQ500. A dataset of head CT scans. http://headctstudy.qure.ai/#dataset

Vollmer J, Mencl R, Mueller H (1999) Improved laplacian smoothing of noisy surface meshes. In: Computer graphics forum. Blackwell Publishers Ltd, Oxford, UK and Boston, USA, pp 131–138
Wang B, Liu Z, Li Y et al (2020) Cranial implant design using a deep learning method with anatomical regularization. In: Cranial implant design challenge, pp 85–93

Chapter 12
Application Study of Electroencephalographic Signals in the Upper Limb Prosthesis Field

Alexandre Ferreira Kleppa, Anderson Luis Szejka, and Leandro dos Santos Coelho

12.1 Introduction

Loss or being born without limbs can significantly affect the level of autonomy and the capability of performing daily living, working and social activities (Cordella et al. 2016). There are many reasons why a person may lose a limb. Congenital circumstances, diseases, industrial and car accidents are among the other causes of lost limbs. In the United States, the most common cause of amputation is diabetes (Geiss et al. 2019), and other researches show that this situation is not limited to the United States of America (Santos et al. 2006; Laclé and Valero-Juan 2012; Hoffstad et al. 2015). Based on this context, current research is seeking new methods and technologies to improve prosthetic limbs manufacturing, usability, flexibility, and versatility to propitiate the most suitable welfare for the user (Canciglieri et al. 2019; Kumar et al. 2019; Kashef et al. 2020).

Prosthetic hands are a type of artificial limb that has received research attention in recent years (Kashef et al. 2020; Badawy and Alfred 2020; Graham et al. 2021; Vaskov and Chestek 2021). The use of prosthetic hand to replace the loss is desirable,

A. F. Kleppa
Control and Automation Engineering Department, Pontifical Catholic University of Parana (PUCPR), Curitiba, Parana, Brazil
e-mail: alexandre.kleppa@pucpr.edu.br

A. L. Szejka (✉) · L. dos Santos Coelho
Industrial and Systems Engineering Graduate Program, Pontifical Catholic University of Parana, Curitiba, Parana, Brazil
e-mail: anderson.szejka@pucpr.br

L. dos Santos Coelho
e-mail: leandro.coelho@pucpr.br

L. dos Santos Coelho
Department of Electrical Engineering (PPGEE), Federal University of Parana (UFPR), Polytechnic Center, Curitiba, Brazil

O. Canciglieri Junior and M. D. Trajanovic (eds.), *Personalized Orthopedics*,
https://doi.org/10.1007/978-3-030-98279-9_12

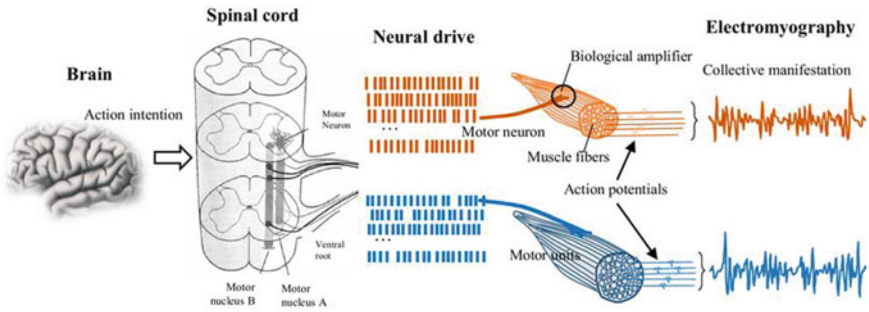

Fig. 12.1 The generation of EMG signals (Yang et al. 2019)

with modern prosthetic hands, which it has evolved from the mechanical nails of yesteryears to sophisticated devices that are electrically powered and offer large numbers of Degrees of Freedom (DOF) (Kumar et al. 2019). The control of the first prosthetic hands was merely mechanical, where the user had to wear a mechanism and when the arm would move in a certain way (Badawy and Alfred 2020). As prosthetic hand presents a large number of DOF and open and close with force and position control, new prosthetic hand control methods are required (Vaskov and Chestek 2021).

The modern hand's owners can perform the control of the hand using electrodes that would give the hand's controller input (Badawy and Alfred 2020). This type of prosthetic control gets a bit more natural, once that the electrode receives the electric signal from the user's muscle and gives it to the system as an output to open or close the hand (Eisenberg et al. 2017). However, the control of the hand using electrodes is complex and require technologies like electromyography (EMG) and modern algorithms to treat the signal and convert it into an output to control the hand movement (Eisenberg et al. 2017; Badawy and Alfred 2020; Graham et al. 2021; Vaskov and Chestek 2021). EMG technology reads the impulse sent by the brain through the spinal cord to the muscles as can be seen in Fig. 12.1.

According to Fig. 12.1, the brain also sent an electric impulse that is generated in the frontal-lobe motor areas that were carried through the spinal cord and sent to the muscle (in this case could be the muscle in the residual limb). The difference from the limb-powered one is that, in this case, the signal will be read by the electrodes placed on the patient's residual limb, and this signal will be used as the information to be processed then moving the prosthesis.

Even though the commercial upper limb electric-powered prosthesis available in the market use in its big majority EMG, the residual limb has muscular limitations, especially the ones after an above-elbow amputation what makes the EMG not enough for the control of prosthesis with multiple degrees of freedom. To solve this problem, there is the proposal of using signal fusion, which is using EMG combining with Electroencephalography (EEG) for having more trustful data (Li et al. 2017). EEG is a method of brain exploration that measures electrical activity in the brain through electrodes placed on the scalp often shown as a trace called an electroencephalogram

(Srinivasan and Nunez 2012). Recently, researchers showed a success rate of 68% using EEG signals to trigger the tasks in a robotic hand system (Saint-Elme et al. 2017; Eisenberg et al. 2017; Badawy and Alfred 2020; Graham et al. 2021; Vaskov and Chestek 2021), which also shows the promising future of the EEG research field.

According to this context, the chapter explores an approach that integrates Principal Component Analysis (PCA) and Recurrent Neural Network (RNN) techniques to evaluate the performance in control a prosthetic hand based on the signals generated from the user's intention of movement recorded from electroencephalographic (EEG). Additionally, the Long-Short Term Memory (LSTM) is a model of RNN of the deep learning field, which will evaluate the performance in face of different Machine Learning methods to control the movement of a prosthetic hand.

The remainder of the paper is structured as follows: Sections 12.2–12.4 explores the related works about the Brain-Computer Interface (BCI), PCA and RNN to support the problem definition. Section 12.5 is dedicated to conceptualizing the integration of PCA with LSTM-RNN to control a prosthetic hand. Section 12.6 presents the application of the approach in an experimental case. Section 12.7 discusses the results, main advantages, and limitations of the research.

12.2 Brain-Computer Interface (BCI)

The BCI is the technique that uses electric signals spotted from the scalp, cortical surface, or brain subcortical areas to activate external devices (Vaskov and Chestek 2021). The electric signals can be captured in an invasive manner or a non-invasive one. The first one is done by the register of a small or big number of neurons, the non-invasive manner is to capture and monitoring the signals by electroencephalography (EEG) (Nuwer and Coutin-Churchman 2014; Srinivasan and Nunez 2012; Machado et al. 2009).

A BCI has, normally, the following components: signal acquisition, preprocessing, feature extraction, classification (or detection), and the application of the interface (Graimann et al. 2010). The explanation can be found in the sequence:

- *Signal acquisition*: This part is responsible for recording the electrophysiological signals that are going to be the input to the BCI.
- *Preprocessing*: This is the task that must enhance the signal-to-noise ratio. To accomplish this task advanced signal processing methods can be useful.
- *Feature extraction*: The objective in this stage is to find an adequate representation of the obtained signals in the previous steps that simplify the classification or detections of the patterns that are going to be studied.
- *Classification*: The goal in this phase is to use the signal features obtained by the previous one to assign the recorded samples into a category of brain patterns.
- *Application of the interface*: As the name may suggest, here is where the BCI system is applied. For advanced applications of the BCI system, it can be found

the output as the controlling of spelling systems or some external devices as prosthetic or multimedia applications.

There is a big interest in this area, once that the implementation of the technique can help to compensate for a motor control loss of patients with a degree more severe of limitation. BCI can be a good indication for patients that suffer from lateral sclerosis amyotrophic, spinal cord injury, stroke, and cerebral palsy, for example, once that BCI captures and modifies the signals that come from brain activity (intension of a movement, for instance) into action, what allows the patient to communicate with the external world (Machado et al. 2009).

When many neurons are activated in the brain, an electric field is formed, EEG is the method used to record and monitor it. Those recorded signals can reveal a data set on cognitive processing, for instance, the intention of a movement (Bäckström and Tidare 2016). To obtain those signals, a technique called electroencephalogram can be done. It is a recording of the brain's electrical potentials done by a set of electrodes placed on the patient scalp (Nunez and Srinivasan 2006).

The electric signals from the brain can also be obtained by intracranial electrodes, implanting them on the animals or epileptic patients for instance, however, as said by Nunez and Srinivasan (2006), although in the second option more detailed and local information can be recorded, it fails to record the general picture of the brain activity. Therefore, in practice, intracranial recordings can just give a different data set of information than the one that can be obtained by the scalp electrodes, not a better one.

According to Bäckström and Tidare (2016), the technique of using EEG signals to control devices through a brain-computer interface is being used for more than a decade now. The appliance the technique resulted, for example, in movement computer cursor, the control of a mobile robot and a virtual keyboard, and some more examples.

12.3 Principal Component Analysis (PCA)

As previously exposed, feature extraction is one of BCI's steps. EEG data can be a large dataset difficult to analyze. To be able to study the EEG data, it can be approached and represented in another way.

Dimensionally reduction is one processing step used to transform features into lower dimension space. One of the most famous unsupervised techniques is the PCA. It is a technique that has the goal of finding the space that better represents the direction of the maximum variance of the data (Tharwat 2016). The PCA has several purposes: finding relationships between observations, extracting the main information from the data, outlier detection and removal, and selecting only the important information of the data reducing its dimensions. The principal components space is composed of orthogonal principal components that are calculated using the covariance matrix or Singular Value Decomposition (SVD) (Tharwat 2016). It can perform dimensionally reduction without any loss of data (Iftikhar et al. 2018).

To use PCA in this study, a background is required, and some concepts must be consolidated. The following sections present a review of the theory that precedes the study of the PCA.

12.3.1 Standard Deviation (s) and Variance (S2)

It is not possible to analyze the features of an entire population, for this reason, studies are normally done using a sample (Tharwat 2016). When a sample of a population is taken for a study, the standard deviation is used to analyze how to spread the individual points of this sample are from the mean. It is a basic statistics technique but will be used in the following steps during the development of the PCA technique. Standard Deviation is calculated by Eq. (12.1) given by

$$s = \sqrt{\frac{\sum_{i=1}^{n} X_i - \overline{X}}{N - 1}} \tag{12.1}$$

where X_i is the value in the data that refers to the point i, X is the mean of the data and N is the number of data points in the population. It shows how distant an observation is from the distribution center. Therefore, if the standard deviation has a great value, it tells that the data is very spread out, while a low standard deviation shows that the data has a small variability. The variance is also a way of verifying the vary between the points of the sample and the mean. Its formula is given by the standard deviation squared (s2). It measures the deviation of the variable from its mean value, which is the standard deviation squared with

$$s^2 = \frac{\sum_{i=1}^{n} X_i - \overline{X}}{N - 1} \tag{12.2}$$

where X_i is the value in the data that refers to the point i, X is the mean of the data and N is the number of the data points in the population.

12.3.2 Covariance (Cov) and Covariance Matrix (Σ)

The standard deviation and the variance are technics that can analyze the characteristics of the attributes of the population's sample only in one dimension, which means that it cannot check the relation between two or more attributes of the sample, however, many times can be interesting to check the influence that they have on each other. For this task, a good solution is calculating the covariance between them. The covariance is measured always in two dimensions, and it is given by

$$cov(X, Y) = \frac{\sum_{i=1}^{n} (X_i - \overline{X})(Y_i - \overline{Y})}{N - 1} \tag{12.3}$$

where X_i is the value in the data that refers to the point i in the attribute X, X is the mean of the data in the attribute X, N is the number of the data points in the population, Y_i is the value in the data that refers to the point i in the attribute Y, Y is the mean of the data in the attribute Y and $co(X,Y)$ is the representation of the covariance between X and Y. If the result is a negative covariance, it means that when one value increases the other decreases. If the covariance is positive, it means that the values of both attributes increase or decrease in a direct proportion. In the case that the result is equal to zero, the interpretation is that the attributes have no relation between them.

Covariance shows if there is a relation between two dimensions, if there are more than two dimensions in one data set, the covariation matrix can be used. The covariation matrix is given by

$$C^{xnx} = (c_{i,j}, c_{i,j} = cov\big(Dim_i, Dim_j\big)) \tag{12.4}$$

From this equation, considering a hypothetical dataset with the dimensions (x, y, z), the possibilities of covariance analyses would be $co(x,y)$, $cov(x,z)$, $cov(y,z)$, and the covariances between each dimension and itself. Therefore, in this hypothetical case, the covariance matrix is given by

$$\Sigma = \begin{pmatrix} cov(x, x) & cov(x, y) & cov(x, z) \\ cov(y, x) & cov(y, y) & cov(y, z) \\ cov(z, x) & cov(z, y) & cov(z, z) \end{pmatrix} \tag{12.5}$$

Calculating the eigenvalues and eigenvectors is the way to solve the covariance matrix (Σ) as shown in Eq. (12.6). Eigenvalues are scalar values and eigenvectors are non-zero vectors, they represent the principal components explained in sequence.

$$V\Sigma = \lambda V \tag{12.6}$$

12.3.3 Calculating of Principal Component Analysis

The principal components (PCs) correspond to the direction of the maximum variance. They are orthonormal and uncorrelated. The PCA space corresponds to n PCs (Tharwat 2016). The first PC represents the direction of the maximum variance of the data (which is the eigenvector with the highest eigenvalue), the second one represents the second largest variance in the data's direction (which is the eigenvector with the second-highest eigenvalue) and so on.

The eigenvectors are ordered considering the eigenvalue (highest to lowest). The eigenvector with the highest eigenvalue will be the principal component of e analysis, and from the order don before, eigenvectors with the lowest eigenvalues can be eliminated without concern for a loss on the data set. With the eigenvectors selected, a feature vector can be done, and a matrix is formed with all of them in the columns given by

$$FeatureVector = (eigen_1, eigen_2, eingen_3, \ldots, eigen_n) \tag{12.7}$$

For good feature extraction and the decision of how many principal components to use, a bar plot can be done, it helps to graphically analyze the PCs and decide which ones are the important ones, how many are needed to represent the biggest variance on the data.

In this case, in both examples the PCA1 and PCA2 would be used, the other ones do not contain much valuable information and can be discarded. After those previous steps, the new data set will be the product between the feature vector transposed and t data adjusted by the mean (transposed as well) given by

$$FinalData = (FeatureVector)^T (DataAdjusted)^T \tag{12.8}$$

These steps will give the output of the original data but in terms of the desired vectors. And now the data points are classified as a combination of the contributions from each of the lines.

12.4 Recurrent Neural Network

Many of the advanced artificial intelligence architectures today are inspired by Recurrent neural networks (RNNs). RNN are a special class of Artificial Neural Networks characterized by internal self-connections for feedback, unlike a traditional feedforward neural network (Bianchi et al. 2017). This feedback loop permits the RNN to model the effects of the earlier parts of the sequence on the later part of the sequence, which is a relevant aspect when it comes to modelling sequences (Hiriyannaiah et al. 2020).

RNN uses an internal state to perform a task (Reimers and Requena-Mesa 2020). Since the new internal state is calculated from the old internal state and the input, it can be understood as one part of the output of the neural network. A RNN presents multiple architectures such as Integer-only Recurrent Neural Network (iRNN); np-Recurrent Neural Network (np-RNN), Long Short Term Memor (LSTM) and Convolutional Neural Network (CNN).

LSTM is very used with short- and long-term dependencies in data. LSTM tries to solve the vanishing gradient problem by not imposing any bias towards recent observations, but it keeps constant error flowing back through time (Reimers and Requena-Mesa 2020). LSTM has been employed in numerous sequence learning applications, especially in the field of classification. an LSTM cell is composed of 5 different nonlinear components, interacting with each other in a particular way. The internal state of a cell is modified by the LSTM only through linear interaction. To control the behavior of each gate, a set of parameters are trained with gradient descent, to solve a target task. Equation (12.9) presents the LSTM modelling (Bianchi et al. 2017) with

$$\begin{aligned}
&forgetgate : \sigma_f[t] = \sigma(W_f x[t] + R_f y[t-1] + b_f,\\
&candidatestate : \tilde{h}[t] = g_1(W_h x[t] + R_h y[t-1] + b_h,\\
&updatestate : \sigma_u[t] = \sigma(W_u x[t] + R_u y[t-1] + b_u,\\
&cellstate : h[t] = \sigma_u[t] \odot \tilde{h}[t] + \sigma_f[t] \odot h[t-1],\\
&outputgate : \sigma_o[t] = \sigma(W_o x[t] + R_o y[t-1] + b_o,\\
&output : y[t] = \sigma_o[t] \odot g_2(h[t])
\end{aligned} \tag{12.9}$$

where $x[t]$ is the input vector at time t. W_f, W_h, W_u, $and W_o$ are rectangular weight matrices, that are applied to the input of the LSTM cell.R_f, R_h, R_u, and R_o are square matrices that define the weights of the recurrent connections, while b_f, b_h, b_u, and b_o are bias vectors. The function $\sigma(\cdot)$ is a sigmoid 2, while $g1(\cdot)$ and $g2(\cdot)$ are pointwise non-linear activation functions, usually implemented as hyperbolic tangents that squash the values in $[-1, 1]$. Finally, $\odot$ is the entry wise multiplication between two vectors (Hadamard product).

12.5 PCA + LSTM-RNN Approach to Control a Prosthetic Hand Based on EEG

As presented in Sect. 12.3, PCA is a technique that has the goal of finding the space that better represents the direction of the maximum variance of the data. In this research, PCA is important since EEG signals are acquired in many channels, and some of them can be not relevant for studying and/or may increase the noise in the dataset. PCA reduces the dimension of the dataset using feature extraction, maintaining just the relevant information for a posterior analysis or classification.

After the PCA, it is necessary to classify the dataset to define the movement which the user intends to carry out. LSTM is an architecture of the neural of RNN that “remembers” the values in arbitrary intervals, and it is adequate to classify temporal series with non-known interval’s durations (Lin et al. 2021) that is the case of EEG signals. In this way, this work is going to use an LSTM architecture for classifying the dataset.

Based on this context, a PCA + LSTM-RNN approach to control a prosthetic hand based on EEG was proposed in Fig. 12.2. The approach is divided into four

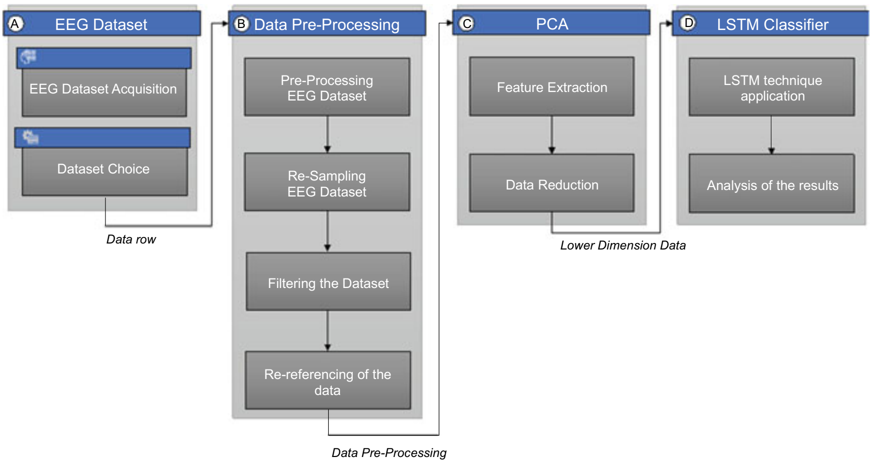

Fig. 12.2 PCA + LSTM-RNN approach to control a prosthetic hand

sections: EEG Dataset Acquisition (Detail "A"), Data Pre-Processing (Detail "B"), PCA (Detail "C"), LSTM Classifier (Detail "D").

In Fig. 12.2, the beginning of the process (Detail "A") can be seen where the data must be acquired through an already existent EEG database. The EEG database must go to the preprocessing part (Detail "B") where the sampling rate is adjusted, and the data is filtered and re-referenced. After this step, the PCA method (Detail "C") is applied, where the features will be extracted, and the data dimensions reduced. In the last part, an LSTM-RNN classifier (Detail "D") was applied and compared with other classifiers to verify the performance and accuracy to understand what kind of movement is necessary to carry out in a prosthetic hand.

12.5.1 Electroencephalographic Signals Database

In the last decades, many works, and research have been developed in the EEG and brain-computer interface field, as discussed in Sect. 12.2. For developing those studies, normally EEG signals were acquired from commercial devices, or other types of devices developed for this finality (Badawy and Alfred 2020; Vaskov and Chestek 2021).

Many of those datasets previously used for research or other applications are available online. On the internet and in related researches, EEG databases can be found, such as motor-imagery (Al-Saegh et al. 2021), emotion-recognition (Gannouni et al. 2021), error-related potentials (Keyl et al. 2019), visual-evoked potentials (Salelkar and Ray 2020), event-related potentials (Kropotov 2016), resting state (Corchs et al. 2019), EEG signals based in the subject's eye-blink (Sovierzoski et al. 2008) and so on.

The purpose of this work is to analyze the EEG signals and checking the possibility of them being the input of a robotic hand's control. Therefore, it is not necessary to acquire a new dataset of EEG and an online dataset is going to be selected. This option will let this study focus on the data processing and analysis, not carrying, in this first moment, for the data acquisition itself.

12.5.2 Data Preprocessing

The EEG recorded is called raw data. This data comes without any filtering or treatment. For the analysis that is going to be done in the next steps, it may be transformed into a format that is better to analyze and work with, this transformation step is called preprocessing.

The signals obtained from EEG are not only significant data, but the spatial information of the brain activity may also have got lost and they can be contaminated by muscle movement or blinking. Additionally, some noise in the data may obscure some weak EEG signals. Irrelevant activity is mixed with relevant activity and more possible problems can contaminate the data. To send a better dataset to the next steps some filtering techniques must be applied.

First, changing the sampling rate of the data is necessary to save the memory and the disk storage. Also, a good data sampling must be selected in this step for the processing time. The EEG recorded data comes in many different frequencies, therefore, many kinds of waves (alpha, beta, theta, and delta). The type of wave that better suits the project is going to be chosen, from that, to work only with the desired ones and a bandpass filter shall be applied.

In EEG a reference electrode must be chosen, the voltage of the other electrodes will be relative to the voltage of the reference one. If the reference electrode was not well chosen, it will contaminate the data, so a re-reference must be done in the preprocessing to send better data to the next steps. With these techniques, it is expected that the preprocessing part of the project will be good if an analysis shows that it not being enough, more techniques can be studied and applied.

12.5.3 PCA Application

After the application of the preprocessing method, the data is already improved for the final user. However, there is still some noise that can interpret this data as a difficult task. This noise must be removed. The feature meaningful features need to be extracted, between many techniques that could be used, such as Common Spatial Patterns, Wavelet Transform, Independent Components, and PCA. The PCA was chosen for two main reasons: (i) it is proven to be a relevant feature extraction method from many researches including (Lekshmi et al. 2014) (Subasi and Ismail

Gursoy 2010) and (Saint-Elme et al. 2017), and (ii) the interest of the author for this specific method.

PCA is a wide method used for pattern recognition and feature extraction (Lekshmi et al. 2014). It can be used in cases where exist a big dimension dataset with some variable redundancy can be reduced to a smaller number of principal components. In the case of this study, the redundant data can be eliminated using PCA. After applying the PCA method, it will be possible to analyze the data in a dimension reduced space, which will facilitate the classification of the variables in the next method.

12.5.4 Data Classification

After the signal is acquired, preprocessed and the features are extracted, the data must be classified before going to the application as an input.

Through the vast area of machine learning and deep learning, the chosen method for classifying the dataset in this project is one type of neural network called RNN. It is a type of neural network where the output of previous steps is fed as an input to the current step. In this model, the neural network allows the information to persist, a recurrent neural network can be thought of as a stack of multiple normal neural networks passing the information to one another (Silva et al. 2018; Modaresi et al. 2018; Lin et al. 2021). An illustration of an RNN can be seen in Fig. 12.3.

Where *A* is the hidden layers of the RNN, *X* the inputs, and *h* the outputs. LSTM is an architecture of the neural of RNN that "remembers" the values in arbitrary intervals, and it is adequate to classify temporal series with non-known interval's durations. To compare LSTM's accuracy with other methods, some Machines Learn methods were chosen, methods as Linear Discriminant Analysis (LDA), Random Forest, AdaBoost (Adaptive Boosting), and Support Vector Machines (SVM).

LDA is a classifier with a linear decision boundary, the classifier is generated by fitting class conditional densities to the data using Bayes's rule. Random Forest

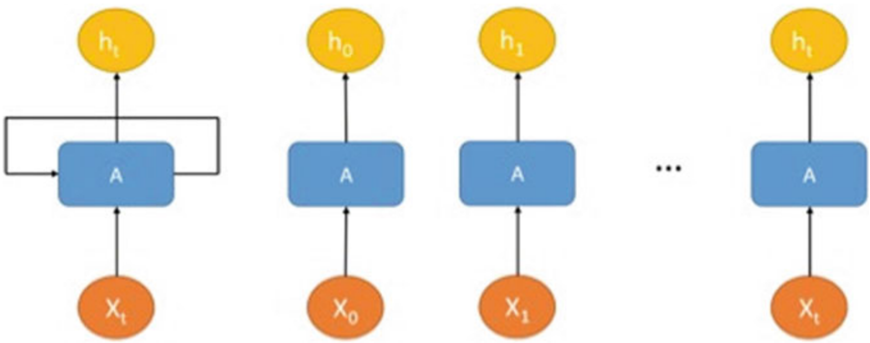

Fig. 12.3 Representation of an RNN

classifier is a machine learning method that fits several decision trees classifiers on various sub-samples of the dataset. Adaboost classifier is a method that works by fitting a classifier on the original dataset and, after that, fitting additional copies of the classifier on the same dataset but it fits in where the weights of the incorrectly classified instances are adjusted. SVM is a set of supervised learning methods that can be used for classifying and regression.

12.6 Application of the Proposed Approach in an Experimental Case

12.6.1 EEG Dataset Selection

The dataset was chosen from the available data from BCI Competition IV. It is a motor imagery dataset that contains 59 EEG channels recorded in around 2,000,000 frames. It contains the values of each EEG signal through time, the voltage between the EEG channel and the ground electrode. The recordings were done for 7 subjects. It is a raw dataset with a sampling rate of 1000 Hz. Firstly, it was in a MATLAB format (.mat), using MATLAB computational environment it was converted to CVS format.

For each one of the subjects, two classes of motor imagery were selected. The options were: left hand, right hand, left foot, and right foot. Therefore, there were three options to be classified (rest, class number one, and class number two). With this way of classifying, it has the same number of classes as the most common way of control a robotic hand, once EEG also considers three classes of control (a contraction of muscle number one, contraction of muscle number two and rest).

12.6.2 Data Pre-processing Applied in the Experimental Case

Although it has been previously band-pass filtered between 0.5 and 100 Hz the digitalized to 1000 Hz, the dataset still provides noise and some not useful information. Figure 12.4 shows the raw data from the EEG acquisition. In this figure, just 20 channels of 59 channels are showed to illustrate the solution. Additionally, as can be seen in Fig. 12.4, it is full of noise and does not represent the desired data for analysis.

The study of EEG signals requires a reference-independent measure of the potential field (Junghöfer 1999). Electrode recordings measure the electrical difference between two points and express them in micro-Volts. One of those two points is the ground electrode, an electrode connected to the ground circuit of the amplifier. Therefore, any electrode signal that can be displayed have as a reference to the so-called ground electrode, this electrode can pick up noise that does not influence the

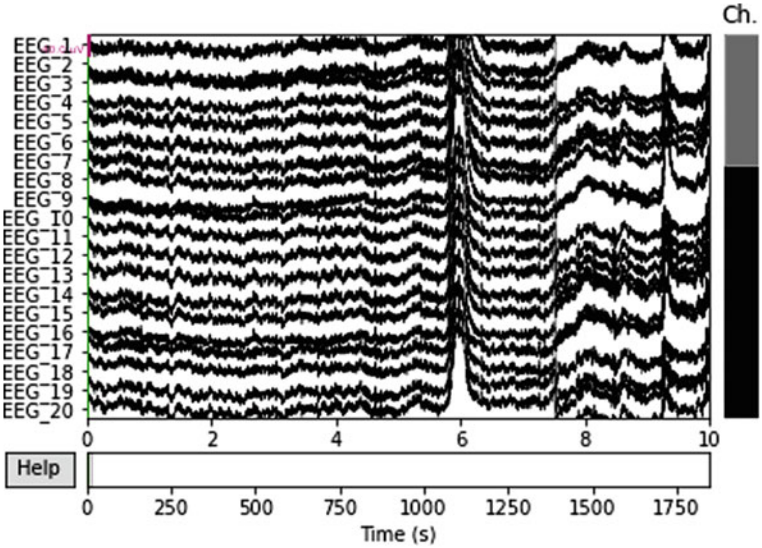

Fig. 12.4 EEG raw data from the 20 more relevant channels

other electrodes (Leuchs 2019). One solution for cleaning the signals from this noise is re-referencing the data.

There are different ways of re-referencing EEG data, and it influences the amplitude of each channel and time point. It redefines the level of the zero voltage and makes all the other EEG signals and channels are related to it (Leuchs 2019).

Average reference is the result of the subtraction of all the EEG signals and the average of all EEG signals through time. It was used here to eliminate part of the noise and can be seen in Fig. 12.5. The figure is the same data as the previous image, re-referenced, with less noise. When using the average re-reference, the amplitudes are overall reduced, and each channel contributes equally to the new reference.

Motor imagery has its power in the alpha (8–12 Hz) and beta (13–30 Hz) frequency bands (Di Nota 2017). To obtain this band a band-pass filter was applied between 7 and 30 Hz. The reduction from the same channels displayed in Figs. 12.4 and 12.5 can be checked in Fig. 12.6, already band-pass filtered.

12.6.3 PCA Application in the Experimental Case

With 59 electrodes placed on the subject's scalp, some not valuable information for classification can also be recorded. This step aims to reduce the number of EEG channels that are going to be analyzed and classified by the neural network.

For accomplishing this step, a matrix was made for each subject with the dimension (frames x channels). For applying PCA, the data needs to be standardized. It

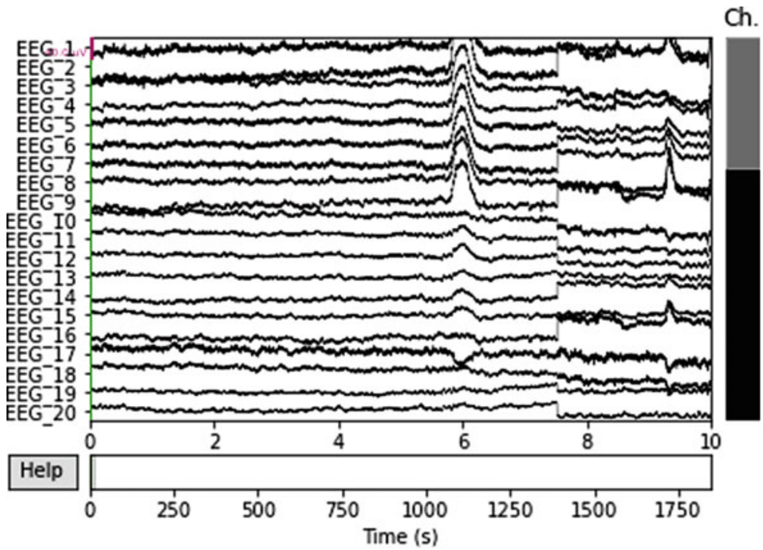

Fig. 12.5 Re-referenced data of EEG raw data

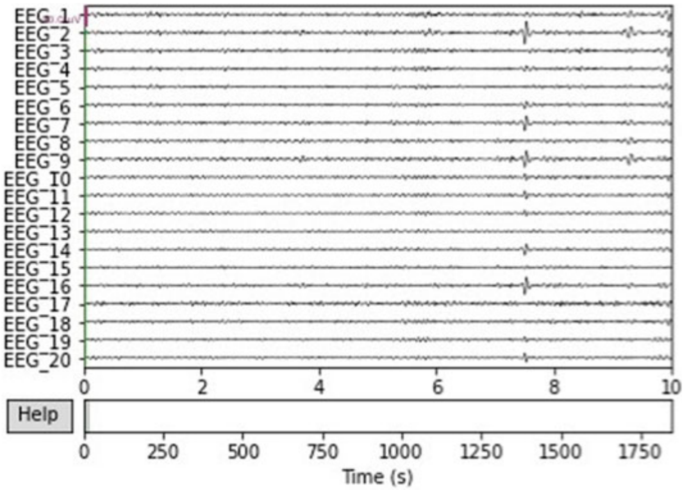

Fig. 12.6 EEG signal filtered (7–30 Hz band-pass filtered)

is done by applying Eq. (12.1) to the dataset. After obtaining the standardized data, a covariance matrix is calculated using Eq. (12.5) for every possible relationship in the dataset. From this covariance matrix, the eigenvectors and eigenvalues were extracted. The eigenvectors were organized in a decreasing form in a matrix according

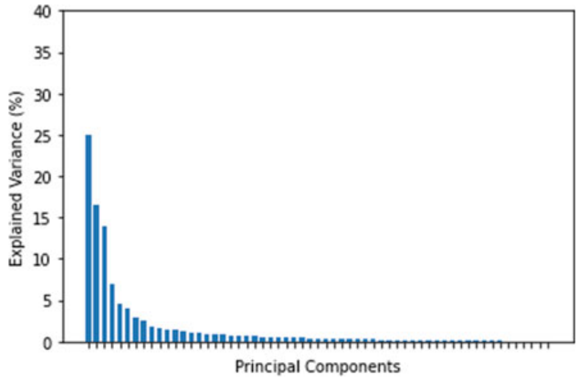

Fig. 12.7 Explained variance of the data

to the value of its respective eigenvalue. These eigenvectors are the principal components. They are the components that explain the biggest part of the variance in the dataset.

For each subject's EEG data that was going to be analyzed, it was verified how many principal components were needed to explain the biggest part of the data, in this case, the number of principal components needed to explain at least 75% of the data's variance. Therefore, the number of channels used as an input for the model was equal to the number of necessary channels to explain the desired percentage of the variance. Based on this, Fig. 12.7 shows a bar plot of all the principal components of the total data. Each of the components has its importance on the data variance and they are ordered by the highest to the lowest considering their percentage on the representativeness of the data's total variance.

As can be observed in Fig. 12.7, some components contribute to a little percentage of the overall variance. Those principal components can be discarded as they would not have a big influence on the final data analysis. With the usage of only 10 of the first PCs together, it is possible to explain 79.67% of the data, as shown in Fig. 12.8. Therefore, the dimension of the dataset could be reduced for those 10 principal components that explain the variance of the biggest part of the data. Instead of analyzing 59 EEG channels, only 10 PCs are going to be analyzed.

Once the dimensionality is reduced by selecting the meaningful principal components that explain the biggest part of the data's variance, the chosen principal components are used in the classification step. Now, with less information to analyze, a more accurate analysis can be done with less computational time.

12.6.4 Data Classification with LSTM Classifier

In this part, the data is classified and tested to check the accuracy of the approach. The PCs were chosen to be used as an input for the RNN classification method. LSTM is an RNN used for time series, and, for its design, the hyperparameters of the

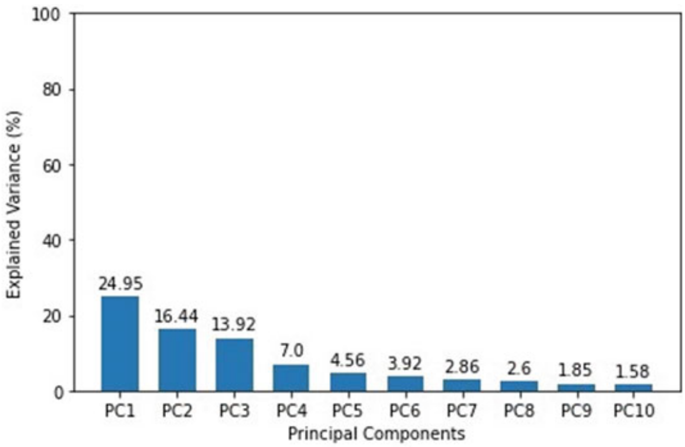

Fig. 12.8 Explained variance of the selected principal components

RNN need to be selected. The number of layers, the number of neurons per layer, the chosen optimizer, the batch size used for the training, and the number of epochs is the parameters to be considered and tested to have a more tuned LSTM. For obtaining better accuracy, different configurations were tested.

A first run was done for choosing the number of layers that would better fit the problem. Different LSTM configurations were tried with a batch size of 32 and 5 epochs as can be seen in Table 12.1. Firstly, a configuration of 20 neurons per layer, using Adam (Adaptive Moment Estimation) optimizer was performed 3 times changing the number of layers each time. It was checked that the LSTM 1 outperformed the other 2 having an accuracy of 84.43% and a mean squared error of 0.11 while the LSTM 2 had an accuracy of 83.43 with a mean squared error of 0.11 and the worst perfume of this first trial was from the LSTM 3 that had an accuracy of 79.54% and a mean squared error of 0.14. With the results shown in Table 12.2,

Table 12.1 Configurations of the first test of LSTMs tuning according to the number of layers

LSTM	1	2	3
Number of layers	3	2	1
Number of neurons per layer	20	20	20
Optimizer	Adam	Adam	Adam
Drop out	0.2	0.2	0.2

Table 12.2 Accuracy and mean squared error from the first LSTM configurations for tuning

LSTM configuration	Accuracy (%)	Mean squared error
1	84.43	0.11
2	83.43	0.11
3	79.54	0.14

Table 12.3 Configuration of the second test of LSTMs tuning according to the number of layers

LSTM	4	5	6	7
Number of layers	1	1	1	1
Number of neurons per layer	1	10	20	30
Optimizer	Adam	Adam	Adam	Adam
Drop out	0.2	0.2	0.2	0.2

the second set of tests was done to find the number of neurons per layer that would be the best fit for the LSTM.

In the second run for finding the best configuration, the aim was to find the number of neurons per layer. They were tested with the same batch size and the same epoch that before, the number of layers equal to one for saving computational time, Adam optimizer was used and a drop out of 0.2. As is shown in Table 12.3, the number of neurons per layer tested were 1, 10, 20, and 30, more than this would take too much computational time.

The second run for tuning the LSTM checked that the highest number of neurons obtained the best accuracy. The LSTM 7 outperformed the LSTMs 4, 5, and 6 with an accuracy of 85.27% while the others achieved the accuracies of 66.67%, 73.67%, and 79.74%, respectively. The mean squared error calculated from the LSTM performance was also better for the last one of them. With a mean squared error of 0.10, the LSTM with the setup #7 had a better result than the other that had the root mean squared errors higher than 0.14 as shown in Table 12.4.

The last run was done to find the number of epochs that best fits the problem. Three tests were done with 1 layer, one neuron per layer, Adam optimizer, and 5 training epochs, using the batch sizes of 32, 128, and 1024, as can be seen in Table 12.5. The results are in Table 12.6.

Table 12.4 Accuracy and mean squared error resulting from the second LSTM configurations for tuning

LSTM configuration	Accuracy (%)	Mean squared error
4	66.67	0.20
5	73.67	0.17
6	79.74	0.14
7	85.27	0.10

Table 12.5 Configurations of the third test of LSTMs tuning according to the number of layers

LSTM	8	9	10
Number of layers	1	1	1
Number of neurons per layer	1	1	1
Optimizer	Adam	Adam	Adam
Drop out	0.2	0.2	0.2
Batch size	32	128	1024

Table 12.6 Accuracy and mean squared error resulting from the third LSTM configurations for tuning

LSTM configuration	Accuracy (%)	Mean squared error
8	66.67	0.20
9	66.70	0.20
10	66.66	0.20

With the results from Table 12.6, the LSTM chosen configuration was an LSTM with 3 layers, 30 neurons per layer, using Adam optimizer a batch size of 128. Another approach was done for classifying the data. After preprocessing the data where 473 epochs were extracted from the dataset. The time point where the subject started one movement, or another was detected and after this time point, 1,000 frames were stored. From this new dataset, 7 features were extracted from each one of the epochs, features as mean, variance, skewness, kurtosis, peak-to-pick distance, and maximum peak-to-peak distance. And those filters were used to classify each epoch. The same LSTM previously found was used in this method.

To sum up, two methods were done, one directly analyzing the continuous signal (Method 1) and another one extracting 8 features from the signal and analyzing the feature vector made from it (Method 2).

12.6.5 The Results of the PCA + LSTM-RNN Approach Application in an Experimental Case

From the tests previously done for choosing the LSTM configuration, in Sect. 12.6.4, an LSTM with 3 layers, 30 neurons per layer, Adam optimizer, 30 epochs and a batch size of 128 was chosen to be the classifier to solve the problem of this research, as shown on Table 12.7.

This configuration was validated with fivefold cross-validation and showed a mean accuracy of 94.41% ± 0.23%. LSTM has its focus on predictions, for using it as a classifier, the numbers it predicted need to be rounded. Once was done, the method's accuracy decreased a bit, and the result was accuracy of 91.05%.

With the algorithm already trained, the model was used to classify a dataset with 370,015 frames and was used to classify each one of those frames, the chosen

Table 12.7 Configuration of the chosen LSTM

Number of layers	3
Drop out	0.2
Neurons per layer	20
Optimizer	Adam
Epochs	30
Batch Size	128

Table 12.8 LSTM Confusion matrix

88,883	6955	1412
9065	166,336	4123
4392	7146	81,703

Table 12.9 Accuracy results from the classification

Machine learning method	Accuracy (%)
LSTM	91.05
SVM	48.21
Random forest	48.46
Adaboost	51.05

configuration was able to classify the dataset with an accuracy of 91.05% of the re-referenced dataset after the principal components had been applied. The confusion matrix shows in its principal diagonal the numbers of the right classifications of the data, it shows that in 336,922 frames, the algorithm was classified correctly (Table 12.8).

To do the comparison of the LSTM accuracy, some machine learning classifiers were used. The related works (Jia et al. 2020; Al-Saegh et al. 2021; Rajapriya et al. 2021; Lin et al. 2021) suggest the methods such as SVM, Random Forest, Adaboost. With the chosen approach, LSTM is the best choice for classifying the data. It outperformed the other methods classifying the data while all the other methods, had their accuracies below 52% (Table 12.9).

For the second approach chosen, where the 7 features were extracted from each one of the epochs after the data had been preprocessed and the dimension had been reduced, the classifiers have shown a low accuracy for classifying the three different classes. LDA showed an accuracy of 53.68%, Random Forest was the best one of the machine learning models that showed an accuracy of 57.89%, AdaBoost had an accuracy of 54.73% and SVM, being the second-best one of the machine learning models, showed an accuracy of 56.84%. With the same approach, LSTM had an accuracy of 63.68% outperforming the other methods (Table 12.10).

Table 12.10 Comparison of the two methods used

Method 1		Method 2	
LSTM	91.05%	LSTM	63.68%
SVM	48.21%	SVM	56.84%
Random forest	48.46%	Random forest	57.89%
Adaboost	51.05%	Adaboost	54.73%
LDA	48.40%	LDA	53.68%

12.7 Conclusion and Future Research

This chapter explored an approach which it integrates PCA and LSTM-RNN approaches to evaluate the performance to control a prosthetic hand based on the signals generated from the user's intention of movement recorded from EEG. The approach proposed in composed of 4 parts: (i) EEG Dataset Acquisition, (ii) Data Pre-Processing, (iii) PCA, and (iv) LSTM Classifier.

Principal component analysis has appeared to be a good approach for this problem, reducing the dimension to be analyzed for only 10 principal components, it performed a dimensionality reduction of 83.05% of the total number of channels to be analyzed and allowed the classification of more meaningful data. LSTM has shown promising results with a mean accuracy of 91.05% on method 1 and 63.08% on method 2, outperforming all the other methods.

The objective of designing a suitable BCI application was not totally accomplished using dimensionality reduction with PCA combined and LSTM-RNN. However, with the results is possible to conclude that the approach of using principal component analysis with a recurrent neural network is an accurate approach for classifying the data. An EEG dataset was well classified in three classes (same number of classes used in a myoelectric hand control), therefore, it is possible to use electroencephalography on the robotic hand's control. On the other hand, for a BCI application, where the processing needs to be done online, the method chosen in this project may not fit its due to its need for a time series to work. BCI applications need real-time data processing, thus, a classical machine learning approach could be a better choice, a more tuned machine learning classifier and a different approach of data reduction could make a better performance.

For the future perspectives for this project would be trying to outperform the LSTM classification with a machine learning approach. Once a promising result of a machine learning approach is found, develop a BCI system, and applied on the control of a robotic hand for checking its real accuracy.

Acknowledgements The authors would like to thank the Pontifical Catholic University of Parana (PUCPR) for financial support to the development of this research.

References

Al-Saegh A, Dawwd SA, Abdul-Jabbar JM (2021) Deep learning for motor imagery EEG-based classification: a review. Biomed Signal Process Control 63:102172. https://doi.org/10.1016/j.bspc.2020.102172

Bäckström M, Tidare J (2016) A brain-actuated robot controller for intuitive and reliable manoeuvring. Master thesis, Mälardalen University

Badawy A, Alfred R (2020) Myoelectric prosthetic hand with a proprioceptive feedback system. J King Saud Univ Eng Sci 32(6):388–395. https://doi.org/10.1016/j.jksues.2019.05.002

Bianchi FM, Maiorino E, Kampffmeyer MC, Rizzi A, Jenssen R (2017) Recurrent neural network architectures. In: Bianchi FM, Maiorino E, Kampffmeyer MC, Rizzi A, Jenssen R (eds) Recurrent

neural networks for short-term load forecasting: an overview and comparative analysis. Springer International Publishing, Cham, pp 23–29
Canciglieri MB, Leite AFCS de M, Szejka AL, Júnior OC (2019) An approach for dental prosthesis design and manufacturing through rapid manufacturing technologies. Int J Comput Integr Manuf, 0(0):1–16. https://doi.org/10.1080/0951192X.2019.1636410
Corchs S, Chioma G, Dondi R, Gasparini F, Manzoni S, Markowska-Kaczmar U, Mauri G, Zoppis I, Morreale A (2019) Computational methods for resting-state EEG of patients with disorders of consciousness. Front Neurosci 13:807. https://doi.org/10.3389/fnins.2019.00807
Cordella F, Ciancio AL, Sacchetti R, Davalli A, Cutti AG, Guglielmelli E, Zollo L (2016) Literature review on needs of upper limb prosthesis users. Front Neurosci 10:209. https://doi.org/10.3389/fnins.2016.00209
dos Santos VP, Silveira DR, Caffaro RA (2006) Risk factors for primary major amputation in diabetic patients. Sao Paulo Med J 124:66–70. https://doi.org/10.1590/S1516-31802006000200004
Eisenberg GD, Fyvie KGHM, Mohamed A-K (2017) Real-time segmentation and feature extraction of electromyography: towards control of a prosthetic hand. IFAC-Pap 50(2):151–156. https://doi.org/10.1016/j.ifacol.2017.12.028
Gannouni S, Aledaily A, Belwafi K, Aboalsamh H (2021) Emotion detection using electroencephalography signals and a zero-time windowing-based epoch estimation and relevant electrode identification. Sci Rep 11(1):7071. https://doi.org/10.1038/s41598-021-86345-5
Geiss LS, Li Y, Hora I, Albright A, Rolka D, Gregg EW (2019) Resurgence of diabetes-related nontraumatic lower-extremity amputation in the young and middle-aged adult U.S. population. Diabetes Care 42(1):50–54. https://doi.org/10.2337/dc18-1380
Graham EM, Hendrycks R, Baschuk CM, Atkins DJ, Keizer L, Duncan CM, Mendenhall SD (2021) Restoring form and function to the partial hand amputee: prosthetic options from the fingertip to the palm. Hand Clin 37(1):167–187. https://doi.org/10.1016/j.hcl.2020.09.013
Graimann B, Allison B, Pfurtscheller G (eds) (2010) Brain-computer interfaces: revolutionizing human-computer interaction. Springer, Berlin Heidelberg
Hiriyannaiah S, Srinivas AMD, Shetty GK, Siddesh GM, Srinivasa KG (2020) Chapter 4—a computationally intelligent agent for detecting fake news using generative adversarial networks. In: Bhattacharyya S, Snášel V, Gupta D, Khanna A (eds) Hybrid computational intelligence. Academic Press, pp 69–96
Hoffstad O, Mitra N, Walsh J, Margolis DJ (2015) Diabetes, lower-extremity amputation, and death. Diabetes Care 38(10):1852–1857. https://doi.org/10.2337/dc15-0536
Iftikhar M, Khan SA, Hassan A (2018) A survey of deep learning and traditional approaches for EEG signal processing and classification. In: 2018 IEEE 9th annual information technology, electronics and mobile communication conference (IEMCON). pp 395–400
Jia G, Lam H-K, Liao J, Wang R (2020) Classification of electromyographic hand gesture signals using machine learning techniques. Neurocomputing 401:236–248. https://doi.org/10.1016/j.neucom.2020.03.009
Kashef SR, Amini S, Akbarzadeh A (2020) Robotic hand: a review on linkage-driven finger mechanisms of prosthetic hands and evaluation of the performance criteria. Mech Mach Theory 145:103677. https://doi.org/10.1016/j.mechmachtheory.2019.103677
Keyl P, Schneiders M, Schuld C, Franz S, Hommelsen M, Weidner N, Rupp R (2019) Differences in characteristics of error-related potentials between individuals with spinal cord injury and age- and sex-matched able-bodied controls. Front Neurol 9:1192. https://doi.org/10.3389/fneur.2018.01192
Kropotov JD (2016) Chapter 1.6—event-related potentials. In: Kropotov JD (ed) Functional neuromarkers for psychiatry. Academic Press, San Diego, pp 59–78
Kumar DK, Jelfs B, Sui X, Arjunana SP (2019) Prosthetic hand control: a multidisciplinary review to identify strengths, shortcomings, and the future. Biomed Signal Process Control 53:101588. https://doi.org/10.1016/j.bspc.2019.101588

Laclé A, Valero-Juan LF (2012) Diabetes-related lower-extremity amputation incidence and risk factors: a prospective seven-year study in Costa Rica. Rev Panam Salud Pública 32:192–198. https://doi.org/10.1590/S1020-49892012000900004
Lekshmi SS, Selvam V, Pallikonda Rajasekaran M (2014) EEG signal classification using principal component analysis and wavelet transform with neural network. IEEE, Melmaruvathur, India, pp 687–690
Li X, Samuel OW, Zhang X, Wang H, Fang P, Li G (2017) A motion-classification strategy based on sEMG-EEG signal combination for upper-limb amputees. J NeuroEngineering Rehabil 14(1):2. https://doi.org/10.1186/s12984-016-0212-z
Lin L, Li M, Ma L, Baziar A, Ali ZM (2021) Hybrid RNN-LSTM deep learning model applied to a fuzzy based wind turbine data uncertainty quantization method. Ad Hoc Netw 123:102658. https://doi.org/10.1016/j.adhoc.2021.102658
Machado S, Cunha M, Velasques B, Minc D, Bastos VH, Budde H, Cagy M, Piedade R, Ribeiro P (2009) Interface cérebro-computador: novas perspectivas para a reabilitação. Rev Neurociências 17(4):329–335. https://doi.org/10.34024/rnc.2009.v17.8525
Modaresi F, Araghinejad S, Ebrahimi K (2018) A comparative assessment of artificial neural network, generalized regression neural network, least-square support vector regression, and K-nearest neighbor regression for monthly streamflow forecasting in linear and nonlinear conditions. Water Resour Manag 32(1):243–258. https://doi.org/10.1007/s11269-017-1807-2
Nunez PL, Srinivasan R (2006) Electric fields of the brain: the neurophysics of EEG, 2nd edn. Oxford University Press, New York
Nuwer MR, Coutin-Churchman P (2014) Brain mapping and quantitative electroencephalogram. In: Aminoff MJ, Daroff RB (eds) Encyclopedia of the neurological sciences, 2nd edn. Academic Press, Oxford, pp 499–504
Rajapriya R, Rajeswari K, Thiruvengadam SJ (2021) Deep learning and machine learning techniques to improve hand movement classification in myoelectric control system. Biocybern Biomed Eng 41(2):554–571. https://doi.org/10.1016/j.bbe.2021.03.006
Reimers C, Requena-Mesa C (2020) Chapter 13—deep learning—an opportunity and a challenge for geo- and astrophysics. In: Škoda P, Adam F (eds) Knowledge discovery in big data from astronomy and earth observation. Elsevier, pp 251–265
Saint-Elme E, Larrier M, Kracinovich C, Renshaw D, Troy K, Popovic M (2017) Design of a biologically accurate prosthetic hand. In: 2017 International symposium on wearable robotics and rehabilitation (WeRob), pp 1–2
Salelkar S, Ray S (2020) Interaction between steady-state visually evoked potentials at nearby flicker frequencies. Sci Rep 10(1):5344. https://doi.org/10.1038/s41598-020-62180-y
Silva R, Rudek M, Szejka AL, Canciglieri Junior O (2018) Machine vision systems for industrial quality control inspections. In: Product lifecycle management to support industry 4.0. Springer Nature Switzerland, Turin, pp 631–641
Sovierzoski MA, Argoud FIM, de Azevedo FM (2008) Identifying eye blinks in EEG signal analysis. In: 2008 International conference on information technology and applications in biomedicine, pp 406–409
Srinivasan R, Nunez PL (2012) Electroencephalography. In: Ramachandran VS (ed) Encyclopedia of human behavior, 2nd edn. Academic Press, San Diego, pp 15–23
Subasi A, Ismail Gursoy M (2010) EEG signal classification using PCA, ICA, LDA and support vector machines. Expert Syst Appl 37(12):8659–8666. https://doi.org/10.1016/j.eswa.2010.06.065
Tharwat A (2016) Principal component analysis—a tutorial. Int J Appl Pattern Recognit 3(3):197–240. https://doi.org/10.1504/IJAPR.2016.079733
Vaskov AK, Chestek CA (2021) Brain-machine interfaces: lessons for prosthetic hand control. Hand Clin 37(3):391–399. https://doi.org/10.1016/j.hcl.2021.04.003
Yang D, Gu Y, Thakor NV, Liu H (2019) Improving the functionality, robustness, and adaptability of myoelectric control for dexterous motion restoration. Exp Brain Res 237(2):291–311. https://doi.org/10.1007/s00221-018-5441-x

Chapter 13
Maxillofacial Prostheses: Assistive Technology in Mutilated Facial Patients

Roberta T. Stramandinoli-Zanicotti, Paola F. Corso, and Maria Elizete Kunkel

13.1 Introduction

Amputation of a body part is a very difficult, delicate, and often unpredictable event. Physical loss has a major impact on life with a series of biopsychosocial changes that can interfere with the roles played by the personal, social, family, and professional fields. The emotional factor increases the resistance to accepting this loss making it more difficult for the individual to recover (Scorchio et al. 2018). The common emotions that arise after amputation are feelings of helplessness, self-strangeness, low self-esteem, loss of identity, anguish, meaninglessness, and motivation, capabilities, and limitations being experienced (Chini and Boemer 2007). The World Health Organization defines the quality of life not only as the absence of disease or illness but also as the individual's perception of their position in life, in the context of the culture and value system in which they live and concerning their goals, expectations, patterns, and concerns (Fleck et al. 2000).

The valued and monitored psychological factors for quality of life are resilience (personal mobilization to adapt to the new reality), acceptance of amputation, depression, and optimism. Psychosocial factors predisposing to quality of life include participation in social activities, working, studying, socializing with friends, associations, among others (Milioli and Vargas 2012). The amputation of any part of the body can lead to depression, performance anxiety and significantly altered relationships, body image and sexual wellbeing (Geertzen et al. 2009; Gallagher et al. 2019).

Facially mutilated individuals are those who have suffered any type of mutilation or amputation in the head and neck region, including anatomical structures such

R. T. Stramandinoli-Zanicotti (✉) · P. F. Corso
Reconstructive Facial Prosthesis Service of Trabalhador Hospital, Curitiba, PR, Brazil
e-mail: robertastramandinoli@yahoo.com.br

M. E. Kunkel
Institute of Science and Technology of Federal, University of São Paulo, São José Dos Campos, SP, Brazil

O. Canciglieri Junior and M. D. Trajanovic (eds.), *Personalized Orthopedics*,
https://doi.org/10.1007/978-3-030-98279-9_13

as ear, nose, eyes, eyelids, hard or soft palate, tongue, and other parts of the face. The etiologies can be congenital, traumatic, or due to diseases, with cancer being the main cause of amputation. Individuals with an absence of a facial structure have few options in 'displaying' their unusual face: covering the amputation site with bandages; carrying a prosthetic device that emulates the missing limb's looks and baring their amputation for others to see it (Yaron et al. 2018). During their rehabilitation trajectory, these individuals commonly receive a facial prosthesis that replaces the lost part. Although this device closely resembles the absent facial area, its artificiality remains (potentially) discernible. Some studies highlight the psychosocial issues associated with facial variance, for instance, depression, social anxiety, or avoidance behavior (Koster and Bergsma 1990; Rumsey and Harcourt 2004). The psychology of appearance offers very few empirical, qualitative investigations into the way facial variance comes into play in the daily life of affected individuals, as they encounter and interact with various others. The facial mutilated individuals need to be included as persons with disabilities so that their rights can be clarified and respected.

After cancer ablation surgery or traumatic amputation, if surgical reconstruction cannot completely restore the surgical defect site, the maxillofacial prosthesis plays an important role in rehabilitation. Maxillofacial prosthesis aims the anatomical, functional and aesthetic rehabilitation, through alloplastic substitutes, of missing or defective regions of the maxilla, mandible and face, such as surgical, traumatic, evolutionary sequelae, or due to congenital malformations or developmental disorders. They can also restore lost functions, although in some cases they are limited. The purpose of the prosthesis is to restore and maintain health and comfort, correct facial defects, appearance disorders, restore and correct speech, swallowing, and chewing functions (Sharma and Beumer 2006; Beumer et al. 2011).

The final maxillofacial prostheses (MP) are fabricated with biocompatible and soft material, such as medical-grade silicone, with high tear resistance and different shore. The MP is made in a personalized way according to the needs of each patient, respecting the mutilated area to be rehabilitated (Fig. 13.1). Although they can also restore lost functions, in some cases they have limited results. The MP can be fixed to the patient's skin with the aid of special glues or osseointegrated implants, with bar-clip systems or magnets. Although the use of implants associated with retention systems in extraoral rehabilitations has presented great advantages over the use of adhesives such as retention, support, and stability of the prosthesis, in addition to being easy to install and daily cleaning (Beumer et al. 2011), in head and neck cancer patients undergoing radiotherapy there is a risk of osteoradionecrosis. Research in animals and humans indicates that irradiated bone has a greater risk of failure and failure in osseointegration than non-irradiated bone (Stefan et al. 2009; Stramandinoli-Zanicotti et al. 2014).

Assistive Technology is based on the application of information and communication technology to meet daily needs and actively engage in everyday activities of persons with disabilities (Peraković et al. 2018). Maxillofacial prostheses are custom assistive technology devices that have benefited from industry 4.0 tools such

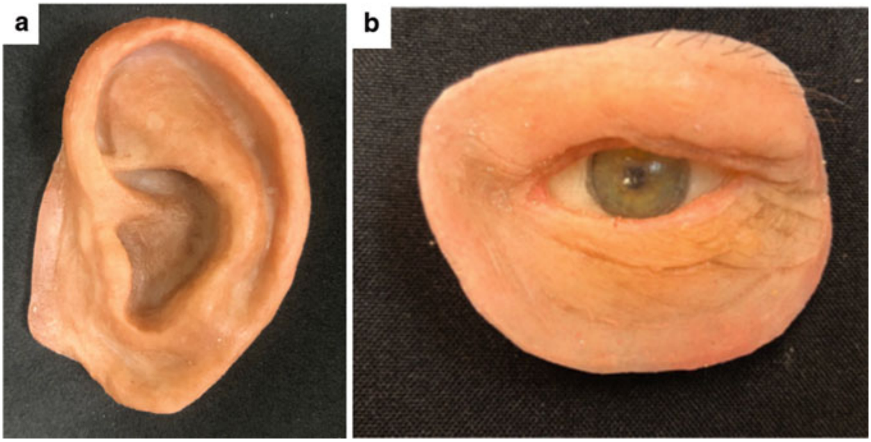

Fig. 13.1 Conventional maxillofacial prostheses: ear prosthesis (**a**) and oculus palpebral prosthesis (**b**)

as 3D scanning and additive manufacturing since the facial reconstruction treatment requires impressions of the entire face, including the defect area.

Additive manufacturing has gradually become an emerging and crucial technology in medicine. The application in healthcare provides many benefits such as better cost-effectiveness, increased productivity, and democratization of design and manufacturing. The literature highlights the use of resources and products made by 3D printing in several areas of Assistive Technology. Additive manufacturing can make objects of the most varied types and sizes, most often using low-cost material and based on a layer overlay system to create three-dimensional models. Using this technology, it is possible to reduce patient discomfort by increasing the accuracy of the directly manufactured maxillofacial prosthesis, without the need for intermediate wax and sculpting steps. The 3D technology optimizes the making of the prosthesis, enabling more favourable and predictable results. With the improvement of existing techniques and the use of additive manufacturing with new materials such as resins, silicones, biomaterials, and osseointegrated implants, the specialty has enabled the manufacture of more aesthetic, realistic, and biocompatible facial prostheses (Fig. 13.2).

In this book chapter, the role of assistive technology for facial patients will be addressed, focusing on additive manufacturing. Since the use of additive manufacturing is the final step in facial prosthesis production, it is necessary to understand all the steps that precede it. For this reason, the phases of image acquisition, segmentation, 3D modeling and printing will also be addressed in the example shown in Fig. 13.2.

Fig. 13.2 Workflow for additive manufacturing of facial prostheses

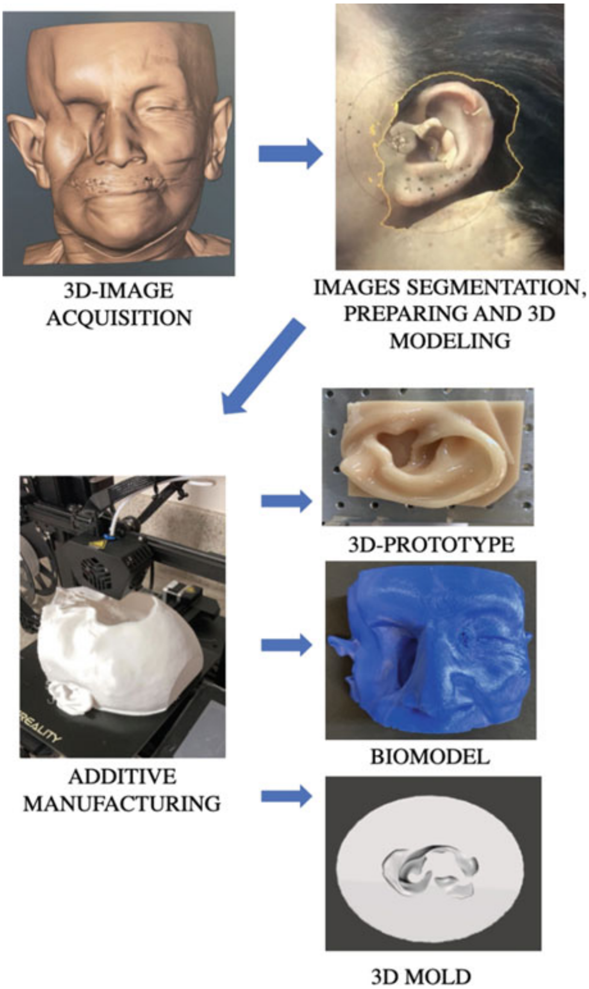

13.2 Images Acquisition

In the maxillofacial prostheses production workflow presented, first, the region of the face of the individual to be fitted needs to be scanned. All volumetric and spatial anatomical information must be provided from an image acquisition method. The structure of the scanned face is represented by a set of points arranged in the shape of a triangle, this mesh is used later to make the 3D modeling and printing of the structure. For the production of maxillofacial prostheses, the most commonly used methods are 3D reconstruction of medical images, 3D scanning and photogrammetry.

13.2.1 3D Reconstruction of Medical Images

This image acquisition method is the most used in the maxillofacial prostheses field. The data can be obtained by Magnetic Resonance Imaging (MRI), Cone Beam Computed Tomography (CBCT), or Multislice Computed Tomography (MSCT). The CBCT exam is the option with the lowest radiation dose and costs. It is the most used for dentistry because it allows a detailed view of the face in a shorter time. The exam enables us to accurately assess the quality of the bone trabeculae and isolate smaller areas of interest during the 3D reconstruction. On the other hand, the MSCT exam despite taking longer to take tomography and emitting more radiation has advantages such as better detailing of regions with thin cortical layers, such as the anterior wall of the maxillary sinus and cortical of the mandibular condyles. In addition, it also presents a better representation of the facial soft tissues involved. It is also worth remembering that the MSCT can be a tomography with a greater field of view, which is interesting in cases of extensive and/or combined maxillofacial prostheses.

The computed tomography images will provide the information of the face structure according to the Hounsfield scale, which is based on the radiodensity of the water being equal to 1 (Hounsfield 1979). Thus, the structure denser will have a higher value (bone and teeth) and the structureless dense will have a lower value (air and fat). After the exam is performed, all data is transported to the software as voxel files. It means that all the information about the volume and spatial position are precisely available. The Digital Imaging and Communications in Medicine (DICOM) format will ensure that all anatomical measurements and positions are standardized, regardless of the software being used.

The 3D reconstruction of medical images requires the segmentation process of the structures to be reconstructed using software and this process can be done manually or automatically. The computed tomography equipment has software that makes it possible to reconstruct a volume formed by all the images of the pact (Fig. 13.3). However, from a DICOM image package, it is possible to use commercial or free software to make the 3D reconstruction of the structure. Figure 13.4 shows the complete workflow of planning a maxillofacial prosthesis.

13.2.2 3D Scanning

The 3D scanner is a device able to achieve digital records from an object, regardless of its composition and density, and transmit it to the computer, making a 3D mesh. The scanner converts the reflected light into digital data using different technologies. Thousands of red laser light points can record the details of the surface of a structure from the confocal points (Van der Meer et al. 2012). It is also possible to add texture to objects, such as identifying different colours of a tooth, gums and skin characteristics.

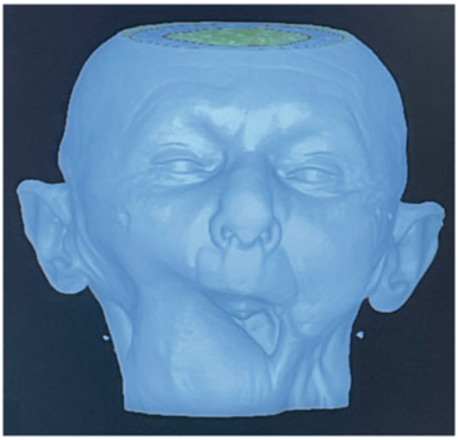

Fig. 13.3 3D face reconstruction from Multislice Computed Tomography images

In this way, when the technique is well done, the scanning will show the whole soft and hard tissues, without failures and density differences.

Previously, it was mentioned the great advantages and applications of using medical images such as MRI, CBCT, or MSCT. So why use 3D scanning? 3D scanning can make it easier to obtain anatomical structures without direct contact with the individual and without ionizing radiation. Digitization using 3D laser scanners works by emitting light, which generates a cloud of points. The point cloud created generates a vector mesh, which forms the virtual model of the scanned object. In the 3D reconstruction of computed tomography, the object appears in a variable amount of structures, depending on object density, which does not occur in scanning.

The 3D scanning technique, compared to photogrammetry, differs in terms of the number of points obtained. 3D Scanning provides a much larger number of surface points, that is, it is the most accurate technique to acquire and represent the surface of an object. Thus, 3D scanning is indicated when only the external face structure information is needed. But some disadvantages of using the scanner should be mentioned, such as the added cost and the impossibility of reaching some anatomical areas in facial mutilated patients due to the limitation of space when compared to the size of the sensor, for example. In these cases, computed tomography turns out to be the most viable option for image acquisition.

13.2.3 Photogrammetry

A third option for obtaining a 3D structure of the face is photogrammetry. There are a few different techniques for this modality. Conventional photography protocols using professional cameras or smartphones have been suggested so that a series of photos at different angles of the same scene are capable of matching 2D data (pixels) so that a 3D object (voxels) is constructed. A more precise methodology involves the use

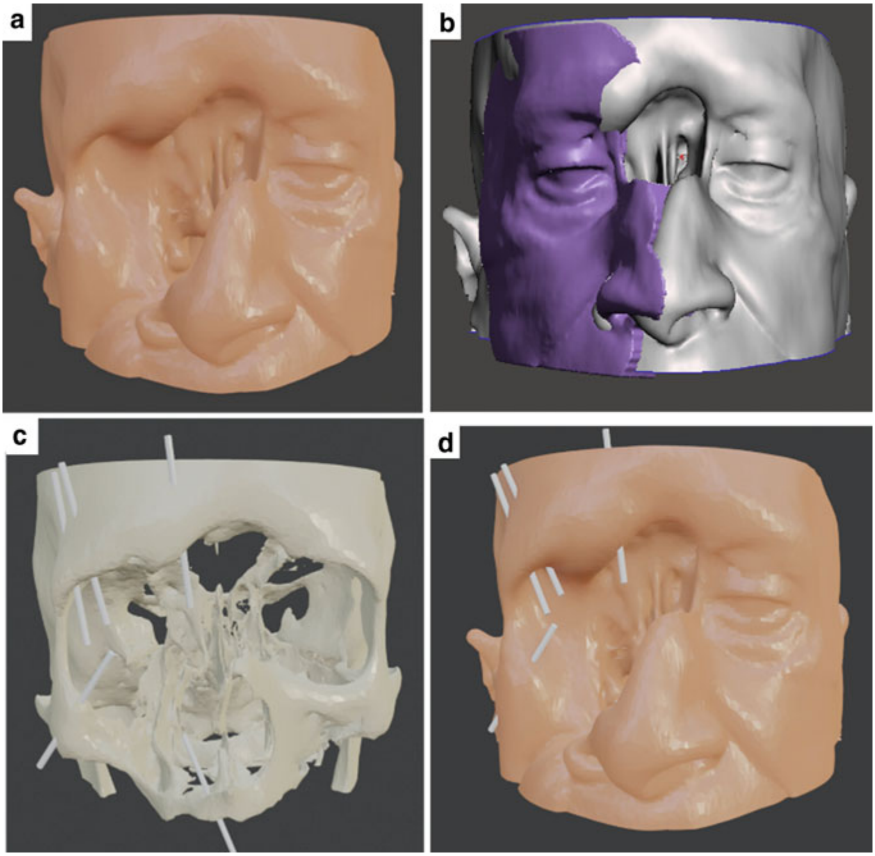

Fig. 13.4 3D face reconstruction from Multislice Computed Tomography images presenting an extensive facial defect after tumour ablation surgery (**a**). Mirroring of the contralateral side for volume and symmetry initial study of the anatomical structures (**b**). 3D evaluation of implant position in bone (**c**) and soft tissue (**d**)

of photo booths, in which numerous cameras are strategically positioned at different angles so that in a few seconds all the information obtained is quickly transformed into 3D data. In this way, there is a much smaller possibility of distortion of the structures. Other ways have also been demonstrated, such as the use of videos in high resolution through specific software, which is very reminiscent of the idea of virtual reality that can be seen in cinema. In addition to the volumetric and spatial data, photogrammetry is also able to provide texture (Ciobanu and Rotariu 2014). The main limitation of 3D scanning and photogrammetry compared to the 3D reconstruction of medical images is the fact that the individual to be scanned has to remain static throughout the process, which can take a few minutes.

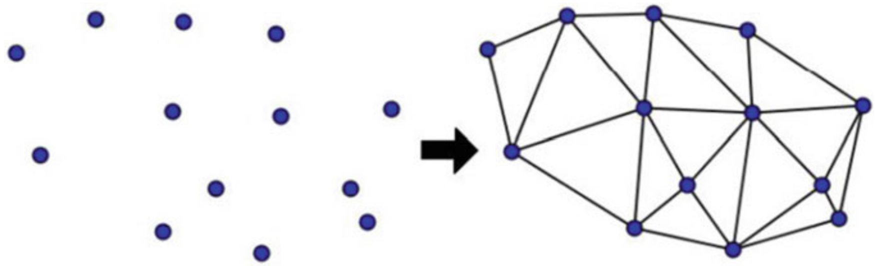

Fig. 13.5 Two-dimensional triangulation technique

13.3 3D Modeling

In this workflow step, the healthy structure of the face is digitally cropped and mirrored to fill the facial defect, this is the 3D modeling of the maxillofacial prosthesis. The modeling process, used to create devices that are attached to the patient's body, starts by scanning the anatomical region. Modeling in 3D means creating and manipulating a computer representation of an object or structure in the real world, which is virtually represented by a cloud of interconnected points, polygons or tetrahedra. When dealing with an object with dimensions, creation can be carried out virtually directly by CAD software (Fig. 13.5).

However, when the object of study has a surface with complex curves, such as the human anatomical structure, modeling becomes difficult. Thus, it is necessary to acquire the surface of this structure to represent it on a computer, as in the case of lower, upper, hip, among others, for the creation of personalized devices (Fabio 2003). Commonly, the digital model of the prosthesis to be printed is converted into a stereolithographic file (.stl file extension) which consists of important data on the surfaces of the 3D model, a 3D mesh. In the "*.stl*" model or mesh, the greater the number of triangles, the greater the resolution of the 3D printed object (Bibb et al. 2010).

13.4 Additive Manufacturing

Additive manufacturing is a production technology by successively adding material in layers through different processes. Additive manufacturing is a fast, customizable, low-cost and lightweight approach that has been used in the last years for orthotics and prosthesis fabrication (Artioli et al. 2018; Santos et al. 2018; Silva et al. 2020; Kunkel et al. 2020; Paula et al. 2021). It is a promising advancement in modern prosthetic fabrication that would alleviate several issues noted in the fabrication and use of prosthetic devices in low and middle-income countries. The long-term effects of these technologies on prosthetics need to be investigated to produce a more sustainable alternative to traditional prosthetics and enhance the field of additive manufacturing.

Table 13.1 Working principle of the main additive manufacturing processes

Process	Working principle	Advantages	Disadvantages
Stereolithography (SLA)	From light-sensitive polymers, solidification occurs after exposure to ultraviolet radiation	Excellent surface quality. Meets complex geometries. Good accuracy	Limited to light-sensitive polymers. Requires support structures. Vapors are harmful to health. Need for post-cure
Selective laser sintering (SLS)	Using a laser beam, it melts and solidifies, one layer at a time, powder-like materials such as elastomers and metals	No additional sintering and support. High range of materials. Produces metal parts without machining	High cost. Rough and porous surfaces. Lots of time and energy Castings require additional processing (leakage). Thickness distortions
Fusion deposition modeling (FDM)	By extruding polymers in a system with an extrusion nozzle that moves along the x, y and z axes	Low cost and wide range of materials. Easy operation and adjustment of the machins	Support structure. Low precision and low speed. The object supports low force in the vertical direction. Rough surface

The most innovative and simplified method in the manufacture of prostheses is the computer-aided design and manufacturing (CAD/CAM) 3D system, combined with a non-contact laser measurement system. The additive manufacturing technology can be classified by the form of the raw material used (liquid, solid and powder) or by the energy used in the processing of the layers (Volpato, 2017) (Table 13.1). The most used additive manufacturing processes in the medical field are stereolithography (SLA), selective laser sintering (SLS) and fusion deposition modeling (FDM) (Bibb et al. 2010; Kunkel and Vasques 2021) (Fig. 13.6).

Three-dimensional printing technology has gradually become an emerging and crucial adjunctive tool in the medicine area (Haleem and Javaid, 2021), including the maxillofacial prosthesis. The application of additive manufacturing in healthcare provides many benefits such as better cost-effectiveness, increased productivity, and democratization of design and manufacturing (Jin et al. 2021). There is a variety of printing materials such as polylactic acid (PLA), nylon, thermoplastic, polyvinyl alcohol (PVA) filament, acrylonitrile butadiene styrene (ABS), resin etc. These materials vary in mechanical strength, flexibility, and biocompatibility. The choice of material will also determine the amount of stress and strain that can be exerted on the prosthetics. The costs and the weight of the 3D printed prosthetics are significantly lower than in traditional prosthetics due to the type of material used and the reduction in manual labour and manufacturing costs (Ventola 2014) (Fig. 13.7).

The 3D-biomodels are indicated in cases of extensive facial mutilations, where it is not possible to perform a face impression using the traditional technique, with impression materials. Biomodels can be printed on different materials and can be

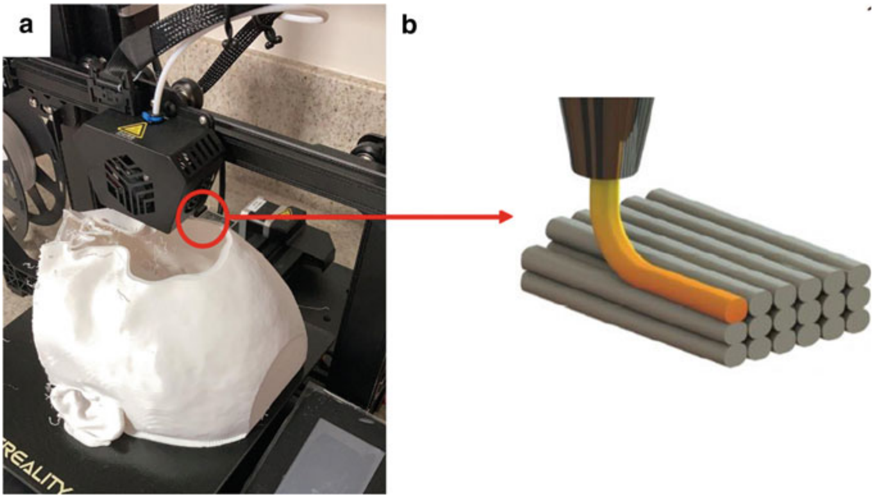

Fig. 13.6 The Fusion deposition modeling process

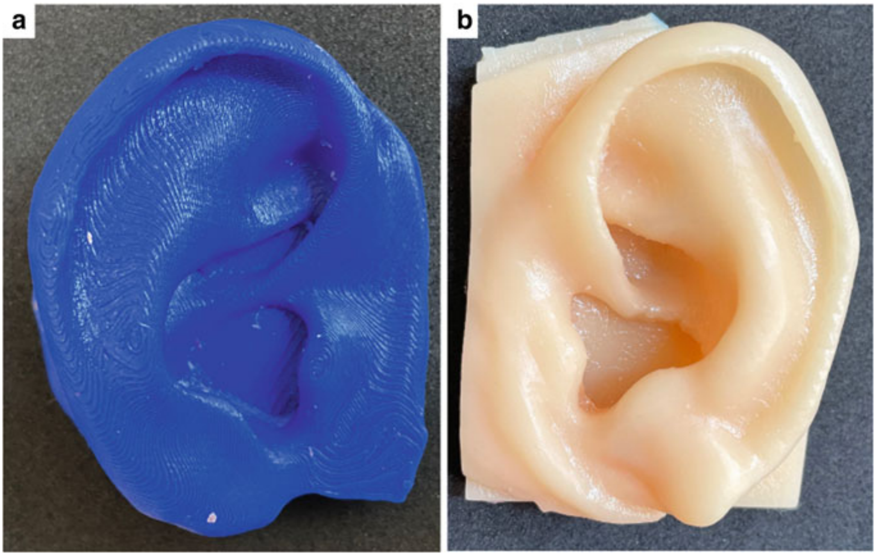

Fig. 13.7 3D printed ears manufactured by different materials and processes: **a** Polylactic acid ear manufactured by the fusion deposition modeling process and, **b** resin ear manufactured by the stereolithography process

used for studying and prosthetic planning, wax sculpting and prosthesis prototyping. A biomodel of the reconstructed digital structure of a deformed face can be obtained by Additive manufacturing, becoming a tool very useful for planning the facial prostheses and can be done in different printing materials (Figs. 13.8 and 13.9).

Additive manufacturing is an innovative technology utilized for prostheses production with the benefits of higher levels of customization and lower production costs (Ribeiro et al. 2021). However, more research and technological advancements are required to fully understand the impact of this technology on patients and how it will affect their daily life. The long-term effects of this technology should be investigated to produce a more sustainable alternative to traditional methods. Additive manufacturing is a promising advancement in modern prosthetic fabrication that alleviates several issues noted with traditional fabrication methods. The technology

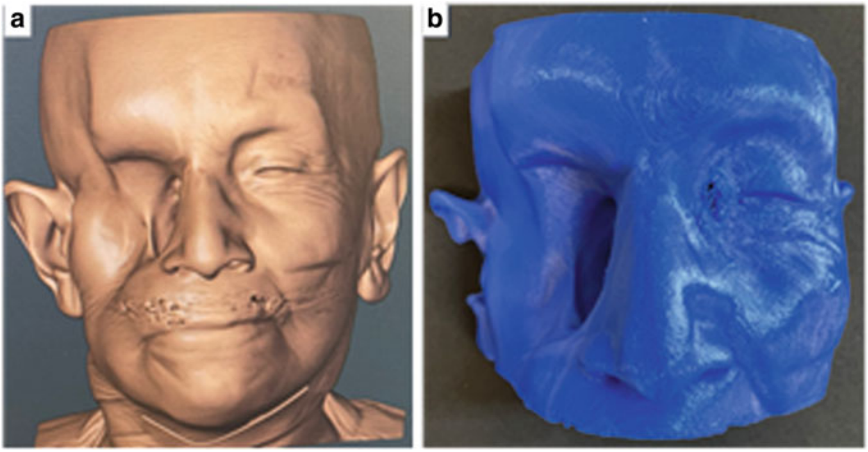

Fig. 13.8 3D face reconstruction from Multislice Computed Tomography images (**a**) and the 3D-biomodel of the face printed in polymeric mate

Fig. 13.9 3D-biomodel of the individual with an extensive face mutilation

encompasses a variety of different printing methods, using an additive manufacturing process that involves heating, excreting and fusing material layer-by-layer slowly building the object (Chimento et al. 2011).

Nowadays, there does not exist a 100% printing technology that could bring the perfect personal skin characteristics, including the many different colours, textures, wrinkles, and nuances for the maxillofacial prosthesis. In this way, the industries have been trying to bring improvements and innovations in different materials so that prostheses are more realistic. While these possibilities are not yet a financially viable option for most professionals, it is possible to have some options aimed at MP: direct printing of a part such as mirrored or virtually modeled prototyping or printing a mold.

The direct 3D printing method refers to the use of a 3D printer to print the organ model itself directly, but not always print the complete model at one time. The model can also be split into several parts for printing, and then assembled in the post-processing step. Printing a complete model at one time is the most convenient, but it has restrictions on some conditions. Indirect 3D printing method refers to the use of 3D printing to manufacture the parts for making the model, but not directly print the prosthesis model itself (Jin et al. 2021).

The indirect 3D printing methods are characterized by lower costs for 3D printers and materials, but more complex workflow and more procedures for traditional analogical methods. On the one hand, manual operation can significantly save the cost of machinery manufacturing, but on the other hand, it will increase the time cost and the error of the model, unless the operator has a high level of proficiency and skill. Generally, the indirect method is more suitable for manufacturing soft blocky structures, such as kidney and liver parenchyma. After all, making those soft materials that cannot be directly 3D printed play a role in organ models is the crucial advantage of indirect methods (Jin et al. 2021).

The directly printed prosthesis has poor mechanical properties and untested biological responses. For these reasons, the best way to fabricate facial prosthesis is to print the prosthesis mold and cure the prosthesis with silicone rubber (Bibb et al. 2010).

It is possible to fabricate soft prostheses with a low-cost desktop 3D printer. One of the methods that can be cited is the Scanning Printing Polishing Casting (SPPC), in which one, a chemical polish can be used to improve the inside of the mold and avoid the layering effect, originating from the AM process, and thus produce a prosthesis with a smoother surface. Using the SPPC method, the total cost of fabricating ear prosthesis is about $30, which is much lower than the current soft prosthesis fabrication methods, in addition to reducing working time (He et al. 2014).

13.5 Improved Construction of Facial Prosthesis by Digital Technologies

For the facial, ear, and ocular palpebral prosthesis the mirrored image is imported to the software and a virtual model of the future prosthesis is obtained for the defect side (Fig. 13.10). The superposition of anatomical structures of a donor is another possibility, mainly used in nasal prostheses. It is possible to use an image of a family member that presents the anatomical structures similar to the patient or a virtual image bank. Initially, the mirrored image is printed and then it is duplicated in wax which is fitted over the defect side. Then, it is conventionally flasked. An impression of the defect side also can be made, and the cast model is obtained in a dental flask.

The patient's skin colour can be digitized using a spectromatch skin colour system or can be checked conventionally. At room temperature, the silicone elastomer is mixed, the intrinsic pigments are added to the patient's skin colour (intrinsic colouring) and then packed into the mold. The silicone is cured conventionally. After the silicone is totally cured, the fine soft prostheses can be removed from the mold. The prosthesis is trimmed and fitted in the patient and sometimes extrinsic colouring is necessary to make the prosthesis more realistic (Figs. 13.11 and 13.12) This method eliminates the conventional laboratory steps and reduces the number of stages of the fabrication of a silicone prosthesis. The negative mold of the defect side allowed direct fabrication of the silicone prosthesis without a need for waxing or flasking procedures. Additionally, these technologies saved time and provided a

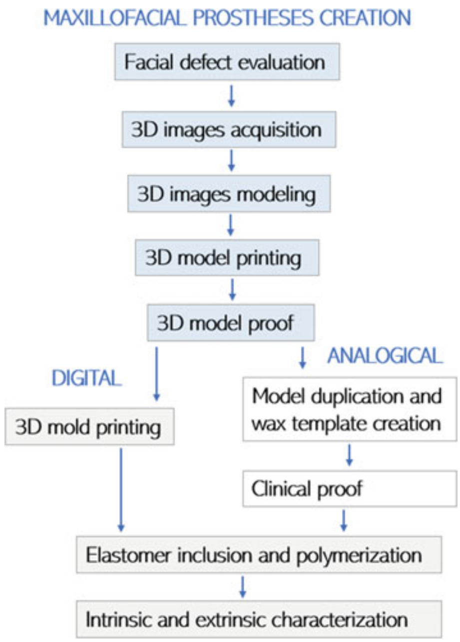

Fig. 13.10 A flowchart demonstrating the difference between the digital and traditional analogical methods

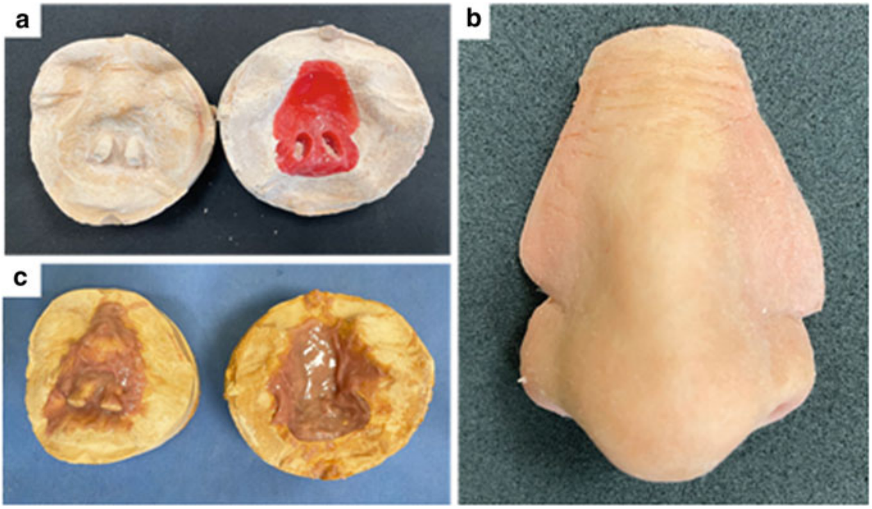

Fig. 13.11 Indirect 3D printing methods using images of a virtual bank. Mold from the final wax (**a**); elastomer with intrinsic pigmentation packed into the mold (**b**) and final prosthesis (**c**)

base for reproducible results regardless of the operator (Nuseir et al. 2015; Cevik and Kocacikli 2020).

13.6 Final Considerations

Because of the new existing technologies, it is also important to reinforce the application of AM in the construction of assistive technology, such as facial prostheses. The ease of access of this manufacturing process resulting from the cost reduction, both of equipment and inputs, associated with the dissemination of knowledge for the production of models, biomodels, prototypes, 3D molds in different materials, can allow, for example, access to low-cost, customized prostheses with a fast fabrication process.

Some studies have investigated the best form of 3D digitization of the human body for the medical field, in the development of customized prostheses (Koutny et al. 2012; Colombo et al. 2013; Ciobanu et al. 2013; Ciobanu and Rotariu 2014; Mohammed et al. 2016). Among the main disadvantages of the digital technological process in the Additive manufacturing of facial prostheses are the acquisition of equipment and supplies such as professional computers with specific configurations, different 3D printer systems, the need to acquire software that often involves costs and a learning curve. One of the biggest advantages is the possibility of visualizing the anatomical defect in different angles and planes. The level of detail of the prosthesis, quality improvement, thinning of the edges and better adaptation of the mutilated area are also considered important benefits.

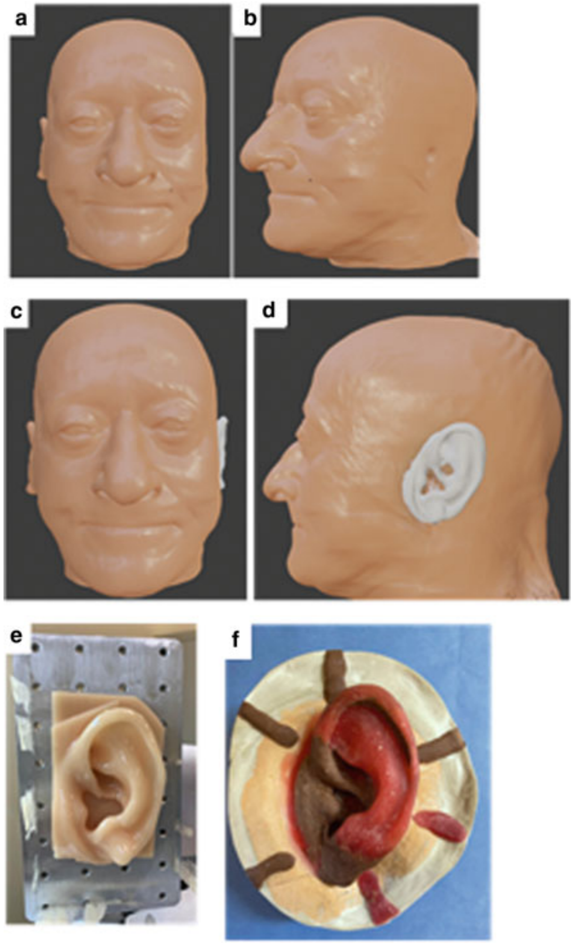

Fig. 13.12 Ear prosthesis confection through 3D mirroring. Computed tomography in a 3D reconstruction in frontal, **a** and lateral, **b** view. Ear mirroring, modeling and adaptation in frontal, **c** and lateral, **d** view. MA of the model, **e** sculpture and mold, **f** before the siliconization

Acknowledgements The authors would like to thank the Pontifical Catholic University of Parana (PUCPR), the National Council for Scientific and Technological Development (CNPq), the International Development Research Centre (IDRC), and the GDS Program. and for financial support to the development of this research.

References

Artioli BO, Kunkel ME, Mestanza SN (2018) Feasibility study of a methodology using additive manufacture to produce silicone ear prosthesis. In: World congress on medical physics and biomedical engineering. Springer, Singapore. pp 211–215. https://doi.org/10.1007/978-981-10-9023-3_38

Beumer J III, Marunick MT, Esposito SJ (2011) Maxillofacial rehabilitation: prosthodontic and surgical management of cancer-related, acquired, and congenital defects of the head and neck, 3rd edn. Quintessence Publishing Co, São Paulo

Bibb R, Eggbeer D, Evans P (2010) Rapid prototyping technologies in soft tissue facial prosthetics: current state of the art. Rapid Prototyping J 130–137. https://doi.org/10.1108/13552541011025852

Cevik P, Kocacikli M (2020) Three-dimensional printing technologies in the fabrication of maxillofacial prosthesis: a case report. Int J Artif Organs 43(5):343–347. https://doi.org/10.1177/0391398819887401

Chimento J, Highsmith M, Nathan C (2011) 3D printed tooling for thermoforming of medical devices. Rapid Prototyping Journal 17:387–392. https://doi.org/10.1108/13552541111156513

Chini GCDO, Boemer MR (2007) Amputation in the perception of those who experience it: a study under the phenomenological. Rev Lat Am Enfermagem 15:330–336

Ciobanu O, Rotariu M (2014) Photogrammetric scanning and applications in medicine. Appl Mech Mater 657:579–583. https://doi.org/10.4028/www.scientific.net/AMM.657.579

Ciobanu O, Xu W, Ciobanu G (2013) The use of 3D scanning and rapid prototyping in medical engineering. In: Fiabilitate si Durabilitate - Fiability & Durability Supplement no 1/ 2013 Editura “Academica Brâncuşi”, Târgu Jiu, pp 241–247

Colombo G, Facoetti G, Rizzi C (2013) A digital patient for computer-aided prosthesis design. Interface Focus 3:20120082. Itália, Dalmine, Univer. de Bergamo. https://doi.org/10.1098/rsfs.2012.0082

Fabio R (2003) From point cloud to surface: the modeling and visualization problem. Int Arch Photogrammetry Remote Sens Spat Inf Sci Zurique, Suíça 24(5):11. https://doi.org/10.3929/ethz-a-004655782

Fleck M, Louzada S, Xavier M et al (2000) Application of the Portuguese version of the abbreviated instrument of quality life WHOQOL-bref. Rev Saude Publica 34(2):178–183

Gallagher P, Coffey L, Desmond DM et al (eds) (2019) Handbook of rehabilitation psychology. American Psychological Association, pp 257–277

Geertzen JH, Van Es G, Dijkstra PU (2009) Sexuality and amputation: a systematic literature review. Disabil Rehabil 31(7):522–527. https://doi.org/10.1080/09638280802240589

Haleem A, Javaid M (2021) 3D printed medical parts with different materials using additive manufacturing. Clin Epidemiol Glob Health 8:215–223. https://doi.org/10.1016/j.cegh.2019.08.002

He Y, Xue GH, Fu JZ (2014) Fabrication of low-cost soft tissue prostheses with the desktop 3D printer. Sci Rep 27(4):6973. https://doi.org/10.1038/srep06973

Hounsfield GN (1979). Computer reconstructed x-ray imaging, vol 292. Phil Trans R Soc Lond A

Jin Z, Li Y, Yu K et al (2021) 3D printing of physical organ models: recent developments and challenges. Adv Sci 8:2101394. https://doi.org/10.1002/advs.202101394

Koster META, Bergsma J (1990) Problems and coping behaviour of facial cancer patients. Soc Sci Med 30(5):569–578. https://doi.org/10.1016/0277-9536(90)90155-L

Koutny D, Palousek D, Koutecky T et al. (2012) 3D digitization of the human body for use in orthotics and prosthetics. World Acad Sci Eng Technol 6(12):1487–1494

Kunkel ME, Cano APD, Ganga TAF et al. (2020) Manufatura Aditiva do Tipo FDM na Engenharia Biomédica. In: Kunkel ME (ed) Fundamentos e Tendências em Inovação Tecnológica, vol 1, 1st edn. Kindle Direct Publishing, Seattle, pp 50–69

Kunkel ME, Vasques MT (2021) Manufatura aditiva por fotopolimerização na odontologia e engenharia biomédica. In: Kunkel ME (ed) Fundamentos e Tendências em Inovação Tecnológica. Kindle Direct Publishing, Seattle, pp 53–75

Milioli R, Vargas MAO (2012) Leal SMC quality of life in patients submitted to amputation. Rev Enferm UFSM 2(2):311–319. https://doi.org/10.5902/217976924703

Mohammed MI, Fitzpatrick A, Gibson I (2016) Customised design and development of patient specific 3D printed whole mandible implant. In: Solid Freeform Fabrication 2016: Proceedings of the 26th annual international solid freeform fabrication symposium—an additive manufacturing conference. Austrália e India, pp 1708–1717

Nuseir A, Hatamleh M, Watson J et al (2015) Improved construction of auricular prosthesis by digital technologies. J Craniofac Surg 26(6):e502–e505. https://doi.org/10.1097/SCS.0000000000002012

Paula FCN, Kunkel ME, Bina TS et al. (2021) Health 4.0 technologies to develop customized external breast prostheses. In: Belinha J, Campos JCR, Fonseca E, Silva MHF, Marques MA, Costa MFG, Oliveira S (eds) Advances and current trends in biomechanics, 1st edn. CRC Press Taylor and Francis Group, Porto

Peraković D, Periša M, Cvitić I (2018) Analysis of the possible application of assistive technology in the concept of industry 4.0. In: Proceedings the 36th symposium on novel technologies in postal and telecommunication traffic –posTel, pp 175–184

Ribeiro D, Cimino SR, Mayo AL et al (2021) 3D printing and amputation: a scoping review. Disabil Rehabil Assist Technol 16(2):221–240. https://doi.org/10.1080/17483107.2019.1646825

Rumsey N, Harcourt D (2004) Body image and disfigurement: issues and interventions. Body Image 1(1):83–97. https://doi.org/10.1016/S1740-1445(03)00005-6

Santos NA, Artioli BO, Goiano E et al (2018) A parametrization approach for 3D modeling of an innovative abduction brace for treatment of developmental hip dysplasia. In: World congress on medical physics and biomedical engineering. Springer, Singapore, pp 227–231. https://doi.org/10.1007/978-981-10-9023-3_41

Scorchio FRS, Teng TK, De Conti MG et al (2018) Art rehabilitation in amputee women with Pandora's myth as a self-esteem and quality of life facilitator resource. Acta Fisiatra 25(1):12–18. https://doi.org/10.11606/issn.2317-0190.v25i1a158827

Sharma AB, Beumer J (2006) Reconstruction of maxillary defects: the case for prosthetic rehabilitation. J Oral Maxillofac Surg 63(12):1770–1773. https://doi.org/10.1016/j.joms.2005.08.013

Silva ATD, Lages AS, Silveira GRP et al (2020) Development and customization of a dennis brown orthosis prototype produced from anthropometric measurements by additive manufacturing. In: Bastos-Filho TF, Caldeira EMO, Frizera-Neto A (eds) Proceedings of CBEB 2020 XXVII Brazilian congress on biomedical engineering, 1st edn. Springer, p 2018

Stefan I, Koop S, Gundlach K et al (2009) Effects of radiation therapy on craniofacial and dental implants: a review of the literature. Oral Surg Oral Med Oral Pathol Oral Radiol Endod 107(1):56–65. https://doi.org/10.1016/j.tripleo.2008.06.014

Stramandinoli-Zanicotti RT, Sassi LM, Schussel JL et al (2014) Effect of radiotherapy on osseointegration of dental implants immediately placed in postextraction sites of minipigs mandibles. Implant Dent 23(5):560–564. https://doi.org/10.1097/ID.0000000000000150

Van der Meer WJ, Andriessen FS, Wismeijer D et al (2012) Application of intra-oral dental scanners in the digital workflow of implantology. PLoS One 7(8):e43312. https://doi.org/10.1371/journal.pone.0043312

Ventola CL (2014) Medical applications for 3D printing: current and projected uses. Pharm Ther Peer-Rev J Formulary Manage 39(10):704–711

Volpato N (2017) Manufatura aditiva: tecnologias e aplicações da impressão 3D. 1st ed. Blucher, São Paulo

Yaron G, Meershoek A, Widdershoven G et al (2018) Recognizing difference: in/visibility in the everyday life of individuals with facial limb absence. Disabil Soc 33(5):743–762. https://doi.org/10.1080/09687599.2018.1454300

Part V
Additive Manufacturing and Personalized Materials

Chapter 14
3D Printing in Orthopedic Surgery

Celso Júnio Aguiar Mendonça and João Antônio Palma Setti

14.1 Introduction

Several areas of medicine, mainly in the surgical field such as orthopedics are using the additive manufacturing (AM) of anatomical models and personalized implants, thus allowing accurate preoperative planning, simulation of surgeries with team training, and better communication with the patient (Zheng et al. 2018a, b; Rankin et al. 2018).

The features of the 3D printing technology currently used in orthopedic surgeries allow the printing of anatomical models precisely reproducing the anatomy of the patients. These can improve the understanding of the surgeon about anatomy and fracture deviations, and in some cases, it helps to make a correct diagnostic interpretation, where it was not apparent in medical images. Besides, it helps to understand the anatomical relationships of structures and geometry of regions with complex anatomy, facilitating accurate preoperative planning. These models assist in the training of surgeons in areas of complex anatomy such as the pelvis, spine, and joint regions.

Virtual 3D planning allows the surgeon to better visualize and understand the full three-dimensional anatomy and to digitally plan, e.g., a corrective osteotomy to restore anatomy and normal function or allow better implant positioning. This

C. J. A. Mendonça (✉)
Postgraduate Program in Electrical Engineering and Industrial Informatics—CPGEI, Federal Technological University of Paraná—UTFPR, Curitiba, Brazil
e-mail: celso.mendonca@hc.ufpr.br

Musculoskeletal System Unit—USME, Hospital of the Federal University of Parana—CHC UFPR, Curitiba, Brazil

J. A. P. Setti
Postgraduate Program in Biomedical Engineering—PPGEB, Federal Technological University of Paraná—UTFPR, Curitiba, Brazil
e-mail: setti@utfpr.edu.br

O. Canciglieri Junior and M. D. Trajanovic (eds.), *Personalized Orthopedics*,
https://doi.org/10.1007/978-3-030-98279-9_14

planning is based on computed tomography (CT) images of the patient, in which various surgical approaches are considered. 3D planning has the potential to increase the accuracy of preoperative planning, increase the accuracy of surgical navigation, decrease postoperative complications, obtain a more economical use of operating rooms, and improve patient satisfaction. To this end, Patient-Specific surgical guides are designed to control the cut and reduction according to the surgical plan, aiming to improve the predictability of osteotomy and fracture treatment procedures (Vaishya et al. 2018; Bagaria and Chaudhary 2017).

Three-dimensional printing allows the use of personalized 3D printed tools and guides for performing osteotomies with precise implant placement to optimize surgical results. Implants, cut and drill guides, orthoses and personalized prostheses can be created according to the individualized anatomy of each patient (Vaishya et al. 2018).

In complex osteotomies and arthroplasties, the production of 3D models helps in planning the surgical procedure. It goes beyond the three-dimensional images usually reconstructed from CT and allows the surgeon to study the problem, not only seeing it in two dimensions but keeping it in his hand, ensuring a 3D perspective in real size.

The main advantages are the ability to assess bone defects, evaluate fracture patterns, guarantee the accuracy of the position of the implants and prosthesis. The printed biomodel offers the opportunity to plan the necessary instrumentation and customized implants, thus optimizing surgery. Surgeons can simulate the procedure and, if necessary, build templates, cutting and drilling guides, and personalized perforations based on the disease, anatomy, and surgeon's preferences (Bagaria and Chaudhary 2017).

The use of 3D technology in orthopedic trauma allows Virtual Surgical Planning (VSP) to provide the reduction of fragments, the choice of implants according to bone geometry. This allows the anatomical model to be printed on a full scale for a better understanding of the anatomy, performing surgical simulation with due training of the team and verification of the pre-selected implants with the possibility of preoperative modeling (bending) of these implants, as in cases where plate and screws are used, adapting the best local bone surface. Also, in orthopedic trauma surgeries, it is possible to use a 3D printing technique to print a mirror image of the bone on the unaffected side in real size (similar to the affected side) to use it in the preoperative for refinement of surgical planning and simulation and in the intraoperative approach to reference the anatomical fracture reduction (Zhang et al. 2017a, b).

14.2 Medical Images

14.2.1 Image Acquisition

The first and most important step in printing objects is the acquisition of images (Shui et al. 2017; Wong et al. 2017; Eijnateen et al. 2018). The quality of the printed

Table 14.1 Parameters for the CT image acquisition used in the printing of anatomical bone models (Bagaria and Chaudhary 2017)

Parameters	Description
Field of view (FOV)	12 × 12 inches
Scout	Depends on the region of interest
Region of interest (ROI)	ROI should be identified
KV	Automatic
mA	Usually, automatic
Pitch	512 × 512
Collimation	1.25–1.5 mm
Slice thickness	1–1.5 mm
Slice increment	0.625–0.75 mm (less than 1 mm)
Kernel/Algorithm	Moderated—soft tissue

model depends on the quality of the processed data (resolution of the images). Therefore, low-resolution images will result in inappropriate models and distortions in the printed object (Marro et al. 2016; Mok et al. 2016; Martelli et al. 2016; Green et al. 2016).

Bone tissue has a high contrast compared to soft tissue in CT images, which makes this type of exam the most indicated for the acquisition of data for 3D modeling (Wong et al. 2017). There is no consensus in the literature on which would be an ideal protocol for image acquisition, mainly from CT images for use in Rapid Prototyping (RP) of 3D anatomical models. Some important parameters in the acquisition of CT images were described in the literature (Eijnatten et al. 2018). Bagaria and Chaudhary (2017) in their study suggest a protocol of parameters for the CT image acquisition used in the printing of anatomical bone models (Table 14.1).

Some studies show that the width of the slices of the images CT scan also influences the quality of volumetric reconstruction of the image being one of the main limiting factors for the quality of prototyping in the medical field (Rankin et al. 2018; Eijnatten et al. 2018; Marro et al. 2016). The slices should be 0.5–2 mm depending on the anatomical region. Anatomical models of the face should have slices with 0.5–1 mm of width as models of long bones, and the pelvis can be sliced up to 2 mm according to Marro et al. (2016). Slices above 2 mm can generate distortions during volumetric reconstruction and printing of objects. Most appliances CT is limited to a slice width of at least 0.625 mm although many 3D printer companies specify a resolution of minus 0.1 mm for their machines (Eley 2017). The ROI must be established for the segmentation, to decrease the work of extracting parts that will not be useful for printing (Shui et al. 2017).

The data acquired (images) on CT scan are processed in software observing a set of standards for the treatment, storage, and transmission of information in an electronic format, structuring a protocol known as the Digital Image Communication in Medicine (DICOM format) (Shui et al. 2017; Eijnatten et al. 2018; Marro et al. 2016; Mulford et al. 2016). This format was created in the 80 s to standardize the formatting of diagnostic images such as CT, Magnetic Resonance Images (MRI), and

Ultrasonography (US) used in the Picture Archiving and Communications System (PACS), a system for storing and exchanging information generated by medical equipment. The DICOM standard has a series of rules that allow medical data and information associated with images to be exchanged with diagnostic equipment that generates images and between the different equipment from different developers.

Image acquisition can be carried out by direct scanning in 3D volume. The scanned images can be exported already in the format of the STL file e.g., to be print (Li et al. 2017).

14.2.1.1 Computed Tomography

Currently, the CT data are the most used medical images in the creation of 3D anatomical models and virtual surgical simulations. Bone tissues have a high contrast compared to soft tissues in CT images, which makes this type of exam the most suitable for the acquisition of data for 3D modeling (Wong et al. 2017) (Fig. 14.1). Van den Broeck et al. (2014) conducted a study whose objective was to quantify errors in absolute dimensions between models reconstructed from CT images and MRI compared to the true model for several bone regions.

3D model images of the tibia were created from segmented CT and MRI images and compared to optical scans of real bones (considered standard). 3D reconstruction using CT images resulted in an error of 0.55 mm, corresponding to an overestimated bone model of CT compared to the real bone. The MRI resulted in an error of 0.56 mm; however, the bone model of MRI was, on average, a small underestimation in comparison with the real bone. Different regions of the bones were analyzed, indicating a difference in accuracy between the diaphysis and the epiphysis. This study shows high accuracy for CT and MRI images, supporting the feasibility of using technology imaging for 3D bone reconstruction in medical applications (Van den Broeck et al. 2014).

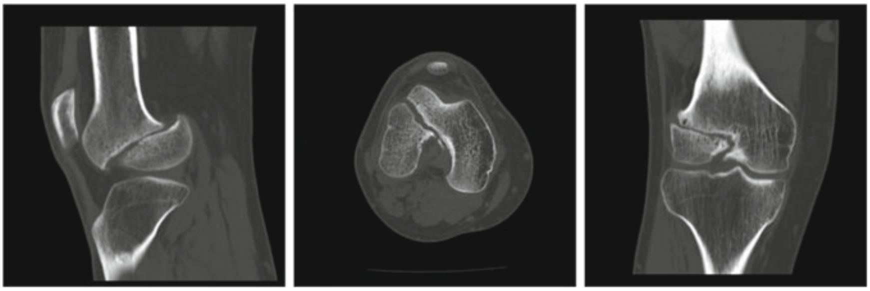

Fig. 14.1 CT of the knee in sagittal, axial, and coronal planes showing a coronal femoral condyle fracture nonunion (Hoffa's fracture)

14.2.1.2 Magnetic Resonance Imaging

The most important aid of the MRI is to show the soft tissue in orthopedics images. Eley et al. (2014) and (2017) described the “Black Bone” MRI and concluded that segmentation of the “Black Bone” MRI datasets was successful with both threshold and volume rendering techniques, demonstrating considerable clinical potential as a non-ionizing alternative to CT.

According to Parthasarathy et al. (2020), bone structures require the “black bone” MRI technique for accurate evaluation. The black bone MRI technique uses a gradient echo. These authors showed that the 3D-created model from MRI with 1 mm slice acquisition is more accurate than the one created from the acquisition of 3 mm slices. The black bone sequence normally is not a routine protocol in MRI acquisition, and its specific requisition is necessary.

14.2.2 Processing and Postprocessing Images

14.2.2.1 Denoising

If the images show random noise (especially if there are metallic implants), noise cleaning should be performed to avoid artifacts in CAD models. So, the first step is the sequential reduction of the data acquired by CT. The smoothing method, which is a computer algorithm, can be used to reduce noise without losing important details and anatomical information (Bagaria and Chaudhary 2017; Green et al. 2016).

14.2.2.2 Segmentation

Segmentation is a process of separating an unwanted area from the desired area, that is, the region of interest (ROI) for future image processing (Bagaria and Chaudhary 2017; Shui et al. 2017; Marro et al. 2016; Green et al. 2016). The separation of the parts depends on the anatomical area and the chosen tissue to be studied (bone, muscle, vascular blood, etc.). For proper segmentation to take place, the threshold of attenuation (density) of the tissue must be chosen (Rankin et al. 2018). This is defined according to the scale of Hounsfield (HU) which is a transformation of the original measure of the coefficient of linear attenuation for a dimensionless scale in X-Ray and CT images. The Hounsfield scale is related to obtaining images from ionizing radiation like X-rays. It transforms the different shades of gray, acquired in imaging with ionizing radiation (e.g., X-ray), into numerical values.

This transformation makes it possible to open windows within the grayscale obtained in the images, allowing greater differentiation between previously very similar colors (and often indistinguishable to the human eye). Visually, the air is identified as completely black area, the water as gray, and the bone as white. On that scale, the radiodensity of distilled water under standard temperature conditions and

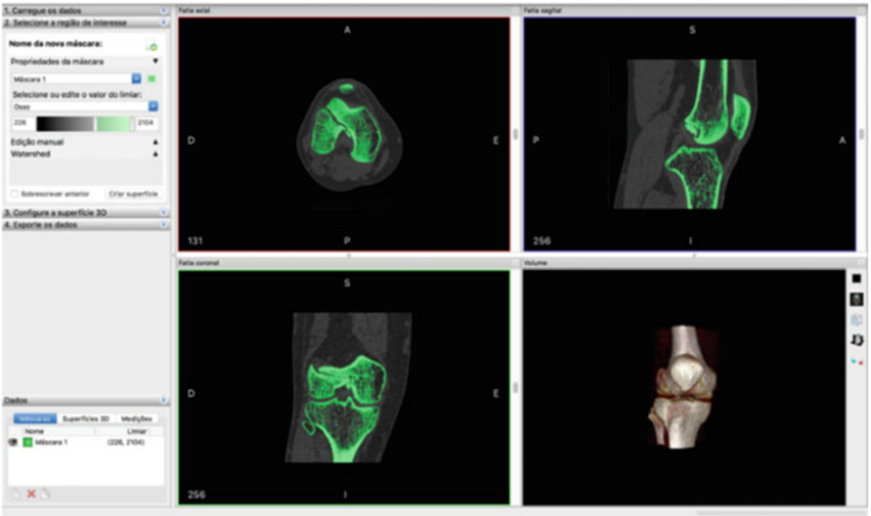

Fig. 14.2 Screen image of the Invesalius v3.1.1 software showing the bone segmentation. After the segmentation process, it was created a mask that appear in green. The automatic segmentation of the bone was performed using an algorithm with the Hounsfield´s scale of 226–2014. In the same image the 3D object created from the DICOM data is shown

pressure is defined as zero (0) Hounsfield unit (HU), while air radiodensity in normal temperature and pressure conditions is defined as −1000 HU. The scale is commonly used between −1000 HU and 3000 HU. Some authors consider that cortical bone is reported to exhibit HU values around 150–1800. These values depend on the sex, age, and health of the bone tissue (Green et al. 2016). The segmentation can be performed manually or through algorithms created for this purpose (Chen et al. 2016). Besides this, bone segmentation can be performed using an automatic algorithm program or manually identifying bone tissue in the thresholding window using the HU. Usually, the software creates a mask to identify the segmented tissue (Fig. 14.2).

According to Eijnatten et al. (2018), threshold determination (thresholding) continues to be the most widely used segmentation method in the manufacture of 3D prints in the medical field. The manual threshold determination is still the best method for transforming the volume reconstruction in STL files (the most used format for manipulating 3D images) according to Rankin et al. (2018).

Van Eijnatten considers this as the most critical and most in-demand phase in the 3D printing process since the generation of low-resolution 3D images can generate low accuracy object printing (Eijnatten et al. 2018). Similarly, the segmentation and mesh generation process can generate significant accuracy between the original DICOM data, and the 3D model generated. It is important to compare the processed data from the area interest with the original images in DICOM format, at each stage to ensure that it remains a true anatomical representation according to Marro et al.

(2016). Some software used to perform the segmentation of CT images are OsiriX, Horos, Invesalius and 3D Slicer.

3D File Formats

After segmentation, the surface is extracted from the volumetric data converting the voxel data into a mesh formed of a series of triangular facets (Marro et al. 2016). That is, there is a conversion of 2D images into 3D images, for the possibility of editing the three-dimensional object (Eijnatten et al. 2018; Eley 2017). At this moment, there is a three-dimensional reconstruction of the images. Currently, the most commonly used file format in medical 3D printing is Stereolithography File (with .STL extension) (Eijnatten et al. 2018). In this format, the object can be manipulated, and the necessary adjustments can be made allowing geometry editing for printing. The process of converting files in DICOM format to 3D volumetric tests templates is one of the biggest causes of inaccurate production of AM in the medical field, according to Van Eijnatten et al. (2018).

There are many types of 3D file formats to perform modeling and rendering besides STL format e.g., Additive Manufacturing File (with the .AMF extension), Wavefront 3D Object File (with the .OBJ extension), and 3D Manufacturing File (with the 0.3MF extension).

14.3 Computer-Aided Design (CAD)

14.3.1 Postprocessing Images—Modeling and Rendering

The selected volume in a 3D file format is then processed to remove unwanted parts and to improve the smoothness of the surface of the object, to make the object as close to the real situation. For this purpose, software with CAD technology is normally used. The most used programs for rendering 3D virtual objects are Mimics, Magics, Meshmixer, Meshlab, Rhinoceros 3D, Blender, and Catia. The use of these CAD software allows the rendering of the virtual bone model with the correction of imperfections and irregularities of the surface and the proper separation of the bone fragments for virtual surgery. The more accurate the segmentation, less distortion or imperfections of the object is generated with less need to correct surface irregularities in the rendering and modeling of the virtual object (Fig. 14.3).

After segmentation and modeling using the data processed within the creation of the 3D object (e.g., virtual bone model) it is possible performing surgical planning, carrying out the study of the spatial geometry of the site (anatomy), performing virtual surgery with resection of parts (e.g., in oncologic surgery), implant placement simulation (e.g., implants and prostheses) (Chen et al. 2016) and repositioning/reduction of fracture fragments (Fig. 14.4).

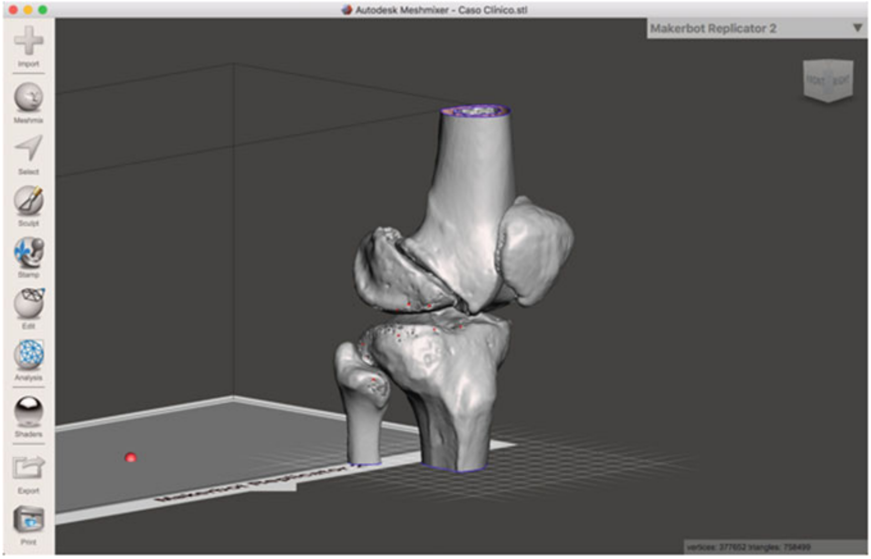

Fig. 14.3 Screen image of the Meshmixer v3.5 software showing the bone modelling (distal femur and proximal tibia)

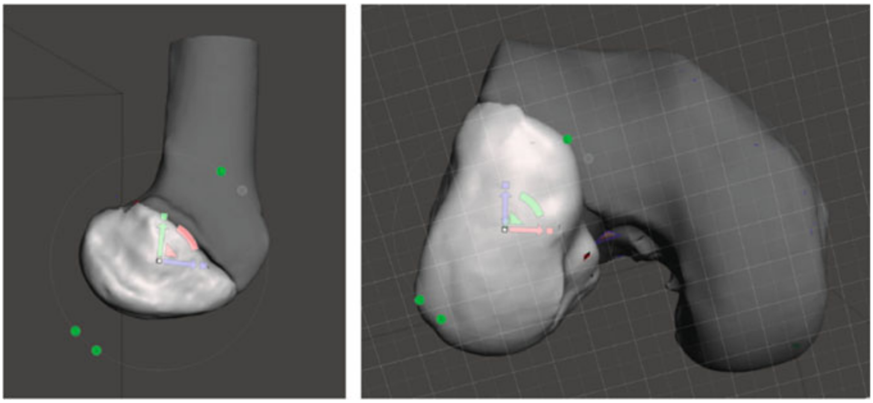

Fig. 14.4 The Virtual Surgical Planning (VSP) with the reduction of the Hoffa's fracture nonunion fragments

14.3.1.1 Mesh Generation

Due to the complexity of geometry and CT resolution, it is necessary to form a mesh to define the places where there are gaps so that they would be corrected with image editing methods, making the surface of the object as smooth as possible (Bagaria and Chaudhary 2017) (Fig. 14.5). The figure shows a screen image of the Meshmixer

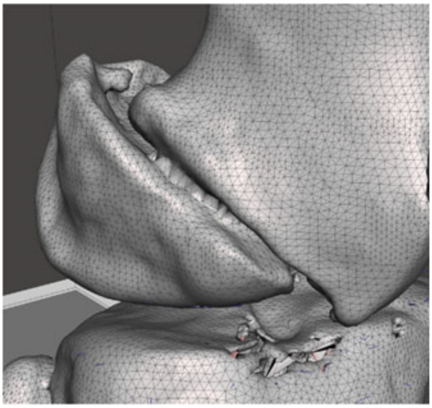

Fig. 14.5 Screen image of the Meshmixer v3.5 software showing the space between the nonunion fragments. A mesh was created to better understand the irregularities and flaws on the surface of the object and to facilitate the later correction of these flaws

v3.5 software where a mesh was created to better understand the irregularities and flaws on the surface of the object and to facilitate the later correction of these flaws.

14.3.1.2 Cleaning

It is often necessary to remove artifacts that make the object irregular and with deformations on the surface created after the segmentation. Other kinds of artifacts are bridges between near surfaces and components. (e.g., connections across the joint or gap fracture) (Green et al. 2016). Some artifacts are due to metallic materials implanted on the patient's body. The spatial smoothing method normally used is an algorithm to reduce these artifacts without losing anatomical information (Bagaria and Chaudhary 2017).

14.3.1.3 Smoothening

Smoothing is the process of making the surface of the object more regular and natural while trying to maintain the original geometry. Manual image smoothing and smoothing algorithms are used to improve the definition and quality of the 3D image to be printed (Bagaria and Chaudhary 2017; Favier et al. 2017). In many cases, there is a need to smooth the surface of the 3D object before printing or during the creation of cut and drilling guides and surgical simulation.

14.3.2 Virtual Surgical Planning (VSP)

Kim et al. (2018) in their study reports the clinical experience with the use of 3D printing techniques in orthopedic trauma, with the following applications:

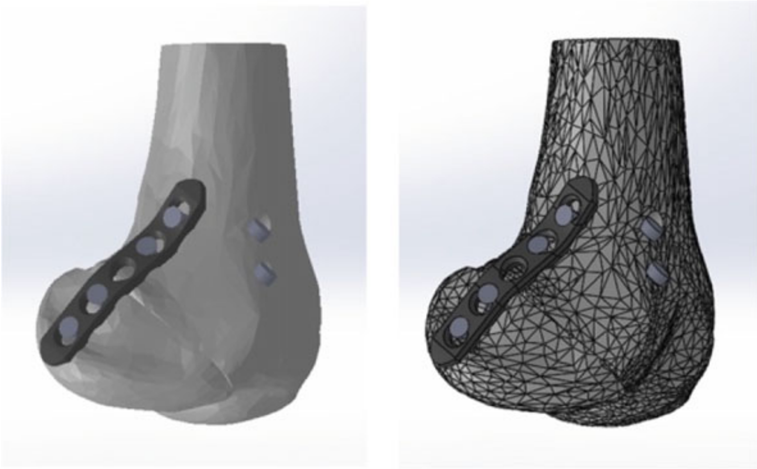

Fig. 14.6 The reduction and Hoffa's fracture nonunion fixation with plate and screws. During VSP, it is possible to choose the best position for the implants in lateral surface of femoral condyle

1. A better understanding of the fracture and anatomical relationships;
2. Preoperative planning;
3. Medical education;
4. Training and surgical simulation.

Preoperative analysis can currently be one of the most common and important applications of useful 3D printing technology. Surgical procedures in areas of complex anatomy with a high damage risk to noble structures (vessels blood and nerves) benefit from rapid prototyping (Rankin et al. 2018). Several CAD software showed before in 14.3.1 item currently allow the performing of VSP with a better understanding of spatial geometry, anatomical relationships mainly in places of complex anatomy, and the possibility of programming less invasive surgical procedures and in the case of orthopedic trauma surgery, and the previous reduction of bone fragments simulating definitive osteosynthesis (Fadero and Shah 2014; Frizziero et al. 2021; Tappa et al. 2019) (Fig. 14.6). The figure depicts the reduction and fracture nonunion fixation with plate and screws. During VSP, it is possible to choose the best position for the implants in lateral surface of femoral condyle.

14.3.3 *Orthopedic Implant Designing*

Additive Manufacturing has great potential for customized implants in the orthopedic application. The fabrication of Patient-Specific Implants (PSI) is the most feasible example of this technology. The implants such as plates and screws, nails, prosthesis

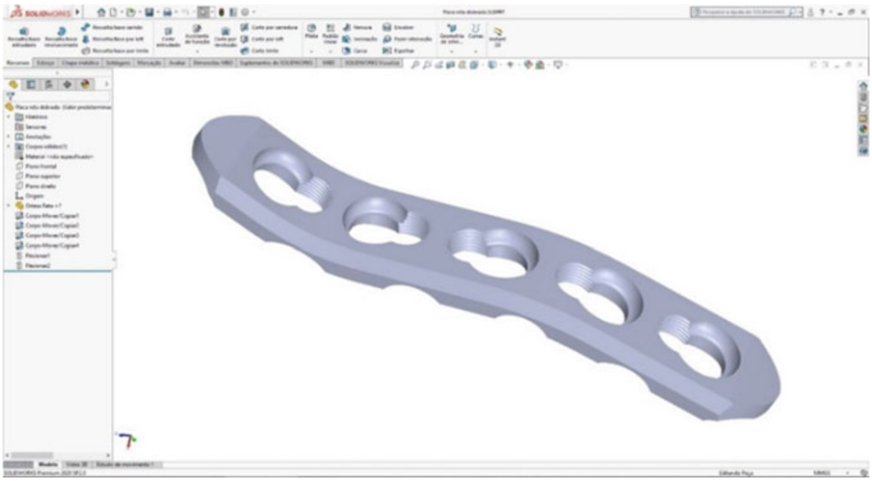

Fig. 14.7 Image of customized implant design using the CAE software SolidWorks

(conventional or unconventional), and endoprosthesis made with 3D printing technology are called PSI since they are personalized (custom made), and they can be used in traumatic situations, in bone loss treatment, or replacement joints in orthopedic surgeries (Tappa et al. 2019; Belvedere et al. 2019; Rathor et al. 2021). For modeling, 3D constructs (implants or prothesis) are necessary to use specific CAD software to design the project accurately. In a CAD environment is it possible to make changes and adjusting the design and make sure about the adaptation of implant or prosthesis to bone geometry (Yan et al. 2020).

The use of PSI technology is an important tool to solve complex bone destructions that require bone loss treatment in severe fractures and oncological bone resection (Tetsworth et al. 2017; Wong et al. 2015). To design PSI in orthopedics these are the currently used software e.g., SolidWorks, Creo Parametric, Autodesk Fusion 360, Autodesk Inventor, Materialise Magics. Figure 14.7 is showing an image of customized implant design (plate) using the CAE software SolidWorks.

14.4 Computer-Aided Engineering (CAE)

The CAE software is an important resource that 3D virtual model volumes may be discretized and analyzed by simulation in silico using the finite elements method (FEM). It is possible to perform the static and dynamic analysis, measure the forces acting in the bone, in the implant, and the bone-implant interface. Thus, it is feasible to measure the stress forces (compression and distraction) and material strain of all-system bone-implant. This kind of analysis is important to define the best mechanical and geometrical characteristics of the 3D printed personalized implant.

14.4.1 Finite Element Analysis (FEA)

The numerical solutions to solve structural mechanical problems are important resources in biomechanics mainly in orthopedic implant projects. Due to the advances in biomechanical studies using CAE technology, it is possible to reach a high level in correlations between computational tests and experimental mechanical assay arriving at 95% (Wieding et al. 2012). An important advantage of Finite Element Analysis (FEA) is that it can analyze the complex geometry of the model and obtain detailed data from the 3D model. During the computational simulation of the project, it is possible to measure the strain levels during different loading conditions analyzed using the FEA. This kind of analysis helps designing orthopedic implants with more mechanical effectiveness and with more accurate anatomical design (Rathor et al. 2021; Yan et al. 2020).

Some software used to perform the FEA in the orthopedics area are SolidWorks, Altair Hypermesh, Abaqus, and Ansys. Figure 14.8 is showing the FEA using the CAE software (Ansys 16.0) to analyze deformation and loads that act in the bone-implant system. During FEA performing it is possible better understanding the osteosynthesis mechanical behave. This analysis showed that the chosen implant demonstrated mechanical resistance to promote bone healing.

14.5 Computer-Aided Manufacturing (CAM)

The bone model created through the acquisition and segmentation methods must be suitable for printing while maintaining the characteristics and dimensions of the real object. Usually, files in the STL and AMF format are then loaded into the slicing that prepares the file for printing by converting it to GCode, numerical control programming language, a universal code to send position, and extrude commands to 3D printers (Rankin et al. 2018). The printing of 3D objects of complex shapes can require different characteristics of solidity and porosity (Mulford et al. 2016).

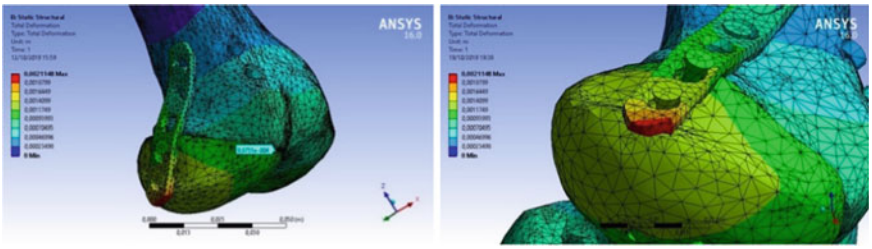

Fig. 14.8 Images showing the FEA using the CAE software (Ansys 16.0) to analyze deformation and loads that act in the bone-implant system. During FEA performing it is possible better understanding the osteosynthesis mechanical behave. This analysis showed that the chosen implant demonstrated mechanical resistance to promote bone healing

The most used CAM environment software for generating GCode and printing 3D models with FDM technology in desktop printers are Makerbot Desktop, Cura, Slic3r, Repetier-Host.

14.5.1 Printing Technologies

14.5.1.1 Fused Deposition Modeling (FDM)

The FDM uses the technique of layered deposition of a polymer heated through an extruder nozzle, layer by layer (Hoang et al. 2016), which immediately hardens after extrusion to form solid layers, making three-dimensional objects with geometric high definition. A filament of material normally thermoplastic or metal wire feeds the nozzle head extruder that heats the filament and expels it, turning it off and on, forming the successive layers (Bagaria et al. 2018).

This technique requires support for the printing of the structures (Marro et al. 2016). Print speed is low, and the print resolution is lower than the SLS technique (Wong et al. 2017; Malik et al. 2015). With FDM technology, it is necessary to consider the small amount of shrinkage that occurs with plastics when they cool to room temperature, around 0.5%, which can be surpassed by the preventive dimensioning of the model (Eley 2017). In this technique, the layer width can be up to 7 μm with an X/Y resolution of up to 2.8 μm (Hoang et al. 2016).

Currently, the most widespread use of the FDM technique in orthopedic surgeries is anatomical models (Marro et al. 2016) as depicted in Fig. 14.9. The figure presents an images of the 3D printed bone model with FDM technology in white ABS, distal femur and fragment of the lateral femoral condyle.

Fig. 14.9 The 3D printed bone model with FDM technology in white ABS, distal femur and fragment of the lateral femoral condyle

The main advantages of FDM for printing biomaterials with making scaffolds are high porosity due to the deposition pattern and good mechanical resistance. A challenge for FDM is the limitation for thermoplastic materials with good melt viscosity properties that have high enough viscosity to build, but low enough for extrusion (Chia and Wu 2015). The materials used in this technique are Acrylonitrile Butadiene Styrene (ABS), Polylactic Acid (PLA), Polyamide, Polycarbonate, Polypropylene, Polyester, and some types of waxes (Hoang et al. 2016).

14.5.1.2 Lithography-Based 3D Printing

This technique is known as vat photopolymerization technology and has three main types: Stereolithography (SLA), Digital Light Processing (DLP), and Continuous Digital Light Processing/Continuous Liquid Interface Production (CDLP/CLIP) (Pagac et al. 2021).

The SLA is a fast and very accurate technique for manufacturing 3D objects by which a computer controls a beam of ultraviolet (UV) laser for the polymerization of liquid resin from the surface to the depth forming successive layers. The polymer is contained in a container whose movement of descension, or ascension is controlled by the program printing. The photopolymer is transformed into semi-solid with heat and then it hardens ("cure"). The entire process uses the triangulated UV laser on the surface using scanning mirrors on the X and Y axis (Bagaria et al. 2018). The kinetics of the healing reactions that occur during polymerization is critical. This affects the curing time and the polymerized layer width. The kinetics can be controlled by the power of the light source, the scanning speed, and the chemistry and quantity of the monomer. Also, UV absorbers can be added to the resin to control the depth of polymerization (Chia and Wu 2015). In this technique, the width of the layer can be up to 2 μm with an X/Y resolution of up to 4 μm (Hoang et al. 2016).

The printing materials most used in resin 3D printing techniques are limited to photopolymers such as Epox and acrylic resins, which can have a high cost (Marro et al. 2016). In the DLP technique, a digital light projector is used to cure the resin, flashing images of whole layers onto the bottom of the tank. A digital light projector is used instead of a mirror to reflect a laser source used in SLA technology to cure the resin. The printing accuracy depends on projector resolution (Pagac et al. 2021).

The CDLP/CLIP technology flashes complete layers at the resin tank, employing digital projection from LEDs. Due to continuous movement of the build platform, is possible to print undisrupted prototype with high speed.

The advantages of the resin 3D printing technique are the ability to create complex shapes with internal architecture (with tubular shapes, lattices). It is possible to easily remove unpolymerized resin and obtain extremely high resolution and highly accurate models with smooth surface finishes. The main disadvantage of the 3D printing technique is the scarcity of biocompatible resins with suitable SLA, DLP, and CDLP/CLIP processing properties (Chia and Wu 2015). In the case of the DLP technique "zoomed out" effect (low accuracy printing process to print big objects) can occur.

The DLP and CDLP/CLIP techniques benefit compared to SLA is building speed, because the entire layer is flashed at once in this technology, instead of a single point in SLA technology. Currently, using this kind of technology is being used in researches in 3D bioprinting and bioinks for bone repair and regeneration (Liang et al. 2021; Luo et al. 2020).

14.5.1.3 Selective Laser Sintering (SLS)/Selective Laser Melting (SLM)

The SLS uses a high-quality CO_2 laser power to sinter a thin layer of powder particles into layers to form the model. The laser draws the shape of the desired object merging it with the layer below; successively layers of the powder are spread over the previous ones, covering them after the laser action on each layer. It can be used to create an extremely precise representation because the precision is limited only by the laser, the powder fineness/granulation of the raw material, and layer thickness. The most used materials are thermoplastics (polycarbonate, polyamide, nylon), metals, glass, or ceramics (Hoang et al. 2016). Selective laser fusion, also known as SLM, is a subtype of SLS being used mainly for printing metals and implant manufacturing. Both SLS and SLM have high resolution and high cost (Hoang et al. 2016; Bagaria et al. 2018).

An advantage of SLS and SLM over other processes of 3D printing is that they do not require support structures during the printing of the models because the objects are supported on the powder. With other printers, support structures are sometimes necessary to prevent the model from collapsing in weak spots. These support structures can be removed manually after the model has been printed. In the SLS and SLM process, they usually leave a rough surface that may require polishing. The surface finish with SLS can be difficult, requiring more post-processing than other methods (Marro et al. 2016).

The SLM and Direct Metal Laser Sintering (DMLS) are the most popular 3D metal printing technologies. Both use a laser to scan and then selectively melt the metal dust particles that bond to each other in layers. The main difference between the two technologies is the ability to print different materials. Both techniques have less than 5% waste of raw material. Although SLM can print just a single metal, DMLS allows printing multiple alloys, just like powder with variable melting points can also fuse at the molecular level in this specific technology. The height of the layer for printing a 3D metal object varies between 20 and 50 μm and depends on the properties of the raw material, such as flow capacity, particle size, shape, and distribution. Modern metal printing standards have an accuracy of less than 100 μm, making them ideal for printing orthopedic implants that need high precision (Bagaria et al. 2018). According to Hoang, in the SLS technique, the layer width can be up to 4–6 μm with X/Y resolution of up to 30–50 μm, while using the DLMS technique layer width can be up to 0.8–1.2 μm with X/Y resolution of up to 12–16 μm (Hoang et al. 2016).

Chia and Wu (2015) in their review of advances in the use of biomaterials in 3D printing reported the use of non-metallic materials printed with the SLS technique such as previously coated ceramic thermoplastics, a mixture of polyvinyl alcohol (PVA) with hydroxyapatite (HA) and polyetheretherketone (PEEK) used for making personalized implants. In these techniques, it is possible to reuse the powder that has been used before, and it is necessary to process it again to allow a new use.

14.5.1.4 Electron Beam Melting (EBM)

A similar process to SLS is the EBM. In this process, what melts the dust is a laser electron beam, powered by high voltage, typically 30–60 kV. The process takes place in a high vacuum to avoid oxidation problems, as it is intended for the construction of high-precision metal parts. Other than that, the process is very similar to SLS. EBM can also process a wide range of pre-connected metals (Wong and Hernandez 2012). This AM technique allows the manufacture of personalized prostheses (such as hip or knee prostheses, endoprosthesis) of metal alloys.

14.5.1.5 Inkjet

In the inkjet printing technique, a print head creates droplets of a liquid binding agent, which are combined with a substrate in powder. Droplets are created using a variety of technologies, such as piezoelectric, electromagnetic, or thermal methods to be distributed on a substrate (Marro et al. 2016). Changing the applied temperature gradient, pressure, frequency of the pulse, and ink viscosity, the droplet size can be modified to different applications in the medical field (Mok et al. 2016). Like SLM, inkjet printing does not require the use of support structures. Besides, they create relatively fast, low-cost models. However, in general, parts are not as durable as those manufactured with the SLS technique. An application of inkjet technology has been used in the bioengineering of 3D printed tissue. Instead of a liquid, the head printing deposits the living cells in scaffolds (Marro et al. 2016).

According to Chia and Wu (2015), the main advantages of bioprinting are room temperature processing (if applicable), direct incorporation, and homogeneous cell distribution. The main disadvantages are stiffness limited mechanics, the critical gelling time delay, the specific correspondence of the material, and the densities of the liquid medium to preserve shapes and low print resolution.

14.5.2 Materials

Various compounds, including photopolymers and thermoplastics, were and are being developed for application in 3D printing technology in the medical area due to cost reduction, good resolution (20–100 μm), and easy use (Rankin et al. 2018). Various types of materials are used for 3D printing in orthopedic surgeries such as metals, natural and synthetic polymers, bioceramics, and biomaterials (Marro et al.

2016; Mok et al. 2016; Chen et al. 2016; Tang et al. 2021). Currently, the most used materials in the printing of models in orthopedic surgery are:

1. Acrylonitrile Butadiene Styrene (ABS) is a rigid and lightweight thermoplastic, resistant and non-toxic, with a melting point of approximately 210 °C to 250 °C. Derived from petroleum, it is not biodegradable, it can release vapors during printing (Fadero and Shah 2014). Used in bone model printing for education, training, and surgical planning (Bagaria and Chaudhary 2017) (Fig. 14.9);
2. Polylactic Acid (PLA) is a thermoplastic of vegetable origin (starch), it has a melting point of approximately 210 °C to 250 °C (Hoang et al. 2016). PLA is easy to print, is biocompatible and biodegradable, but its strength degrades over time and the print has a certain texture roughness (Bagaria et al. 2018). It is used in printing of bone models and printing of surgical guides (Mok et al. 2016). PLA is brittle and has low mechanical resistance;
3. Polyetheretherketone (PEEK) is used in the manufacture of implantable medical materials because it is biocompatible and biodegradable. Devices made with such material may show greater similarity to bone strength, stiffness, and elasticity. Also, it provides better patient comfort compared to titanium, exhibiting less thermal conductivity and lower density. Radiolucency is often cited as a great benefit for the improvement of the postoperative image which is particularly valuable in cancer cases. This material is suitable for intraoperative format adjustments as it allows the removal of part of the material (Peel et al. 2017);
4. Nylon/Polyamide is a resistant and low-cost synthetic polymer, but it requires high temperature for modeling (210 °C to 250 °C) (Bagaria et al. 2018). Used in the printing of anatomical bone models for surgical programming and simulation, as well as surgical guides;
5. Polycarbonate is used in the printing of bone models for education, training, and surgical planning.

As for metal printing, several materials are approved for printing implants and prostheses such as Stainless-Steel alloys (AISI 316L), Titanium alloys (Ti4ALV6), Tantalum (TA), and Chrome-Cobalt (CrCo).

14.6 Application of 3D Printing Technology in Orthopedic Surgery

The use of 3D printing technology is growing exponentially in various areas of medicine including orthopedic surgery. According to orthopedic literature, the biomedical use of technology 3D printing has four important uses (Bagaria et al. 2018):

1. Anatomical models printing;
2. Guides and Surgical Templates printing (cutting and drilling guides);
3. Implants, Prostheses, and Orthoses printing;

Table 14.2 Advantages and disadvantages of using 3D printing in surgeries (Martelli et al. 2016)

	Advantages	Disadvantages
Preoperative planning	Better anticipation of surgical difficulties with complex anatomy and direct visualization of malformations	Additional preparation time during the planning and production of the 3D model
Accuracy	Great precision of the surgical guides Improvement in intraoperative positioning of surgical guides	Possible distortions between the 3D model and the real object due to the resolution of medical images
Surgical time	Decrease	
Risks and complications	Decreased the radiological exposure during surgery Decrease incidence of postoperative complications such as blood loss and infection	Increased patient's radiological exposure on imaging studies Allergic reactions due to waste materials used (polymers)

4. Scaffolds and cell printing.

In some situations, in the treatment of orthopedic problems the technology 3D printing has been used according to Bagaria et al. (2018):

1. Periarticular and fractures of the hip, knee, ankle, shoulder, and elbow;
2. Complex arthroplasties with bone defects;
3. Complex spinal deformities;
4. Deformities and fractures of the face;
5. Deformities and changes due to congenital malformation;
6. Planning for osteotomies.

Martelli et al. (2016) on a systematic review about the advantages and disadvantages of using 3D printing in surgeries describe them according to Table 14.2.

14.6.1 Biomodel Printing

The manufacture of anatomical models is currently the largest application of this type of 3D printing technology for the versatility of possibilities of use in several medical areas. One possibility of using the anatomical model includes patient-relative orientation. Regarding the communication between the medical team and the patient, some studies demonstrate the use of anatomical models to inform about the type of surgical treatment proposed, promoting a better understanding of the clinical condition of patients, surgical schedule, rehabilitation, and greater adherence to treatment, contributing to an improvement in the doctor-patient relationship (Zheng et al. 2018a, b; Bizzotto et al. 2015; Tack et al. 2016; Wilcox et al. 2017; Chen et al. 2019; Yang et al. 2016a, b).

14.6.1.1 Medical Education

The 3D printed anatomical models are a promising means of medical education for students in health sciences, resident doctors, and an improved form of communication with patients (Zheng et al. 2016).

Some works show the use of 3D-printed anatomical models in surgical training. A wide variety of domains including simulation accuracy, anatomical similarity, training in the use of surgical instruments use printed models for the training of surgeons (Hoang et al. 2016; Tack et al. 2016; Langridge et al. 2018). The use of 3D printing technology in the teaching process of health professionals has complemented, or even traditional teaching methods have been supplanted. Concerning the acquisition of knowledge of anatomy according to some studies as shown in the paper review by Langridge et al. (2018). This author reports that a 3D-printed anatomical model offers "feedback" that can facilitate the acquisition of surgical skills, accelerating the learning curve in some training models (Hoang et al. 2016; Zheng et al. 2016; Langridge et al. 2018).

Several studies have shown the effective application of the use of 3D printing technology in medical education and orthopedic training (Shui et al. 2017; Marro et al. 2016; Eley 2017; Mulford et al. 2016; Malik et al. 2015; Langridge et al. 2018; Bagaria et al. 2011; Cromeens et al. 2017) mainly associated with surgical procedures in complex anatomical regions. Huang et al. (2018) concluded in their study about the acetabular fracture surgical training with the aid of 3D anatomical models that the 3D printing technology was the most valuable tool for understanding this type of fracture. The data demonstrated that 3D-printed models of real fractures are an effective tool in learning the morphology of the acetabulum and promote student interest.

14.6.1.2 Preoperative Planning

The printing of biomodels provides additional information to conventional images with increased knowledge concerning the anatomopathology of the disease to be treated (Vaishya et al. 2018; Marro et al. 2016; Zheng et al. 2016; Bagaria et al. 2011; Zhang et al. 2017a, b).

An accurate navigation technique is essential for transferring the 3D preoperative surgical planning to the patient during surgery. Kim et al. (2018) in their study concluded that the 3D printing technique provided surgeons with a better understanding of the fracture pattern and anatomy and it was effectively used for preoperative planning, educating interns, and performing surgical simulations to improve the intraoperative technical results. Some studies have shown that 3D printing technology in planning and carrying out surgical procedures leads to a decrease in the surgical time (Bagaria and Chaudhary 2017; Malik et al. 2015; Tack et al. 2016; Zheng et al. 2016; Giannetti et al. 2017; Mobbs et al. 2018; Yang et al. 2016a, b; Ozturk et al. 2020), decreased blood loss during surgery (Bagaria and Chaudhary 2017; Mobbs et al. 2018; Yang et al. 2016a, b; Ozturk et al. 2020), decrease in time of exposure to ionizing radiation during the surgical procedure (Tack et al. 2016; Giannetti et al. 2017; Mobbs et al. 2018; Yang et al. 2016a, b; Ozturk et al. 2020), reduction of complications (Bagaria and Chaudhary 2017; Martelli et al. 2016; Kaye et al. 2016), a decrease of tourniquet time (Ozturk et al. 2020) and likely improvement in surgical results (Bagaria and Chaudhary 2017; Tack et al. 2016; Zheng et al. 2016).

Regarding the decrease in surgical time, Wilcox et al. (2017) in their systematic review reported that the reduction in surgical time was 15–20% in various scenarios of surgical procedures. The highlighted reasons given for reducing the time of surgery included a deeper understanding of pathologies, such as location and surgical approach, and the facilitation of preoperative instrumentation decisions. In a recent publication, Morgan et al. (2020) in systematic review and meta-analysis have concluded that their results suggest the use of 3D printing in pre-operative planning in orthopedic trauma reduces operative time, intraoperative blood loss, and the number of times fluoroscopy used.

One controversial point in orthopedics literature is the improvement of results using 3D printing in orthopedic surgery. Langridge et al. (2018) show in their study works suggesting that surgical planning with 3D technology leads to a better understanding of the anatomy which can lead to better surgical results.

However, there is no consensus in the orthopedics literature to improve the surgical result, in general, using 3D printing technology in orthopedic surgery and further trials are needed to highlight this aspect.

14.6.1.3 Preoperative Simulation

A preoperative simulation of a surgical procedure allows the prior evaluation and reproduction of complex operative stages, without suffering the time restriction of a real procedure. An effective surgical simulation requires faithful anatomical reproduction and must also behave similarly to the tissue of the patient (Rankin et al. 2018). This way 3D printing is useful in surgical simulation, surgical planning, in referencing the anatomical structures in the intraoperative step, in the preoperative choice of implants and guides to be used (Shui et al. 2017; Martelli et al. 2016; Van den Broeck et al. 2014; Zhang et al. 2017a, b; Trauner 2018) mainly regarding the understanding of geometry (distances, scales, shapes) and identification of complex anatomy (Vaishya et al. 2018; Shui et al. 2017; Marro et al. 2016; Mulford et al. 2016; Fadero and Shah 2014; Hoang et al. 2016; Wilcox et al. 2017; Langridge et al. 2018; Cromeens et al. 2017; Zhang et al. 2017a, b). Other advantages are a better choice of access to bone defects, a better understanding of the fracture pattern, and better choice in the positioning of bone implants (Zheng et al. 2018a, b; Vaishya et al. 2018; Bagaria and Chaudhary 2017; Eijnatten et al. 2018; Tetsworth et al. 2017; Karlin et al. 2017; Chana-Rodríguez et al. 2016; Huang et al. 2020; Cai et al. 2018) as depicted in Fig. 14.10.

Fig. 14.10 3D printed bone model fixated with the plate and screws on the anatomical model (lateral side of distal femur)

According to Malik et al. (2015), a lot of time is spent intraoperatively to measure and bending the implant before placement during surgery to treat acetabular fractures. When performing the steps of reduction and positioning of the implant in a 3D model preoperatively, valuable time is saved during the procedure surgical, as the surgeon has more time to focus on the approach, reduction, and correction; that is, the choice of implant and preoperative bending of the implant is carried out in a free of stress environment before the procedure. In a study on osteotomy using 3D printing technique in the treatment of tibial plateau fractures malunion, Yang et al. (2016a, b) performing virtual surgical planning and using an anatomical model in scale reported an improvement in the understanding of the deformity for osteotomy programming with surgical simulation using the anatomical model (osteotomy, reduction of joint sinking and fixation with plate and screw). They report that with this technique they successfully reproduced preoperative planning with reduced surgical time, little loss of intraoperative blood, and accuracy in reducing collapse of the joint surface. These authors list the advantages of assisted surgery with 3D printing techniques compared to traditional surgery methods: Full-scale anatomical models improve understanding of the anatomy and morphology of the deformity such as details of the location, diversion, and sinking. Important details in planning the osteotomy location. Individualized surgical planning, with the possibility of less damage to soft parts due to the precise choice of surgical access and accuracy in reduction of deformity with less surgical time. The technique does not require sophisticated instruments and keeps the cost relatively low when printing the anatomical model.

The use of 3D printing technology in preoperative surgical planning has been shown to facilitate the procedure with satisfactory results, especially in complex articular fractures of the spine, pelvis, acetabulum, and sacro (Bagaria and Chaudhary 2017; Fadero and Shah 2014; Bagaria et al. 2011; Huang et al. 2020; Courvoisier et al. 2018; Zeng et al. 2016), knee (Kim et al. 2018; Bagaria et al. 2011; Giannetti et al. 2017), tibial plateau (Zheng et al. 2018a, b; Ozturk et al. 2020), tibial pilon (plafond) (Zheng et al. 2018a, b), ankle (Yang et al. 2016a, b), calcaneus (Fadero and Shah 2014; Bagaria et al. 2011), clavicle (Shon et al. 2020), shoulder and elbow (Zheng et al. 2018a, b; Kim et al. 2018) and distal radius (Bizzotto et al. 2015; Chen et al. 2019).

The utilization of the 3D anatomical model in preoperative planning allows the study and better understanding of anatomy, especially in articular and periarticular joints; improved visualization of specific fracture details confirming the pattern of fractures; better determining the displacement/deviation and the number of fracture fragments; better confirming the collapse and comminute condition of the joint surface; better checking the potential presence of bone defects; better determining whether the graft is needed. This type of virtual planning allows fracture fragments reduced in the best possible way and the most appropriate implants chosen and used, in addition to the possibility of the best choice of approach surgery at the injury site (Fadero and Shah 2014; Zheng et al. 2018a, b). VSP combined with 3D printing technology allows the surgeon to view the entire preoperative reduction process and guide intraoperative reduction, making the reduction less time-consuming and more precise (Giannetti et al. 2017; Ma et al. 2017) with less chance of surgical complications (Zheng et al. 2018a, b) (Fig. 14.11). It also allows adequate planning of percutaneous fixings in situations of irregular bone fractures (Fadero and Shah 2014).

The 3D anatomical models of complex joint fractures increase considerably the number of important information needed for the appropriate treatment compared to radiographic and CT images. This one benefit that 3D printing favors are also dependent on the experience of the surgeon according to Bagaria and Chaudhary (2017). For the treatment of unilateral severe fractures of the lower limbs, Zhang et al. (2017a, b) described a technique for mirroring CT images of long bones for programming fracture reduction and programming of the implants to be used.

In his study on the use of 3D technology in the treatment of humeral intercondylar fractures, Zheng et al. (2018a, b) made a comparison between the group control that was submitted to conventional treatment and the group submitted to surgical treatment using 3D technology in preoperative planning (virtual surgery and anatomical model printing) and found a statistically significant difference in the following aspects: duration of surgery, blood loss, fluoroscopy time. The group submitted to treatment with the use of 3D technology showed a lower index in these three aspects with a value of $p < 0.001$. However, there was no statistical difference regarding the length of consolidation and clinical results.

In a randomized, single-blinded, prospective clinical trial conducted to evaluate the efficacy of using 3D printing in the treatment of distal radius fracture Chen et al. (2019) concluded in their study that 3D printing models effectively help the doctors plan and perform the surgery and provide more effective communication

Fig. 14.11 Complete surgical wound healing after 3 weeks postoperative and the motion range of the right knee joint close to normal (**a**, **b**, **c**). One-year postoperative X-ray images showing nonunion healing with anatomical reduction and restored articular surface. The implant positioning performed during the surgery was according to preoperative VSP (Fig. 14.9) and the preoperative surgical simulation (Fig. 14.10) (**d**, **e**)

between doctors and patients, but cannot improve postoperative function compared with routine treatment.

Considering the anatomical complexity of acetabular fractures, several studies have reported the benefits of 3D printed models with preoperative planning (Bagaria and Chaudhary 2017; Kim et al. 2018; Fadero and Shah 2014; Malik et al. 2015; Bagaria et al. 2011, Courvoisier et al. 2018; Zeng et al. 2016). The use of technology of AM in the treatment of acetabular fractures provides the study of accurate fracture morphology; performing VSP; allows for a better choice surgical approach; pre-bent (pre-contoured) of implants with greater accuracy in their positioning (Courvoisier et al. 2018; Maini et al. 2018). Huang et al. (2020) in their study described a minimally invasive technique with an anterior approach combined with 3D printing for anterior plate fixation of the sacral fracture using VSP and preoperative simulation surgery for pre-bent implants. This author described that the postoperative x-Rays images have shown that the sacral fractures of all cases (12 patients) were successfully reduced and internally fixated.

Some authors have described the use of AM technology in the treatment of fractures of the tibial plateau. Giannetti et al. conducted a study whose proposal was to compare the surgical time, intraoperative blood loss, and postoperative clinical and radiographic results in the treatment of complex tibial plateau fractures operated with and without the pre and intraoperative use of real anatomical models of fractures printed in 3D. They concluded that patients operated with the aid of anatomical models printed with the 3D technology have seen a significant reduction in the time of surgery. However, in surgeries of patients operated without the use of anatomical models, there was an increased time of exposure to ionizing radiation (Giannetti et al. 2017). Huang et al. (2018) in a series of 6 cases submitted to surgical treatment of tibial plateau fracture performed preoperative planning with fracture reduction and positioning of the plate and screws, and 3D surgical guides were printed (PSI) according to the planning for positioning the screws and the board. Deviations in the positioning of the screws were evaluated before and after surgery comparing size, entry point, and direction of screws. They reported that there was no statistical difference in terms of size, entrance, and the projection of the ideal and real angle of the direction (trajectory) of the screw. They concluded that this technology increases the accuracy and efficiency of internal fixation using PSI. In their study, Ozturk et al. (2020) concluded that the use of the 3D life-size anatomical models assisting surgical planning maximized the possibility of ideal anatomical reduction and provided individualized information concerning tibial plateau fractures.

Zheng et al. (2018a, b) in their study on the feasibility of 3D printing in the treatment of tibial pilon (plafond) fracture and its effect on doctor-patient communication carried out a prospective study (100 patients) randomized into two groups: one group undergoing conventional treatment and another group undergoing treatment with the use of 3D printing technology. The latter group was subjected to virtual planning and virtual simulation of fracture reduction with mirroring of the contralateral side. The printing of the anatomical model and surgical simulation using an anatomical model printed in full scale for choosing and modeling of implants was also used. The statistical analysis of data was of the double-blind type. This study concluded that the 3D printing technology is safe and effective for treating adults with fractures tibial plateau with significantly shorter surgical time, less intraoperative blood loss, fewer fluoroscopy times, higher rate of anatomical reduction, and better results compared to the group that did not use these resources, finding any statistic differences regarding the complication rate comparing the groups. They also concluded that 3D printing can help doctors improve their theoretical knowledge and practical skills, reduce the learning curves, improve surgical quality, and provide better communication between doctors and patients.

14.6.2 Surgical Guides and Surgical Tools Printing

The cutting, drilling, and reduction guides made with 3D printing technology are called Patient-Specific Instrument (PSI) since they are customized and used in various situations in orthopedic surgeries.

These guides are personalized molds that fit the bone of the patient, with cutting guides and screw hole guides to position directly previously planned surgical instruments (Caiti et al. 2018) with bone graft removal cut guides and cutting and drilling guides in osteotomy and arthroplasty (Vaishya et al. 2018; Hoang et al. 2016; Tack et al. 2016; Zheng et al. 2016; Nam 2015; Woo et al. 2020). In addition to this minor or percutaneous surgical approaches are possible using this technique (Bagaria et al. 2018).

The PSI has been developed as an alternative to navigation systems. PSI was originally developed for Total Knee Arthroplasty (TKA). Other applications have been used as the insertion of pedicle screws in spine surgeries, Total Hip Arthroplasty (THA), and corrective osteotomy. The PSI technology has been adapted for tumor surgery bones: the customized cutting guides are designed with smooth surfaces specific to fit the bone in a unique position to direct the desired resection plans (Gouin et al. 2014).

Possible benefits of PSI printing are preoperative surgical planning reproducibility, reduced surgical time, and optimized efficiency and cost-effectiveness. Despite the proposed benefits, it is not yet proven to be better than standard techniques. In 2014 in Australia, this technique was used in 6.8% of all TKA according to Mulford et al. (2016).

In oncological surgeries, preoperative planning associated with PSI may result in greater surgical accuracy concerning resection of free margins and precision in bone cuts (Gouin et al. 2014).

Studies show that the use of PSI in bone tumor resections in the pelvis, simplify the surgical procedure (Sallent et al. 2017). In the same way the use of the combination of 3D models associated with computerized navigation results in increased surgical accuracy in tumor resection (Fadero and Shah 2014; Zhang et al. 2017a, b). Jentzsch et al. (2016) reported in a series of cases the use of cutting guides in performing osteotomies in surgeries for hemipelvectomy in the treatment of pelvic tumors. They concluded that the virtual surgical planning associated with intraoperative use of 3D models and PSI anatomical assist in visualizing the anatomy and surgical accuracy.

Cutting guides for block osteotomies assist in the adequate resection of the injury with safety margins (Jentzsch et al. 2016). The use of 3D image modeling has led to an improvement in the design of various instruments (cutting and drilling guides) and implants used in orthopedic surgery, mainly in those whose realization occurs in places of complex anatomy such as pelvis, spine, and scapular waist (Mok et al. 2016; Malik et al. 2015; Zhang et al. 2017a, b). PSI prototyping has become a technological advance with an impact on TKA and THA, oncological surgery, and spine surgery (Chen et al. 2016; Malik et al. 2015; Trauner et al. 2018).

The use of PSI in spine surgery allows planning the screw trajectories reducing the risk of deviations out of the body and the vertebral pedicle reducing the risk of vascular and nerve damage, in addition to making custom implants according to Mobbs et al. (2018). Intraoperative guides, created with specific patient data, in spine surgeries may have the ability to decrease the risks associated with these procedures according to Wilcox et al. (2017). In their systematic review, numerous studies have shown that guides help shorten operations, suggesting that this may decrease complications related to operative time (e.g., infection). Other benefits include decreased intraoperative radiation; simplicity of use; elimination of subjectivity of the procedure; improved preoperative planning; and moderate cost compared to other techniques.

In the same way as deformity correction planning in orthopedic trauma, the making of personalized surgical instruments is one of the great benefits of 3D printing technology (Fadero and Shah 2014). For the treatment of malunion fracture, Hoekstra et al. (2016) described a long bone corrective osteotomy technique using specific individualized guides printed with 3D technology. This process is summarized in:

1. Image acquisition of the segment that has vicious consolidation in CT. It is necessary to acquire the contralateral limb to perform the technique;
2. Creation of the 3D virtual model and realization of the mirroring of the contralateral side to define the variables to be corrected (rotation, angulation, and length);
3. Choosing of osteotomy position and orientation (addition wedge or subtraction e.g.) and determining the corrected position of the bone, the location of the implants is defined. This one step is performing virtual surgical planning (VSP);
4. Printing of the cut and drill guide (PSI) and the anatomical model;
5. Performing surgery with exposure of the osteotomy site, positioning of the guide, and provisional fixation of the guide with Kirschner's wire; In this step, the holes of the definitive screws can be pre-drilled;
6. Performing the osteotomy with the cutting guide according to the VSP;
7. Performing osteotomy reduction to the corrected site. Kirschner's wires can be used to perform the reduction;
8. Fixating of osteotomy as planned with plate and screw;
9. Performing postoperative CT.

Caiti et al. (2018) showed in their study on radio osteotomy that the positioning error of the PSI (cutting guides) depends on the mounting location. That must be carefully considered when using 3D printing during surgery, recommending the use of extended guides, as it increases the accuracy of surgical navigation. Several studies cite that despite the creation of personalized guides for angular correction surgery with osteotomy the cutting guide and plate positioning may lead to unsatisfactory surgical procedures (Hoekstra et al. 2016; de Muinck Keizer et al. 2017; Rosseels et al. 2019).

According to Rosseels et al. (2019) in their study on the use of guides printed with 3D technology (PSI) to perform osteotomies found four big traps using the 3D printing technique. They are:

1. Careful placement of the planned guide is mandatory since that the sub-optimal positioning of the guide is the main cause of the incomplete correction;
2. The use of screw holes (pre-drilled) does not guarantee the proper screw placement;
3. The translation of bone fragments over the osteotomy planes in an oblique osteotomy is a potential risk;
4. The depth of the osteotomy is difficult to estimate and can lead to cartilage lesions in peri-articular regions.

Tack et al. (2016) in their systematic review regarding the use of 3D technology in the medical field report that many recent studies mention that there is no difference in clinical outcomes between TKA surgeries that used standardized cuts compared to surgeries that used cutting guides obtained through 3D printing technology. This same author claims that recent studies showing the cost–benefit assessment of the use of custom cut guides suggest that 3D printing technology does not offer advantages to cover the cost associated with using these personalized cut guides. Besides, Tack mentions that some studies show an increased time in preparing and discussing surgical planning with the use of 3D technology. The use of customized cutting guides in TKA requires a long period of programming the surgery that is much longer than the reduction of time in the TKA surgical procedure. These studies suggest that surgical planning is more accurate when performed by an orthopedist compared to other professionals.

14.6.3 Orthopedics Implants Printing

A major advantage of using AM technology is the ability to make personalized implants—PSI (Mobbs et al. 2018) being a resource increasingly used in orthopedic surgeries (Bagaria and Chaudhary 2017; Eijnatten et al. 2018; Chen et al. 2016; Tack et al. 2016; Kaye et al. 2016; Sallent et al. 2017; Rosseels et al. 2019). The use of PSI is an effective method with great reproduction accuracy of preoperative planning (Malik et al. 2015; Caiti et al. 2018; Sallent et al. 2017). Besides the accuracy, these printed materials must have two other important characteristics: they must have mechanical resistance and be sterilizable (Rankin et al. 2018).

The possibility of printing personalized implants as mentioned by Ma et al. where a 3D printed titanium mesh tray was used in the treatment of a complex comminuted mandibular fracture can provide more predictable aesthetic and functional results. In this study, Ma et al. described a case where virtual surgery was performed to simulate the process reduction of the displaced fragments in the preoperative. The team conducted a study on the morphology of fractured sites to be reduced. The tray fabric was manufactured by 3D printing technology based on the anatomic model serving as an intraoperative template. All of these factors led to a reduction in the time of surgery and better results (Ma et al. 2017).

Regarding the use of customized implants used in spinal surgery, Wilcox et al. (2017) described in their systematic review that the cases performed so far are limited anatomically to rare pathologies and challenging in which an individualized solution to restore a patient's anatomy specificity is a key prognostic factor. Also, most custom prostheses were made of titanium alloy (TiV6Al4) due to their biocompatibility and ability to improve bone healing by porosity optimization to match the trabecular bone structure.

In a retrospective study of a series of cases, Li et al. (2016) described the use of acetabular components printed with 3D printing technology in THA revision surgeries with severe bone loss. This study concluded that the use of custom acetabular components using prototyping technology and 3D printing seems to provide stable fixation and good short-term functionalities in this series of cases. As further improvements in the design and the manufacturing process are made, future studies should evaluate groups with larger numbers of patients for longer and ideally compare this approach with other alternative approaches for treating this type of complex bone defect in THA reviews.

Wong et al. (2015) reported a clinical case of partial resection of the acetabulum in a patient with pelvic chondrosarcoma and performed a reconstruction with a personalized pelvic implant. Bone resection was virtually planned, and an implant was designed using CAD software to fill in the bone defect. The implant was evaluated biomechanically and made with titanium 3D printing technology (Ti6Al4V) with the SLM technique. A cutting guide (PSI) was used to reproduce the planned resection (osteotomy in VSP) to suit the custom implant. The accuracy of free margin resection was validated by comparing the obtained resection and the implant position with that planned. There was no recurrence of the injury or loosening of the implanted material in an 11-month postoperative follow-up.

Liang et al. (2017) described a reconstruction technique for treating tumors in the pelvis using modular pelvic endoprosthesis printed with 3D printing technology in titanium alloy by EBM technique. Based on their report of a series of 35 patients, the study concluded that the use of prostheses pelvic floor using 3D printing technology for reconstruction of defect bone after excision of pelvic tumors is possible and safe with good functional results in a 30-month follow-up.

With the development of AM technology, it was possible to make structures to replace complex bone defects and even whole bones. Tetsworth et al. (2017) described a reconstruction technique for bone defects with the use of a printed implant with 3D technology for the treatment of massive segmental defects of long bones. They performed virtual planning (VSP) and constructed the customized metal structure (PSI) titanium lattice type. Based on mirroring of the contralateral limb, the titanium lattice was made according to the original bone geometry. The truss design was defined according to the implants used to fixate the bone-implant set. Imanishi and Choong (2015) described a clinical case of using a calcaneus prosthesis printed with 3D technology after total calcanectomy. The patient had calcaneus chondrosarcoma that was completely resected, and a heel prosthesis was placed. The VSP was performed using the mirroring technique on the contralateral side, and a prosthesis of the calcaneus with EBM titanium technology was made. The articular surface was submitted to polishing treatment. Tendon and ligament reinsertion were performed in the prosthesis for stabilization. With a 5-month follow-up, the patient did not present surgical complications nor pain. This was the first case of calcaneus prosthesis created with AM technology. Xie et al. (2018) described reconstructive surgery for the treatment of Kienböck disease in stage IIIC, using a metallic prosthesis 3D printed semilunar bone. The shape and size of the prosthesis were determined by mirroring the contralateral side based on CT images. In this case, the author does not mention the technology for printing the prosthesis, nor the material used in printing. Choy et al. (2017) described a clinical case of treatment of primary bone tumor in the spine undergoing reconstruction after vertebrectomy. The T9 body was printed with 3D technology in titanium restoring the local anatomy, with a good result in a 6-month follow-up.

In a systematic review concerning the technique of 3D printing in the medical field, Tack et al. (2016) report that the most commonly used materials in making custom implants are titanium (Ti), PEEK, hydroxyapatite (HA), PMMA. Researches are being carried out concerning the manufacturing of customized meshes using biodegradable materials such as HA and PLA (Ma et al. 2017). Qiao et al. (2015) described the use of AM technology in the printing of a customized external fixator to aid in reducing the fracture, reporting advantages such as easy handling, accurate reduction, and minimally invasive procedure.

Other possibilities for using AM technology are e.g., the printing of surgical instruments for hand fractures surgery as described by Fuller et al. (2014) and the making of hand prostheses printed with 3D technology for the treatment of children who suffered hand amputation due to traumatic or malformation, as described by Burn et al. (2016).

14.6.4 Scaffold and Cell Printing

With the progressive technological advancements, a new frontier was reached in health research with the establishment of the "State of the Art" in medical science with the structuring of two new areas of knowledge: regenerative medicine (RM) and tissue engineering (TE). RM combines the principles of engineering and biology for the production of structures that can restore or strengthen the functions of human organs and tissues (Arealis and Nikolaou 2015). TE is a transdisciplinary and translational field that aims to combine knowledge about cells and tissues, biomaterials, biochemical factors, and biomechanics to create biological structures to replace and/or regenerate tissues (Wong et al. 2017).

Bioprinting is a rapid prototyping technology for the printing of biologically active cells and cellular matrices. The development of culture media and cell growth systems allowed for the direct printing of biological materials in scaffolds (3D structures that serve as frameworks used for transplantation with or without cells). The scaffolds are critical to providing structure for infiltration and cell proliferation, space for extracellular matrix generation, and remodeling providing biochemical signals to direct cellular behavior and physical connections to injured tissue. According to Chia and Wu (2015). when printing scaffolds, it is necessary to evaluate the architecture at the macro, micro, and nano-level to provide structural conditions, nutrient transport, and cell–matrix interaction. Macro architecture is the general form of the structure that can be complex (e.g., patient and organ specificities, anatomical features). Microarchitecture reflects fabric architecture (e.g., pore size, shape, porosity, spatial distribution, and pore interconnection). Nanoarchitecture is the modification of the surface (e.g., fixation of biomolecules for adhesion, proliferation, and cell differentiation). It is possible to print scaffolds, fabrics, or even biologically active organs through various methodologies including constructions of biodegradable materials associated with cell seeding, bio-jet printing ink, microextrusion bioprinting, or laser-assisted bioprinting (Rankin et al. 2018). Tang et al. (2021) described the specific features that ideal scaffolds material should present:

1. Excellent biocompatibility to support the adhesion and proliferation of bone-forming cells;
2. High mechanical properties for load bearing;
3. Suitable pore interconnectivity and size for transport of nutrients and oxygen.
4. Tailored biodegradation or bioresorbability to provide growth space of new bone tissue;
5. Allowable incorporation of biological cues and signals for cell adhesion, proliferation, metabolism, and differentiation.

Bone Tissue Engineering (BTE) in the field of RM develops alternative treatment options for treating bone defects. According to Arealis and Nikolaou (2015), BTE has four methods for creating bone grafts in vitro:

1. Printing a scaffold in which all other components will be loaded. Ideally, it should imitate the bone structure, reabsorb the fee that allows the native bone to fill the defect and at the same time protect and provide nutrients to the cellular components of the graft (osteoconduction);
2. The second component is the cells. They can be osteoblasts or pluripotent progenitor cells that differ from osteoblasts bone producers with osteogenic function;
3. For cells to proliferate and differentiate into osteoblasts, morphogenic or osteoinductive signs are needed. Protein bone morphogenetic (BMP) and similar inducing molecules are the third components required;
4. For the graft to develop and be incorporated in vivo, sufficient vascularization to meet the growing metabolic tissue is needed.

Therefore, a possibility of using scaffolds is their use on bone defect treatments (post-traumatic, congenital, or post-arthroplasty), with osteoconductive function. Currently, bioceramics such as HA and calcium phosphate—or even bioactive glass—are biomaterials for manufacturing porous structures, as they are highly biocompatible and biodegradable. However, the low mechanical strength is a major challenge, and most scaffolds are used only in unloaded regions (Wong et al. 2017). For reconstructing bone defects that require mechanical support such as long bone (femur, tibia) metal materials are used in scaffolds. The two more used are Ti alloy and tantalum (Ta) as bone trabecular metal to create a biomimetic structure that occupies the bone defect and allows scaffold cellularization (Tang et al. 2021).

Currently, research is underway to develop other types of natural and synthetic polymers, composites, and biomaterials used in 3D printed scaffolds for the treatment of bone defects. In the last years, scholars have made important progress in BTE technology concerning biomaterial development, bioprinting cells, and using of the bone bioreactor to promote viable substitutes to bone regeneration (Liang et al. 2021; Luo et al. 2020).

References

Arealis G, Nikolaou VS (2015) Bone printing: new frontiers in the treatment of bone defects. Injury 46(8):S20–S22

Bagaria V, Bhansali R, Pawar P (2018) 3D printing creating a blueprint for the future of orthopedics: current concept review and the road ahead! J Clin Orthop Trauma 9(3):207–212

Bagaria V, Chaudhary K (2017) A paradigm shift in surgical planning and simulation using 3Dgraphy: experience of first 50 surgeries done using 3D-printed biomodels. Injury 48(11):2501–2508

Bagaria V, Deshpande S, Rasalkar DD, Kuthe A, Paunipagar BK (2011) Use of rapid prototyping and three-dimensional reconstruction modeling in the management of complex fractures. Eur J Radiol 80(3):814–820

Belvedere C, Siegler S, Fortunato A, Caravaggi P, Liverani E, Durante S (2019) New comprehensive procedure for custom-made total ankle replacements: medical imaging, joint modeling, prosthesis design, and 3D printing. J Orthop Res 37(3):760–768

Bizzotto N, Tami I, Santucci A, Romani D, Cosentino A (2015) 3D Printed replica of articular fractures for surgical planning and patient consent: a 3 years multi-centric experience. 3D Print Med, 2(1):2

Burn MB, Ta A, Gogola GR (2016) Three-dimensional printing of prosthetic hands for children. J Hand Surg Am 41(5):e103–e109

Cai L, Zhang Y, Chen C, Lou Y, Guo X, Wang J (2018) 3D printing-based minimally invasive cannulated screw treatment of unstable pelvic fracture. J Orthop Surg Res 13(1):71

Caiti G, Dobbe JGG, Strijkers GJ, Strackee SD, Streekstra GJ, Caiti BG (2018) Positioning error of custom 3D-printed surgical guides for the radius: influence of fitting location and guide design. Int J Comput Assist Radiol Surg 13(4):507–518

Chana-Rodríguez F, Mañanes RP, Rojo-Manaute J, Gil P, Martínez-Gómiz JM, Vaquero-Martín J (2016) 3D surgical printing and pre contoured plates for acetabular fractures. Injury 47(11):2507–2511

Chen C, Cai L, Zheng W, Wang J, Guo X, Chen H (2019) The efficacy of using 3D printing models in the treatment of fractures: A randomised clinical trial. BMC Musculoskelet Disord 20(1):65

Chen X, Xu L, Wang W, Li X, Sun Y, Politis C (2016) Computer-aided design and manufacturing of surgical templates and their clinical applications: a review. Expert Rev Med Devices 13(9):853–864

Chia HN, Wu BM (2015) Recent advances in 3D printing of biomaterials. J Biol Eng 9(1):4

Choy WJ, Mobbs RJ, Wilcox B, Phan S, Phan K, Sutterlin III CE (2017) Reconstruction of the thoracic spine using a personalized 3D-printed vertebral body in an adolescent with a T9 primary bone tumour: case report. World Neurosurg 105:1032e13–1032e17

Courvoisier A, Boudissa M, Chabanas M, Tonetti J (2018) Computer assisted surgery in preoperative planning of acetabular fracture surgery: state of the art. Expert Rev Med Devices 15(1):81–89

Cromeens BP, Ray WC, Hoehne B, Abayneh F, Adler B, Besner GE (2017) Facilitating surgeon understanding of complex anatomy using a three-dimensional printed model. J Surg Res 216:18–25

de Muinck Keizer RJO, Lechner KM, Mulders MAM, Schep NWL, Eygendaal D, Goslings JC (2017) Three-dimensional virtual planning of corrective osteotomies of distal radius malunions: a systematic review and meta-analysis. Strateg Trauma Limb Reconstr 12(2):77–89

van Eijnatten M, van Dijk R, Dobbe J, Streekstra G, Koivisto J, Wolff J (2018) CT image segmentation methods for bone used in medical additive manufacturing. Med Eng Phys 51:6–16

Eley KA, Watt-Smith SR, Sheerin F, Golding SJ (2014) "Black Bone" MRI: a potential alternative to CT with three-dimensional reconstruction of the craniofacial skeleton in the diagnosis of craniosynostosis. Eur Radiol 24(10):2417–2426

Eley KA, Watt-smith SR, Golding SJ (2017) "Black Bone" MRI: a novel imaging technique for 3D printing. Dentomaxillofacial Radiol 46(3):20160407

Eley KA (2017) Centralised 3D printing in the NHS: a radiological review. Clin Radiol 72(4):269–275

Fadero PE, Shah M (2014) Three dimensional (3D) modelling and surgical planning in trauma and orthopaedics. Surgeon 12(6):328–333

Favier V, Zemiti N, Mora OC, Subsol G, Captier G, Lebrun R et al (2017) Geometric and mechanical evaluation of 3D-printing materials for skull base anatomical education and endoscopic surgery simulation—a first step to create reliable customized simulators. PLoS ONE 12(12):e0189486

Frizziero L, Pagliari C, Donnici G, Liverani A, Santi GM, Papaleo P et al (2021) Effectiveness assessment of CAD simulation in complex orthopedic surgery practices. Symmetry (basel) 13(5):850

Fuller SM, Butz DR, Vevang CB, Makhlouf MV (2014) Application of 3-dimensional printing in hand surgery for production of a novel bone reduction clamp. J Hand Surg Am 39(9):1840–1845

Giannetti S, Bizzotto N, Stancati A, Santucci A (2017) Minimally invasive fixation in tibial plateau fractures using an pre-operative and intra-operative real size 3D printing. Injury 48(3):784–788

Gouin F, Paul L, Odri GA, Cartiaux O (2014) Computer-assisted planning and patient-specific instruments for bone tumor resection within the pelvis: a series of 11 patients. Sarcoma 2014:842709

Green N, Glatt V, Tetsworth K, Wilson LJ, Grant CA (2016) A practical guide to image processing in the creation of 3D models for orthopedics. Tech Orthop 31(3):153–163

Hoang D, Perrault D, Stevanovic M, Ghiassi A (2016) Surgical applications of three-dimensional printing: a review of the current literature & how to get started. Ann Transl Med 4(23):456

Hoekstra H, Rosseels W, Sermon A, Nijs S (2016) Corrective limb osteotomy using patient specific 3D-printed guides: a technical note. Injury 47(10):2375–2380

Huang H, Xing W, Zeng C, Huang W (2020) Pararectus approach combined with three-dimensional printing for anterior plate fixation of sacral fractures. Injury 52(10):2719–2724

Huang Z, Song W, Zhang Y, Zhang Q, Zhou D, Zhou X et al (2018) Three-dimensional printing model improves morphological understanding in acetabular fracture learning: a multicenter, randomized, controlled study. PLoS ONE 13(1):e0191328

Imanishi J, Choong PFM (2015) Three-dimensional printed calcaneal prosthesis following total calcanectomy. Int J Surg Case Rep 10:83–87

Jentzsch T, Vlachopoulos L, Fürnstahl P, Müller DA, Fuchs B (2016) Tumor resection at the pelvis using three-dimensional planning and patient-specific instruments: a case series. World J Surg Oncol 14(1):249

Karlin L, Weinstock P, Hedequist D, Prabhu SP (2017) The surgical treatment of spinal deformity in children with myelomeningocele: the role of personalized three-dimensional printed models. J Pediatr Orthop B 26(4):375–382

Kaye R, Goldstein T, Zeltsman D, Grande DA, Smith LP (2016) Three dimensional printing: a review on the utility within medicine and otolaryngology. Int J Pediatr Otorhinolaryngol 89:145–148

Kim JW, Lee Y, Seo J, Park JH, Seo YM, Kim SS et al (2018) Clinical experience with three-dimensional printing techniques in orthopedic trauma. J Orthop Sci 23(2):383–388

Langridge B, Momin S, Coumbe B, Woin E, Griffin M, Butler P (2018) Systematic review of the use of 3-Dimensional printing in surgical teaching and assessment. J Surg Educ 75(1):209–221

Li H, Qu X, Mao Y, Dai K, Zhu Z (2016) Custom acetabular cages offer stable fixation and improved hip scores for revision THA with severe bone defects. Clin Orthop Relat Res 474(3):731–740

Li L, Yu F, Shi J, Shen S, Teng H, Yang J et al (2017) In situ repair of bone and cartilage defects using 3D scanning and 3D printing. Sci Rep 7(1):9416

Liang H, Ji T, Zhang Y, Wang Y, Guo W (2017) Reconstruction with 3D-printed pelvic endoprostheses after resection of a pelvic tumour. Bone Joint J 99-B(2):267–275

Liang R, Gu Y, Wu Y, Bunpetch V, Zhang S (2021) Lithography-Based 3D bioprinting and bioinks for bone repair and regeneration. ACS Biomater Sci Eng 7(3):806–816

Luo Y, Pan H, Jiang J, Zhao C, Zhang J, Chen P et al (2020) Desktop-stereolithography 3D printing of a polyporous extracellular matrix bioink for bone defect regeneration. Front Bioeng Biotechnol 8:589094

Ma J, Ma L, Wang Z, Zhu X, Wang W (2017) The use of 3D-printed titanium mesh tray in treating complex comminuted mandibular fractures A case report. Medicine (baltimore) 96(27):e7250

Maini L, Verma T, Sharma A, Sharma A, Mishra A, Jha S (2018) Evaluation of accuracy of virtual surgical planning for patient-specific pre-contoured plate in acetabular fracture fixation. Arch Orthop Trauma Surg 138(4):495–504

Malik HH, Darwood ARJ, Shaunak S, Kulatilake P, El-Hilly AA, Mulki O et al (2015) Three-dimensional printing in surgery: a review of current surgical applications. J Surg Res 199(2):512–522

Marro A, Bandukwala T, Mak W (2016) Three-dimensional printing and medical imaging: a review of the methods and applications. Curr Probl Diagn Radiol 45(1):2–9

Martelli N, Serrano C, van den Brink H, Pineau J, Prognon P, Borget I et al (2016) Advantages and disadvantages of 3-dimensional printing in surgery: a systematic review. Surgery 159(6):1485–1500

Mobbs RJ, Choy WJ, Wilson P, McEvoy A, Phan K, Parr WCH (2018) L5 En-bloc vertebrectomy with customized reconstructive implant: comparison of patient-specific versus off-the-shelf implant. World Neurosurg 112:94–100

Mok S-W, Nizak R, Fu S-C, Ho K-WK, Qin L, Saris DBF et al (2016) From the printer: potential of three-dimensional printing for orthopaedic applications. J Orthop Transl 6:42–49

Morgan C, Khatri C, Hanna SA, Ashrafian H, Sarraf KM (2020) Use of three-dimensional printing in preoperative planning in orthopaedic trauma surgery: a systematic review and meta-analysis. World J Orthop 11(1):57–67

Mulford JS, Babazadeh S, Mackay N (2016) Three-dimensional printing in orthopaedic surgery: review of current and future applications. ANZ J Surg 86(9):648–653

Nam D (2015) Patient-specific instrumentation (PSI) in total knee arthroplasty (TKA) [Internet]. In: Surgical techniques in total knee arthroplasty (TKA) and alternative procedures. Woodhead Publishing Limited, pp 207–227

Ozturk AM, Suer O, Derin O, Ozer MA, Govsa F, Aktuglu K (2020) Surgical advantages of using 3D patient-specific models in high-energy tibial plateau fractures. Eur J Trauma Emerg Surg 46(5):1183–1194

Pagac M, Hajnys J, Ma Q, Jancar L, Jansa J, Stefek P et al (2021) A review of vat photopolymerization technology: materials, applications, challenges, and future trends of 3D printing. Polymers (basel) 13(4):598

Parthasarathy J, Krishnamurthy R, Ostendorf A, Shinoka T, Krishnamurthy R (2020) 3D printing with MRI in pediatric applications. J Magn Reson Imaging 51(6):1641–1658

Peel S, Bhatia S, Eggbeer D, Morris DS, Hayhurst C (2017) Evolution of design considerations in complex craniofacial reconstruction using patient-specific implants. Proc Inst Mech Eng H 231(6):509–524

Qiao F, Li D, Jin Z, Gao Y, Zhou T, He J et al (2015) Application of 3D printed customized external fixator in fracture reduction. Injury 46(6):1150–1155

Rankin TM, Wormer BA, Miller JD, Giovinco NA, Al Kassis S, Armstrong DG (2018) Image once, print thrice? Three-dimensional printing of replacement parts. Br J Radiol 91(1083):20170374

Rathor S, Jena J, Uddanwadikar R, Apte A (2021) Finite element analysis of type I and type II fracture with PFN implant—a comparative study. In: Kalamkar V, Monkova K (eds) Advances in mechanical engineering. Lecture notes in mechanical engineering. Springer, Singapore, pp 243–251

Rosseels W, Herteleer M, Sermon A, Nijs S, Hoekstra H (2019) Corrective osteotomies using patient-specific 3D-printed guides: a critical appraisal. Eur J Trauma Emerg Sur 45(2):299–307

Sallent A, Vicente M, Reverté MM, Lopez A, Rodríguez-Baeza A, Pérz-Domínguez M et al (2017) How 3D patient-specific instruments improve accuracy of pelvic bone tumour resection in a cadaveric study. Bone Joint Res 6(10):577–583

Shon HC, Bang JY, Lee Y, Koh KH, Kim JW (2020) Optimal plate position in minimally invasive plate osteosynthesis for mid-shaft clavicle fractures: simulation using 3D-printed models of actual clinical cases. Eur J Trauma Emerg Surg 1–7

Shui W, Zhou M, Chen S, Pan Z, Deng Q, Yao Y et al (2017) The production of digital and printed resources from multiple modalities using visualization and three-dimensional printing techniques. Int J Comput Assist Radiol Surg 12(1):13–23

Tack P, Victor J, Gemmel P, Annemans L (2016) 3D-printing techniques in a medical setting: a systematic literature review. Biomed Eng Online 15(1):115

Tang G, Liu Z, Liu Y, Yu J, Wang X, Tan Z et al (2021) Recent trends in the development of bone regenerative biomaterials. Front Cell Dev Biol 9:665813

Tappa K, Jammalamadaka U, Weisman JA, Ballard DH, Wolford DD, Pascual-Garrido C et al (2019) 3D printing custom bioactive and absorbable surgical screws, pins, and bone plates for localized drug delivery. J Funct Biomater 10(2):17

Tetsworth K, Block S, Glatt V (2017) Putting 3D modelling and 3D printing into practice: virtual surgery and preoperative planning to reconstruct complex post-traumatic skeletal deformities and defects. SICOT J 3:16

Trauner KB (2018) The emerging role of 3D printing in arthroplasty and orthopedics. J Arthroplasty 33(8):2352–2354

Vaishya R, Patralekh MK, Vaish A, Agarwal AK, Vijay V (2018) Publication trends and knowledge mapping in 3D printing in orthopaedics. J Clin Orthop Trauma 9(3):194–201

Van den Broeck J, Vereecke E, Wirix-Speetjens R, Vander Sloten J (2014) Segmentation accuracy of long bones. Med Eng Phys 36(7):949–953

Wieding J, Souffrant R, Fritsche A, Mittelmeier W, Bader R (2012) Finite element analysis of osteosynthesis screw fixation in the bone stock: an appropriate method for automatic screw modelling. PLoS ONE 7(3):e33776

Wilcox B, Mobbs RJ, Wu A-M, Phan K (2017) Systematic review of 3D printing in spinal surgery: the current state of play. J Spine Surg 3(3):433–443

Wong KC, Kumta SM, Gee NVL, Demol J (2015) One-step reconstruction with a 3D-printed, biomechanically evaluated custom implant after complex pelvic tumor resection. Comput Aided Surg 20(1):14–23

Wong KV, Hernandez A (2012) A review of additive manufacturing. ISRN Mech Eng 2012:208760

Wong TM, Jin J, Lau TW, Fang C, Yan CH, Yeung K et al (2017) The use of three-dimensional printing technology in orthopaedic surgery: a review. J Orthop Surg (hong Kong) 25(1):2309499016684077

Woo S-H, Sung M-J, Park K-S, Yoon T-R (2020) Three-dimensional-printing technology in hip and pelvic surgery: current landscape. Hip Pelvis 32(1):1–10

Xie M, Tang K, Yuan C (2018) 3D printing lunate prosthesis for stage IIIc Kienböck's disease: a case report. Arch Orthop Trauma Surg 138(4):447–451

Yan L, Lim JL, Lee JW, Tia CSH, O'Neill GK, Chong DYR (2020) Finite element analysis of bone and implant stresses for customized 3D-printed orthopaedic implants in fracture fixation. Med Biol Eng Comput 58(5):921–931

Yang L, Shang XW, Fan JN, He ZX, Wang JJ, Liu M et al (2016a) Application of 3D printing in the surgical planning of trimalleolar fracture and doctor-patient communication. Biomed Res Int 2016:2482086

Yang P, Du D, Zhou Z, Lu N, Fu Q, Ma J et al (2016b) 3D printing-assisted osteotomy treatment for the malunion of lateral tibial plateau fracture. Injury 47(12):2816–2821

Zeng C, Xing W, Wu Z, Huang H, Huang W (2016) A combination of three-dimensional printing and computer-assisted virtual surgical procedure for preoperative planning of acetabular fracture reduction. Injury 47(10):2223–2227

Zhang W, Ji Y, Wang X, Liu J, Li D (2017a) Can the recovery of lower limb fractures be achieved by use of 3D printing mirror model? Injury 48(11):2485–2495

Zhang Y, Wen L, Zhang J, Yan G, Zhou Y, Huang B (2017b) Three-dimensional printing and computer navigation assisted hemipelvectomy for en bloc resection of osteochondroma. Medicine (baltimore) 96(12):e6414

Zheng YX, Yu DF, Zhao JG, Wu YL, Zheng B (2016) 3D printout models vs. 3D-rendered images: which is better for preoperative planning? J Surg Educ 73(3):518–523

Zheng W, Chen C, Zhang C, Tao Z, Cai L (2018a) The feasibility of 3D printing technology on the treatment of Pilon fracture and its effect on doctor-patient communication. Biomed Res Int 2018:8054698

Zheng W, Su J, Cai L, Lou Y, Wang J, Guo X et al (2018b) Application of 3D printing technology in the treatment of humeral intercondylar fractures. Orthop Traumatol Surg Res 104(1):83–88

Chapter 15
Natural Hydrogels and 3D-Bioprinting

Beatriz Luci Fernandes and Clayton Fernandes de Souza

15.1 Introduction

The future medicine will incorporate technologies that will transform healthcare services, providing highly automated and smart solutions. These advances will lead to lower health care costs, resulting in more efficient treatments and an exponential increase of innovative and disruptive industries. Several studies indicate the 3D Bioprinting market with a high Compound Annual Growth Rate (GAGR) of 25.49% through 2025. Other prospects suggest that the global 3D bioprinting market size is expected to reach USD 4.2 billion by 2027, expanding at a CAGR of about 17.4%. The medical segment of biofabrication dominated this market with a share of 21.1% in 2019, justified by increased investment in R&D.

A prospect on bases Scopus and Web of Science was carried out between 2000 and 2020 on this topic, indicating significant growth in publications related to biomaterials and bioprinting processes. The results are illustrated in Fig. 15.1. From these results, since the beginning of the 2000s, one can see that the development of hydrogels is linked to tissue engineering and 3D bioprinting, representing the most significant bioengineering challenges towards the in vitro manufacture of tissues.

Present Address:
B. L. Fernandes (✉)
Health Technology Graduate Program, Pontifícia Universidade Católica do Paraná, Curitiba, Paraná, Brazil
e-mail: beatriz.fernandes@pucpr.br

Polytechnic School, Chemical Engineering Undergraduate Course, Pontifícia Universiade Católica do Paraná, Curitiba, Brazil

C. F. de Souza
School of Education and Humanities, Chemistry Undergraduate Course, Pontifícia Universidade Católica do Paraná, Curitiba, Paraná, Curitiba, Brazil
e-mail: clayton.souza@grupomarista.org.br

O. Canciglieri Junior and M. D. Trajanovic (eds.), *Personalized Orthopedics*,
https://doi.org/10.1007/978-3-030-98279-9_15

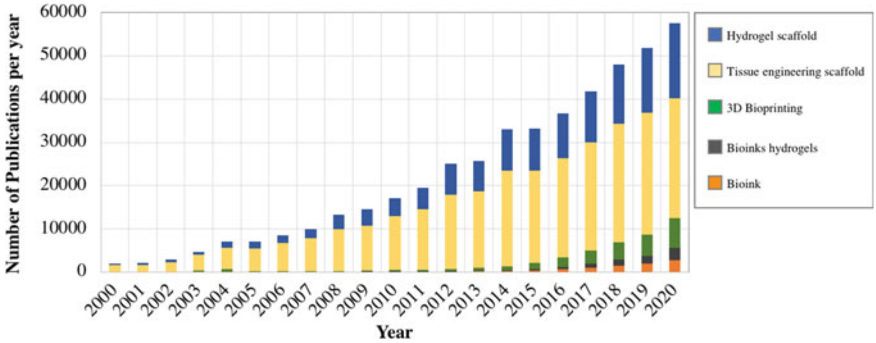

Fig. 15.1 The number of publications per year related to biomaterials and bioprinting processes based on the hydrogel. *Source* Scopus, Web of Science

The advances of additive manufacturing technology were taken to bioprinting to create complex structures necessary to restore the function of tissues. However, the key to the success of perfect bioprinting is the material used, defined in this context as "*bioink*", which are biocompatible hydrogels.

The advances of additive manufacturing technology were taken to bioprinting to create complex structures necessary to restore the function of tissues. However, the key to the success of perfect bioprinting is the material used, defined in this context as "*bioink*", which are biocompatible hydrogels.

Initially, *bioink* was referred to as the cells aggregate applied over a biomaterial print known as "*biopaper*". In this context, Mironov (2003) reported fibrinogen gel deposition using a syringe in a three-axis robotic system. The deposition occurred layer by layer using a thrombin solution as a crosslinking agent to harden the gel. In addition, Wilson and Boland (2003) reported their first experience transforming the hardware and software of an inkjet printer into a cell printer commanded by a computer. They shifted the paper by a poly [N-isopropylacrylamide-co-2-(N, N-dimethylamino)-ethyl acrylate] copolymer and the ink by bovine aortal endothelial cells.

Thus, biopaper was no longer proper, and the term "*bioink*" was adopted (Groll et al. 2019). Bioink, therefore, can be defined as a system composed of an extracellular matrix-like gel biomaterial with proper rheological behavior and living cells, forming a stable scaffold after being manufactured through a 3D printer technology or bioprinting. The gel biomaterial must allow the attached cells to grow and proliferate and, in some cases, to differentiate.

The development and consolidation of 3D Bioprinting techniques, new biocompatible and non-toxic natural and synthetic hydrogels are intensely explored. Therefore, the success of 3D bioprinting techniques includes the raw materials used, called "*bioinks*", and the combination of correct process parameters.

Several biomimetic systems can be developed by 3D Bioprinting techniques using natural, synthetic, or hybrid hydrogels, as illustrated in Fig. 15.2. Researchers have been improving bioprinting through the years, setting viscous materials to be

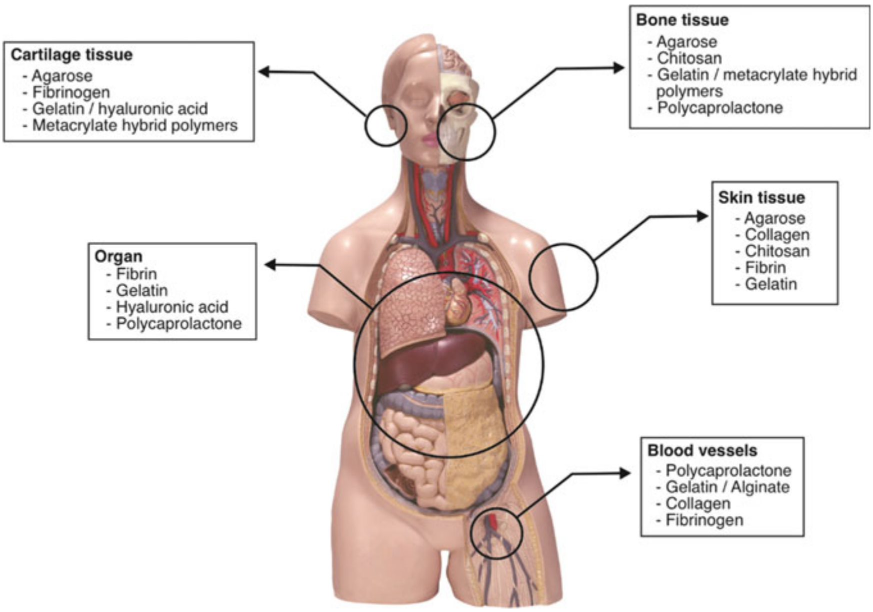

Fig. 15.2 Some biomimetic systems obtained by 3D printing techniques with hydrogels based on natural polymers for biomedical applications

deposited layer by layer assisted by a computer, creating a 3D mimetic model, associating them to new terms and concepts (Maharjan et al. 2021; Su et al. 2021; Tröndle et al. 2021; Xu et al. 2021; Abdollahiyan et al. 2020; Thomas et al. 2020; Li et al. 2020; Lam et al. 2019; Wang et al. 2018; Temple et al. 2014).

However, what are hydrogels? Which ones are available for bioprinting? What are the primary physical, chemical, mechanical and biological characteristics needed for a hydrogel to be suitable for bioprinting? This chapter aims to develop and characterize "*bioinks*" based on natural polymers as supports for cell growth, incorporating new materials and aggregating relevant information for 3D Bioprinting technology in the field of Health Technology.

15.2 Hydrogels Used as "*Bioink*"

The bioinks may contain or not living cells. However, it must support cell adhesion, proliferation, and differentiation after printing. Some requirements are fundamental for the bioprinting process to obtain the best biomimetic construct. For example, considering the bioink with cells, the printing temperature must be physiological and allow gelation and crosslinking formation with incorporated bioactive substances (Gao et al. 2018).

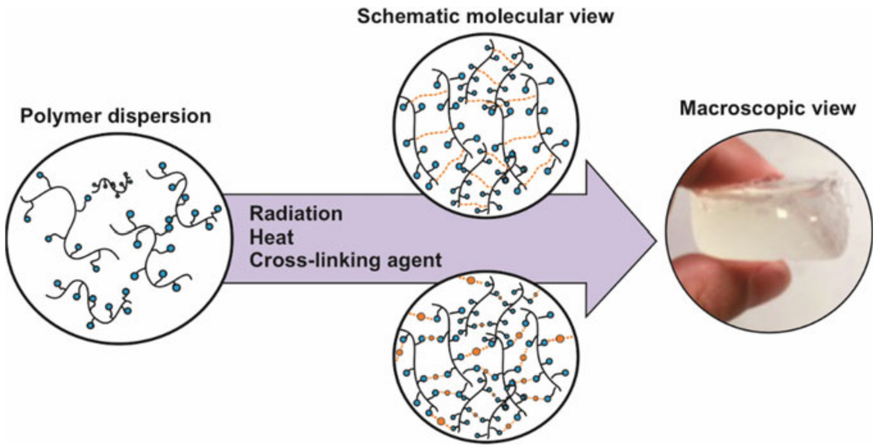

Fig. 15.3 Process of hydrogel formation by the water-soluble polymeric solution

Those conditions are possible with hydrogels, which can encapsulate cells due to their microstructural morphology and interconnected porous network. Besides, to guarantee a stable material for biomedical applications, it is necessary to create semi-permanent interactions between chains and a 3D network to retain water (Dash et al. 2011).

In general, this crosslinked biomaterial is called permanent, and a simple way to obtain such materials is by using chemical or physical crosslink agents in water-soluble polymers (Caló and Khutoryanskiy 2015). In both cases, the self-assembly using covalent or non-covalent crosslinking enables the production of workable biomaterials to flow at several extrusion in 3D-bioprinting conditions. This process is illustrated in Fig. 15.3.

We can consider the hydrogel as a solid-like three-dimensional network of hydrophilic polymeric chains having at least 10% of their total volume formed by water. They belong to polymeric materials that can retain substantial amounts of a liquid fluid, considerably increasing their volume without losing their chemical characteristics. Some powder polymeric materials, natural or synthetic ones, can be hydrated, trapping liquid between its long chains, forming gels.

By chemical process, some typical bioinks are obtained by covalently crosslinked conditions by radiation process, promoting in situ polymerization reactions, resulting in a permanent network. The advantage of those bioinks is good shear-thinning behaviour, pH stability, and improved mechanical properties. However, most common crosslink agents are toxic and need some purification process for biomedical applications (Zandi et al. 2021).

On the other hand, the crosslinking process involves heating, hydrophilic (or hydrophobic) interactions, including hydrogen bonds, complexation, or aggregation when applying the physical method to obtain hydrogels. In this system, only hydrophilic groups are not enough to form a hydrogel able to be printed. It is necessary to build crosslinks between the backbones of the polymer to guarantee that the gel will not be soluble in water and remains stable as a scaffold. In this way, because of the capacity to retain water from their hydrophilic functional groups like amine (–NH_2), hydroxyl (–OH), amide (–$CONH^-$, –$CONH_2$), and sulfate (–SO_4^{2-}), hydrogels are like living tissues (Bahram et al. 2016; Ahmadi et al. 2015; Kaczmarek-Szczepańska et al. 2021).

The hydrophilic functional groups, pending the polymeric main chain, have a thermodynamic affinity with water. The water absorbed by the hydrogel can be free or have no bonding to the polymer molecules or the functional groups directly influencing the swelling capacity of the material. The water can also form hydrogen bonds to the polymeric chains and, together with the crosslinks, affect inversely the water absorption by the hydrogel (Ahmadi et al. 2015).

Those characteristics inspired their use as an artificial and less complex extracellular matrix (ECM). The artificial ECM has a high water content and porosity that entraps and modulates the bioactive substances such as growth factors, nutrients, and cells, allowing their diffusion with the consequent spatial distribution of cells and biomolecules in the substrate. Those characteristics are analogous to the noncellular porous media present in all human tissues. Therefore, the cells can migrate and proliferate (Abar et al., 2021; Garreta et al. 2017).

Mainly composed of water, proteins, and polysaccharides, the natural ECM has a specific hole for each tissue depending on its function (Frantz et al. 2010). So, it is easy to realize why hydrogel is considered excellent material for providing scaffolds for cells and bioactive substances, or in other words, an artificial ECM, as long it is biocompatible.

The essential properties of hydrogels for bioinks are their biodegradability, low toxicity, and easiness to be excreted or metabolized. However, these properties depend on the substrate structure, chemical bonds, and stability that can be broken by the substances present in the body fluids (Akhtar et al. 2015).

The candidate hydrogels for bioprinting in biomedical applications can be natural, synthetic, or hybrid, as long as they are bioprintable, cytocompatible, and provide adequate mechanical properties after impression. In the following topics, the main natural polymers used in bioinks are presented.

15.2.1 Natural Polymer Based-Hydrogels

Natural-based hydrogels constitute an attractive group of natural polymers due to their capability to form highly viscous solutions in water. Some advantages and disadvantages are presented in Table 15.1 and exposed in this topic. In case of proteins and polysaccharides are more available in this group due to easy obtaining and industrialization.

Table 15.1 Typical natural-based-hydrogels raw materials used in 3D-bioprinting techniques

Natural Polymer	Source	Group	Advantages	Disadvantages	References
Agarose	Agar seaweed algae	Polysaccharide	Non-toxic; high stability; self-crosslinking; rapid gelation kinetics, high potential for further chemical functionalization	Gelling dependent on concentration; low degradability, and low cellular adhesion	Nadernezhad et al. (2019); Yang et al. (2009)
Alginate	Brown seaweed algae	Polysaccharide	Specific, quick, and high gelation conditions; high biocompatibility	Low kinetic degradation; low cellular adhesion	Adhikari et al. (2021); Neves (2020)
Cellulose	Plants and bacterial	Polysaccharide	High biocompatibility, good shear thinning and high shape fidelity, good mechanical properties	Need pre-treatments and defibrillation	Muthukrishnan (2021); Kuzmenko et al. (2018); Markstedt et al. (2015);
Collagen	Different tissues of bovine and porcine sources	Protein	High biocompatibility; low antigenicity	High acid solubility	Brown (2005)
Chitosan	Exoskeletons of crustaceans	Polysaccharide	High biocompatibility; antibacterial properties	Low gelation rate; low water solubility	Adhikari et al. (2021)
Fibrin	Blood plasma	Protein	High biocompatibility; fast gelation time	Poor mechanical properties	De Melo et al. (2020)
Gelatin	Different tissues of bovine and porcine sources	Protein	High biocompatibility; water-soluble; thermoreversible gelation	Poor shape fidelity; limited rigidity	Xu et al. (2021); Li et al. (2020); Noh et al. (2019)
Hyaluronic acid	Connective tissue, skin, the eye, and synovial fluid	Polysaccharide	Quickly and high gelation conditions; high cell proliferation	Low stability, poor mechanical properties	Antich et al. (2020); Kiyotake et al. (2019); Lam et al. (2019)

These macromolecules are extracted by chemical processes, being isolated from animals, vegetables, and microorganisms. After extracted and purified, their biocompatibility depends on the structure and functional groups present in the polymer backbone. The functional groups like amine ($–NH_2$), hydroxyl (–OH), amide ($–CONH^-$, $–CONH_2$) and sulphate ($–SO_4{}^{2-}$) are normally founded in natural polymers, modulating the biological activity, important for health technology purposes and the printability, referred to gelation and other mechanical properties (Adhikari et al. 2021; Antich et al. 2020; Aswathy et al. 2020; De Melo et al. 2020; Li et al. 2020; Neves et al. 2020; Kiyotake et al. 2019; Noh et al. 2019; Nadernezhad et al. 2019; Chirani et al. 2015; Markstedt et al. 2015; De Souza et al. 2013; Yang et al. 2009; Brown et al. 2005; Stringer 2005).

Even so, some authors highlight the limitation of producing bioinks with natural hydrogels due to these systems instability and poor mechanical properties (Aswathy et al. 2020). Some studies have shown that it is difficult to reproduce their final structure artificially due to their natural origin and dependence on the gelation conditions. It is worth noticing that the natural hydrogels were not built to be used in bioprinting (Chirani et al. 2015).

Nevertheless, hydrogels based on natural polymers have the advantages of being biocompatible, biodegradable, and low cost. Currently, the raw materials and typical natural hydrogels commercially available with potential in 3D-bioprinting applications are Agarose, Alginate, Cellulose, Collagen, Chitosan, Fibrin, Gelatin and Hyaluronic Acid will be discussed in the next topics.

15.2.2 Agarose

Agarose is a complex group of polysaccharides extracted from the agarocytes of *Rhodophyceae*, marine algae, and consists of the D-galactose and 3,6-anhydrous-L-galactose repeating unities, with residual D-galactose, occasionally substituted with negatively charged groups such as sulfate and pyruvate, giving a fixed negative charge (Stringer 2005). The agar extraction and purification is a typical for several biopolymers (Fig. 15.4). The process involves milling, alkaline pre-treatment, centrifugation and filtration processes at high temperatures, several strategies to eliminate water content and drying processes (Martínez-Sanz et al. 2019).

It is insoluble in cold water but dissolves readily in boiling water. Upon cooling, the agarose chains form side-by-side aggregates, which condense into a double helix arrangement. The interlocking network is held together by non-covalent hydrogen bonds, resulting in high mechanical strength at low concentrations.

Some initial researches have already demonstrated the potential of Agarose for the production of artificial organs. One example is the encapsulation of pancreatic islets into agarose microbeads which effectively prolonged their functioning in a diabetic mouse, without using any immunosuppressive drug (Iwata et al. 1992). However, Agarose forms high viscous hydrogel and, at about 5%w/v, inhibits the diffusion of biomolecules (Iwata et al. 1994).

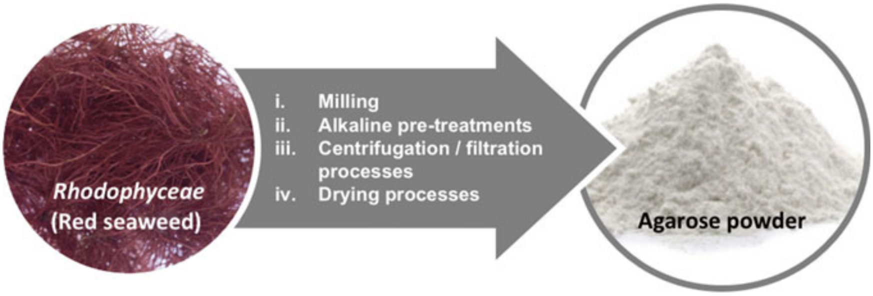

Fig. 15.4 Typical process of agarose extraction from *Rhodophyceae* algae species. Adapted from Iwata et al. (1992)

Due to three-dimensional organization with a pore diameters range of 500–800 nm, Agarose is used mainly as a molecular sieve, including selective DNA separation and cell culture media (Weinberger 2000).

Gel-based Agarose seems to maintain the viability of the cells for several days (Yang et al. 2009). Also, the Agarose matrix might incorporate the sequential application of different growth factors, with improved mechanical properties for the functional tissue engineering of articular cartilage (Lima et al. 2007). It might provide the differentiation and functional maturation of bovine mesenchymal stem cells and bovine articular chondrocytes, with significative mechanical properties (Mauck et al., 2006).

Some studies on Agarose hydrogels for neural regeneration reveal their ability to organize, support, and direct neurite extension of neural cells (Stokols and Tuszynski 2006; Balgude et al. 2001). These works show the potential application for this hydrogel to be explored as bioink.

However, the diffusion of nutrients in Agarose scaffolds depends on the molds fabrication process (Norotte et al. 2009). It allows the units to build in various shapes (pyramid, square), including spheroids that facilitate the induction of cell proliferation (Tan et al. 2014). Therefore, Agarose can be used as support for spheroids formation and cell expansion.

Another important application of Agarose is in cells culture in static suspension. It is well known that the three-dimensional cell culture provides an environment similar to the in vivo ECM, allowing the maintenance of the cells to form 3D spheroid structures. Such structures can create cell-ECM networks favoring the cell to cell communication and their proliferation keeping their phenotype. To enable the cells to create spheroids and to control their sizes, the culture plate must be non-adherent to the cells. A layer of Agarose provides such a non-adherent environment (Ryu et al. 2019).

15.2.3 Alginate

Alginate is a substance extracted from brown algae. It is a non-toxic, bioinert, and limited biodegradation block copolymer composed of 1,4-linked β-D-mannuronic acid and l-guluronic acid (Gyles et al. 2017; Jia et al. 2014), easily dissolved in water. Among the natural polymers, alginate is the one that has good rheological properties for bioprinting.

The bioinert property of the alginate hydrogel came from its high hydrophilicity, which prevents the adsorption of proteins, limiting the cell interactions. Therefore, some substances that provide biological activity are necessary, usually peptides like arginine-guanidine-aspartate, which give the alginate environment a characteristic similar to the ECM, favouring migration, proliferation, and differentiation of cells. However, like other natural hydrogels, the Alginate has no adequate mechanical properties to produce a stable scaffold. So, chemical modifications such as reinforcement with fibers, or powders, or blending are necessary (Zhu et al. 2012).

In relation to rheological properties of alginate, one alternative for producing a printable and cell-friendly hydrogel is to add the crosslink agents divalent cations such as Ca^{2+}, Ba^{2+}, Mn^{2+}, Sr^{2+}, Zn^{2+}, and Mg^{2+}, or even trivalent cátion such as Fe^{3+} from water solved salts. Those cations interact mainly with the free carboxylate groups that compose the alginate structure and modulate the gel strength (Pradhan et al. 2021; Benwood et al. 2021). However, some studies indicate that hydrogel-based of Alginate is limited to good printability.

However, some studies indicate that hydrogel-based of Alginate is limited to good printability, suggesting addition of viscous agents to obtain solid-like behaviour. Mixtures of Alginate and Gelatin combine the good rheological properties of the Alginate and the fluidity of the Gelatin. Also, there are the alginate-methacrylate and alginate-norben, which provide a UV photo-crosslinking (Badhe and Nipate 2020; Malda et al. 2013).

The temperature and pH also influence the gelation of Alginate. Increasing the temperature, the speed of gelation also increases. Regarding the pH, an alkaline environment destabilizes the hydrogel due to the pronation of the carboxyl groups causing the repulsion between them (Pradhan et al. 2021).

15.2.4 Cellulose

Cellulose is the most abundant natural polymer and promising to be explored in biomedical applications. Structurally, it is a biopolymer composed of unbranched $\beta(1 \rightarrow 4)$D-glucose units. When biosynthesized are self-assembled into microfibrils, showing crystalline and amorphous regions and this organization depends on the natural source. Due to its high commercial demand, there are several sources for obtaining this raw material and major sources are plant fibers, wood, and by microorganisms.

For biomedical applications, the bacterial cellulose has more advantages in relation to cellulose by other sources, including high crystallinity without lignin presence, good mechanical properties, biocompatibility. In addition, using bacterial cellulose as substrate its able to adsorb bioactive molecules to produce for example drug delivery systems or be coated by nanoparticles on surface to produce occlusive biocuratives with antimicrobial activity or accelerate the wound healing process (De Souza et al. 2013).

Cellulose and its derivatives, such as carboxymethylcellulose and cellulose acetate, are widely used viscosity agents in cosmetic formulations. However, hydrogels with these derivatives show more viscoelastic behavior, i.e., not forming a true gel, making it difficult to use these hydrogels alone due to poor printability. To improve the gel strength of cellulose, an alternative is the increase their surface area, producing micro- and nanocellulose.

When these cellulose micro- and nanofibrils are dispersed in presence of water, the hydrogen bonds between water and hydroxyl groups of cellulose, promote high swelling forming hydrogels. Considering good printable conditions, some studies show that in concentrations ranged at 2% to 10%, some systems present shear thinning behavior and mechanical strength interesting for application as bioinks (Badhe and Nipate 2020; Kuzmenko et al. 2018).

However, cellulose at micro- or nanofibrils are only the substrate and other functions and requisites to explore this biopolymer as bioink has been improved. Incorporation of nanoparticles and bioactive antimicrobial molecules has been reported and authors relate such properties with advantage to increase cell growth.

In this way, new dressings have been developed using natural polymers, such as alginate, chitosan and cellulose derivatives (methylcellulose, carboxymethylcellulose, and others). Blending different polymers with cellulose allows the improvement of biocomposites to generate charged surfaces with variable functional characteristics, resulting in a friendly surface to adhesion, proliferation and differentiate cells.

For example, Souza et al. (2021) evaluated the cellulose nanocomposite with gellan gum and xyloglucan seeded with mesenchymal stem cells (MSCs) as wound dressing. The authors concluded that the membranes seeded with MSCs improved the healing process, reduced acute/chronic inflammatory infiltrates, accelerated resolution of the inflammatory process, increased vascular proliferation, and stimulated epithelialization and a higher rate of collagen deposition, reducing the wound area in less time, and collagen deposition.

Wu et al. (2018) used cellulose nanocrystals (CNCs) with alginate. The rheological analysis reveal that only with incorporation of CNCs was possible to obtain hydrogels with solid-like behavior and printability tests of bioink displayed excellent shear-thinning property, extrudability, and shape fidelity after deposition.

15.2.5 Collagen

The Collagen present as the most abundant protein in the natural ECM has inspired the collagen hydrogel to be used in bioprinting. The ECM collagen interacts with cells contributing to their migration, proliferation, and differentiation. Therefore, the hydrogel collagen is supposed to have the same interactions.

However, the properties of collagen hydrogel are strongly dependent on the fabrication parameters and the sources (bovine or porcine, for example), and the method of extraction (Antoine et al. 2014).

Type I is commonly used to produce hydrogels among the collagen types because it is the most abundant and easy to obtain from tendons, bones, and skin. This Collagen, formed by amino acid chains arranged in a triple alpha-helices structure, self-organizes into fibrils in the physiological environment (Osidak et al. 2020; Lee et al. 2021).

Type I Collagen can be dissolved in water, between 5 mg/ml and 10 mg/ml, to produce a hydrogel in nearly neutral pH through natural crosslink bonds formed between the Collagen fibrils (Antoine et al. 2014; Osidak et al. 2020). This kind of Collagen can be provided by maintaining the temperature between 20 oC and 37 °C, and the pH between 6.5 and 8.5 (Lee et al. 2021).

Some strategies are required to make the Collagen hydrogel suitable for bioprinting since it has low viscosity and is unstable in solution. One method is to mix Collagen with Alginate hydrogel and calcium ions (Moeinzadeh et al. 2021). Another way to improve its physical strength is by chemical crosslinker agents such as glutaraldehyde, genipin, and riboflavin (Nair et al. 2020).

However, further crosslinks must be achieved with chemicals such as aldehydes to improve the mechanical properties providing stable scaffolds (Dinescu et al. 2018). In this case, the use of chemicals prevent the addition of cells during the printing process (Lee et al. 2021).

Another possibility is the mixture of about 80 mg/ml of Collagen with NaCl with temperature control, forming a high viscous bioink and favoring a stable printable structure. Such bioink is available on the market under the trade name Viscoll, which permits the viability in vitro of the NIH 3T3 cells (mammal cells) after printing (Osidak et al. 2020).

15.2.6 Chitosan

Chitosan is an amino polysaccharide derived from the Chitin, poly(β-(1-4)-poly-N-acetyl-D-glucosamine). Chitin is the principal organic constituent extracted mainly from the exoskeletons of crustaceans and, therefore, is an abundant substance. Its chemical structure has high stability and low solubility. A variety of chitin structures are associated with the specimen from which it was extracted, presenting specific proteins, degree of mineralization, and interactions between the molecules, which influence the properties of this material (Ahmadi et al. 2015; Fu et al. 2018). Although Chitosan is synthetically derived from Chitin, it can be considered a natural polymer.

So, the deacetylated Chitin is called Chitosan. The degree of deacetylation represents the molar percentage of the amino groups and is between 50 and 100% deacetylation, generally using an alkaline solution (Shen et al. 2016). The acetylated groups are responsible for the rigidity and poor solubility of the Chitin. Therefore, its partial deacetylation provides the fabrication of a gel material suitable for bioprinting. However, the smaller the degree of deacetylation, the lower the crystallinity, which decreases the degradability of the Chitosan.

Some studies have shown that Chitosan presents antimicrobial and immunomodulatory properties and seems osteoinductive (Benwood et al. 2021; EzEldeen et al. 2021). Besides, the chemical structure and properties of the Chitosan are similar to the glycosaminoglycan (GAG) abundant in the natural ECM.

Due to the apolar character of the amino groups, Chitosan is not soluble in water or organic solvents. It is soluble in acid solutions at pH < 6.0, transforming it into a cationic electrolyte because of the creation of protonated amino groups (Domalik-Pyzik et al. 2018). The positive charges interact with the glycoprotein providing the adhesive characteristic of the Chitosan. In this case, as the degree of deacetylation increases, more positive charges are formed, and higher is the adhesive force (Akhtar et al. 2016; Croisier and Jérôme 2013). Therefore, the rise in the degree of deacetylation transforms the Chitosan into a more viscous hydrogel. The high viscosity difficult the migration of cells and other bioactive substances, making it less biocompatible.

Concerning hydrogel formation, there is no necessity for additives to form a gel of Chitosan. However, some studies report that the increase in positive charges leads to an increase in vitro biocompatibility because of the interactions of those charges with cells (Croisier and Jérôme 2013).

A gel is easily formed because of the adhesive characteristic of the Chitosan pointed earlier, involving the neutralization of the protonated amino groups by the glycoproteins. The only additional work is to create a repulsion between the backbone molecules by forming hydrogen bonds, hydrophobic interactions, or crystallization (Lam et al. 2019; Croisier and Jérôme 2013).

Chitosan hydrogels are mechanically weak and can be dissolved due to the physical molecular interactions, leading to limited applications as bioink. However, as with other biopolymers, incorporating other hydrogels (e.g., Alginate) improves its mechanical and thickening properties adequate to bioprinting techniques (Adhikari et al. 2021).

As illustrated in Fig. 15.5, to obtain good properties of chitosan systems as bioink, just like other natural polymers, chitosan can be modified or blended with crosslinking agents. For example, it is possible to create a covalent crosslink in Chitosan hydrogel using glyoxal, glutaraldehyde, and the natural crosslinking agent called genipin (EzEldeen et al. 2021; Zhou et al. 2019). Irreversible Chitosan hydrogel can be produced chemically inducing covalent bonds between the chains. However, there is no guarantee that the reaction delivers non-toxic residues compromising its use in biomedical applications.

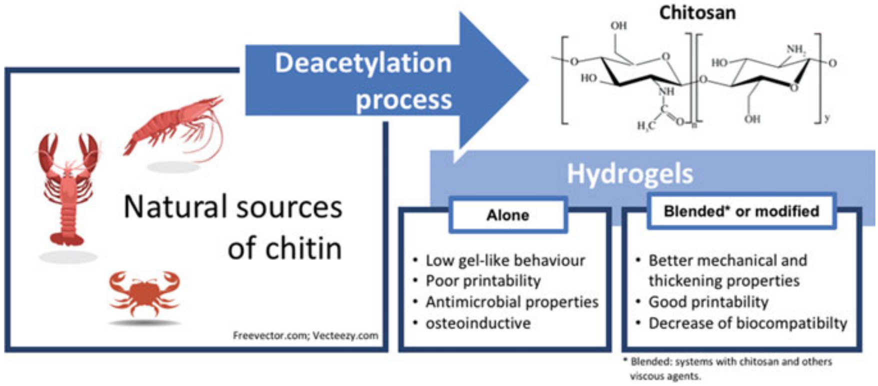

Fig. 15.5 Achievement of chitosan from different natural sources and their prospect as bioink

Also, the cationic characteristic of Chitosan dissolved in acid solution favours electrostatic interactions with phosphates, sulphates, and citrates, and negatively charged ions, allowing Chitosan to form a hydrogel. Proteins and anionic polysaccharides can also be used for this purpose (Croisier and Jérôme 2013).

15.2.7 Fibrin

Fibrin is a natural biopolymer formed after thrombin cleavage of fibrinopeptide A from fibrinogen Alpha-chains, resulting in a fibrous matrix. Fibrin plays important overlapping roles in blood clotting, fibrinolysis, cellular and matrix interactions, inflammation, wound healing, and neoplasia (Mosesson 2005). The isolation and application of fibrin membranes as a scaffold for wound healing are illustrated in Fig. 15.6, which follows a well-known protocol involving blood collection from venous access, centrifugation using tubes free of anticoagulant agent, and isolation of the fibrin clot which is one of the three layers formed.

The fibrin clot is full of platelets and leukocytes. This antibacterial 3D network stimulates the migration of fibroblasts to the wound site and induces the proliferation of essential elements for improving wound healing, such as collagen type I and fibronectin. However, like other natural hydrogels, the fibrin has poor mechanical resistance and needs to be blended with another natural or synthetic hydrogel (de Carvalho et al. 2020).

The hydrogel formation from Fibrin is based on its natural polymerization process with thrombin following vascular injury. The mechanism indicates a cleavage at two amino acids of fibrinogen by thrombin followed by fast polymerization of single fibrinogen molecules to a 3D fibrin network achieved by covalent crosslinking (Schneider-Barthold et al. 2016).

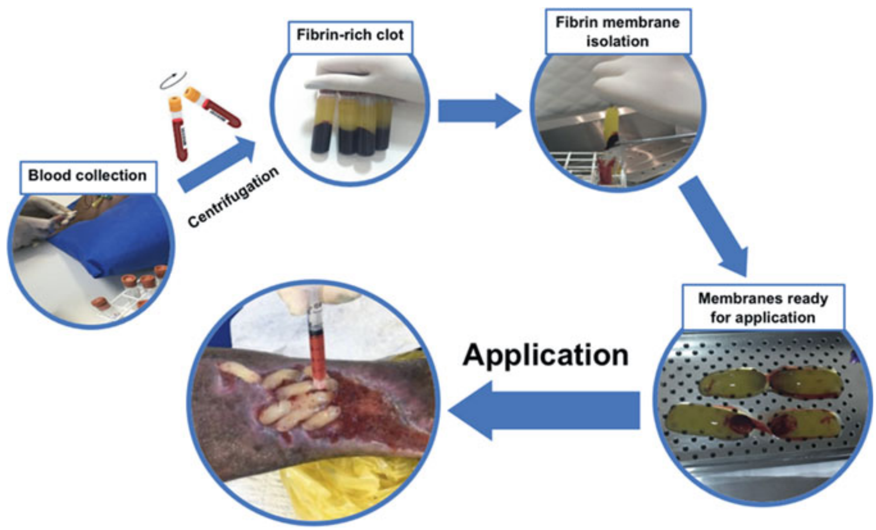

Fig. 15.6 Manufacture of autologous fibrin membranes substrate for wound healing applications

Its biocompatibility and fast polymerization can be explored for drug and cell delivery, wound healing, and tissue engineering (Dubnika et al. 2021; Deller et al. 2019). Although fibrin forms hydrogel, the isolate solutions of this polymer show low shear-thinning behaviour and low mechanical properties, limiting its use in bioprinting techniques (De Melo et al. 2020; Weisel 2004).

However, to explore this hydrogel in 3D-bioprinting process, the tuneable mechanical and nanofibrous structural properties occur only in the presence of the other polymers that improve these parameters to promote better printer conditions (De Melo et al. 2020).

15.2.8 Gelatin

Gelatin is composed of protein usually extracted by partial hydrolysis of Collagen, the organic component present in soft tissues such as tendons, cartilage, and skin, and also present in bones (Rashid et al. 2019). It is soluble in hot water, forming a hydrogel during its cooling.

Gelatin contains about 18 amino acids, including glycine, alanine, and proline. Although the components vary depending on the source (Rashid et al. 2019), amino acids are essential to maintain cellular viability. Therefore, Gelatin is used together with other natural bioprintable polymers to improve printability and provide a suitable environment for the cells to proliferate and maintain their viability.

The Gelatin alone, even though be printable, cannot form a stable scaffold after the bioprinting process since it solubilizes at physiological temperature (37 °C) (Leucht et al. 2020). This characteristic allows the hydrogel to be used as a sacrificial one to form channels simulating vessels and arteries.

The necessary mechanical resistance to be used as a support for cells must be achieved by creating crosslinks by chemical means. Various studies have been done with Gelatin and metacryl forming the Gelatin methacryloyl (GelMA), which is biocompatible, degradable, and has custom-made mechanical properties by controlling the degree of methacryloylation (Zhu et al. 2019). The addition of hydroxyapatite to the GelMA bioink has been showing to provide osteoinduction (Leucht et al. 2020; Bartnikowski et al. 2016). Therefore, depending on the substance mixed to the GelMA bioink can support and proliferate specific cells after the bioprinting process.

Cell attachment and proliferation can be improved when Gelatin is mixed with Collagen, because of their favorable composition with components present in the natural ECM (Gao et al. 2018). The hydrogel Gelatin-Alginate is another viable alternative since Alginate offers a stable scaffold through crosslinked by divalent cations.

Besides improving printability, Gelatin provides amino acids that enhance the environment to the viability of the cells. However, the proportion of Aginate and Gelatin must be carefully evaluated for each injection speed to guarantee printability without losing the printable structure's stability (Gao et al. 2018).

15.2.9 Hyaluronic Acid

Hyaluronic acid (HA) is a glycosaminoglycan composed of a linear chain polysaccharide consisting of a repeating disaccharide β-1,4-glucuronic acid and β-1,3 N-acetylglucosamine. It exists primarily in the extracellular tissue matrix of vertebrates (Lam et al. 2019).

Hyaluronan and networks in plasma fluidic have many physiological functions that include tissue and matrix water regulation, structural and space-filling properties, lubrication, and several other functions (Kiyotake et al. 2019).

HA acts as a signaling molecule for cell migration and proliferation. In this way, this hydrogel has been extensively used in biomedical applications (Kiyotake et al. 2019). However, its gelling properties are not suitable to be applied as bioink (Antich et al. 2020).

Because of the low viscosity of HA in solution, the blends involving natural gelling agents are an alternative to formulate bioinks with this hydrogel (Petta et al. 2020; Noh et al. 2019). There are some challenges concerning the HA hydrogel since it seems that it does not allow cells adherence and spreading, so it must be improved (Kiyotake et al. 2019).

Blends can be prepared, for example, adding allyl-functionalized poly(glycidol)s (P(AGE-co-G)) as a cytocompatible crosslinker, which improves cell viability and printability. The crosslinker decreases the elastic modulus and increases the swelling ratio, resulting in good cell viability. The thermoplastic poly(ε-caprolactone) can be added to form bioink to bioprint in articular cartilage scaffolds (Stichler et al. 2017).

Another possibility to form an appropriate bioink is to blend HA with sodium alginate (SA), using ions Ca^{2+} as crosslink agent. Different ratios of HA, vary the cell viability and proliferation. Besides, the SA modulates the viscosity, provides printable conditions for the hydrogel, and allows structural stability of the scaffold, comparing to the HA alone. This blend is suitable for scaffolds focused on soft tissue regeneration (Lee et al. 2021).

15.3 Optimizing Natural Based-Hydrogels as Bioinks

3D printing involves some steps to obtain precise objects, and this conception is illustrated in Fig. 15.7. The steps involve the concept, 3D design, material selection (plastic, rubber, gels, metal), printer settings, slice, and printing (Ashammakhi et al. 2019).

Due to complexity, the 3D design must be as faithful as possible to the natural tissues. One way to do that is by exploring computer-aided design and computer-aided manufacturing (CAD-CAM) tools and mathematical modelling to rendering images. High-resolution images can be obtained by ultrasound, MRI, and X-ray equipment. The three-dimensional images can be treated to transform into functional and biomimetic tissue-like constructs.

A study performed by Busse et al. (2018) to exemplify this step evaluates soft tissue 3D histology with a cytoplasm-specific staining method tailored for computed tomography (CT) X-ray that enables a routine and efficient 3D volume screening at high resolutions. The results showed the anatomical morphology of different tissues in the submicrometric dimension.

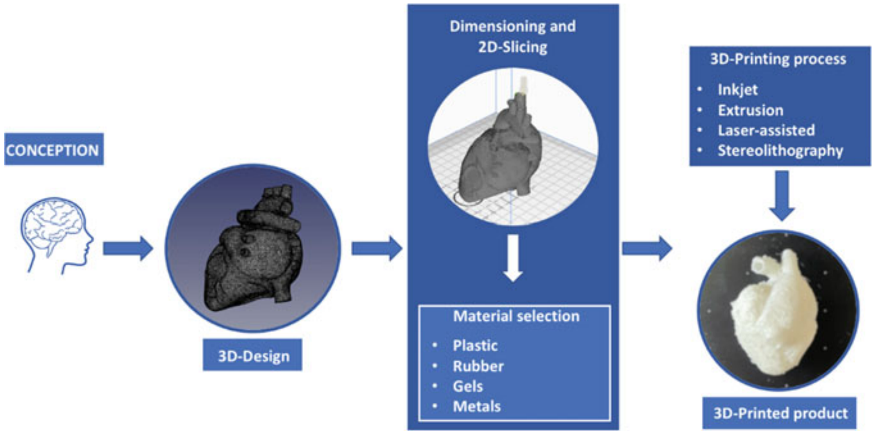

Fig. 15.7 Schematic illustration of steps to produce objects by 3D printing process

The 3D-rendered images are divided into thin 2D horizontal slices (with customizable size and orientation) that provide the bioprinter systems instructions for layer-by-layer depositions (Murphy and Atala 2014).

Analogous to the conventional 3D printing process, the biomimetic structure is obtained by deposition the substrate layer-by-layer. The bioinks are dependent on printing techniques. In all cases, the rheological properties and crosslinking mechanism reflect the printability of the bioinks (Chopin-Doroteo et al. 2021).

In this context, according to the behavior of hydrogels in solution and their applicability, three systems can be used, nozzle-based 3D-printing, inkjet printer-based 3D-printing based in fused deposition modeling (FDM) technology, and laser-based 3D printing based in FDM and stereolithography (SLA) technology (Fig. 15.8).

In inkjet printing (Fig. 15.8a), a ceramic piezoelectric component generates a mechanical pulse to promote a flow of bioink to the nozzle as droplets. As advantage, inkjet-based bioprinting has low cost, medium print speeds, and good resolution (Chopin-Doroteo et al. 2021). However, among the problems there is low droplet directionality and unreliable cell encapsulation due to the low concentration and high viscosity of the bioink, resulting in the weak mechanical integrity of the construct (Kačarević et al. 2018; Williams et al. 2018).

The microextrusion printers (Fig. 15.8b) present pneumatic, piston-driven, or screw-driven robotic dispensing systems, controlling the bioink by a continuous stream of hydrogel-containing cells. It has the advantage of working with a wide range of bioinks with different fluid properties and viscosity from 30 mPa/s to 60 kPa/s,

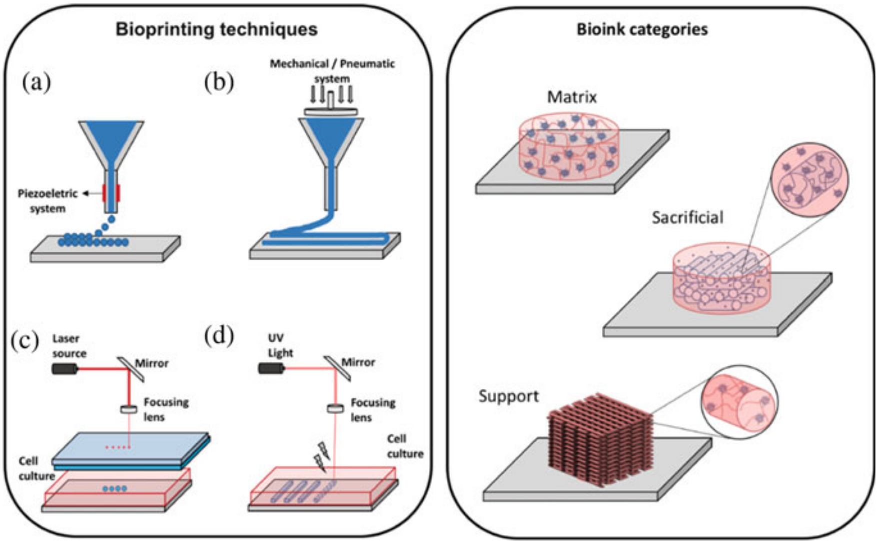

Fig. 15.8 Illustration of different techniques: inkjet printer-based 3D-bioprinting (**a**), nozzle-based 3D-bioprinting (**b**), laser-assisted 3D-bioprinting (**c**), and stereolithographic 3D-bioprinting (**d**); and bioink categories. Groll et al. (2019), Sundaramurthi et al. (2016)

with limitations in build the structure more complex and enhancing print speed and resolution.

The laser-assisted 3D printing (Fig. 15.8c, d) uses an absorbing layer to create laser pulse pressure. It induces a vapor bubble through cell-laden hydrogel to transfer cell-encapsulating hydrogel droplets onto a substrate (Sundaramurthi et al. 2016). The extrusion temperature must be lower than the conventional 3D printing process to avoid denaturation and killing the cells. In the ECM, the inkjet printer-based and nozzle-based 3D-bioprinting extrusion occur at about 37 °C (Theus et al. 2020). The gelation of bioink by physical or chemical processes can happen simultaneously with the printing process to guarantee the fidelity of the scaffold.

On laser-assisted 3D-printing process, are explored light-emitting diodes (LEDs) that emit either ultraviolet (UV) (~365 nm) radiation or near-ultraviolet (~405 nm) radiation sources to in situ photocrosslinking hydrogels. In this case, penetrating UV radiation can damage and limit cell viability (Zheng et al. 2021). However, Godar et al. (2019) evaluated the exposition of L929 mouse fibroblast cells by UV and compared them with human mesenchymal stem cells (hMSC), simulating the conditions of 3D-microextrusion. In this study, the authors observed more sensitivity of hMSC in polymerization conditions proposed concerning L929 cells, indicating some limitations to explore this 3D-printing process with the ECM hydrogel systems.

Recently, it is proposed to divide the term bioink into three categories: matrix, sacrificial, and support bioinks (Fig. 15.8). The suggested discrimination between the different classes is:

(i) *Matrix bioinks*: materials designed to support cell populations during delivery and act as an artificial extracellular matrix as cells multiply;
(ii) *Sacrificial bioinks*: temporary materials that can be rapidly removed to form internal voids or channels within a printed construct;
(iii) *Support bioinks*: are used to provide mechanical integrity to printed structures and may also be fugitive but over a relatively long time.

According to techniques presented in Fig. 15.8, the printability of the bioink depends on the different parameters such as viscosity of the solution, surface tension, the ability to crosslink on its own and surface properties of printer nozzle. In general, the authors improve the hydrogels printability increasing the polymer concentration or crosslink density with formulations ranged at 0.8wt% to 40wt% (Malda et al. 2013).

To understand the influence of these parameters, we can exemplify with the inkjet and microextrusion printer. In the work mechanical to 3D-printing process, the pressure applied to induce the flow of the bioink, the viscoelastic gel is changed, becomes more fluidic, and comes out in the needle smoothly. However, is desired that the hydrogel which came out of the needle recovery initial viscoelasticity, and the pressure is stopped, the hydrogel inside the reservoir regains the initial viscoelasticity.

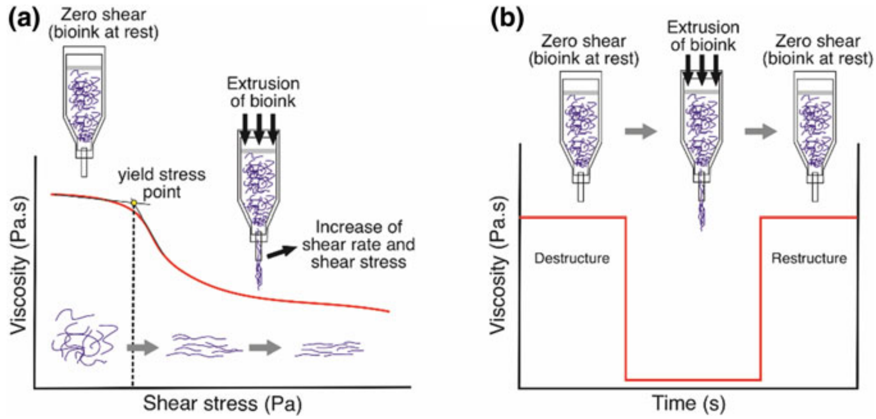

Fig. 15.9 Schematic representation of steady conditions rheological parameters evaluation to optimize 3D-printing process by natural hydrogels bioinks

The challenge is developed a system that show low resistance to flow upon application of stress, i.e., during 3D-printing process and a solid-like behavior after deposition, to obtain an optimal shape fidelity. Thus, define steady and dynamic oscillatory shear rheological properties show us as mandatory to application of the hydrogels as bioink. In case to evaluate the rheological parameters of the bioink, this is summarized in Fig. 15.9, where the steps to obtain the information to improve the printing process.

According to illustration of Fig. 15.9a, the first step is analysis the flow behavior of hydrogels. The non-Newtonian systems, such as hydrogels, the viscosity are dependent of the shear rate at constant temperature. On case of 3D-printing process, the ideal conditions is that viscosity decrease with increasing shear rates. As the viscosity of the hydrogles is shear-dependent, the shear condition can be modulate by gauge of the printer nozzle (considering an ideal concentration).

Additionally, in this condition of the rheological analysis, we can evaluate the yield stress point, that is minimum force to make the bioink flowing during printing process. In this case, is the force that must be exceeded in order to break down a hydrogel structure at rest, and thus make it flow.

For example, the yield stress for PHA pressed through a 27G (i.e., 0.21 mm diameter) nozzle is about 1000 Pa, where PHA formulations with yield stress beyond 1000 Pa form printed construct with choppy layers. While the yield stress can be a direct indicator of printability, a material can be printed with high shape fidelity if the viscosity is high enough to delay the material during printing.

Therefore, the viscosity of a bioink is a vital parameter because it determines how much pressure is necessary to keep the material extruding at the desired flow rate. Thus, in addition to determining the shear-thinning behavior, the yield stress is a critical characteristic to maintain the shape of the printed structure (Kiyotake et al. 2019).

When the bioink stay at rest after a sharply switched shear rate, the structure of the hydrogels can be modified resulting in changes of the initial viscosity, before of the flow. In the extrusion process, occur moments at rest of the flow of the bioink (low shear rate) and others with high flow (high shear rate). To simulate this, it is interesting evaluating time-dependent controlled-shear-rate test. As illustrated in the graph of Fig. 15.9b, the viscosity measurement consist one step with very low shear rate (bioink at rest), followed by a high shear rate (bioink with shear-thinning behavior) and finally a step with the same low shear rate of the first step (bioink at rest again). The aim of this measurement is observe the three-dimensional structure regeneration of the hydrogel, during and after extrusion under constant shear conditions.

The final test is measure the viscoelastic behavior of the hydrogels. As exposed in this chapter, an ideal bioink result in high fidelity after printing process. Thus, we must evaluate the behavior of the systems when submitted at quick movements during the extrusion. This condition result in higher shear rate and according to temperature and frequency of oscillation, the hydrogel can exhibit a liquid-like or solid-like behavior. So, this measurement consist in find the ideal conditions (temperature, velocity and frequency) of printing process, without break out the structure of the hydrogel, i.e., work at linear viscoelastic conditions.

According to illustrated at Fig. 15.10, are obtained when submit the sample at dinamic oscilatory rheological measurements. When is finded the linear viscoelastic conditions, two mechanical parameters are obtained: the storage modulus (G') and the loss modulus (G''). Basically, the G' represent the solid-state behavior and G'' liquid-state of the sample. The graphical representation of this measurement indicate a $G' > G''$, typical solid-like behavior, due to intermolecular association of the bioink. The higher variation of the G' in relation to the G'', higher the solid-like behavior of the bioink, ideal conditions of rapid solidification upon printing and higher fidelity construct (Siqueira et al. 2017).

Even though the 3D-printing process is in full development, a new technique related to additive manufacturing is rising which is 4D printing. This is a great promise for health application since uses the same principle of 3D printing together with some stress applied to the hydrogel during the 2 D or 3D construct formation. Smart materials such as shape memory polymers can be used to produce hydrogels appropriate for this application. The stresses applied during printing can be temperature, magnetic field, solvent, or pH variation (Piedade 2019).

For example, Kuzmenko et al. (2018) develop conductive inks from cellulose nanofibrils with carbon nanotubes for neural tissue engineering. According to the authors, with this conductive ink was possible to print guidelines with a diameter below 1 mm and electrical conductivity of $3{,}8 \times 10^{-1}$ S cm^{-1}. At 2wt% aqueous dispersion of nanocellulose was enough to obtain shear thinning flow behavior during the printing process and a storage modulus (G') substantially higher than loss modulus (G''), resulting in a rapid solidification of hydrogel when is deposited on surface.

Nature is an inspiration to produce 4 D constructs using, as printable material, acrylamide reinforced by cellulose fibrils having their direction previously arranged. When swelled with water, the construct mimics the plant architecture. A magnetic

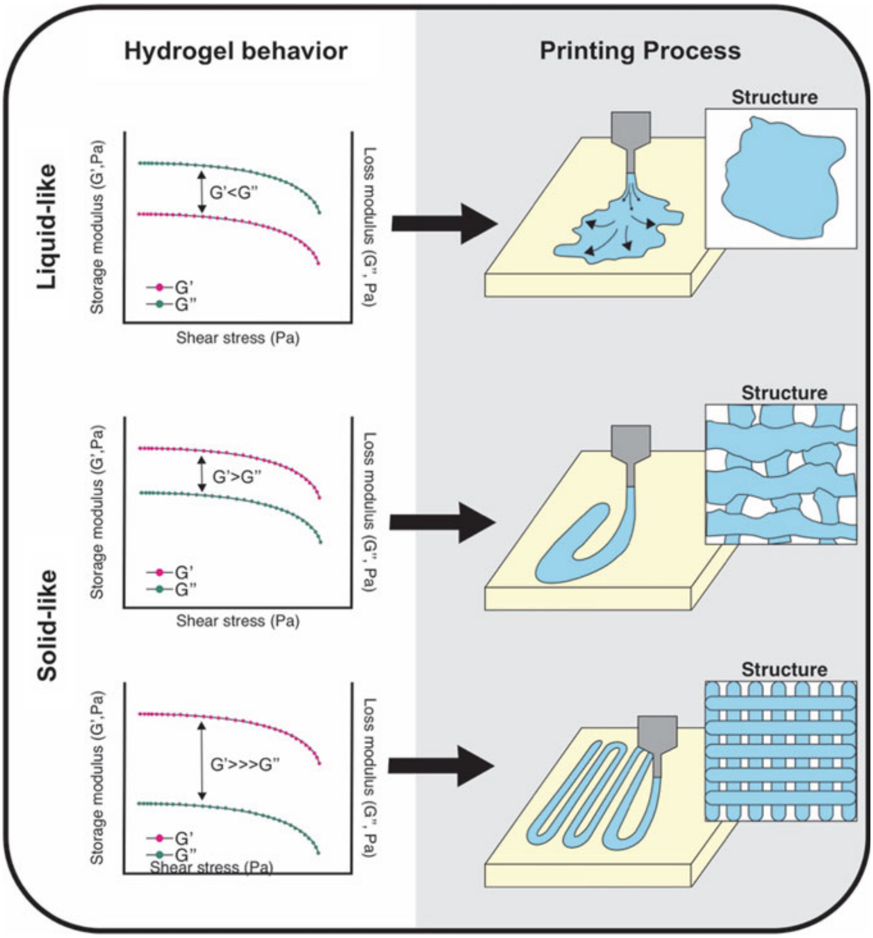

Fig. 15.10 Oscillatory conditions rheological parameters evaluation to optimize 3D-printing process by natural hydrogels bioinks and a simulate reproduction of fidelity construct of hydrogel

field can change the shapes of printed hydrogels impregnated with metal particles like poly(urethane acrylate) and aluminum.

Manipulating polymer blends with different glass transition temperatures (*Tg*) is possible to change the shapes of constructs submitting them to ranges of temperatures. Poly (2-vinyl pyridine) blended with acrylonitrile–butadiene–styrene (ABS) is an example of hydrogel that changes its shape according to pH variation (Piedade 2019). Those are some examples of hydrogels that have been studied for future biomedical applications.

15.4 Conclusion

Regenerative medicine has, presently, a great ally in 3D printing and, more recently, 4D printing. Hydrogels and bioinks have been improved each year and seems that there are no limits for discoveries and new mixtures. Also, the 3D cell proliferation and their aggregation to the hydrogels have been breaking barriers.

Until now, there are a limited number of natural printable biomaterials, and developing new bioinks is challenging because of the combined physical, mechanical, chemical, and biological properties. Like synthetic hydrogels, natural ones presents advantages and disadvantages to be explored as bioink. The main advantage of natural hydrogels is their capacity to mimic the extracellular matrix allowing the cells to continue to produce their signaling and maintaining their activities in vitro. Besides, although their relative abundance, they can be expensive.

In this chapter, we mentioned the natural hydrogels commonly studied to be used as bioinks that are Agarose, Alginate, Cellulose, Collagen, Chitosan, Fibrin, Gallatin, and Hyaluronic Acid. As discussed, they rarely are used alone because the blends provide better printability and construct stability.

Since the characteristics of the bioinks are strongly dependent on the hydrogels' mixture, most of the bioinks are developed by trial-and-error, which is neither efficient nor comparable across materials, limiting the efficiency studies. Therefore, a study front could be the development of standard methods to improve and characterize natural bioinks.

Many bioinks formulations have been reported from cell-biomaterials-based bioinks to cell-based bioinks such as cell aggregates and tissue spheroids for tissue engineering and regenerative medicine applications. Interestingly, more tunable bioinks, which are biocompatible for live cells, printable, and mechanically stable after printing are emerging with the help of functional polymeric biomaterials, their modifications, and blending of cells and hydrogels. These approaches show the immense potential of these bioinks to produce more complex tissue/organ structures using 3D bioprinting in the future and more recently for 4D bioprinting process.

Acknowledgements The authors would like to thank the Pontifical Catholic University of Parana (PUCPR) for financial support to the development of this research.

References

Abar B, Alonso-Calleja A, Kelly A, Kelly C, Gall K, West JL (2021) 3D printing of high-strength, porous, elastomeric structures to promote tissue integration of implants. J Biomed Mater Res A 109:54–63. https://doi.org/10.1002/jbm.a.37006

Abdollahiyan P, Oroojalian F, Mokhtarzadeh A, De la Guardia M (2020) Hydrogel-based 3D bioprinting for bone and cartilage tissue engineering. Biotechnol J 15:2000095. https://doi.org/10.1002/biot.202000095

Adhikari J, Perwez MS, Das A, Saha P (2021) Development of hydroxyapatite reinforced Alginate–Chitosan based printable biomaterial-ink. Nano Struct Nano Object 25:100630. https://doi.org/10.1016/j.nanoso.2020.100630

Ahmadi F, Oveisi Z, Samani SM, Amoozgar Z (2015) Chitosan based hydrogels: characteristics and pharmaceutical applications. Res Pharm Sci 10(1):1–16

Akhtar MF, Hanif M, Ranjha NM (2016) Methods of synthesis of hydrogels-a review. Saudi Pharm J 24:554–559. https://doi.org/10.1016/j.jsps.2015.03.022

Antich C, De Vicente J, Jiménez G, Chocarro C, Carrillo E, Montañez E, Gálvez-Martín P, Marchal JA (2020) Bio-inspired hydrogel composed of hyaluronic acid and alginate as a potential bioink for 3D bioprinting of articular cartilage engineering constructs. Acta Biomater 106:114–123. https://doi.org/10.1016/j.actbio.2020.01.046

Antoine EE, Vlachos PP, Rylander MN (2014) Review of Collagen i hydrogels for bioengineered tissue microenvironments: characterization of mechanics, structure, and transport. Tissue Eng Part B 20(6):683–696. https://doi.org/10.1089/ten.teb.2014.0086

Aswathy SH, Narendrakumar U, Manjubala I (2020) Commercial hydrogels for biomedical applications. Heliyon 6:e03719. https://doi.org/10.1016/j.heliyon.2020.e03719

Ashammakhi N, Ahadian S, Xu C, Montazerian H, Ko H, Nasiri R et al (2019) Bioinks and bioprinting technologies to make heterogeneous and biomimetic tissue constructs. Mater Today Bio [Internet], 1:100008. https://doi.org/10.1016/j.mtbio.2019.100008

Badhe RV, Nipate SS (2020) Cellulosic materials as bioinks for 3D printing applications. In: Toit L, Kumar P, Choonara Y, Pillay V (eds) Advanced 3D-printed systems and nanosystems for drug delivery and tissue engineering. Woodhead Publishing Series in Biomaterials, Elsevier, pp 109–137

Bahram M, Mohseni N, Moghtader M (2016) An introduction to hydrogels and some recent applications, emerging concepts in analysis and applications of hydrogels. Sutapa Biswas Majee IntechOpen. https://doi.org/10.5772/64301

Balgude AP, Yu X, Szymanski A, Bellamkonda RV (2001) Agarose gel stiffness determines rate of DRG neurite extension in 3D cultures. Biomaterials 22:1077–1084. https://doi.org/10.1016/S0142-9612(00)00350-1

Bartnikowski M, Akkineni AR, Gelinsky M, Woodruff MA, Klein TJ (2016) A hydrogel model incorporating 3D-plotted hydroxyapatite for osteochondral tissue engineering. Mater (Basel, Switzerland) 9(4):285 PMID: 28773410

Benwood C, Chrenek J, Kirsch RL, Masri NZ, Richards H, Teetzen K, Willerth SM (2021) Natural biomaterials and their use as bioinks for printing tissues. Bioeng 8(27):2–19. https://doi.org/10.3390/bioengineering8020027

Busse M, Müller M, Kimm MA, Ferstl S, Allner S, Achterhold K et al (2018) Three-dimensional virtual histology enabled through cytoplasm-specific X-ray stain for microscopic and nanoscopic computed tomography. Proc Natl Acad Sci USA 115(10):2293–2298

Brown K, Broadhurst K, Mathahs M et al (2005) Expression of HSP47, a collagen-specific chaperone, in normal and diseased human liver. Lab Invest 85:789–797. https://doi.org/10.1038/labinvest.3700271

Caló E, Khutoryanskiy VV (2015) Biomedical applications of hydrogels: a review of patents and commercial products. Eur Polym J 65:252–267. https://doi.org/10.1016/j.eurpolymj.2014.11.024

Chirani N, Yahia L'H, Gritsch L, Motta FL, Chirani S, Faré S (2015) History and applications of hydrogels. J Biom Sc 4:2. https://doi.org/10.4172/2254-609X.100013

Croisier F, Jérôme C (2013) Chitosan-based biomaterials for tissue engineering. Eur Polym J 49:780–792. https://doi.org/10.1016/j.eurpolymj.2012.12.009

Chopin-Doroteo M, Mandujano-Tinoco EA, Krötzsch E (2021) Tailoring of the rheological properties of bioinks to improve bioprinting and bioassembly for tissue replacement. Biochim Biophys Acta—Gen Subj [Internet] 1865(2):129782. https://doi.org/10.1016/j.bbagen.2020.129782

Dubnika A, Egle K, Skrinda-Melne M, Skadins I, Rajadas J, Salma I (2021) Development of vancomycin delivery systems based on autologous 3D platelet-rich fibrin matrices for bone tissue engineering. Biomedicines 9(7):814. https://doi.org/10.3390/biomedicines9070814

De Carvalho CKL, Fernandes BL, de Souza MA (2020) Autologous matrix of platelet-rich fibrin in wound care settings: a systematic review of randomized clinical trials. J Funct Biomater 11(31):1. https://doi.org/10.3390/jfb11020031

De Melo BAG, Jodat YA, Cruz EM, Benincasa JC, Shin SR, Porcionatto MA (2020) Strategies to use fibrinogen as bioink for 3D bioprinting fibrin-based soft and hard tissues. Acta Biomater 117:60–76. https://doi.org/10.1016/j.actbio.2020.09.024

Deller RC, Richardson T, Richardson R, Bevan L, Zampetakis I, Scarpa F et al (2019) Artificial cell membrane binding thrombin constructs drive in situ fibrin hydrogel formation. Nat Commun [internet] 10(1):1887. https://doi.org/10.1038/s41467-019-09763-0

Dinescu S, Albu KM, Chitoiu L, Ignat S, Kaya DA, Costache M. (2018) Collagen-based hydrogels and their applications for tissue engineering and regenerative medicine. In: Mondal M (eds) Cellulose-based superabsorbent hydrogels. Polymers and polymeric composites: a reference series. Springer, Cham. https://doi.org/10.1007/978-3-319-76573-0_54-1

Domalik-Pyzik P, Chłopek J, Pielichowska K (2018) Chitosan-based hydrogels: preparation, properties, and applications. Int J Biol Macromol 115:194–220. https://doi.org/10.1016/j.ijbiomac.2018.04.034

De Souza CF, Lucyszyn N, Woehl MA, Riegel-Vidotti IC, Borsali R, Sierakowski M-R (2013) Property evaluations of dry-cast reconstituted bacterial cellulose/tamarind xyloglucan biocomposites. Carbohydr Polym 93:144–153. https://doi.org/10.1016/j.carbpol.2012.04.062

Dash M, Chiellini F, Ottenbriteb RM, Chiellini E (2011) Chitosan—a versatile semi-synthetic polymer in biomedical applications. Progr Pol Sc 36:981–1014. https://doi.org/10.1016/j.progpolymsci.2011.02.001

EzEldeen M, Loos J, Nejad ZM, Cristaldi M, Murgia D, Braem A, Jacobs R (2021) 3D-printing-assisted fabrication of chitosan scaffolds from different sources and crosslinkers for dental tissue engineering. Eur Cells Mat 41:485–501. https://doi.org/10.22203/eCM.v041a31

Fu J, Yang F, Guo Z (2018) The chitosan hydrogels: from structure to function. New J Chem 42:17162–17180. https://doi.org/10.1039/C8NJ03482F

Frantz C, Stewart KM, Weaver VM (2010) The extracellular matrix at a glance. J Cell Sc 123:4195–4200. https://doi.org/10.1242/jcs.023820

Gao T, Gillispie GJ, Copus JS, Pr AK, Seol Y-J, Atala A, Yoo JJ, Lee SJ (2018) Optimization of gelatin-alginate composite bioink printability using rheological parameters: a systematic approach., Biofabrication 10:34106. https://doi.org/10.1088/1758-5090/aacdc7

Garreta E, Oria R, Tarantino C, Pla-Roca M, Prado P, Fernández-Avilés F, Campistol JM, Samitier J, Montserrat N (2017) Tissue engineering by decellularization and 3D bioprinting. Mater Today 20:166–178. https://doi.org/10.1016/j.mattod.2016.12.005

Godar DE, Gurunathan C, Ilev I (2019) 3D bioprinting with UVA1 radiation and photoinitiator irgacure 2959: can the ASTM standard L929 cells predict human stem cell cytotoxicity? Photochem Photobiol 95(2):581–586. https://doi.org/10.1111/php.13028

Groll J, Burdick JA, Cho D-W, Derby B, Gelinsky M, Heilshorn SC, Jüngst T, Malda J, Mironov VA, Nakayama K, Ovsianikov A, Sun Takeuchi WS, Yoo JJ, Woodfield TB (2019) A definition of bioinks and their distinction from biomaterial inks. Biofabrication 11. https://doi.org/10.1088/1758-5090/aaec52

Gyles DA, Castro LD, Silva Júnior JOC, Ribeiro-Costa RM (2017) The designs and prominent biomedical advances of natural and synthetic hydrogel formulations. Eur Pol J 88:373–392. https://doi.org/10.1016/j.eurpolymj.2017.01.027

Iwata H, Kobayashi K, Takagi T, Oka T, Yang H, Amemiya H, Tsuji T, Ito F (1994) Feasibility of agarose microbeads with xenogeneic islets as a bioartificial pancreas. J Biomed Mater Res 28:1003–1011. https://doi.org/10.1002/jbm.820280905

Iwata H, Takagi T, Amemiya H, Shimizu H, Yamashita K, Kobayashi K, Akutsu T (1992) Agarose for a bioartificial pancreas. J Biomed Mater Res 26:967–977. https://doi.org/10.1002/jbm.820260711

Jia J, Richards DJ, Pollard S, Tan Y, Rodriguez J, Visconti RP, Trusk TC, Yost MJ, Yao H, Markwald RR, Mei Y (2014) Engineering alginate as bioink for bioprinting. Acta Biomater 10:4323–4331. https://doi.org/10.1016/j.eurpolymj.2017.01.027

Kaczmarek-Szczepańska B, Sosik A, Małkowska A, Zasada L, Michalska-Sionkowska M (2021) The study of physicochemical properties and blood compatibility of sodium alginate-based materials via tannic acid addition. Materials 14(17):4905. https://doi.org/10.3390/ma14174905

Kačarević ŽP, Rider PM, Alkildani S, Retnasingh S, Smeets R, Jung O et al (2018) An introduction to 3D bioprinting: possibilities, challenges and future aspects. Mater (basel, Switzerland) 11(11):2199. https://doi.org/10.3390/ma11112199

Kiyotake EA, Douglas AW, Thomas EE, Nimmo SL, Detamore MS (2019) Development and quantitative characterization of the precursor rheology of hyaluronic acid hydrogels for bioprinting. Acta Biomater 95:176–187. https://doi.org/10.1016/j.actbio.2019.01.041

Kuzmenko V, Karabulut E, Pernevik E, Enoksson P, Gatenholm P (2018) Tailor-made conductive inks from cellulose nanofibrils for 3D printing of neural guidelines. Carbohydr Polym 189:22–30. https://doi.org/10.1016/j.carbpol.2018.01.097

Lam T, Dehne T, Krüger JP, Hondke S, Endres M, Thomas A, Lauster R, Sittinger M, Kloke L (2019) Photopolymerizable gelatin and hyaluronic acid for stereolithographic 3D bioprinting of tissue-engineered cartilage. J Biomed Mater Res Part B Appl Biomater 107:2649–2657. https://doi.org/10.1002/jbm.b.34354

Lee JM, Suen SKQ, Ng WL, Ma WC, Yeong WY (2021) Bioprinting of Collagen: considerations, potentials, and applications. Macrom Biosc 21:1–18. https://doi.org/10.1002/mabi.202000280

Leucht A, Volz A-C, Rogal J, Borchers K, Kluger PJ (2020) Advanced gelatin-based vascularization bioinks for extrusion-based bioprinting of vascularized bone equivalents. Sci Rep [internet] 10(1):5330. https://doi.org/10.1038/s41598-020-62166-w

Li L, Qin S, Peng J, Chen A, Nie Y, Liu T, Song K (2020) Engineering gelatin-based alginate/carbon nanotubes blend bioink for direct 3D printing of vessel constructs. Int J Biol Macromol 145:262–271. https://doi.org/10.1016/j.ijbiomac.2019.12.174

Lima EG, Bian L, Ng KW, Mauck RL, Byers BA, Tuan RS, Ateshian GA, Hung CT (2007) The beneficial effect of delayed compressive loading on tissue-engineered cartilage constructs cultured with TGF-beta3. Osteoarthr Cartil 15:1025–1033. https://doi.org/10.1016/j.joca.2007.03.008

Maharjan B, Park J, Kaliannagounder VK, Awasthi GP, Joshi MK, Park CH, Kim CS (2021) Regenerated cellulose nanofiber reinforced chitosan hydrogel scaffolds for bone tissue engineering. Carbohydr Polym 251:117023. https://doi.org/10.1016/j.carbpol.2020.117023

Malda J, Visser J, Melchels FP, Jüngst T, Hennink WE, Dhert WJA, Groll J, Hutmacher DW (2013) 25th anniversary article: engineering hydrogels for biofabrication. Adv Mater 25:5011–5028. https://doi.org/10.1002/adma.201302042

Markstedt K, Mantas A, Tournier I, Martínez Ávila H, Hägg D, Gatenholm P (2015) 3D bioprinting human chondrocytes with nanocellulose—alginate bioink for cartilage tissue engineering applications. Biomacromol 16:1489–1496. https://doi.org/10.1021/acs.biomac.5b00188

Martínez-Sanz M, Gómez-Mascaraque LG, Ballester AR, Martínez-Abad A, Brodkorb A, López-Rubio A (2019) Production of unpurified agar-based extracts from red seaweed Gelidium sesquipedale by means of simplified extraction protocols. Algal Res 38:101420. https://doi.org/10.1016/j.algal.2019.101420

Mauck RL, Yuan X, Tuan RS (2006) Chondrogenic differentiation and functional maturation of bovine mesenchymal stem cells in long-term agarose culture. Osteoarthr Cartil 14:179–189. https://doi.org/10.1016/j.joca.2005.09.002

Mironov V (2003) Printing technology to produce living tissue. Expert Opin Biol Ther 701–704. https://doi.org/10.1517/14712598.3.5.701

Moeinzadeh S, Park Y, Lin S, Yang YP (2021) In-situ stable injectable collagen-based hydrogels for cell and growth factor delivery. Materialia 15:100954. https://doi.org/10.1016/j.mtla.2020.100954

Mosesson MW (2005) Fibrinogen and fibrin structure and functions. J Thromb Haemost 3:1894–1904. https://doi.org/10.1111/j.1538-7836.2005.01365.x

Muthukrishnan L (2021) Imminent antimicrobial bioink deploying cellulose alginate EPS and synthetic polymers for 3D bioprinting of tissue constructs. Carbohydrate Polymers 260117774-https://doi.org/10.1016/j.carbpol.2021.117774

Murphy SV, Atala A (2014) 3D bioprinting of tissues and organs. Nat Biotechnol [internet] 32(8):773–785. https://doi.org/10.1038/nbt.2958

Nadernezhad A, Caliskan OS, TopuzF AF, Erman B, Koc B (2019) Nanocomposite bioinks based on agarose and 2D nanosilicates with tunable flow properties and bioactivity for 3D bioprinting. ACS Appl Bio Mater 2:796–806. https://doi.org/10.1021/acsabm.8b00665

Neves MI, Moroni L, Barrias CC (2020) Modulating alginate hydrogels for improved biological performance as cellular 3D microenvironments. Front Bioeng Biotechnol 8:665. https://doi.org/10.3389/fbioe.2020.00665

Noh I, Kim N, Tran HN, Lee J, Lee C (2019) 3D printable hyaluronic acid-based hydrogel for its potential application as a bioink in tissue engineering. Biomater Res 23:3. https://doi.org/10.1186/s40824-018-0152-8

Norotte C, Marga FS, Niklason LE, Forgacs G (2009) Scaffold-free vascular tissue engineering using bioprinting. Biomaterials 30:5910–5917. https://doi.org/10.1016/j.biomaterials.2009.06.034

Nair M, Best SM, Cameron RE (2020) Crosslinking collagen constructs: achieving cellular selectivity through modifications of physical and chemical properties. Appl Sci 10(19):6911. https://doi.org/10.3390/app10196911

Osidak EO, Kozhukhov VI, Osidak MS, Domogatsky SP (2020) Collagen as bioink for bioprinting: a comprehensive review. Int J Bioprint 6(3):270. https://doi.org/10.18063/ijb.v6i3.270

Pradhan RA, Rahman SS, Qureshi A, Ullah A (2021) Biopolymers: opportunities and challenges for 3D printing. In: Thomas S, Gopi S, Amalraj A (eds) Biopolymers and their Industrial Applications. From Plant, Animal, and Marine Sources, to Functional Products. Elsevier, pp 281–303

Petta D, D'Amora U, Ambrosio L, Grijpma DW, Eglin D, D'Este M (2020) Hyaluronic acid as a bioink for extrusion-based 3D printing. Biofabrication 12(3):32001. https://doi.org/10.1088/1758-5090/ab8752

Piedade AP (2019) 4D Printing: the shape-morphing in additive manufacturing. J Funct Biomater 10(9):1. https://doi.org/10.3390/jfb10010009

Rashid TU, Sharmeen S, Biswas S, Ahmed T, Mallik AK, Shahruzzaman M et al. (2019) Gelatin-based hydrogels. In: Mondal MIH (ed) Cellulose-based superabsorbent hydrogels. Springer, Cham, pp 1601–1641. https://doi.org/10.1007/978-3-319-77830-3_53

Ryu N-E, Lee S-H, Park H (2019) Spheroid culture system methods and applications for mesenchymal stem cells. Cells 8:1620. https://doi.org/10.3390/cells8121620

Siqueira G, Kokkinis D, Libanori R, Hausmann MK, Gladman AS, Neels A, & Studart AR (2017) Cellulose Nanocrystal Inks for 3D Printing of Textured Cellular Architectures. Advanced Functional Materials 27(12) 1604619-https://doi.org/10.1002/adfm.201604619

Souza CMCOS, de Souza CF, Mogharbel BF, Irioda AC, Franco CRC, Sierakowski MR, de Carvalho KAT (2021) Nanostructured cellulose–gellan–xyloglucan–lysozyme dressing seeded with mesenchymal stem cells for deep second-degree burn treatment. Int J Nanomed 16:833–850. https://doi.org/10.2147/IJN.S289868

Schneider-Barthold C, Baganz S, Wilhelmi M, Scheper T, Pepelanova I (2016) Hydrogels based on collagen and fibrin—frontiers and applications. BioNanoMaterials 17(1–2):3–12. https://doi.org/10.1515/bnm-2015-0025

Shen X, Shamshina JL, Berton P, Gurau G, Rogers RD (2016) Hydrogels based on cellulose and Chitin: fabrication, properties, and applications. Green Chem 18:53–75. https://doi.org/10.1039/c5gc02396c

Stichler S, Böck T, Paxton N, Bertlein S, Levato R, Schill V et al (2017) Double printing of hyaluronic acid/poly(glycidol) hybrid hydrogels with poly(ε -caprolactone) for MSC chondrogenesis. Biofabrication 9(4):044108. https://doi.org/10.1088/1758-5090/aa8cb7

Stokols S, Tuszynski MH (2006) Freeze-dried agarose scaffolds with uniaxial channels stimulate and guide linear axonal growth following spinal cord injury. Biomaterials 27:443–451. https://doi.org/10.1016/j.biomaterials.2005.06.039

Stringer R (2005) Electrophoresis | overview. In: Worsfold P, Townshend A, Poole C (eds) Encyclopedia of analytical science, 2nd edn. Elsevier, Oxford, pp 356–363
Su T, Zhang M, Zeng Q, Pan W, Huang Y, Qian Y, Dong W, Qi X, Shen J (2021) Mussel-inspired agarose hydrogel scaffolds for skin tissue engineering. Bioact Mater 6:579–588. https://doi.org/10.1016/j.bioactmat.2020.09.004
Sundaramurthi D, Rauf S, Hauser C (2016) 3D bioprinting technology for regenerative medicine applications. Int J Bioprinting 2(2). https://doi.org/10.18063/IJB.2016.02.010
Tan Y, Richards DJ, Trusk TC, Visconti RP, Yost MJ, Kindy MS, Drake CJ, Argraves WS, Markwald RR, Mei Y (2014) 3D printing facilitated scaffold-free tissue unit fabrication. Biofabrication 6:24111. https://doi.org/10.1088/1758-5082/6/2/024111
Thomas A, Orellano I, Lam T, Noichl B, Geiger M-A, Amler A-K, Kreuder A-E, Palmer C, Duda G, Lauster R, Kloke L (2020) Vascular bioprinting with enzymatically degradable bioinks via multi-material projection-based stereolithography. Acta Biomater 117:121–132. https://doi.org/10.1016/j.actbio.2020.09.033
Theus AS, Ning L, Hwang B, Gil C, Chen S, Wombwell A et al (2020) Bioprintability: physiomechanical and biological requirements of materials for 3D bioprinting processes. Polymers 12(10):2262. https://doi.org/10.3390/polym12102262
Tröndle K, Rizzo L, Pichler R, Koch F, Itani A, Zengerle R, Lienkamp SS, Koltay P, Zimmermann S (2021) Scalable fabrication of renal spheroids and nephron-like tubules by bioprinting and controlled self-assembly of epithelial cells. Biofabrication 13:035019. https://doi.org/10.1088/1758-5090/abe185
Wang Z, Lee SJ, Cheng HJ, Yoo JJ, Atala A (2018) 3D bioprinted functional and contractile cardiac tissue constructs. Acta Biomater 70:48–56. https://doi.org/10.1016/j.actbio.2018.02.007
Wu Y, Lin ZY, Wenger AC, Tam KC, Tang X (2018) 3D bioprinting of liver-mimetic construct with alginate/cellulose nanocrystal hybrid bioink. Bioprinting 9:1–6. https://doi.org/10.1016/j.bprint.2017.12.001
Weinberger R (2000) Size separations in capillary gels and polymer networks. In: Weinberger R (ed) Practical capillary electrophoresis. Academic Press, San Diego, pp 245–292
Weisel JW (2004) The mechanical properties of fibrin for basic scientists and clinicians. Biophys Chem 112(2):267–276. https://doi.org/10.1016/j.bpc.2004.07.029
Williams D, Thayer P, Martinez H, Gatenholm E, Khademhosseini A (2018) A perspective on the physical, mechanical and biological specifications of bioinks and the development of functional tissues in 3D bioprinting. Bioprinting 9:19–36. https://doi.org/10.1016/j.bprint.2018.02.003
Wilson WC Jr, Boland T (2003) Cell and organ printing 1: protein and cell printers. Anat Rec Part A 272A:491–496. https://doi.org/10.1002/ar.a.10057
Xu J, Fang H, Zheng S, Li L, Jiao Z, Wang H, Nie Y, Liu T, Song K (2021) A biological functional hybrid scaffold based on decellularized extracellular matrix/gelatin/chitosan with high biocompatibility and antibacterial activity for skin tissue engineering. Int J Biol Macromol 187:840–849. https://doi.org/10.1016/j.ijbiomac.2021.07.162
Yang L, Li C, Chen L, Li Z (2009) An agarose-gel based method for transporting cell lines. Curr Chem Genomics 3:50–53. https://doi.org/10.2174/1875397300903010050
Zandi N, Sani ES, Mostafavi E, Ibrahim DM, Saleh B, Shokrgozar MA, Tamjid E, Weiss PS, Simchi S, Annabi N (2021) Nanoengineered shear-thinning and bioprintable hydrogel as a versatile platform for biomedical applications. Biomaterials 267:120476. https://doi.org/10.1016/j.biomaterials.2020.120476
Zhu X, Su M, Tang S et al (2012) Synthesis of thiolated chitosan and preparation nanoparticles with sodium alginate for ocular drug delivery. Mol vis 18:1973–1982 PMID: 22876124
Zhou P, Li X, Zhang B, Shi Q, Li D, Ju X (2019) A human umbilical cord mesenchymal stem cell-conditioned medium/chitosan/collagen/β-glycerophosphate thermosensitive hydrogel promotes burn injury healing in mice. Biomed Res Int 5768285. https://doi.org/10.1155/2019/5768285
Zhu M, Wang Y, Ferracci G, Zheng J, Cho N-J, Lee BH (2019) Gelatin methacryloyl and its hydrogels with an exceptional degree of controllability and batch-to-batch consistency. Sci Rep 9(1):6863. https://doi.org/10.1038/s41598-019-42186-x

Zheng Z, Eglin D, Alini M, Richards GR, Qin L, Lai Y (2021) Visible Light-Induced 3D Bioprinting Technologies and Corresponding Bioink Materials for Tissue Engineering: A Review. Engineering 7(7) 966-978 https://doi.org/10.1016/j.eng.2020.05.021

Part VI
Prediction, Optimization, and Monitoring

Chapter 16
Computational Modelling and Machine Learning Based Image Processing in Spine Research

Tijana Šušteršič, Vojin Kovačević, Vesna Ranković, Lukas Rasulić, and Nenad Filipović

16.1 Theoretical Background

16.1.1 Short Overview of Disc Herniation

The spine consists of 24 bones called vertebrae and of sacral and coccygeal bones which represent fused vertebrae. Sacral and coccygeal bone form final, lower part of the spine. The first five vertebrae above sacral bone make lumbar spine. The lumbar (lower back) segment of the spine carries most of the body's weight. Five lumbar vertebrae are numbered from L1 to L5. The vertebrae are separated by spinal discs, which serve as shock absorbers stopping the vertebrae to be in direct contact. Fibrous annulus represents the outer ring of the disc and has fibrous bands connected to each vertebral body. Beside the annulus, each disc has a gel-filled core called the nucleus. The most important function of the spine is to protect spinal cord and spinal nerves from damage. A very important part are also spinal nerves that leave the spinal cord at each disc level and branch out to the body forming dermatome maps (Bogduk 2016).

The first step in many types of degenerative spine disease is degeneration of intervertebral disc. Process of disc degeneration is often identified with the term herniated disc. Herniated disc occurs when the gel-like material in the middle of the disc ruptures through a tear in annulus. This gel substance irritates the spinal nerves, creating chemical and mechanical irritation, which results in the inflammation of the spinal nerve and swelling caused by the pressure of the herniated disc (Fig. 16.1).

T. Šušteršič · V. Kovačević · V. Ranković · L. Rasulić · N. Filipović (✉)
Faculty of Engineering, University of Kragujevac, Kragujevac, Serbia
e-mail: fica@kg.ac.rs

Bioengineering Research and Development Center (BioIRC), Kragujevac, Serbia

Steinbeis Advanced Risk Technologies Institute Doo Kragujevac (SARTIK), Kragujevac, Serbia

O. Canciglieri Junior and M. D. Trajanovic (eds.), *Personalized Orthopedics*,
https://doi.org/10.1007/978-3-030-98279-9_16

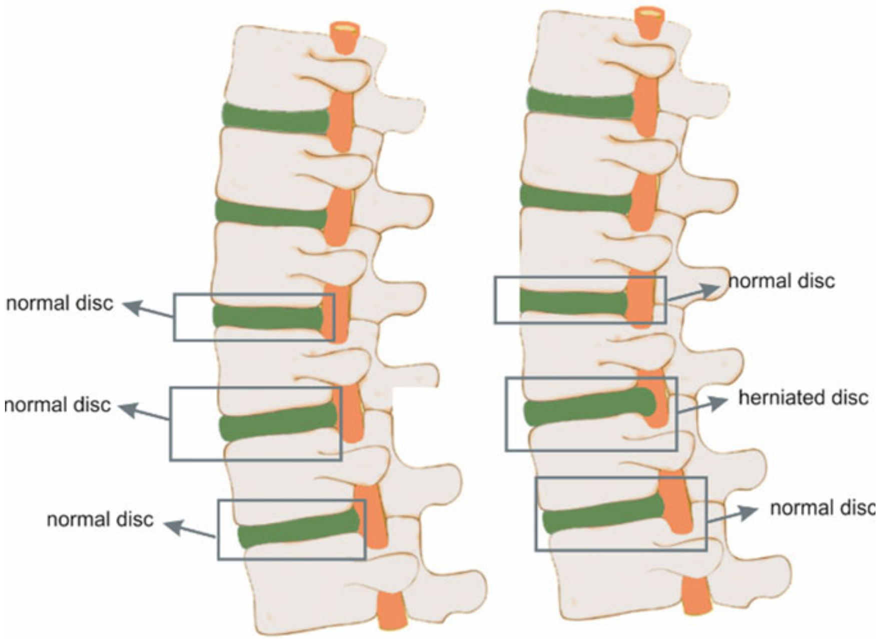

Fig. 16.1 Comparison of the normal and herniated discs

In time, herniation can develop in two directions. It can continue to shrink when partial or total pain relief may happen. But also, it can cause severe damage of neural tissue (nerves), which in return places need for surgery. Different stages of herniation can occur (Fardon et al. 2014; Winn 2016):

- bulging disc (protrusion)–this condition happens when disc annulus remains intact, but forms an outpouching that may pressure the nerves; a slipped disc bulges without rupturing the annulus fibrosis (Fig. 16.2a)

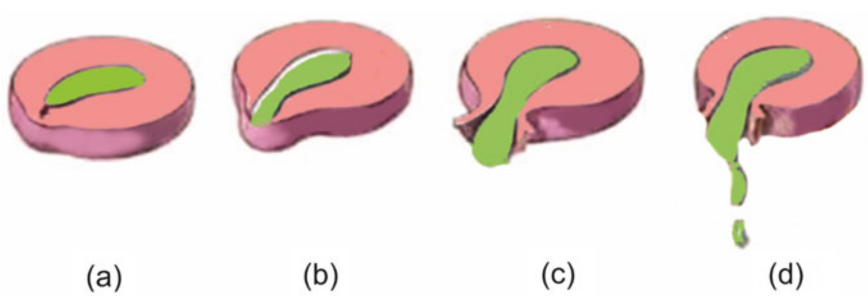

Fig. 16.2 Comparison of different grades of herniation **a** protrusion, **b** prolapse, **c** extrusion, **d** sequestration

- prolapse—it is usually the next grade in herniation where nucleus pulposus migrates to the outermost fibers of the annulus fibrosis (Fig. 16.2b)
- extrusion—genuine herniated disc (also called a broken or slipped disc) happens when the disc breaks or ruptures, causing the gel-filled core to be squeezed out (Fig. 16.2c)
- sequestration - sometimes the herniation is so extreme that there is a free fragment, which means that the piece has broken entirely free from the disc and goes into the spinal canal (Fardon et al. 2014; Winn 2016) (Fig. 16.2d).

The vast majority of herniated discs arise in the lumbar spine, where the spinal nerves run out between the lumbar vertebrae, and then come together again to form the sciatic and femoral nerve that pass down the anterior/posterior aspect of the thigh and leg (Winn 2016).

Symptoms and clinical signs of herniated disc differ significantly based on the site of herniation and individual reaction to pain. Herniated lumbar disc can cause pain that radiates from lower back, either or both legs, and occasionally to feet (called sciatica). Pain can be like an electrical shock that is intense, whether standing, walking or sitting down. Activities such as bending, standing up/down, twisting, and sitting may increase discomfort. Lying flat on the back with knees bent can be the most relaxed because it relieves the downward pressure on the nerve. In addition to pain, muscle weakness in the leg or lack of knee or ankle reflex may occur. In the most severe cases, foot drop or a lack of control of the intestine or bladder may occur (Fardon et al. 2014; Greenberg 2016).

Some of the causes for discs bulging or herniation can be due to injury and improper lifting or may even occur spontaneously. Since age is a large factor in disc herniation, as with aging, the discs get harder and the strong fibrous outer wall of the disc are weakened (Cummins et al. 2006). The gel-like nucleus can bulge or crack through a tear in the disc wall, causing pain when it comes into contact with the nerves. Genetics, smoking and a variety of occupational and recreational daily practices can contribute to early disc degeneration (Mobbs et al. 2001; Longo et al. 2011).

Herniated discs are more prevalent in individuals between the ages of 30 and 40, while middle-aged and older people are marginally more at risk if they are engaged in strenuous physical exercise. Lumbar disc herniation is one of the most frequent forms of lower back pain associated with leg pain which happens 15 times more frequently than cervical (neck) disc herniation. Disc herniation happens 8% of the time in the cervical (neck) region and just 1–2% of the time in the upper-to-mid-back (thoracic) region (Jordan et al. 2011).

16.1.2 Diagnostic Testing for Lumbar Disc Herniation (LDH)

Main diagnostic testing for lumbar disk herniation are imaging techniques such as X-ray, myelography, computed tomography (CT) and Magnetic Resonance Imaging

(MR) scan. With the X-rays alone, it is not possible to detect a herniated disc, however, X ray can provide additional information about the position of the vertebrae, arthritic changes, bone spurs, or fractures. Magnetic Resonance Imaging (MRI) or MR scan is a non-invasive imaging procedure that combines magnetic field and radiofrequency waves to provide a clear image of the soft tissues of the spine. Unlike X-rays, nerves and discs are easily visible in MRI images. Imaging may or may not be performed with a dye (contrast agent) that is injected into the bloodstream. The MRI presents a golden standard in diagnosing disc herniation. Bone overgrowth, spinal cord lesions, or abscesses can also be observed. Myelography is a specialized X-ray technique in which a dye is used to be injected into the spinal canal but today it is rarely in use due to its invasive character. This examination could be accompanied by a CT scan. Computed tomography (CT) scan is also a non-invasive diagnostic technique that uses an X-ray beam and a device to make 2-dimensional images of the spine (Vitosevic et al. 2019). It may or may not be performed with a dye (contrast agent) that is injected into the bloodstream (Fardon et al. 2014; Jarvik and Deyo 2002).

Other techniques, that are not imaging are electromyography (EMG) and Nerve Conduction Studies (NCS). EMG tests measure the muscles' electrical function. Small needles are inserted in the muscles and the effects are registered by special machine. NCS are similar, except it tests how far the nerves transfer the electrical signal from one end of the nerve to the other. These tests can diagnose muscle weakness and nerve damage (Fardon et al. 2014; Jarvik and Deyo 2002).

16.1.3 Treatments of LDH

Conservative non-surgical intervention is the first step towards rehabilitation which can involve medicine, rest, physical activity, home workout, hydrotherapy, epidural steroid injection (ESI), chiropractic manipulation, and pain control. With such treatment, 80% of patients with back pain will recover in around 6 weeks and return to daily life. In cases where conservative treatment dos not give results, the doctor may recommend surgery (Jordan et al. 2011; Rasulić et al. 2020).

16.1.3.1 Nonsurgical Treatments of LDH

In most cases, herniated disc pain will weaken within a few days and will be fully healed within 4–6 weeks. Restricting your movement, ice/heat treatment, and taking the counter medicine will help in recovery. Recommended medical drugs can range from pain relievers, nonsteroidal anti-inflammatory drugs (NSAIDs), muscle relaxants, and steroids. Steroid injections therapy is performed under x-ray fluoroscopy which includes the injection of corticosteroids and numbing agents into the epidural space of the spine. The drug is offered next to the sore area to alleviate the swelling and inflammation of the nerves. About 50% of patients will notice improvement after an epidural injection, but the effects appear to be transient. Injections are conducted in accordance with a Physical and/or Home Workout Regimen. Physical therapy as a way towards the relief of the pain is performed to help people get back to normal activities as quickly as possible and avoid re-injury. Physical trainers will advise on correct balance, lifting, and walking exercises, primarily to improve lower back, leg, and stomach muscles. They will also allow to extend and improve the versatility of back and legs. Exercise and strengthening techniques are essential aspects of recovery and further healthy lifestyle (Fardon et al. 2014; Kambin 2005).

16.1.3.2 Surgical Treatments of LDH

Surgery for herniated lumbar disc, named discectomy, could be an alternative if the symptoms do not change dramatically with conservative therapies. Surgery can also be recommended if there are symptoms of nerve injury, such as fatigue, muscle weakness or lack of sensation in the legs. Microsurgical discectomy starts with 1–2-in. length skin incision in the midline of the back. In order to access the injured disc, the spinal muscles are dissected and moved aside to reveal the vertebra. A part of the bone is removed to easily approach the root of the nerve and disc. The part of the damaged disc that touches the spinal nerve is gently removed using surgical microscope and other special equipment.

Alternative to microdiscectomy in some cases is minimally invasive endoscopic discectomy. It is performed in such a way that the surgeon makes a minor incision in the back. Small tubes called dilators are used with a diameter that increases in order to widen the tunnel to the vertebrae. In addition, the procedure is similar to microdiscectomy. A part of the bone is removed to expose the root of the nerve to the disc, which will be removed. While microdiscectomy (MD) is now widely recognized as the preferred surgical procedure for lumbar disc herniation, regular discectomy (without use of surgical microscope) is still used by many neurosurgeons (SD) (Kovačević et al. 2017). About 80–85% of patients have successfully recovered from a discectomy and are able to return to daily work after about 6 weeks (Fardon et al. 2014; Kambin 2005).

16.2 Computational Modelling and Machine Learning in Spine Research

16.2.1 Machine Learning in Image Segmentation

Researchers have used many approaches for intervertebral disc diagnosis of lumbar spine diseases. Peng et al. (2006) developed both quantitative and visualization workflow using an image segmentation method to extract six features derived from MRI images of the patients. Extracted features include the distribution of the protruded disc and the ratio of the protruded portion to the dural sac and its relative signal intensity. Ghosh and Chaudhary (2014) proposed a majority voting system for the diagnosis of lumbar herniation that used intensity, planar shape features, and texture features derived from the Gray Level Co-Occurrence Matrix. The proposed methodology was tested on a dataset with 35 subjects achieving the accuracy of 94.86%. Bhole et al. (2009) have also developed a system for segmentation of lumbar discs and vertebrae from MRI images using geometric data from T2 axial, T2 sagittal and T1 sagittal views. Reported results included 98.8% accuracy on the testing subset of 67 sagittal views. Oktay and Akgul (2011) proposed another approach using pyramidal histogram of directed gradients (HOG) and SVM and obtained the accuracy of 95% percent tested on 40 images. Koh et al. (2011) have proposed unsupervised approach using active contour model for segmentation of region of interest on spinal images. Results obtained show dice coefficient of 0.71 dice tested on 60 images. Schmidt et al. (2007a, b) suggested a probabilistic model that calculates the various locations of the intervertebral disc in MRI images. Using 30 images for testing, they achieved the accuracy of 91%.

Other researchers such as Pekar et al. (2007) have established a labeling method for automated scanning of MRI images by using two dimensional images of horizontal spinal and finding the adequate candidates. They achieved 0.833% accuracy for lumbar regions and 97% for cervical scans. This proposed method is a step beyond the state-of-the-art proposed by Peng et al. (2006). Peng uses the methodology to select the best sagittal slice, perform edge detection using canny edge operator. Horsfield et al. (2010) have also proposed a semi-automatic approach to identify spinal cord in MRI images by using active surface models to diagnose multiple sclerosis. Ayed et al. (2011) suggested a procedure based on the segmentation of the graph to delineate the intervertebral discs in the MRI images of the spine. Michopoulou et al. (2009) with their method obtained 86–88% accuracy for classification of normal and degenerated disc in images. They used fuzzy C-means to perform semi-automatic atlas-based disc segmentation with texture features and then further implemented Bayesian Classifier, only to achieve 94% accuracy on a test set of 50 manually segmented discs. Neubert et al. (2013) use signal intensity and shape features to diagnose herniated discs and degeneration in MRI images in order to classify pathologies. Unal et al. (2015) had the aim to diagnose disc abnormalities from the axial view MRI with a hybrid model that uses features obtained manually by the technician.

However, all of these methods are mostly semi-automatic, as they require user-expert interaction to set up initial contours/conditions, extraction of the features manually etc. Similarly, Hoad and Martel (2002) used a semi-automatic technique for segmentation of vertebrae and spinal cord on MRI images. The initialization process involved user intervention to manually detect the middle of the spinal cord at every level of the spine or to manually select 4 points for each vertebral body. After this, an active contour algorithm overtook in order to segment the spinal canal. Tsai (1987) observed herniation on 3D MRI and CT disc volumes using geometrical features such as shape, size and location. Although this methodology is interesting, very rarely are 3D MRI images are available as part of the regular diagnosis. Another interesting methodology was used by Corso et al. (2008) who implemented a two-level probabilistic model for identification of MRI scans to try to resolve the issue of adjusting the light strength of MR images and achieved 96.6% accuracy.

Some fully automatic methods were also investigated, such as the work by Alomari et al. (2014) who performed automatic herniation detection using a GVF snake for an initial disc contour and then further trained a Bayesian classifier on the obtained resulting shape attributes. Although the accuracy results are promising with 92.5%, poor sensitivity of 86.4% is not convincing that this method can be used in real praxis. Ghosh et al. (2011) suggested five different classifiers and merged them to produce the best results of a fully automatic diagnosis of lumbar hernia, achieving 94.86% of accuracy and 95.90% of specificity. Other authors (Ebrahimzadeh et al. 2018) created a combination of the traditional methods and novel methods to diagnose lumbar disc herniation in MRI images. Otsu thresholding is combined with the feature extraction by measuring the form function, after which Multi-Layer Perceptron (MLP), K-Nearest Neighbors (KNN) and Support Vector Machine (SVM) were used for classification. The MLP and KNN classifications demonstrated the accuracy of 91.90% and 92.38%, respectively. Similarly, Chevrefils et al. (2007) merged two approaches, watershed and morphological methods, in order to detect discs in MR images. This automatic method was proposed to control the initial values of the cluster centroid using intuitive fuzzy clustering. They claim to have formed a supplement for intuitive fuzzy clustering. Proposed methodology was evaluated using Jaccard coefficient and dice coefficient, as well as recall and precision. Other methods include cervical intervertebral disc segmentation using Hough transform and predictive form-conscious deformable models, such as those proposed by Marquardt et al. (2012). Although many papers have achieved potentially good results, the findings have been limited due to the lack of standardized magnetic resonance imaging of the phenotype of spinal degeneration (Steffens et al. 2016).

As a result, many researchers have abandoned traditional methods and adopted deep learning techniques. Jackson et al. (1989) have developed deep learning techniques for detecting and segmenting intervertebral discs and vertebrae from 2D images or volumetric data. Simonyan and Zisserman (2014), He et al. (2016), Dou et al. (2017) have developed several approaches focused on deep learning to identify and locate intervertebral discs (IVDs) and vertebrae from 2D images. Cai et al. (2016) performed detection of IVDs using 3D hierarchical model and accomplished segmentation by using features derived from deep neural networks. Studies performed by Chen et al. (2018) and Suzani et al. (2015) used deep learning methods, specifically Chen et al. focused on Convolutional Neural Networks (CNN), while Suzani et al. concentrated on feed forward neural networks. Harun et al. (2012) have developed a convolutional neural network workflow to automatically detect intervertebral discs and vertebrae using a set of radiological ratings. Other studies such as those performed by Al-Kafri et al. (2019) proposed deep learning neural networks (specifically Segnet architecture) to help clinicians to diagnose lumbar spinal stenosis by delineating lumbar disc MRI scans. Haq et al. (2015) used statistical shape model to identify intervertebral discs and vertebrae in high-resolution magnetic resonance images. Zhou et al. (2019) had the idea for a novel method of detection using a convolutional neural network to detect the spine from L1 to S, achieving better results than others. Wang et al. (2018) established a deep learning method for segmentation and labeling of axial MRI slices. Mbarki et al. (2020) propose to use convolutional neural networks, particularly VGG16 to detect the L1-L2, L2-L3, L3-L4, L4-L5 and L5-S1 discs, as well as apophyse, as well as classify the herniated and the normal lumbar discs. Although they claim to achieve better than state-of-the-art results with 93.3% accuracy, there were some manual interventions such as cropping the image, as well as the fact that they only use axial view to diagnose the herniation (bulging, protrusion, extrusion or exclusion).

There is an additional approach towards diagnosing discus herniation using sensor measurements. A group of authors described the medical background connection between the ending nerves on feet (dermatome maps on feet) and discus hernia on certain level (Peulić et al. 2020), only to establish the foundation for the development of the platform with sensors to measure foot forces at several distinctive points (Peulić et al. 2019). Another study by the same group of authors (Sustersic et al. 2019) examined the use of the Bayes theorem to localize the level of disc hernia using foot force measurements. A detailed examination of classifiers in biomedical signal processing as a decision support system in disc hernia diagnosis was described in (Šušteršič et al. 2020). Ranković et al. (2015) also propose adaptive neuro-fuzzy inference architecture for supporting the diagnosis of lumbar disc herniation. However, in these studies, no images were analyzed and we will focus on medical image processing in this chapter.

It is true that localization of axial lumbar discs is a difficult, yet very interesting task, due to variations in size, shape and appearance of discs and vertebrae. This is especially the case when the problem is coupled with diagnosis of the level and side of the herniation. Traditional segmentation and thresholding strategies have several disadvantages, therefore deep learning methods should be given a priority. Automation of the segmentation process for medical images is a complex and ultimate task, as simple features do not exist. In order to create a Computer-Aided Design (CAD) system for diagnostic purposes, it must go through several steps—image enhancement, interest extraction region, herniated lumbar disc identification and finally herniated herniation classification detected as different types. In this chapter, we propose the use of U-net for segmentation of discs on both sagittal and axial view. It is only possible to correctly diagnose the level of herniation by looking at both views, which is a work that has not been examined so far from a computational point of view and ML based automatic detection.

16.2.2 Computational Modelling in Spine Research

The complexity of analyzing human lumbar spinal section analyses is evident (Dietrich et al. 1992; Eberlein et al. 2002; Glema et al. 2004). This is primarily due to the geometry, the nonlinear properties of the materials (bones, ligaments, etc.) and the challenge of calculating all properties of the materials, i.e. viscosity. In addition, simplifications in numerical models can have a great impact on the results. Even the validation of the obtained results is not so simple with the studies carried out on the human, which in return raises many ethical questions and makes it harder to adopt final conclusions (Glema et al. 2004).

Using special solvers, Finite Element Method (FEM) allows the simulations of complex structures by dividing the structure into various, simple finite elements, each of which is able to describe with certain rules and model mathematically (Li and Wang 2006). FEM is adequate for modelling the bone system, even with its complex structure. Based on the detailed biomechanical characteristics of the lumbar, FEM provides in-depth results on stress, strain, strain energy etc. (Li and Wang 2006).

The first step in simulating the biomechanical system is the correct description of the geometry of the model, after which boundary conditions need to be pre prescribed, as well as material properties. There were many research studies using FE modelling to investigate the spine biomechanics (Park et al. 2013; Dreischarf et al. 2014; Allison et al. 2015).

As intervertebral disc and ligaments play the most important role in the spinal kinematics, Glema et al. (2004) based their attention on these two parts in the numerical simulation of the L4-L5 section. They perform Finite Element Analysis (FEA) modeling of intervertebral disc to provide a 3D mechanical disc model that can be used more in the modeling of human lumbar spinal segments in surgery, spinal balance analysis and stabilization. The simulations were conducted using the ABAQUS. Obtained results were fields of deformation, contact surfaces with their interactions, as well as total tension and stress conditions, load-displacement relationships etc. (Glema et al. 2004). Some research has been performed in order to determine the effect of degeneration on disc joint dynamics by modifying structural properties (Schmidt et al. 2007a, b; Rohlmann et al. 2006a, b, c). Developing models that imitate native joint dynamics helps researchers to test the impact of degeneration of individual sub-components on intradiscal deformations (Schmidt et al. 2007a, b; Mengoni et al. 2017; Yang and O'Connell 2019; Yang et al. 2019; Yang and O'Connell 2017). This models usually use hyperelastic material to explain significant deformations in biological tissues, but these models do not account for tissue swelling that has been found in many biological tissues (Schmidt et al. 2007a, b; Mengoni et al. 2017; Yang and O'Connell 2019). Li and Wang (2006) created a 3D finite element representation of the L1–L2 section on the basis of a geometric model. Loads that simulate the pressure from above have been added to the FEM, while a boundary condition defining the relative L1–L2 displacement has been put on the FEM to account for 3D physiological states. This simulation, similarly to the previous, investigates the distribution of stress and pressure and the deformation of the spine (Li and Wang 2006).

In most studies, detailed data of the material properties are not available, so researchers use either available data online or calculate the values as a function of other materials. Goto et al. developed a three-dimensional finite element (FEM) model of the 4th and 5th vertebrae using computed tomography (CT) images of a healthy man. They proposed the use of intradiscal pressure in the nucleus pulposus to assess the material properties of the nucleus pulposus of the intervertebral disc. Von Mises stress on the vertebral endplates and the annulus fibrosus are calculated and the authors specifically paid attention von Mises stress on the vertebral endplate in normal and degenerative discs (Goto et al. 2002). Overview of the material models of the vertebral body and the articular facet joints, the intervertebral plate, the nucleus pulposus, the annulus fibrosus, the ligaments etc. are given in (Kurutz and Oroszváry 2012).

Although there are many studies that investigate the stress and displacements in spinal system, not many analyze the problem of disc herniation. One such study by Du et al. (2016) developed a comprehensive FE model of the full normal lumbar disc integrated with the surrounding muscles, and used a graphic technique to create a degenerative lumbar model with disc herniation as well as a facet joint dislocation, followed by a biomechanical analysis of the press-extension massage technique for lumbar disc herniation. The results demonstrated that the press-extension techniques add an obvious induction effect to the annuli fibrosi and raise the strain in the pressure in the front region. This study concluded that the finite element simulation of the lumbar spine is adequate for the investigation of the press-extension technique affecting the lumbar intervertebral disc biomechanics and provide the basis for further analysis of disc herniation using simulations. Greater understanding of the biomechanical features of surgical procedures would potentially lead to better diagnosis and treatment of intervertebral herniation (Du et al. 2016). Another study by Xie et al. (2017) used FEM approach to analyze the mechanical behavior of stable and herniated intervertebral disc (IVD). In order to compare IVD's reactions under various loading conditions for IVD's annulus fibrosus, hyperelastic (Neo-Hookean model) and elastic constitutive models were investigated in the analysis. Numerical findings indicate that the mechanical behavior of IVD is best defined using hyperelastic FE models rather than by elastic ones (Xie et al. 2017).

Most of the studies use commercial software such as ANSYS, ABAQUS, or COMSOL, however there are few studies that use other in-house software. Lavecchia et al. (2018) used Matlab developed toolbox named lumbar model generator (LMG) to generate a population of models using subject-specific dimensions obtained from data scans or averaged dimensions evaluated from the correlation analysis. This toolbox allowed for patient-specific assessment, taking into account individual morphological variation (Lavecchia et al. 2018). Already mentioned research by Du et al. (2016) use self-developed biomechanical software. Kojic et al. (2001) investigate static response of the segment of human spinal motion (SMS) and analyze it using in-house solver PAK, developed at the Faculty of Engineering, University of Kragujevac, Serbia. In this example, the static response of human healthy SMS is analyzed on the basis of a poroelastic model, subjected to axial loading. Three-dimensional finite elements are used and half of the SMS is modeled due to symmetry, with appropriate boundary conditions on the symmetry plane (Kojić et al. 2008).

Taking into account the review of the literature, there is a need for development of the model that will be compatible with FE simulations, in an automatic manner, starting from MRI/CT scans. Most of the previous studies perform the segmentation on images manually, after which commercial software is used in the analysis of the 3D model. Also, there is a lack of models that deal with disc herniation, especially adaptable models, only available through in-house software, that can be expanded with additional equations describing various phenomena. This chapter aims to develop an automated technique to obtain a parametric anatomically representative models of lumbar discs and corresponding vertebrae, which can be used to evaluate the effects of herniation on the discs. The models would have applications in various areas such as design process of new devices, evaluating the biomechanics of the spine as well as helping clinicians when deciding on treatment strategies.

16.3 Materials and Methods

This section deals with two main approaches—machine learning and computational modelling in order to investigate the computational methods that would provide additional information about disc herniation based on medical MR images.

16.3.1 Automatic Segmentation of Disc Material in Medical Images

In order to extract relevant parameters for automatic diagnosis of disc herniation, automatic segmentation of disc material in medical images needs to be performed first.

16.3.1.1 Dataset for Machine Learning

The dataset used in this research was obtained from the Clinical Centre of Kragujevac, Serbia (https://www.kc-kg.rs/) and consists of 69 sagittal images and 69 axial images from 10 patients diagnosed with lumbar discus hernia. The dataset consists of 6 female and 4 male patients, and age of patients in the form of mean ± standard deviation was 42.9 ± 7.52 years. Distribution of the type and side of discus hernia is presented in Fig. 16.3.

Due to a relatively small number of images in the dataset, which is often a case in fields such as biomedicine, where large amount of biomedical data is often unavailable (Bloice et al. 2019), a process called augmentation has been utilized in order to increase the segmentation performances (Bloice et al. 2017). The augmentation procedure was performed with the aim to artificially increase the training and validation dataset (Farda et al. 2020), while the testing dataset remained the same and consisted of only original and unseen images.

In this particular study, a set of several operations were utilized in order to increase the dataset, specifically:

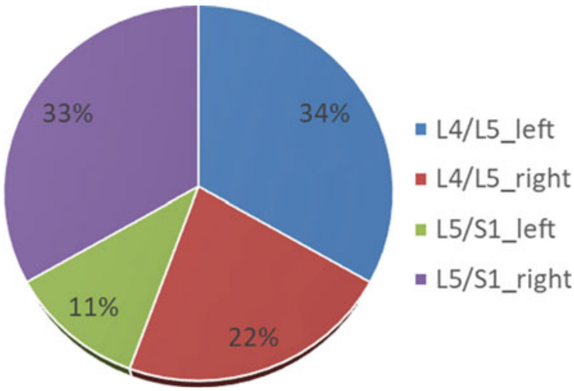

Fig. 16.3 Distribution of disc hernia type and side in the dataset

- horizontal flip (equivalent to the mirroring along the y axis)
- brightness (HSV (hue, saturation, lightness) colorspace is utilized for this task, which means that the greater the values of saturation and value matrices are, the brightness is bigger. Therefore, in order to increase the brightness, matrices are multiplied by a value greater than 1 and to reduce brightness, matrices are multiplied by a value less than 1) (Fig. 16.4)

Only geometrical transformations in combination with multiplication of all image pixels with a certain factor were used for data augmentation in order to keep the entire data of the image and do not lose any information. Other techniques, could result in removing important parts of the image, so they were considered inappropriate due to the nature of the problem. Also, other techniques such as vertical flip were considered inappropriate, as they do not have physical meaning (no spine upside down image can be found in real life situations).

By using the augmentation process described in the previous paragraphs, a new augmented dataset of 207 images was created. It is important to emphasize that augmented dataset was used only in the training and validation phases, while testing was performed only on original unseen images that were not modified. Division of the whole dataset was performed in the ratio of 80:10:10 for the training, validation and testing dataset, respectively. This means that the number of images in the subsets was 167-20-20.

The presented training dataset was used for the training of U-net convolutional neural network, while validation dataset was used for optimization of network hyper-parameters and the testing subset was used for the evaluation of the segmentation performance.

The processing hardware were 64 GB of RAM, a GPU NVIDIA Quadro RTX 6000, and an Intel(R) Xeon(R) Gold, 6240R, CPU @2.40 GHz. The network implementation was done in the Python environment with Tensorflow and Keras (Available: https://www.tensorflow.org/).

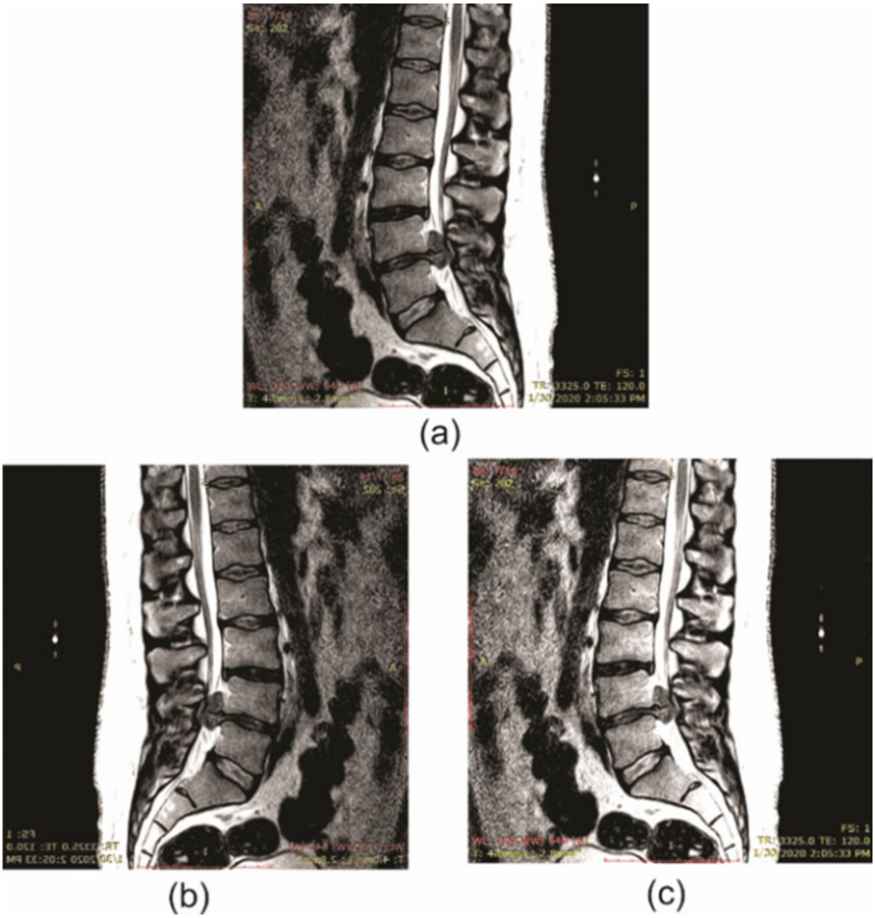

Fig. 16.4 Overview of image augmentation procedure **a** original image; **b** horizontally flipped image; **c** image with improved brightness; **d** zoomed in image

16.3.1.2 U-Net Architecture

U-net neural network architecture has proven to be applicable to various medical image segmentation issues (Moradi et al. 2019; Ronneberger et al. 2015). U-net architecture, adapted for the purposes of this study is presented in Fig. 16.5**.** It should be emphasized that the methodology is presented for sagittal view images, but the same methodology was applied on axial view images.

As it can be seen from the figure, U-net has the shape of the letter U and consists of contraction path (named encoder) and expansion path (named decoder). Contraction path consisted of two 3×3 convolutional layers and 2×2 max pooling at each level. This means that size of the input image gradually reduces while the depth gradually

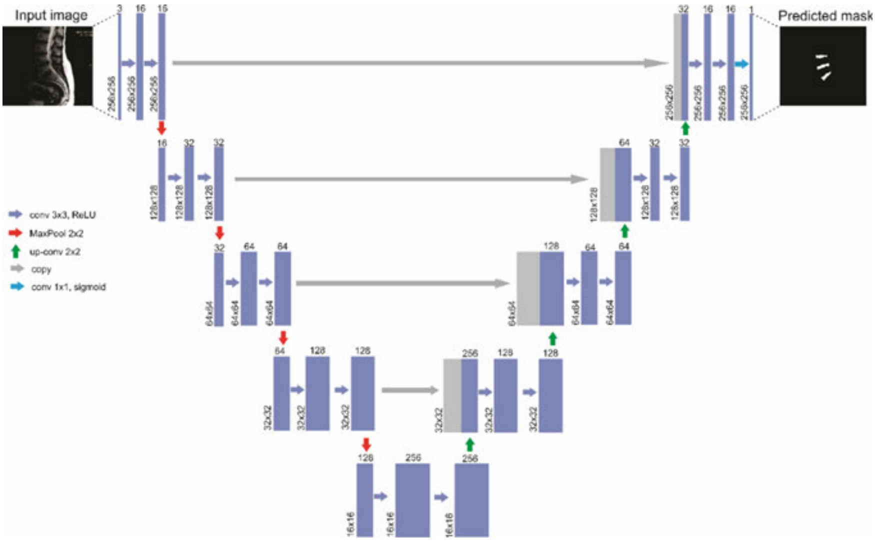

Fig. 16.5 U-net architecture

increases, and more advanced features are extracted. This means that the contraction path is performed following the idea:

conv_layer1 $\Rightarrow$ conv_layer2 $\Rightarrow$ max_pooling $\Rightarrow$ dropout(optional)

Each process consists of two convolution layers and a number of channels that change from 3 $\rightarrow$ 16, because the convolution process connects the depth of the image. The red arrow pointing down is the max pooling procedure that halves the size of the image (size will be reduced from 256 $\times$ 256 $\rightarrow$ 128 $\times$ 128 and the padding used in this application is padding = "same") (Fig. 16.6).

Described process can be implemented in Python using Keras library (Gulli and Pal 2017) (Code snippet 16.1):

Please note that in our case start_neurons = 16. This process is repeated 3 more times (Fig. 16.7):

Which can be implemented in Python in the following manner (Code snippet 16.2):

The bottom of the U network is reached with only two convolutional layers, without max pooling (Fig. 16.8).

Which can be implemented in Python in the following manner (Code snippet 16.3):

The current image size has been changed to 16 $\times$ 16x256. Further, the process is continued with the expansion path (decoder). In the decoder, the size of the image

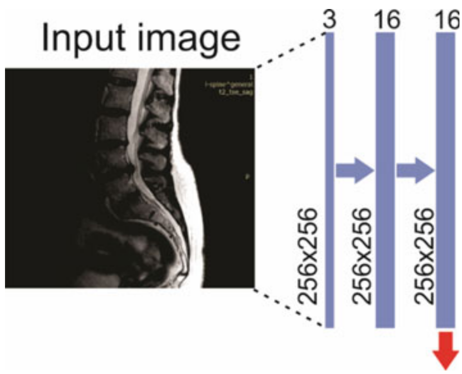

Fig. 16.6 First step in contraction path

```
conv1 = Conv2D(start_neurons * 1, (3, 3), activation="relu", padding="same")(input_layer)
conv1 = Conv2D(start_neurons * 1, (3, 3), activation="relu", padding="same")(conv1)
pool1 = MaxPooling2D((2, 2))(conv1)
pool1 = Dropout(0.25)(pool1)
```

Code snippet 16.1 First step in contraction path

gradually increases and the depth gradually decreases. In each step on the expansion path, two consecutive 2 × 2 up-conv and two 3 × 3 convolutional layers are implemented. This means that the expansion path is performed following the formula:

$$\text{conv\_2d\_transpose} \Rightarrow \text{concatenate} \Rightarrow \text{conv\_layer} \Rightarrow \text{conv\_layer2}$$

First part of the expansion path recovers the information from the original image, using the described methodology (Fig. 16.9). Transposed convolution is a sampling technique that expands the size of an image. After the transposed convolution, this image is merged with the corresponding image from the contraction path and together create an image of size 32 × 32 × 256. The reason for combining the information from the previous layers is to get a more accurate prediction. Following this process, two convolutional layers are added.

Which can be implemented in Python in the following manner (Code snippet 16.4):

Simple expansion path recovers the size of segmentation map, but with loss of the localization information. Because fine-grained features may be lost in down-sampling stage, there are cross-over connections used by concatenating feature maps that are equally sized, to help give localization information from contraction path to expansion path.

As before, this process is repeated three times (Fig. 16.10).

Which can be implemented in Python in the following manner (Code snippet 16.5):

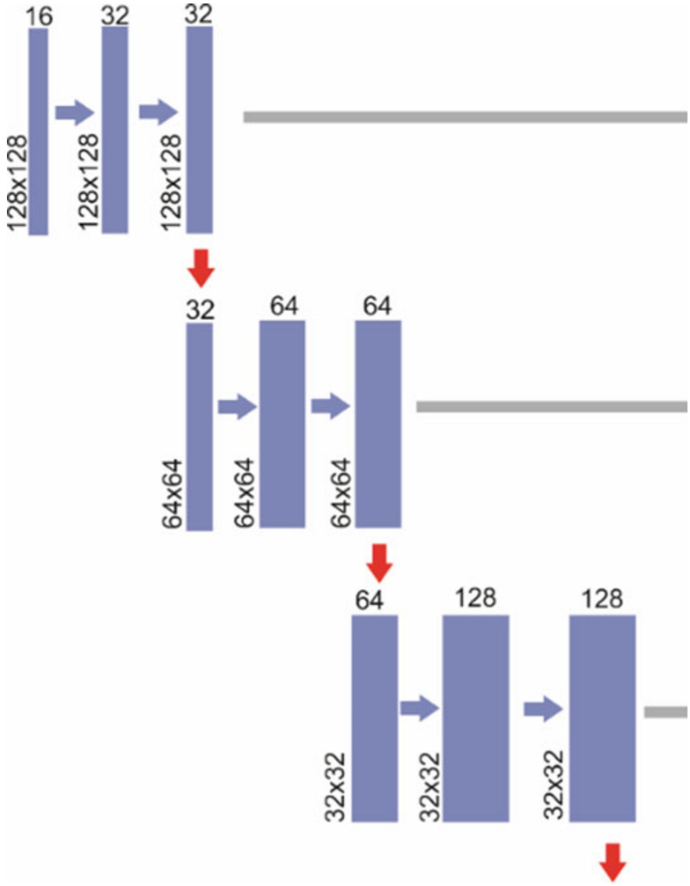

Fig. 16.7 Convolution and MaxPooling is repeated three times

The final step is to reshape the image to meet the prediction requirements. This means that the last layer is a convolutional layer with 1 filter of size 1 × 1 (there is no dense layer in the network) (Fig. 16.11).

Which can be implemented in Python in the following manner (Code snippet 16.6):

To summarize, and explain the U-net architecture in a more implementation manner, Fig. 16.12 is created.

In Fig. 16.12 the following notation was used:

- 2@conv layers means that two consecutive convolution layers are used
- c1, c2, …, c9 are the output tensors of convolutional layers
- p1, p2, p3 and p4 are the output tensors of Max Pooling Layers
- u6, u7, u8 and u9 are the output tensors of up-sampling (transposed convolutional) layers.

```
conv2 = Conv2D(start_neurons * 2, (3, 3), activation="relu", padding="same")(pool1)
conv2 = Conv2D(start_neurons * 2, (3, 3), activation="relu", padding="same")(conv2)
pool2 = MaxPooling2D((2, 2))(conv2)
pool2 = Dropout(0.5)(pool2)

conv3 = Conv2D(start_neurons * 4, (3, 3), activation="relu", padding="same")(pool2)
conv3 = Conv2D(start_neurons * 4, (3, 3), activation="relu", padding="same")(conv3)
pool3 = MaxPooling2D((2, 2))(conv3)
pool3 = Dropout(0.5)(pool3)

conv4 = Conv2D(start_neurons * 8, (3, 3), activation="relu", padding="same")(pool3)
conv4 = Conv2D(start_neurons * 8, (3, 3), activation="relu", padding="same")(conv4)
pool4 = MaxPooling2D((2, 2))(conv4)
pool4 = Dropout(0.5)(pool4)
```

Code snippet 16.2 Convolution and MaxPooling is repeated three times

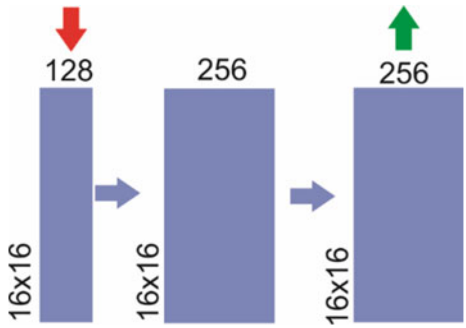

Fig. 16.8 Bottom part of the U net

```
# Middle
convm = Conv2D(start_neurons * 16, (3, 3), activation="relu", padding="same")(pool4)
convm = Conv2D(start_neurons * 16, (3, 3), activation="relu", padding="same")(convm)
```

Code snippet 16.3 Bottom part of the U net

This is what gives the architecture a symmetric U-shape, hence the name U-net. This basically means the network learns in the encoder path the "WHAT" information in the image, however it has lost the "WHERE" information. Intuitively, the Decoder recovers the "WHERE" information (precise localization) by gradually applying up-sampling. To get better precise locations, at every step of the decoder we use skip connections by concatenating the output of the transposed convolution layers with the feature maps from the Encoder at the same level:

Fig. 16.9 First part of the expansion path

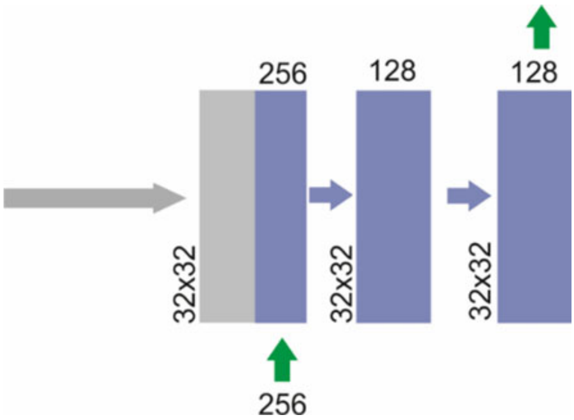


```
deconv4 = Conv2DTranspose(start_neurons * 8, (3, 3), strides=(2, 2), padding="same")(convm)
uconv4 = concatenate([deconv4, conv4])
uconv4 = Dropout(0.5)(uconv4)
uconv4 = Conv2D(start_neurons * 8, (3, 3), activation="relu", padding="same")(uconv4)
uconv4 = Conv2D(start_neurons * 8, (3, 3), activation="relu", padding="same")(uconv4)
```

Code snippet 16.4 First part of the expansion path

$$
\begin{aligned}
\mathrm{u6} &= \mathrm{u6} + \mathrm{c4} \\
\mathrm{u7} &= \mathrm{u7} + \mathrm{c3} \\
\mathrm{u8} &= \mathrm{u8} + \mathrm{c2} \\
\mathrm{u9} &= \mathrm{u9} + \mathrm{c1}
\end{aligned}
$$

After every concatenation we again apply two consecutive regular convolutions so that the model can learn to assemble a more precise output.

The U-Net model provides several advantages for segmentation tasks, among which are the fact that the model allows the simultaneous use of global location and context, it also works with very few training samples and provides better performance for segmentation tasks, in comparison to other convolutional networks, as well as that the pipeline processes the entire image in the front passage from end to end and directly creates segmentation maps (Liu et al. 2020). All this ensures that U-net preserves the full context of the input images, which is a major advantage over patch-based segmentation approaches (Liu et al. 2020). The only obvious disadvantage of the U-net architecture is that learning can be slowed down in the middle layers of deeper models, so there is a certain risk that the network learns to ignore the layers where abstract characteristics are represented. This is because the gradients are increasingly diluted, where the error is calculated, resulting in slower learning for distant weights. Overfitting of the training dataset can occur if there are too many epochs, while underfitting can occur if there are too few. Early stopping is a

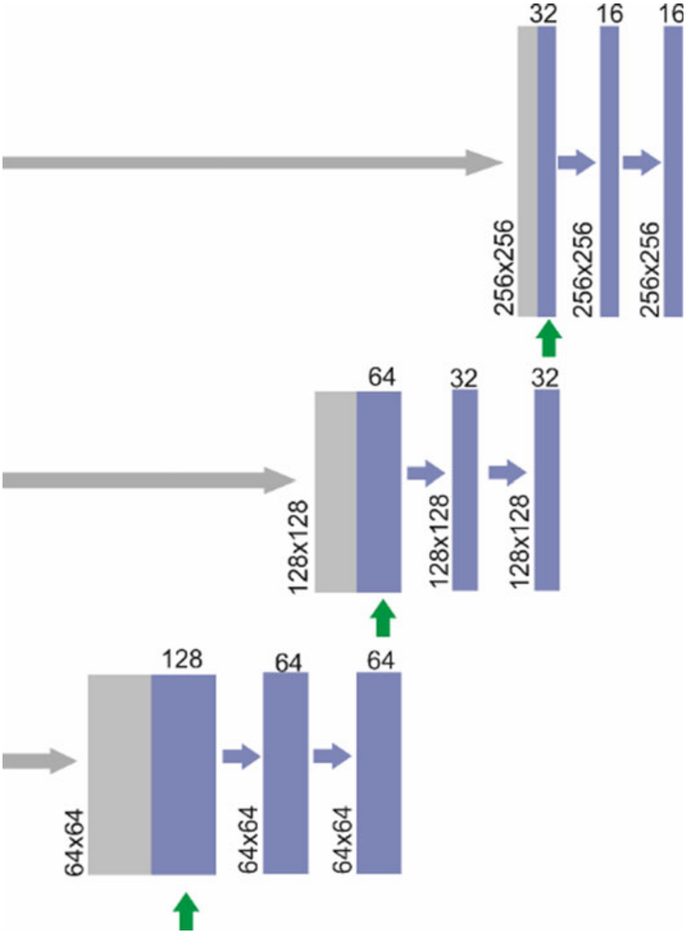

Fig. 16.10 Transposed convolution, concatenate and convolution is repeated three times

technique that allows you to designate an arbitrarily large number of training epochs and then stop training when the model performance on a holdout validation dataset stops improving. We have used Early Stopping with a monitoring of validation loss, and a patience of 10.

The training process was set for 100 epochs, stochastic gradient descent was used with the defined learning rate that was varied to investigate its effect on the results, as well as the batch size. ReLU activation function was used. The data is fed to the network, which then propagates along the described paths (contraction, expansion, and concatenation) after which the final result is a binary segmented image. The same process is repeated independently for sagittal and axial view images.

```
deconv3 = Conv2DTranspose(start_neurons * 4, (3, 3), strides=(2, 2), padding="same")(uconv4)
uconv3 = concatenate([deconv3, conv3])
uconv3 = Dropout(0.5)(uconv3)
uconv3 = Conv2D(start_neurons * 4, (3, 3), activation="relu", padding="same")(uconv3)
uconv3 = Conv2D(start_neurons * 4, (3, 3), activation="relu", padding="same")(uconv3)

deconv2 = Conv2DTranspose(start_neurons * 2, (3, 3), strides=(2, 2), padding="same")(uconv3)
uconv2 = concatenate([deconv2, conv2])
uconv2 = Dropout(0.5)(uconv2)
uconv2 = Conv2D(start_neurons * 2, (3, 3), activation="relu", padding="same")(uconv2)
uconv2 = Conv2D(start_neurons * 2, (3, 3), activation="relu", padding="same")(uconv2)

deconv1 = Conv2DTranspose(start_neurons * 1, (3, 3), strides=(2, 2), padding="same")(uconv2)
uconv1 = concatenate([deconv1, conv1])
uconv1 = Dropout(0.5)(uconv1)
uconv1 = Conv2D(start_neurons * 1, (3, 3), activation="relu", padding="same")(uconv1)
uconv1 = Conv2D(start_neurons * 1, (3, 3), activation="relu", padding="same")(uconv1)
```

Code snippet 16.5 Transposed convolution, concatenate and convolution is repeated two times

Fig. 16.11 Last step on the expansion path before creating the predicted mask

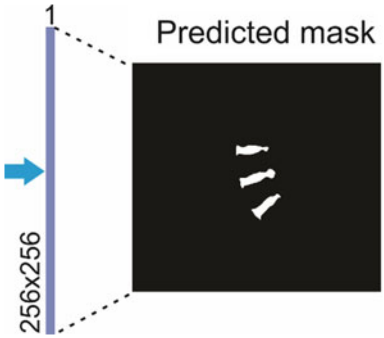


```
output_layer = Conv2D(1, (1,1), padding="same", activation="sigmoid")(uconv1)
```

Code snippet 16.6 Last step on the expansion path before creating the predicted mask

16.3.1.3 Evaluation Metrics

Segmentation accuracy of the proposed automatic method was compared to the manual segmentation. Manual segmentation was performed by neurologist expert. In the training, validation and testing phase, evaluation metrics were calculated—accuracy, precision, recall, Dice, Intersection over union (Jaccard coefficient).

We have used the dice similarity coefficient D (Lin et al. 2003) to calculate the overlapping regions between the automatic segmentation area marked as S and the ground truth area marked as G:

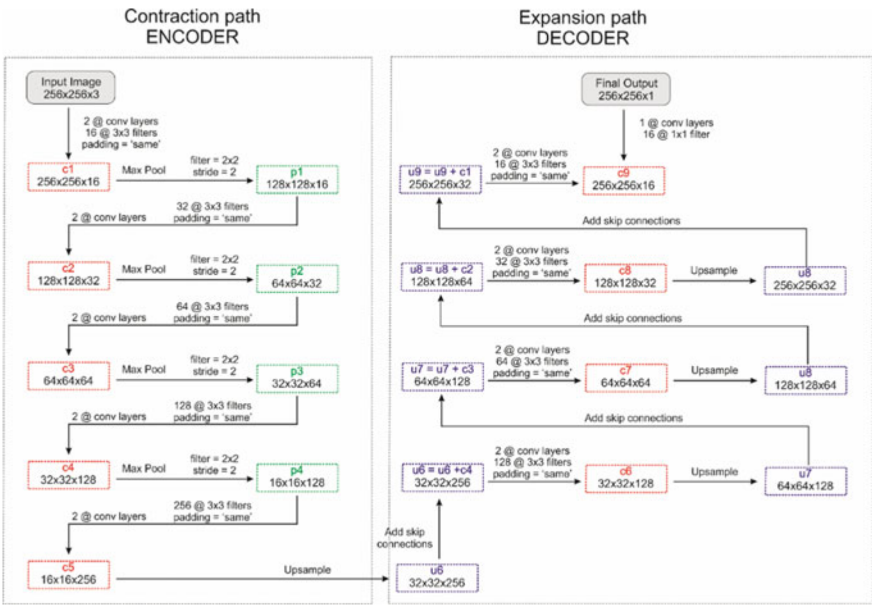

Fig. 16.12 U net architecture in the implementation manner

$$D = \frac{2|S \cap G|}{|S| + |G|}$$

Another metric, Jaccard coefficient (JC) or intersection over union (IOU) is calculated similarly to D and is generally used to compare the similarity and diversity of two segmented areas. It is defined as the number of pixels of the intersected area, divided by the number of pixels that represent the union area.

$$JC = \frac{|S \cap G|}{|S \cup G|}$$

16.3.2 Computational Modelling Methodology

A simulation using the Finite Element Method (FEM) as a way of mechanical analysis to investigate the biomechanics of lumbar vertebrates under sagittal motions would be useful. For this reason, it is important to create a patient-specific model that accurately depicts the geometry of spinal area of a person. Creating such model would involve the inclusion of the properties specific for the human body, such as materials and constants. However, the human nucleus pulposus of the intervertebral discs is not uniform and the degeneration of the derived nucleus pulposi happens rapidly, so that there are actually no experimentally calculated values for particular materials and constants and usually literature values are used.

In FE modeling, depending on the quality of the images, vertebral body, cancellous core and endplates are generally differentiated. Baroud et al. (2003) used 1 mm cortex and 0.5 mm endplate thickness. Cartilage layer thickness of facet joint Schmidt et al. (2009) considered 0.2 mm. When it comes to modeling of the intervertebral disc – nucleus and annulus are differentiatied. For the volumetric relation between annulus and nucleus, ratio 3:7 is generally used for the lumbar part L1-S1 (Moramarco 2010; Goto et al. 2002). Chen et al. (2001) on the other hand proposed 30–50% proportion between the nucleus and annulus in disc cross section.

Described proposed methodology for modelling is given in Fig. 16.13**.** For our model, we have used MRI scans at slice thicknes of 2 mm, in a 40-year-old man with dicus hernia on the level L4/L5. Another model was created with no discus herniation in order to simulate the before and after herniation situations. Volume of disc outside the intervertebral disc area was calculated and model without herniation was reconstructed.

The scan images were were in DICOM format, after which each vertebra in the region (L3–S5) and discs (L3/L4, L4/L5 and L5/S1) were extracted from images using semiautomatic segmentation tools, and corresponding 3D solid geometry was reconstructed precisely. Due to the fact that the images were taken only at representative cross sections, it was not possible to distinguish between the cancellous and trabecular bone in vertebrae, as well as between nucleus and annulus. Therefore,

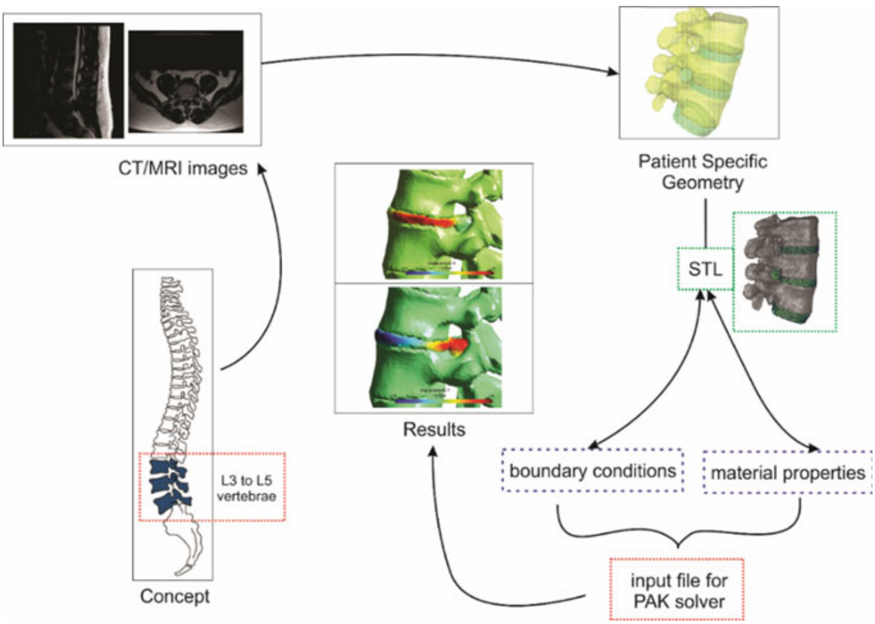

Fig. 16.13 Proposed methodology for reconstruction of human spine

this model contains only one material for bone and one material for disc structure. Boundary conditions were set in such a way that movement of vetrwbrae was possible only in the z direction (vertical direction), while the disc material could be moved in any direction. Additionaly, on the bottom of the L5/S1 disc, a support was set, in order not to allow the whole model to be translated as a result of the compression. The bone and disc elements of vertebrae were modeled as 3D solid continuum isoparametric 8-node hexahedral (brick) elements. Summary of number of nodes and elements for the healthy person and person with disc herniation are given in Table 16.1.

The models of heathly person and person with disc herniation are given in Fig. 16.14**,** with vertebrae as wire structures and discs as full solid structures. The main difference lies in the disc area where the height of the herniated disc is reduced and is 1.5 mm smaller than the normal disc height. This was calculated based on the volume of disc outside the intervertebral disc space in order to simulate before herniation situation. It is visible in Fig. 16.13 that the model of healthy L4/L5 disc

Table 16.1 Summary of number of nodes and elements for models

	Bone structure	Disc structure	Total	
	Number of elements	Number of elements	Number of nodes	Number of elements
Model with healthy discs	369,356	127,840	575,178	497,196
Model with disc herniation	369,192	126,032	573,114	495,224

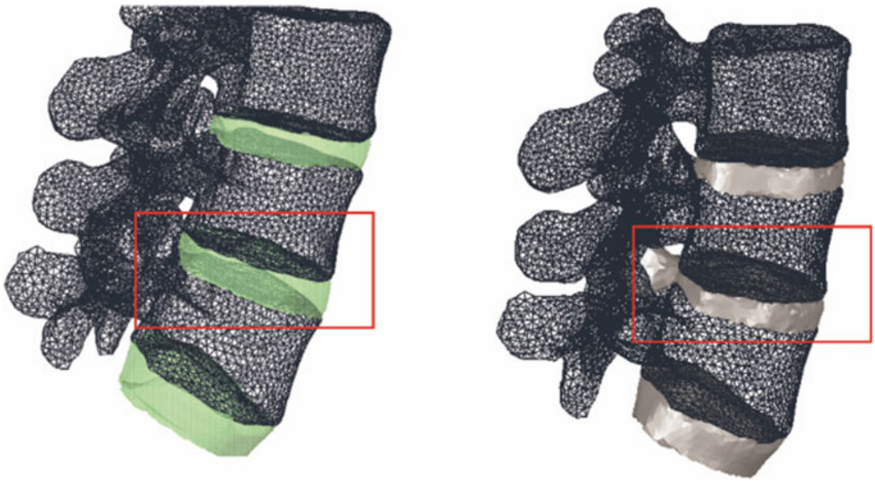

Fig. 16.14 Comparison of the models of healthy person (left) and person with disc herniation (right)

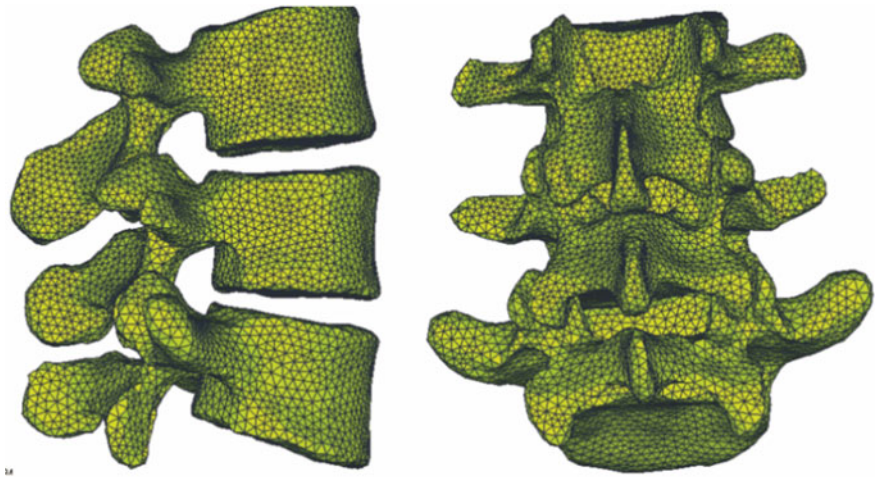

Fig. 16.15 L3-L5 vertebrae models with surface mesh

does not contain any material outside the intervertebral space, whilst the model with disc herniation contains the volume outside the intervertebral space.

The complete vertebrae with surface mesh from two different views are given in Fig. 16.15. The vertebrae bodies of L3, L4 and L5 are created, including anterior, as well as posterior parts. Each vertebra had around 6500–7500 surface elements.

When it comes to disc material, for the healthy person, each disc contained around 2500–3000 surface elements (Fig. 16.16).

When it comes to herniated disc material, for the person with disc herniation, L4/L5 disc contained around 2800 surface elements (Fig. 16.17). Disc height of the herniated L4/L5 disc is 1.5 mm smaller than the healthy disc and contains extruded material.

The changes in geometry and material properties are the main characteristics used to simulate the degeneration. Other authors used the same methodology in modelling degeneration of the lumbar discs (Kurutz and Oroszváry 2012). They apply the methodology for posterior annulus to be weakened with inner annulus fibers tearing, and allow herniation of nuclear material into the outer annular structure. A more detailed view of the herniated geometry is shown in Fig. 16.18.

In order to simulate the before and after herniation situation, normal L4/L5 disc was reconstructed by calculating the volume of extruded material. Comparison between discs before and after herniation is given in Fig. 16.19.

We have performed the calculation using in-house solver PAK for FEM analysis, developed at the Faculty of Engineering, University of Kragujevac, Serbia (Kojic et al. 2001). Material properties and prescribed loads will be described in detail in the following sections.

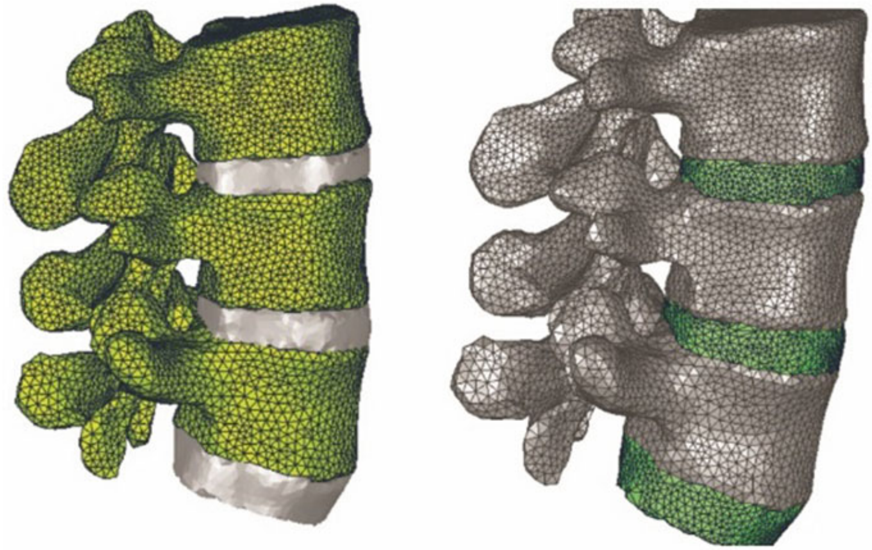

Fig. 16.16 Whole model of discs and vertebrate with surface mesh for healthy person

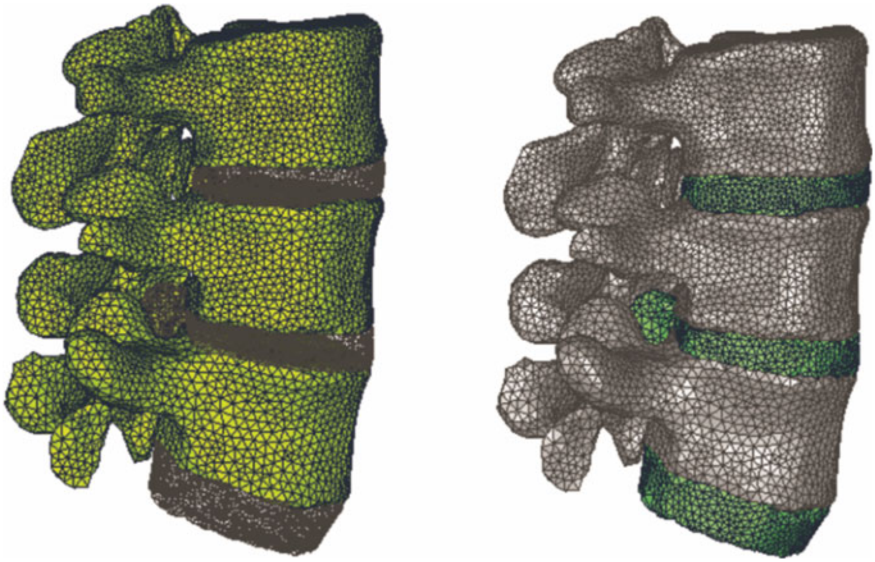

Fig. 16.17 Whole model of discs and vertebrate with surface mesh for the person with disc herniation

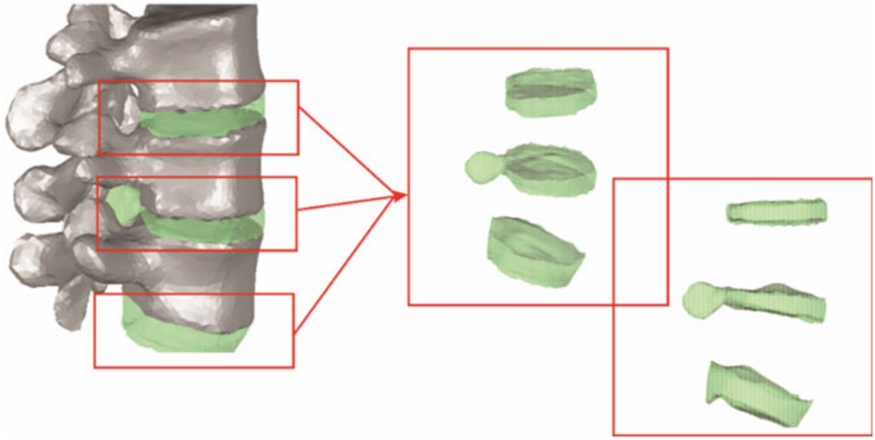

Fig. 16.18 A more detailed view of the reconstructed herniated disc L4/L5 and normal discs L3/L4 and L5/S1

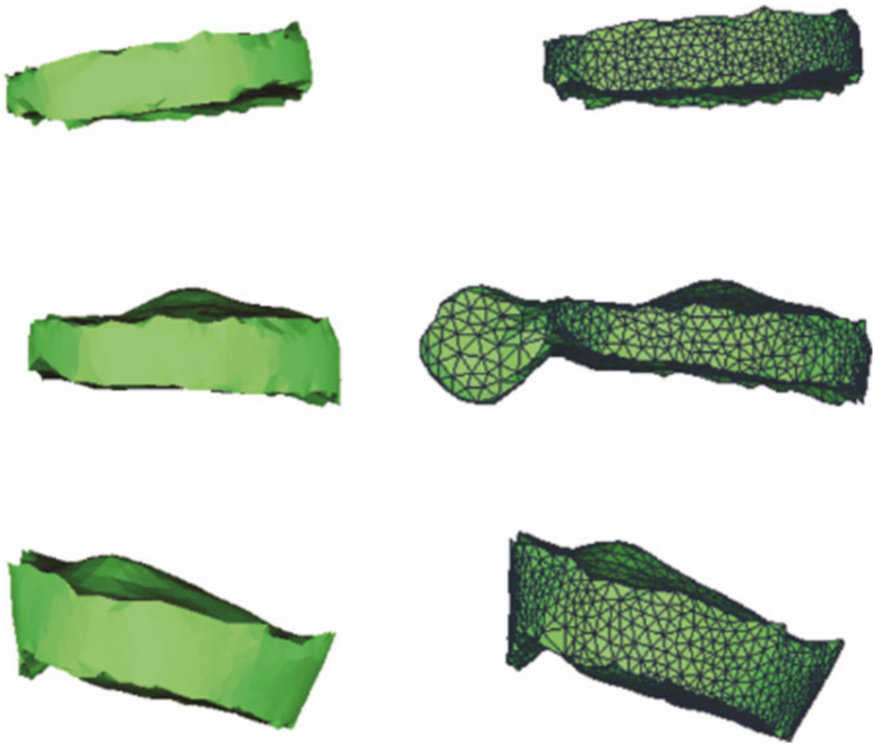

Fig. 16.19 Comparison between discs before (left) and after herniation (right)

16.3.2.1 Material Models of the Vertebrae and Discs

The high strength of the cortical vertebral shell is commonly assumed to be linear elastic isotropic or transversely isotropic orthotropic material as seen in Table 16.2. Vertebral cancellous bone is usually modeled by linear elastic isotropic or transversely isotropic or even orthotropic material (Table 16.3**).** In the following tables, E denotes Young's modulus, while ν denotes Poisson's ratio.

The material of disc nucleus is commonly assumed to be linear elastic isotropic as seen in Table 16.4. Disc annulus is usually modeled by linear elastic isotropic tension only with elastic fibers (Table 16.5). It should be emphasized that these values are for the nucleus and annulus that is healthy, meaning no degeneration has occurred.

Aging type degeneration usually starts in the nucleus which loses its incompressibility during and becomes stiffer, meaning it transforms from fluid to solid material. This form of nucleus degeneration can be modeled by using a decreased value for Poisson's ratio and increased value for Young's modulus (Kurutz and Oroszváry 2012). This action is usually followed by a stiffening mechanism of the disk as a whole and by a decrease in the volume of the nucleus and an increase in the volume of the annulus, as well as a reduction in the height of the disk. Many geometrical models of the degenerated disk use the reduction of the disk height (Kurutz and Oroszváry 2012). At the same time, annulus tears cause the extrusion of the material outside the disc space.

Unlike age-related degeneration, the nucleus can lose its incompressibility without any stiffening or volume shift process as a consequence of an unexpected traumatic

Table 16.2 Review of properties used in FE models of lumbar vertebral cortical bone

Material model	E (MPa)	ν	References
Linear elastic, isotropic	5000	0.3	Rohlmann et al. (2006a, b, c), Zander et al. (2006)
linear elastic, isotropic	10,000	0.3	Rohlmann et al. (2006a, b, c), Rohlmann et al. (2006a, b, c), Rohlmann et al. (2007), Zhang and Zhu (2019)
Linear elastic, isotropic	11,300	0.2	Little et al. (2008)
Linear elastic, isotropic	12,000	0.3	Goto et al. (2002), Xie et al. (2017), Hassan et al (2020), Zhang et al. (2009), Kurutz and Oroszváry (2010)
Linear elastic	11,300	0.48	Schmidt et al. (2009)
Transversely	11,300	0.20	
Isotropic	22,000	0.20	
Linear elastic	8000	0.40	Schmidt et al. (2009)
Transversely	8000	0.23	
Isotropic	12,000	0.35	
Poroelastic	10,000	0.3	Ferguson and Steffen (2003)

Table 16.3 Review of properties used in FE models of lumbar vertebral cancellous bone

Material model	E (MPa)	ν	References
Linear elastic, isotropic	10	0.2	Zhong et al. (2006), Ruberté et al. (2009)
Linear elastic, isotropic	50	0.2	Rohlmann et al. (2006a, b, c)
	81	0.2	Baroud et al. (2003)
	140	0.2	Little, et al. (2008)
	100	0.29	Zhang et al. (2009)
	100	0.2	Hassan et al. (2020), Goto et al. (2002)
	150	0.3	Kurutz and Oroszváry (2010)
	500	0.2	Rohlmann et al. (2006a, b, c), Zander et al. (2006)
Poroelastic	100	0.2	Williams et al. (2007)
Linear elastic, transversely isotropic	200 140	0.45 0.315	Rohlmann et al. (2007), Rohlmann et al. (2006a, b, c)
Linear elastic	140	0.45	Malandrino et al. (2009)
Transversely	140	0.176	

Table 16.4 Review of properties used in FE models of lumbar disc nucleus

Material model	E (MPa)	ν	References
Fluid-like solid, linear elastic, isotropic	1	0.499	Ruberté et al. (2009), Kurutz and Oroszváry (2010), Zhang, et al. (2009)
	4	0.499	Li and Wang (2006), Hassan et al. (2020)
	10	0.4	Chen et al. (2008)
Incompressible fluid			Little et al. (2008), Zander et al. (2006), Rohlmann et al. (2006a, b, c), Rohlmann et al. (2006a, b, c)
Quasi incompressible			Rohlmann et al. (2007)
Hyperelastic, neo-Hookean			Moramarco et al. (2010)
Mooney-Rivlin incompressible			Baroud et al. (2003), Schmidt et al. (2007a, b)
Poroelastic	Varied	0.17	Malandrino et al. (2009)
	1	0.45	Williams et al. (2007)
Viscoelastic solid	2	0.49	Wang et al. (2000)
Osmoviscoelastic	0.15	0.17	Schroeder et al. (2006)

Table 16.5 Review of properties used in FE models of lumbar disc annulus

Material model	Ground substance		Fibers		References
	E (MPa)	ν	E (MPa)	ν	
Linear elastic, isotropic matrix, tension only, elastic fibers	4	0.4	500	–	Glema et al. (2004)
	4	0.45	500	0.3	Fagan et al. (2002)
	4	0.45	400/500/300	0.3	Kurutz and Oroszváry (2010)
	4.2	0.45	450	–	Zhong et al. (2006), Goto et al. (2002)
	4.2	0.45	175	–	Chen et al. (2001)

loading impact. In this case, the nucleus can quasi burst and the hydrostatic compression can unexpectedly cease in it. This form of nucleus degeneration can be modeled by a sudden decrease in the ratio of Poisson with the Young nucleus module remaining the same (Kurutz and Oroszváry 2010). This action is usually triggered or followed by ripping or buckling of the internal annulus, splitting of the annular fibers, fracturing of the endplates, or collapsing of the bone in the spine, depending on the age at which the accidental occurrence occurs. In other words, accidental disc failures may also occur in a young age. This situation can be modeled by the sudden damage to the tissues with all the components involved. In order to simulate the effect of degeneration on the biomechanical activity of the segment, Rohlmann et al. (2006a, b, c) developed a FE model of the lumbar motion segment of various age-related disk degeneration classes. Three rates of disk degeneration were introduced: mild, moderate and severe degeneration. Compared to the healthy disk, the three classes are 20%, 40% and 60% in smaller height, respectively. At the same time as the disk height decreases, the length of the annulus fibers was also decreased by offsetting their nonlinear stiffness curves. Schmidt et al. (2007a, b) confirmed the theory that with an increase in disk degeneration, the internal pressure and disk stresses will also reduce the likelihood of disk prolapse. They proposed a mildly, moderately and severe disc degeneration with 16.5, 49.5 and 82.5% decreased height, and assumed a rise in osteophyte formations with gradual degeneration. Zhang et al. (2009) modelled healthy and two degenerated grades in the L4-5 motion simulation segment. For Grade 1, the elastic modulus of the nucleus of the disk was two times the elastic modulus of the annulus of the intact model and the ratio of Poisson was implemented to be the same as annulus, with a decrease in disc height by 20%. For grade 2, the elastic module of the annulus was doubled and the volume of the annulus fiber was decreased by 25% and the disc height was reduced by 40%, taking into account the research by Rohlmann et al. (2006a, b, c). Kurutz and Oroszváry (2010) introduced five classes of age-related degeneration starting from healthy (1) to completely degenerated (5) cases, and modeled the loss of hydrostatic state in the nucleus by decreasing the ratio of Poisson ($\nu = 0.499, 0.45, 0.40, 0.35, 0.30$), and increasing Young's modulus (E = 1, 3, 9, 27, 81 MPa). At the same time, they used a gradual increase in the annulus matrix (E = 4.0, 4.5, 5.0, 5.5, 6.0 MPa) in the annulus

Table 16.6 Summary of used material properties

	Bone structure		Disc structure	
	E (MPa)	ν	E (MPa)	ν
Model with healthy discs	12	0.3	4	0.45
Model with disc herniation	10	0.3	8	0.45

matrix and a gradual decline in Young's modulus in the vertebral cancellous bone (E = 150, 125, 100, 75, 50 MPa) and endplates (E = 10, 80, 60, 40, 20 MPa). The age-related shift in tensile modules of annulus ground material and nucleus (E = 0.4, 1.0, 1.6, 2.2, 2.8 MPa) was modeled using a parameter identification approach based on in vivo determined lumbar elongation by Kurutz (2006).

Based on all previous stated, we have used the following data in our model (Table 16.6). In addition, a reduction of 1.5 mm in disc height for the degenerated disc is modelled, which corresponds to 40% reduction of the disc height, as used in other studies by different authors (Rohlmann et al. 2006a, b, c; Schmidt et al. 2007a, b; Zhang et al. 2009; Kurutz and Oroszváry 2010). Material properties for the degenerated disc were set as Young's module of elasticity to be double of the module in normal disc material, while Poisson coefficient remained the same. Also, as part of the degenerative process, bone structure was affected by reducing the Young's module of elasticity in comparison to the healthy vertebrae. This assumption was adopted based on (Rohlmann et al. 2006a, b, c; Zhang et al. 2009). For both healthy and degenerative model, density of the bone was adopted to be $\rho = 1.83$ g/cm3 (Wang et al. 2019), and density of the disc material to be $\rho = 1$ g/cm3 (Glema et al. 2004; Wang et al. 2019).

16.3.2.2 Loads on Lumbar Spinal Motion Segments

In the FE modeling, loading of lumbar spinal motion segments phase depends on the objectives of the study and analysis type. The investigated segment is usually supported rigidly at the lower endplate of the lowest vertebrae of interest, so the loads are generally applied to the upper endplate of the highest vertebrae of interest. Loads may be used as static or dynamic loads. Constant static loads or incrementally shifting quasi-static loads are commonly used in lumbar spine analysis. Most commonly used loading types are force or displacement, in order to mimic the load or displacement operated device.

Chen et al. (2001) used 10 Nm for flexion, expansion, lateral bending and axial torsion under 150 N preload in the study of adjacent segment rigid fixation syndrome. Goto et al. (2002) studied numerically the L4-5 section lumbar vertebrae using gradual loading instruments to apply intradiscal pressure in the nucleus. In ten steps, compressive loading was carried out at 294 N, followed by flexion and extension loads of 15 Nm in 15 steps. Intradiscal pressure was set as 1.32 MPa for flexed and standing position; then for extended position pressure was set at 0.6 MPa and for degenerated disc model, zero pressure was assumed. Schmidt et al. (2007a, b) used an unconstrained moment load of 7.5 Nm with varying directions of loading between each pair of main anatomical planes to model variations of anatomical loads, e.g. rotation with lateral bending, etc. Both these loading cases were additionally coupled with an axial compressive preload of 500 N. Chen et al. (2008) contrasted the inter-body fusion and fixation strategies by adding a compressive preload of 150 N along with four distinct forms of 10 Nm moments simulating physiological loading events. Zhang et al. (2009) tested the load transfer of a dynamic stabilization system under compression by applying an axial compressive force of 2000 N to validate the model and 1000 N to analyze the load transmitting properties of the various implants.

Due to the larger numerical stability of solution when using displacements as load rather than forces in our in-house software PAK, we have relied upon the recommendation from Baroud et al. (2003) that have applied displacement in load FE analysis of L4-5 segment, by applying quasi-static compression load of 2.8 mm in steps of 0.2 mm. We have used the same methodology by applying 2.8 mm in the steps of 0.1 mm in 10 time steps.

16.3.2.3 Type of Analysis

Bone tissue is the essential constituent of the body. It refers to a community of helping connective tissues. Like some, this connective tissue has two components: cells and an intercellular material. The basic chemical compound of the intercellular material and the internal composition of the fibrous materials decide the rigidity as the key trait of the bone tissue. Bone is a functional tissue with irreversible biochemical modifications and therefore represents a constant mechanism for remodeling, resorption and tissue formation. Bone tissue homeostasis is regulated by systemic hormones and parathyroid glandular hormones. Any discrepancy in resorption and bone tissue development (homeostasis disorder) leads to significant complications and loss of essential bone function. Therefore, the general rules of the FE simulation of systems are applicable here (Milasinovic et al. 2020). The static or dynamic equilibrium equations can also be used. The bone structure is typically modeled by 3D finite elements to capture bone geometry, and here we give a dynamic motion equation for a 3D finite element (Kojić et al. 2008):

$$\mathbf{M}^{n+1}\ddot{\mathbf{U}}+^{n}\mathbf{K}\mathbf{U} =^{\mathrm{n+1}} \mathbf{F}^{\mathrm{ext}} \tag{16.1}$$

where $\mathbf{M}$ and ${}^{\mathrm{n}}\mathbf{K}$ are the element mass and stiffness matrices, ${}^{\mathrm{n+1}}\ddot{\mathbf{U}}$ and $\mathbf{U}$ are the nodal acceleration and displacement vectors, and ${}^{\mathrm{n+1}}\mathbf{F}^{\mathrm{ext}}$ is the external nodal force which includes the structural external forces and the action of the surrounding elements. The motion equation refers to the time step 'n' where the upper left indices 'n' and '$n+1$' represent the start and end of the time step, respectively. The stiffness matrix can be written in the form (Kojić et al. 2008):

$$ {}^{n}\mathbf{K} = \int_V \mathbf{B}^{\mathrm{T}\,n}\mathbf{C}\mathbf{B}dV \tag{16.2} $$

where $\mathbf{B}$ is the strain–displacement matrix and ${}^{n}\mathbf{C}$ is the constitutive matrix. In the case of isotropic material, the constitutive matrix is given in (16.3), where elastic constants are E and ν. The upper left index 'n' is used to indicate that the axial modulus (16.4) corresponding to the strain rate ${}^{n}\dot{e}$ can be used when the rate effects are significant. In Eq. (16.4), where $\mathrm{E}_{\mathrm{axial}}$ is the elastic modulus of bone of apparent density ρ, tested at strain rate of $\dot{\mathrm{e}}[\mathrm{s}^{-1}]$; and E_c is the elastic modulus of bone with an apparent density of ρ_c tested at strain rate of 1.0 s^{-1}.

$$ \mathrm{C} = \frac{\mathrm{E}(1-\nu)}{(1+\nu)(1-2\nu)} \begin{bmatrix} 1 & \frac{\nu}{(1-\nu)} & \frac{\nu}{(1-\nu)} & 0 & 0 & 0 \\ \frac{\nu}{(1-\nu)} & 1 & \frac{\nu}{(1-\nu)} & 0 & 0 & 0 \\ \frac{\nu}{(1-\nu)} & \frac{\nu}{(1-\nu)} & 0 & 0 & 0 & 0 \\ 0 & 0 & 0 & \frac{1-2\nu}{2(1-\nu)} & 0 & 0 \\ 0 & 0 & 0 & 0 & \frac{1-2\nu}{2(1-\nu)} & 0 \\ 0 & 0 & 0 & 0 & 0 & \frac{1-2\nu}{2(1-\nu)} \end{bmatrix} \tag{16.3} $$

$$ E_{axial} = E_c \dot{e}^{0.06} \left(\frac{\rho}{\rho_c} \right)^3 \tag{16.4} $$

Cartilage is considered to be a porous deformable medium whose pores are filled with fluid. The current configuration at time t, is denoted by ${}^{\mathrm{t}}\boldsymbol{B}$. The coordinates of the material point P are denoted as ${}^{\mathrm{t}}\mathbf{x}$, where the upper left index denotes the moment of time t. The physical quantities at the material point are: displacement of the solid $\mathbf{u}$, relative velocity of the fluid in relation to the solid (Darcy velocity) $\mathbf{q}$, fluid pressure p, inflation pressure $\mathrm{p_c}$, or electric potential ϕ. Next, the basic equations for the previously described coupled problem are derived (Kojić et al. 2008). The equation of equilibrium for the solid is considered first

$$ (1-n)\mathbf{L}^{\mathrm{T}}\boldsymbol{\sigma}_s + (1-n)\rho_s\mathbf{b} + \mathbf{k}^{-1}n\mathbf{q} - (1-n)\rho_s\ddot{\mathbf{u}} = 0 \tag{16.5} $$

where: $\boldsymbol{\sigma}_{\mathrm{s}}$ is stress in the solid phase, n—porosity, $\mathbf{k}$—permeability matrix, ρ_{s}—solid density, $\mathbf{b}$ volume force per unit mass, $\mathbf{q}$—relative fluid velocity, $\ddot{\mathbf{u}}$- solid acceleration. The $\mathbf{L}^{\mathrm{T}}$ operator is defined as (Kojić et al. 2008):

$$ \mathbf{L}^{\mathrm{T}} = \begin{bmatrix} \frac{\partial}{\partial x_1} & 0 & 0 & \frac{\partial}{\partial x_2} & 0 & \frac{\partial}{\partial x_3} \\ 0 & \frac{\partial}{\partial x_2} & 0 & \frac{\partial}{\partial x_1} & \frac{\partial}{\partial x_3} & 0 \\ 0 & 0 & \frac{\partial}{\partial x_3} & 0 & \frac{\partial}{\partial x_2} & \frac{\partial}{\partial x_1} \end{bmatrix} \tag{16.6} $$

Equation (16.5) corresponds to the current configuration ${}^{t}\boldsymbol{B}$; in this section, time indices are used in labels only where necessary for clarity. The equilibrium equation for the fluid phase is (without electrokinetic coupling):

$$n\nabla p + n\rho_f \mathbf{b} - \mathbf{k}^{-1} n\mathbf{q} - n\rho_f \dot{\mathbf{v}}_f = \mathbf{0} \tag{16.7}$$

where p is the fluid pressure in the pores, ρ_f is the density of the fluid and $\dot{\mathbf{v}}_f$ is the acceleration of the fluid. Equation (16.7) is known as the generalized Darcy law. Both equilibrium Eqs. (16.5) and (16.7) refer to the unit volume of the mixture. From Eqs. (16.5) and (16.7) it follows (Kojić et al. 2008):

$$\mathbf{L}^{\mathrm{T}}\sigma + \rho\mathbf{b} - \rho\ddot{\mathbf{u}} - \rho_f \dot{\mathbf{q}} = \mathbf{0} \tag{16.8}$$

where $\boldsymbol{\sigma}$ is the total voltage that can be expressed through the terms $\boldsymbol{\sigma}_{\mathrm{s}}$ and p as:

$$\mathbf{L}^{\mathrm{T}}\sigma + \rho\mathbf{b} - \rho\ddot{\mathbf{u}} - \rho_f \dot{\mathbf{q}} = \mathbf{0} \tag{16.9}$$

and $\rho = (1 - \mathrm{n})\rho_{\mathrm{s}} + \mathrm{n}\rho_{\mathrm{f}}$ is the density of the mixture. The constant vector $\mathbf{m}$ is defined as $\mathbf{m}^{\mathrm{T}} = \{1\ 1\ 1\ 0\ 0\ 0\}$ and indicates that the contribution of fluid pressure refers only to normal stresses. It is also taken into account that the fluid pressure has a positive sign in the direction of compression, as well as that the tensile stresses and strains are positive. Further analysis uses the effective voltage defined as:

$$\boldsymbol{\sigma}' = \boldsymbol{\sigma} + \mathbf{m}\mathrm{p} \tag{16.10}$$

and is used to represent constitutive relations for solid. Relative fluid velocity (Darcy velocity) $\mathbf{q}$ is defined as the volume of fluid that passes through the unit area of the mixture in a unit of time,

$$\mathbf{q} = n\left(\mathbf{v}_f - \dot{\mathbf{u}}\right) \tag{16.11}$$

Equation (16.7) can be written as:

$$-\nabla p + \rho_f \mathbf{b} - \mathbf{k}^{-1}\mathbf{q} - \rho_f \ddot{\mathbf{u}} - \frac{\rho_f}{n}\dot{\mathbf{q}} = \mathbf{0} \tag{16.12}$$

The next equation is the constitutive relation for solid:

$$\sigma' = \mathbf{C}^{\mathrm{E}}(\mathbf{e} - \mathbf{e}_{\mathrm{p}}) \tag{16.13}$$

where $\mathbf{C}^{\mathrm{E}}$ is the elastic constitutive matrix of the solids skeleton, $\mathbf{e}$ is the total deformation, and $\mathbf{e}_{\mathrm{p}}$ is the deformation of the solid due to the action of fluid pressure (Filipovic 1999):

$$\mathbf{e}_{\mathrm{p}} = -\frac{\mathbf{m}}{3K_s} p \tag{16.14}$$

where K_s is the volume modulus of the solid grains. The fluid continuity equation reads (Filipovic 1999):

$$Q_v + Q_p + Q_\rho + Q_s + \nabla^{\mathrm{T}}(\rho_f \mathbf{q}) = 0 \tag{16.15}$$

where volume deformation velocity is defined as:

$$Q_v = \rho_f \frac{\partial e_v}{\partial t} = \rho_f \mathbf{m}^{\mathrm{T}} \frac{\partial \mathbf{e}}{\partial \mathbf{t}} \tag{16.16}$$

$$Q_p = \rho_f \frac{1-n}{K_s} \frac{\partial p}{\partial t} \tag{16.17}$$

wherein $\mathrm{K_f}$ represents the volume modulus of the fluid. Compressibility of solid grains due to the action of effective stress is defined as $\boldsymbol{\sigma}^{,}$:

$$Q_s = -\frac{\rho_f}{3K_s} \mathbf{m}^{\mathrm{T}} \frac{\partial \sigma^{,}}{\partial t} \tag{16.18}$$

Using the elastic constitutive law and Eqs. (16.16)–(16.18), the continuity Eq. (16.15) can be written as:

$$\nabla^{\mathrm{T}}\mathbf{q} + \left(\mathbf{m}^{\mathrm{T}} - \frac{\mathbf{m}^{\mathrm{T}}\mathbf{C}^{\mathrm{E}}}{3K_s}\right)\dot{\mathbf{e}} + \left(\frac{1-n}{K_s} + \frac{n}{K_f} - \frac{\mathbf{m}^{\mathrm{T}}\mathbf{C}^{\mathrm{E}}\mathbf{m}}{9K_s^2}\right)\dot{p} = 0 \tag{16.19}$$

Equations (16.19) refers to the current configuration and the current porosity n. However, in the incremental analysis of problem solving, it is necessary to take into account the change in porosity. It is necessary to define the change of porosity in differential equations. Namely, the continuity equation for fluid can be written as:

$$\nabla^T(\rho_f \mathbf{q}) + \frac{\partial(\rho_f n)}{\partial t} = 0 \tag{16.20}$$

or, using Eq. (16.17), as:

$$\nabla^T(\rho_f \mathbf{q}) + \frac{n\rho_f}{K_f} \frac{\partial p}{\partial t} + \rho \frac{\partial n}{\partial t} = 0 \tag{16.21}$$

This equation will be used later to calculate the incremental porosity change in the time integration step Δt. It is necessary to define the deformation rate. In the case of small displacements of the solid, the tensor of small deformations is defined as

$$\mathbf{e} = \frac{1}{2}(\nabla\mathbf{u} + (\nabla\mathbf{u})^{\mathrm{T}}) \tag{16.22}$$

However, in the case of large displacements, other measures of deformation in the constitutive relation Eq. (16.3) are used. One of the most commonly used measures of deformation is logarithmic deformation (also called natural deformation). For the current configuration ${}^{t}\mathbf{B}$ the left Cauchy-Green deformation tensor ${}_{0}^{t}\mathbf{B}$ at the material point P is defined as:

$$ {}_{0}^{t}\mathbf{B} = {}_{0}^{t}\mathbf{F}{}_{0}^{t}\mathbf{F}^{\mathrm{T}} \tag{16.23}$$

where ${}_{0}^{t}\mathbf{F}$ is the strain tensor:

$$ {}_{0}^{t}\mathbf{F} = \frac{\partial^{t}\mathbf{x}}{\partial^{0}\mathbf{x}} \tag{16.24}$$

with components ${}_{0}^{t}\mathbf{F}_{ij} = \partial^{t}x_i/\partial^{0}x_j$. Here ${}^{t}\mathbf{x}$ and ${}^{0}\ \mathbf{x}$ are the position vectors in the ${}^{t}\mathbf{B}$ configuration and in the initial ${}^{0}\mathbf{B}$ configuration. Using standard eigenvalue analysis, the principal directions ${}^{t}\mathbf{p}_{\mathrm{i}}$ and the eigenvalues ${}_{0}^{t}\lambda_i^2$ of the tensor ${}_{0}^{t}\mathbf{B}$ can be obtained, where ${}_{0}^{t}\lambda_i$ are the elongations in the direction of the principal directions, so that it is valid that ${}_{0}^{t}\mathbf{B}$ is defined as:

$$ {}_{0}^{t}\mathbf{B} = \sum_{i=1}^{3} {}_{0}^{t}\lambda_i^{2\,t}\mathbf{p}_i{}^{t}\mathbf{p}_i \tag{16.25}$$

Logarithmic deformations are defined as:

$$ {}_{0}^{t}\mathbf{e} = \sum_{i=1}^{3} ln{}_{0}^{t}\lambda_i{}^{t}\mathbf{p}_i{}^{t}\mathbf{p}_i \tag{16.26}$$

Finally, the effect of “swelling” p_c pressure is considered. First of all, it is necessary to define the total pressure p_{tot}, over the sum of fluid pressure p and “swelling” pressure p_c (Filipovic 1999)

$$ p_{tot} = p + p_c \tag{16.27}$$

Total pressure refers to the pressure already described through Darcy’s generalized law (16.7). There are several definitions of “swelling” pressure. According to (Filipovic 1999), “swelling” pressure can be represented as a nonlinear function of the change in water content ζ,

$$ p_c = p_{co} + k_c(\zeta)\zeta \tag{16.28}$$

where p_{co} is the initial “swelling” pressure, and $k_c(\zeta)$ is a nonlinear function that is determined empirically. The variable ζ is expressed in terms of the relative displacement of the fluid $\mathbf{w}$ as:

$$\zeta = \nabla^{\mathrm{T}}\mathbf{w} \tag{16.29}$$

Another way of expressing "swelling" pressure is through the ionic concentration c. Namely, a relation is introduced to define the concentration deformation e_c as:

$$e_c = \alpha_c c \tag{16.30}$$

where α_c is the coefficient of chemical contraction. The deformation defined by Eq. (16.30) has the characteristic of thermal deformation in the constitutive relation for the effective stress $\boldsymbol{\sigma}'$. Otherwise, concentration is defined through Fick's law

$$\nabla^{\mathrm{T}}(\beta_c \nabla c) - \frac{\partial c}{\partial t} = 0 \tag{16.31}$$

where β_c is the ion diffusion coefficient. The ion diffusion rate is high compared to the relative fluid velocity, so the concentration field can be considered stationary (Filipovic 1999). A third possibility for interpreting the effects of "swelling" pressure is through electrokinetic coupling. Namely, the combination of Om's and Darcy's law established the following relations (Filipovic 1999):

$$\begin{Bmatrix} \mathbf{q} \\ \mathbf{j} \end{Bmatrix} = \begin{bmatrix} -k_{11} & k_{12} \\ k_{21} & -k_{22} \end{bmatrix} \begin{Bmatrix} \nabla p \\ \nabla \phi \end{Bmatrix} \tag{16.32}$$

where: $\mathbf{j}$ is the density of the electric current, ϕ is the electric potential, k_{11} is the Darcy hydraulic permeability, k_{22} is the electrical conductivity; and k_{12} and k_{21} are electrokinetic coupling coefficients equal to Osinger's reciprocal values. Using Eq. (16.32), equilibrium Eq. (16.7) can be generalized to include electrokinetic coupling. From the first equation of the system (16.30), the resistance force of the fluid $\mathbf{F}_{\mathrm{w}}$ can be defined (Kojić et al. 2008):

$$\mathbf{F}_w = -k_{11}^{-1}\mathbf{q} + k_{11}^{-1}k_{12}\nabla\phi \tag{16.33}$$

so that now the equilibrium Eq. (16.7) becomes:

$$-\nabla p + \rho_f \mathbf{b} - k_{11}^{-1}\mathbf{q} + k_{11}^{-1}k_{12}\nabla\phi - \rho_f \ddot{\mathbf{u}} - \frac{\rho_f}{n}\dot{\mathbf{q}} = \mathbf{0} \tag{16.34}$$

It is noticed that Eq. (16.34) corresponds to the isotropic conditions of the solid skeleton and represents a generalized form of Darcy's law. Also, based on the shape of Eq. (16.33), the existence of a "swelling" effect can be concluded through electrokinetic coupling. In electrokinetic coupling, an additional equation is the equation of continuity for current density $\mathbf{j}$:

$$\nabla^{\mathrm{T}}\mathbf{j} = 0 \tag{16.35}$$

By substituting the current density $\mathbf{j}$ from the second equation of the system of Eq. (16.34) into Eq. (16.35), we obtain:

$$k_{21}\nabla^{\mathrm{T}}\nabla p - k_{22}\nabla^{\mathrm{T}}\nabla\phi = 0 \tag{16.36}$$

Further derivations assume large displacements and large deformations of the solid, as well as elastic material with a constitutive relation Eq. (16.3). The effects of "swelling" pressure are presented through electrokinetic coupling. Other possibilities of presenting "swelling" pressure can be considered as special cases in further execution. Applying the principle of virtual work and assuming that the material is elastic, we obtain:

$$\begin{aligned}
&\int\limits_{{}^tV} \delta\mathbf{e}^{\mathrm{T}}\mathbf{C}^{\mathrm{E}}\mathbf{e}dV + \int\limits_{{}^tV} \delta\mathbf{e}^{\mathrm{T}}\left(\frac{\mathbf{C}^{\mathrm{E}}\mathbf{m}}{3K_s} - \mathbf{m}\right)pdV \\
&\quad + \int\limits_{{}^tV} \delta\mathbf{u}^{\mathrm{T}}\rho\ddot{\mathbf{u}}dV + \int\limits_{{}^tV} \delta\mathbf{u}^{\mathrm{T}}\rho_f\dot{\mathbf{q}}dV \\
&= \int\limits_{{}^tV} \delta\mathbf{u}^{\mathrm{T}}\rho\mathbf{b}dV + \int\limits_{{}^tA} \delta\mathbf{u}^{\mathrm{T}}\mathbf{t}dA
\end{aligned} \tag{16.37}$$

where the upper left index "t" denotes the configuration ${}^{\mathrm{t}}\mathbf{B}$ (at time t). Further, by applying Galerkin's method, ie. by multiplying Eq. (16.34) by the interpolation matrix $\mathbf{H}_q^{\mathrm{T}}$ for the relative velocity of the fluid $\mathbf{q}$, and integrating by the volume of the finite element ${}^tV$, we obtain:

$$\begin{aligned}
&-\int\limits_{{}^tV} \mathbf{H}_q^{\mathrm{T}}\nabla pdV + k_{11}^{-1}k_{12}\int\limits_{{}^tV} \mathbf{H}_q^{\mathrm{T}}\nabla\phi dV \\
&+\int\limits_{{}^tV} \mathbf{H}_q^{\mathrm{T}}\rho_f\mathbf{b}dV - k_{11}^{-1}\int\limits_{{}^tV} \mathbf{H}_q^{\mathrm{T}}\mathbf{q}dV \\
&-\int\limits_{{}^tV} \mathbf{H}_q^{\mathrm{T}}\rho_f\ddot{\mathbf{u}}dV - \int\limits_{{}^tV} \mathbf{H}_q^{\mathrm{T}}\frac{\rho_f}{n}\dot{\mathbf{q}}dV = \mathbf{0}
\end{aligned} \tag{16.38}$$

Analogously, by multiplying the continuity Eq. (16.15) by an interpolation fluid pressure matrix $\mathbf{H}_p^{\mathrm{T}}$ (which is a column vector), we obtain

$$\begin{aligned}
&\int\limits_{{}^tV} \mathbf{H}_p^{\mathrm{T}}\nabla^{\mathrm{T}}\mathbf{q}dV + \int\limits_{{}^tV} \mathbf{H}_p^{\mathrm{T}}\left(\mathbf{m}^{\mathrm{T}} - \frac{\mathbf{m}^{\mathrm{T}}\mathbf{C}^{\mathrm{E}}}{3K_s}\right)\dot{\mathbf{e}}dV \\
&\quad + \int\limits_{{}^tV} \mathbf{H}_p^{\mathrm{T}}\left(\frac{1-n}{K_s} + \frac{n}{K_f} - \frac{\mathbf{m}^{\mathrm{T}}\mathbf{C}^{\mathrm{E}}\mathbf{m}}{9K_s^2}\right)\dot{p}dV = \mathbf{0}
\end{aligned} \tag{16.39}$$

Table 16.7 Comparative view of the number of unknown quantities per element type

Element type	Number of nodes per element	Number of unknown sizes by element	
		Fluid velocity and solid displacement	Fluid pressures and electric potential
2-D	4	4	1 + 1
	9	9 + 9	4 + 4
3-D	8	8 + 8	1 + 1
	21	21 + 21	8 + 8
	27	27 + 27	8 + 8

Finally, by multiplying the continuity Eq. (16.38) by the interpolation matrix for the electric potential and integrating by the volume of the finite element ${}^{t}V$, we obtain:

$$k_{21}\int_{{}^{t}V}\mathbf{H}_{\phi}^{\mathrm{T}}\nabla^{\mathrm{T}}\nabla p\,dV - k_{22}\int_{{}^{t}V}\mathbf{H}_{\phi}^{\mathrm{T}}\nabla^{\mathrm{T}}\nabla\phi\,dV = \mathbf{0} \tag{16.40}$$

Table 16.7 gives a comparative view of the number of unknown quantities depending on the type of element.

The standard procedure for integration by volume of a finite element for Eq. (16.37)–(16.39) is applied. The obtained system of finite element equations is solved incrementally in the time step Δt, provided that the balance equations are satisfied at the end of each time step (t + Δt). This gives the following system of equations:

$$\begin{bmatrix} \mathbf{m}_{\mathbf{uu}} & 0 & 0 & 0 \\ 0 & 0 & 0 & 0 \\ \mathbf{m}_{qu} & 0 & 0 & 0 \\ 0 & 0 & 0 & 0 \end{bmatrix}\begin{Bmatrix} {}^{t+\Delta t}\ddot{\underline{\mathbf{u}}} \\ {}^{t+\Delta t}\ddot{\underline{\mathbf{p}}} \\ {}^{t+\Delta t}\ddot{\underline{\mathbf{q}}} \\ {}^{t+\Delta t}\ddot{\underline{\phi}} \end{Bmatrix} + \begin{bmatrix} 0 & 0 & \mathbf{c}_{\mathbf{uq}} & 0 \\ \mathbf{c}_{pu} & \mathbf{c}_{pp} & 0 & 0 \\ 0 & 0 & \mathbf{c}_{qq} & 0 \\ 0 & 0 & 0 & 0 \end{bmatrix}\begin{Bmatrix} {}^{t+\Delta t}\dot{\underline{\mathbf{u}}} \\ {}^{t+\Delta t}\dot{\underline{\mathbf{p}}} \\ {}^{t+\Delta t}\dot{\underline{\mathbf{q}}} \\ {}^{t+\Delta t}\dot{\underline{\phi}} \end{Bmatrix}$$

$$+\begin{bmatrix} \mathbf{k}_{\mathbf{uu}} & \mathbf{k}_{\mathbf{u}p} & 0 & 0 \\ 0 & 0 & \mathbf{k}_{pq} & 0 \\ 0 & \mathbf{k}_{qp} & \mathbf{k}_{qq} & \mathbf{k}_{q\phi} \\ 0 & \mathbf{k}_{\phi p} & 0 & \mathbf{k}_{\phi\phi} \end{bmatrix}\begin{Bmatrix} \Delta\underline{\mathbf{u}} \\ \Delta\underline{\mathbf{p}} \\ \Delta\underline{\mathbf{q}} \\ \Delta\underline{\phi} \end{Bmatrix} = \begin{Bmatrix} {}^{t+\Delta t}\mathbf{f}_{\mathbf{u}} \\ {}^{t+\Delta t}\mathbf{f}_{p} \\ {}^{t+\Delta t}\mathbf{f}_{q} \\ {}^{t+\Delta t}\mathbf{f}_{\phi} \end{Bmatrix} \tag{16.41}$$

The matrices and vectors in Eq. (16.41) are defined as:

$$\mathbf{m}_{uu} = \int_{{}^{t}\mathbf{V}}\mathbf{H}_{u}^{\mathrm{T}}\rho\mathbf{H}_{u}\,dV$$

$$\mathbf{m}_{qu} = \int_{{}^{t}\mathbf{V}}\mathbf{H}_{q}^{\mathrm{T}}\rho_{f}\mathbf{H}_{u}\,dV$$

$$\mathbf{c}_{uq} = \mathbf{m}_{qu}^{\mathrm{T}} = \int_{{}^t\mathbf{V}} \mathbf{H}_u^{\mathrm{T}} \rho_f \mathbf{H}_q dV$$

$$\mathbf{c}_{pu} = -\int_{{}^t\mathbf{V}} \mathbf{H}_p^{\mathrm{T}} \left(\mathbf{m}^{\mathrm{T}} - \frac{\mathbf{m}^{\mathrm{T}} \mathbf{C}^{\mathrm{E}}}{3K_s} \right) {}^t\mathbf{B} dV$$

$$\mathbf{c}_{pp} = -\int_{{}^t\mathbf{V}} \mathbf{H}_p^{\mathrm{T}} \left(\frac{1-n}{K_s} + \frac{n}{K_f} - \frac{\mathbf{m}^{\mathrm{T}} \mathbf{C}^{\mathrm{E}} \mathbf{m}}{9K_s^2} \right) \mathbf{H}_p dV$$

$$\mathbf{c}_{qq} = \int_{{}^t\mathbf{V}} \mathbf{H}_q^{\mathrm{T}} \frac{\rho_f}{n} \mathbf{H}_q dV$$

$$\mathbf{k}_{uu} = \int_{{}^t\mathbf{V}} {}^t\mathbf{B}^{\mathrm{T}} \mathbf{C}^{\mathrm{E}t} \mathbf{B} dV$$

$$\mathbf{k}_{up} = \mathbf{c}_{pu}^{\mathrm{T}} = \int_{{}^t\mathbf{V}} {}^t\mathbf{B}^{\mathrm{T}} \left(\frac{\mathbf{C}^{\mathrm{E}} \mathbf{m}}{3K_s} - \mathbf{m} \right) \mathbf{H}_p dV$$

$$\mathbf{k}_{pq} = \int_{{}^t\mathbf{V}} \mathbf{H}_p^{\mathrm{T}} \mathbf{H}_{q,\mathbf{x}} dV$$

$$\mathbf{k}_{qp} = \mathbf{k}_{pq}^{\mathrm{T}} = \int_{{}^t\mathbf{V}} \mathbf{H}_{q,\mathbf{x}}^{\mathrm{T}} \mathbf{H}_p dV$$

(1.3.6)

$$\mathbf{k}_{qq} = \int_{{}^t\mathbf{V}} \mathbf{H}_q^{\mathrm{T}} \mathbf{k}^{-1} \mathbf{H}_q dV$$

$$\mathbf{k}_{q\phi} = -k_{11}^{-1} k_{12} \int_{{}^t\mathbf{V}} \mathbf{H}_q^{\mathrm{T}} \mathbf{H}_{\phi,\mathbf{x}} dV$$

$$\mathbf{k}_{\phi q} = k_{21} \int_{{}^t\mathbf{V}} \mathbf{H}_{\phi,\mathbf{x}}^{\mathrm{T}} \mathbf{H}_{q,\mathbf{x}} dV$$

$$\mathbf{k}_{\phi\phi} = -k_{22} \int_{{}^t\mathbf{V}} \mathbf{H}_{\phi,\mathbf{x}}^{\mathrm{T}} \mathbf{H}_{\phi,\mathbf{x}} dV$$

$${}^{t+\Delta t}\mathbf{f}_{\mathbf{u}} = \int_{{}^tV} \mathbf{H}_u^{\mathrm{T}} \rho^{t+\Delta t} \mathbf{b} dV + \int_{{}^tA} \mathbf{H}_u^{\mathrm{T}t+\Delta t} \mathbf{t} dA - \int_{{}^tV} \mathbf{B}^{\mathrm{T}t} \sigma dV - \mathbf{k}_{up}{}^t p$$

$${}^{t+\Delta t}\mathbf{f}_p = \int_{{}^tA} \mathbf{H}_p^{\mathrm{T}} \mathbf{n}^{\mathrm{T}t} \mathbf{q} dA - \mathbf{k}_{pq}{}^t\mathbf{q}$$

$${}^{t+\Delta t}\mathbf{f}_q = \int_{{}^t\mathbf{V}} \mathbf{H}_q^{\mathrm{T}} \rho_f{}^{t+\Delta t} \mathbf{b} dV - \mathbf{k}_{qp}{}^t\mathbf{p} - \mathbf{k}_{qq}{}^t\mathbf{q} - \mathbf{k}_{q\phi}{}^t\phi$$

$$^{t+\Delta t}\mathbf{f}_{\phi} = \int\limits_{^tA} \mathbf{H}_{\phi}^{T\,t}\mathbf{n}^{T}\mathbf{j}dA - \mathbf{k}_{\phi p}{}^{t}\mathbf{p} - \mathbf{k}_{\phi\phi}{}^{t}\phi \tag{16.42}$$

In the previous expressions, $^{t}\mathbf{n}$ is the vector of the normal to the boundary, and $^{t}\mathbf{B}$ is the transformation matrix between deformations and displacements (linear matrix $\mathbf{B}_{L}$). To improve the convergence rate, a nonlinear part ($\mathbf{K}_{uu}$) can be added to the $\mathbf{K}_{uu}$ matrix (Filipovic 1999).

As can be seen from Eq. (16.38), the unknown quantities per finite element nodes are: solid displacements $\mathbf{u}$, relative fluid velocities $\underline{\mathbf{q}}$, fluid pressures $\underline{\mathbf{p}}$, and electric potential $\underline{\boldsymbol{\phi}}$. Boundary conditions include: general boundary conditions for solids, relative velocities, surface pressures, current density and electric potential.

When analyzing the system of differential equations, it is noticed that the system is asymmetric and nonlinear. Only in the case of small displacements and constant porosity does the system become linear. The system is symmetric if the inertial effects are neglected and if there is no electrokinetic coupling. For all the previously mentioned cases, the Newmark method of integration in time is applied. In the case of nonlinearity of the system, an iterative system of equations is formed, which is solved until the convergence criterion is reached. In the iterative procedure of solving the system of equations, all volume and surface integrals refer to the last configuration $^{t+\Delta t}\mathbf{B}^{(i-1)}$, and the deformation $^{t+\Delta t}_{0}\mathbf{e}^{(i-1)}$, where "i" is the current equilibrium iteration. For the density of the mixture ρ, and the porosity n, for the sake of simplicity, however, values are taken from the beginning of the time step, meaning $^{t}\rho$ and ^{t}n. After achieving convergence, the porosity is calculated by the following relation (Filipovic 1999):

$$^{t+\Delta t}n = {}^{t}n - \Delta t\left[{}^{t}n^{t}\left(\frac{\partial p}{\partial t}\right)\frac{1}{K_f} + \underline{\nabla}^{T\,t}\mathbf{q}\right] \tag{16.43}$$

when deriving Eq. (16.43), the spatial changes of fluid density were neglected, meaning $\partial \rho_f/\partial x_i = 0$,. When the effects of "swelling" pressure are taken into account according to Eq. (16.27), then in the system of Eqs. (16.42) the force $^{t+\Delta t}\mathbf{f}_q$ contains an additional term $^{t}\mathbf{f}_{q}^{c}$

$$^{t}\mathbf{f}_{q}^{c} = -\int\limits_{^tV} \mathbf{H}_{q}^{T}\underline{\nabla}^{t}p_c dV \tag{16.44}$$

Here, $^{t}p_c$ is calculated at the beginning of the step and $^{t}\zeta$ is defined as:

$$^{t}\zeta = \Delta t\underline{\nabla}^{T\,t}\mathbf{q} \tag{16.45}$$

Of course, in the system of Eq. (16.41) the types and columns related to the electric potential ϕ are omitted. Finally, if the effects of "swelling" pressure are described via Eq. (30), then there are no terms that take into account electrokinetic coupling, and an additional term is introduced in Eq. (16.42) as (Filipovic 1999):

$$
{}^{t}\mathbf{f}_u^c = \frac{\alpha_c E}{1-2\nu} \int\limits_{{}^{t}V} {}^{t}\mathbf{B}\mathbf{m} c dV \tag{16.46}
$$

16.4 Results and Discussion

This section presents independent results using the two aforementioned main approaches—machine learning and computational modelling.

16.4.1 Results for the ML Model

This section presents the main results in the aspect of implementation of machine learning methods for automatic segmentation of region of interest (disc material). The influence of training parameters is also investigated to achieve best possible results.

16.4.1.1 Influence of Training Parameters

1. Epoch

Training and validation were performed independently on sagittal and axial view images. Regarding the analysis of number of epochs (EP) on sagittal view images, the results with three different learning rates (LR), LR = 0.1, LR = 0.01 and LR = 0.001 on a training and validation subsets are shown in Fig. 16.20.

If we compare the training-validation loss curves under different LR values, where the maximum EP number is 100, it can be seen, that the loss curves become stable after EP = 40 with LR = 0.1 and 0.01. However, for LR = 0.001, the training loss becomes stable after few more epochs. Also, after 40 epochs the model tends to overfit, leading to the conclusion that EP = 40 was selected in subsequent investigations.

This effect is also visible when looking into Dice coefficient, where the dice was the highest when LR = 0.01 and it becomes stable after EP = 40 with the value of around 84% (Fig. 16.21). It is understanding that with the LR = 0.001, the learning is the slowest and the achieved dice coefficient becomes stable after the largest number of epochs in comparison to the other investigated LRs.

The same investigation regarding the investigation of the number of epochs is performed on axial images. The results with three different learning rates (LR), LR = 0.1, LR = 0.01 and LR = 0.001 on a training and validation subsets are shown

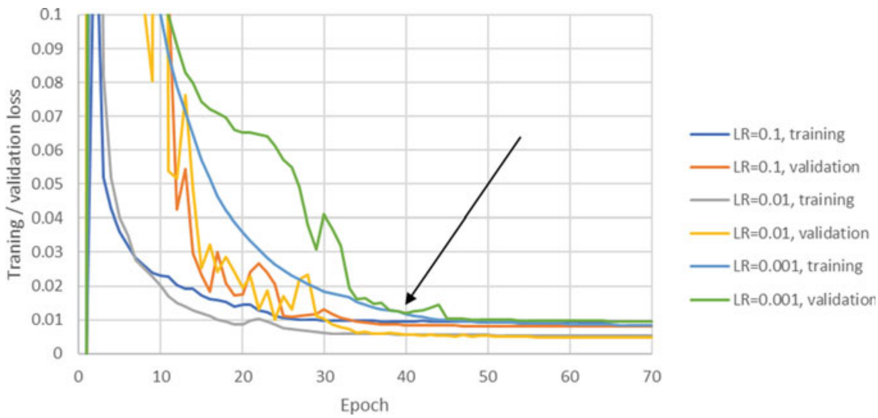

Fig. 16.20 Influence of EP on the training-validation loss curves for different LR values on sagittal view images

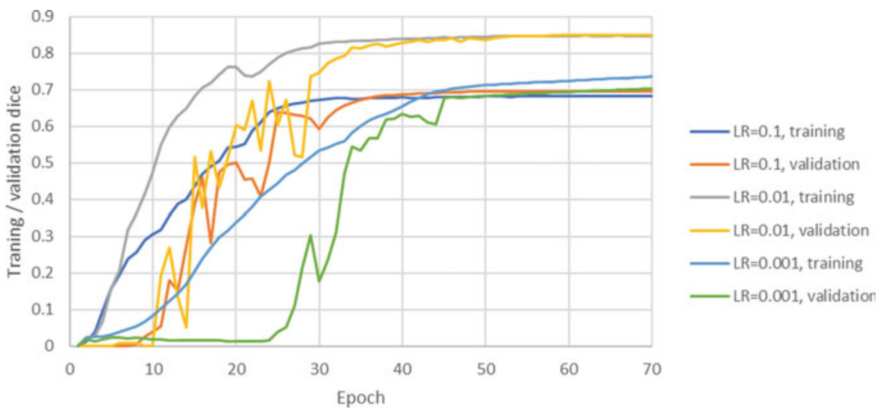

Fig. 16.21 Influence of EP on the training-validation dice curves for different LR values on sagittal view images

in Fig. 16.22. It should be noted that early stopping method resulted in stopping the learning after 82 epochs.

If we compare the training-validation loss curves under different LR values, where the maximum EP number is 100, it can be seen, that the loss curves have more instability in comparison to the analysis on sagittal view image and become stable after EP = 40 with LR = 0.01 and 0.001. However, for LR = 0.1, the validation loss becomes stable after few more epochs. Also, the model for training on axial view images did not have the problem of overfitting.

This same "flickering" effect is also visible when looking into Dice coefficient, where the dice was the highest when LR = 0.01 and it becomes stable after EP = 40 with the value of around 94% (Fig. 16.23).

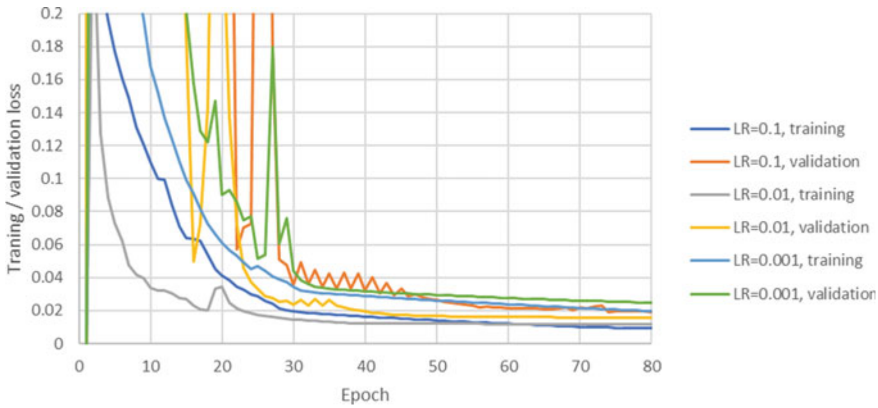

Fig. 16.22 Influence of EP on the training-validation loss curves for different LR values on axial view images

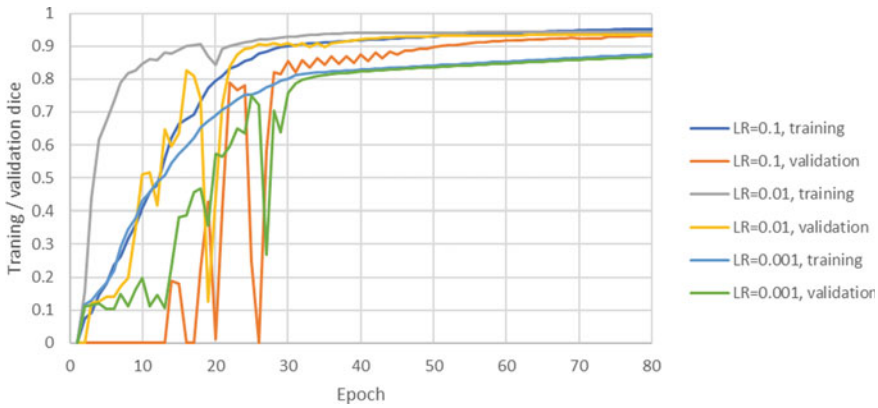

Fig. 16.23 Influence of EP on the training-validation dice curves for different LR values on axial view images

As a result, it can be concluded that 40 epochs are a compromise for both type of views and will be further used in the analysis.

2. Batch Size

The influence of batch size (BS) was evaluated according to the GPU memory occupation ratio (OR) and mean dice over all images from the validation set with EP = 40. In our study, GPU memory occupation was 4% - 6% at all times and did not have larger deviation. Therefore, we have focused on the analysis of as the BS with values 6–12, with an increment of 2. As a result, BS = 10 was selected for the final network training to achieve good segmentation performance with reasonable GPU memory availability.

3. Dropout

The influence of dropout was evaluated according also to the GPU memory occupation ratio (OR) and mean dice over all images from the validation set with EP = 40. No larger influence was noticed on the expense of GPU memory occupation with the change of dropout from 0.1 to 0.5 with an increment of 0.1. As a result, dropout = 0.1 was selected for the final network training as the best in achieving good segmentation performance.

4. Number of Kernel Features

The influence of the number of kernels in the layers was also investigated. We have tried with the several combinations, including 8, 16, 32, 64 and 16, 32, 64, 128 numbers of kernels in subsequent layers, coming to the conclusion that with the EP = 40 and combination of 16, 32, 64, 128 numbers of kernels was the optimal choice in achieving best segmentation performance.

5. Learning Rate

Regarding the analysis of sagittal view images, we have found that different LR values have greater impact on the segmentation performance of the training network. The validation loss curves under different LR values are compared in Fig. 16.24. As shown in this figure, when all learning rates resulted in oscillation up to the around EP = 25, after which a stability is achieved. By comparing the different LR values, specifically LR = 0.1, LR = 0.01, LR = 0.02, LR = 0.03, LR = 0.05, we found that with LR = 0.01 the best results are achieved.

To support previous conclusion that LR = 0.01 was the best, mean dice of the validation set was plotted against epochs, as shown in Fig. 16.25. The highest mean dice of the validation set was achieved with LR = 0.01 with the value of 84%. Through comprehensive consideration of these aspects, LR = 0.01 was selected when training the final U-Net network model.

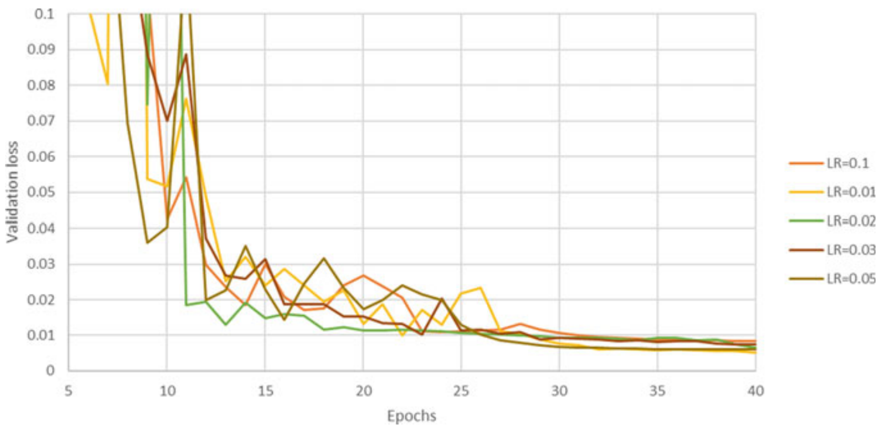

Fig. 16.24 Influence of LR on the validation loss curves on sagittal view images

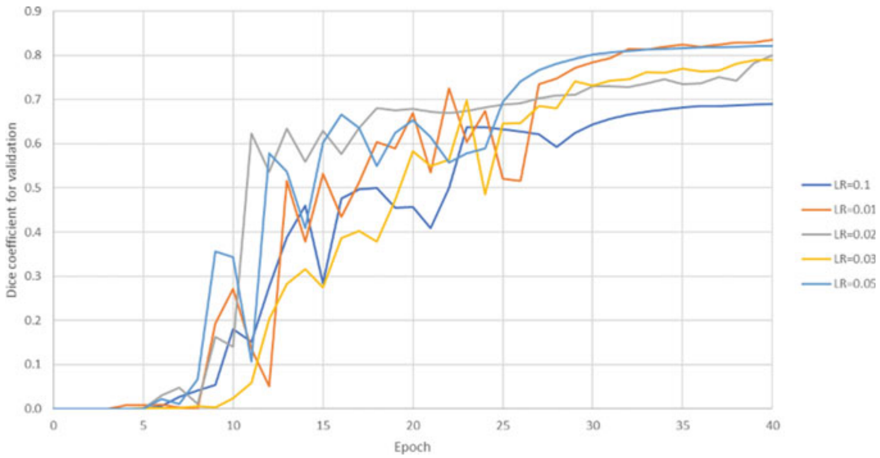

Fig. 16.25 Influence of LR on the dice value curves on sagittal view images

Regarding the analysis of axial view images, we have also found that different LR values have greater impact on the segmentation performance. The validation loss curves for axial view images under different LR values are compared in Fig. 16.26. As shown in this figure, when all learning rates resulted in oscillation up to the around EP = 27, after which a stability is achieved for most of the LR (except LR = 0.1). By comparing the different LR values, specifically LR = 0.1, LR = 0.01, LR = 0.02, LR = 0.03, LR = 0.05, we found that also in this view analysis, the best results are achieved with LR = 0.01.

To support previous conclusion that LR = 0.01 was the best, mean dice of the validation set was plotted against epochs, as shown in Fig. 16.27. The highest mean dice of the validation set was achieved with LR = 0.01 with the value of 94%.

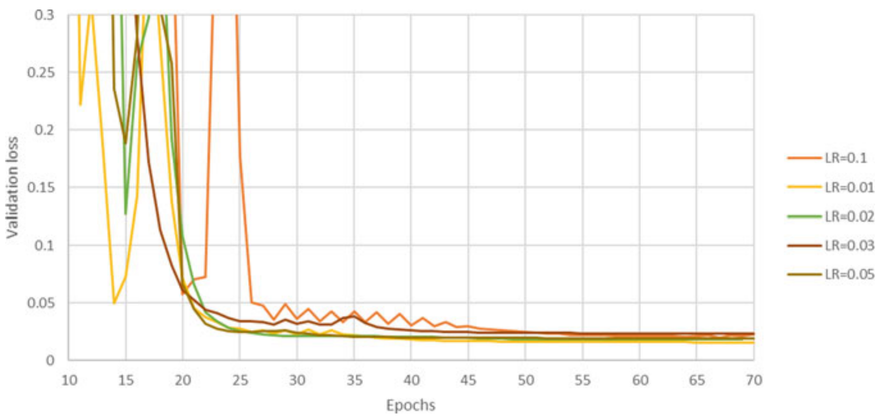

Fig. 16.26 Influence of LR on the validation loss curves on axial view images

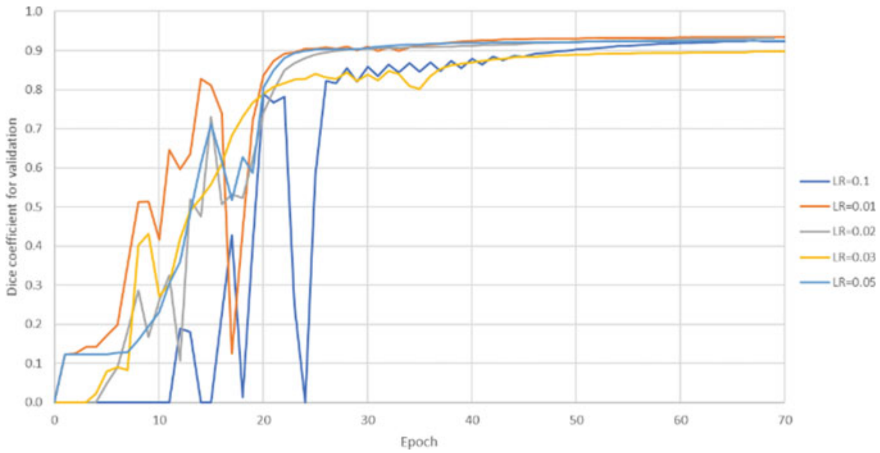

Fig. 16.27 Influence of LR on the dice value curves on axial view images

Through comprehensive consideration of these aspects, LR = 0.01 was also selected when training the final U-Net network model for axial view images.

16.4.1.2 Evaluation and Segmentation

Finally, EP = 40, BS = 10, and LR = 0.01 were used in our implementation as training parameters. The training time was approximately 25 min for the training set (167 images), and segmentation time was around than 20 s for 20 images (~1 s/image). GPU utilization was 5 ± 1% for training. Loss function for training and validation on sagittal view images is shown in Fig. 16.28.

Dice value for training and validation on sagittal view images is shown in Fig. 16.29, achieving highest stable value of around 84%.

Since we have also investigated intersection over union (IOU) metric as a statistical measure of network performance, we give dependance of IOU as a function of number of EP in Fig. 16.30, where the highest value of 72.2% for training and 71.7% for validation was achieved on sagittal view images.

Visual output of the segmentation for the patient with L4/L5 herniation on sagittal view images is given in Fig. 16.31. It should be noted that confidential patient data are covered with black rectangles in the original image to comply with the confidentiality standards. The results show that there is a tendency for underestimation of the surface outside the disc area on the level L4/L5 (herniated level). Further investigation in this direction would include additional post processing methods for erosion/dilatation etc. Also, we will investigate the extraction of relevant geometrical parameters such as lengths, heights, circumferences, surface area etc.

The values of accuracy, dice, IOU, precision and recall for sagittal view images for the training, validation and test subsets are given in Table 16.8.

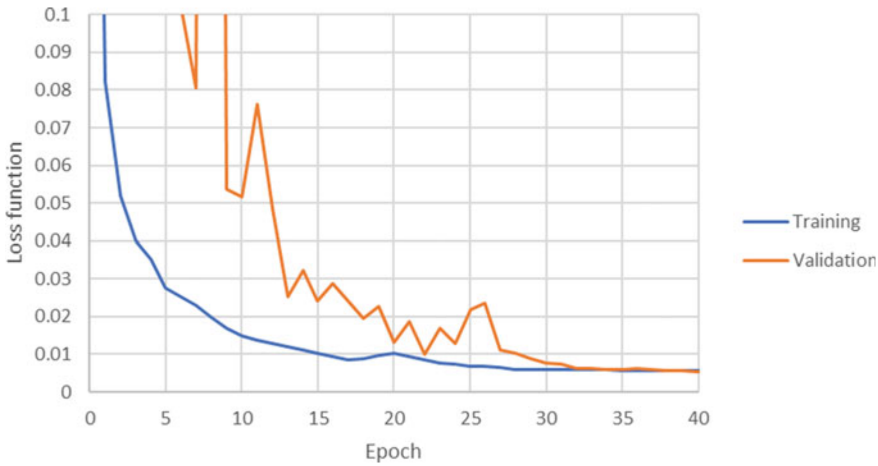

Fig. 16.28 Training-validation loss curves for optimized values EP = 40, BS = 10, and LR = 0.01 on sagittal view images

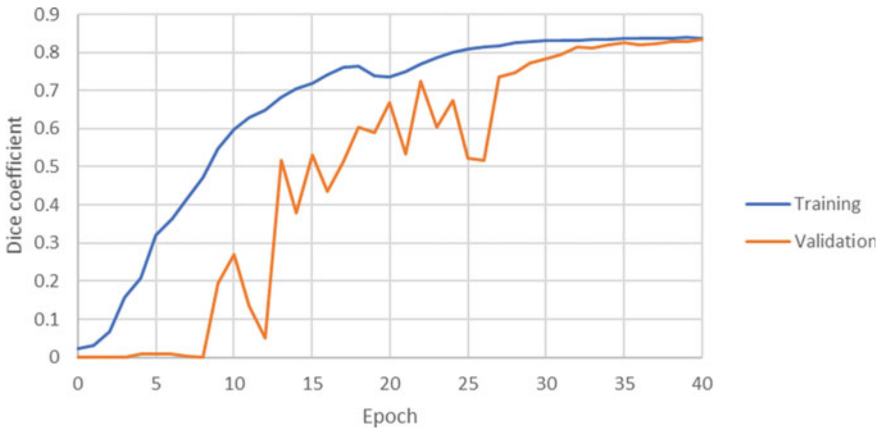

Fig. 16.29 Training-validation dice value for optimized values EP = 40, BS = 10, and LR = 0.01 on sagittal view images

The same methodology was applied to see the performance of the network on axial view images. Loss function for training and validation on axial view images is shown in Fig. 16.32.

Dice value for training and validation on axial view images is shown in Fig. 16.33, achieving highest stable value of around 95%.

Since we have also investigated IOU metric as a statistical measure of network performance, we give dependance of IOU as a function of number of EP in Fig. 16.34, where the highest value of 89.3% for training and 87.7% for validation was achieved on axial view images.

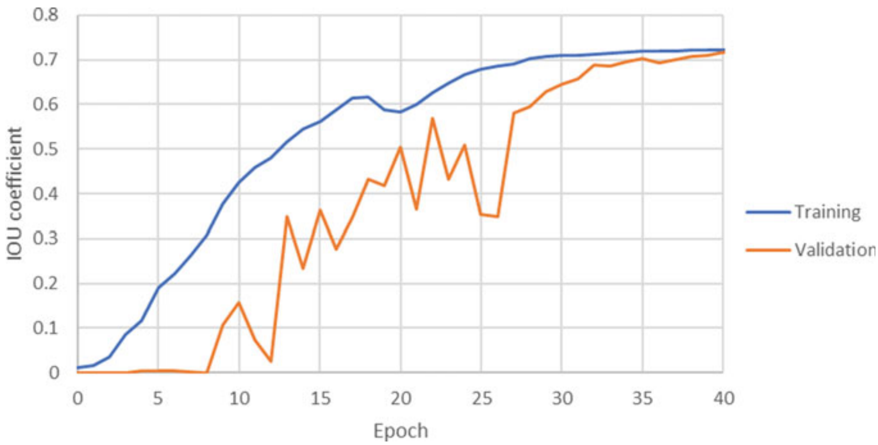

Fig. 16.30 Training-validation IOU value for optimized values EP = 40, BS = 10, and LR = 0.01 on sagittal view images

Fig. 16.31 Comparison of original image (left), manual annotation (center) and automatic segmentation (right) for optimized values EP = 40, BS = 10, and LR = 0.01 on axial view images

Table 16.8 Statistical measures for training, validation and test sets using optimized values EP = 40, BS = 10, and LR = 0.01 on sagittal view images

	Statistical measure				
	Accuracy	Dice	IOU	Precision	Recall
Training	0.996	0.838	0.722	0.950	0.839
Validation	0.996	0.835	0.717	0.972	0.796
Test	0.995	0.791	0.659	0.910	0.792

Visual output of the segmentation for the patient with herniation in axial view is given in Fig. 16.35. It should be noted that confidential patient data are covered in the original image with black rectangles to comply with the confidentiality standards. The results show that there is a tendency for underestimation of the surface outside the

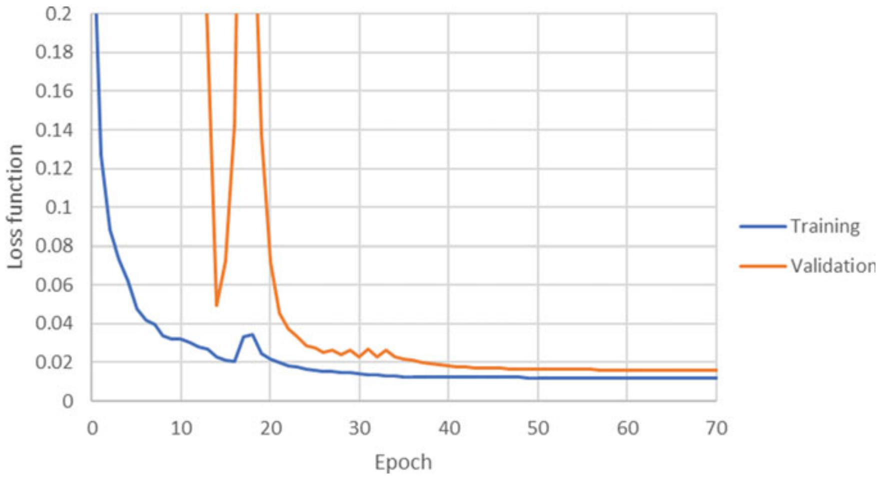

Fig. 16.32 Training-validation loss curves for optimized values EP = 40, BS = 10, and LR = 0.01 on axial view images

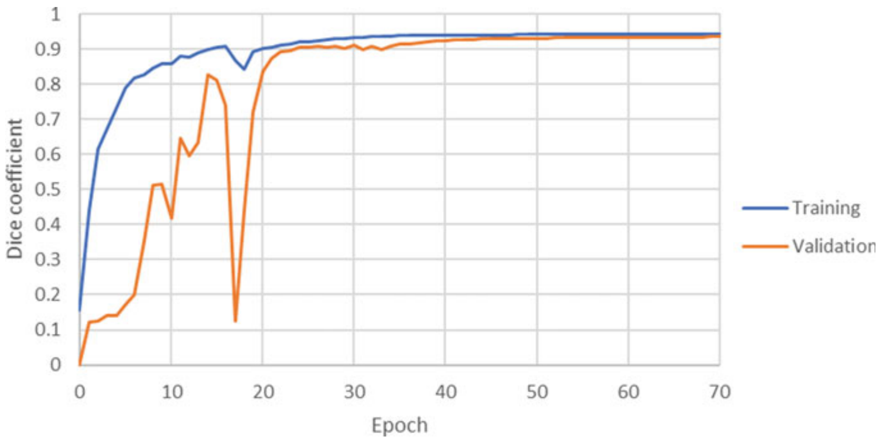

Fig. 16.33 Training-validation dice value for optimized values EP = 40, BS = 10, and LR = 0.01 on axial view images

disc area (herniated part). Further investigation in this direction would include additional post processing methods for erosion/dilatation etc. Also, we will investigate the extraction of relevant geometrical parameters such as lengths, circumferences, surface area etc.

The values of accuracy, dice, IOU, precision and recall for axial view images for the training, validation and test subsets are given in Table 16.9**.**

The utilization of neural network makes the segmentation process fast and robust. The traditional contour-based method requires the initial snake contour be close

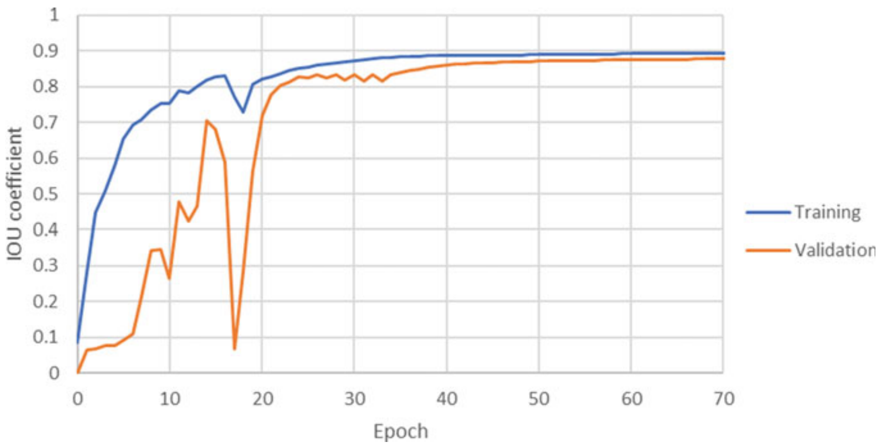

Fig. 16.34 Training-validation IOU value for optimized values EP = 40, BS = 10, and LR = 0.01 on axial view images

Fig. 16.35 Comparison of original image (left), manual annotation (center) and automatic segmentation (right) for optimized values EP = 40, BS = 10, and LR = 0.01 on axial view images

Table 16.9 Statistical measures for training, validation and test sets using optimized values EP = 40, BS = 10, and LR = 0.01 on axial view images

	Statistical measure				
	Accuracy	Dice	IOU	Precision	Recall
Training	0.994	0.947	0.893	0.970	0.960
Validation	0.993	0.935	0.877	0.970	0.938
Test	0.991	0.926	0.863	0.964	0.926

to the real contour; otherwise, the algorithm requires a large number of iterations to converge to the final solution. It should be also noted that in the dataset, both healthy and herniated discs were present in images, meaning that the system is able to segment both herniated and healthy discs. In conclusion, we have presented a rapid, accurate, and automated segmentation method for spinal images (both sagittal and axial) images based on a machine learning network model. The present work can provide guidance for making decision about diagnosis about disc herniation on a certain level. This methodology presents the first step in automatic diagnosis and additional analysis of disc herniation.

16.4.2 Results for the FEM Model

Effective displacements of the region of interest are illustrated in Fig. 16.36, including the normal lumbar and herniated lumbar disc L4/L5. It can be noticed that displacements for the herniated disc (2.1 mm) are larger than for the normal disc (maximum 1.77 mm), which is understandable, considering the fact that displaced part of herniated disc lies beyond the constrained area between the vertebrae. The stress values of herniated disc were also larger than those of normal one.

Looking more into the values of effective displacement for the normal healthy disc from several views, it can be seen that it is denoted with red (1.77 mm of displacement) (Fig. 16.37). Those values are present on the top of the L4/L5 disc, which is understandable, as L4 vertebra is pressing the disc from that direction. The values decrease towards the spinal canal (around 1.0 mm).

In contrast, effective displacements for the herniated disc shows higher maximal value (2.1 mm) (Fig. 16.38). This value is present in the area inside the spinal canal, outside the intervertebral space. That volume is denoted with red (2.1 mm of displacement). This result is understandable, as this section is moved outside the intervertebral space.

Considering displacements in x and y direction, for the normal disc before herniation, maximal value in x direction is 1.19 mm and in y direction is 1.31 mm (Fig. 16.39). It should be noted that vertebrae in the Fig. 16.34 are not included in the presentation of displacements, but are only colored green to show the position of the disc between the two vertebrae. Disc material results in the x direction show the highest value towards the spinal canal, indication the start of the herniation and movement of the disc material outside the intervertebral space. Similar results are

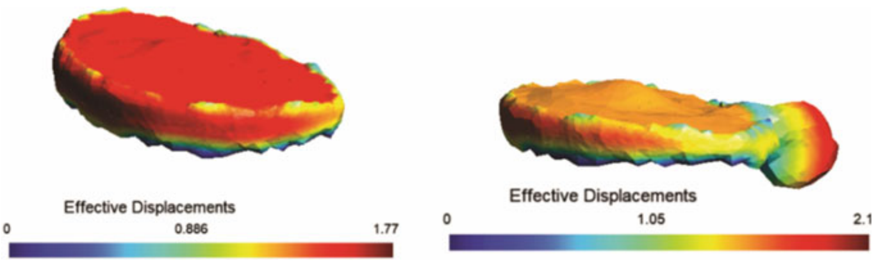

Fig. 16.36 Comparison of normal (left) and herniated (right) L4/L5 lumbar disc

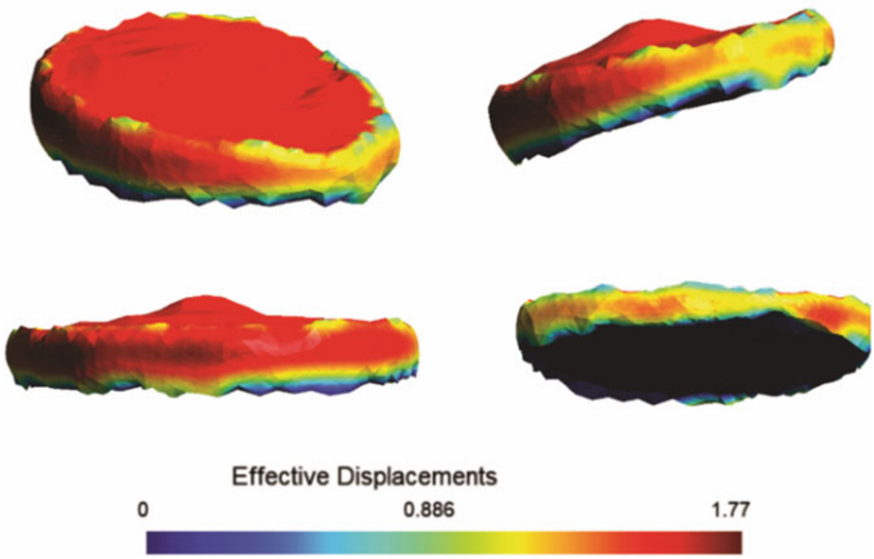

Fig. 16.37 Effective displacements of normal healthy L4/L5 disc in several views

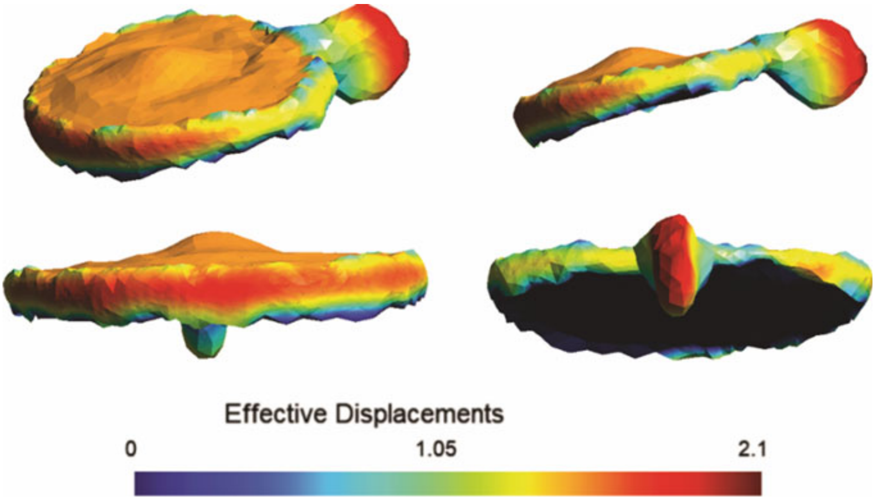

Fig. 16.38 Effective displacements of herniated L4/L5 disc in several views

present also for the y direction with the highest value of 1.31 mm. All this indicated the start of herniation and movement of the disc material towards spinal canal.

Considering displacements in x and y direction, for the herniated disc, maximal value in x direction is 1.25 mm and in y direction is 1.45 mm, which is higher in comparison to the healthy disc (Fig. 16.40). It should be also noted that vertebrae

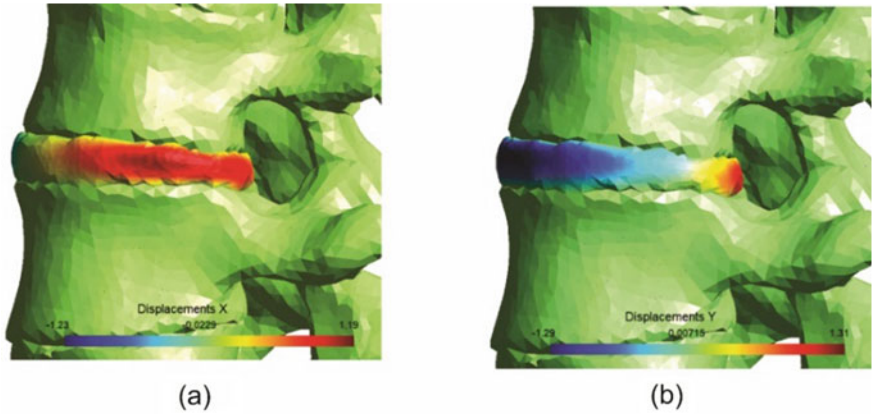

Fig. 16.39 Displacements of normal healthy L4/L5 disc in x direction (**a**) and y direction (**b**)

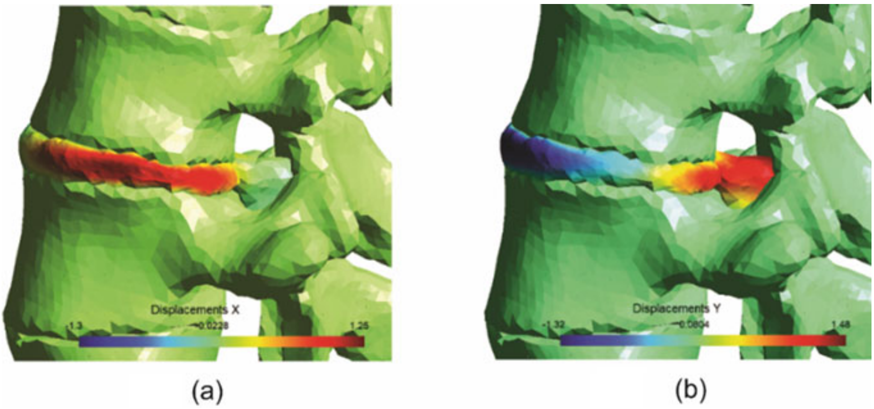

Fig. 16.40 Displacements of herniated L4/L5 disc in x direction (**a**) and y direction (**b**)

in the Fig. 16.35 are not included in the presentation of displacements, but are only colored green to show the position of the disc between the two vertebrae. Disc material results in the x direction show the highest value towards the spinal canal, indication the largest movements of the material towards the spinal canal, while for the y direction the highest values are for the herniated area, as the movement of that section was not constrained in any way (we did not include the spinal cord in the simulation). This section would put pressure onto the spine and cause back pain. Future analysis can investigate into more cases of herniation and their differences in displacements in order to connect displacement values with level of pain in the patients.

Most of the studies investigate the stresses and forces in discs/vertebrae, under different loadings. However, in order to account for the geometrical movements of the disc material, medical experts often propose displacements as a feature that would provide additional information. Li and Wang (2006) therefore examine the connection between the load forces and maximum displacement of FE model. Although their results cannot be directly compared with results of our study, they show that under the loading ranges of 500–2500 N, maximum displacements are form 0.5 to 2.2 mm, which is comparable with our study. They also imply that posterior direction has a more obvious tendency to extrude than others; at the same time, the bilateral direction is easily to extrude out than the anterior. This agrees with observations on the patient and our study, showing that posterior-lateral of the disc is the region where annulus fiber mostly ruptures and nucleus populous extrusion occurs. Xie et al. (2017) also look into displacements of annulus fibrosus (mm) which for different models and different types of loading (flexion, extension, bending) was in the same order of magnitude as in our study ranging between the 0.2 mm to 2.989 mm. The distribution of displacement is also in accordance to the results from our study. Similar findings are confirmed by Du et al. (2016).

All this shows that FEM analysis can provide additional information in the analysis of the spinal problems and connection between visible effect of herniation (i.e. back pain) and displacement of the disc material using simulation. Such information could be helpful in determination of adequate therapy.

16.4.3 Coupling Between the Computational Modelling and Machine Learning

This chapter presented the machine learning methods for automatic detection and segmentation of region of interest in MRI images, specifically disc area. This is necessary in order to extract disc material, which can be later processed in order to extract geometrical parameters of interest, which could imply the level of disc herniation. The main limitation of this section is small number of patients (10 patients were available), and therefore small number of images (not all images were with herniated discs, but also images included healthy disc cross sections). This results in some underestimation of the herniated areas. However, the methodology presented shows promising results and can be applied when larger number of images is available.

Additionally, we have presented the methodology for computational modelling using FEM to determine displacements and stresses in a created 3D model of human vertebrae (L3, L4 and L5) and intervertebral discs (L3/L4, L4/L5 and L5/S1). In order to accompany for differences between the healthy individual and individual with disc herniation, we have investigated two 3D models (disc herniation was on level L4/L5 for the diseased patient). Such methodology can imply what areas are under larger stress and possibly how those affect the human body (i.e. pain). In such a way, doctors can have help in determining and prescribing adequate therapy. The main limitation of this study is that we were not able to reconstruct and differentiate between the cancellous and cortical bone, as well as between the nucleus pulposus and annulus fibrosis. The number of images per patient and resolution were not enough to accurately differentiate between the different materials. However, the reconstructed vertebrae and discs are patient specific and most of other authors use simplified models with flat planes, in contrast to our model which follows every patient specific curve. Such patient specific models can be further used in future analyses of creating a parametric model.

Coupling between the machine learning and computational modelling can be performed in such a way that 3D parametric model is created for the three investigated vertebrae and intervertebral discs and personalized based on the output from MRI scans analysis using ML. Relevant parameters from the scans will be forwarded to the parametric model and 3D personalized parametric model will be created. Further investigation of stresses and displacements can be used not only in diagnosing but also for prescribing adequate therapy. This will be achieved in future research and this chapter represents a first step in accomplishing such complex ML and FEM coupling goals.

16.5 Conclusions

This chapter presents a unique investigation of automatic methods for analysis of disc herniation in MRI medical images. State-of-the art methods usually focus only on one approach—3D modelling or Machine Learning. This chapter is the first to propose machine learning algorithms to perform automatic segmentation of regions of interest (vertebrae, discs etc.) and computational modelling using finite element method to investigate the displacements and stress distribution in spinal discs and vertebrae.

The chapter begins with medical background including a short overview of disc herniation and medical methods for diagnosis and treating such disease, only to review existing methods and solutions in the fields of machine learning and computational modelling. The dataset used in this research consisted of 69 sagittal images and 69 axial images from 10 patients diagnosed with lumbar discus hernia. As in standard ML procedure with smaller datasets, data augmentation was introduced in training and validation phases. Proposed method, as part of the segmentation process, U net convolutional neural network has been implemented to segment disc area which can be further used in the analysis of relevant parameters (i.e. pelvic incidence, pelvic tilt, lumbar lordosis angle, sacral slope, grade of spondylolisthesis). Sagittal and axial view are independently analyzed, and their results will be combined in future research. Influence of different hyper-parameters of the network such as number of epochs, learning rate, batch size, dropout, kernel size in convolutional layers are investigated. It was shown that with EP = 40, BS = 10, and LR = 0.01 the results were the best, achieving accuracy = 0.995, dice = 0.791, IOU = 0.659, precision = 0.910 and recall = 0.792 for the sagittal view images and accuracy = 0.991, dice = 0.926, IOU = 0.863, precision = 0.964 and recall = 0.926 for the axial view images. Further post processing methods could possibly increase the accuracy of segmentation.

Computational modelling has been used to investigate between the differences in displacements of the disc for the healthy pre herniated model and herniated model. Using FEM analysis and setting up adequate material properties for the healthy and degenerative disc, under appropriate loads and using boundary conditions, it was shown that effective displacements for the herniated disc (maximal value of 2.1 mm) are generally higher in comparison to the normal disc (maximal value of 1.77 mm). Disc material displacements in the x and y direction also indicate the largest movements of the disc material towards the spinal canal, which will in return put pressure onto the spine and cause back pain. Future analysis can investigate into more cases of herniation and their differences in displacements in order to connect displacement values with level of pain in the patients. Moreover, numerical simulation techniques have the potential to reduce costs and to save time during the development of new effective spinal treatment methods or implants.

Such methodology would help in creating a decision support system for disc hernia diagnosis. Additionally, currently independent systems for ML and FEM can be combined into one parametric model, which can be adaptable using ML methods for segmentation and then further analyzed using FEM. This chapter represents first step towards such parametric model. A computer diagnostic system can be helpful in generating diagnostic results in a short time with reduced time for treatment decision (operation/drugs etc.). In addition, the accuracy of the diagnosis can be increased and human errors caused by environmental factors or visual errors of the non-experienced radiologists can be eliminated.

Acknowledgements This research is funded by Serbian Ministry of Education, Science, and Technological Development [451-03-68/2020-14/200107 (Faculty of Engineering, University of Kragujevac)]. This research is also supported by the projects that have received funding from the European Union's Horizon 2020 research and innovation programmes under grant agreements No 952603 (SGABU project) and No 760921 (PANBioRA project). This article reflects only the author's view. The Commission is not responsible for any use that may be made of the information it contains.

References

Al-Kafri AS et al (2019) Boundary delineation of MRI images for lumbar spinal stenosis detection through semantic segmentation using deep neural networks. IEEE Access 7:43487–43501

Allison L et al (2015) Finite element analysis predicts experimental failure patterns in vertebral bodies loaded via intervertebral discs up to large deformation. Med Eng Phys 37:599–604

Alomari RS, Corso JJ, Chaudhary V, Dhillon G (2014) Lumbar spine disc herniation diagnosis with a joint shape model. Springer, Cham, pp 87–98

Ayed IB et al (2011) Graph cuts with invariant object-interaction priors: application to intervertebral disc segmentation. Springer, Berlin, Heidelberg, s.n., pp 221–232

Baroud G, Nemes J, Heini P, Steffen T (2003) Load shift of the intervertebral disc after a vertebroplasty: a finite element study. Eur Spine J 12(4):421–426

Bhole C, Kompalli S, Chaudhary V (2009) Context sensitive labeling of spinal structure in MR images. Medical imaging 2009: computer-aided diagnosis, vol 7260. International Society for Optics and Photonics, p 72603P

Bloice MD, Roth PM, Holzinger A (2019) Biomedical image augmentation using Augmentor. Bioinformatics 35(21):4522–4524

Bloice MD, Stocker C, Holzinger A (2017) Augmentor: an image augmentation library for machine learning, p 1708.04680

Bogduk N (2016) Functional anatomy of the spine. In: Handbook of clinical neurology, vol 136. Elsevier, pp 675–688

Cai Y et al (2016) Multi-modal vertebrae recognition using transformed deep convolution network. Comput Med Imaging Graph 51:11–19

Chen CS, Cheng CK, Liu CL, Lo WH (2001) Stress analysis of the disc adjacent to interbody fusion in lumbar spine. Med Eng Phys 23(7):483–491

Chen H et al (2018) VoxResNet: Deep voxelwise residual networks for brain segmentation from 3D MR images. Neuroimage 170:446–455

Chen S et al (2008) Biomechanical comparison of a new stand-alone anterior lumbar interbody fusion cage with established fixation techniques—A three-dimensional finite element analysis. BMC Muscoskeletal Disorders 9(88):1–10

Chevrefils C, Chériet F, Grimard G, Aubin CE (2007) Watershed segmentation of intervertebral disk and spinal canal from MRI images. Springer, Berlin, Heidelberg, pp 1017–1027

Clinical Centre of Kragujevac Website. Available at https://www.kc-kg.rs/. Accessed 21 Dec 2020

Corso JJ, Raja'SA, Chaudhary V (2008) Lumbar disc localization and labeling with a probabilistic model on both pixel and object features. Springer, Berlin, Heidelberg, s.n., pp 202–210

Cummins J et al (2006) Descriptive epidemiology and prior healthcare utilization of patients in the spine patient outcomes research trial's (sport) three observational cohorts: disc herniation, spinal stenosis and degenerative spondylolisthesis. Spine 31(7):806

Dietrich M, Kedzior K, Wittek A, Zagrajek T (1992) Non-linear finite element analysis of formation and treatment of intervertebral disc Herniae, pp 225–231.

Dou Q et al (2017) 3D deeply supervised network for automated segmentation of volumetric medical images. Med Image Anal 41:10–54

Dreischarf M et al (2014) Comparison of eight published static finite element models of the intact lumbar spine: predictive power of models improves when combined together. J Biomech 47:1757–1766

Du HG et al (2016) Biomechanical analysis of press-extension technique on degenerative lumbar with disc herniation and staggered facet joint. Saudi Pharmaceut J 24(3):305–311

Eberlein R, Holzapfel G, Schulze-Bauer C (2002) Assessment of a spinal implant by means of advanced FE modeling of intact human intervertebral discs. Vienna, Austria

Ebrahimzadeh E, Fayaz F, Ahmadi F, Nikravan M (2018) A machine learning-based method in order to diagnose lumbar disc herniation disease by MR image processing. MedLife Open Access 1(1):1

Fagan M, Julian S, Siddall D, Mohsen A (2002) Patient specific spine models. Part 1: finite element analysis of the lumbar intervertebral disc—A material sensitivity study. Proc Inst Mech Eng Part H 216(5):299–314

Farda NA et al (2020) Sanders classification of calcaneal fractures in CT images with deep learning and differential data augmentation techniques. Injury.

Fardon DF et al (2014) Lumbar disc nomenclature: version 2.0: recommendations of the combined task forces of the North American Spine Society, the American Society of Spine Radiology and the American Society of Neuroradiology. Spine J 14(11):2525–2545

Ferguson S, Steffen T (2003) Biomechanics of the aging spine. Eur Spine J 2:S97–S103

Filipovic N (1999) Numerical solution of coupled problems of a deformable solid body and fluid flow (In Serbian). Faculty of Mechanical Enginireeing, University of Kragujevac, Kragujevac

Ghosh S, Chaudhary V (2014) Supervised methods for detection and segmentation of tissues in clinical lumbar MRI. Comput Med Imaging Graph 38(7):639–649

Ghosh S, Raja'S A, Chaudhary V, Dhillon G (2011) Composite features for automatic diagnosis of intervertebral disc herniation from lumbar MRI, pp 5068–5071

Glema A et al (2004) Modeling of intervertebral discs in the numerical analysis of spinal segment. ECCOMAS 2004

Goto K et al (2002) Mechanical analysis of the lumbar vertebrae in a three-dimensional finite element method model in which intradiscal pressure in the nucleus pulposus was used to establish the model. J Orthopaedic Sci 7(2):243–246

Greenberg MS (2016) Spine and spinal cord. In: Handbook of neurosurgery. 8th edn. New York Thieme, p 1102

Gulli A, Pal S (2017) Deep learning with Keras. Packt Publishing Ltd.

Haq R et al (2015) 3D lumbar spine intervertebral disc segmentation and compression simulation from MRI using shape-aware models. Int J Comput Assist Radiol Surg 10(1):45–54

Harun NF, Yusof KM, Jamaludin MZ, Hassan SAHS (2012) Motivation in problem-based learning implementation. Procedia Soc Behav Sci 56:233–242

Hassan CR, Lee W, Komatsu DE Qin YX (2020) Evaluation of nucleus pulposus fluid velocity and pressure alteration induced by cartilage endplate sclerosis using a poroelastic finite element analysis. In: Biomech Model Mechanobiol 1–11

He K, Zhang X, Ren S, Sun, J (2016) Deep residual learning for image recognition. In Proceedings of the IEEE conference on computer vision and pattern recognition, pp 770–778

Hoad CL, Martel AL (2002) Segmentation of MR images for computer-assisted surgery of the lumbar spine. Phys Med Biol 47(19):3503

Horsfield MA et al (2010) Rapid semi-automatic segmentation of the spinal cord from magnetic resonance images: application in multiple sclerosis. Neuroimage 50(2):446–455

Jackson RP et al (1989) The neuroradiographic diagnosis of lumbar herniated nucleus pulposus: II. A comparison of computed tomography (CT), myelography, CT-myelography, and magnetic resonance. Spine **14**(2):1362–1367

Jarvik JG, Deyo RA (2002) Diagnostic evaluation of low back pain with emphasis on imaging. Ann Intern Med 137(7):586–597

Jordan J, Konstantinou K, O'Dowd J (2011) Herniated lumbar disc. BMJ Clin Evidence Arch 2009:1118

Kambin P (2005) Arthroscopic and endoscopic spinal surgery: text and Atlas. Humana Press, New Jersey

Koh J, Scott PD, Chaudhary V, Dhillon G (2011) An automatic segmentation method of the spinal canal from clinical MR images based on an attention model and an active contour model. In 2011 IEEE International symposium on biomedical imaging: from nano to macro. IEEE, pp 1467–1471

Kojić M, Filipović N, Stojanović B, Kojić N (2008) Computer modeling in bioengineering: theoretical background, examples and software. John Wiley & Sons

Kojic M, Filipovic N, Živkovic M & Slavkovic G (2001) PAK-FS finite element program for fluid-structure interaction. Kragujevac, Serbia

Kovačević V et al (2017) Standard lumbar discectomy versus microdiscectomy-differences in clinical outcome and reoperation rate. Acta Clin Croat 56(3):391–398

Kurutz M (2006) Age-sensitivity of time-related in vivo deformability of human lumbar motion segments and discs in pure centric tension. J Biomech 39(1):147–157

Kurutz M, Oroszváry L (2010) Finite element analysis of weightbath hydrotraction treatment of degenerated lumbar spine segments in elastic phase. J Biomech 43(3):433–441

Kurutz M, Oroszváry L (2012) Finite element modeling and simulation of healthy and degenerated human lumbar spine. In: Finite element analysis: from biomedical applications to industrial developments. p 193.

Lavecchia CE, Espino DM, Moerman KM, Tse KM et al (2018) Lumbar model generator: a tool for the automated generation of a parametric scalable model of the lumbar spine. J R Soc Interface 15(138):20170829

Li H, Wang H (2006) Intervertebral disc biomechanical analysis using the finite element modeling based on medical images. Comput Med Imaging Graph 30(6–7):363–370

Lin N, Yu W, Duncan J (2003) Combinative multi-scale level set framework for echocardiographic image segmentation. Med Image Anal 7:529–537

Little J, Pearcy M, Adam C (2008) Are coupled rotations in the lumbar spine largely due to the osseo-ligamentous anatomy?—A modeling study. Comput Methods Biomech Biomed Eng 11(1):95–103

Liu L et al (2020) A survey on U-shaped networks in medical image segmentations. Neurocomputing 409:244–258

Longo UG et al (2011) Symptomatic disc herniation and serum lipid levels. Eur Spine J 20(10):1658–1662

Malandrino A, Planell J, Lacroix D (2009) Statistical factorial analysis on the poroelastic material properties sensitivity of the lumbar intervertebral disc under compression, flexion and axial rotation. J Biomech 42(3):341–348

Marquardt G et al (2012) Ultra-long-term outcome of surgically treated far-lateral, extraforaminal lumbar disc herniations: a single-center series. Eur Spine J 21(4):660–665

Mbarki W et al (2020) Lumbar spine discs classification based on deep convolutional neural networks using axial view MRI. Interdisc Neurosur 22:100837

Mengoni M et al (2017) Annulus fibrosus functional extrafibrillar and fibrous mechanical behaviour: experimental and computational characterisation. Roy Soc Open Sci 4:170807

Michopoulou SK et al (2009) Atlas-based segmentation of degenerated lumbar intervertebral discs from MR images of the spine. IEEE Trans Biomed Eng 56(9):2225–2231

Milasinovic D, Vukicevic A, Filipovic N (2020) dfemtoolz: An open-source C++ framework for efficient imposition of material and boundary conditions in finite element biomedical simulations. Comput Phys Commun 249:106996.

Mobbs RJ, Newcombe RL, Chandran KN (2001) Lumbar discectomy and the diabetic patient: incidence and outcome. J Clin Neurosci 8(1):10–13

Moradi S, Alizadehasl A, Dhooge J et al (2019) MFP-Unet: a novel deep learning based approach for left ventricle segmentation in echocardiography. Phys Medica 58–69

Moramarco V, Palomar A, Pappalettere C, Doblaré M (2010a) An accurate validation of a computational model of human lumbosacral segment. J Biomech 43(2):334–342

Neubert A et al (2013) Three-dimensional morphological and signal intensity features for detection of intervertebral disc degeneration from magnetic resonance images. J Am Med Inform Assoc 20(6):1082–1090

Oktay AB, Akgul YS (2011) Localization of the lumbar discs using machine learning and exact probabilistic inference. Springer, Berlin, Heidelberg, s.n., pp 158–165

Park WM, Kim K, Kim YH (2013) Effects of degenerated intervertebral discs on intersegmental rotations, intradiscal pressures, and facet joint forces of the whole lumbar spine. Comput Biol Med 43:1234–1240

Pekar V et al (2007) Automated planning of scan geometries in spine MRI scans. Springer, Berlin, Heidelberg, s.n., pp 601–608

Peng B et al (2006) Possible pathogenesis of painful intervertebral disc degeneration. Spine 31(5):560–566

Peulić A, Šušteršič T, Peulić M (2019) Non-invasive improved technique for lumbar discus hernia classification based on fuzzy logic. Biomed Eng/Biomedizinische Technik 64(4):421–428

Peulić M, Joković M, Šušteršič T & Peulić A (2020) A noninvasive assistant system in diagnosis of lumbar disc herniation. Comput Math Methods Med 6320126

Ranković V et al (2015) November. A fuzzy model for supporting the diagnosis of lumbar disc herniation. Belgrade, Serbia

Rasulić L et al (2020) Viable C5 and C6 proximal stump use in reconstructive surgery of the adult brachial plexus traction injuries. Neurosurgery 86(3):400–409

Rohlmann A et al (2006a) Determination of trunk muscle forces for flexion and extension by using a validated finite element model of the lumbar spine and measured in vivo data. J Biomech 39(6):981–989

Rohlmann A, Burra N, Zander T, Bergmann G (2007) Comparison of the effect of bilateral posterior dynamic and rigid fixation devices ont he loads in the lumbar spine: a finite element analysis. Eur Spine J 16(8):1223–1231

Rohlmann A, Zander T, Bergmann G (2006b) Spinal loads after osteoporotic vertebral fractures treatedby vertebroplasty or kyphoplasty. Eur Spine J 15(8):1255–1264

Rohlmann A et al (2006c) Analysis of the influence of disc degeneration on the mechanical behaviour of a lumbar motion segment using the finite element method. J Biomech 39(13):2484–2490

Ronneberger O, Fischer P, Brox T (2015) October. U-net: convolutional networks for biomedical image segmentation. In International conference on medical image computing and computer-assisted intervention. Springer, Cham, pp 234–241

Ruberté L, Natarajan R, Andersson G (2009) Influence of single-level lumbar degenerative disc disease on the behavior of the adjacent segments—A finite element model study. J Biomech 42(3):341–348

Schmidt H, Heuer F, Wilke H (2009) Which axial and bending stiffnesses of posterior implants are required to design a flexible lumbar stabilization system? J Biomech 42(1):48–54

Schmidt H et al (2007a) The risk of disc prolapses with complex loading in different degrees of disc degeneration—A finite element analysis. Clin Biomech 22:988–998

Schmidt S et al (2007b) Spine detection and labeling using a parts-based graphical model. Springer, Berlin, Heidelberg, s.n., pp 122–133

Schroeder Y, Wilson W, Huyghe J, Baaijens P (2006) Osmoviscoelastic finite element mdel of the intervertebral disc. Eur Spine J 15(Suppl 3):361–371

Simonyan K, Zisserman A (2014) Very deep convolutional networks for large-scale image recognition, vol 1409, p 1556

Steffens D et al (2016) Do MRI findings identify patients with low back pain or sciatica who respond better to particular interventions? systematic review. Eur Spine J 25(4):1170–1187

Šušteršič T, Milovanović V, Ranković V, Filipović N (2020) A comparison of classifiers in biomedical signal processing as a decision support system in disc hernia diagnosis. Comput Biol Med 125:103978

Sustersic T, Rankovic V, Peulić M, Peulic A (2019) An early disc herniation identification system for advancement in the standard medical screening procedure based on Bayes theorem. IEEE J Biomed Health Inform 24(1):151–159

Suzani A et al (2015) Fast automatic vertebrae detection and localization in pathological CT scans-a deep learning approach. In International conference on medical image computing and computer-assisted intervention. Springer, Cham, pp 678–686

Tensorflow. Available at https://www.tensorflow.org/. Accessed 5 Oct 2019

Tsai R (1987) A versatile camera calibration technique for high-accuracy 3D machine vision metrology using off-the-shelf TV cameras and lenses. IEEE J Robot Autom 3(4):323–344

Unal Y, Polat K, Kocer HE, Hariharan M (2015) Detection of abnormalities in lumbar discs from clinical lumbar MRI with hybrid models. Appl Soft Comput 33:65–76

Vitosevic F, Rasulic L, Medenica SM (2019) Morphological characteristics of the posterior cerebral circulation: an analysis based on non-invasive imaging. Turk Neurosurg 29(5):625–630

Wang G et al (2018) Interactive medical image segmentation using deep learning with image-specific fine tuning. IEEE Trans Med Imaging 37(7):1562–1573

Wang J, Parnianpour M, Shirazi-Adl A, Engin A (2000) Viscoelastic finite element analysis of a lumbar motion segment in combined compression and sagittal flexion. Spine 25(3):310–318

Wang T et al (2019) Development of a three-dimensional finite element model of thoracolumbar kyphotic deformity following vertebral column decancellation. Appl Bionics Biomech. Article ID 5109285

Williams J, Natarajan R, Andersson G (2007) Inclusion of regional poroelastic material properties better predicts biomechanical behaviour of lumbar discs subjected to dynamic loading. J Biomech 40(9):1981–1987

Winn H (2016) Youmans & Winn neurological surgery. 7th edn. Elsevier

Xie F, Zhou H, Zhao W, Huang L (2017) A comparative study on the mechanical behavior of intervertebral disc using hyperelastic finite element model. Technol Health Care 25(S1):177–187

Yang B, Lu Y, Um C, O'Connell G (2019) Relative nucleus pulposus area and position alter disk joint mechanics. J Biomech Eng 141:051004

Yang B, O'Connell G (2017) Effect of collagen fibre orientation on intervertebral disc torsion mechanics. Biomech Model Mechanobiol 16:2005–2015

Yang B, O'Connell G (2019) Intervertebral disc swelling maintains strain homeostasis throughout the annulus fibrosus: a finite element analysis of healthy and degenerated discs. Acta Biomater 100:61–74

Zander T, Rohlmann A, Burra N, Bergmann G (2006) Effect of a posterior dynamic implant adjacent to a rigid spinal fixator. Clin Biomech 21(8):767–774

Zhang H, Zhu W (2019) The path to deliver the most realistic follower load for a lumbar spine in standing posture: a finite element study. J Biomech Eng 141(3):1–10

Zhang Q, Zhou Y, Petit D, Teo E (2009) Evaluation of load transfer characteristics of a dynamic stabilization device on disc loading under compression. Med Eng Phys 31(5):533–538

Zhong Z et al (2006) Finite element analysis of the lumbar spine with a new cage using a topology optimization method. Med Eng Phys 28(1):90–98

Zhou Y et al (2019) Automatic lumbar MRI detection and identification based on deep learning. J Digit Imaging 32(3):513–520

Chapter 17
Structural Analysis and Optimization of Fixation Devices Used in Treatment of Proximal Femoral Fractures

Nikola Korunovic and Jovan Arandjelovic

17.1 Introduction

Long bone fractures, especially proximal femoral fractures, are often treated using internal fixation, which is based on biomechanical properties of bone (Mittal and Banerjee 2012). A desired feature of bone fractures fixation is to allow fractured bone segments to remain mutually mobile in terms of axial translation (Perren 2002) resulting in the compression between bone segments after surgery, which benefits the growth of a callus. Internal fixation of bone fractures may result in considerable loading of the fixation device that is likely to instigate problems related to its durability, stability or strength (Floyd et al. 2009; Lunsjö et al. 1999; Pavic et al. 2013). Some of the tools that are commonly used to avoid these problems are structural analysis (Hibbeler and Kiang 2015) and structural optimization (Christensen and Klarbring 2008).

Today, the prevailing method for structural analysis of bone-implant assemblies is the finite element method (FEM). It is used to calculate deformation, strain and stress state of bones and implants, and thus assess implant strength and durability and the prospects of successful bone healing. The existence of a finite element (FE) model, which consists of bone and implant models, is a prerequisite for performance of a finite element analysis (FEA) of bone-implant assembly. FE models of bones and implant are usually created from the corresponding computer-aided design (CAD) models. Their creation is related to a number of specific issues, which arise from the fact that patient data must be obtained in vivo, using the appropriate medical imaging techniques (Petrovic and Korunovic 2018).

A sensitivity (design) study typically contains several FEAs, in which the values of chosen design variables are changed to observe their influence on model's shape

N. Korunovic (✉) · J. Arandjelovic
Faculty of Mechanical Engineering, University of Nis, Aleksandra Medvedeva 14, 18000 Nis, Serbia
e-mail: nikola.korunovic@masfak.ni.ac.rs

O. Canciglieri Junior and M. D. Trajanovic (eds.), *Personalized Orthopedics*,
https://doi.org/10.1007/978-3-030-98279-9_17

and/or mechanical behavior. A structural optimization or optimization design study relies on methods of mathematical optimization to find optimal values of design variables for given optimization goals (Christensen and Klarbring 2008). Within a sensitivity or an optimization study, a large number of structural analyses must be performed, which in this context represent virtual experiments. If these analyses are based on FEM, each of them requires that a different FE model is built based on a unique set of values of design variables. For the optimization procedure to take less time and less user effort, the building of corresponding FE models must be automated to the highest possible degree. It also means that the underlying CAD model, on which the FE model is based, must be adequately parameterized and robust to allow the uninterrupted creation of any possible assembly configuration. If the geometry and structure of a fixation device are relatively simple, this task is not particularly demanding. If a more complex structure is present, special care must be taken when the CAD model is built.

To illustrate the stages in structural analysis and optimization processes, the research performed by the authors is presented through several sections. The research was conducted on the Selfdynamisable Internal Fixator (SIF) by Mitkovic (Mitkovic et al. 2012; Micic et al. 2010), having a specific structure. After the introduction, an overview of the current research relating to structural analysis and optimization of internal fixation devices used in treatment of proximal femoral fractures is given. The subsequent sections present the SIF, creation of CAD models of femur based on medical images, creation of flexible and robust parametric CAD models of the femur-SIF assembly, material modeling issues related to the femur, creation of suitable FE models for structural analysis, sensitivity studies and structural optimization studies.

17.2 Literature Review

The most important issues related to CAD and FE models of bones are representation of complex bone geometry, characterization of specific material properties and universal definition of anatomical landmarks. Implant models are simpler to build than bone models, as their shapes and material properties are less complex. However, care must be taken to create suitable references for their assembly with bone models. Anatomical landmarks are used as positioning markers in the creation of the bone-implant assembly.

Automatic definition of bone geometry based on medical images has lately become a popular research topic. The first step along the way that leads from medical image to 3D model of the bone is the segmentation of medical image, i.e., the accurate recognition of borders between bones of interest and surrounding tissue. For example, in the paper by Zou et al. (2017) a semi-automatic method is proposed for accurate segmentation of femur from hip joint, where the user has to provide only the high-level information. A fully automatic femoral segmentation was performed by Almeida et al. (2016) adapting a template mesh of the femoral volume to medical images, whereby an adaptation of the active shape model (ASM) technique based on the statistical shape model (SSM) and local appearance model (LAM) were used. A promising approach, which implies 3D reconstruction of anatomical structures from 2D X-ray images, is performed at the Zuse Institute Berlin (Ehlke et al. 2013; Kainmueller et al. 2009). It has several advantages. Firstly, the 3D geometry is obtained from 2D X-ray images, thus the patient receives a much smaller radiation dose than with CT. Secondly, the variable material properties of the bone throughout its volume are also modeled, using the technique of virtual X-ray imaging. Finally, the bone landmarks are also automatically extracted during the process. Automated extraction of bone landmarks, with purpose of optimal prosthesis placement in total hip arthroplasty is also reported in the paper by Almeida et al. (2017). The method is used to identify femoral middle diaphysis axis, medullary cavity (medullary canal) axis, femoral neck axis, femoral head center, greater and lesser trochanter and neck saddle point.

Appropriate modeling of boundary conditions and loads must be performed for FE analysis results to be valid. However, it is not a simple task as intensity, direction and impact surfaces cannot be determined directly. Thus, various techniques are used to assess those indirectly. For example, a free boundary condition modeling approach is used in the paper by Phillips (2009), by which the femur is treated as a complete musculoskeletal construct. It implies the explicit inclusion of muscles and ligaments, spanning both the hip joint and the knee joint, modeled as springs. In the paper by Edwards et al. (2016) static and dynamic optimization methods were used to obtain muscle forces, which they applied on FE model of femur in order to calculate its strains. Additionally, it should be considered that different physical activities result in different load cases for the FE model. A study (Pakhaliuk and Poliakov 2018) was presented where the load conditions have been applied and compared for typical activities of patients' daily living (ADL: level walking, stair ascending-stair descending, chair sitting-chair rising and deep squatting) in the case of an applied total hip arthroplasty (THA) implant. The results indicate that the wear values of the sliding cup material differ between different ADL, and that they are visibly higher than in the case of level walking.

Structural analysis has often been used to compare the suitability of various fixation devices for a certain fracture type. In the paper by Eberle et al. (2010), FEA was performed to compare the stress of a common Gamma Nail (GN) and a reinforced GN (larger diameter of the proximal shaft and thicker walls) for two types of subtrochanteric femoral fracture. A synthetic standardized femur model (whole bone, with two assigned materials for cortical and cancellous bones) with implant was utilized for the FEA, with boundary conditions that simulate human gait using two approaches: a single force acting on the femoral head, and a force acting on the femoral head in combination with a force on the major trochanter that simulates the muscles being attached in this region. The FEA showed a decrease of stress in the reinforced GN compared to a common GN, while there was no increase in stress shielding in the surrounding bone. Even though the standardized bone models are the starting point for comparable results of FEA studies of different authors, additional factors such as material characteristics, boundary conditions, etc. also influence the acceptability of comparison. A study was presented by Sowmianarayanan et al. (2008) that compared the application of a Dynamic Hip Screw (DHS), Dynamic Condylar Screw (DCS), and Proximal Femoral Nail (PFN) in subtrochanteric fractures. In this study, a standardized femur model was also used but five different materials were assigned to specific regions of cortical and cancellous bone. A force on the femoral head was applied in combination with three additional forces simulating the action of connected muscles. The results indicate that when DHS and DCS implants are used the fractured femur has a stress state that is more similar to the intact femur, than in the case of using a PFN implant. Other studies use bone models that are created through reverse engineering (RE) and thus are patient specific. A study by Samsami et al. (2015) was carried out to determine the best fixation method for femoral neck fractures. The authors compared cannulated screws (CSs), Dynamic Hip Screw with Derotational Screw (DHS + DS) and Proximal Femoral Locking Plate (PFLP) using FEA and validated these results through mechanical testing of cadaveric femur. A femur model was created from CT images. It represented the proximal part of bone, with three assigned materials: two for cancellous bone and one for cortical bone). CAD assemblies containing different implants where created, while the boundary conditions modeled a single leg stance case, with a single force acting on the femoral head. Both mechanical test and FEA indicated that DHS + DS implant underwent the minimal femoral head displacement and minimal failure load, which is why it is a better choice for this type of fracture when compared to PFLP and CSs.

In described studies, bone material properties were modeled by dividing the bone model into segments and assigning homogenous averaged material characteristics to each segment. A more accurate model can be created by local material mapping, which implies that each finite element is assigned specific material properties, according to empirical relationships between the CT image greyscale, bone density and material constants. In the paper by Wu et al. (2015) a study is presented that compared the behavior of Proximal Femoral Nail Antirotation for Asia (PFNA-II) and Expert Asian FemoralNail (A2FN) implants in treatment of subtrochanteric femoral fractures. A patient-specific femur model was created from CT and material properties were assigned to each finite element, while the implants which were designed in CAD where later attached to the bone model in HyperMesh software. Additionally, the research considers two types of materials for the callus ("soft" and "hard"), for two different stages of fracture healing. The maximum implant stress decreased between the first and second healing stage, but the difference was much larger for the A2FN implant in addition to which it also had a lower stress on the implant, thus indicating the superiority of the A2FN implant.

Sensitivity studies or optimization studies have been employed to find the optimal configuration and position of an existing fixation device or to optimize the shape and dimensions of a new one. In the paper by Konya and Verim (2017) a study is described in which the optimization of position of proximal locking screws used in PFN system was performed. The automatic optimization procedure was facilitated by bidirectional connection between the CAD and the FEM models, where two angles and one distance defining the position of the locking screw were defined as design

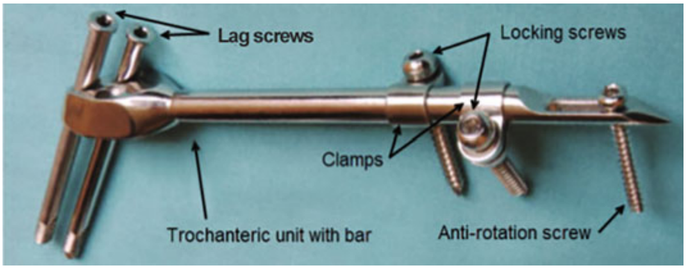

Fig. 17.1 Selfdynamisable Internal Fixator (SIF)—a configuration used in subtrochanteric femoral fracture treatment (Korunovic et al. 2019)[1]

variables and the stress in fixating device was minimized. Optimization of position and configuration of Selfdynamisable Internal Fixator (SIF) used in treatment of subtrochanteric femoral fracture is presented in the paper by Korunovic et al. (2019). The CAD model of SIF was assembled to the CAD model of femur using specific anatomical landmarks. Because of the flexibility of the CAD and FE model, numerous instances of femur and SIF assemblies were easily created. A sensitivity study was performed to check how the changes in bar length and clamp distance affected the stress distribution. In another paper by Korunovic et al. (2015) a sensitivity study of a SIF used in subtrochanteric femoral fracture treatment is presented. Local material mapping was used to assign location specific modulus of elasticity to each finite element, while in the fracture zone three different materials were assigned depending on the stage of the healing process. Through the parametric study it was analyzed how the change of bar length, number of distal screws and fracture zone modulus of elasticity affected SIF stress distribution. Because of local material mapping, the FE model needed to be prepared manually for each different parameter combination.

17.3 Selfdynamisable Internal Fixator (SIF)

The SIF, invented by Prof. Mitkovic (Mitkovic et al. 2012; Micic et al. 2010) is intended for fixation of long bone fractures. Like other fixation devices, it is designed to withstand the load during the whole fracture healing process, minimizing the chance of mechanical failures (like screw breaking or bar bending) or any other complications. The structure of SIF is modular and Fig. 17.1 shows its typical configuration. For its connection with upper femur, two sliding (lag) screws and the two corresponding holes in the trochanteric unit (of three in total) are used. One of the sliding screws is always placed in the top hole of the fixator, while its axis is passing close to the center of the femoral head. The other sliding screw is placed in one of the other two holes, depending on whether the left or the right femur is fixed. As for

[1] In Silico Optimization of Femoral Fixator Position and Configuration by Parametric CAD Model by N. Korunovic et al. is licensed under CC BY/"Dynamic hip screws" changed to "Lag screws".

the clamps, those may rotate around the fixator bar. They may be positioned with locking screw holes on the same side or on the different sides of the bar. In this way, it is possible to achieve an excellent 3D stability of the fixator (Mitkovic et al. 2012). Finally, the anti-rotation screw is used to limit the axial movement and to contribute to the fixator rotational stability.

Mitkovic et al. performed several studies in which the SIF was applied on 726 patients. Fixations screw braking occurred in 2.6% and the bar broke at the transition to trochanteric unit in 0.3% cases (Mitkovic et al. 2012). Although the recorded percentage of failures was small, it was the indication that SIF durability could be improved.

For an experienced orthopedic surgeon, using of SIF in the treatment of common fractures is usually a routine process. If a less experienced surgeon performs the surgery or if the fracture is complex, then the application of SIF can be more complicated considering its configuration and placement on the underlying bone. Nevertheless, even the most experienced orthopedic surgeons cannot predict the durability-wise optimal SIF configuration and placement, which is characterized by minimal stress in its components. One of the goals of the research described in next section was to aid the orthopedists in surgery planning. Structural analysis based on FEM, sensitivity studies and structural optimization were used to find the best configuration and position of SIF for given fracture. The goal of the studies was to minimize SIF stress, respecting the constraints related to implant positioning and surgery related trauma. In an ideal case, a structural optimization study should be performed for each patient-specific trauma, which is not always a feasible option. Instead, the knowledge on trends related to change of SIF stress with change of SIF configuration and position for a specific fracture type, gained from previous studies, can help the orthopedic surgeon make the right decision.

17.4 Creation of Computer-Aided Design (CAD) Models

Throughout the research described in this monograph chapter, various approaches to creation of FE models of femur-implant assembly were used, resulting in creation of different CAD models. CAD models of femur were mostly based on CT images of the patients. Some of the models contained only the outer boundary, while some contained the inner zones that corresponded to cortical bone, cancellous bone and medullary cavity. The choice of inner structure was dependent on the approach to bone material modeling, as described in Sects. 17.4.1 and 17.5. Parametric CAD models of SIF were easily created using standard solid modeling techniques (Chang 2014). Non-parametric assembling was used for standard FEAs, while special attention was paid to building of flexible and robust parametric models for structural optimization studies, as described in Sect. 17.4.2.

17.4.1 Creation of CAD Models of Femur Based on Medical Images

This section describes a typical procedure for creation of solid CAD models of long bones based on subject-specific CT image sets. The resulting solid model does not contain any inner structures. Those, if needed, may be constructed in FE model discretization phase, as described in Sect. 17.5.

In current research, the subject specific CAD models of femur based on CT image sets were created, through the two main steps: creation of the polygonal model and creation of the solid model.

17.4.1.1 Creation of the Polygonal Model

The polygonal model represents a set of flat triangular surfaces, based on the point cloud that is created through separation of various tissue types. This model is primarily used for data visualization, or for data transfer to a CAD system. After the polygonal model is "cleaned" and "healed" it can be used as a basis for the creation of surface and solid models of bones (Vulovic et al. 2011), or for production of physical bone models by additive manufacturing technologies (Stojkovic et al. 2009).

In this procedure, a subject-specific CT image set of lower extremities was used as the basis for CAD and FE femur models creation. A CT image set, or tomogram, is a series of two-dimensional X-ray images (Fig. 17.2) that are placed in parallel planes, which are usually equally spaced. It is obtained using CT scanners, which produce very sharp and detailed images of bones but also generate a significant radiation dose to a patient.

In the software for medical image processing Materialize Mimics (ver. 17, Materialise Company, Leuven, Belgium), a region of interest (ROI) was selected that contained patient's right femur. A function that recognizes the tissue type based on density was used to create a point cloud, which was composed of points corresponding to the outer femoral surface and points corresponding to the separating surface between compact bone and medullary cavity. The CT set was acquired by scanning of a patient who had vascular problems; therefore, a contrast agent was injected into his veins before scanning to enable their detection by the scanner. Nevertheless, as the density of contrast material was similar to the density of the bone, the resulting point cloud also contained a certain part of the vascular system. This may be seen in the image of the corresponding polygonal model (Fig. 17.3). Finally, a model representing the femur only was created by unnecessary portions removal from the polygonal model, which belonged to the vascular system. (Fig. 17.4).

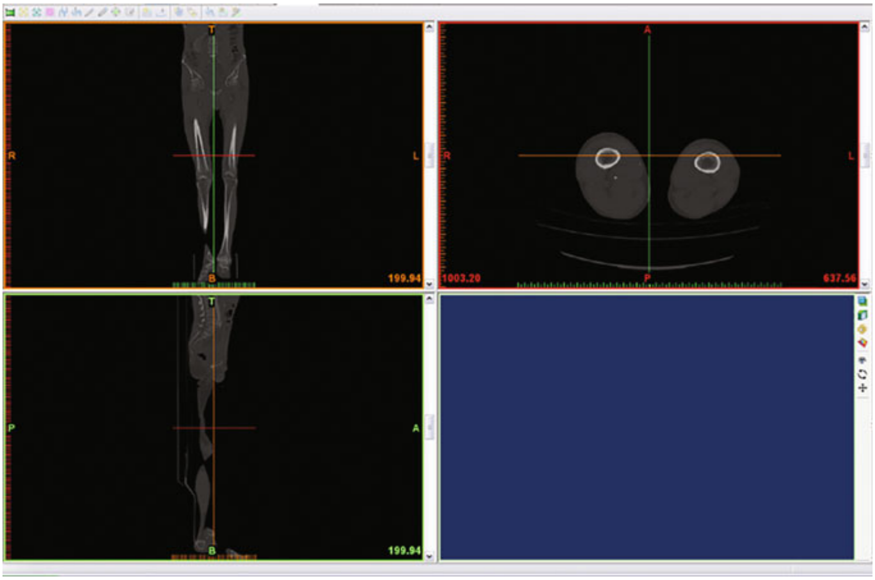

Fig. 17.2 A CT image set of lower extremities (Korunovic et al. 2010)

Fig. 17.3 A point cloud extracted from a CT image set containing a part of vascular system, used to create the polygonal model of the femur (Korunovic et al. 2010)

Fig. 17.4 Polygonal model of the femur, after the removal of the unnecessary portions (Korunovic et al. 2010)

17.4.1.2 Creation of the Solid Model

After the excess polygons were removed from the polygonal model, it was subjected to "cleaning". In this phase, the polygons created inside the femur, based either on medullary cavity or on the trabecular (cancellous) bone structure (Fig. 17.5), were also removed. All cleaning operations were performed in CATIA (V5R21, Dassault Systèmes, Paris, France Company, Waltham, MA, USA).

After the inner portion of polygonal model was removed, the remaining part of the model still did not fully represent the outer surface of the femur. There were

Fig. 17.5 Internal portion of the polygonal model before cleaning (Korunovic et al. 2010)

still some surface segments left that penetrated deeper into the inside of the femur (Fig. 17.6a), as well as the cracks and holes on femoral surface (Fig. 17.6b). To fix those, the model had to be "cleaned" and "healed".

After cleaning and healing, the polygonal model was smoothed, to be more suitable for creation of surface model. The surface model, representing the outer surface of the femur, was created by approximation of polygonal model, as a closed set of NURBS surfaces (Fig. 17.7). Finally, the solid model of the femur was created by filling of the surface model.

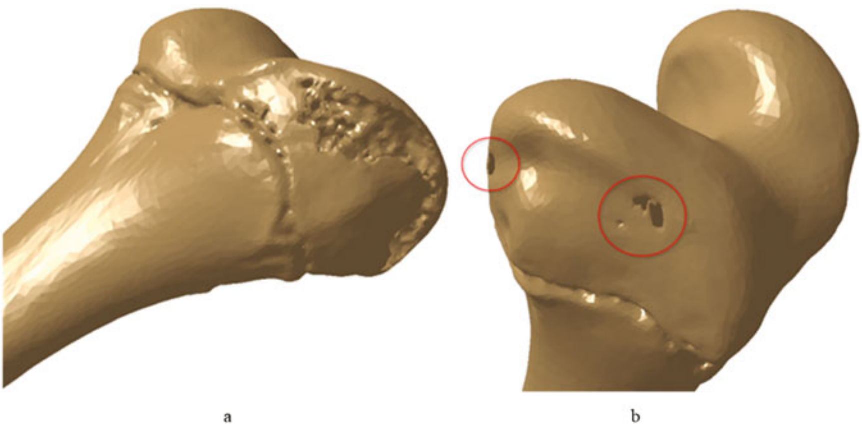

Fig. 17.6 **a** Zones of the polygonal model, penetrating into the bone deeper than expected. Those "chaotically" arranged polygons were created because the cortical bone was too thin or nonexistent as the consequence of the osteoporotic changes, **b** the surface of the polygonal model contained holes that were connected with larger groups of irregularly spaced polygons. This is the consequence of both osteoporotic changes and the fact that a part of spongious bone was present in the polygonal model (Korunovic et al. 2010)

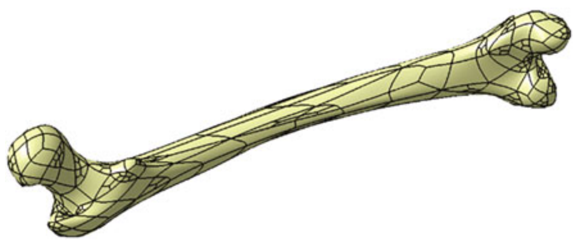

Fig. 17.7 Surface model of the femur created by surface approximation of the polygonal model (Korunovic et al. 2010)

17.4.2 Creation of Parametric CAD Models of the Femur-Fixator Assembly

This section describes the study that was performed to prove that, within the CAD model of femur-SIF assembly, it was possible to parametrize the placement of SIF relatively to the femur in such way that a valid CAD model was created for each possible combination of design variables values. This is an important step towards the automation of the SIF optimization process, as it supports the continuous performance of sensitivity and optimization studies.

Complexity of SIF is greater than in some other long bones fixation devices, as there are clamps between screws and implant stem (implant body). In fact, its modular design is similar to that of external fixators (Mitkovic et al. 2012). In the context of CAD, it is not an easy task to parametrize the position of SIF on the femur. Therefore, the methodology was developed for positioning of the SIF relatively to the underlying femur, ensuring the femur-SIF assembly is robust during all possible changes in the values of SIF design variables.

To represent femur geometry, a subject-specific, non-parametric solid model described in Sect. 17.4.1 was used. No inner structure was created, for the model to be simple and to enable focusing on parametrization of SIF placement and configuration. To prepare the CAD model of the femur for assembling with SIF model, it has been enhanced by landmark creation. Landmark set was comprised of axes, points, curves, and planes that served as geometrical references for fixator positioning as well as for loads and boundary conditions definition for subsequent FEA. The preparation of the model was performed manually, by following the predefined procedure that may be used for any subject-specific femur. Ultimately, the landmark creation procedure should be automated, to make it faster and easier to perform. The position of the parametric CAD model of SIF was defined using assembly constraints. CAD modeling was performed in SolidWorks (ver. 2016, Dassault Systèmes, Paris, France Company, Waltham, MA, USA).

17.4.2.1 Anatomical Landmarks

Following the procedure similar to the one described in (Vitkovic et al. 2013), the creation of anatomical landmarks started with creation of two points: the point of the intercondylar fossa and the center point of the femoral head. Then, the mechanical axis passing through both points was constructed (Fig. 17.8). It was later used to define the direction of force simulating body weight of the patient in FEA. Additionally, the lateral and medial epicondyle points were constructed (extreme points of the distal femur), defining the anteroposterior (A-P) plane together with the center point of the femoral head. Next, the sagittal or lateral-medial (L-M) plane was constructed, as the plane containing the mechanical axis and being perpendicular to A-P plane (Fig. 17.8). The details on construction of all necessary axes, points, curves and

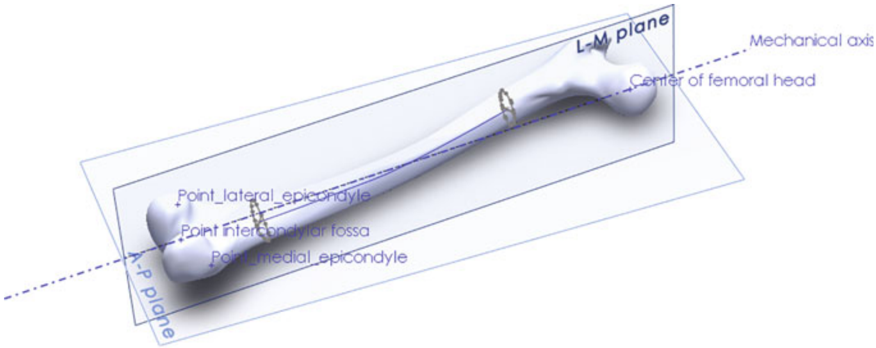

Fig. 17.8 Anatomical axes, points, and planes on the femur

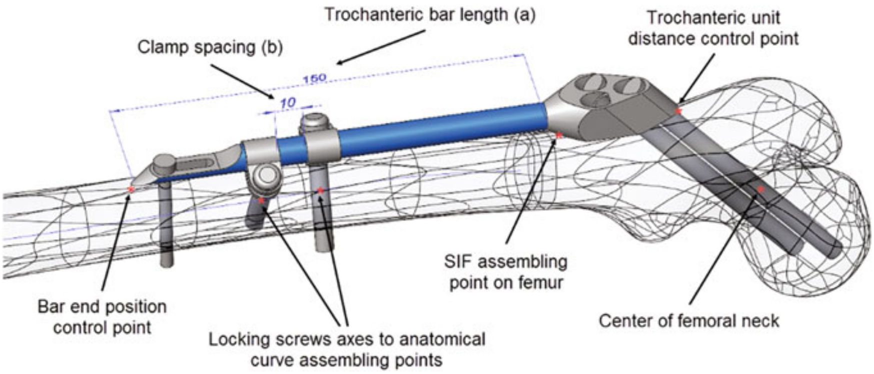

Fig. 17.9 Design variables (trochanteric bar length (**a**) and clamp spacing (**b**)) and specific points on CAD model of femur (Korunovic et al. 2019)[2]

planes may be found in (Vitkovic et al. 2013). In addition to the mentioned anatomical landmarks, the anatomical curve was created as a spline curve connecting the centers of gravity of several femoral shaft cross-sections parallel to the horizontal or transversal plane (which is perpendicular to both A-P and L-M planes).

17.4.2.2 Configuration of SIF and Assembly Constraints

A number of points on femur model and the anatomical curve were used for positioning of the fixator in relation to the femur (Fig. 17.9). The chosen assembly constraints and reference points played the most important role in achieving the robustness of femur-SIF assembly. Robustness of the assembly implied that mutual

[2] In Silico Optimization of Femoral Fixator Position and Configuration by Parametric CAD Model by N. Korunovic et al. is licensed under CC BY.

position of SIF and femur would still satisfy the requirements of an orthopedic surgeon after an arbitrary change of design variables values, inside the permissible boundaries, would be performed.

The SIF is characterized by a modular design, as shown in Sect. 17.3. The research did not consider the change of module shapes (design improvement). It took into account only the current practice, in which the orthopedic surgeon must choose between standard module sizes and position the SIF correctly. Currently, the surgeon may choose between four bar lengths: 100, 150, 200, and 250 mm. The most common situation, where two clamps are used, was considered, in which their position is generally arbitrary. Nevertheless, the length of the distal surgical cut that is created during the surgery depends on the clamp spacing (distance between the clamps), and it should not be too long, to lessen the trauma of a patient. In this study, one of the clamps was placed near the bar edge (1 mm from the edge), as being often done in practice, and clamp spacing was limited to the representative interval of 1–28 mm.

Considering the previous analysis, only the assembly constraints that could be changed during the surgery, and not the dimensions of SIF modules, were chosen as design variables. Those design variables were (Fig. 17.9):

a. Trochanteric bar length (discrete)
b. Clamp spacing (continuous).

In clinical practice, to determine the initial position of the fixator in relation to the underlying femur during the surgery, visible anatomical landmarks are used. Those are the specific points on greater trochanter, lesser trochanter, femoral head, or femoral neck. The exact position of fixator, especially of the screws, is determined using fluoroscopy (live X-ray imaging). Surgeons describe fixator position by using descriptive empirical constraints. In the case of SIF, they may pay attention that the axis of the first sliding screw is situated near femoral head center, while the tip of the sliding screw does not penetrate femoral head surface and is located about five millimeters from it. They would also strive to keep the second sliding screw inside the bone, with its tip a couple of millimeters away from the surface of the femoral neck. Replacing those empirical constraints with design variables and geometrical constraints within the CAD model was one of the tasks of this research. Thereby, some of the landmarks used by the surgeons were replaced by more suitable ones, as described next.

The first component of SIF that was placed on the femur, within the femur-fixator assembly, was the implant body, consisting of the trochanteric unit and the bar. In doing so, the following positioning constraints were used:

1. The coincidence between the axis of the proximal sliding screw hole and the point that lies in the center of femoral neck.
2. The coincidence of trochanteric unit symmetry plane and a newly created point on femoral surface. The point lies on A-P plane, between edge of the fracture and breakthrough point of the sliding screw into the bone, at approximately equal distances from them (Fig. 17.9, “SIF assembling point on femur”).
3. The distance between femoral surface and the trochanteric unit, measured at a specific point on femoral surface (Fig. 17.10, “Point for distance control”).

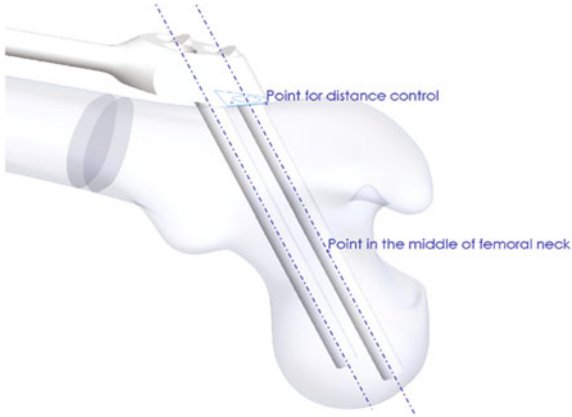

Fig. 17.10 Position of the trochanteric unit on the femur

4. The position of the end of the bar, closely following the anatomical axis. It is defined as the coincidence of a point created at an offset from the bar end and a point created in a new empty part in the assembly. The latter point is at the same time coincident with the projection of the anatomical curve onto the femoral surface. Bar end offset point is used instead of the bar end point, to prevent penetration of the bar into the bone and to control the distance of the bar end from the femoral surface.

17.5 Material Modeling Issues Related to Femur

The accuracy of FEA results largely depends on the accuracy of material models used in the analysis. While it is common to describe standard engineering materials (like steel or aluminum) using homogenous, isotropic, linear elastic material models, describing bone material is a more challenging task. The reason for this lies in the remodeling process that is constantly taking place within the bone tissue. It causes the structure and density of bone tissue to vary through the bone, depending on direction and intensity of stress caused by external loads. Hence, the bone material tends to get pronouncedly inhomogeneous and anisotropic.

Characterization of bone material for FEA is usually done either by zoning the FE model and assigning the averaged material properties to each zone, or by performing so called material mapping, where radiological density values, obtained from CT scans, are used to estimate the values of material constants. Both approaches have their advantages and drawbacks, depending on the application.

Among the factors that affect the accuracy of material characterization, the most important ones are the selection of material model, material properties averaging technique, parameters of x-ray tube, calibration of CT scanner, relations between radiological density and bone density, and relations between bone density and material constants. These are discussed in more detail in (Korunovic et al. 2013).

Usually, bone material is modeled either as linear isotropic or as anisotropic (commonly orthotropic). In a number of studies, it was found that the second approach was more accurate (Baca et al. 2008; Yang et al. 2010). However, it is also true that the characterization and application of anisotropic materials models can represent quite challenging tasks, which may not be worth the extra effort (Peng et al. 2006).

A more detailed description of the two approaches to bone material modeling, that are most often used in FEA, is given in the rest of the section. Those are:

1. Zoning, i.e., the division of CAD model into zones that are assigned averaged material characteristics,
2. Local material mapping, i.e., assignment of material properties to each finite element separately, where empirical relations between radiological density and bone density, as well as between bone density and elastic constants are used.

According to the first approach, the zones that correspond to the internal femoral structure are created. The zones that can be distinctly separated are compact (cortical) bone, cancellous (trabecular, cancellous) bone and medullary cavity. The zone corresponding to cancellous bone may further be subdivided into zones that are characterized by significantly different trabecular density (Fig. 17.11). While the concept is simple, it has several shortcomings. The main one lies in the fact that the averaged mechanical properties are assigned to the zones spanning quite large areas of the bone, while elastic properties of the bone show significant variation over the bone. For long bones, like tibia or femur, this is especially true. Also, significant effort and time may be required for recognition and creation of zones.

According to the second approach, local material mapping, the unique elastic properties are assigned to each finite element, based on local bone tissue density being estimated from CT images. To establish the relations between radiological density and bone tissue density, as well as between bone tissue density and elastic constants, empirical equations are used (Schileo et al. 2008; Helgason et al. 2008).

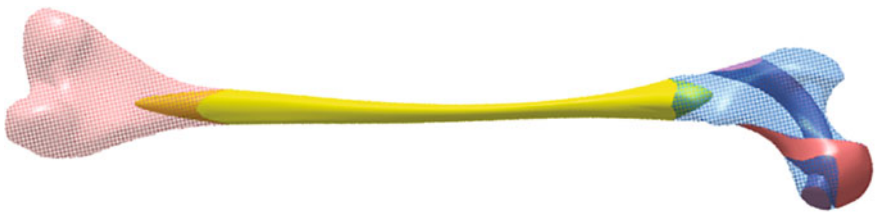

Fig. 17.11 Zones created in the solid CAD model of the femur. For clarity, the zone representing the cortical bone is hidden. Distal segment of cancellous bone is shown in light red. Proximal segment of cancellous bone with sparser trabeculae is shown in light blue. Proximal segments of cancellous bone with denser trabeculae are shown in dark blue and dark red. Medullary cavity is shown in yellow (Korunovic et al. 2010)

Available FEA programs usually accept a limited number of material property definitions. Thus, the entire range of possible values of an elastic constant (e.g., of Young's modulus), is usually divided into several intervals. Then, a mid-value of the interval to which the calculated value of an elastic constant at the location of a finite element belongs, is assigned to that finite element. In practice, this approach is often used, as it considers local variation of bone density and enables relatively fast creation of FE model. Nevertheless, errors in local characterization of material properties may still be present, especially if the FE mesh is coarse, when the dimensions of some finite elements may get significantly larger than the thickness of particular bone segments.

Both approaches described above had been used throughout authors' practice in FEA of human femur, as portrayed next.

17.5.1 Zoning Approach to Material Modeling of the Femur

To represent the cortical bone and medullary cavity, two separate zones in CAD models of the femur were created (Korunovic et al. 2013). The rest of the model, corresponding to spongious bone, was divided into several zones, following the typical trabecular density distribution (Fig. 17.12). The constant values of Young's modulus were assigned to each of the zones, i.e., to the finite elements that were crated inside the zones. To simulate the properties of bone marrow, medullary cavity zone was assigned a very small value of Young's modulus. The values of $E_{cortical}$ and $E_{trabecular}$ were determined based on the trial-and-error approach, so that the maximum displacement of the FE model was the same as the displacement of the FE model in which local material mapping was used (as described in Sect. 17.5.2). The resulting FE model, in which the typical element edge size was set to 3 mm and fast element growth from the surface to the interior of the model was used, is shown in Fig. 17.12. Using the mentioned settings, 149,712 tetrahedron elements with quadratic shape functions were created.

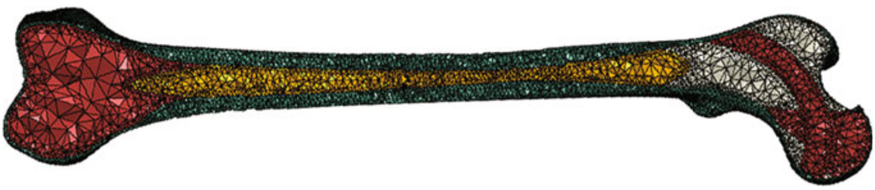

Fig. 17.12 The zones and the corresponding FE mesh of the femur model. Green: trabecular bone, E = 12.7 GPa. Red: cancellous bone (denser trabeculae), E = 0.3GPa. White: cancellous bone (sparser trabeculae), E = 0.07 GPa. Yellow: Bone marrow, 1 MPa (Korunovic et al. 2010)

17.5.2 Local Material Mapping Approach to Material Modeling of the Femur

Based on CT images, only the external surface of the femur was modeled. The volume of the femur was meshed using tetrahedron elements with quadratic shape functions (Fig. 17.13). Once again, the typical element edge size was set to 3 mm and fast element growth from the surface to the interior of the model was used (Korunovic et al. 2013). To assign material properties, local material mapping was performed, based on the following empirical equations: the relation between values of Hounsfield units (HU) and bone density (Eq. 17.1) and the relation between bone density and Young's modulus (Eq. 17.2). Both equations are described in (Morgan et al. 2003). Three different variations of FE model were created, in which 20, 100 or 300 discrete values of Young's modulus were used, as presented in (Korunovic et al. 2013). Using the mentioned settings, 59,926 tetrahedron elements with quadratic shape functions were created.

$$\rho_{app}[g/cm^3] = 0.1957 + 0.001053\,HU \tag{17.1}$$

$$E[N/mm^2] = 6950 \cdot \rho_{app}^{1.49} \tag{17.2}$$

17.6 Creation of FE Model of Femur-Fixator Assembly

This section describes the FE models of femur-implant assemblies that were used by the authors during the ongoing research. In various studies, different models were built. The choice of the model depended on several factors, like the availability of CT scans, necessary detail level or FE software used. Those models were mutually different by:

1. Material modeling of the femur, as described in the previous section. The following models were created:

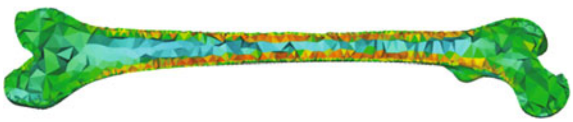

Fig. 17.13 FE model in which different values of elastic modulus, corresponding to different colors, were assigned to individual finite elements using the local material mapping approach. Lowest values are shown in light blue, while the highest ones are shown in red (Korunovic et al. 2013)

a. Mapped model, which represents a FE model of the femur based on the solid CAD model with outer surface only, where local material mapping is used for the whole model (Fig. 17.13).
b. Zoned model with averaged material properties (Fig. 17.12).
c. Zoned + mapped model: the model is divided into two zones, one corresponding to cortical bone and the other to the union of the spongious bone and medullary cavity. Mesh is created within each of the zones and material properties assigned by local material mapping. This approach, described in more detail in (Korunovic et al. 2013), is considered to be more accurate than local material mapping alone, as there are no elements that partially belong to the cortical bone volume and partially belong to spongious or medullary cavity volume, and therefore the material property averaging errors are lesser.
d. Non-zoned model with averaged material properties, which implies the whole femur volume is assigned a uniform elasticity modulus. This approach is, as a preliminary one, used in creation of flexible and robust femur-SIF assemblies for structural optimization, to simplify the FE model of the femur and concentrate on the CAD model parametrization.

2. Landmark creation and model parametrization. The following models were used:

a. Non-parametric model, in which the fixator was approximately positioned on femur, according to surgeon's recommendations.
b. Parametric model (Sect. 17.4.2), in which landmarks were created on the femur, and SIF position on the femur was parametrized.

In this section, the procedure for creation of parametric femur-SIF FE model in ABAQUS, with local material mapping, is described, as the one requiring the most steps and user effort. In the first step, the CAD model of the fixator (Fig. 17.14) was created using standard form features such as extruded or revolved cuts and protrusions, holes, chamfers, and rounds. Linear positions and angles of clamps and the length of trochanteric bar were parametrized, to enable the creation of all possible SIF configurations and positions on the femur. This was done because the standard SIF configurations differ by bar length, which may take values of 100 mm, 150 mm, 200 mm, or 250 mm. Also, the clamps are linearly positioned and rotated during the surgery, to adapt to the shape of the femur and fracture position. The CAD model of SIF was assembled with non-parametric CAD model of the femur (created as

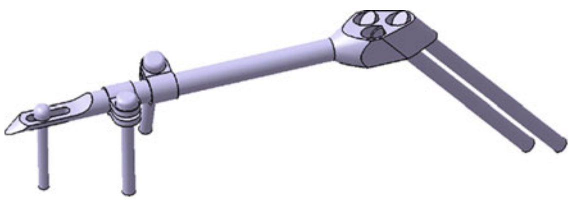

Fig. 17.14 CAD model of SIF, where bar length equals 150 mm

Fig. 17.15 FE model of femur with material properties assigned (shown in different colors). Screw holes are also visible on the model. Lowest values are shown in light blue, while the highest ones are shown in red (Korunovic et al. 2015)

described in Sect. 17.4.1.). By subtraction of SIF CAD model from femur CAD model, the screw holes in the femur were created (Fig. 17.15).

Next step was the creation of two surface partitions on femoral surface (Fig. 17.17). The surface partition that was created on the head of the femur was later used to define the force acting on the femur as the consequence of the contact with acetabulum. The surface partition that was created on femoral condyles was later used to place the support fixing the lower part of the bone. After the CAD model of the assembly was imported into ABAQUS, two mutually parallel planes were created just below the greater trochanter, to define the limits of the fracture zone. The planes were then used to cut the femur and create the volume that represented a simple subtrochanteric fracture (Fig. 17.17).

Elasticity modulus equal to 1160 N was assigned to the fracture zone, simulating its elasticity 3 weeks after surgery. To simulate the elasticity of the fracture zone 6 and 12 weeks after surgery, values of 2055 N and 4220 N were used respectively. Those values were based on rat femur data reported in (Komatsubara et al. 2005), multiplied by typical ratio of human to rat femoral modules, as no similar studies performed on humans were available. The material of SIF, stainless steel ASTM F 138-2, was characterized by elasticity modulus equal to 2.1 GPa and yield strength of 795 N/mm^2 (Oldani and Dominguez 2012). The yield strength of cortical bone was set to 112 N/mm^2, as it was expected to take values between 104 and 120 N/mm^2 (Ko 1953; Burstein et al. 1976; Vincentelli and Grigoroy 1985). The coefficient of friction between the bone and each component of SIF was set to 0.34 (Mischler and Pax 2002) and between any two components of SIF to 0.7. Temporary material properties, i.e., arbitrary values of Young's modulus and Poisson's ratio were assigned to the femur, to enable the creation of the initial FE model. This model was exported from ABAQUS and imported into a medical imaging program in which the material mapping process was performed. One hundred incremental values of Young's modulus were thereby used, where the lowest one was equal to 1 N/mm^2 and the highest was equal to 17,500 N/mm^2 (Fig. 17.15).

After the material mapping procedure was finished, the resulting FE model, containing material properties definitions, was exported from medical imaging software. It was then imported into ABAQUS as "orphan mesh" (containing only finite elements and no geometry), in which it was used to replace the initial FE model within the duplicated femur-SIF assembly model. After the femur model was replaced,

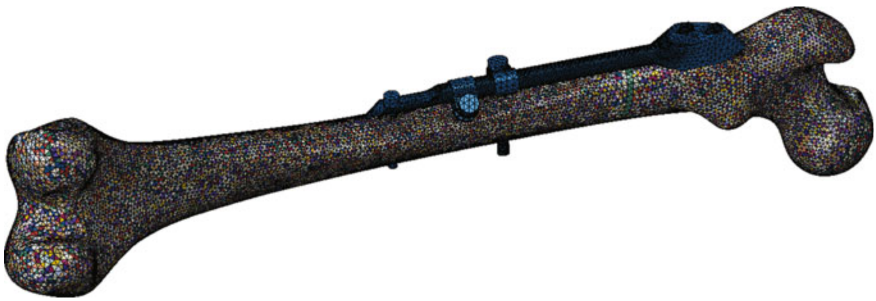

Fig. 17.16 Final FE model of femur-SIF assembly, containing the fracture zone (Korunovic et al. 2015)

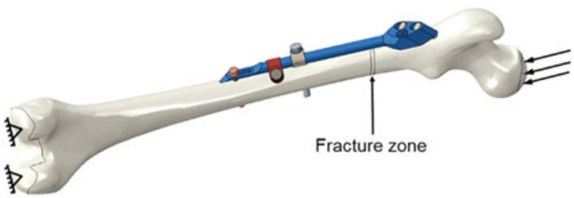

Fig. 17.17 Loads and supports imposed on FE model of femur-SIF assembly. Surface partitions used for load definition, as well as fracture zone are visible in the image (Korunovic et al. 2015)

contact definitions were lost and thus had to be recreated. Figure 17.16 represents the final FE model of femur-SIF assembly, where each different color corresponds to a fixed value of elasticity modulus. For this reason, the components of SIF and the fracture zone contain the finite elements shown by uniform colors, while the elements belonging to the rest of the femur are shown in many different colors. The number of colors is, in fact, equal to one hundred, as one hundred values of Young's modulus were used during material mapping.

Loads and supports were defined to resemble the one-legged stance, or more precisely, to mimic the mechanical test that is often performed on cadaveric femurs. On the surface partition that was created in the distal part of the femur, displacement of element nodes was fixed in all directions. On the other surface partition, which was created on the femoral head, a distributed load of 883 N acting in the direction of the mechanical axis was set to simulate the force resulting from body weight of 90 kg (Fig. 17.17).

17.7 Sensitivity Studies

Previous sections were mostly dedicated to various steps in creation of FE models of femur-implant assembly. After a FE model is built, it is used in structural analysis, to find the values of displacements, strains, stresses or contact pressures of the fixator and of the bone. Those values may be used to predict possible implant failures or bone degradation during the healing process, as it is shown in the following example.

Distribution of equivalent stress, obtained by FEA of a femur-SIF model for a predefined bar size and position of SIF on the femur, where SIF is loaded as depicted in Fig. 17.17, is shown in Fig. 17.18. It may be concluded that the bar and the sliding screws are predominantly loaded in bending.

The highest values of stress, reaching 112.7 N/mm^2, were found at the upper part of sliding screws and at one of the sliding screws holes in the trochanteric unit. Femur stresses were the highest in the vicinity of screw holes, taking values up to 29.58 N/mm^2. For the presented SIF configuration and placement, and for the presented load case (one-legged stance), the lowest values of safety factor related to stress were 3.51 on femur and 6.58 on SIF. This leads to the conclusion that the fixator can withstand the imposed loads during the whole healing process.

Previous results are, however, valid only for a specific load case and geometrical configuration of the femur-SIF assembly. During the fracture healing process, fixator is usually exposed to various loading conditions, including dynamic loads. It is, thus, important to identify the situations with highest stresses and to perform accurate modeling of the loads. It may also be important to combine more loading scenarios in one analysis, especially if durability analysis is performed.

Even if all elements of a FE model, including geometry, materials, and loads, are accurately defined, one must bear in mind that the obtained results are valid only for a single specific case. Thus, a single finite element analysis may not be used to find the optimal configuration or placement of the implant, but just to check the validity of the configuration and placement that were determined empirically by the surgeon. To help in surgery planning and decreasing the probability of fixation failure, FEA must be combined with optimization techniques (as described in the next section) or at

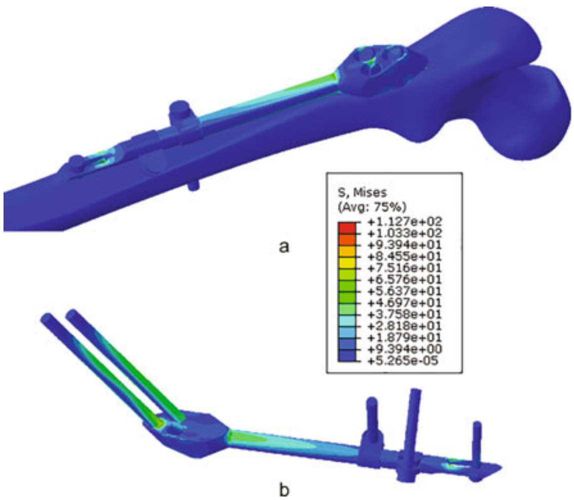

Fig. 17.18 Equivalent stress in: **a** femur-SIF assembly, **b** SIF subassembly (Korunovic et al. 2015)

least a sensitivity study must be performed. A sensitivity study implies changing the values of chosen design variables to observe their influence on mechanical behavior of the structure. If a sensitivity study is to be performed using the FE model of femur-fixator assembly, it is very important that the underlying CAD model, in which the values of design variables are changed to produce the new geometry and update the FE model, is flexible and robust, as described in Sect. 17.4.2.

In the continuation of this section a sensitivity study is presented, which was performed using the FE model based on the CAD model from Sect. 17.4.2. The goal of the study was to find the dependence of SIF stress on the change of two design variables: trochanteric bar length (a) and clamp spacing (b) (Fig. 17.9).

The initial FE model of femur-SIF assembly was based on the CAD model that was configured using the default values of design variables (a = 150 mm and b = 10 mm). The CAD model was imported from Solidworks to ANSYS Workbench (ver. 17.1, Ansys Inc., Canonsburg, PA, USA) via the Workbench associative interface, to establish the bidirectional connection between CAD and FEA models and enable the automatic propagation of geometry changes from CAD to FEA software and vice versa (SolidWorks et al. 2015; Ansys 2016). The details on the FE model and analysis settings may be found in (Korunovic et al. 2019). Loading conditions were set to model the one-legged stance, as described in the previous section.

Sensitivity analysis was performed by defining a design table in ANSYS that contained 16 instances of femur-SIF assembly and running the 16 corresponding analyses continuously. To illustrate the difference between the resulting FE models, the models that correspond to the instances based on minimal and maximal values of design variables are shown in Fig. 17.19.

The values of design variables for each design point (a row in design table corresponding to a different assembly instance), as well as the corresponding value of maximal implant stress, are shown in Table 17.1. The sensitivity of equivalent SIF stress to the change of the two design variables may better be observed in Fig. 17.20, where it is presented in the form of a three-dimensional graph.

Based on Fig. 17.20 it may be concluded that bar length has a significantly larger influence on SIF stress than clamp spacing. For an arbitrary constant value of clamp spacing, SIF stress gets notably larger with shortening of the bar. For an arbitrary

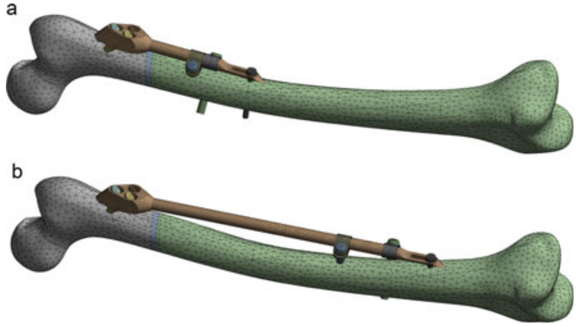

Fig. 17.19 Sample instances of the FE model of femur–SIF assembly: **a** Bar length 100 mm, clamp spacing 1 mm. **b** Bar length 250 mm, clamp spacing 28 mm (Korunovic et al. 2019)[2]

Table 17.1 Femur-SIF assembly instances, the values of the design variables, and the calculated values of maximal fixator stress (Korunovic et al. 2019)[2]

Instance Number	Bar Length (a) (mm)	Clamp Spacing (b) (mm)	Maximal Implant Stress (MPa)
1	100	1	353.26
2	100	10	341.41
3	100	19	330.54
4	100	28	333.15
5	150	1	307.04
6	150	10	317.18
7	150	19	297.94
8	150	28	312.13
9	200	1	270.38
10	200	10	261.84
11	200	19	255.28
12	200	28	251.45
13	250	1	222.59
14	250	10	217.08
15	250	19	216.63
16	250	28	208.15

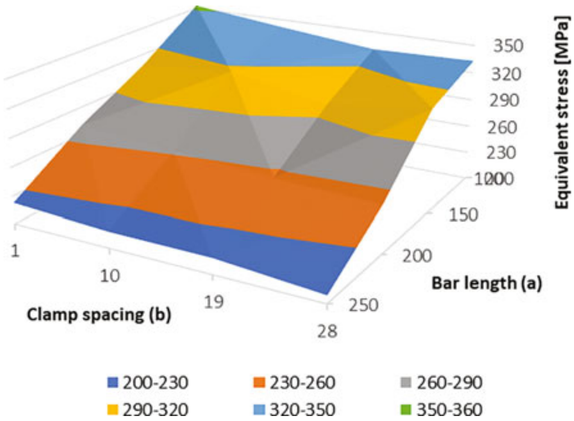

Fig. 17.20 Equivalent stress of SIF, as a function of bar length (**a**) and clamp spacing (**b**) (Korunovic et al. 2019)[2]

constant value of bar length, as clamp spacing gets larger SIF stress gets slightly lower. As only two design variables were defined, and the surface representing the SIF stress as a function of those was smooth and monotonic, even without structural optimization it could be concluded that the optimal values of design variables concerning minimization of SIF stress were a = 250 mm and b = 28 mm. In other words, the surgeon should strive to maximize both bar length and clamp spacing to ensure the maximum durability of SIF if there are no other factors influencing this choice, such as the location of the fracture, the condition of underlying bone or surgical cut length.

17.8 Optimization Studies

The goal of a structural optimization study is to find the structure that supports the load in the "best" way. For example, the best structure may be sought for transferring a load from a known area in space to a fixed support. For the mathematical optimization to be possible, the term "the best" must be mathematically described in the context of the structure, typically as "minimal mass" or "maximal stiffness". In each optimization study, one or more functions mathematically define a selected output variable (e.g., displacement, stress, or mass) as a function of design variables. Those are called the objective functions (goals) and are maximized or minimized to find the optimal solution, which is a set of optimal values of design variables. Some constraints must also exist for the optimization task to be fulfilled successfully. For example, if stiffness is maximized without constraints, mass may tend to infinity (Christensen and Klarbring 2008).

There are several types of structural optimization: size, shape, topology, and material optimization. In the case of shape optimization, which is the topic of this section, some of the variable dimensions of the parametric CAD model are considered as design variables. Design variables control the shape of the structure, and their values are changed to achieve targeted mechanical properties i.e., to design the implant having satisfactory structural strength (Milovanovic et al. 2020). It is also possible to include the values of material constants and loads in the shape optimization process. Structural optimization method by which the small segments of material may disappear and reappear is called topology optimization. Resulting geometry is thereby very irregular and organic, as only the necessary parts of the material are kept. It may be very useful in custom implant design, especially if fixators are being produced by additive manufacturing methods that allow great part complexity and design freedom (Cucinotta et al. 2019).{Cucinotta, 2019}.

To find the optimal shape of SIF, response surface optimization (RSO) was performed in DesignXplorer, a module of ANSYS. In RSO, design of experiments (DOE), response surfaces (meta-models), and mathematical optimization methods are used to find the optimal values of design variables (Ansys 2016). The experiments which are required in DOE phase are performed as virtual ones, by means of FEA. Thereby, the underlying CAD model, on which the FE model is based, must be adequately parameterized and robust. Such a model allows the successful creation of any permissible assembly configuration and enables the uninterrupted performance of all required virtual experiments (FEAs).

17.8.1 Optimization Study 1

In the first study, the exact same model of femur-SIF assembly that was utilized in the sensitivity study described in previous section was used. The goal of this multi-criteria optimization study was to simultaneously minimize the values of maximal equivalent stress of SIF and maximal equivalent stress of femur. The same design variables were kept as in the sensitivity analysis, only in this case the trochanteric bar length was defined as a continuous design variable. The lower and an upper bound of design variables were set as:

a. Trochanteric bar length (100–250 mm)
b. Clamp spacing (1–28 mm).

Central composite design (CCD), face centered, enhanced type of DOE was used, resulting in definition of 17 different combinations of design variables values that covered the design space, including extreme points, very well. After all the analyses, i.e., virtual experiments, were finished successfully, response surface of "genetic aggregation" type were fitted to the resulting data. In Fig. 17.21 one of the surfaces is shown together with the data obtained in DOE phase. Similar conclusions may be drawn from this graph as from the one obtained by sensitivity study (Fig. 17.20), suggesting that the inclusion of the femur stress in the optimization did not have significant effect on the results regarding sensitivity.

Finally, the optimization was performed based on the obtained response surface, using the multi-objective genetic algorithm (MOGA). Three sets of optimal values of design variables (candidate points) were obtained, as shown in Table 17.2. The differences between calculated values were minimal, and all the values were close to the ones obtained by sensitivity analysis, i.e., the upper bonds of both design

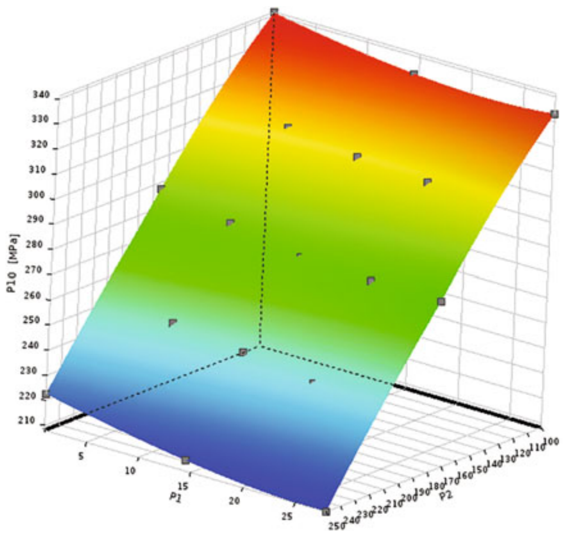

Fig. 17.21 Equivalent stress of SIF (P10), as a function of bar length (P2) and clamp spacing (P1) obtained by RSO

Table 17.2 Three sets of suggested optimal values obtained by RSO

Input and output variables	Candidate Point 1	Candidate Point 2	Candidate Point 3
P1—clamp spacing [mm]	**27.99**	27.84	27.71
P2—bar length [mm]	**249.96**	249.94	249.98
P4—fixator stress [N/mm^2]	**208.60**	208.67	208.68
P5—femur stress [N/mm^2]	**10.73**	10.74	10.74
P12—fixator mass [kg]	**0.312**	0.312	0.312

The set that was selected as the best one is shown in bold letters

variables. Nevertheless, the first set of design variables values was selected as optimal, since its values of stress were the lowest. In practice, the upper bounds of design variables could be used as optimal values, as they are very close to the results of the optimization.

The previous optimization study did not bring much more benefits than the preceding sensitivity study, except for the automated process of optimal values determination. It is because the optimization task was simple, as only two design variables that were considered had influenced the output variables in a monotonic way.

17.8.2 Optimization Study 2

The second example presents a more complex optimization study, in which the modified design of SIF and more design variables were considered. Namely, a radius was introduced between the trochanteric unit and the bar, and four extra design variables were created. This was done by allowing the mentioned radius and three more dimensions that were fixed in the standard design to be changed (bar diameter, bar end thickness and bar radius). The suggested modifications of SIF design were made to reduce the stress while lowering the mass of SIF, in order to enhance fixator durability, save material and lower the trauma for the patient. Therefore, the six design variables and their limits were introduced as (Fig. 17.22):

- P1—Bar length (100–250 mm)
- P2—Bar diameter (8–10 mm)

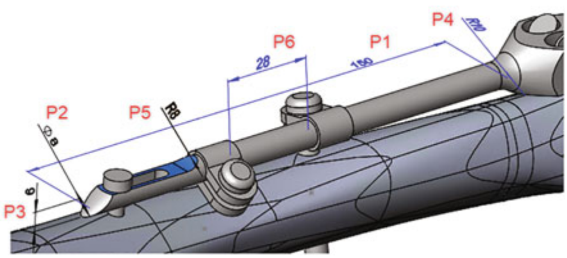

Fig. 17.22 Design variables used in the second optimization study

- P3—Bar end thickness (4–6.5 mm)
- P4—Radius at trochanteric unit (3–10 mm)
- P5—Radius at bar end (6–10 mm)
- P6—Clamp spacing (1–28 mm).

It is a common occurrence that some design variables have a more significant influence on the observed output variables than the other design variables. In addition, performing the optimization study with too many design variables may lead to very long computational times, as there are many virtual experiments to perform. Also, the optimization algorithms may be less efficient when too many variables are used and the optimization results obtained using too many input variables may be tedious to analyze. Therefore, a parameters correlation analysis is often performed to filter out a limited number of the most influential design variables that will be used in design optimization study as input variables. Such an analysis was performed in DesignXplorer and the following variables were selected as the most important ones (the value of calculated Relevance parameter is given in brackets):

- P1—Bar length (1)
- P3—Bar end thickness (1)
- P2—Bar diameter (0.62366).

The other design variables were filtered out, as the values of their Relevance parameters were lower than 0.29, whereas the default threshold was equal to 0.5. The optimization study was therefore performed using the three above design variables and their earlier defined ranges, while the values of other three design variables were fixed at the following values: P4 = 10 mm, P5 = 8 mm, P6 = 28 mm.

Once again, central composite design (CCD), face centered, enhanced type of DOE was used, resulting in definition of 29 different combinations for design variables values. The response surfaces of "genetic aggregation" type were fitted to the resulting data. Some of those are shown in Fig. 17.23, together with the data obtained in DOE phase.

Detailed results of the RSO are too extensive to be shown. Nevertheless, some conclusions may be drawn from the presented data. Firstly, the response surfaces do not follow the DOE obtained data as closely as in the previous example, which should be expected as the number of design variables is larger. Some data points are very far from the response surface, as, for example, the SIF stress at P1 = 100, P2 = 8 and P3 = 5.25, implying the meta-model has local inaccuracies. There are techniques that may be performed to lessen the surface approximation error, such as creation of verification and refinement points or selection of different response surface type. In this example, the accuracy was considered as acceptable for the optimization to be carried out.

The optimization was performed based on the obtained response surfaces, using the MOGA. Two different sets of objectives and constraints were set. In the first case, the objective was to minimize maximal SIF stress and the constraints were the upper and the lower bounds of design variables. In the second case, two different objectives were defined that had to be satisfied simultaneously: minimization of maximal SIF

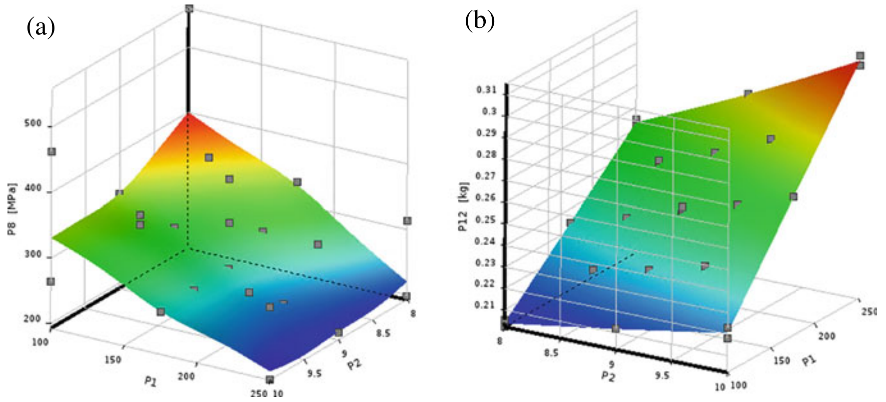

Fig. 17.23 Some of the surfaces obtained in the second optimization study: **a** equivalent stress of SIF (P8), as a function of bar length (P1) and bar end thickness (P2); **b** SIF mass (P12), as a function of the same design variables. Both surfaces are shown for the fixed value of bar diameter (P3), equal to 5.25 mm

stress and minimization of SIF mass. The constraints were also the bounds of design variables, plus the upper limit of 220 N/mm^2 was set as a constraint on SIF stress. The results of the two optimizations are given in Table 17.3, where the shown values of fixator stress are verified by FEA, and in Table 17.4.

In the first case, candidate point 2 has the lowest maximal SIF stress value of 170.32 N/mm^2, which is considerably lower than the value obtained in the previous study, 208.6 N/mm^2, when only two design variables were allowed to be changed. The mass is also lower, as it is equal to 0.294 kg and was equal to 0.312 kg. Therefore, it may be concluded that SIF design has been improved both concerning durability and mass. In the second case, the best solution is considered to be candidate point 2, where maximum SIF stress is equal to 216.41 N/mm^2 and SIF mass equals to 0.253 kg. Here, SIF mass is considerably lower than in the first case and in the previous study, while the maximum SIF stress is a bit higher than in the first optimization study (208.60 N\mm^2). As the change of maximum SIF stress is small and the mass is considerably lower, it may be concluded that mass optimization was successful. There is also a possibility to rerun the optimization with changed objectives importance, to

Table 17.3 The results of the first optimization task in optimization study 2

Input and output variables	Candidate Point 1	Candidate Point 2	Candidate Point 3
P1—bar length [mm]	249.79	**249.59**	249.37
P2—bar end thickness [mm]	9.28	**9.23**	9.29
P3—bar diameter [mm]	6.01	**6.05**	6.01
P8—fixator stress [N/mm^2]	173.67	**170.32**	171.52
P12——fixator mass [kg]	0.295	**0.294**	0.295

The set of optimal values that was selected as the best one is shown in bold letters

Table 17.4 The results of the second optimization task in optimization study 2

Input and output variables	Candidate Point 1	Candidate Point 2	Candidate Point 3
P1—bar length [mm]	182.33	**189.48**	197.49
P2—bar end thickness [mm]	8.87	**8.73**	8.56
P3—bar diameter [mm]	6.43	**6.48**	6.41
P8—fixator stress [N/mm^2]	218.17	**216.41**	218.19
P12—fixator mass [kg]	0.252	**0.253**	0.254

The set of optimal values that was selected as the best one is shown in bold letters

emphasize either the mass minimization or the stress minimization objective. In this way, the trade-off between mutually opposite objectives may be controlled.

17.9 Concluding Remarks

The intention of this chapter was to illustrate how structural analysis based on FEM and structural optimization may jointly be used to plan proximal femoral fracture surgery and to decrease the probability of femoral fixation failures. Various stages in FE model building, structural analysis and structural optimization were illustrated through the studies performed by the authors.

Although the presented methods are well known, the complex freeform geometry of femur, as well as the nature of the bone material, make the creation of FEA models that may be used in automated optimization studies a very complex task. The main challenges lie in creation of flexible and robust CAD models that serve as the basis for FE model creation and in the accurate bone geometry and bone material modeling.

The presented methodology may be used in optimization of various fixation devices utilized in long bone fractures surgical treatment. There is a lot of space for presented methods improvement and many researchers are already working on various related topics. Their ultimate goal is achieving a completely automatic and fast procedure for subject-specific optimization of fixation devices, that would be introduced into clinical practice.

Acknowledgments This research was financially supported by the Ministry of Education, Science and Technological Development of the Republic of Serbia (Agreement no. 451-03-9/2021-14/200109).

References

Almeida D, Ruben R, Folgado J, Fernandes P, Audenaert E, Verhegghe B, De Beule M (2016) Fully automatic segmentation of femurs with medullary canal definition in high and in low resolution CT scans. Med Eng Phys 38(12):1474–1480

Almeida D, Ruben R, Folgado J, Fernandes P, Gamelas J, Verhegghe B, De Beule M (2017) Automated femoral landmark extraction for optimal prosthesis placement in total hip arthroplasty. International Journal for Numerical Methods in Biomedical Engineering, 33(8):e2844

Ansys C (2016) Reference Guide, Release 17.1. ANSYS Inc., Canonsburg, PA

Baca V, Horak Z, Mikulenka P, Dzupa V (2008) Comparison of an inhomogeneous orthotropic and isotropic material models used for FE analyses. Med Eng Phys 30(7):924–930

Burstein AH, Reilly DT, Martens M (1976) Aging of bone tissue: mechanical properties. The J Bone Joint Surg Am 58(1):82–86

Chang K-H (2014) Product design modeling using CAD/CAE: the computer aided engineering design series. Academic Press

Christensen P, Klarbring A (2008) An introduction to structural optimization, vol 153. Springer Science & Business Media

Cucinotta F, Guglielmino E, Longo G, Risitano G, Santonocito D, Sfravara F (2019) Topology optimization additive manufacturing-oriented for a biomedical application. In: Advances on mechanics, design engineering and manufacturing II. Springer. pp 184–193

Eberle S, Gerber C, Von Oldenburg G, Högel F, Augat P (2010) A biomechanical evaluation of orthopaedic implants for hip fractures by finite element analysis and in-vitro tests. Proc Inst Mech Eng [h] 224(10):1141–1152

Edwards B, Miller R, Derrick T (2016) Femoral strain during walking predicted with muscle forces from static and dynamic optimization. J Biomech 49(7):1206–1213

Ehlke M, Ramm H, Lamecker H, Hege H-C, Zachow S (2013) Fast generation of virtual X-ray images for reconstruction of 3D anatomy. IEEE Trans Visual Comput Graphics 19(12):2673–2682

Floyd J, O'toole R, Stall A, Forward D, Nabili M, Shillingburg D, Hsieh A, Nascone J (2009) Biomechanical comparison of proximal locking plates and blade plates for the treatment of comminuted subtrochanteric femoral fractures. J Orthop Trauma 23(9):628–633

Helgason B, Perilli E, Schileo E, Taddei F, Brynjólfsson S, Viceconti M (2008) Mathematical relationships between bone density and mechanical properties: a literature review. Clin Biomech 23(2):135–146

Hibbeler RC, Kiang T (2015) Structural analysis. Pearson Prentice Hall Upper Saddle River

Kainmueller D, Lamecker H, Zachow S, Hege H-C An articulated statistical shape model for accurate hip joint segmentation. In: Engineering in medicine and biology society, 2009. EMBC 2009. Annual international conference of the IEEE, 2009. IEEE. pp 6345–6351

Ko R (1953) The tension test upon the compact substance of the long bones of human extremities. J Kyoto Pref Med Univ 53:503

Komatsubara S, Mori S, Mashiba T, Nonaka K, Seki A, Akiyama T, Miyamoto K, Cao Y, Manabe T, Norimatsu H (2005) Human parathyroid hormone (1–34) accelerates the fracture healing process of woven to lamellar bone replacement and new cortical shell formation in rat femora. Bone 36(4):678–687

Konya M, Verim Ö (2017) Numerical optimization of the position in femoral head of proximal locking screws of proximal femoral nail system; biomechanical study. Balkan Med J 34(5):425

Korunovic N, Marinkovic D, Trajanovic M, Zehn M, Mitkovic M, Affatato S (2019) In silico optimization of femoral fixator position and configuration by parametric CAD model. Materials 12(14):2326

Korunovic N, Trajanovic M, Mitkovic M, Vulovic S (2010) From CT scan to FEA model of human femur. IMK-14-Istrazivanje i razvoj 16(2):45–48 (in Serbian)

Korunovic N, Trajanovic M, Stevanovic D, Vitkovic N, Stojkovic M, Milovanovic J, Ilic D Material characterization issues in FEA of long bones. In: SEECCM III 3rd South-East European conference on computational mechanics—an ECCOMAS and IACM special interest conference, Kos Island, Greece, 2013, pp 12–14
Korunovic N, Trajanovic M, Mitkovic M, Vitkovic N, Stevanovic D (2015) A parametric study of selfdynamisable internal fixator used in femoral fracture treatment. Paper presented at the NAFEMS world congress 2015 inc. 2nd International SPDM Conference, San Diego, 21–24 June
Lunsjö K, Ceder L, Tidermark J, Hamberg P, Larsson B-E, Ragnarsson B, Knebel RW, Allvin I, Hjalmars K, Norberg S (1999) Extramedullar fixation of 107 subtrochanteric fractures: a randomized multicenter trial of the Medoff sliding plate versus 3 other screw-plate systems. Acta Orthop Scand 70(5):459–466
Micic I, Mitkovic M, Park I-H, Mladenovic D, Stojiljkovic P, Golubovic Z, Jeon I-H (2010) Treatment of subtrochanteric femoral fractures using selfdynamisable internal fixator. Clin Orthop Surg 2(4):227–231
Milovanovic J, Stojkovic M, Husain K, Korunovic N, Arandjelovic J (2020) Holistic approach in designing the personalized bone scaffold: the case of reconstruction of large missing piece of mandible caused by congenital anatomic anomaly. J Healthc Eng 2020:6689961
Mischler S, Pax G (2002) Tribological behavior of titanium sliding against bone. Eur Cell Mater 3(1):28–29
Mitkovic M, Milenkovic S, Micic I, Mladenovic D, Mitkovic M (2012) Results of the femur fractures treated with the new selfdynamisable internal fixator (SIF). Eur J Trauma Emerg Surg 38(2):191–200
Mittal R, Banerjee S (2012) Proximal femoral fractures: principles of management and review of literature. J Clin Orthop Trauma 3(1):15–23
Morgan EF, Bayraktar HH, Keaveny TM (2003) Trabecular bone modulus—density relationships depend on anatomic site. J Biomech 36(7):897–904
Oldani C, Dominguez A (2012) Titanium as a biomaterial for implants. Recent Adv Arthroplasty 218:149–162
Pakhaliuk V, Poliakov A (2018) Simulation of wear in a spherical joint with a polymeric component of the total hip replacement considering activities of daily living. Facta Universitatis-Ser Mech Eng 16(1):51–63
Pavic A, Kodvanj J, Surjak M (2013) Determining the stability of novel external fixator by using measuring system Aramis. Tehnički Vjesnik 20(6):995–999
Peng L, Bai J, Zeng X, Zhou Y (2006) Comparison of isotropic and orthotropic material property assignments on femoral finite element models under two loading conditions. Med Eng Phys 28(3):227–233
Perren S (2002) Evolution of the internal fixation of long bone fractures: the scientific basis of biological internal fixation: choosing a new balance between stability and biology. J Bone Joint Surg Br 84(8):1093–1110
Petrovic S, Korunovic N (2018) Imaging in clinical and preclinical practice. In: Biomaterials in clinical practice. Springer, pp 539–572
Phillips A (2009) The femur as a musculo-skeletal construct: a free boundary condition modelling approach. Med Eng Phys 31(6):673–680
Samsami S, Saberi S, Sadighi S, Rouhi G (2015) Comparison of three fixation methods for femoral neck fracture in young adults: experimental and numerical investigations. J Med Biol Eng 35(5):566–579
Schileo E, Dall'Ara E, Taddei F, Malandrino A, Schotkamp T, Baleani M, Viceconti M (2008) An accurate estimation of bone density improves the accuracy of subject-specific finite element models. J biomech 41(11):2483–2491
SolidWorks DS, Street W, Waltham M (2015) SOLIDWORKS 2016. Online help. Accessed Mar 2020

Sowmianarayanan S, Chandrasekaran A, Kumar K (2008) Finite element analysis of a subtrochanteric fractured femur with dynamic hip screw, dynamic condylar screw, and proximal femur nail implants - a comparative study. Proc Inst Mech Eng [h] 222(1):117–127

Stojkovic M, Trajanovic M, Vitkovic N, Milovanovic J, Arsić S, Mitković M (2009) Referential geometrical entities for reverse modeling of geometry of femur. Paper presented at the VIPIMAGE 2009, Porto, Portugal

Vincentelli R, Grigoroy M (1985) The effect of Haversian remodeling on the tensile properties of human cortical bone. J Biomech 18(3):201–207

Vitkovic N, Milovanovic J, Korunovic N, Trajanovic M, Stojkovic M, Mišic D, Arsic S (2013) Software system for creation of human femur customized polygonal models. Comput Sci Inf Syst 10(3):1473–1497

Vulovic S, Korunovic N, Trajanovic M, Grujovic N, Vitkovic N (2011) Finite element analysis of CT based femur model using finite element program PAK. J Serb Soc Comput Mech 5(2):160–166

Wu X, Yang M, Wu L, Niu W (2015) A biomechanical comparison of two intramedullary implants for subtrochanteric fracture in two healing stages: a finite element analysis. Appl Bionics Biomech 2015

Yang H, Ma X, Guo T (2010) Some factors that affect the comparison between isotropic and orthotropic inhomogeneous finite element material models of femur. Med Eng Phys 32(6):553–560

Zou Z, Liao S-H, Luo S-D, Liu Q, Liu S-J (2017) Semi-automatic segmentation of femur based on harmonic barrier. Comput Methods Programs Biomed 143:171–184

Chapter 18
Overview of AI-Based Approaches to Remote Monitoring and Assistance in Orthopedic Rehabilitation

Dragan Misic and Milan Zdravkovic

18.1 Introduction

The recent years have seen the unprecedented rise in computational power and storage. Both have become widespread, thanks to the major cloud providers. Today, Graphical Processing Units in application clouds are becoming available at minimum or no cost, facilitating efficient training of models and increased productivity in numerical experiments. In such circumstances, the Machine Learning tools and approaches started to emerge at extremely fast pace, as the flagship technology for implementing the concept of the Artificial Intelligence (AI). Besides accessibility of computational infrastructures, this pace is also facilitated by the trend of overall digitalization, leading to collection, creation, curation, and storage of vast data that can today be used for training different models.

The main purpose of ML models is to address incompleteness of deterministic models in case of complex problems. While sometimes a phenomenon in the specific domain can be represented by the mathematical equation (deterministic approach), in great most of those complex cases, using experience engraved in the vast data is much more reliable approach for its modeling. That experience is recognized and extracted by using the existing data to train the selected ML methods and thus, create the model that is capable to solve different classes of prediction problems.

Challenges in medicine are the most difficult because their solutions are strongly founded on the experimental methods. They rely on big data to train the diagnostic models which can then classify diseases based on the Real-Time data streams, for example, incoming from the wearable devices. Real-Time patient monitoring systems help to improve the diagnostics (based on data collected in real life situations), to identify clinical emergency and to monitor the therapeutic process. Many different signals

D. Misic (✉) · M. Zdravkovic
Facuty of Mechanical Engineering, Nis, Serbia
e-mail: dragan.misic@masfak.ni.ac.rs

O. Canciglieri Junior and M. D. Trajanovic (eds.), *Personalized Orthopedics*,
https://doi.org/10.1007/978-3-030-98279-9_18

of physiological origin can be tracked: pulse oximetry, respiration rate, temperature, heart rate, heart rate variability, arterial blood pressure, skin temperature, skin conductance, blood alcohol concentration, and others. They can be combined with environmental (air temperature, humidity, atmospheric pressure) and location data to feed the processing algorithms which can infer the features indicative to a person health status.

This paper aims to define the state of the art in using the AI/ML to facilitate prediction and decisions in remote monitoring and assistance in orthopedic rehabilitation.

To the best of our knowledge, there is no systematic review of the overall use of AI/ML methods in orthopedics that could be used to paint a big picture on the overall potential impact of the new disruptive technologies to that domain. Murali et al. (2020) published a loosely structured narrative review with identifying only directions of applications. Groot et al. (2020) have carried out the systematic review of comparing performance of ML methods and clinicians in classifying orthopedic abnormalities on medical images. Myers et al. (2020) provided a very superficial introduction for clinicians on the use of AI methods in orthopedics and identified the potential domains of use as image recognition, risk prediction, patient-specific payment models, and clinical decision-making. Van Eetvelde et al. (2021) have done the systematic review of the use of ML methods in sport injury prediction and prevention.

In this paper, after introducing the major ML algorithms and approaches, we analyze AI applications in orthopedics for patient rehabilitation, remote monitoring and rehabilitation follow-up. In the last section, the guidelines for the future research in this area are provided.

18.2 Machine Learning

Machine Learning is the study of approaches and algorithms to solve different classes of prediction or decision problems (that cannot be effectively solved analytically or programmatically) in the domains described by experience, where this experience, represented by data is used to automatically improve the effectiveness of those solutions (adapted from Mitchell 1997). Traditionally, ML approaches and applications are divided into three categories (although there are many different ML methods which do not fit into this categorization): supervised, unsupervised and reinforcement learning.

In supervised learning, a selected algorithm learns from the existing data to map the selected input into the selected output. For example, the time series interval of data recorded by using IMU sensors can be mapped to the specific movement of the patient, and thus used for actually recording the movements, based on the Real-Time data. In supervised learning, output data are often labels, associated to each of the individual sets of input data by a human, typically an expert. For example, orthopedic surgeons can map the regions of the medical image to the specific diagnosis. The ML algorithm can be trained to distinguish between normal and pathological state by learning from the large set of medical images. Each image is associated with one of the labels—nominal output features (normal, pathological), where those associations were made by orthopedic surgeon. ML algorithm, trained with the existing data is then called ML model and that model can be used for predicting the output feature (continual or nominal), based on incoming input data (not present in the training set). There are many different algorithms, broadly divided into the classification and regression algorithms, depending on whether the output feature is a nominal or continual one, respectively. The most commonly used traditional supervised learning algorithms are Naive Bayes, Linear and Logistic Regression, Decision Trees and Support Vector Machine (SVM) (Cortes and Vladimir 1995). Ensemble methods (also traditional algorithms) (Opitz and Maclin 1999) combine multiple algorithms in the specific way (such as bagging, voting, and boosting) to improve the prediction performance of the used individual algorithms. Random Forest (Ho 1995) and Gradient Boosting (Breiman 1997) are today considered as the most effective traditional ML algorithms.

Unsupervised learning is used to discover meaningful patterns or structures in the existing data. It is often used as a data processing activity that precedes the training of some supervised learning algorithm. Clustering, namely grouping of data instances of some similar characteristics is one of the most frequent problems addressed by unsupervised learning algorithms. The most commonly used traditional algorithms for clustering are k-means clustering (MacQueen 1967) and k-nearest neighbors (Altman 1992). Dimensionality reduction is an unsupervised learning technique aiming at reducing the number of features in order to avoid overfitting (incapability of the prediction model to generalize beyond the training data), increase the training and prediction performance or even improve prediction accuracies. The most commonly used algorithm for dimensionality reduction is Principal Component Analysis (PCA). Finally, anomaly detection (Zimek and Schubert 2017) is another class of problems typically addressed by some unsupervised learning approach (although supervised learning and semi-supervised learning techniques are sometimes also used). Anomalies are often defined as occurrences or values of items, events or observations significantly differing from the vast majority of data. Anomaly detection is therefore devoted to identifying these data points.

The development of Artificial Neural Networks (ANN) and especially new deep learning architectures, such as convolutional (LeCun and Bengio 1998), recurrent (Rumelhart and McClelland 1987) and attention-based neural networks (Vaswani et al. 2017) are probably the most significant drivers for innovative and practical application of machine learning for addressing each of the ML groups of problems listed above. Convolutional Neural Networks (CNN) effectively implement a feature engineering method to reduce the complexity of very large datasets (such as images), while improving the data representation. For this reason, they are most often used for addressing computer vision problems such as image classification, object localization, classification and segmentation. Encoder-Decoder neural networks, namely the Recurrent Neural Networks (RNN) and Long Short-Term Memory architectures—LSTM (Hochreiter and Schmidhuber 1997) are designed to address the problems related to sequential datasets, such as time-series, natural language, speech and videos. In a nutshell, both RNN and LSTM networks maintain a single so-called hidden state vector which stores the context of the entire sequence of data. All those architectures are composed of two individual models—Encoder encodes the entire sequence into the hidden state vector, while Decoder decodes this vector into another sequence of output data. While many of the disadvantages arising from the strictly sequential processing of data by RNN architectures are addressed by the LSTMs, the degrading effect of lagged data ("weakened" representation of past data in a hidden state vector) is solved by so-called attention mechanisms, which maintain many multiple lagged hidden states.

As the use of AI algorithms and approaches increase, the issue of the right of the individuals, enterprise and its supply chain as well as society at large, to understand the effect of the decisions made by AI-enabled EIS (Enterprise Information Systems) will emerge. Growing concern on potential bias in AI models and a demand for model transparency and interpretability is addressed by the Explainable AI (XAI) stack of methods and approaches (Gilpin et al. 2018). XAI helps to highlight evidence that the prediction model is trustworthy, that it is not biased, or that is compliant with regulation. It typically refers to post-modelling explainability of pre-developed models. Global explainability refers to discovering the features' importance while looking at the whole model (trained with all available data). Local explainability relates to facilitating understanding of how input data is used by a model to make a prediction or a forecast for an instance of a class (for example, individual predicted ranking of a recruited candidate). Different explanation families can be used for different purposes, such as importance scores (saliency heatmaps), decision rules, decision trees, dependency plots and others. Some of the most commonly used approaches to local explanation are Local Interpretable Model-agnostic Explanations (LIME) (Ribeiro et al. 2016) and SHAP (SHapley Additive exPlanations) (Lundberg and Lee 2017). Model explainability is a prerequisite for building trust and facilitating adoption in the areas which are characterized by high privacy, reliability and safety requirements, as well as those where AI-facilitated decisions have significant socio-economic implications.

18.3 Applications

Various artificial intelligence (AI) methods are becoming more popular in different branches of medicine, and orthopedics is not an exception. AI applications in orthopedics were described by Jayakumar and colleagues through three aspects: advanced data discovery and extraction, improved diagnostics and prediction, and enhanced clinical and decision support (Jayakumar et al. 2019). Other studies are disease-specific, for example, Cabitza et al. (2018) analyzed AI applications for fracture detection, spinal pathology assessments, skeletal bone age detection, shoulder strength assessment, gait classification, osteoarthritis prediction and detection, optimal injection point localization, ACL/PCL (Anterior Cruciate Ligament/Posterior Cruciate Ligament) detection, and bone and cartilage image segmentation.

In this chapter, we will analyze AI applications in orthopedics for patient rehabilitation and rehabilitation monitoring.

18.3.1 Rehabilitation

Rehabilitation may be defined as a "set of measures that assist individuals who experience, or are likely to experience, disability to achieve and maintain optimal functioning in interaction with their environments" (WHO 2011).

For some patients, rehabilitation is necessary to be able to proceed with everyday life. Rehabilitation is voluntary, so for some patients, the assistance of medical professionals might be crucial for continuing and benefiting from the rehabilitation process. In the case of insufficient capacity, as well as the fact that rehabilitation is often conducted outside medical facilities, the application of AI tools might contribute to better patient recovery.

Rehabilitation can be analyzed in a few ways. Here we will consider the following applications: predicting rehabilitation success, using wearable sensors for rehabilitation tracking, and assistance in the postoperative process. These applications areas are necessarily overlapping. For example, wearable sensors are used for handling sports injuries, in the postoperative process, and for predicting rehabilitation success. However, this division helps for focusing on important fields of AI applications.

18.3.1.1 Predicting Rehabilitation Success

One of the first studies for predicting rehabilitation success using AI techniques originates from 2007 (Zhu et al. 2007). Although in this work the authors studied the rehabilitation of older patients with Alzheimer's disease, it is relevant in orthopedics as well, since it is one of the first applications of AI methods for predicting rehabilitation success. The authors showed that basic algorithms such as k-Nearest Neighbors (k-NN) and Support Vector Machine (SVM) may improve decision-making and predictions when compared to standard clinical protocols. The data used in this analyze are obtained from the Resident Assessment Instrument—Home Care (RAI-HC) system used in Canada. Assessment items include personal items, referral information, cognition, communication and hearing, vision, mood and behavior, informal support services, physical functioning etc.

One of the latest studies related to recovery prediction, by Verma et al. (2021), analyzed the possibility of using the data collected during and after rehabilitation to predict the results of the proposed therapy and rehabilitation. The data were collected through questionnaires filled by patients. This study reviews the work on prediction of rehabilitation after cancer surgery, prediction of depression treatments, pain volatility, and a few studies related to the rehabilitation after the total joint arthroplasty. The authors conclude that AI applications on this type of data may be beneficial and should be studied further, especially considering the much easier data collection using mobile applications.

Tschuggnall et al. (2021) analyzed the questionnaire data on hip, foot, and knee injuries provided by patients, but combined with the clinical data. Rehabilitation for these types of injuries often requires several weeks or even months. Based on experience, medical professionals may be able to predict if the treatment will be successful, but it remains unclear how specific factors influence such a conclusion.

To discover the most relevant factors influencing rehabilitation success, in addition to the questionnaire data, clinical data are also used. The clinical data comes from the patients' electronic health record and includes variables assessed by a clinician, e.g., the Range of Motion (ROM) of the hip joint, the perimeter of the knee, or the Timed Up and Go (TUG) test value. Questionnaire data, which are subjective, are reported by patients and include the pain assessment, Barthel Index (physical disability assessment) obtained from the assessment of everyday life activity, and others.

To predict the rehabilitation success, the researchers used several ML algorithms: Random Forest, Extra Trees, Support Vector Classification, Naive Bayes, and Linear Discriminant Analysis. Comparison of the results obtained from these algorithms showed that the best performance was achieved with non-linear algorithms based on trees: Random Forest and Extra Tree.

Another study predicting rehabilitation success after hip and knee replacement was described by Huber et al. (2019). The input data were reported by patients and collected monthly and yearly by the National Health Services (NHS). This study compared different ML algorithms with the prediction provided by the NHS that were based on a linear regression model. Since ML algorithms are sensitive to imbalanced datasets, the authors upsampled the less frequent examples in the training data. The test data remained representative of the population. The following algorithms were selected for comparison: Logistic Regression, Extreme Gradient Boosting, Multi-step Adaptive Elastic Net, Random Forest, Neural Net, Naive Bayes, K-Nearest Neighbors, and Boosted Logistic Regression. The comparison showed that Extreme Gradient Boosting delivered the highest overall performance, as measured by J-statistic (Youden 1950), followed closely by the linear model, Multi-step Elastic Net, and Neural Net.

Fontana et al. (2019) also analyze the questionnaire data, in this case after the total joint arthroplasty. Their main aim was to use ML algorithms to predict if the patient's state will be improved enough by conducting a surgery. The improvement assessment is usually obtained from the comparison of the patient's response before and two years after the surgery, and the algorithms were designed to predict the patient's response two years after the surgery. The authors used the logistic LASSO, Random Forest, and linear SVM and concluded that machine learning has the potential to improve clinical decision-making and patient care by informing presurgical discussions of likely outcomes from total joint arthroplasty.

Polce et al. (2020) analyzed patients' satisfaction two years after total shoulder arthroplasty. They used 16 variables collected prior to surgery to predict if the patient will be satisfied. The variables included age (as a continuous variable), body mass index (continuous), sex (male/female), insurance status (workers and non-workers compensation), and others. To reduce the number of features, the authors applied

Recursive Feature Elimination through the Random Forest algorithm. This procedure reduced the number of features to ten that were the most significant for classification. The data with the selected features were then provided as input to the ML algorithms. The following ML algorithms were explored: Stochastic Gradient Boosting, Random Forest, SVM, Neural Network, and Elastic Net-penalized Logistic Regression, with SVM performing best. The five most relevant features contributing to the SVM model were obtained by averaging across all patients (global variable importance) and included the baseline SANE (Single Assessment Numeric Evaluation) score, exercise and activity, insurance status, diagnosis, and preoperative duration of symptoms.

One other study (Harris et al. 2019) also analyzed the patients' states after knee or hip arthroplasty, but with the aim of discovering possible complications that might arise in the postoperative period, in the first 30 days after the operation. The complications that were analyzed might be serious and potentially lead to the patient's death. The authors used LASSO algorithm and were able to better predict complications like renal, death and cardiac complication. Venous thromboembolism and other complications appeared to be much more challenging for prediction.

18.3.1.2 Wearable Sensors for Rehabilitation

The term wearable technology (wearable devices) refers to small electronic devices (sensors) that can be easily installed on the body and in the clothes. Nowadays, there is a variety of such sensors that can track different health-related parameters. For example, sensors, such as accelerometer, gyroscope, magnetometer, and GPS, can track movement, but there are also sensors that monitor the heart, measure the blood pressure, and pedometers that count the number of steps taken.

One of the most significant applications of wearable devices, which is also of most interest here, is probably monitoring physical activity. Even though there are many studies related to this topic, the application of this technology in clinical practice is still in its infancy. The main challenge is the lack of standardization of sensors coming from different manufacturers, as well as the integration of these data into existing electronic health records (Smuck et al. 2021).

In this overview, we will consider the application of wearable sensors in orthopedics for remote monitory and help for patients' rehabilitation. Wearable sensors enable precise movement monitoring that allows monitoring and assessment of the patients during rehabilitation. The sensors' size makes them easy to set up and wear, so they can be used during everyday activities. These sensors provide a lot of data which is the basis for artificial intelligence analysis.

Some of the sensors that are most commonly used for rehabilitation monitoring are sensors based on the force, accelerometer, gyroscope, magnetometer, and GPS sensor.

Force sensors are usually set up on footwear and measure the interaction of the body and the surface while walking. They often contain triggers that are sensitive to pressure. The sensors can be installed on the heel, in which case they detect the heel hitting the ground and the walking phase, but it is also possible to mount multiple sensors on the shoe pad to examine the walking strategy (Porciuncula et al. 2018). However, these sensors are very susceptible to mechanical wear and might also move inside the pad which will influence the quality of the data.

One of the most frequently used sensors in rehabilitation is accelerometer. Accelerometers measure the body movement by detecting the changes in the speed: measuring the acceleration. They can measure the acceleration in three axes, and are used to monitor walking, but also daily activities. The main drawbacks of these sensors are that they are not reliable in the resting state and are influenced by gravity. To overcome these drawbacks, different signal processing techniques are used.

Another sensor that is frequently used in rehabilitation is gyroscope. Gyroscope is the device that measure changes in angular velocity in up to three axes. One of the advantages of gyroscopes is that they are not sensitive to gravity or vibrations.

Magnetometer is the sensor measuring the strength of the magnetic field or the magnetic moment. The readings from the magnetometer enable to define the orientation of the body with respect to gravity. Since these devices are not sensitive to accelerations occurring due to movements, they can be used in combination with accelerometer to separate the gravitational component from kinetic data.

Accelerometers, gyroscopes, and magnetometers are useful for determining the individual components of the movement (acceleration, angular velocity, and magnetic field), but combining these data leads to much more accurate results. That is why today they are rarely build separately, but instead are made as a part of the Inertial Measurement Unit (IMU) that include all these three sensors. IMUs are very precise in determining the movement and orientation.

The main characteristic of the described sensors is that they generate large amount of data. This leads to another challenge: how to use such data. For that purpose, ML methods are becoming more popular. In the text below, we will describe some ML applications on the sensor data for improving the rehabilitation outcome after orthopedic interventions or remote monitoring.

Pereira et al. (2019), for example, use a combination of inertial and surface electromyography (sEMG) sensors to monitor movement and muscular activation. They conducted an experiment in which the patients were performed a set of predefined activities with sensors attached to them. For each activity, the physiotherapist also defined two types of deviations that occur when the activity is not performed correctly. The aim was to predict, based on the collected data, if the patient has performed the activity correctly or not. This is a classification problem in the ML context. The first step authors utilized was feature selection to remove correlated features. After that, the authors used Decision Trees, k-NN, SVM, and Random Forest for classification. The best results were obtained with the k-NN algorithm followed by Decision Tree. Due to faster execution time and minor performance change, the authors suggested Decision Tree as an algorithm for this purpose.

One of the most important physical parameters in rehabilitation that is often monitored is the joint angle (e.g., of hip, knee, etc.). The ability to continuously assess the joint angle, outside the clinic provides better and realistic insight into the performance of the rehabilitation process. Joint angle can be assessed continuously by using wearable IMUs and ML models. Argent et al. (2019) used sensors mounted on eight positions on the body to monitor performance of activities prescribed in rehabilitation after hip or knee surgery. In that way, they aimed to determine if sensor data and ML methods can be used to predict the joint angle equally well as when using standardized techniques. For ML methods, they used Linear Regression, Polynomial Regression, Decision Tree and Random Forest regression. No single algorithm was found the have the best performance, but instead the best algorithm depended on the type of angle which is measured.

One of the fields where it is important to determine the movement angle is also gait assessment. Conte et al. (2021) used deep learning methods for this purpose. The data were obtained from four IMU units mounted on lower extremities (pelvis, foot, lower leg, upper leg). Regarding the sequential and nonlinear characteristics of the kinematic gait signals, authors considered, nonlinear autoregressive network with exogenous inputs, and LSTM networks for black box modeling between the kinematic gait data and the lower body joint angles in the sagittal plane. The evaluation results based on the root mean square error (RMSE) show that LSTM networks deliver superior performance in nonlinear modeling of the lower limb joint angles compared to other approaches.

Bevilacqua et al. (2018) also investigated the correctness of exercises during the rehabilitation following total knee replacement. In this paper, the authors used one IMU unit placed in a neoprene sleeve at the midpoint of the shin, in the midline of the thigh on the anterior aspect. The patient cohort was instructed to repeat the exercise ten times in a correct way and ten times in an incorrect way. The system was set to determine if the exercise was performed correctly based on the readings from the IMU units. There was a total of four types of exercises. This is a classification task and the ML algorithms used were Random Forest, SVM, AdaBoost, and Decision Tree. For two types of exercises the best performance was achieved by SVM, while Random Forest was the best for the other two types.

In the study by LeMoyne et al. (2015) there was described a system for improving ankle rehabilitation. Instead of separate inertial units, the authors used smart phone sensors. Most of the smart phones have various embedded sensors, such as accelerometer or gyroscope. This study used gyroscope data and applied ML to classify between an affected ankle and unaffected ankle hemiplegic pair. They used SVM for classification achieving 97% accuracy.

Another area where wearable devices are becoming increasingly popular are sport injuries. Sport injuries are very frequent, and it is crucial for athletes to recover as soon as possible. Unfortunately, there are not many studies that analyze specifically the rehabilitation and recovery after sport injuries. Most of the research on sport injuries is focused on predicting when the injury will occur and assessing the risk. One of the studies that analyzed the rehabilitation after sport injuries was performed by Xiao and Yuan (2021). The authors attempted to recognize if the top athletes suffered from an injury. Namely, in some less serious injuries it cannot be definitively determined what type of injury has occurred and how it will influence the athlete's capabilities to achieve top results. With that aim, the authors have developed an algorithm that followed the movement and gestures of the athletes and used that data to determine if an injury occurred. The data were collected using wearable sensors. For the data analysis, they did not use traditional ML methods, but instead developed a custom convolutional neural network (CNN). The input for the CNN was the time-frequency graph of the sensor data. At the same time, they performed a conversion of one-dimensional time series collected by the sensor into two-dimensional images. They proposed a new residual module of porous convolutional kernel, which improved the model's ability to extract features at different scales while effectively controlling parameters scale. Based on this module, a sensor-based motion recognition algorithm was developed.

18.3.2 Remote Monitoring

Remote monitoring refers to the collection of physiological data from patients that are not located in a medical facility. These data are collected via digital technologies and sent back to healthcare providers located elsewhere. The devices collecting the data are often wearable devices described in the previous section, so these two fields partially overlap.

The information obtained in this manner is used for monitoring the patient's state, providing health advice, and adapting the patient's care plan. This reduces the number of hospitalizations, readmission rates, as well as the patient's length of stay. Although the application of these technologies alone represents a significant improvement in comparison to traditional methods, additional benefits arise when AI is applied for the analysis of these data. In that case, the decision-making process related to monitoring may be automated.

Remote monitoring in orthopedics is usually employed during rehabilitation, and after the surgery. For example, Ramkumar et al. (2019) monitored the recovery and behavior of patients after total knee arthroplasty. This pilot study followed 25 patients. For the monitoring, the authors used mobile phones with an application installed that was based on open-source software development kit (SDK). The application was developed by a Californian company Focus Ventures. Prior to the operation, the data on steps made by the patients as well as patients questionnaire data were collected. The same data was collected after the operation and additionally the data on knee flexion, medication usage, and on following prescribed exercises. The authors observed that most of the patients positively evaluated the application. These data may be very useful for further ML analysis, but the authors did not provide much detail in that regard.

Hu et al. (2020) examined the limb rehabilitation remote monitoring using a combination of sensors consisting of velocity meter and accelerometer. The task was to determine if the patient has been running or walking slowly. The data were not analyzed directly, but instead first transformed to energy signals, so that activity recognition was done based on energy distribution. The authors used SVM algorithm achieving 100% accuracy.

This result matches the results from (Misic et al. 2018), where the authors demonstrated how the device made possible to make real-time observations on behavior of the patient with fractured tibia in homecare. For the experiment the accelerometer was set up in the same place where the fixator was set after tibia fracture, with the aim of embedding sensors on the orthopedic fixators making them smart fixators. Sensors would enable the monitoring of patient's daily activities (remote monitoring). This way the medical professionals could track if the rehabilitation was going as planned and suggest adjustments as necessary. In this work, ML was used for activity recognition. Following the results by Hu et al. (2020), the authors here also showed that it is possible to distinguish between running and walking using wearable sensors and ML. In addition to walking and running, light running, going up and down the stairs was also analyzed (Misic et al. 2018), but the accuracy of recognizing these activities was lower than recognizing running and walking. For the analysis, the authors used Random Forest, Naive Bayes, and k-NN. Algorithm with the best performance was k-NN, followed by Random Forest and Naive Bayes.

18.3.3 Rehabilitation Follow-Up

One of the elements influencing the success of orthopedic operations is rehabilitation follow-up. The main aim of the follow-up is to enable the medical facility to provide services to patients that were released from the hospital. Traditionally, such services were offered via telephone calls, electronic mail, and follow-up check-ups in the hospital. However, these methods require a lot of medical resources. The rapid progress of AI, as well as telemedicine, enable the computers and mobile devices to replace people in such tasks.

The research has long ago shown that the clear communication between patients and surgeons is important and leads to increased patient satisfaction and improves clinical outcomes (Tongue et al. 2005). However, communication with orthopedic trauma patients remains challenging at times.

On the other hand, the mobile phone usage is drastically increased in the last decade. Today almost every adult owns a mobile phone, so there is a great potential of using the phones for rehabilitation follow-up. The first studies in this field considered the use of text messages over the phone. For that purpose, automated mobile phone messaging robots ("chat bots") where used. A chat bot is a computer program that simulates human conversation through voice commands text chats or both. Chat bot, short for chatterbot, is an AI feature that can be embedded and used through any major messaging application.

Chat bots are also used in orthopedics. One of the first applications was for automatic text message exchange with the patients (Anthony et al. 2018). In that paper, the authors proposed an automatic text messaging platform for recovery monitoring that might replace existing approaches to data collection, such as questionnaires, phone calls, or home journals. The study followed if the patients felt pain after the operation, and how much medications they used. The patients were receiving text messaging three times a day inquiring about the pain level they were feeling, and once a day they were asked about the number of pain medications they had taken.

This study showed that a high percentage of patients accepted this type of communication and remained in contact with the hospital (88%), which is an increase in comparison to traditional types of communication.

Bian et al. (2020) went one step further in the application of chat bot technologies. The AI-assisted follow-up system obtained baseline information for each discharged patient including the ID number, gender, age, discharge date, diagnosis, telephone number, and caller location. The system called patients via automated speech telephony delivered in batches from 8:30 AM to 8:30 PM every day allowing hundreds of calls to be made daily. Interactions between the system and patients were based on ML, speech recognition, spoken language understanding, and human voice simulation technology. Communication contents included patient satisfaction in the hospital environment, nursing, and health education; wound recovery; functional training; postoperative complications; and other surgery-related medical consulting. The system was able to identify dialects in different parts of China via speech recognition technology and voice information was converted into text in Real-Time. A report was generated and automatically uploaded to the cloud afterwards. Surgeons and nurses could review the report and respond to patient feedback, if necessary.

The study also compared manual and automated follow-up. The results showed that it took around 9 h for a medical professional to talk to 100 patients. The automated system performed the same in 87 s without any human participation. The authors concluded that these systems were promising and could be used to replace traditional ways of communication.

18.3.3.1 Rehabilitation Assessment

Medical image analysis is the most reliable way to assess the progress and success of the rehabilitation. In the medicine, different types of imaging techniques are used to diagnose diseases. These imaging techniques include projection imaging (e.g., x-ray), computed tomography (CT), ultrasound, magnetic resonance imaging (MRI), and other techniques. In orthopedics, image analysis represents the best way to determine if a defect occurred and what type of defect occurred.

Image analysis is one of the fields with the most significant improvements in terms of AI applications in recent years. Although many different ML algorithms may be used for image analysis, the largest difference was made by the intensive application of deep learning methods.

Recent applications of deep learning in medical image analysis involve various computer vision-related tasks such as image classification, object detection and segmentation, and registration. Among them, classification, detection, and segmentation are fundamental and the most widely used tasks (Liu et al. 2021).

Image classification is one of the main tasks in computer vision. In medical science, this translates to classification between images coming from patients with a certain disease and healthy individuals. This is not always a binary classification (e.g., diseased versus healthy), but can also be a multi-class classification (e.g., multiple diseases or multiple stages of the disease).

Another application area is object detection in medical images. Within that application, there are two tasks: identification and localization. Identification task refers to finding if an object of a certain class exists in the region of interest, while localization means determining the exact position of that object in the image.

Image segmentation in medical image analysis is used to determine the organ contours or the anatomic structure in the image.

For image analysis, the most frequently used method is the Convolutional Neural Network. There are many different CNN architectures tailored to specific tasks (classification, object detection, and segmentation) (Liu et al. 2021). For example, for image classification, used neural networks include VGGNet (Simonyan and Zisserman 2014), ResNet (He et al. 2016), and DenseNet (Huang et al. 2017). For object detection, CNN architectures such as Faster-RCNN (Ren et al. 2017) and Mask-RCNN (He et al. 2017), as well as newer CornerNet (Law 2018). Architectures like FCNN (Long et al. 2014) and its implementation U-Net (Ronneberger et al. 2015) are some of the architectures used in image segmentation.

Image analysis is currently very popular, but the main question regarding its application in medicine is if this automated analysis can lead to equally good or better results compared to medical professionals who traditionally perform that task. There are several studies comparing the performance of algorithms to the performance of medical doctors and they show that algorithms can compete with the doctors and in some cases perform even better (Groot et al. 2020; Liu et al. 2019). One of the challenges is that deep learning methods require a lot of data to perform well, so it is necessary to provide a sufficient amount of data for training these methods.

In orthopedics, image analysis is often used in diagnostics, but may also be used during post-surgery rehabilitation. The optimal approach to determine the success of the surgery and follow the recovery is to make a new image.

For example, Borjali et al. (2020) used CNN for detecting mechanical loosening of total hip replacement implants. One of the challenges of applying deep learning is the lack of interpretability of the methods: it is not clear how the method reached its prediction. The authors of this study focused on this issue and proposed two different methods to visualize two main levels of CNN: (1) the CNN classification level and (2) the CNN feature detection level. For the first level, they suggest the use of image-specific saliency maps, and for the second activation maximization. These techniques enable a better understanding of the CNN function and shed light on its decision-making process to build more trust in the method.

Another example of AI application for image analysis after surgery is described by Kang et al. (2019). The authors there analyzed the possibility of automatic recognition of hip arthroplasty designs. In hip surgeries, it is often necessary to replace the implant after a certain number of years. For that purpose, the surgeons need to know what the previous implant was, so that they may successfully plan the interventions. On the other hand, the information on the type of implant that was used previously is often unavailable. In those cases, it is common to attempt to interpret the X-ray image, since stem type, taper size, and design differences among appliance companies are very important for selecting a surgical option. The authors used Yolov3 algorithms for recognition (Redmon and Farhadi 2018) achieving promising results. They stated that their workflow has 99% accuracy in identifying the used implant.

18.4 Discussion

When considering the success of the works in this overview and some specific methodological choices, there are two different aspects that are extremely relevant for the success of research in automated prediction and decision making in orthopedic rehabilitation and remote monitoring. Those aspects are of general nature and they span all domains of ML applications: data and algorithms that are trained with that data.

18.4.1 Data

One of the important issues for the successful ML-driven prediction is completeness and representativeness of data, namely its quality in context of the prediction model they are used to train. Many applications rely exclusively (Verma et al. 2021; Huber et al. 2019; Fontana et al. 2019; Polce et al. 2020) or partially (Tschuggnall et al. 2021; Harris et al. 2019) on the subjective data collected by using questionnaires. Lots of quality reduction risks are involved in such approaches, from the subjective bias of the respondents to the lack of coverage among the selected target groups (including age groups, genders, races, health risks, etc.). Similar remark also stands for clinical data, acquired from the Electronic Health Record. Besides measured features (for example, blood analyses), clinical data includes data that is assessed by the clinicians, typically only one per assessment. The risk of inaccurate data in the above case is also relatively high. Third type of data are Real-Time data streams incoming from the sensors (for example, wearables). There are several challenges that need to be dealt with when data streaming is considered. First, integration of these data is sometimes an issue, due to lack of standardization in the domain (Smuck et al. 2021). Second, data streams generate extremely large amount of data that cannot be effectively and efficiently processed as a whole. That means that some feature engineering or dimensionality reduction approaches are required to identify the most relevant features of those data streams for the purpose they are intended to. This is demonstrated by Misic et al. (2018) in the feature engineering of the data stream incoming from the IMU sensor, in attempt to classify human activity based on its readings.

Feature engineering is one of the most important steps in ML method implementation pipeline. It is especially valuable in reducing the dimensionality, while effectively ensuring proper representation of extremely large datasets, such as those made of images. In the latter cases, Convolutional Neural Network architectures are used as they integrate the feature engineering and classification steps. This approach was successfully demonstrated in the work of Xiao and Yuan (2021) who developed the CNN-based model that followed the movement and gestures of the athletes and used that data to determine if an injury occurred, based on time-frequency graph images of sensor data.

As it was previously stressed out (Huber et al. 2019), another important factor for the data quality is its balance, in terms of different predicted categories (in case of, for example, disease classification problems). Data stratification is important step in the preparation of the dataset for training the models.

18.4.2 Algorithms

Another factor of success for the effective prediction model is the choice of the appropriate algorithm and its configuration. The overview of application of ML methods in rehabilitation and remote monitoring in orthopedics shows different classes of data used for addressing different problems.

In several cases, patient survey data is used to train models. This data is mostly of categorical type. When considering the traditional algorithms, Decision Tree-based algorithms (or ensemble algorithms based on the Decision Trees) achieve the best success in prediction, especially in case of predominantly categorical data (Verma et al. 2021; Tschuggnall et al. 2021; Huber et al. 2019). However, one must be careful in interpretation of metrics from those experiments as it must also include the assessment of actual data coverage. Namely, Decision Tree-based algorithms tend to overfit—instead of generalizing it, they adapt to work the best on the actual data and typically fail when new unseen data is introduced. When data is sparse (for example, one-hot encoded categorical data), it is very likely that SVM will demonstrate very good performance in the experiments (Polce et al. 2020).

While traditional methods are sufficient in case of limited data availability (which is most often the case when data is collected by using patient questionnaires), as the volume of data grows, the typical metrics of traditional methods plateaus at some point. Even with additional data collection, after that point, the performance of traditional algorithms is not improving. This is when Deep Learning models and architectures are deployed.

Wearables and remote monitoring in general are typical cases in which the collection of huge amounts of data is possible. This data is streamed 24 h, data collection effort is minimal if not none. This data is sequential or so-called time series—order of incoming data matters for its interpretation. In some cases, the ordered data dependency is short-termed, such as the example of interpretation of IMU signals for classification of human activity in rehabilitation (Misic et al. 2018). As it is shown in the referenced paper, in those cases, effective feature engineering practice will help reducing the problem (without any loss) from time-series to conventional classification with kept potential to use conventional ML algorithms. However, sometimes, the ordered data dependency is long-termed, as it is the case in modeling dependency between the kinematic gait data and the lower body joint angles in the sagittal plane

(Conte et al. 2021). In such cases, complex autoregressive networks, such as LSTM architectures show superior performance.

18.5 Conclusion

This paper presents the overview of applications of Machine Learning methods and approaches in orthopedics for patient rehabilitation, remote monitoring and rehabilitation follow-up. Today, ML is considered as mature technology for automatization in many different domains. As it is shown in this paper, there exists quite a large number of works in the area of rehabilitation and recovery in orthopedics, demonstrating the effectiveness and efficiency of ML in actual medical practice. Those works are classified in the categories of rehabilitation (predicting rehabilitation success, wearable sensors for rehabilitation), remote monitoring and rehabilitation follow-up (rehabilitation assessment).

There are sufficient body of evidence showing that Machine Learning and especially Deep Learning architectures have matured to facilitate automated or at least assisted decision making in the clinical practice and specifically—in remote monitoring and assistance in orthopedic rehabilitation. In some cases, the results of the experiments clearly demonstrate that the accuracy of trained prediction models exceeds the accuracy of clinicians.

However, two possible problems of quite different nature still prevent steeper trend in implementing AI solutions in clinical practice.

First problem is related to difficulties to achieve training and testing data quality and diversity, at the rate which will guarantee the complete, non-biased and representative prediction models. The sources of this problem are risk of endangering the data privacy (despite many different anonymization approaches) and lack of integration of Electronic Health Records.

Second issue lays in undefined liability and responsibility for errors in the rehabilitation process, when automated or assisted decision making is used. We believe that the solution of this problem can be found in the application of Explainable AI (XAI) methods and approaches. XAI can help to infer the set of arguments that made one algorithm making the specific decision or suggesting it to the clinician.

References

Altman NS (1992) An introduction to Kernel and nearest-neighbor nonparametric regression. Am Stat 46:175–185. https://doi.org/10.1080/00031305.1992.10475879

Anthony CA, Volkmar A, Shah AS et al (2018) Communication with orthopedic trauma patients via an automated mobile phone messaging robot. Telemed J E Health 24:504–509. https://doi.org/10.1089/tmj.2017.0188

Argent R, Drummond S, Remus A et al. (2019) Evaluating the use of machine learning in the assessment of joint angle using a single inertial sensor. J Rehabil Assistive Technol Eng 6. https://doi.org/10.1177/2055668319868544
Bevilacqua A, Huang B, Argent R et al (2018) Automatic classification of knee rehabilitation exercises using a single inertial sensor: a case study. IEEE 15th international conference on wearable and implantable body sensor networks (BSN). https://doi.org/10.1109/BSN.2018.8329649
Bian Y, Xiang Y, Tong B et al (2020) Artificial intelligence—assisted system in postoperative follow-up of orthopedic patients: exploratory quantitative and qualitative study. J Med Internet Res 22:e16896. https://doi.org/10.2196/16896
Borjali A, Chen AF, Muratoglu OK et al (2020) Deep learning in orthopedics: how do we build trust in the machine? Healthc Transform. https://doi.org/10.1089/heat.2019.0006
Breiman L (1997) Arcing the edge. Technical report 486. Statistics Department, University of California, Berkeley
Cabitza F, Locoro A, Banfi G (2018) Machine learning in orthopedics: a literature review. Front Bioeng Biotechnol 6:75. https://doi.org/10.3389/fbioe.2018.00075
Conte A, Moghaddamnia S, Peissig J (2021) Efficiency of deep neural networks for joint angle modeling in digital gait assessment. EURASIP J Adv Sig Process 10. https://doi.org/10.1186/s13634-020-00715-1
Cortes C, Vladimir V (1995) Support-vector networks. Mach Learn 20:273–297. https://doi.org/10.1007/BF00994018
Fontana MA, Lyman S, Sarker GK et al (2019) Can machine learning algorithms predict which patients will achieve minimally clinically important differences from total joint arthroplasty? Clin Orthop Relat Res 477:1267–1279
Gilpin LH, Bau D, Yuan BZ et al (2018) Explaining explanations: an overview of interpretability of machine learning. In: IEEE 5th international conference on data science and advanced analytics (DSAA), pp 80–89. https://doi.org/10.1109/DSAA.2018.00018
Groot OQ, Bongers MER, Ogink PT et al (2020) Does artificial intelligence outperform natural intelligence in interpreting musculoskeletal radiological studies? a systematic review. Clin Orthop Relat Res 478:2751–2764. https://doi.org/10.1097/CORR.0000000000001360
Harris AH, Kuo AC, Weng Y et al (2019) Can machine learning methods produce accurate and easy-to-use prediction models of 30-day complications and mortality after knee or hip arthroplasty? Clin Orthop Relat Res 477:452–460. https://doi.org/10.1097/CORR.0000000000000601
He K, Zhang X, Ren S et al (2016) Deep residual learning for image recognition. In: 2016 IEEE conference on computer vision and pattern recognition (CVPR), pp 770–778. https://doi.org/10.1109/CVPR.2016.90
He K, Gkioxari G, Dollar P et al (2017) Mask R-CNN. In: proceedings of the IEEE international conference on computer vision (ICCV), 2980–2988. https://doi.org/10.1109/ICCV.2017.322
Ho TK (1995) Random decision forests. In: Proceedings of 3rd international conference on document analysis and recognition. IEEE Comput. Soc. Press. Montreal, Que., Canada, pp 278–282. https://doi.org/10.1109/ICDAR.1995.598994
Hochreiter S, Schmidhuber J (1997) Long short-term memory. Neural Comput 9:1735–1780. https://doi.org/10.1162/neco.1997.9.8.1735
Hu W, Zhang J, Huang B et al (2020) Design of remote monitoring system for limb rehabilitation training based on action recognition. J Phys Conf Ser 1550:32067. https://doi.org/10.1088/1742-6596/1550/3/032067
Huang H, Liu Y, Van Der Maaten L et al (2017) Densely connected convolutional networks. In: 2017 IEEE conference on computer vision and pattern recognition (CVPR). Honolulu, HI, USA. https://doi.org/10.1109/CVPR.2017.243
Huber M, Kurz C, Leidl R (2019) Predicting patient-reported outcomes following hip and knee replacement surgery using supervised machine learning. BMC Med Inf Decis Making 19. https://doi.org/10.1186/s12911-018-0731-6

Jayakumar P, Moore MLG, Bozic KJ (2019) Value-based healthcare: can artificial intelligence provide value in orthopaedic surgery? Clin Orthop Relat Res 477:1777–1780. https://doi.org/10.1097/CORR.0000000000000873

Kang Y, Yoo J, Cha YH et al (2019) Machine learning–based identification of hip arthroplasty designs. J Orthop Translat 21:13–17. https://doi.org/10.1016/j.jot.2019.11.004

Law H (2018) CornerNet: detecting objects as paired keypoints. In: Ferrari V, Hebert M, Sminchisescu C, Weiss Y (eds) Computer vision—ECCV 2018. Lecture notes in computer science, vol 11218. Springer, Cham, pp 765–781

LeCun Y, Bengio Y (1998) Convolutional networks for images, speech, and time series. In: The handbook of brain theory and neural networks, pp 255–58. https://doi.org/10.5555/303568.303704

LeMoyne R, Mastroianni T, Hessel A et al (2015) Ankle rehabilitation system with feedback from a smartphone wireless gyroscope platform and machine learning classification. In: IEEE 14th international conference on machine learning and applications (ICMLA), pp 406–409. https://doi.org/10.1109/ICMLA.2015.213

Liu X, Faes L, Kale AU, Wagner SK et al (2019) A comparison of deep learning performance against health-care professionals in detecting diseases from medical imaging: a systematic review and meta-analysis. Lancet Digit Health 1:e271–e297. https://doi.org/10.1016/S2589-7500(19)30123-2

Liu X, Gao K, Liu B et al (2021) Advances in deep learning-based medical image analysis. Health Data Science. https://doi.org/10.34133/2021/8786793

Long J, Shelhamer E, Darrell T (2014) Fully convolutional networks for semantic segmentation. IEEE Trans Pattern Anal Mach Intel 39:640–651. https://doi.org/10.1109/CVPR.2015.7298965

Lundberg SM, Lee S (2017) A unified approach to interpreting model predictions. In: Guyon I, Luxburg UV, Bengio S, Wallach H, Fergus R, Vishwanathan S, Garnett R (eds) Advances in neural information processing systems. Curran Associates Inc., 30, pp 4765–4774

MacQueen J (1967) Some methods for classification and analysis of multivariate observations. In: Proceedings of the fifth berkeley symposium on mathematical statistics and probability, pp 281–297

Misic D, Zdravkovic M, Mitkovic M et al (2018) Real-time monitoring of bone fracture recovery by using aware, sensing, smart, and active orthopedic devices. IEEE Internet Things J 5:4466–4473. https://doi.org/10.1109/JIOT.2018.2819623

Mitchell T (1997) Machine learning. McGraw-Hill series in computer science. McGraw-Hill, New York

Murali, Poduval A, Ghose S, Manchanda V, Bagaria A, Sinha (2020) Artificial Intelligence and Machine Learning: A New Disruptive Force in Orthopaedics. Indian Journal of Orthopaedics 54(2):109–122. https://doi.org/10.1007/s43465-019-00023-3

Myers TG, Ramkumar PN, Ricciardi BF et al (2020) Artificial intelligence and orthopaedics: an introduction for clinicians. J Bone Joint Surg 102:830–840. https://doi.org/10.2106/JBJS.19.01128

Opitz D, Maclin R (1999) Popular ensemble methods: an empirical study. J Artif Intell Res 11:169–198. https://doi.org/10.1613/jair.614

Pereira A, Folgado D, Nunes F et al (2019) Using inertial sensors to evaluate exercise correctness in electromyography-based home rehabilitation systems. In: 2019 IEEE international symposium on medical measurements and applications (MeMeA). https://doi.org/10.1109/MeMeA.2019.8802152

Polce EM, Kunze KN, Fu M et al (2020) Development of supervised machine learning algorithms for prediction of satisfaction at two years following total shoulder arthroplasty. J Shoulder Elb Surg 30:e290–e299

Porciuncula F, Roto AV, Kumar D et al (2018) Wearable movement sensors for rehabilitation: a focused review of technological and clinical advances. PMR 10:S220–S232. https://doi.org/10.1016/j.pmrj.2018.06.013

Ramkumar PN, Haeberle HS, Ramanathan D et al (2019) Remote patient monitoring using mobile health for total knee arthroplasty: validation of a wearable and machine learning-based surveillance platform. J Arthroplasty 34(10):2253–2259. https://doi.org/10.1016/j.arth.2019.05.021

Redmon J, Farhadi A (2018) YOLOv3: An incremental improvement. Tech Report, https://doi.org/10.48550/arXiv.1804.02767

Ren S, He K, Girshick R et al (2017) Faster R-CNN: towards Real-Time object detection with region proposal networks. IEEE Trans Pattern Anal Mach Intell 39:1137–1149. https://doi.org/10.1109/TPAMI.2016.2577031

Ribeiro MT, Singh S, Guestrin C (2016) Model-Agnostic Interpretability of Machine Learning. ICML Workshop on Human Interpretability in Machine Learning, 91–95. https://doi.org/10.48550/arXiv.1606.05386

Ronneberger O, Fischer P, Brox T (2015) U-Net: convolutional networks for biomedical image segmentation. In: Navab N, Hornegger J, Wells W, Frangi A (eds) Medical image computing and computer-assisted intervention—MICCAI 2015. Lecture notes in computer science, vol 9351 Springer, Cham

Rumelhart DE, McClelland J (1987) Learning internal representations by error propagation. In: Parallel distributed processing: explorations in the microstructure of cognition: foundations. MIT Press, pp 318–362

Simonyan K, Zisserman A (2014) Very deep convolutional networks for large-scale image recognition. In: Computer, international conference on learning representations, San Diego, CA, USA

Smuck M, Odonkor CA, Wilt JK et al (2021) The emerging clinical role of wearables: factors for successful implementation in healthcare. NPJ Digit Med 4. https://doi.org/10.1038/s41746-021-00418-3

Tongue JR, Epps HR, Forese LL (2005) Communication skills for patient-centered care: research-based, easily learned techniques for medical interviews that benefit orthopaedic surgeons and their patients. J Bone Joint Surg Am 87:652–658. https://doi.org/10.2106/00004623-200503000-00027

Tschuggnall M, Grote V, Pirchl M et al. (2021) Machine learning approaches to predict rehabilitation success based on clinical and patient-reported outcome measures. Inform Med Unlocked 24. https://doi.org/10.1016/j.imu.2021.100598

Van Eetvelde H, Mendonça LD, Ley C et al (2021) Machine learning methods in sport injury prediction and prevention: a systematic review. J Exp Orthop 8:27. https://doi.org/10.1186/s40634-021-00346-x

Vaswani A, Shazeer N, Parmar N et al (2017) Attention is all you need. In: NIPS'17: proceedings of the 31st international conference on neural information processing systems, Curran Associates Inc., USA, pp 6000–6010

Verma D, Bach K, Mork PJ (2021) Application of machine learning methods on patient reported outcome measurements for predicting outcomes: a literature review. Informatics 8:56. https://doi.org/10.3390/informatics8030056

WHO (2011) World report on disability. World Health Organization. https://www.who.int/teams/noncommunicable-diseases/sensory-functions-disability-and-rehabilitation/world-report-on-disability. Accessed 10 Oct 2021

Xiao C, Yuan GL (2021) Sports injury rehabilitation intervention algorithm based on visual analysis technology. Mob Inf Syst 2021:9993677:1–9993677:8. https://doi.org/10.1155/2021/9993677

Youden WJ (1950) Index for rating diagnostic tests. Cancer 3:32–35

Zhu M, Chen W, Hirdes JP, Stolee P (2007) The K-nearest neighbor algorithm predicted rehabilitation potential better than current Clinical Assessment Protocol. J Clin Epidemiol 60:1015–1021. https://doi.org/10.1016/j.jclinepi.2007.06.001

Zimek A, Schubert E (2017) Outlier detection. In: Liu L, Özsu MT (eds) Encyclopedia of database systems. Springer, New York, pp 1–5. https://doi.org/10.1007/978-1-4899-7993-3_80719-1